Gold Nanoparticle-mediated enhancement of radiotherapy responses in 2D and 3D models

Cristiana Ferreira de Matos

A thesis submitted in partial fulfilment of the requirements of Sheffield Hallam University for the degree of Doctor of Philosophy

October 2024

CANDIDATE DECLARATION

I hereby declare that:

- I have not been enrolled for another award of the University, or other academic or professional organisation, whilst undertaking my research degree.
- None of the material contained in the thesis has been used in any other submission for an academic award.
- I am aware of and understand the University's policy on plagiarism and certify that this thesis is my own work. The use of all published or other sources of material consulted have been properly and fully acknowledged. The TEM and Hyperspectral Microscopy data presented in this thesis was obtained in experiments carried out by Dr Francis Sweeney (SHU) and Dr Christopher (UoS), and Dr Niall Byrne and his team (QUB), respectively. I played a major role in the preparation of the experiment, and the data analysis and interpretation are entirely my own work. Any contributions from colleagues in the collaboration are explicitly referenced in the text.
- The work undertaken towards the thesis has been conducted in accordance with the SHU Principles of Integrity in Research and the SHU Research Ethics Policy.
- The word count of the thesis is 62 401.

Name	Cristiana Ferreira de Matos
Award	PhD
Date of Submission	4th October 2024
Research Institute	Biomolecular Sciences Research Centre
Director of Studies	Dr Neil Cross

ACKNOWLEDGEMENTS

Firstly, I would like to thank my supervisory team and the DTA for accepting me into the DTA3/COFUND Marie Skłodowska-Curie PhD Fellowship Programme and for giving me the opportunity to work on this project. This was, without a shadow of a doubt, the most challenging thing I have ever done and probably will ever do. I am extremely proud of myself for making it here and for not giving up, so yay me! But it wasn't just me. There are many people who made this possible, and to whom I am forever grateful.

To Dr Neil Cross, I could not have asked for a better Director of Studies. I genuinely believe you are one of the most brilliant minds in our field and to have had the pleasure of working alongside you was an honour and a privilege. You have always steered me in the right direction, supported my crazy ideas, and motivated me to carry on when times were tough. But the thing I most grateful for is your untiring support, for listening to my rants without judgement, and for always making sure I was ok. More importantly, for reassuring me that it was ok to not be ok. I will never be able to thank you enough. You are an inspiration. To Dr Neil Bricklebank, for being my chemistry guide – God knows I needed one – and for making everything sound simple. For the support, for always checking on me, for the motivation, thank you. To Dr Rebecca Leyland, who unfortunately did not make it to the end, but was there when it mattered. Thank you for all the support and motivation, for all our chats and for never letting me quit.

To every single person that crossed my path in the BMRC and the University of Sheffield, students and staff. To Dr Catherine Duckett, thank you for all your help with the mass-spec work, and to Dr Sue Campbell for being the most dedicated PGRT we could have asked for. To Celine, you were the light all of us needed and you showed up at the exact right time. Thank you for everything. And Svetlana, at UoS, for always being so accommodating every time I visited your facilities. Without you, there would be nothing to write about. I would also like to extend my gratitude to Dr Francis Sweeney, Libby Allcock, and Tiffany Tran (SHU), Dr Christopher Hill (UoS), and Drs Jonathan Coulter and Niall Byrne (QUB) for their contributions to this thesis.

(Now is the bit I'm going to struggle to write without drowning in my own tears. It's going to be long so feel free to skip, sorry not sorry.)

To my BMRC war companions, especially those who started with me, you have made these years worthwhile, and for that I am forever thankful. A special shout-out to Alex, for everything, and Muna, (for everything as well, of course) especially for these last few months. You have been a rock, thank you for tirelessly listening to me, we've made it! To those who have since left but were there when it all began, thank you for all the moments we shared. Katie, in particular, you quickly became a sister to me, and I will be forever grateful to have met you.

To my Portuguese crew, my Luso waste, my family away from home. I am the luckiest to be able to call you my friends. For always being here, for never giving up on me, for every drunken night, every hungover day, every cheeky Wednesday pint and every Sunday coffee, thank you. Nelma, you have been an inspiration since we first met in 2018, in Walkabout of all places. I am so incredibly thankful for every conversation, every word of advice, and for being there for me

from the smallest insignificant things to the major milestones. Filipe, for being the laugh we always need, the life of the party, the Patricia we all know and love. But also, for being a shoulder to cry on, a rock and true friend. For always showing up, no matter when or where. Madalena, for every time you held my hand when I wanted to give up. For being a source of unconditional support and for showing me no matter how bad things get, at the end of the day we will always have each other. I love you all so much, and I can't imagine my life without you. Thank you.

To my barbie girls, Lucy, Meg and Ameera. You have been the light of my life for the past two years. Thank you for the motivation, for lifting me off the ground when I needed it the most, for showing me I am much more than the bad things that happen. Meg and Lucy, thank you for opening your door to me when I was at my lowest. You have become true sisters and fundamental pillars in my life. Thank you for the girls' nights, in or out, and for the never-ending TikTok chains that never fail to make laugh. For everything you continue to do, I look forward to our next reunion and margarita tally. I love you so much, I am so lucky you adopted me into your little family.

To the friends I left back home, thank you for never making me feel left out. To Serrinha, Catalin and Renato, thank you for our yearly power ranger reunions. No matter when I go to Portugal, how long I stay or where I go, you always make time to come see me and that means the world to me. To Harrison, my clowning buddy, I appreciate you more than words can say. Thanks for fighting dragons with me. To Margarida, Majó, Madalena, and Gonçalo, thank you for always being one call away, for keeping our group chat alive and always making me smile. I miss you every day. To Maria and Raquel, I will never have the words to express how lucky I feel to have you in my life, how much you mean to me, and how much it hurts to be away from you. Thank you for always being here, I love you and miss you so much.

To my Biquinha (yes, I am thanking my cat) for being my emotional support fur baby, for all the cuddles and purrs. You will never know, mainly because you can't read, how much you've helped me get here. To Killick, who was there since the start and has been a source of support for years. Thank you especially for the past few months, for making my life easier so I'd have time to write. For listening to me vent, for holding me while I cried, for making me laugh and for cooking me pasta. It took us a while, but we got there in the end. I love you.

To my family, for their unconditional support. To my grandmother, for the constant messages, for all the prayers and candles. For always having time to see me when I come home and for always being with me, even when you're not. I love you nan. To my parents, for being with me at all times. For everything you did for me so I could be here today. For all the sacrifices, for giving me everything, for the love I never lacked, for being examples of effort and dedication, and for being my safe haven. I am who I am thanks to you, and I am where I am because you have always supported me. Dad, we both know how difficult it was not being together all the time, but despite the distance you were never absent. Thank you for always being the source of optimism that pulls me up and for always being up for everything. For always knowing what and when to say it. Mum, for having been a mother and a father for years, you are the biggest reason I am here today (even if I couldn't always see it). For being the best advisor and my best friend, and for being the hug that brings the most comfort. Mããããeeeee, you are the person I admire most in the world and I hope one day I can be a third of the

woman you are. Dear Mum and Dad, words will never be enough to thank you and it will never be possible to express how much I love you. I miss you every day. You can't choose your family, but I would always choose you.

À minha familia, pelo apoio inconcional. À minha avó, pelas constantes mensagens, por todas as rezas e velinhas. Por teres sempre tempo para me ver quando vou a casa e por estares sempre comigo, mesmo quando não estás. Amo-te avozinha. Aos meus pais, por estarem comigo em todos os momentos. Por tudo o que fizeram por mim para que eu podesse estar aqui hoje. Por todos os sacrificios, por me darem tudo, pelo amor nunca faltou, por serem exemplos de esforço e dedicação, e por serem o meu porto de abrigo. Sou o que sou graças a vocês e estou onde estou porque sempre me apoiaram. Papá, ambos sabemos o quão dificil foi não podermos ter-te sempre por perto, mas embora a distancia nunca te senti ausente. Obrigada por seres sempre a fonte de otimismo que me puxa para cima e por alinhares sempre comigo em tudo. Por saberes sempre o que e quando o dizer. Mamã, por teres sido mãe e pai durante anos, és a maior razao de estar aqui hoje (ainda que nem sempre o conseguisse ver). Por seres a melhor conselheira e a minha melhor amiga, e por seres o abraço que mais traz conforto. Mããããeeeee, és a pessoa que mais admiro no mundo e espero um dia conseguir ser um terço da mulher que és. Papás, palavras nunca vão ser suficientes para vos agradecer e nunca será possível exprimir o quanto vos amo. Tenho saudades vossas todos os dias. A família não se escolhe, mas eu escolher-vos-ia sempre.

And finally, to my grandad and godmother. I miss you every day and I will always love you. You're the reason this research exists, and this thesis is for you.

COVID-19 IMPACT STATEMENT

In March of 2020 Sheffield Hallam University and the BMRC were forced to close their doors due to the Covid-19 pandemic. For seven months we had no access to laboratory facilities, meaning this project was put on hold, and no data collection took place in that time.

Upon return, in September of the same year, social distancing measures were put in place: a three-day rota was created, meaning students were only allowed in the labs 3 days a week, for a maximum of 8h. Moreover, due to the dimensions of our cell culture facilities, the access to this lab was restricted to 3h/day. With this project being cell-culture based in almost its entirety, I saw my average laboratory working hours being cut from ≈30 to 9h/week, which deeply impacted the progress of this study. Most of cell-model set up and preparation would require more than the time allotted, meaning I had to split my workload into smaller, achievable tasks, which significantly delayed every deadline we had initially planned, consequently impairing the progress of this study. It also impeded all assays we had planned that required multiple time points, which dramatically reduced the number of techniques we could employ in this research. This socially distanced way of working and the restrictions associated lasted another 9 months, with laboratories only being fully operational in June 2021.

Furthermore, all the irradiation experiments performed in this study were done in the University of Sheffield, which also had Covid-19 related restrictions. For weeks I was unable to access the irradiation facilities, as this was limited to UoS students. These additional restrictions further delayed the collection of data.

Even though all PhD students impacted by the pandemic-related restrictions received a deadline extension of 6 months, this was not enough considering how much time was effectively lost – 6 full months of full closured combined with another 9 of limited access and restricted work.

OUTPUTS OF THIS THESIS

Manuscripts in preparation:

- De-Matos, C. Bricklebank, N. Cross, N. Differences in response to radiation exposure between 2D and 3D cell culture models.
- De-Matos, C. Bricklebank, N. Cross, N. Gold nanoparticle radiosensitisation of 2D and 3D cancer cell models.
- De-Matos, C. Bricklebank, N. Cross, N. TPP-Functionalised gold nanoparticle-mediated radiosensitisation of 2D and 3D cancer cell models.

Poster Presentations:

- **Sheffield Hallam University (SHU).** Winter Poster Event. Sheffield, England.
    - December 2019. Presentation title: Nanoparticle Mediated Enhancement of Radiotherapy Responses in 3D Cell Culture.
    - December 2021. Presentation title: Comparing Radiosensitivity between 2D and 3D cell line models.
- **European Association of Cancer Research (EACR):** 1st-3rd November 2022. Presentation title: Radiosensitivity of cells grown in 2D cell culture vs 3D cell culture models. Cellular Bases for Patient Response to Conventional Cancer Therapies. Berlin, Germany.
- **British Association of Cancer Research (BACR) and American Association of Radiation (ARR):** 4th-6th June 2023. Presentation Title: Gold nanoparticle-mediated enhancement of radiation responses in 2d and 3d cell culture. Radiation Research Conference 2023. Glasgow, Scotland.
- **British Association of Cancer Research (BACR) and Cancer Research UK (CRUK):** 22nd-23rd June 2023. Presentation title: Gold nanoparticle-mediated enhancement of radiation responses in 2d and 3d cell culture. Trailblazers in Cancer Research, The Next Generation. Manchester, England.

Oral Presentations:

- **Sheffield Radiotherapy Research Network:** 26th May 2023. Presentation title: Gold nanoparticle-mediated enhancement of radiation responses in 2d and 3d cell culture. Sheffield Teaching Hospitals, Sheffield, England.

ABSTRACT

Radiotherapy is commonly used as a treatment in over 50% of cancer patients, where radiation is used to kill cancer cells by inducing DNA damage. However, it presents many disadvantages which can be minimised through the use of radiosensitisers, such as gold nanoparticles. Since 3D cultures better mimic *in vivo* conditions such as tumour resistance, it is important to investigate the responses of these models to radiation treatment as well as develop methods to investigate gold nanoparticle uptake and distribution within them.

In this study I used cell lines representative of epithelial and mesenchymal tumours and developed the methods to assess the radio-sensitising potential of uncoated (AuNP), nuclear-targeted (NLS-AuNP) and mitochondrial-target gold nanoparticles, in both 2D and 3D cell culture models. Cell models were incubated with AuNPs and irradiated with doses ranging from 1.25 to 20 Gy of γ-radiation using a Caesium-137 source. Our results show that both uncoated and mitochondrial-targeted nanoparticles were successfully internalised by cells and produced a significant radiosensitising effect in monolayer cultures, translated by a decrease in colony formation, disruption of the cell cycle and increased number of γ-H2AX foci. Whilst 3D models are significantly more resistant, both nanoparticles successfully produced acute sensitisation, with levels of cell death increasing 24h post-treatment. While prolonged effects were not observed, this acute effect could potentially be enhanced by fractioned dosing, inhibiting damage repair and proliferation. Whilst cellular uptake was not observed for NLS-AuNPs, these nanoparticles still produced an increase in radiation-induced DNA damage and a reduction in the acute viability of osteosarcoma spheroids, which could offer new strategies for treatment of these inherently radio-resistant tumours.

CONTENTS

ABBREVIATIONS

•OH - Hydroxyl Radical

^{137}Cs - Caesium-137

3D-CRT - 3D Conformational Radiotherapy

ATP - Adenosine Triphosphate

AuNP - Gold Nanoparticle

BSA - Bovine Serum Albumin

$CaCl_2$ – Calcium Chloride

CAS - Cellular Apoptosis Susceptibility Protein

CDK - Cyclin-Dependent Kinase

CKI - Cyclin-Dependent Kinase Inhibitors

CPRC - Castration-Resistant Prostate Cancer

CSC - Cancer Stem Cell

CT - Computed Tomography

DCM - Dichloromethane

DDR - DNA Damage Response

DMEM - Dulbecco's Modified Eagle Medium

DNA - Deoxyribonucleic Acid

DSB - Double Strand Break

EBRT - External Beam Radiotherapy

ECM - Extracellular Matrix

EGFR - Epidermal Growth Factor Receptor

EMT - Epithelial-To-Mesenchymal Transition

EPR - Enhanced Permeability and Retention

ERG - ETS-Related Gene

ETC - Electron Transport Chain

ETS - E-26 Transformation-Specific Transcription Factor

FBS - Foetal Bovine Serum

FDR - False Discovery Rate

FSC - Front Scatter Channel

H - Hoechst 33342

$HAuCl_4$ - Gold Chloride

HDR - High-Dose Rate

HIF - Hypoxia-Inducible Factors

HR - Homologous Recombination

IFN-γ - Interferon-Gamma

IGRT - Image Guided Radiotherapy

IMRT - Intensity Modulated Radiotherapy

ISUP - International Society of Urological Pathologists

kV - Kilovoltage

LA-ICP-MSI - Laser Ablation Inductively Coupled Plasma Mass Spectrometry Imaging

LDR - Low-Dose Rate

LET - Linear Energy Transfer

LINAC - Linear Accelerator

MCTS – Multicellular Tumour Spheroid

MRI - Magnetic Resonance Imaging

mtDNA - Mitochondrial DNA

MV – Megavoltage

NaCl - Sodium Chloride

NHEJ - Non-Homologous End Joining

NLS - Nuclear Localisation Sequence

NMR - Nuclear Magnetic Resonance

NP - Nanoparticle

NPC - Nuclear Pore Complex

Nrf-2 - Nuclear Factor Erythroid 2-Related Factor 2

NSCLC - Non-Small Cell Lung Cancer

OS - Osteosarcoma

OXPHOS - Oxidative Phosphorylation

PBS - Phosphate-Buffered Saline

PDGF - Platelet-Derived Growth Factor

PDT - Photodynamic Therapy

PE – Plating Efficiency

PEG - Polyethylene Glycol

PET - Positron Emission Tomography

PFA - Paraformaldehyde

PI - Propidium Iodide

PSA - Prostate-Specific Antigen

Rb - Retinoblastoma Protein

RGD - Arginine-Glycine-Aspartic Acid

RIBE - Radiation-Induced Bystander Effect

RM - Repeated Measures

ROI - Region of Interest

ROS - Reactive Oxygen Species

RT - Radiotherapy

RTK - Receptor Tyrosine Kinase

SASP - Senescence-Associated Secretory Phenotype

SBRT - Stereotactic Body Radiation Therapy

SE - Standard Error

SF - Surviving Fraction

SMT - Somatic Mutation Theory

SPR - Surface Plasmon Resonance

SSC - Side Scatter Channel

Tat - Transactivator Protein

TEM - Transmission Electron Microscopy

TGF-A - Tumour Growth Factor A

TME - Tumour Microenvironment

TMPRSS2 - Transmembrane Protease Serine 2

TPP - Triphenylphosphine

TSG - Tumour Suppressor Gene

TSP1 - Thrombospondin-1

UICC - Union for International Cancer Control

ULA – Ultra-Low Attachment

VEGF - Vascular Endothelial Growth Factor

VMAT - Volumetric Modulated Arc Therapy

Z - Atomic Number

αMEM - Alpha Modified Eagle Medium

LIST OF TABLES

LIST OF FIGURES

Chapter 1. Introduction

1.1. Cancer

Cancer is a complex genetic disease, with unique features, that occurs as result of a continuous acquisition of genetic and epigenetic deregulations such as point mutations, gene amplification, chromosome instability, deletions, and gene silencing (Wang et al., 2020). Consequently, this set of mutations can disrupt the normal regulatory mechanisms of cell growth, division, and death, allowing cancer cells to promote their own proliferation and grow uncontrollably (Sinkala, 2023).

Despite significant advances in diagnosis and treatment, cancer represents the second most important cause of death and morbidity in Europe, with more than 2.7 million new cases and 1.3 million deaths each year. The highest mortality rates are associated with lung, colorectal, stomach, liver, and breast cancers (European Commission, 2022). The aetiology of cancer is multifactorial, involving an interplay between genetic, environmental and lifestyle factors (Mbemi et al., 2020). Habits such as smoking, alcohol consumption, an unhealthy diet, and lack of physical activity are major risk factors for the development of cancer (Cancer Research UK, 2020). The lifetime probability of being diagnosed with an invasive cancer is higher for men (40.1%) than women (38.7%), and although it can occur at any age the risk of developing cancer increases significantly over the age of 50, due to biological changes related to the ageing process (Berben et al., 2021; Mbemi et al., 2020).

1.1.1. Classification and nomenclature of tumours

Cancer can result from the abnormal proliferation of any kind of cell, which means there are over 100 types of cancer. When any of the different cell types in the body starts proliferating uncontrollably, a neoplasm can originate. This abnormal growth can either be benign, if it remains encapsulated in the tissue of origin, or malignant, if it has acquired the ability of invading the surrounding structures and migrate to distant sites in the body (Cooper, 2000a). Benign tumours are designated by the suffix “-oma” attached to the cell type from which the tumour occurs. Malignant neoplasms are designated according to the type of tissue from which they arise. Tumours that originate in epithelial tissues are called carcinomas. These are further subdivided depending on their growth pattern –

squamous cell carcinoma or adenocarcinoma if their pattern is glandular. If the neoplasm origin is mesenchymal, these are called sarcomas. Tumours that derive from blood cells are include leukaemias or lymphomas, and neoplasms that originate in melanocytes are called melanomas (Kumar et al., 2018).

1.1.2. Grading and staging of malignant tumours

The primary characteristics of all cancers include the tumour site, its profile (histopathology, morphology, molecular and genetic characteristics) and the disease extent, i.e. the tumour stage. Tumour grading systems are used to assess the aggressiveness (e.g. mitotic count and necrosis) and cytological features, such as cellular differentiation and presence of dysplasia, and they also guide treatment decisions (Carbone, 2020). While most tumours are graded using a three- our four-tier numerical system, like osteosarcoma (three grades: low – well differentiated, slow growth –, intermediate – cells look more abnormal than low grade, moderate growth –, and high – poor differentiation, rapid growth and very likely to metastasise), some tumours have specific grading systems based on their unique characteristics (Carbone, 2020; Lilienthal & Herold, 2020; Varma et al., 2023).

Prostate cancers have typically been graded using a Gleason score, where pathologists analyse the histology of the tumour and attribute one grade for the most predominant pattern and another for the second most predominant. The Gleason system identified five different grades, based on the cellular patterns observed, from cells that resemble normal prostate tissue, with well-formed glands (pattern 1); to cells that do not form glands and look very abnormal (pattern 5). The overall score would be the sum of both grades, scoring from 2-10, with 2-4 indicating less aggressive tumours, 5-6 moderately differentiated, and 7-10 poorly differentiated and highly aggressive cancers (European Association of Urology, 2024; Kweldam et al., 2019). In 2014 the Gleason grading system was upgraded to improve accuracy and provide more clarity. Since the Gleason score was a sum of two different patterns, low scores of 2-5 were never attributed, leading to confusion. Moreover, the same score could indicate different prognostic implications (e.g. a score of 7 could be 3+4 or 4+3), therefore, to simplify interpretation, the International Society of Urological Pathologists (ISUP) introduced a new system – the Grade Group system – which categorises prostate cancer into five groups based on the Gleason score: Group 1 – Gleason score 6

(3+3), 2 – 7 (3+4), 3 – 7 (4+3), 4 – 8 (4+4, 3+5, 5+3), and 5 – scores 9 and 10 (4+5, 5+4, 5+5) (Cancer Research, 2022a; European Association of Urology, 2024; Kweldam et al., 2019).

Breast cancers are graded using the Nottingham Grading System or Nottingham Histologic Score, which evaluates three key features of breast cancer cells: tubule formation – how much tumour cells form glandular structures, scored from 1 (most cells form tubules) to 3 (few or no tubules) –, nuclear pleomorphism – how different cancer cells look compared to normal tissue, scored from 1 (cells look similar to normal tissue) to 3 (cells look very different) –, and mitotic count – how many cells are dividing, scored from 1 (few cells) to 3 (many cells). The scores of each of these tumoral characteristics are added together to give a total score ranging from 3 to 9. The total score then assigns the grade of the tumour: grade 1 (3-5 points) is low grade, well differentiated; and grade 3 (8-9 points) is high grade, poorly differentiated (Takahashi, H. et al., 2020; van Dooijeweert et al., 2022).

Tumour staging is based on the TNM system, developed by Pierre Denoix and the Union for International Cancer Control (UICC), and has been recognised as determinant of prognosis (Brierley et al., 2016). It gives information regarding the tumour size (T) – between T1 and T4, with progressive enlargement –, whether there is lymph node involvement (N) – N0, if the tumour has not yet spread to any lymph nodes, or, N1 to N3, with progressive distal spread –, and if it has metastasised to other parts of the body (M) – M0 or M1 if metastasis is present or not (Cancer Research, 2014; Rosen & Sapra, 2024). The stage of osteosarcomas can also be determined using the Enneking system for staging of malignant musculoskeletal tumours, based on the grading of the tumour, the local extent and the presence or absence of metastasis. The lesions are divided into stages I and II, regarding cellular differentiation, cytological atypia and risk of metastasis, and further subdivided into A and B on the basis of involvement of anatomical barriers to tumour growth, i.e. cortical bone, articular cartilage, fascial septa, or joint capsules, where A is intracompartmental – contained in a well-defined compartment – and B is intercompartmental. Stage III lesions are lesions that have metastasised, regardless of size and grade (Kundu, 2014).

1.1.3. Carcinogenesis

Normal cells are continuously exposed to mutagenic agents that induce DNA damage. However, cells possess a range of repair mechanisms that allows their progression through the stages of the cell cycle (Chatterjee & Walker, 2017). Malignant tumours are a result of a multistep phenomenon that involves a series of genetic and epigenetic alterations that the cells cannot repair, which lead to defective tumour suppressor genes and/or hyperactive oncogenes that promote tumorigenesis (Zhu et al., 2015).

1.1.3.1. Oncogenes

In normal conditions, proto-oncogenes control cell proliferation and survival which means that mutations causing overexpression of these genes - now called oncogenes - induce abnormal cell proliferation and thus tumour development (Lee & Muller, 2010; Shortt & Johnstone, 2012). The activation of an oncogene involves a *gain-of-function* mutation which can be a deletion or point mutation in the gene or regulatory region, resulting in the constitutive activation of the protein or the overexpression of the gene; a chromosomal rearrangement, leading to the fusion of two genes or translocation to a neighbouring regulatory sequence, causing gene overexpression; an amplification of a DNA segment which translates into excessive amounts of the gene product; or an increase in mRNA stability – the mRNA stays active in the cell, promoting the overproduction of the encoded protein (Chial, 2008a; Pierotti et al., 2003; Rosenberg & Rosenberg, 2012).

There are numerous proto-oncogenes which can be divided into six subcategories: growth factors, like *c-Sis*, which encodes for platelet-derived growth factor (PDGF) that induces cell proliferation; receptor tyrosine kinases (RTKs), like the epidermal growth factor receptor (EGFR), that receive cell growth inducive signals; cytoplasmic tyrosine kinases, like *Src*, that mediate cell proliferation, migration, differentiation and survival; cytoplasmic serine/threonine kinases, such as Raf kinase, that are involved in cell cycle regulation, survival and apoptosis; regulatory GTPases, such as *Ras*, involved in pathways of cell proliferation; and transcription factors/transcription factor regulators, such as *Myc*, a direct transcription factor involved in cell proliferation, and Cyclin D1 (CCND1) which indirectly promotes the transcription of genes needed for cell

proliferation (Brown, 2021; Capra et al., 2006; Chial, 2008a; Jung et al., 2020; Lee & Muller, 2010; Paul & Mukhopadhyay, 2004).

1.1.3.1.1. Oncogenes in Breast and Prostate Adenocarcinoma.

The most commonly deregulated oncogenes in breast cancer are ErbB2, PI3K, MYC, and CCND1, with ErbB2 (HER-2) assuming special importance considering 20-30% of human breast cancers show elevated levels of this gene, due to genomic amplification. The overexpression of HER-2, a member of the EGFR family of receptor tyrosine kinases that assists in differentiation and cell growth, correlates with negative clinical prognosis and is also a predictive marker for therapeutic response (Lee & Muller, 2010).

In prostate cancer, several oncogenes have now been identified and characterised in the molecular progression of the disease, such as IGF1R – a receptor tyrosine kinase that mediates the actions of the insulin-like growth factor 1, and is involved in cell growth –, other members of the EGRF family, MYC, PI3K, and, most importantly due to its correlation with the Gleason Score, ERG. ERG (ETS-related gene) is a member of the E-26 transformation-specific (ETS) transcription factor. ETS proteins are nuclear-DNA binding phosphoproteins that act as activators or repressors of transcription (Adamo & Ladomery, 2016). In prostate cancer, the overexpression of ERG or ETV1 (ETS variant transcription factor 1- another gene of the ETS family) are usually linked to the fusion of the promoter region of the transmembrane protease serine 2 (TMPRSS2) gene, which contains androgen sensitive elements, with the coding region of ERG or ETV1, driving the overexpression of ERG in the presence of androgens, which consequentially correlates with malignancy and cancer progression (Adamo & Ladomery, 2016; Dasgupta et al., 2012; Tomlins et al., 2005; Wang et al., 2021).

1.1.3.2. Tumour Suppressor Genes

As opposed to oncogenes, proteins encoded by tumour suppressor genes (TSGs) are either growth inhibitors, pro-apoptotic or trigger the arrest of the cell cycle. The activation of TSGs is usually linked to a *loss-of-function* mutation which are often point mutations or small deletions and are generally recessive in activity – cells need to lose both copies of the gene to become cancerous (Chial, 2008b). The inactivation of TSGs can also be consequence of chromosomal deletions or breaks, promoter hypermethylation, and epigenetic silencing, which can involve histone modification, the binding of repressive proteins or aberrant methylation of

CpG islands – stretches of DNA rich in CpG dinucleotides often found near the transcription initiation sites. The methylation of CpG islands or promoters typically leads to the silencing of the associated gene by inhibiting the binding of transcription factors (Chial, 2008b; Jung & Pfeifer, 2013; Keohane, 2020; Llauradó et al., 2012; Moore et al., 2013).

The proteins encoded by TSGs can be categorised into five different classes: cell cycle regulators, like p16 and pRb; receptors or signal transducers involved in preventing cell proliferation, such as TGFβ; check-point control for cell cycle arrest, like p53; pro-apoptotic proteins, such as BAX; and, finally, enzymes that participate in DNA damage repair (Lodish et al., 2008). These last examples are encoded by stability genes or caretakers. These genes are responsible for repairing mutations during DNA replication, mitotic recombination, and chromosomal segregation. Caretaker genes maintain the cells genome mutation-free, therefore, when inactivated, the rate of alterations in other genes increases drastically, enhancing the probability of occurrence of a neoplasm (Cooper, 2000b; Lee et al., 2024; Wang et al., 2018).

1.1.3.3. Theories of carcinogenesis

Various theories have been proposed to explain the mechanisms underlying carcinogenesis, each providing insights into how cancer develops and progresses (Stewart, 2019).

Somatic Mutation Theory *(first proposed by Theodor Boveri, 1914)*

The somatic mutation theory (SMT) is one of the earliest and most prevalent models to explain carcinogenesis. According to SMT, cancer is a clonal disease, primarily caused by genetic mutations in somatic cells. These mutations can result from exposure to carcinogens, such as chemicals, radiation, or viruses; or they can arise spontaneously during DNA replication. The accumulation of these mutations leads to a disruption in the normal regulatory mechanisms of cell growth and proliferation, ultimately leading to the development of cancer (Soto & Sonnenschein, 2011).

Multi-Hit Model *(first proposed by Alfred Knudson, 1971)*

The multi-hit model of carcinogenesis expands on the somatic mutation theory by emphasizing that cancer development requires multiple genetic alterations. Knudson's "two-hit hypothesis", based on his studies in retinoblastoma, suggests

that both alleles of a tumour suppressor gene must be inactivated for cancer to develop. Furthermore, his observations showed that patients with an inherited germline mutation would only need a somatic mutation in the other allele of the gene for the tumour to occur, meaning they would develop cancer much earlier than individuals who did not inherit a mutation and would therefore need two “hits” to occur somatically within a single cell over time. He also showed that patients with inherited mutations were more likely to develop multiple tumours. This model underscores the idea that cancer is a multistep process, where successive genetic alterations accumulate to drive malignance (Chial, 2008b).

Clonal Evolution Model *(first proposed by Peter Nowell, 1976)*

The clonal evolution model of carcinogenesis builds on the concept of the multi-hit model by describing how cancer cells evolve over time. This theory states that genetic and epigenetic changes occur in individual cells and, if these mutations confer selective advantage, they allow the cells to proliferate, forming clones. As the tumour progresses, additional mutations occur, further enhancing the survival and proliferation of these cells. Clonal evolution leads to tumour heterogeneity, as multiple subclones in a single patient have different phenotypes and levels of aggressiveness. The clonal evolution model explains the genetic diversity seen within tumours and the development of resistance to therapies, as different subclones may respond differently to treatment (Greaves & Maley, 2012; Shackleton et al., 2009).

Cancer Stem Cell Theory *(first proposed by Dominique Bonnet and John Dick, 1997)*

The concept of Cancer Stem Cells (CSCs) has evolved through the years, with research as early as 1855, by Virchow, proposing a stem cell origin of cancer. But it was not until 1997 that researchers Bonnet and Dick provided experimental evidence supporting this theory, by demonstrating and isolating a small subset of cells with extensive proliferative potential in acute myeloid leukaemia – CSCs – characterised by a $CD34^{+}CD38^{-}$ phenotype (Bonnet & Dick, 1997). Thus, the cancer stem cell theory postulates that CSCs possess the ability to self-renew and differentiate into various cell types, suggesting the growth and progression of a tumour is driven by this cell population. Moreover, the cancer stem cell model proposes that many cancers are hierarchically organised in the same manner as normal tissues, with CSCs undergoing epigenetic alterations analogous to the

differentiation of normal stem cells, forming tumour cell populations with different phenotypes. According to this theory, CSCs are responsible for tumour initiation, maintenance, and recurrence, and these cells are thought to be resistant to conventional therapies, like chemotherapy and radiation, that typically target rapidly dividing cells but may not effectively eliminate CSCs (Chu et al., 2024; Shackleton et al., 2009).

Epigenetic Theory *(first proposed by Peter Jones and Stephen Baylin, 2002)*
The epigenetic theory of carcinogenesis focuses on changes in gene expression that do not involve alterations in the DNA sequence. Epigenetic modifications, such as DNA methylation, histone modification, and non-coding RNA expression, can regulate gene activity and contribute to cancer development. Aberrant epigenetic changes can silence tumour suppressor genes or activate oncogenes, driving cancer development and progression. Unlike genetic mutations, epigenetic changes are potentially reversible, making them a promising target for therapeutic interventions (Baylin & Jones, 2016; Sadida et al., 2023).

1.1.3.4. Hallmarks of Cancer

Developed by Hanahan and Weinberg, the hallmarks of cancer were originally six biological capabilities acquired by cancer cells in the multistep process of tumorigenesis (Hanahan & Weinberg, 2000) (Figure 1.1A). In a 2011 update, the hallmarks increased to eight biological capabilities and two enabling characteristics (Hanahan & Weinberg, 2011) (Figure 1.1B). In the most recent elaboration of the concept, Hanahan proposed a new model, including 10 core hallmarks (H) and 4 enabling characteristics (EC) (Hanahan, 2022) (Figure 1.1C).

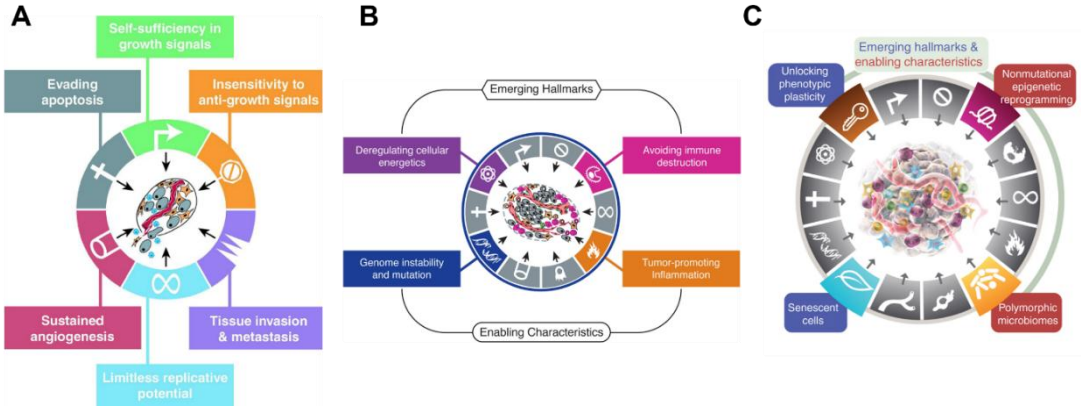

Figure 1.1 - The Hallmarks of Cancer. A – the first six proposed hallmarks **(Hanahan & Weinberg, 2000). B –** revised model including two new emerging hallmarks and two enabling characteristics **(Hanahan & Weinberg, 2011)**. **C –** the latest updated concept,

including two new emerging hallmarks and an additional two enabling characteristics **(Hanahan, 2022)**.

Sustaining Proliferative Signalling (H)

Contrary to normal cells, that depend on external growth signals to proliferate, cancer cells can trigger their own growth. This can be achieved through a variety of mechanisms, mainly:

- Internal production of growth factors, such as EGF (epidermal growth factor), PDGF (platelet-derived growth factor), and TGF-α (tumour growth factor α), creating a positive feedback signalling loop known as autocrine stimulation. This leads to a constant stimulation of cyclin production, especially cyclin D1, ultimately driving the transcription of genes necessary for DNA replication (Casimiro et al., 2012; Hanahan & Weinberg, 2000; Wang, 2021).
- Overexpression or constitutive activation of growth factor receptors, rendering the cells either hyperresponsive to ambient levels of growth signal, or allowing cell proliferation in the absence of ligand binding, respectively. Cancer cells with mutant or overactive receptors continually activate pathways like Ras-Raf-MAPK or PI3K-AKT which ultimately lead to the activation of cyclins and cyclin-dependent kinases (CDKs) and DNA replication (Dulińska-Litewka et al., 2022; Hanahan & Weinberg, 2000, 2011; Poch et al., 2001).
- Constitutive activation of downstream signalling pathways, when cancer cells possess mutated signalling molecules such as Ras, Raf, or PI3K, that stop needing upstream signals to drive cell growth. The continuous activation of these pathways leads to the constant expression of cyclin D1, which activates CDK4/6. This complex then phosphorylates the retinoblastoma protein (Rb), which releases the transcription factor E2F which, in turn, drives the transcription of genes necessary for DNA replication (Hanahan & Weinberg, 2000, 2011; Sherr & McCormick, 2002; Stanciu et al., 2023).
- Paracrine signalling manipulation, by influencing the tumour microenvironment (TME) to secrete growth factors and other soluble molecules that drive cell proliferation (Thomas et al., 2020).

Evading Growth Suppressors (H)

One of the key elements of homeostasis is the presence of antiproliferative signals that keep cell growth within normal limits, preventing excessive cell division and maintaining tissue integrity (Hanahan & Weinberg, 2000, 2011). Anti-proliferative signals work by controlling cell cycle checkpoints and activating tumour suppressor pathways. To be able to achieve uncontrolled proliferation, cancer cells acquire mechanisms to evade these growth suppressors, bypassing the regulatory checkpoints that would otherwise limit their growth (Amin et al., 2015). Two of the most important tumour suppressors that regulate cell growth are the pRb and p53 proteins. The pRb protein is a regulator of the G1/S checkpoint, which controls when cells enter the S phase of DNA synthesis. When pRb is activated, it binds to and inhibits E2F. To evade this mechanism, tumour cells often mutate RB1, the coding gene for pRb, which becomes nonfunctional; or overexpress cyclins or CDKs, that inactivate pRb (Amin et al., 2015; Engeland, 2022; Hanahan & Weinberg, 2000, 2011; Sherr & McCormick, 2002). TP53 is a tumour suppressor that responds to DNA damage and other stress signals. When activated, p53 stops the cell cycle to allow DNA repair or induces apoptosis if the damage is too extensive and cannot be repaired. Many cancer cells acquire mutations in the TP53 gene (which encodes p53) or increase the expression of MDM2, a protein that degrades p53. With p53 inactive, cells avoid cell cycle arrest and apoptosis, allowing them to proliferate (Amin et al., 2015; Engeland, 2022; Hanahan & Weinberg, 2000, 2011; Sherr & McCormick, 2002).

Cancer cells may also inactivate growth-inhibitory signals, such as TGF-β (Transforming Growth Factor β), an external signal that inhibits cell proliferation by promoting the expression of CDK inhibitors (CKIs) that block the activity of cyclin-CDK complexes, through the mutation of proteins involved in the TGF-β signalling pathway, like Smad proteins, or by downregulating the expression of TGF-β receptors (Hanahan & Weinberg, 2000, 2011; Seoane & Gomis, 2017). Likewise, tumour cells may also dysregulate CKIs like p16 or p21, through mutations in the genes that encode them. This leads to unchecked cyclin-CDK activity, promoting uncontrolled cell growth (Schirripa et al., 2022).

Resisting Cell Death (H)

Apoptosis is a mechanism of programmed cell death that occurs when cells are infected, unnecessary or possess damage too extensive to repair. It ensures

tissue integrity and homeostasis and involves a series of cellular mechanisms that culminate with the activation of caspases (Fernald & Kurokawa, 2013; Hanahan & Weinberg, 2000, 2011). In response to apoptotic stimuli, initiator caspases are activated, leading to the cleavage and activation of executor caspases. This results in the proteolytic cleavage of cellular substrates and cell death (Jan & Chaudhry, 2019). There are two pathways that regulate programmed cell death: the intrinsic or mitochondrial pathway, triggered by internal signals such as DNA damage or oxidative stress, which involves proteins like Bcl-2 and cytochrome *c*. Members of the BCL2 family such as PUMA, NOXA and BAD initiate the apoptotic cascade in response to internal stress signals by neutralizing the activity of anti-apoptotic proteins like Bcl-2. Pro-apoptotic signals (BAX and BAK) are then activated and translocated to the mitochondrial outer membrane, where they form pores leading to mitochondrial membrane permeabilization, which allows for the release of pro-apoptotic factors like cytochrome *c* and ultimately leads to caspase-9 activation via the formation of apoptosomes. The extrinsic or death receptor pathway is activated by external signals, such as immune cells activating death receptors such as FAS, TNFR or DR4/5 leading to caspase-8 activation and subsequently activation of the executioner caspases including caspase-3 (Ai et al., 2024; Jan & Chaudhry, 2019).

Since cancer cells are under constant stress (e.g. oncogenic stress, genomic instability, and hypoxia) they often acquire mechanisms in order to evade apoptosis and proliferate uncontrollably (Fernald & Kurokawa, 2013). In response to such stimuli, the intrinsic pathway would normally be triggered, therefore, cancer cells may resist this process by:

- Overexpressing anti-apoptotic proteins, such as Bcl-2 or Bcl-xL, which block the mitochondrial pathway by inhibiting BAX and BAK, preventing the release of cytochrome c from the mitochondria, thus blocking the activation of caspases (Qian et al., 2022).
- Loss of pro-apoptotic proteins, such as BAX, BAK, or PUMA, impeding apoptosis (Qian et al., 2022; Sharma et al., 2019)
- Disrupting the p53 pathway, often by mutating TP53, meaning p53 is nonfunctional or absent. This means it will no longer trigger the transcription of pro-apoptotic genes like PUMA or NOXA, which promote mitochondrial membrane permeabilization and induce apoptosis (Wang, H. et al., 2023).

These mechanisms are not mutually exclusive and cancer cells may trigger one or more of these processes to evade apoptosis (Fernald & Kurokawa, 2013).

Enabling Replicative Immortality (H)

Normal cells have limited replicative potential before they enter senescence – a permanent growth arrest state – or undergo apoptosis. This is primarily due to the telomere shortening (Yaswen et al., 2015). Telomeres are repetitive DNA sequences at the end of chromosomes that protect them from genome instability. With each round of cell division, a small portion of the telomeres is lost due to the inability of DNA polymerase to completely replicate the ends of linear chromosomes, a phenomenon known as “end-replication problem”. Once telomeres become critically short, they can no longer protect the chromosome ends, which become recognised by the cell’s DNA repair machinery as a double-strand break, leading to senescence or apoptosis. This telomere shortening acts as a natural limit to the number of times somatic cells can divide (Victorelli & Passos, 2017; Yaswen et al., 2015). In cancer cells, this limit is bypassed through telomere maintenance. Ninety percent of malignant cells upregulate the expression of telomerase, an enzyme that extends telomeres and prevents their shortening. Normally inactive in most somatic cells, telomerase is reactivated in tumours, allowing for continued cell division without triggering senescence (Hanahan & Weinberg, 2000, 2011). Cancer cells also disable key tumour suppressor pathways, such as p53 and Rb, which normally respond to telomere shortening by inducing cell cycle arrest or apoptosis. By inactivating these pathways, cancer cells can continue dividing even when telomeres reach critically short lengths, avoiding the DNA damage response that would normally stop proliferation (Hanahan & Weinberg, 2000, 2011; Victorelli & Passos, 2017).

Inducing Angiogenesis (H)

Angiogenesis refers to the formation of new blood and lymphatic vessels from pre-existing vasculature, a process essential to tumour growth as it supplies oxygen and nutrients to cancer cells (Elebiyo et al., 2022). To ensure a constant supply of blood, cancer cells switch to angiogenesis by shifting the balance between pro-angiogenic and anti-angiogenic factors in favour of the former, leading to a pro-angiogenic state. A major regulator of this process is the vascular endothelial growth factor A (VEGF-A), a signalling protein that stimulates the formation of new blood vessels, the production of which is often upregulated in

response to hypoxia, a common feature of rapidly growing tumours (Duffy et al., 2013; Elebiyo et al., 2022; Hanahan & Weinberg, 2000, 2011; Saman et al., 2020). At the same time, cancer cells and the TME can downregulate or inhibit anti-angiogenic factors, like thrombospondin-1 (TSP1), to further promote blood vessel formation (Kaur et al., 2021; Saman et al., 2020). As tumours grow and become more vascularised, these new blood vessels tend to be abnormal – disorganised, leaky, and inefficient at delivering oxygen (Orozco-García et al., 2023). This disordered vasculature can promote further tumour growth and even metastasis by providing easier access for cancer cells to enter the bloodstream (Cooper, 2000a). Additionally, these abnormal blood vessels can create regions of hypoxia within the tumour, which in turn drives even more aggressive angiogenesis (Cooper, 2000a; Muz et al., 2015).

Activating Invasion and Metastasis (H)

Metastasis is one of the most prominent causes of cancer therapy failure and mortality, and it remains poorly understood (Fares et al., 2020). The formation of secondary tumours occurs when cancer cells escape the primary tumour site and spread through the bloodstream or lymphatic system, establishing new colonies in distant organs, where nutrients and space are abundant (Fares et al., 2020; Hanahan & Weinberg, 2000, 2011). The process through which cancer cells adopt invasive properties, disseminate and survive in the circulation and acquire capabilities to colonize distant tissues is called the metastatic cascade and it involves an epithelial-to-mesenchymal transition (EMT) (Liu, Q. et al., 2021). During EMT, cancer cells lose their epithelial characteristics, such as cell adhesion – often translated by and aberrant expression of cell adhesion molecules (CAMs) such as cadherins and integrins, disrupting cell-cell and cell-matrix interactions – and acquire mesenchymal traits, including enhanced mobility and invasiveness (Martin et al., 2013; Ribatti et al., 2020).

Genome Instability and Mutation (EC)

To drive tumour progression, cancer cells depend on the occurrence of various alterations in their genome that favour tumoral growth and dominance over the local tissue environment (Hanahan & Weinberg, 2011). While in normal cells the DNA is maintained through a range of protective mechanisms such as DNA damage repair pathways and cell cycle checkpoints, in cancer cells these mechanisms are often faulty, leading to a high rate of mutations, chromosomal

rearrangements, and other genetic abnormalities, like epigenetic changes (Hanahan & Weinberg, 2011; Jurkovicova et al., 2022). This genomic instability is achieved through disruptions in the components that normally preserve genome integrity – the caretaker genes – such as BRCA1/2 which mediate the homologous recombination repair pathway (Hanahan & Weinberg, 2011; Ledermann et al., 2016). Similarly, malfunctioning of cell cycle checkpoints, particularly those regulated by p53 – the "guardian of the genome" –, allows cells with damaged DNA to continue dividing, passing on mutations to daughter cells. Over time, these accumulated mutations can activate oncogenes or inactivate tumour suppressor genes, driving cancer progression (Hanahan & Weinberg, 2011; Wang, H. et al., 2023). In addition to mutations at the gene level, cancer cells often exhibit larger-scale genomic changes, such as chromosomal instability (CIN), leading to abnormalities, both numerical (gain or loss of a chromosome or sets of chromosomes) and structural (deletions, amplifications, inversions, and translocations), which further disrupt normal cellular functions. As these genetic changes accumulate, tumours become more heterogeneous, with different subpopulations of cells possessing unique mutations, some of which confer advantages such as resistance to treatment or enhanced metastatic potential (Hosea et al., 2024).

Tumour-promoting Inflammation (EC)

Inflammation is closely related with all stages of tumorigenesis, especially chronic inflammation, which is involved in immunosuppression and provides a preferred microenvironment for tumour development, progression and metastasis (Zhao et al., 2021). While the immune system typically defends the body against infections and abnormal cells, cancer can exploit certain inflammatory processes to create an environment that supports tumour growth (Greten & Grivennikov, 2019; Hanahan & Weinberg, 2011). This persistent inflammation provides growth factors, survival signals, and promotes tissue remodelling, all of which contribute to cancer progression. For example, immune cells such as macrophages, neutrophils, and T-cells can be recruited by cancer cells upon infiltration in the TME to support tumour growth, releasing factors like cytokines and chemokines that promote cell proliferation, angiogenesis and metastasis, and also aid in anti-tumour immune suppression (Cendrowicz et al., 2021; Greten & Grivennikov, 2019). Moreover, inflammation promotes genome instability through the

generation of ROS that damage the DNA, accelerating the mutation rate of cancer cells (Hanahan & Weinberg, 2011; Yu et al., 2024). Additionally, inflammatory signalling pathways, such as NF-κB and STAT3 – transcription factors involved in development, differentiation, immunity, and metabolism –, are often activated in cancer cells and immune cells in the tumour microenvironment, sustaining pro-tumour inflammation (Zhang et al., 2021).

Deregulating Cellular Energetics (H)

Cancer cells are able to reprogramme their metabolism to support rapid growth and survival. In normal cells, under aerobic conditions, glucose is processed through glycolysis in the cytosol followed by oxidative phosphorylation in the mitochondria to produce energy in the form of ATP molecules. In contrast, cancer cells often reprogramme their glucose metabolism and energy production to aerobic glycolysis – cells convert glucose into lactate through fermentation (Warburg Effect) instead of fully oxidising it in the mitochondria (Hanahan & Weinberg, 2011; Liberti & Locasale, 2016). Despite being less efficient than oxidative phosphorylation (36 ATP:1 glucose), aerobic glycolysis (2 ATP:1 glucose) produces energy at a faster rate, supporting the high metabolic demands of rapidly proliferating cancer cells (Fadaka et al., 2017). Furthermore, the intermediate products of this process (e.g. pyruvate and lactate) feed into other biosynthetic pathways such as nucleotide, amino acid, and lipid production, which are essential for cell proliferation. Finally, the upregulation of glycolysis contributes to microenvironmental acidosis, which in turn promotes tissue invasion and immune cell inhibition (Gatenby & Gillies, 2004; Hanahan & Weinberg, 2011).

Evading Immune Destruction (H)

Under normal circumstances, the immune system identifies and destroys abnormal cells, including early cancer cells, through mechanisms of immune surveillance – tumour cells are recognised by T cells, which become activated and secrete interferon-gamma (IFN-γ). Activated $CD8^+$ T cells release cytotoxic molecules such as perforin and granzyme that trigger apoptosis, while in parallel IFNγ enhances these cytotoxic effects and helps recruit addition immune cells. However, as the tumour progresses, cancer cells evolve multiple ways to bypass this defence by developing strategies to avoid being recognised and eliminated by immune cells (Hanahan & Weinberg, 2011; Kim & Cho, 2022). Some of the

strategies through which cancer cells are capable of immune evasion include altering the expression of surface proteins that immune cells recognise as *non-self* – for example, cancer cells may downregulate MHC class I molecules, which present tumour antigens to cytotoxic T cells –, or express immune checkpoint proteins, including PD-L1, which binds to its receptor PD-1 present on the surface of T cells, inhibiting their activity (Taylor & Balko, 2022; Yu et al., 2020); and creating an immunosuppressive microenvironment, by recruiting regulatory immune cells such as regulatory T cells (T_{reg}) and myeloid-derived suppressor cells (MDSCs), that express inhibitory factors that ultimately supress the proliferation of T cells and IFN-γ (Kim & Cho, 2022).

Unlocking Phenotypic Plasticity (H)

During embryonic development, progenitor cells differentiate into different cell types with specific functions, after which they normally stop growing, achieving terminal differentiation, a determinant aspect that allows cells to produce the necessary factors to achieve homeostatic functions (Hanahan, 2022; Tímár et al., 2023). In most cases, this end point is an antiproliferative state, which, in the context of cancer, constitutes a barrier to cell growth and proliferation. Therefore, tumour cells unlock the capability of phenotypic plasticity to escape the state of terminal differentiation, which can be done through dedifferentiation – mature cells revert back to a progenitor-like, less differentiated state, regaining proliferative potential –, blocked differentiation – cancer cells that arise from progenitor cells short-circuit the differentiation pathway, maintaining uncontrolled proliferative capacity –, and transdifferentiation – cells committed to one differentiation pathway transform directly into a distinct cell type (Hanahan, 2022; Tímár et al., 2023). Phenotypic plasticity is also associated with cancer stem cells, which can differentiate into various cell types within the tumour, promoting tumour heterogeneity, resistance to chemotherapy or radiation, and driving tumour recurrence. The properties of CSCs are often related to the activation of the EMT program, thus contributing to invasiveness and metastatic potential (Gupta et al., 2019). Pathways including Wnt, Notch, and Hedgehog are intimately related to phenotypic plasticity as they regulate processes in cell fate determination, differentiation and stem cell maintenance (Kumar et al., 2021).

Nonmutational Epigenetic Reprogramming (EC)

Disrupting the epigenetic programme of gene expression is a capability acquired by cancer cells to promote tumorigenesis, dynamically and quickly adapting to different stresses without the need for permanent mutations (Costa et al., 2023; Hanahan, 2022). Epigenetic modifications include DNA methylation, histone modifications, and the action of non-coding RNAs. For instance, hypermethylation of tumour suppressor gene promoters can silence these genes, allowing uncontrolled cell growth, while histone modifications can alter the chromatin structure to activate oncogenes or silence differentiation genes (Xu et al., 2023). Nonmutational epigenetic reprogramming is closely linked to phenotypic plasticity because it allows cancer cells to shift between different cell states – such as switching between more differentiated and stem-like states – enabling tumours to adapt to various stresses, including immune surveillance and cancer therapies, thus enhancing tumour heterogeneity and survival (Hanahan, 2022; Wainwright & Scaffidi, 2017).

Polymorphic Microbiomes (EC)

Diverse communities of microorganisms like bacteria and fungi exist in different environments within the body, and these microbiomes influence tumour development, progression, and response to treatment. The composition of the microbiome can vary significantly between individuals and even across different tissues in the same individual, and these variations, or polymorphisms, can have different effects on cancer biology (Bhatt et al., 2017; Hanahan, 2022). The microbiome can contribute to cancer in several ways. Certain microbes produce pro-inflammatory molecules that create a chronic inflammatory environment, promoting DNA damage and increasing the risk of mutations that lead to cancer (Bhatt et al., 2017). Others can directly affect cancer cell behaviour by modulating signalling pathways involved in cell proliferation, immune evasion, and metastasis. For example, gut microbiota can influence the immune response to cancer, either helping tumours evade immune destruction or reducing the effectiveness of immunotherapy (Chen et al., 2023; Li et al., 2024). In addition to promoting cancer, the microbiome can also affect treatment outcomes. Some microorganisms metabolise cancer drugs, either activating or deactivating them, which can alter their effectiveness. For instance, *E. coli* can alter the effectiveness of chemotherapy drugs, increasing the toxicity of some and reducing the toxicity

of others (Filippou et al., 2024). Furthermore, certain microbiomes may contribute to therapy resistance by protecting cancer cells from drug toxicity, like *Mycoplasma hyorhinis*, that can metabolise gemcitabine into an inactive form, or supporting tumour-promoting inflammation. As a result, cancer patients with different microbiomes may respond differently to the same treatment (Bhatt et al., 2017; Filippou et al., 2024; Francescone et al., 2014).

Senescent Cells (H)

Senescent cells are cells that have permanently exited the cell cycle and no longer divide, typically in response to stress or damage, such as DNA damage, oxidative stress, damage to cellular components or imbalances in cellular signalling pathways (Hanahan, 2022). While senescence is a natural mechanism that prevents damaged cells from proliferating and becoming cancerous, the accumulation of senescent cells in the tumour microenvironment can paradoxically promote cancer progression (Schmitt et al., 2022). Despite being non-proliferative, senescent cells remain metabolically active and secrete a variety of pro-inflammatory molecules, growth factors, and enzymes known as the senescence-associated secretory phenotype (SASP) (Hanahan, 2022). The SASP can create a local environment that promotes cancer by inducing chronic inflammation, encouraging tissue remodelling, and supporting tumour cell growth and invasion. These secreted factors can also stimulate angiogenesis and suppress immune responses, allowing cancer cells to evade immune destruction (Coppé et al., 2010; Hanahan, 2022; Schmitt et al., 2022). Moreover, cancer treatments such as radiation and chemotherapy can induce senescence in both tumour and normal cells. While this may initially interrupt tumour growth, the SASP from therapy-induced senescent cells can promote tumour recurrence, contribute to therapy resistance, and facilitate metastasis (Prasanna et al., 2021; Xiao et al., 2023).

1.1.4. Diagnosis and Treatment

Cancer diagnosis and treatment involve a structured multidisciplinary approach based on the type of cancer, its stage, and individual patient characteristics (Berardi et al., 2020). Cancer may be identified through routine screening – like mammograms for breast cancer or PSA tests for prostate cancer – or through symptoms – like lumps, pain or unexpected weight loss – prompting a series of diagnostic tests. When neoplasia is suspected, imaging techniques such as X-

rays, CT scans, MRI, PET scans or ultrasounds are used to visualise tumours and assess their location (Fass, 2008; Maxim et al., 2014). Nonetheless, a definite cancer diagnosis is always given by a pathological examination of a tumour sample, usually a biopsy. This can be achieved through a series of tests that can go from a simple histochemical stain to more complex techniques such as immunohistochemistry or molecular diagnosis (e.g. *in situ* hybridization) (Connolly et al., 2003; Taniere et al., 2019). The histological and molecular testing of tumour tissue aims to determine the grading and staging of tumours as well as identifying specific cancer subtypes which will guide treatment decisions, i.e. the treatment of a tumour may vary, subject to its type, stage/grade, and molecular biomarkers (Carbone, 2020).

1.1.4.1. Diagnosis and treatment of breast cancer

Most cancer treatments include a combination of surgery, chemo- and/or radiotherapy. For example, the treatment of early-stage breast cancer (ductal carcinoma *in situ*, stage I, and stage II) usually involves surgery – lumpectomy or mastectomy – usually followed by radiation. Then, depending on hormonal receptor (HR) status, ER/PR+, HER2- tumours receive hormonal therapy (e.g. tamoxifen or aromatase inhibitors); for HER2+ tumours, HER2-targeted therapy is recommended (like trastuzumab) combined with chemotherapy (often with docetaxel). Triple negative breast cancers (stages I and II) cannot receive targeted therapy, meaning chemotherapy is the main component of treatment, with patients often undergoing regimens of anthracyclines (doxorubicin) and taxane (paclitaxel). Stage III breast cancer patients are usually submitted to courses of chemotherapy prior to surgery, for tumour shrinkage. The treatment that follows is similar to the one for stage I and II, for HR+ or HER2+ tumours (radiotherapy + targeted therapy). High-risk triple negative breast cancer patients usually receive immunotherapy with immune checkpoint inhibitors combined with chemotherapy. Patients with metastatic (stage IV) cancer usually receive hormone therapy (if HR+) combined with chemotherapy, depending on the aggressiveness of the tumour, HER2-targeted therapy (if HER2+) combined with chemotherapy. If triple-negative, patients receive immunotherapy and may also be subjected to treatment with PARP (Poly (ADP-ribose) polymerase) inhibitors if they have BRCA mutations (BRCA-mutant cells have defective double-strand break (DSB) repair mechanisms, having to rely on proteins such as PARP,

involved in the repair of single-strand breaks. By inhibiting PARP, the DNA accumulates damage that cannot be repaired, resulting in cell death) (American Cancer Society, 2022; Bryant et al., 2005; Cancer Research, 2023; Chino et al., 2024; Helleday et al., 2005).

1.1.4.2. Diagnosis and treatment of prostate cancer

As for prostate adenocarcinomas, their treatment is based on the stage, grade, and the presence of androgen receptors (AR), which drive cancer growth through androgen hormones such as testosterone. For stage I and II cancers, the treatment course is designed based on the Gleason score and PSA (prostate-specific antigen) levels: low risk patients (Gleason ≤6, PSA <10 ng/mL) are put on active surveillance and receive treatment – surgery (radical prostatectomy) or radiotherapy (external beam or brachytherapy, detailed in the section 1.2.2.) – if the cancer progresses; for intermediate risk patients (Gleason 7, PSA 10-20 ng/mL) surgery is recommended, often followed by radiation if the margins are positive or there's high risk of recurrence. Radiotherapy can be combined with androgen deprivation therapy (ADT) to reduce testosterone levels and improve outcomes; high risk patients (Gleason 8-10, PSA >20 ng/mL) receive the same treatment as intermediate risk patients, maintaining ADT for 2 to 3 years to suppress androgen receptor signalling and slow cancer progression. Stage III cancer patients receive radiation therapy combined with long-term ADT, and surgery may be performed in select cases. Patients with metastatic prostate cancer (stage IV) usually receive ADT through LHRH (luteinising hormone-releasing hormone) analogues and antagonists, which stop the testes from producing testosterone, or anti-androgens to block testosterone from binding to testosterone receptors. Other treatment modalities may include chemotherapy, PARP inhibitors, immunotherapy and radiopharmaceuticals. Prostate cancer cells almost universally express androgen receptors and the growth of prostate cancer is primarily driven by androgens (testosterone and dihydrotestosterone). As aforementioned, hormone therapy targets this pathway, but resistance can develop over time, leading to castration-resistant prostate cancer (CRPC), where cancer progresses despite low testosterone levels. In this case, patients may receive next generation AR-targeting therapies like enzalutamide or abiraterone, which block the remaining AR activity, as well as chemotherapy, PARP inhibitors (in BRCA-mutant cases) and immunotherapy (Cancer Research, 2022b;

Congregado Ruiz et al., 2023; PDQ Adult Treatment Editorial Board, 2023; Prostate Cancer, 2024).

1.1.4.3. Diagnosis and treatment of osteosarcomas

The treatment of osteosarcomas is stage and grade dependent. Patients with localised osteosarcomas (stage I and II) can be high or low grade, the latter rarer and less aggressive. In low-grade osteosarcoma patients, surgery is frequently the primary treatment (limb-sparing surgery or amputation), and no chemotherapy or radiation is usually needed. High-grade osteosarcoma patients normally receive neoadjuvant chemotherapy to shrink the tumour and destroy any undetected metastasis, often with drugs such as doxorubicin, cisplatin, mifamurtide, and methotrexate. Following chemotherapy, surgery is performed to remove the tumour. Limb-sparing surgery is preferred in most cases, but amputation may be required in some situations where the tumour has invaded critical structures, such as blood vessels or nerves. After the tumour is removed, additional chemotherapy is administered to kill any remaining cancer cells and reduce the risk of relapse. Osteosarcoma cells are usually resistant to radiation; therefore, radiotherapy is not usually performed, with the exception of cases where surgery fails to remove the entirety of the tumour or is not possible altogether. The treatment of patients with metastatic osteosarcoma (stage III) is more complex as it involves addressing both the primary tumour and the metastases. It usually involves neoadjuvant chemotherapy, surgery for the primary tumour, surgery for metastatic lesions and adjuvant chemotherapy, and the prognosis is very poor (Cancer Research, 2021; Frampton, 2010; Rathore & Van Tine, 2021; Smeland et al., 2019; Spałek et al., 2021).

1.2. Radiation Therapy

Radiotherapy is commonly used as a primary or adjuvant treatment in over 50% of cancer patients where high energy Gamma (γ) or X-radiation is used to damage or kill cancer cells, while sparing the surrounding normal tissue as much as possible. This treatment exploits the fact that cancer cells typically lack effective DNA damage repair mechanisms, leading to the accumulation of genetic mutations upon irradiation, ultimately impairing the viability of these cells (Liu, Y. et al., 2021).

1.2.1. Radiation and DNA Damage

In order to effectively treat or reduce the size of tumours, these can be treated with high energy radiation – electromagnetic (γ- or X-rays) or particulate (e.g. electrons and protons) – that interacts with cellular components, primarily DNA (Mehta et al., 2010). Radiation interacts with molecules by transferring enough energy to eject orbital electrons from their atoms, i.e. ionising them, and radiation deposition ultimately results in DNA damage, manifested by single- and double-strand breaks in the sugar-phosphate backbone of the DNA molecule (Liu, Y. et al., 2021). Radiation can have a direct effect on the genome by ionising the DNA's bases or the sugar phosphate backbone (Figure 1.2A). However, as water is the most abundant molecule in cells, ionising radiation predominantly leads to the formation of radical species (like •OH) that cause oxidative stress and damage to proteins, membrane components and nucleic acids (Nickoloff et al., 2021). This indirect effect of radiation causes strand breaks, base sugar damage and cross-links between macromolecules (Figure 1.2B) (Borrego-Soto et al., 2015; Mehta et al., 2010; Nickoloff et al., 2021).

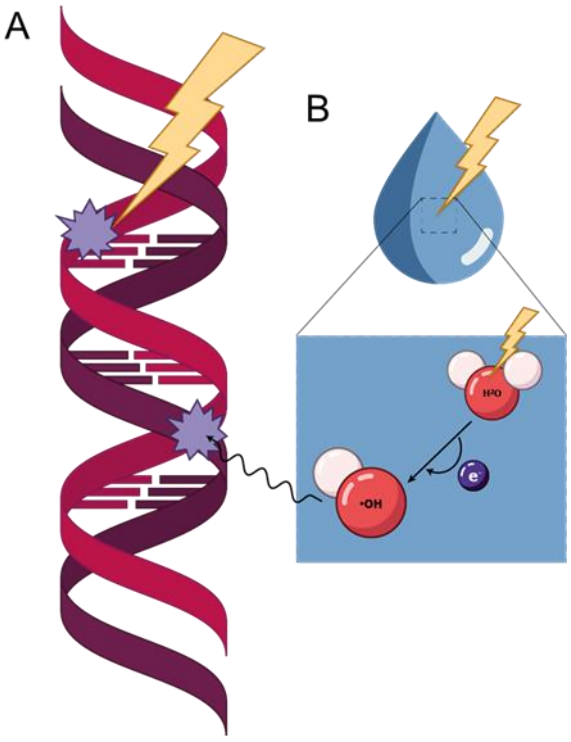

Figure 1.2 - Ionising radiation can induce DNA damage through direct or indirect mechanisms. A – ionising radiation interacts with the DNA double-helix directly, leading to DNA damage. **B** – radiation may also react with other components of the cell, mainly water, leading to the formation of ROS that indirectly damage the DNA.

Double-strand breaks are the most lethal form of radiation-induced DNA damage because they disrupt both strands of the DNA helix, which result in chromosomal aberrations, cell death, or senescence (Penninckx et al., 2021).

1.2.1.1. Cellular response to double-strand breaks

Despite the occurrence of 10^4–10^5 spontaneous DNA lesions a day per cell, which include ≈50 double-strand breaks, cells continue to survive due to the existence of multiple checkpoints to inspect genome damage as well as repair mechanisms that maintain its integrity, collectively known as DNA damage response (DDR) (Nickoloff et al., 2021). While single strand breaks are usually repaired through base excision repair, nucleotide excision repair or mismatch repair, when a DSB occurs, the cell activates signalling pathways to sense, process and repair the damage, and ATM and ATR are the main proteins responsible for coordinating these responses (Groelly et al., 2023). ATM is recruited by the MRN complex, which detects altered DNA, initiating the DDR by phosphorylating downstream proteins such as CHK2 (checkpoint kinase 2) which will then downregulate the activity of cyclin-dependent kinases and activate p53 to halt cell cycle progression. ATM also promotes the phosphorylation of histone H2AX around the DSB site (forming γ-H2AX), which recruits MDC1 (mediator of DNA damage checkpoint protein 1) and other DNA damage mediator proteins like 53BP1 and BRCA1 (Groelly et al., 2023; Qiu & Huang, 2021). After the DNA damage signal has been propagated, the cell repairs the DSB via one of two repair pathways:

- Non-Homologous End Joining (NHEJ) – happens in the G0/1 and S phases of the cell cycle and is initiated by the recruitment of the Ku70/Ku80 complex that binds to the DNA and recruits and activates DNA-PKcs (DNA-dependent protein kinase catalytic subunits) which tether the DNA ends to promote ligation. DNA-end ligation is performed by LIG4, XRCC4 and XLF or PAXX (Figure 1.3). Since it is time efficient, cells preferentially use NHEJ to repair DSBs. However, this pathway is error-prone, as it does not rely on a homologous template for repair (Groelly et al., 2023).
- Homologous Recombination (HR) – this pathway happens in the S and G2 phases of the cell cycle and it uses a homologous DNA strand as a template to perform repair. It is initiated by the MRN complex and CtIP that digest the DNA at the DSB site, creating single-strand DNA (ssDNA) overhangs – DNA

end resection – that are coated by replication protein A (RPA). The RPA-ssDNA complex recruits ATR-interacting protein (ATRIP), which activates ATR. Upon activation, ATR phosphorylates downstream effectors like

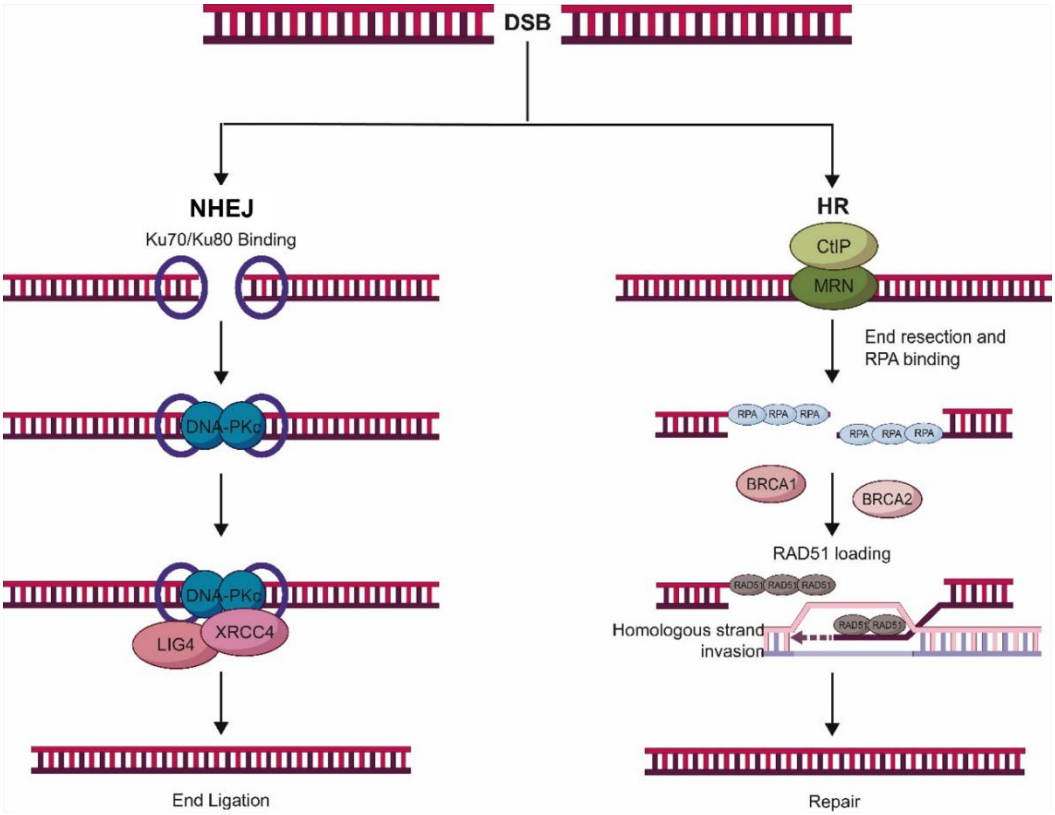

BRCA1, that combined with BRCA 2 and PALB2 load RAD51 onto ssDNA, displacing RPA. RAD51 then forms nucleoprotein filaments that mediate strand invasion into the homologous DNA strand, allowing DNA polymerases to use it as a template for repair (Figure 1.3) (Groelly et al., 2023).

Figure 1.3 - Double-strand break repair pathways. DSBs can be repaired through Non-Homologous End Joining or Homologous Repair. Adapted from (Ketley & Gullerova, 2020).

The fate of a cell after DNA damage depends on several factors, including the extent of damage, the cell type, and its proliferative status (Blanpain et al., 2011). While normal cells can often repair sublethal damage and survive, cancer cells, due to their high rates of proliferation and genetic instability, are more likely to undergo mitotic catastrophe or apoptosis following radiation-induced DNA damage (Liu, Y. et al., 2021).

1.2.2. Radiotherapy in Clinic

Radiotherapy can be administered for different outcomes: it can be curative in early-stage cancers, neo-adjuvant or adjuvant to surgery to shrink tumour size or eliminate residual disease, respectively, or palliative in advance cases to relieve

symptoms (Baskar et al., 2012a). The course of treatment, the type of radiotherapy, and its timing depend on several factors, including the tumour type, size, location, and stage (Demaria et al., 2021). Therefore, the process of radiotherapy planning is individualised and involves multiple steps to ensure the most effective treatment for each patient, like determining the target – which includes the gross tumour volume (GTV), determined by imaging techniques like CT, MRI or PET scans; any microscopic spread which determines the clinical target volume (CTV); and margins to account for patient movement, internal organ motion or setup errors, which together define the planning target volume (PVT) –, planning the patient's immobilisation – which ensures the patient is in a position that is comfortable and reproducible, reducing the risk of systematic set up errors –, dose prescription – based on the cancer type, stage and sensitivity. The dose, usually measured in Gray (Gy), must be high enough to control or eliminate the tumour while minimising the damage to normal tissues, and it is divided into fractions, usually 2 Gy or less a day delivered 5 days a week –, and beam arrangement and optimisation – the angle of shaping of the beams are modulated to match the geometry of the tumour and minimise the exposure of normal tissue to radiation (Barrett et al., 2009).

1.2.2.1. Types of Radiotherapy

There are several types of radiotherapy, categorised based on how the radiation is delivered to the tumour. These include external beam radiotherapy (EBRT), brachytherapy, and systemic radiotherapy. Each has specific applications and techniques depending on cancer type, size, location, and the patient's overall condition (Koka et al., 2022).

External Beam Radiotherapy

EBRT, the most commonly used form of radiotherapy, delivers high-energy beams of radiation – gamma- and X-rays, or electron beams (4 to 25 MV) – to the tumour from outside the body using a linear accelerator (LINAC). Particle radiation, such as proton and neutron beams, can also be used to treat deep-seated tumours (Koka et al., 2022). There are different sub-types of EBRT which include 3D conformational radiotherapy (3D-CRT) – uses imaging techniques like CT (computed tomography), MRI (magnetic resonance imaging) or PET (positron emission tomography) scans to create a 3D image of the tumour to precisely plan the treatment area, i.e. the optimal beam placement, minimising radiation

exposure of healthy tissue. It is used to treat brain, breast, gastrointestinal (GI), lung and gynaecologic malignancies – intensity modulated radiotherapy (IMRT) – a more advanced form of 3D-CRT where the intensity of the radiation beams can be modulated within each treatment session to deliver higher doses of radiation to certain parts of the tumour. It is used to treat head and neck, prostate, breast, brain, lung, gynaecologic and GI tumours – volumetric modulated arc therapy (VMAT) – a variation of IMRT that delivers radiation in a continuous arc around the patient, allowing for greater precision. It is used to treat head and neck, non-small cell lung cancer (NSCLC), prostate, gastrointestinal, gynaecological, thoracic, central nervous system, and breast cancers – image guided radiotherapy (IGRT) – a variation of IMRT that uses imaging to not only plan the treatment but also to guide it during irradiation. It is used to treat prostate, lung, and head and neck tumours – stereotactic body radiation therapy (SBRT) – delivers focused, very high doses to small and well-defined tumours. It is used to treat prostate, head and neck, spinal, renal, and pancreatic malignancies as well as oligo metastases – and particle therapy – like proton beams, which due to a physical property called Bragg peak, are able to deposit the maximum energy at the site of the tumour while minimising damage to exit dose beyond the tumour (Gupta et al., 2012; Koka et al., 2022; National Cancer Institute, 2018).

Brachytherapy

Brachytherapy is a high precision technique used to treat tumours from a short distance, by placing radioactive sources, such as Iridium-192, Iodine-125, Palladium-103, and Caesium-137, on or near the tumour site. These sources can be loaded within body cavities (intracavitary), implanted into tissues (interstitial), within the lumen of organs (intraluminal), or supported in a mould over a tumour (superficial brachytherapy) (Blake, 2007). Depending on the clinical need, brachytherapy can be delivered over different periods of time – permanent or temporary (if the radioactive sources are permanently placed inside the body or are inserted into the tumour or nearby and subsequently removed) – and at different dose rates – low- (0.4-2.0 Gy/h), medium- (2-12 Gy/h), or high-dose rate (>12 Gy/h). Permanent low-dose rate (LDR) brachytherapy is commonly used as a monotherapy for low-grade prostate cancer, by placing small radioactive seeds that are evenly distributed throughout the entire gland, while temporary high-dose

rate (HDR) brachytherapy is often used to treat cervical cancer (Blake, 2007; Lim & Kim, 2021; Stish et al., 2018).

Systemic Radiotherapy

Also known as radiopharmaceutical therapy, systemic radiotherapy uses radionuclides to deliver cytotoxic radiation to cancer cells. The radiopharmaceuticals can either accumulate naturally at the tumour site or target specific cells, through the conjugation of molecules such as peptides and antibodies, and have been used to treat haematological malignancies, thyroid, prostate, breast, hepatic and colorectal cancer (Sgouros et al., 2020).

1.2.2.2. Radiotherapy in breast, prostate cancer, and osteosarcoma

The type of radiotherapy selected depends on tumour location, grade/stage, size, and whether it is localised or metastatic. Other factors include the patient's overall health and the proximity of the tumour to critical structures (Barrett et al., 2009). The table below describes the most commonly used radiotherapy dose escalations for breast cancer, prostate cancer, and osteosarcoma.

Table 1.1 - Most commonly used radiation dose escalations for breast cancer, prostate cancer, and osteosarcoma (Chadha, 2011; Hirsch et al., 2022; Spałek et al., 2021; Teh et al., 2011).

Type	Stage	Technique	Dose
Breast Cancer	DCIS	Adjuvant whole-breast EBRT (3D-CRT or IMRT) after lumpectomy	Total of 50 Gy in 25 daily fractions + 10 Gy boost in 5 daily fractions OR Total of 46.8 Gy in 26 daily fractions + boost of 14 Gy in 7 daily fractions OR 40.5-42.5 Gy in 15-16 daily fractions with concomitant boost to 4.5-4.8 Gy in 15 fractions, or sequential boost to 10 Gy in 4 daily fractions
	Stage I/II	Adjuvant whole-breast EBRT (3D-CRT or	As above

		IMRT) after lumpectomy. Partial breast irradiation (brachytherapy or EBRT) in select cases.	

	Stage III	Adjuvant EBRT to target breast, axillary and supraclavicular nodes (usually 3D-CRT or IMRT)	Conventional dose – total of 50-50.4 Gt at 1.8 to 2.0 Gy daily. Regional lymph nodes – 50.4 Gy in 1.8 Gy per fraction
	Stage IV (metastatic)	Palliative EBRT for control of symptoms (e.g. bone pain)	Single fraction 8 Gy OR 30 Gy in 10 fractions
Prostate Cancer	Low risk (stage I-II, Gleason ≤6)	If radical prostatectomy is not performed - LDR brachytherapy or IGRT	Brachytherapy: permanent seed implant (110-160 Gy depending on radionuclide) IGRT – 76 to 80 Gy in 1.8-2 Gy per fraction
	Intermediate risk (stage II, Gleason 7)	If radical prostatectomy is not performed – IGRT with or without brachytherapy boost	IGRT only: ≥78 Gy in 43 fractions IGRT + brachytherapy: EBRT 40-50 Gy
	High-risk (stage III, Gleason ≥8)	If radical prostatectomy is not performed – IGRT with or without HDR brachytherapy boost If radical prostatectomy is performed – Adjuvant EBRT	IGRT only: ≥78 Gy in 43 fractions IGRT + brachytherapy: EBRT 40-50 Gy
	Stage IV (metastatic)	Palliative EBRT for control of symptoms (e.g. bone pain)	Single fraction 8 Gy OR 30 Gy in 10 fractions
Osteosarcoma	Localised (stage I & II) non-resectable	IMRT or proton therapy	Case dependent (usually ≈70 Gy, fractioned)
	Advanced/metastatic	Palliative IMRT or proton therapy	Case dependent (usually ≈20 Gy in 5 fractions or single dose 8 Gy)

1.2.3. Disadvantages of radiotherapy

Despite its effectiveness, the use of radiation as a treatment method has many shortcomings, primarily its impact on healthy tissue surrounding the tumour site. To minimise these adverse effects, radiotherapy treatments are often administrated in fractionated doses. Fractionation maximises the potential of tumour growth control without exceeding the tolerance levels of normal cells, reducing the likelihood of severe toxicity (Ghaderi et al., 2022; Marcu, 2010). Moreover, due to intra-tumoral heterogeneity in genotypes and phenotypes of cancer cells as well as a diverseness of tumour microenvironments, different tumour types present different radio-sensitivity (Bleaney et al., 2024). However, the main challenge of radiotherapy is tumour resistance to radiation, often related to hypoxia within the tumour. Since the main mechanism of action of radiation treatment is generating reactive oxygen species that damage cellular DNA, low levels of oxygen represent a major obstacle to treatment. Even though most ROS are formed through the hydrolysis of water molecules, oxygen enhances their effectiveness, by reacting with ROS-damaged DNA, forming peroxides, which make the DNA damage irreversible and lethal (Boulefour et al., 2021). Additionally, tumour cells may also neutralise the ROS generated by radiation by upregulating antioxidant systems, like increasing their glutathione and superoxide dismutase (SOD) levels. This reduces the extent of DNA damage, leading to enhanced survival, radio-resistance, and relapse (Liu et al., 2022). The cell cycle stage at the time of irradiation may also determine response to treatment, as cells are the most sensitive when in the G2/M phase due to DNA condensation, moderately resistant in G1, since they are able to pause the cell cycle and activate DDR, and most resistant in S phase, when they are actively replicating DNA and the DNA damage repair mechanisms are active (Bleaney et al., 2024; Wu et al., 2023). Lastly, radiation therapy is only as effective as the amount of death-inducing DNA damage it can produce. Therefore, tumour cells capable of initiating an effective DNA damage response, undermine this process. By activating or bypassing cell cycle checkpoints, modulating CDK activity and/or recruiting DNA repair enzymes, cancer cells can efficiently repair radiation-induced damage, promoting continued proliferation and contributing to increased radiation resistance (Carlos-Reyes et al., 2021; Liu, Y. et al., 2021; Wu et al., 2023).

To overcome these challenges, the use of radiosensitizers, i.e. agents that enhance the susceptibility of tumour tissue to injury by radiation, is of extreme relevance. This translates in the administration of the same amount of radiation with less nefarious effects to normal tissue therefore improving survival rates and the patients' overall quality of life (Gong et al., 2021).

1.3. Radiosensitisers

As previously mentioned, radiotherapy is a fundamental tool for cancer therapy, with clinical studies revealing that over 50% of cancer patients receive RT in the course of their treatment, and in some cases as a monotherapy. Therefore, there is a need to mitigate the side effects of radiotherapy, concomitantly improving its efficiency (Gong et al., 2021). The use of radiosensitisers aims to address this by either increasing the vulnerability of tumour cells to radiation-induced damage or by impairing their ability to repair it (Deng, S. et al., 2022; Sriramulu et al., 2023). Several chemotherapy drugs are commonly used as radiosensitisers, such as cisplatin, a platinum-based drug that binds to DNA destabilising the double helix which may hinder transcription and replication, and inhibit DNA repair, which in turn sensitises the tumour cells to radiation-induce damage (Dong et al., 2017). Other examples include 5-fluorouracil, a proven radiosensitiser for colorectal cancer that inhibits DNA synthesis, and nimorazole, an oxygen mimetic compound that sensitises hypoxic tumour cells to radiation in pharynx and supraglottic tumours (Lee, Y. et al., 2019; Overgaard et al., 1991; Tang et al., 2017). Tumour-specific targeted radiosensitisers, such as cetuximab – a monoclonal antibody that targets the extracellular component of EGFR, inhibiting its activation – have also been gaining prominence in combined therapies (Zhao et al., 2023).

1.3.1. Cancer nanotechnology

The development of radiosensitisers continues to be a constant-evolving area of research in the field of radiobiology, with the goal of creating more targeted, less toxic compounds. The integration of nanotechnology offers innovative to solutions to the current challenges of radiation therapy (Verma et al., 2018). Nanotechnology is, by definition, all science and engineering that can be applied across different fields like biology, chemistry, and medicine, and uses materials and devices with dimensions on the nanometre scale (1-100nm) (Saini et al., 2010). There is currently a vast number of nanoparticles being studied and

applied to personalised therapeutics, mainly for cancer treatment. Due to their unique characteristics, these nanomaterials allow not only controlled drug delivery and amplification of existing therapies but also sensitive and specific diagnosis and imaging. In the context of radiotherapy, nanoparticles have emerged as a promising class of radiosensitisers due to their ability to improve the delivery and efficacy of radiotherapy (Sim & Wong, 2021; Song et al., 2023). Unlike traditional radiosensitisers, nanoparticles can be engineered to specifically accumulate at the tumour site through the enhanced permeability and retention (EPR) effect – due to high permeability of tumour vessels and dysfunctional lymphatic drainage, macromolecules tend to selectively accumulate in tumour tissues – which allows for more precise radiation targeting. Additionally, their surface can be functionalised with several biomolecules to target specific tumour cells and/or organelles within them, increasing specificity and reducing off-target effects (Kim, J. et al., 2023; Villalobos Gutiérrez et al., 2023).

1.3.2. Gold nanoparticles

In recent years, many nanostructures have been studied and developed for cancer therapy, which include both organic (e.g. polymers and liposomes) and inorganic (e.g. gold and silver) nanocarriers. Nanoparticles (NPs) are particles <100 nm in size and can be class into three groups, depending on their composition – organic (such as dendrimers, micelles and liposomes, are biodegradable and non-toxic), carbon-based (such as fullerenes, graphene, carbon nanotubes and nanofibers) and inorganic (mainly composed of metal, metal oxides, and semiconductor materials) (Villalobos Gutiérrez et al., 2023). The study of gold nanoparticles (AuNPs) has been gaining special prominence in multiple therapeutic and diagnostic modalities, including drug delivery, imaging, and radiosensitisation. This is due to their many distinctive physicochemical properties:

- Straightforward synthesis and size tunability – nanoparticles can be easily synthesised in a range of sizes, which can be accurately controlled. This is important as AuNPs need to be small enough to penetrate tumour tissue but large enough to avoid being cleared in the kidneys or invading into capillaries (Siddique & Chow, 2020; Yang et al., 2022).
- Surface plasmon resonance (SPR) – gold nanoparticles can absorb light at specific wavelengths, giving them photoacoustic and photothermal

properties, useful for hyperthermic cancer treatments (e.g. photothermal and photodynamic therapy) and medical imaging applications (Vines et al., 2019).

- Biocompatibility – gold is inert and non-toxic and presents strong interactions with biomolecules such as enzymes, receptors, and antibodies (D'Acunto et al., 2021).
- Easy surface functionalisation – functionalising the surface of AuNPs with ligands, drugs, or targeting molecules is a straightforward process, allowing their application in diagnostics and targeted therapies (Bai et al., 2020; Yang et al., 2022).
- High atomic number (Z) – the high atomic number of gold makes AuNPs efficiently absorb radiation, which results in significant differences in mass energy absorption compared to soft tissue, allowing for their use as radiosensitisers (Penninckx et al., 2020).

1.3.2.1. Gold nanoparticle synthesis

Even though gold nanomaterials can be synthesised using different methods that produce different compounds – e.g. gold nanocages, nanorods and nanospikes – spherical gold nanoparticles have shown to be the nanostructure that produces the highest cellular responses and the maximum cellular uptake, with the lowest cytotoxicity (Lee, Y. J. et al., 2019; Ma et al., 2017). The first method of gold nanoparticle synthesis was published by Faraday (Faraday, 1857). The formation on AuNPs by chemical reaction is usually a two-step process that consists of reducing gold ions, typically from chloroauric acid, using reduction agents such as borohydrides, citric and oxalic acids, hydrogen peroxide or sulphites; and the stabilisation of the new formed particles, to prevent aggregation, through the use of agents like sodium citrate, thiolates, phosphorus ligands, polymers or surfactants (Daruich De Souza et al., 2019). The most commonly used technique to produce gold nanoparticles nowadays is the Turkevich-Frens method that enables the synthesis of colloidal AuNPs with different sizes (Fuentes-García et al., 2021). Typically, a gold chloride ($HAuCl_4$) solution is heated with vigorous stirring until it reaches the boiling point, after which a solution of trisodium citrate is injected. It is the molar ratio of sodium citrate to $HauCl_4$ that determines the particle size. The synthesis is complete when the colour of the suspension no longer changes, and it usually takes 2-5 minutes (Dong, J. et al., 2020).

1.3.2.2. Surface functionalisation

Functionalisation refers to the surface modification of AuNPs with various molecules, such as polymers, peptides, antibodies, or drugs, with enable specific targeting, improve biocompatibility, and facilitate the delivery of therapeutic agents. Surface functionalisation can be achieved through an array of methods, both physical and chemical, that produce a stable bond between the nanoparticle surface and the functional molecule (Arcos Rosero et al., 2024). One of the most common approaches is the use of thiol compounds, where the sulphur-containing thiol groups (-SH) form covalent bonds with the AuNP surface. These gold-sulphur bonds are highly stable and enable the attachment of other thiol-functionalised ligands. Electrostatic interactions may also be used as a functionalisation method, as AuNPs have a negatively charged surface, which can be exploited to attach positively charged molecules (Salamone et al., 2023; Shiue et al., 2020). Click chemistry, a group of reactions that are fast, simple, versatile, and easy to purify, can also be used to functionalise AuNPs. The most commonly used type of click reaction is the Cu(I)-catalysed 1,3-dipolar cycloaddition of azides and alkynes (CuAAC), which forms a stable triazole ring between azide and alkyne groups. Click chemistry offers the advantage of precise control over the functionalisation process and is particularly useful in attaching bioactive molecules, such as antibodies or peptides, which need to maintain their functional integrity (Chen et al., 2016; Chen, Y. et al., 2017; Hein et al., 2008).

The functionalisation of AuNPs with polymers such as polyethylene glycol (PEG) is widely researched, mainly to improve their biocompatibility and circulation time in the bloodstream. PEG is a hydrophilic synthetic polymer with low immunogenicity, used as a coating agent to prevent aggregation, reduce non-specific binding with cells and proteins and increase cellular uptake. Moreover, PEG extends the circulation half-life of AuNPs *in vivo* by promoting steric stabilisation and control of the surface charge, preventing the formation of protein coronas around the AuNPs, thus avoiding recognition and destruction by the immune system (Okła et al., 2023; Reznickova et al., 2019). Gold nanoparticles can also be functionalised with specific molecules and ligands that promote their delivery to particular sites of the body, which can be of great significance in both imaging and therapy. Some of these include short peptide sequences such as the arginine-glycine-aspartic acid (RGD) peptide, which are often attached to AuNPs to promote binding to cell surface receptors and cell internalisation, as

well as other cell-penetrating peptides such as Tat (transactivator protein) or poly-arginine sequences (R_5-R_9) commonly used for the transport of proteins or nucleic acids (Gessner & Neundorf, 2020; Wu et al., 2017). Other classes of molecules used for AuNP functionalisation include antibodies, which enable specific targeting of cells that express certain antigens; and nuclei acids, such as DNA aptamers and siRNA sequences, useful for targeting specific targets, like proteins or cells, or for gene silencing (Babu et al., 2016; Cruz & Kayser, 2019; Kim et al., 2022b).

1.3.2.3. Gold nanoparticles for imaging and drug delivery

Due to their unique optoelectronic properties, AuNPs can be used as contrast agents for imaging diagnosis and can be employed in techniques such as MRI, CT, and nuclear imaging. Because AuNPs absorb radiation more efficiently than tissues, they can provide clearer and more defined images of tumour sites, which is particularly advantageous when imaging small, early-stage tumours that would otherwise be difficult to detect using standard contrast agents (Khademi et al., 2019; Luo et al., 2021). Moreover, due to their strong and manipulatable optical absorption, resulting from the SPR effect, gold nanoparticles can also be used as a contrast agent in techniques such as photoacoustic imaging, a biomedical imaging modality that offers information about cellular and molecular signatures of tissue by using contrast agents (Li & Chen, 2015).

To improve the specificity and efficacy of existing drugs, gold nanoparticles can also be employed as carriers. This not only allows for a higher delivered dose to tumour cells but also decreases non-specific effects, since due to their small size, AuNPs tend to passively accumulate in tumour tissues through the EPR effect. Additionally, functionalising the nanoparticles with cell-specific moieties can further increase direct delivery of chemotherapeutic agents to cancer cells and modulate drug release (Huang et al., 2023; Kong et al., 2017; Yafout et al., 2021). This active targeting approach further increases the specificity of drug delivery, reducing off-target effects and improving therapeutic efficacy (Bajracharya et al., 2022; Kong et al., 2017). Gold nanoparticles can be directly conjugated with drug molecules through physical absorption, covalent and ionic bonding and can also be engineered to carry multiple therapeutic agents simultaneously, allowing for combination therapies in a single nano-platform. For instance, functionalising the surface of gold nanoparticles with siRNAs and chemotherapeutic drugs, allows

for concurrent tumour growth inhibition and suppression of resistance pathways (Huang et al., 2023; Tunç & Aydin, 2022).

1.3.2.4. Gold nanoparticles as radiosensitisers

Gold nanoparticles are proven radio-sensitizers at kilovoltage (kV) and megavoltage (MV) photon energies, with kV photons producing higher radio-sensitization (Penninckx et al., 2020). As previously mentioned, since gold has a high atomic number, it is capable of absorbing a greater proportion of ionising radiation than biological tissues, which have much lower atomic numbers. Moreover, when interacting with radiation, AuNPs are able to release low energy electrons via the Auger effect, leading to localised energy deposition, therefore increasing the radiation dose delivered to cancer cells (Shrestha et al., 2016). The Auger effect occurs when an atom is excited and an inner-shell electron is released, leaving a vacancy that is filled by another electron from a higher energy level, leading to the release of energy – either a photon is emitted, or the energy is transferred to another electron that is ejected from the atom. This second low energy electron is called an Auger electron (Auger, 1975) (Figure 1.4). Auger electrons can cause damage to the DNA chain by either directly interacting with it, leading to strand breaks, or by interacting with water. When a low energy electron reacts with a water molecule, a hydroxyl radical is produced (•OH) which will then interact with DNA chains inducing single- and double-strand breaks, base modifications, and/or cross-linking (Haume et al., 2016; Zheng & Sanche, 2023).

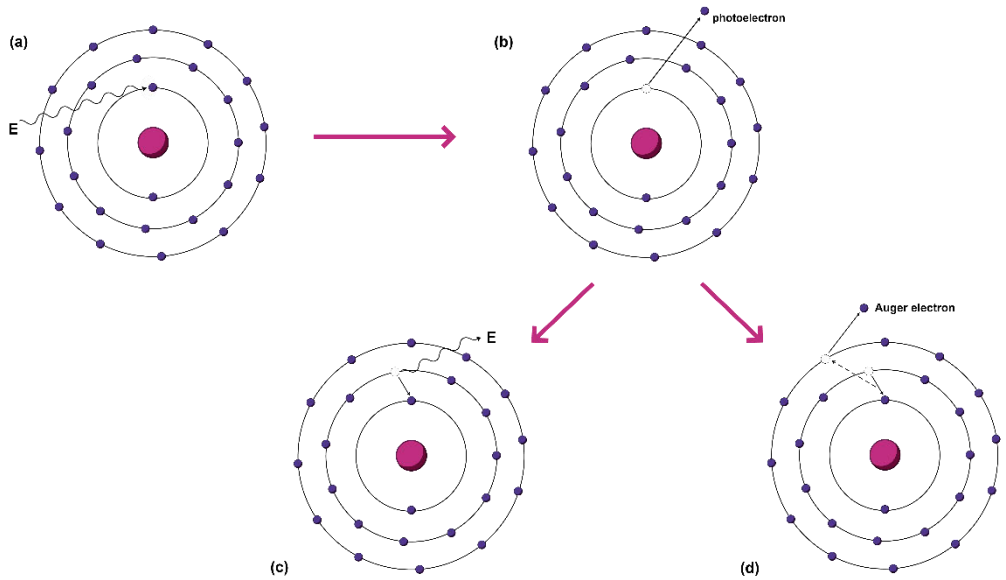

Figure 1.4 - The Auger effect. (a) When an atom is excited by a photon (E), **(b)** this causes an electron from an inner shell to be released. The vacancy left by the latter is filled by an electron from a higher energy level, leading to a release of energy by either **(c)** a photon or **(d)** an auger electron.

The increased ROS production by AuNPs is important in cancer cells, which are often more susceptible to oxidative stress than normal cells due to their altered redox balance. This selective vulnerability means that cancer cells are more likely to undergo cell death in response to increased ROS levels during radiotherapy in the presence of AuNPs. By amplifying ROS production, AuNPs function as radiosensitisers, rendering cancer cells more prone to radiation-induced damage while sparing healthy cells (Abdal Dayem et al., 2017; Cui et al., 2017). The generation of ROS can be monitored through the use of molecules such as dihydrorhodamine 123 (DHR-123) – a known ROS sensor – by tagging them to PEGylated gold nanoparticles and analysing the results using multispectral fluorescence imaging (Choi et al., 2018).

The first evidence of the *in vivo* radiosensitising effect of gold nanoparticles was provided by a study led by Hainfeld (2004), where 1.9nm AuNPs were intravenously injected into mice with EMT-6 mammary xenograft tumours. After irradiation with 250 kVp X-rays, the tumours were completely eliminated in 30 days, and a high sensitisation of AuNPs was observed (Hainfeld et al., 2004). Hainfeld and collaborators further verified this effect by applying AuNPs to different tumour types (Hainfeld et al., 2010, 2013). Since then, the radiosensitising effect of gold nanoparticles has been supported by various experimental data and studies have suggested that the biodistribution of AuNPs,

influenced by their size, shape, surface chemistry and surface modification, is a determining factor for RT efficiency (Chen et al., 2020a; Haume et al., 2016). While undecorated nanoparticles can accumulate in the tumour site through the EPR effect, functionalising them can improve the efficacy of radiotherapy, either by passive targeting – by conjugating the AuNPs with molecules that improve their biocompatibility, circulation time and tumour uptake (like PEG) – or active targeting – by attaching target-specific molecules to the AuNP surface (such as proteins, antibodies and aptamers) (Chen et al., 2020a). For instance, it has been shown that functionalising AuNPs with folic acid increases the rate of cellular uptake, as many tumours upregulate folic acid receptors (Ahmadi Kamalabadi et al., 2022; Samani et al., 2020). Additionally, tagging cell-specific ligands to the surface of AuNPs increases preferential uptake by cells of interest, as shown by Luo et al. (2019) who used gold nanoparticles functionalised with prostate-specific membrane antigen (PSMA) to target tumoral prostate cells in mice. Using fluorophores, they were able to demonstrate preferential uptake of the tagged nanoparticles by the PSMA receptor positive cells (Luo et al., 2019). Hara et al. (2022) used the same functionalisation method *in vitro*, using prostate cancer cell lines to test the effectiveness of targeted AuNPs in boosting the radiation-induced bystander effect (RIBE) – the biological effects that occur in cells that have not been directly exposed to radiation but exhibit similar radiation-induced damage as a result of signals received from nearby irradiated cells. Their results showed that PSMA-functionalised AuNPs not only induced a radiosensitising effect in irradiated cells, but they also boosted the RIBE in non-irradiated cells, treated with the same AuNPs, in contrast to untreated cells, which did not show increased RIBE-associated cell death (Hara et al., 2022). Strategies to localise AuNPs in close proximity to DNA have also been explored. Since the Auger electrons generated during ionisation are low energy and only travel a short distance, targeting the nanoparticles to the nucleus or the mitochondria of the cell can translate in more efficient radiosensitisation as demonstrated by Özçelik and Pratx (2020), who showed high levels of radiation in A549 lung cancer cells, using gold nanoparticles conjugated with PEG, RGD, and NLS (nuclear localisation sequence) that accumulated in the cell nucleus (Özçelik & Pratx, 2020); and Deng et all (2020) who showed that functionalising AuNPs with Triphenylphosphine (TPP) groups leads to their accumulation in the mitochondria. Upon irradiation, the formation of cytotoxic amounts of oxygen radicals triggered the loss of

membrane potential, leading to apoptosis of cancer cells (Deng et al., 2020). Nuclear- and mitochondrial-targeting of AuNPs is further detailed in Chapters 5 and 6 of this thesis.

Gold nanoparticles can be used as radiosensitisers and drug deliverers simultaneously to maximise the potential of both therapies. For example, by functionalizing the AuNPs with Doxorubicin and Trastuzumab, it is possible to inhibit the tumour growth of HER2+ breast cancers and improve the efficacy of subsequent radiation treatments (Żelechowska-Matysiak et al., 2023). Similarly, Khorshid et al. (2023) have designed gold nanoparticles functionalised with anti a HER-2 aptamer for effective targeted delivery of Dasatinib, resulting in higher cytotoxicity induced by the combined effect of radiation-induced damage in radio-sensitised cells and action of the kinase inhibitor Dasatinib (Khorshid et al., 2023). Furthermore, Luan et al. (2022) have demonstrated that by loading acid-responsive gold nanoparticles with Doxorubicin these accumulate preferentially in oesophageal cancer cells, leading to radiosensitisation and specific delivery and release of the chemotherapeutic agent, resulting in higher levels of DNA damage and apoptosis, in a synergistic effect (Luan et al., 2022).

In conclusion, AuNPs have proven to be highly effective radiosensitisers due to their ability to enhance radiation absorption, induce the Auger effect, promote ROS production, and facilitate targeted delivery to cancer cells. These properties allow for more effective radiotherapy with reduced radiation doses, improving patient outcomes and reducing side effects (Chen et al., 2020a; Haume et al., 2016; Zheng & Sanche, 2023). However, despite significant advances in the field, there is still a gap in knowledge when it comes to the use of gold nanoparticles as radiosensitisers in three-dimensional models, with the majority of results coming from monolayer studies. While traditional two-dimensional cell cultures have provided valuable insights into the mechanisms of AuNP radiosensitisation, they often fail to accurately replicate the complex microenvironment of tumours (Gerken et al., 2023). 3D cell models, such as multicellular spheroids and organoids, bridge this gap by better mimicking the structural, biological, and functional characteristics of solid tumours (Gerken et al., 2023; Hoarau-Véchot et al., 2018).

1.4. Aims and Objectives

The aim of this study was to test the hypothesis that 3D cell models become more susceptible to radiation-induced damage and cell death when sensitised with gold-nanoparticles. To assess this, the following objectives were completed:

1- Develop methods for assessing radiotherapy responses in 3D cell culture models and compare radio-sensitivity of 2D and 3D cell culture models.
2- Develop methods to track gold nanoparticle distribution in 3D cell culture models.
3- Investigate the radiosensitising potential of undecorated AuNPs in 2D and 3D cell culture models.
4- Assess the radiosensitising potential of nuclear-targeted gold nanoparticles in 2D and 3D cell culture models.
5- Assess the radiosensitising potential of mitochondrial-targeted gold nanoparticles in 2D and 3D cell culture models.

Chapter 2. Materials and Methods

2.1. Mammalian Cell Culture

2.1.1. Reagents and Materials

Table 2.1 - List of reagents and materials used in mammalian cell culture.

Reagents	**Cat. no.**	**Supplier**
Dulbecco's Modified Eagle Medium (DMEM)	10741574	Gibco, ThermoFisher Scientific
Alpha Modified Eagle Medium (αMEM)	11635190	Lonza
Heat-inactivated Foetal Bovine Serum (FBS)	A5256801	Gibco, ThermoFisher Scientific
Penicillin-Streptomycin	15-140-163	Gibco, ThermoFisher Scientific
Phosphate Buffered Saline (PBS)	10-010-023	Gibco, ThermoFisher Scientific
Trypsin-EDTA	25-200-114	Gibco, ThermoFisher Scientific
MycoAlertTM Mycoplasma Detection Kit	LT07-318	Lonza
0.4% Trypan Blue	17-942E	Lonza
Sodium Chloride (NaCl)	10316943	Fisher Scientific
Calcium Chloride ($CaCl_2$)	11964171	Fisher Scientific
Alginic acid sodium salt from brown algae	9005-38-3	Sigma Aldrich
Sodium Citrate	10183433	Fisher Scientific
EDTA	11408920	Sigma Aldrich
UltraPure™ Agarose	16500500	Invitrogen
Dimethylsulfoxide (DMSO)	786-1323	G Biosciences
Materials		**Supplier**
Culture Flasks (T25/T75/T175)		Nunclon, ThermoFisher Scientific
Stripettes (5mL/10mL/25mL)		Corning
Pipettes (P10/P100/P1000)		ErgOne
Multichannel pipettes (P50/P200)		BRAND
Pipette tips		Starlab
Conical centrifuge tubes (15mL/50mL)		Falcon
Bijoux tubes (5mL)		Corning
Millex® syringe-driven filter unit		Millipore
Microcentrifuge tubes (1.5mL)		Falcon
Countess™ slides		ThermoFisher Scientific
CELLSTAR® 96-well plates with cell repellent surface		Greiner Bio-One
Syringes (2mL/5mL)		Terumo
Agani™ Needle 21G		Terumo
96-well plates		Nunclon, ThermoFisher Scientific
Cryovials		Nunclon, ThermoFisher Scientific
Glass bottles		ThermoFisher Scientific
Equipment		**Supplier**
MCO-170AICUV-PE IncuSafe CO_2 Incubator		PHC
Mega Star 1.6R Centrifuge		VWR
AE2000 Binocular Inverted Microscope		Mitoc

2.1.2. Cell lines

2.1.2.1. PC3

PC-3 cells (CRL-1435) are originated from a bone metastasis of a grade VI prostatic adenocarcinoma from a 62-year-old male. They are an adherent cell line and present an epithelial morphology (Kaighn et al., 1979).

2.1.2.2. LNCaP

LNCaP (CRL-1740) cells are originated from a needle aspiration biopsy of the left supraclavicular lymph node of a metastatic prostate carcinoma from a 50-year-old male. These cells are adherent and can grow as single cells and loosely attached clusters (Horoszewicz et al., 1983).

2.1.1.1. MDA-MB-231

MDA-MB-231 cells (HTB-26) were isolated from a pleural effusion of a 51-year-old female with invasive ductal carcinoma, and present adherent growth properties (Brinkley et al., 1980).

2.1.1.2. MCF-7

MCF-7 cells (HTB-22) were derived from a pleural effusion of a 69-year-old female with metastatic adenocarcinoma. This cell-line presents epithelial features and an adherent growth pattern (Brandes & Hermonat, 1983).

2.1.1.3. MG-63

MG-63 cells (CRL-1427) are originated from the bone of a 14-year-old male with osteosarcoma. They are adherent and have a fibroblast morphology (Billiau et al., 1977).

2.1.1.4. Saos-2

Saos-2 cells (HTB-85) were isolated from a primary osteosarcoma of an 11-year-old female. These cells have an epithelial morphology and present an adherent growth pattern (Banerjee et al., 1996).

All cell lines used in this study were purchased from ATCC and routinely tested for contamination with MycoAlert™ Mycoplasma Detection Kit. For experimental purposes, all cell lines were used between passages 4 and 40.

2.1.3. Cell passaging

PC-3, LNCaP, MDA-MB-231 and MFC-7 cell lines were cultured in Dulbecco's Modified Eagle Medium (DMEM), supplemented with 10% (v/v) heat-inactivated foetal bovine serum (FBS) and 1% (w/v) penicillin/streptomycin.

MG-63 and Saos-2 cell lines were cultured in Alpha Modified Eagle Medium (αMEM), supplemented with 10% (v/v) FBS and 1% (w/v) penicillin/streptomycin. All cell lines were cultured in T175, T75 and T25 flasks, maintained at 37°C, 5% CO_2, and sub-cultured when a confluency of around 80% was reached. For passaging, the media was removed, and the cells were washed with PBS. The flasks were then incubated with trypsin-EDTA (1mL per T25 flask, 2 mL per T75 flask, 3 mL per T175 flask) to allow cell detachment, for 3-5 min at 37°C, 5% CO_2. To stop trypsin action, 4-7 mL of appropriate medium was added. The cell suspensions were then transferred to 50 mL tubes and centrifuged (200 x *g* for 5 min). After removing the supernatant, the pellet was resuspended in fresh medium in a specific volume depending on the intended split ratio.

2.1.4. Cell freezing

To keep low-passage cell stocks, cells were harvested following the previously described method. After the centrifugation step, the pellet was resuspended in 1mL of appropriate medium and a small aliquot of this cell suspension (10 µL) was mixed with a solution of 0.4% trypan blue, in a 1:1 ratio. 10 µL of the trypan blue-cell mixture was then pipetted into the chamber of a Countess™ slide. Using the Countess™ automated cell counter, the number of cells per millilitre and percentage viability were determined.

After counting, the desired volume of cells was centrifuged, and then resuspended in FBS containing 10% DMSO at a density of $1.5x10^6$ cells/mL. The cell suspension was aliquoted into cryovials, which were subsequently placed in a freezing container with isopropyl alcohol. The cryovials were kept at -80°C for 24 hours before being transferred to liquid nitrogen for long-term storage.

2.1.5. Monolayer culture – harvesting cells for radiation treatment

Depending on the assay conducted post-treatment, the cells were either irradiated in suspension or monolayer culture (T25 flasks and 96-well plates).

To determinate the correct number of cells for each assay, cells were harvested and counted using the method described above.

The necessary volume of cell suspension for each experiment was calculated using the following formula:

$$volume\ needed\ (\mu L) = \frac{number\ of\ cells\ needed\ \times 1000 \mu L}{number\ of\ cells\ counted}$$

If the assay to be performed following treatment did not require the use of a 96-well plate or a T25 flask, the cells were irradiated in suspension - due to the dimensions of the metal canister used for irradiation, most vessels have to be placed inside it at an angle of approximately 80°, which can result in media loss or cells drying out. For this purpose, the appropriate volume of cell suspension was pipetted into a bijoux tube containing 2-3 mL of appropriate media. For assays requiring T25 flasks or 96-well plates, cells were seeded at the appropriate density for each experiment.

2.1.6. 3D models

2.1.6.1. Multicellular Tumour Spheroids (MCTS)

MCTS are cohesive cell aggregates that form in low-adhesive plates. The special surface treatment of the wells discourages cell adhesion to the bottom, causing the cells to come together in the centre of the well, where they self-assemble into compact, rounded structures.

To form spheroids, cells were harvested using the method above. After trypsinization and counting, cells were cultured in CELLSTAR® 96-well plates with cell repellent surface at a density of 1.0×10^4 cells per well in 120 µL of appropriate media. Spheroids were grown for 3-5 days at 37°C, 5% CO_2.

2.1.6.2. Alginate spheres

Alginate spheres are three-dimensional cell structures resembling the *in vivo* tissue environment that are formed by encapsulating cells in a gel-like matric using a solution of alginic acid.

2.1.6.2.1. Preparation of Solutions

0.15 M NaCl

8.766 g of NaCl were dissolved in 1 L of dH_2O. The solution was then autoclaved for sterilisation.

0.2 M $CaCl_2$

29.402 g of $CaCl_2$ were dissolved in 1 L of dH2O. The solution was then autoclaved for sterilisation.

1.2% Alginic Acid

To sterilize the alginate powder, a sufficient amount was added to cover the bottom of a petri dish. The powder was then immersed in 70% ethanol and left in the flow hood to evaporate. Once the ethanol had completely evaporated, an appropriate quantity of the sterilized alginate was used to fill a pre-weighed 1.5 mL microcentrifuge tube. The tube's weight was recorded again after adding the alginate. The total content of the tube was then transferred to a previously sterilised glass bottle containing a magnetic flea. To achieve a final concentration of 1.2% (w/v), sterile 0.15 M NaCl was added to the bottle. To ensure the contents were fully dissolved, the alginate solution was left on a magnetic stirrer at room temperature for 24 hours, after which it was stored at 2-8°C.

2.1.6.2.2. Sphere formation

For the preparation of these models, cells were harvested using the previously outlined method. After trypsinization and counting, cells were washed with 0.15M NaCl and resuspended in a solution of 1.2% alginic acid in 0.15 M NaCl at a density of $5.0x10^4$ cells/mL. The cells were gently mixed using a P1000 pipette to avoid the formation of air bubbles for approximately 3 min. Subsequently, the cell/alginate mixture was placed in a sterile syringe. The mixture was then transferred to a sterile syringe and dispersed as droplets into a 0.2 M CaCl2 solution using a 21G needle. The newly formed alginate spheres were incubated for 10min at 37°C, 5% CO_2, and then washed three times with 0.15 M NaCl. Finally, the spheres were transferred to appropriate medium and cultured in upright T25 flasks for 10-15 days, except for spheres used for colony diameter assays (section 2.3.3.), for which they were grown for 3 days.

2.2. Radiation treatment

2D and 3D cell models treated using a using a Caesium-137 (^{137}Cs) source delivering 0.6 MV photon energies at 14.4 s/Gy (Medical School, University of Sheffield). 2D models were treated in suspension or 96-well plates, and 3D models in their respective culturing vessels. Cells were transported using Styrofoam boxes to maintain the incubation temperature for as long as possible and treated with doses between 0.6 Gy and 20 Gy. After treatment, cells were returned to cell culture facilities in the BMRC and incubated at 37°C, 5% CO_2.

2.3. Treatment evaluation assays

After treatment, the effects of radiation were evaluated using an array of different assays: cell viability was determined via imaging, cell proliferation was determined using clonogenic assays (2D) and colony diameter measurements (3D); apoptosis was determined via imaging, and flow cytometry; DNA damage was evaluated by detecting Gamma-H2AX protein levels via Western Blot and its localization using Immunofluorescence; and cell cycle analysis by DNA quantification using Flow Cytometry.

2.3.1. Hoechst 33342/Propidium Iodide (H/PI) assay

Hoechst 33342 (2'-[4-ethoxyphenyl]-5-[4-methyl-1-piperazinyl]-2,5'-bi-1H-benzimidazole trihydrochloride trihydrate) is a permeable nuclear dye that binds to DNA chains. It is excited by ultra-violet light and emits blue fluorescence at 460 to 490 nm.

Propidium Iodide (PI) is a red-fluorescent nuclear stain that intercalates between DNA bases. Contrary to Hoechst 33342, PI is not permeant to live cells, only staining the nucleus of cells with disrupted membranes.

2.3.1.1. Reagents and Materials

Table 2.2. List of reagents and materials used in the Hoechst 33342/Propidium Iodide assay

Reagents	**Cat. no.**	**Supplier**
Hoechst 33342	875756-97-1	Cayman Chemical
Propidium Iodide	25535-16-4	Sigma
PBS, 1X	10-010-023	Gibco, ThermoFisher Scientific
Materials		**Supplier**
Pipettes (P10/P100/P1000)		ErgOne
Multichannel pipettes (P50/P200)		BRAND
Pipette tips		Starlab
96-well plates		Nunclon, ThermoFisher Scientific
Equipment		**Supplier**
MCO-170AICUV-PE IncuSafe CO_2 Incubator		PHC
Mega Star 1.6R Centrifuge		VWR
AE2000 Binocular Inverted Microscope		Mitoc
BioTek Cytation 5		Agilent

2.3.1.2. Experimental procedure

After 24 hours of treatment, cell models were stained with a solution of Hoechst/Propidium Iodide (10 µg/mL in PBS, 1X) and incubated for 20 minutes at 37°C and 5% CO_2. Subsequently, the cell models were imaged using the BioTek Cytation 5 imaging system, and the images were analysed using ImageJ (NIH).

2.3.2. Clonogenic Assay

The clonogenic assay is the gold standard method of determining cell reproductive death after treatment with ionizing radiation *in vitro* (Oike et al., 2020).

2.3.2.1. Reagents and Materials

Table 2.3. List of reagents and materials used in the clonogenic assay.

Reagents	**Cat. no.**	**Supplier**
Acetic Acid	64-19-7	Sigma
Methanol	L13255.0F	ThermoFisher Scientific
Crystal Violet	022866.14	ThermoFisher Scientific
Materials		**Supplier**
6-well/96-well plates		Nunclon, ThermoFisher Scientific
Pipette (P1000)		ErgOne
Pipette tips		Starlab
Stripettes (5mL/10mL/25mL)		Corning
Glass bottles		ThermoFisher Scientific
Equipment		**Supplier**
BX60 Brightfield Microscope		Olympus
CLARIOstar® Plus		BMG LabTech

2.3.2.2. Crystal violet staining

Colony formation in 2D models was assessed by plating cells in Nunc 6-well plates at clonal density ($2.0x10^3$ cells per well) immediately after radiotherapy (RT) treatment. The cells were incubated at 37°C with 5% CO_2, and on the 10th day post-treatment, they were fixed with a 15-minute treatment of acetic acid in methanol (1:9 v/v) at room temperature. Subsequently, the cells were stained with a 0.5% crystal violet solution for 1 hour. To remove the crystal violet stain, the plates were rinsed under running water and left to dry overnight.

2.3.2.3. Colony counting

Colonies were counted the following day using the BX60 Brightfield Microscope. Plating efficiency (PE) was calculated using this formula:

$$PE = \frac{\text{number of colonies formed (control plate)}}{\text{number of cells plated}}$$

And the surviving fraction (SF) was calculated using this formula:

$$SF = \frac{\text{number of colonies formed}}{\text{number of cells plated}} \; x \; \text{PE}$$

2.3.2.4. Absorbance reading

To account for the variation in colony morphology among different cell lines and eliminate potential human error in colony counting, the clonogenic capability of the 2D models was additionally assessed using a plate reader. For this purpose, cells were seeded in Nunc 96-well plates at clonal density ($2.0x10^2$ cells per well) immediately after RT treatment. The cells were then incubated at 37°C with 5% CO_2, and on the 10th day post-treatment, they were stained with crystal violet following the same procedure as described earlier. To establish background levels, wells with no cells were also stained with crystal violet. After the plates dried, the stain was dissolved in methanol (200 µL/well), and the optical density at 570 nm (OD570) was measured using the CLARIOstar® Plus microplate reader. Background interference was accounted for by subtracting the OD570 of the wells without cells from the OD570 of the wells with cells.

2.3.3. Colony diameter measurement in 3D

2.3.3.1. Reagents and Materials

Table 2.4. List of reagents and materials used in the colony measurement assay.

Reagents	**Cat. no.**	**Supplier**
Hoechst 33342	875756-97-1	Cayman Chemical
Propidium Iodide	25535-16-4	Sigma
PBS, 1X	10-010-023	Gibco, ThermoFisher Scientific
Materials		**Supplier**
Pipettes (P10/P100/P1000)		ErgOne
Multichannel pipettes (P50/P200)		BRAND
Pipette tips		Starlab
96-well plates		Nunclon, ThermoFisher Scientific
Equipment		**Supplier**
MCO-170AICUV-PE IncuSafe CO_2 Incubator		PHC
BioTek Cytation 5		Agilent

2.3.3.2. Experimental procedure

For this assay, alginate spheres were irradiated three days post-formation, to ensure the colonies were in a young state with growth potential post-treatment. Before irradiation, on the treatment day, three spheres were stained with H/PI, and bright-field as well as DAPI+Texas Red fluorescent Z-stack images of the spheres were captured using the BioTek Cytation 5 (Agilent, United States). The colony measurements were performed using ImageJ (NIH, United States). Following the treatment, the spheres were returned to the incubator, and the colonies were allowed to grow for an additional seven days at 37°C with 5% CO_2. After this period, the colonies were measured again using the same method.

2.3.4. Flow Cytometry analysis of Annexin V/PI

2.3.4.1. Reagents and Materials

Table 2.5. List of reagents and materials used in the Flow Cytometry analysis of Annexin V/PI.

Reagents	**Cat. no.**	**Supplier**
Alginate dissolving buffer	N/A	N/A
Trypsin-EDTA	25-200-114	Gibco, ThermoFisher Scientific
Cell Staining buffer	420201	BioLegend
Annexin V(APC)/PI staining kit	640932	BioLegend
Materials		**Supplier**
Pipettes (P10/P100/P1000)		ErgOne
Pipette tips		Starlab
Conical centrifuge tubes (15mL/50mL)		Falcon
Microcentrifuge tubes (1.5mL)		Falcon
Round bottom flow tubes		Falcon
Equipment		**Supplier**
FACSCalibur™		BD Biosciences

2.3.4.2. Sample preparation

This assay was performed to confirm the results obtained using the H/PI stain, and apoptosis was determined in 2D using an Annexin V (APC)/PI staining kit. Cells were harvested through the trypsinisation method described in section 2.3.1 and the cell suspensions were washed two times with ice cold cell staining buffer, transferred to 1.5 mL microcentrifuge tubes and resuspended in 200 µL of Annexin-V binding buffer after the final wash. 2 µL of Annexin-V (APC) was added to each tube and cells were incubated at room temperature, in the dark, for 15 min. The stain was washed using Annexin-V binding buffer and resuspended in 300 µL of the same solution. 3 µL of PI were added and the cell suspension was transferred to flow tubes.

2.3.4.3. Flow cytometry analysis

Flow Cytometry analysis of samples was performed using the FACSCalibur™, using the CellQuest™ Pro software. Cell populations were gated using the front scatter (FSC) and side scatter (SSC) channels and single cells were gated using the FL2 channel. Cells positive for Annexin V were detected using the FL4 channel and cells positive for PI were detected using the FL1 channel. Data acquired was processed using the FlowJo software (FlowJo LLC, Becton Dickinson).

2.3.5. Gamma-H2AX detection

DNA double-strand breaks can be monitored by detecting the phosphorylation of the Ser-139 residue of the H2AX histone, an early cellular response to DNA

damage (Mah et al., 2010). This is a common marker used to study the effects of radiation since its mechanism of action is the production of DSB in DNA chains.

2.3.5.1. Immunoblotting

2.3.5.1.1. Reagents and Materials

Table 2.6. List of reagents and materials used in immunoblotting.

Reagents	**Cat. no.**	**Supplier**
CelLytic™ M	C3228	Sigma-Aldrich
cOmplete™ Protease Inhibitor Cocktail (PIC) tablets	04693116001	Roche
PBS, 1X	10-010-023	Gibco, ThermoFisher Scientific
Qubit™ Protein Assay kit	Q33211	Invitrogen
Qubit™ Standards	Q33235	Invitrogen
NuPAGE™ LDS sample buffer (4x)	NP0008	ThermoFisher Scientific
2-mercaptoethanol	60-24-2	VWR
Chameleon® Duo Pre-stained Protein Ladder	928-60000	LiCor
Glycine	10101620	Fisher Scientific
Tris	10376743	Fisher Scientific
Sodium dodecyl sulfate (SDS)	10593355	Fisher Scientific
Marvel Original Dried Skimmed Milk	310663484	Tesco
Sodium Chloride (NaCl)	10316943	Fisher Scientific
Hydrochloric Acid (HCl)	15606880	Fisher Scientific
Tween-20	9005-64-5	Sigma-Aldrich
Antibodies		**Supplier**
Rabbit anti-Human Histone H2AX [p Ser139] – clone NB100-384		NovusBio
Mouse anti-Human βactin – clone mAbcam 8226		Abcam
Goat anti-mouse IRDye 680RD		LiCor
Goat anti-rabbit IRDye 800CW		LiCor
Materials		**Supplier**
Pipettes (P10/P100/P1000)		ErgOne
Pipette tips		Starlab
Qubit™ Assay tubes		Invitrogen
4-20% Precast Gels Mini-PROTEAN® TGX™		BioRad
Trans-Blot® Turbo™ RTA Mini 0.2µm Nitrocellulose Transfer Kit		BioRad
Equipment		**Supplier**
Axygen® Axyspin Refrigerated Microcentrifuge		Axygen, Corning
Qubit™ Fluorometer		Invitrogen
MiniPROTEAN® Handcast System		BioRad
Trans-Blot® Turbo™ Transfer System		BioRad
Odyssey Scanner		LiCor

2.3.5.1.2. Preparation of solutions

Lysis Buffer

One cOmplete™ Protease Inhibitor Cocktail (PIC) tablet was dissolved in 1mL of PBS and stored at -20°C. Before each extraction, 150 µL of this solution were added per 1 mL of CelLytic™ M.

10X SDS Running Buffer (25 mM Tris pH 8.3, 250 mM glycine, 0.1% w/v SDS)
30.2 g of Tris were dissolved in 900 mL of dH_2O and the pH was measured and adjusted to 8.3. Subsequently, 144 g of glycine and 10 g of SDS were added to the solution, along with 100 mL of dH2O, and the solution was placed in a magnetic stirrer overnight to ensure complete dissolution.

10X TBS (20 mM Tris-HCl, 150 mM NaCl)
24 g of Tris and 88 g of NaCl were dissolved in 900 mL of dH_2O and the pH was measured and adjusted to 7.6. To achieve the final volume of 1 L, an additional 100 mL of dH_2O were added.

TBS-T (TBS, 0.1% Tween-20)
100 µL of Tween-20 were dissolved in a previously made solution of 100 mL TBS and 900 mL dH2O.

2.3.5.1.3. Protein extraction
For this assay, 2D cell suspensions were plated in Nunc 6-well plates at a density of $3.0x10^5$ cells/well immediately after RT treatment, while 3D models were simply returned to the incubator in their original culturing vessels. All cell models were harvested 24h post-treatment. Monolayer cultures were washed with ice-cold PBS, and each well was treated with 160 µL of lysis buffer and incubated on an orbital shaker at 4°C. Lysates were collected and transferred to ice-cold 1.5 mL microcentrifuge tubes. Alginate spheres were dissociated using alginate dissolving buffer (55 mM sodium citrate, 30 mM EDTA, 0.15 M NaCl) for 10 min at 37°C, breaking up the beads in solution with a pipette. MCTS were harvested from their wells, centrifuged at 200 x g for 5 min to remove media, washed with PBS and resuspended in trypsin-EDTA to dismantle the spheroids. The samples were incubated for 5 min at 37°C, 5%CO_2 and to ensure full dissociation of the 3D models, these were carefully aspirated and released a few times using a P1000 pipette. The single-cell suspensions obtained from both 3D models were then washed with ice-cold PBS. Cell pellets were resuspended in the appropriate amount of lysis buffer in 1.5 mL microcentrifuge tubes and incubated at 4°C. All samples were then centrifuged at 12000 x g for 10 min at 4°C and supernatants were transferred to new ice-cold tubes.

2.3.5.1.4. Protein quantification

The protein content was quantified using the Qubit™ Fluorometric Quantification assay. Qubit™ working solution was prepared by adding 199n µL of Qubit™ buffer, where n corresponds to the number of samples being analysed + 3 standards included in the kit, to n µL of Qubit™ reagent. Qubit™ tubes were prepared by adding 199 µL of working solution to sample tubes and 190 µL to standard tubes. 1 µL of sample was added to the respective sample tube and 10 µL of each standard were added to the respective standard tube. The fluorescence intensity of the standards was firstly determined to calibrate the Qubit™ Fluorometer (automatic standard curve) followed by the readings of each sample (µg/mL).

2.3.5.1.5. Western blot analysis

SDS-page samples were prepared by mixing the sample volume correspondent to 150 µg of protein to a third of that volume worth of NuPAGE™ LDS sample buffer supplemented with 10% 2-mercaptoethanol. Subsequently, these were boiled in a hot plate at 95°C for 5 min to ensure protein denaturation and left to cool down. 30 µg of protein lysate were loaded on the wells of a 4-20% Precast Gels Mini-PROTEAN® TGX™. Gel electrophoresis was performed on the MiniPROTEAN® Handcast System in 1X running buffer at 120 V for ≈60-90 min. 2µL of Chameleon® Duo Pre-stained Protein Ladder were used as a molecular marker. The gels were then semi-dried transferred onto a nitrocellulose membrane using the Trans-Blot Turbo Transfer System at 25 V, 1,300 A, for 7 min. The transfer sandwich was prepared by soaking the stacking paper, membrane, and gel in transfer buffer (buffer, IMS, water) for 3min and the components were stacked in the following order: stacking paper – membrane – gel – stacking paper. After transfer, membranes were blocked in 5% milk in TBS-T for 1h at room temperature, followed by primary antibody incubation – rabbit anti-Human Histone H2AX [p Ser139] antibody (1:5000 dilution) and mouse anti-Human β-actin antibody (1:2000) – at 4°C overnight. After three washes with TBS-T, the membranes were incubated with Licor secondary antibodies for 1h at room temperature, followed by three more washes with TBS-T. Membranes were visualised and quantified on a LiCor Odyssey Scanner with Image Studio Lite software.

2.3.5.2. Immunofluorescence

2.3.5.2.1. Reagents and Materials

Table 2.7. List of reagents and materials used in immunofluorescence.

Reagents	**Cat. no.**	**Supplier**
Phosphate-buffered saline (PBS)	10-010-023	Gibco
4% Paraformaldehyde in PBS (PFA)	15424389	Fisher Scientific
Tween-20	9005-64-5	Sigma-Aldrich
Triton X-100	9002-93-1	VWR
Bovine serum albumin (BSA)	9048-46-8	Sigma-Aldrich
ProLong™ Diamond Antifade Mountant with DAPI	P36962	Invitrogen
Antibodies	**Cat. no.**	**Supplier**
Rabbit anti-Human Histone H2AX [p Ser139]	NB100-384	NovusBio
Goat anti-Rabbit IgG (H+L) AlexaFluor™ Plus 488	A-11008	Invitrogen
Materials		**Supplier**
Pipettes (P10/P100/P1000)		ErgOne
Pipette tips		Starlab
Stripettes (5mL/10mL/25mL)		Corning
Microcentrifuge tubes (1.5mL)		Falcon
Round coverglass (⌀ 13mm)		VWR
Superfrost™Plus Adhesion Microscope Slides		Epredia
Equipment		**Supplier**
LSM 800 Confocal Microscope		Zeiss

2.3.5.2.2. Immunofluorescence assay

To locate the Gamma-H2AX foci, suspensions of 2D cultures were plated in Nunc 24-well plates containing sterile round coverslips (⌀ 13 mm) at a density of $7x10^4$ cells/well, directly after RT. The Gamma-H2AX stain was performed inside the wells. To remove the media, the samples were rinsed with PBS three times, after which they were fixed in PFA for 20 min at room temperature. PFA was removed, and the samples were washed with PBS, followed by permeabilization with 0.1% Triton X-100 in PBS for 15 min at room temperature. Following three consecutive washes with PBST the samples were incubated in 2% Bovine Serum Albumin (BSA) at room temperature for 1h and subsequently in primary antibody (1:5000 dilution in BSA) at 4°C overnight. The following day, excess primary antibody was removed with three consecutive washes of PBS-T and the samples were incubated for 1h in a fluorescent dye-labelled secondary antibody at a concentration of 5 µg/mL diluted in BSA, at room temperature and protected from the light. Finally, following three further PBST washes, ProLong™ Diamond Antifade Mountant with DAPI was used to mount the slides, which were left to cure for at least 24h at 4°C before visualization.

2.3.5.2.3. Confocal imaging and analysis

Imaging was performed in the Zeiss LSM 800 confocal microscope combined with the Zeiss ZEN 2.3 (blue edition) software for data processing and analysis. For excitatory imaging at 488 nm, a 40x plan-apochromat oil objective and a 488nm diode laser with maximum output of 1.0 % laser transmission were used. Additionally, a 561 nm laser with maximum output of 5.0% laser transmission was used for excitatory imaging at 594 nm. Image acquisition was performed by maximum intensity orthogonal projection of a Z-stack. The analysis of Gamma-H2AX foci was conducted using the same software by processing the captured images using automatic detection of 488 nm fluorescent foci. Using a cell-by-cell analysis, foci were counted using a pre-set threshold value for all the cells in the same image. A singular threshold setup for all images was not possible due to fluctuations of fluorescence between different captured cells. At least 50 cells were captured blindly for counts of Gamma-H2AX foci per replicate.

2.3.6. Cell cycle analysis

2.3.6.1. Reagents and Materials

Table 2.8. List of reagents and materials used in cell cycle analysis by flow cytometry.

Reagents	**Cat. no.**	**Supplier**
PBS, 1X	10-010-023	Gibco, ThermoFisher Scientific
Alginate dissolving buffer	N/A	N/A
Industrial Methylated Spirit (IMS)	10552904	ThermoFisher Scientific
RNAse A	70856-3	Merck
Propidium Iodide	P4864	Sigma-Aldrich
Materials		**Supplier**
Pipettes (P10/P100/P1000)		ErgOne
Pipette tips		Starlab
Conical centrifuge tubes (15mL/50mL)		Falcon
Microcentrifuge tubes (1.5mL)		Falcon
Round bottom flow tubes		Falcon
Equipment		**Supplier**
CytoFLEX		Beckman Coulter

2.3.6.2. Sample preparation

To investigate cell cycle arrest following RT treatment, cells were stained with Propidium Iodide and analysed through flow cytometry. As mentioned before, PI is a fluorescent dye that binds to the cells' DNA. In this case, when the cells are subjected to flow cytometry, the fluorescence emitted from the dye is proportional to their DNA content.

The cell cycle consists of the following phases:

1. G0/G1: The cell stays in G1 (or G0, a quiescent-like state) until the extracellular conditions are favourable for replication. In this phase, the DNA content is diploid (2N).
2. S: Period in which the DNA is replicated. By the end of S phase, the cell has twice the DNA content (4N).
3. G2: Gap between the S phase and mitosis. The DNA replication is complete, and cells are preparing for division (4N).
4. M: mitosis – cell division occurs, and each new cell has one copy of each chromosome (2N) (Alberts et al., 2002)

By analysing the DNA content using flow cytometry, it is possible to quantify the relative distribution of the cell population in the different stages of the cell cycle.

Because flow cytometry is dependent on single cells passing through a laser, a single-cell suspension is required for this type of analysis. Therefore, 3D models needed to be dismantled prior to staining. Cells from alginate spheres were released by dissolving the alginate scaffold in approximately 500 µL of alginate dissolving buffer (55 mM Sodium Citrate, 30 mM EDTA, 0.15 M NaCl*)* per bead. The spheres were incubated in this solution for 10min at 37°C, 5% CO_2. Subsequently, colonies were centrifuged for 5min at 200 x *g*. To further dissociate the colonies, the cell pellet was resuspended in trypsin-EDTA and incubated at 37°C, 5% CO_2 for 3-5 min. The solution was then mixed thoroughly using a P200 pipette, to ensure disaggregation of these models, until a single-cell suspension was acquired.

The MCTS were harvested from the ULA plates, dissociated using trypsin-EDTA and incubated at 37°C, 5% CO_2 for 5-10 min until a single cell suspension was obtained.

2D cells were harvested from their culturing vessels using the trypsinisation method described in section 2.1.3.

The obtained cell suspensions were then washed with ice-cold PBS and fixed using ice-cold 70% IMS, added drop by drop and while vortexing, to avoid clumping. Cells were fixed for 1h at -20°C and washed twice with PBS to remove the ethanol. To remove any RNA content, 50 µL of RNAse (100µg/mL) were added to each sample, followed by 300 µL of PI (50µg/mL) in PBS. These were left to incubate at room temperature for 15 min, protected from the light.

2.3.6.3. Flow cytometry analysis

The samples were transferred to flow tubes and analysed on the CytoFLEX, using the CytExpert softare. Cell populations were gated using the front scatter (FSC) and side scatter (SSC) channels and single cells were gated using the SSC and SSC-H channels. PI intensity was measured using the PE channel. The data acquired was processed using the FlowJo software (FlowJo LLC, Becton Dickinson).

2.4. Statistical analysis

All statistical assessments were performed using the GraphPad Prism 7 software (GraphPad Software, Inc), with a significance of $p<0.05$. Data was subjected to Shapiro-Wilk normality test: when a normal distribution was observed, data was analysed using one-way ANOVA followed by Dunnet's *post-hoc* test and multiple *t-tests* followed by the Holm-Sidak correction method of multiple comparisons; non-parametric data was analysed by Conover-Iman multiple comparisons of two groups, followed by Bonferroni correction, as well as a Kruskal-Wallis test for comparison of three or more groups followed by Dunn's correction *post-hoc* test. Asterisks indicate respective statistical significance as follows: *$p<0.05$; **$p<0.01$; and ***$p<0.001$. Detailed p-values are included in the caption of each figure. Normally distributed data is presented as mean with standard deviation, represented as mean±SD, and non-parametric data is presented as median with range, indicated as median±range.

2.5. Gold synthesis and functionalisation

2.5.1. Gold nanoparticle functionalisation attempts

2.5.1.1. Reagents and Materials

Table 2.9. List of reagents and materials used in AuNP functionalisation.

Reagents	**Cat. no.**	**Supplier**
Gold nanoparticles, 50 nm diameter, OD 1, stabilized suspension in 0.1 mM PBS, reactant free	753645-25ML	Sigma-Aldrich
mPEG-SH 2000	11469717	ThermoFisher Scientific
RGD peptide (Custom made)	N/A	ThermoFisher Scientific
NLS-FITC peptide (Custom made)	N/A	ThermoFisher Scientific
Materials		**Supplier**
Pipettes (P1000/P100/P10)		ErgOne
Pipette tips		Starlab
Microcentrifuge tubes (1.5 mL)		Falcon
Equipment		**Supplier**
Heraeus Pico™ 17 Microcentrifuge		ThermoFisher Scientific

Two custom-made peptides were purchased from ThermoFisher Scientific: an RGD peptide – [NH_2]RGDRGDRGDRGDPGC[COOH] – and an NLS-FITC peptide – [NH_2]GGGPKKKRKVGGC[FITC].

2.5.1.2. AuNP functionalisation

The functionalisation of gold nanoparticles was carried out using a method based on the one published by Mackey et al (2013), where gold nanocages and nanospheres are tagged with RGD and NLS peptides (Mackey et al., 2013).

Prior to peptide conjugation, 1 mL of the 0.1 mM PBS 50 nm diameter gold nanoparticles (Sigma) solution was centrifuged at 12000 x g for 15min, and the pellet was resuspended in a 0.2 mM solution of thiol-terminated polyethylene glycol (mPEG-SH 5000). The gold nanoparticles were incubated with PEG for 24h at room temperature, after which excess PEG was removed via centrifugation (12000 x g, 15 min). The pellet was resuspended in 1 mL dH_2O, mixed with 150 µL of 0.5 mM solution of RGD peptide and allowed to incubate for 48h RT. Excess peptide was removed by centrifugation and the RGD-PEG-AuNP pellet was resuspended in 1 mL dH_2O. To this solution, 150 µL of 0.5 mM NLS were added, and the samples were incubated at room temperature for 48h. The excess peptide was removed by centrifugation and the NLS-FITC-RGD-PEG-AuNP pellet was resuspended in cell culture media.

2.5.2. Gold nanoparticle synthesis and TPP-functionalisation

All the synthesis, functionalisation and characterization of gold nanoparticles was carried out by Tiffany Tran with the supervision of Neil Bricklebank.

2.5.2.1. Reagents and Materials

Reagents	**Cat. no.**	**Supplier**
3(bromopropyl)triphenylphosphonium bromide	3607-17-8	Sigma-Aldrich
Sodium thiosulfate ($Na_2S_2O_3$)	7772-98-7	Sigma-Aldrich
Methanol	34860	Merck
Dichloromethane (DCM)	34856	Merck
Gold(III) chloride trihydrate ($HAuCl_4$)	520918	Sigma-Aldrich
Magnesium sulfate ($MgSO_4$)	M7506	Sigma-Aldrich
Sodium Borohydride (NaBH4)	452882	Sigma-Aldrich
Materials		**Supplier**
Thin-layer chromatography plates (Alugram SIL G/UV254)		Fisher
Pasteur pipettes		Fisher
Equipment		**Supplier**
Glassware (round bottomed flasks, beakers, conical flasks)		Fisher Brand
Stirrer Hotplate		Ika
Rotary Evaporator		Buchi Rotavapor R-100
Nuclear Magnetic Resonance Spectrometer		Bruker Avance III Ultra Shield 400 (400MHz) spectrometer
Infrared Spectrometer		Bruker Alpha Platinum ATR spectrometer
UV-visible Spectrometer		Jenway 6715 Spectrophotometer
Mass spectrometer		Finnigan MAT LCQ LC-MS

2.5.2.2. Synthesis of Phosphonium Zwitterion

The 3-triphenylphosphoniopropylthiosulfate zwitterion was synthesised using methods by Ju-Nam and colleagues (Ju-Nam et al., 2006; Ju-Nam, 2007) In brief, 3-bromopropyl triphenyl phosphonium bromide (0.75 mmol) and sodium thiosulfate (1.125 mmol) were dissolved in aqueous ethanol and refluxed for 24 hours. Reaction progress was monitored by thin-layer chromatography (TLC), using 20% methanol: 80% DCM. After reaction completion, the product was extracted using DCM (3x10 mL), the organic layer was collected, and rotary evaporated to give a cream solid. The product was triturated using cold diethyl ether to give an off-white solid product which was characterised by Fourier-transform infrared spectroscopy (FTIR), Electrospray Ionisation Mass Spectrometry (ESI-MS) and Nuclear Magnetic Resonance (NMR).

2.5.2.3. Synthesis of Phosphonium-functionalised gold nanoparticles

Phosphonium-functionalised AuNPs were synthesised based on methods described previously (Chen, 2014; Ju-Nam et al., 2012); To a solution of 3-triphenylphosphinopropyl thiosulfate in DCM (0.19 mmol), potassium tetrachloroaurate (0.095 mmol) was added. The solution was vigorously stirred for 10 minutes until the gold salt had completely dissolved. Reduction was carried out by adding a freshly prepared solution of aqueous sodium borohydride (400 mmolL-1) dropwise with vigorous stirring, and 15 mL of deionised water was added to the mixture. The stirring was stopped after 24 hours, and DCM extractions (3x10 mL) were carried out for the purification of the aqueous phase. The final product remained in aqueous solution.

2.6. Cell incubation with gold nanoparticles

2.6.1. Reagents and Materials

Reagents	**Cat. no.**	**Supplier**
Dulbecco's Modified Eagle Medium (DMEM)	10741574	Gibco, ThermoFisher Scientific
Alpha Modified Eagle Medium (αMEM)	11635190	Lonza
Gold nanoparticles, 0 nm diameter, OD 1, stabilized suspension in 0.1 mM PBS, reactant free	753645-25ML	Sigma-Aldrich
In Vivo Functionalized Spherical Gold Nanoparticles, 50 nm, NLS/FITC labelled, long circulation In Vivo polymer, 2.5 mg/mL, 5 mL, Saline	Custom made	Nanopartz
TPP-conjugated gold nanoparticles in dH_2O	N/A	In house
Materials		**Supplier**
Culture Flasks (T25/T75/T175)		Nunclon, ThermoFisher Scientific
Stripettes (5 mL/10 mL/25 mL)		Corning
Pipettes (P10/P100/P1000)		ErgOne
Multichannel pipettes (P50/P200)		BRAND
Pipette tips		Starlab
96-well plates		Nunclon, ThermoFisher Scientific
Equipment		Supplier
MCO-170AICUV-PE IncuSafe CO_2 Incubator		PHC

2.6.2. Gold treatments

Prior to radiation treatment, all models were incubated in growth media containing non-functionalised gold nanoparticles, NLS-conjugated AuNPs or TPP-conjugated AuNPs at a final concentration of 10 μg/mL for 24h at 37°C, 5% CO_2.

2.7. Mass Spectrometry Analysis

2.7.1. Reagents and Materials

Reagents	**Cat. no.**	**Supplier**
Alginate dissolving buffer	N/A	N/A
4% Paraformaldehyde in PBS (PFA)	15424389	Fisher Scientific
Histogel™	12006679	Epredia
Neg-50™ Frozen Section Medium	11912365	Epredia
Materials		**Supplier**
Pipettes (P10/P100/P1000)		ErgOne
Pipette tips		Starlab
Stripettes (5 mL/10 mL/25 mL)		Corning
Microcentrifuge tubes (1.5 mL)		Falcon
Cork Discs, 20 mm Diameter, 3 mm Thick		Fisher Scientific
Superfrost™Plus Adhesion Microscope Slides		Epredia
Low-Profile Disposable Blades		Leica
Equipment		**Supplier**
CM1860 Cryostat		Leica
LSM 800 Confocal Microscope		Zeiss
NexION 350X ICPMS		PerkinElmer
ImageBio 266		Elemental Scientific Lasers

2.7.2. Sample preparation

2.7.2.1. Monolayer cultures

Following gold nanoparticle treatment, the cells were harvested using the method described in 2.1.3 and the cell pellet was fixed in 4% PFA for 1h at 2ºC. The fixing reagent was removed by centrifugation (200 x g, 5 min) and warm Histogel™ was added to the samples, in a volume equal to the size of the cell pellet. The samples were centrifuged at 300 x g for 1 min and stored in the -80ºC freezer for a minimum of 1h prior to cryosectioning.

2.7.2.2. 3D cultures

Samples were incubated in cell culture media containing gold nanoparticles for 24h, after which they were harvested from their culturing vessels. MCTS were fixed in PFA for 1h, placed in cork disks and covered Neg-50™ Frozen Section Medium. The discs were transferred to the -80ºC freezer and kept for a minimum of 1h prior to cryosectioning. Since the alginate matrix doesn't sustain fixation and produces low-quality sections, the alginate spheres were dissolved prior to

mass spectrometry analysis, using the method detailed in section 2.3.6.2. and the cell pellet treated in the same manner described above, in section 2.7.2.1.

2.7.2.3. Cryosectioning

Prior to laser ablation, the samples were sectioned in the CS1860 Cryostat (Leica). 10 µm sections were collected in Superfrost™Plus Adhesion microscope slides (Epredia) and stored in the -20ºC freezer. In the hour preceding mass spectrometry analysis, the slides were thawed at room temperature.

2.7.3. LA-ICP-MS gold detection in 2D samples

Experiments to determine gold uptake by cells cultured in monolayer were conducted using a NexION 350X ICP-MS (PerkinElmer, USA) coupled to a ImageBio 266 laser unit (Elemental Scientific Lasers, Bozeman MT, USA). The laser was tuned using a NIST glass and the laser parameters were optimised to a 5 µm spot size with a 20 µm/sec scan speed using the XYR shutter and a 4.95 µm overlap. The repetition rate of the laser was set to 400 Hz, and the laser power was operated at 37%. The sample was ablated in a single 8 mm line. The ICP-MS was operated in standard mode using the Syngistix software (PerkinElmer, USA) and ^{13}C, ^{66}Zn and ^{197}Au isotopes were monitored. The resulting raw data from the laser logs was analysed using Microsoft Excel and GraphPad Prism.

2.7.4. LA-ICP-MSI gold localization in 3D cultures

The experiments to localize the gold nanoparticles within 3D cultures were conducted in the same manner described in the section above. The samples were ablated using a raster covering the whole sample or an area of interest and, therefore, variable in size. The ICP-MS was operated in standard mode using the Syngistix software (PerkinElmer, USA) and ^{25}Mg, ^{66}Zn and ^{197}Au isotopes were monitored. The resulting raw data from the laser logs was analysed using Microsoft Excel and GraphPad Prism, for gold quantification. For nanoparticle localization, the data was analysed, and images were produced using the Iolite 4.4.6 software (Elemental Scientific Lasers, Bozeman MT, USA).

2.8. Transmission Electron Microscopy

The TEM work presented in this thesis was carried out by Dr Francis Sweeney, at MERI-SHU, and Dr Christopher Hill at the School of Biosciences of the University of Sheffield.

Suspensions of gold-treated cells were fixed overnight in fresh 3% Glutaraldehyde in 0.1 M PBS at 4ºC. The specimens were then washed twice

with 0.1 M PBS in 30 min intervals at 4ºC. Secondary fixation was carried out in 2% aqueous osmium tetroxide for 1h room temperature and washed in PBS. The samples were then dehydrated through a graded series of ethanol and dried over anhydrous Copper Sulphate. Infiltration was accomplished by placing the specimens in a 50/50 mixture of Propylene oxide/Araldite resin overnight at room temperature, after which the samples were transferred to full strength Araldite resin for 6h-8h at room temperature. Before sectioning, specimens were embedded in fresh resin for 48-72h at 60ºC. Sections of 0.5 µm were obtained using a Reichert Ultracut E ultramicrotome and stained with 1% Toluidine blue in 1% Borax. The sections were examined using a FEI Tecnai transmission electron microscope at an accelerating voltage of 80 Kv. Electron micrographs were taken using a Gatan digital camera.

2.9. Hyperspectral Microscopy

Samples were prepared by seeding PC3 cells at a density of $1.5x10^5$ cells/well in an 8-chamber slide. Cells were allowed to attach to the bottom of the well for 12-24h at 37ºC, 5% CO_2, after which they were treated with 10 µg/mL gold nanoparticle solutions (unfunctionalised 50 nm AuNP and NLS-FITC-AuNP) for 24h at 37ºC, 5% CO_2. Following treatment, the cells were fixed with 4% PFA for 10min at -20ºC. MCTS were treated with the same concentration of AuNPs and harvested from their wells, after which they were processed in the same manner described in section 2.7.2.2. Prior to imaging, all slides were mounted using coverslips and the ProLong™ Diamond Antifade Mountant with DAPI. Following sample preparation, all hyperspectral microscopy work was carried out by Dr Niall Byrne and his team at the School of Pharmacy of Queen's University Belfast.

The samples were imaged using a dark field fluorescent microscope and Ocular software, and the hyperspectral imaging was performed at 60X magnification using spectral angle mapping, with the Envi 4.8 software.

Chapter 3. Comparing *in vitro* radio-sensitivity between 2D and 3D cell culture models

3.1. Introduction

Radiotherapy is one of the most common treatment modalities in cancer, with approximately 50% of patients receiving radiation as part of their treatment plan, and it translates to 40% of curative therapy (Baskar et al., 2012b). Due to its prevalence in cancer care, radiotherapy remains a focal point of cancer research, with special emphasis on the field of radiobiology. This research focuses on understanding the cancer cells' mechanisms of sensitivity and resistance to radiation (Chen & Kuo, 2017), thus providing the rationale for the development of techniques that enable precise dose delivery, minimising the occurrence of side effects, particularly the damage to normal tissue surrounding the tumour site (Choi & Cho, 2016). *In vitro* radio-sensitivity studies play a pivotal role in cancer research and radiation oncology, allowing for precise assessment of cellular response in a controlled environment, leading to the understanding of cellular and molecular interactions as an effect of radiation-induced damage (Claridge Mackonis et al., 2012).

Monolayer culture has been the *gold standard* for the assessment of radiation responses, since growing cells attached to a plastic surface is a reliable, reproducible, and cost-effective method of evaluating cellular behaviour (Kapałczyńska et al., 2018). Intrinsic tumoral responses to radiation can be assessed through a variety of methods. Among these, survival assays that evaluate clonogenic growth after treatment and molecular studies investigating DNA damage repair mechanisms stand out as the most widely recognized techniques (Dunne et al., 2003).

Despite being a valuable tool for prediction of patient response to radiotherapy, these models fail to recapitulate most aspects of an *in vivo* tumour, mainly the three-dimensional configuration that allows effective cell-cell communication and the passing of important survival signals, the presence of a complex tumour microenvironment and extracellular matrix (ECM) that play a critical role in regulating cell behaviour, as well as oxygen and nutrient gradients that create hypoxic areas within the tumour, which play an important role in tumour resistance to treatment (Raitanen et al., 2023). Moreover, there are also fundamental differences regarding cell morphology and proliferation,

differentiation and protein expression that strongly impact response to therapy (Flint et al., 2020; Fontana et al., 2020).

Consequently, the use of 3D cell culture systems that better mimic the *in vivo* tumour structure and biomechanics is of extreme relevance. Such models not only provide a better resemblance to tumoral biology and architecture, but they also have the potential to bridge the gap between *in vitro* and *in vivo* animal models (Hoarau-Véchot et al., 2018). The use of 3D cell models has exponentially grown in recent years, with a wide range of systems being developed including cell aggregates and organoids – grown in low-attachment surfaces or encapsulated in biopolymers and hydrogels – organ-on-chips and 3D bioprinting (Antonelli, 2023). This study focuses on the use of spheroids grown in ultra-low attachment (ULA) conditions and in an alginate matrix.

The most used 3D model in the context of radiobiology studies is the multicellular tumour spheroid (MCTS), which consists of cell clusters formed via forced aggregation in low attachment surfaces (Figure 3.1). These systems can recapitulate architectural and morphological aspects of solid tumours, forming hypoxic cores – an essential characteristic associated with radio-resistance (Wishart et al., 2021).

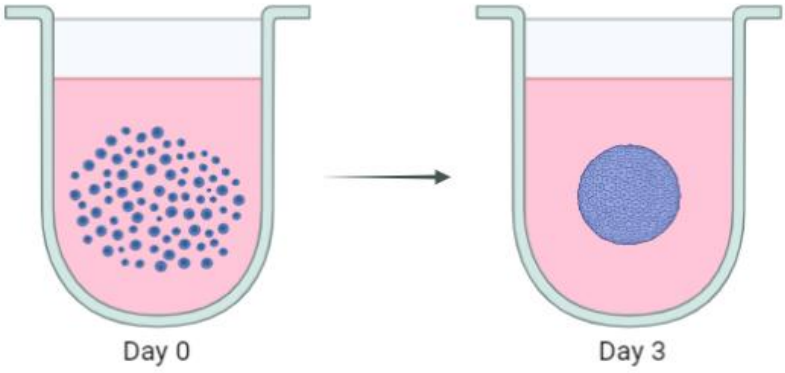

Figure 3.1 - Multicellular tumour spheroid formation. MCTS are formed through the clustering of a single cell suspension in low adhesion plates. Image created using BioRender.

Several research groups have now shown the relevance of using MCTS as platforms for evaluating radiation responses, as these show higher resistance to ionizing radiation, demonstrated by increased cell viability and lower levels of DNA damage (Brüningk et al., 2020; Debeb et al., 2010; Dubois et al., 2019) . While MCTS are the most prominent 3D cell culture model used in radiobiological studies, no single 3D model can fully capture the complexity of the tumour microenvironment (Carter et al., 2021). Therefore, to gain a more comprehensive

understanding of radiation responses in 3D and to gain further insight as to how cancer cells might behave differently in different three-dimensional systems, an alginate-based model was also incorporated in this study.

Obtained from the cell wall of brown algae, alginate is a biopolymer that forms a gel-like structure when in contact with calcium ions. Since it provides *in situ* crosslinking, it is an ideal scaffold for 3D cell culture, being able to encapsulate single cells in isotonic solutions, maintaining physiological conditions of temperature and pH (Ahmad Raus et al., 2021). Like MCTS, alginate cultures also replicate a range of characteristics of *in vivo* tumours, with the additional advantage of the alginate matrix providing physical support for colony growth (Figure 3.2) and a microenvironment with some similarities to the ECM – a complex network of proteins and carbohydrates that play a crucial role in regulating cell behaviour and signalling. Finally, the porosity of alginate also allows for oxygen, nutrient, and growth factor exchange (Ahmad Raus et al., 2021; Kang et al., 2021). Even though alginate spheres have been established as a versatile 3D construct with multiple applications in cancer research, there is still a gap in their use as a platform for radiobiological studies (Read et al., 2018).

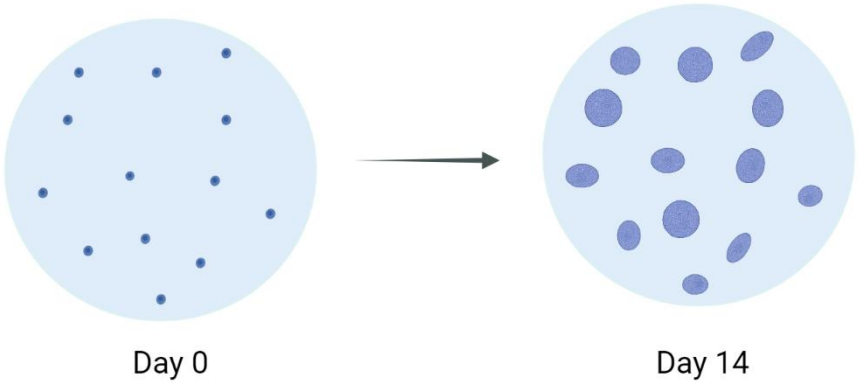

Figure 3.2 - Clonal growth in alginate spheres. Single cells are encapsulated in an alginate-based matrix and incubated for 14 days to allow colony proliferation and spheroid formation. Image created using BioRender.

Overall, it has been systematically proven that there is a need for a shift towards utilizing 3D cell culture models for radiobiological studies, underscored by the evidence presented by several research groups (Table 3.1). This paradigm shift is crucial, since 3D models more accurately mirror *in vivo* conditions of tumour resistance to radiation, enhancing the translation relevance of experimental outcomes in the landscape of radiation research.

Table 3.1 - Studies comparing radiosensitivity between 2D and 3D cell culture models.

Research Group	Cell line(s)	Culture methods	Radiation dose	Output measured	Results
(Fazeli et al., 2007)	DU145 (Prostate carcinoma)	2D vs. 3D spheroids	1 Gy, 3 Gy, 5 Gy	Survival (trypan blue assay), clonogenic potential (clonogenic assay), DNA damage (comet assay).	Lower viability in 2D vs. 3D correlated to higher levels of DNA damage in 2D.
(Bodgi et al., 2019)	RT4, T24, UM-UC-3 (Bladder cancer)	2D vs. 3D Matrigel™-based cultures	2 Gy-10 Gy	Clonogenicity (surviving fraction in 2D vs. sphere forming unit in 3D).	Different cell lines show different results, suggesting 2D and 3D platforms should be used concomitantly
(Koch et al., 2021)	CaCo2, Colo205, HCT116, SW480 - Colorectal cancer (CRC)	2D vs. 3D spheroids	1 Gy, 4 Gy, 10 Gy	Proliferation (Ki67 IHC), apoptosis (TUNEL assay and annexin V/PI flow cytometry), DNA damage (γ-H2AX immunoblotting).	CRC cell lines are more resistant to radiation when cultured in 3D vs. 2D.
(Raitanen et al., 2023)	PC-3, LNCaP (prostate cancer), T-47D (breast cancer)	2D vs. 3D spheroids	1 Gy-20 Gy	Growth analysis (clonogenic and resazurin assays), DNA Damage (γ-H2AX immunoblotting).	Lower radiosensitivity of 3D spheroids compared to monolayer cultures.

3.1.1. Aims of this chapter

Before using radiosensitisers, it is essential to determine the base-level sensitivity to radiation of the 2D and 3D models. To test the hypothesis that 3D cell cultures are more radio-resistant than 2D models and to determine if both 3D models have a similar response to radiation, the aim of this chapter is to assess radiotherapy responses in human osteosarcoma, and prostate and breast adenocarcinoma cell lines grown in monolayer culture and compare them to the responses shown by cells grown in multicellular tumour spheroids and alginate spheres. To achieve this, cell viability post-treatment was measured acutely, using a Hoechst 33342/PI stain, and confirmed with flow cytometry analysis using Annexin V and PI. Clonal growth was evaluated using crystal violet clonogenic assays in 2D and colony diameter measurements in 3D. DNA damage was assessed by determining numbers of γ-H2AX foci through immunofluorescence and cell cycle analysis was performed through the detection of propidium iodide-stained DNA using flow cytometry.

3.2. Results

3.2.1. Sensitivity of cell lines to radiation treatments in 2D colony formation assays.

As previously stated, the clonogenic assay is the *gold standard* method to assess radiotherapy responses in monolayer cultures. Osteosarcoma (MG-63 and Saos-2), prostate adenocarcinoma (PC3 and LNCaP) and breast adenocarcinoma (MDA-MB-231 and MCF-7) cells were irradiated with increasing doses of ionising radiation (0.6 Gy, 1.25 Gy, 2.5 Gy and 5 Gy) and plated at a clonal density ($2x10^3$ cells/well in a 6-well plate). They were then incubated for 10 days to allow colony formation and stained with 0.5% crystal violet (Figure 3.3A). Colonies were counted under the microscope and for the purpose of standardisation, only colonies with 30+ cells were counted. The plating efficiency was calculated by diving the number of colonies of the untreated control by the number of cells plated. The surviving fraction of each dose was obtained by dividing the number of colonies counted by the previously calculated plating efficiency. The surviving fraction values were plotted in log scale (Figure 3.3B) and linear quadratic curves were plotted from which alpha (α) – intrinsic radiosensitivity of cells – and beta (β) – ability of cells to repair sub-lethal damage – values were calculated for each cell line to determine the α/β ratio, a measure of sensitivity of cells to radiation

treatments. The α and β values were calculated by GraphPad Prism, with a confidence interval of 95%. Analysis of each cell line's response to different radiation doses was also conducted and all datasets successfully passed a Shapiro-Wilk normality test at a significance level (alpha) of 0.05. To investigate the level of significance of sensitivity to each radiation dose, each cell line's responses were analysed using one-way ANOVA. Additionally, datasets were subjected to multiple comparisons, using Dunnet's correction as a *post-hoc* test, to assess the significance of the response to each dose, when compared to the untreated control (0 Gy).

The sensitivity of cell lines of the same cancer type was compared by measuring the area under curve (AUC) with a 95% confidence interval and comparing the overlap, followed by a one-way ANOVA test. To assess which *p values* were small enough to investigate further, the multiple comparisons were corrected using the Sidak method with a 95% confidence interval.

3.2.1.1. Sensitivity to radiation of osteosarcoma cell lines.

Ten days post-treatment, the surviving fraction of MG-63 cells was 0.8 (±0.03), 0.72 (±0.06), 0.6 (±0.03) and 0.34 (±0.06) after 0.6, 1.25, 2.5 and 5 Gy doses, respectively. When compared to the untreated control, the reduction in viability is statistically significant at all doses with *p values* <0.001 (Figure 3.3Bi). For Saos-2 cells, the surviving fraction was 0.76 (±0.09), 0.52 (±0.02), 0.25 (±0.03) and 0.07 (±0.03) after treatment with 0.6, 1.25, 2.5 and 5Gy doses of γ-radiation, respectively. The reduction in viability was statistically significant, with *p values* smaller than 0.001 at all doses, when compared to the untreated control (Figure 3.3Bi). Comparing the AUC of both cell lines, the lack of overlap between the two suggests a significant difference in response, which was confirmed using an extra sum-of-squares F-test, that showed Saos-2 presents higher sensitivity to treatment than MG-63 (*p* <0.001). This difference in response is significant at all doses except 0.6 Gy, with a *p value* smaller than 0.001 (Figure 3.3Bi).

3.2.1.2. Sensitivity to radiation of prostate adenocarcinoma cell lines.

Ten days post-treatment, the surviving fraction of PC3 cells was 0.82 (±0.13), 0.68 (±0.13), 0.44 (±0.09) and 0.25 (±0.11) after 0.6, 1.25, 2.5 and 5 Gy doses, respectively. When compared to the untreated control, the reduction in viability is statistically significant at 1.25 Gy, 2.5 Gy and 5 Gy with *p values* of 0.012 at 1.25 Gy and <0.001 at 2.5 Gy and 5 Gy (Figure 3.3Bii). For LNCaP cells, the surviving

fraction was 0.54 (±0.11), 0.31 (±0.10), 0.12 (±0.04) and 0.007 (±0.003) after treatment with 0.6, 1.25, 2.5 and 5 Gy doses of γ-radiation, respectively. The reduction in viability was statistically significant at all doses when compared to the untreated control, with *p values* of smaller than <0.001 (Figure 3.3Bii). The difference in response between PC3 and LNCaP translated by the different AUC of both cell lines was confirmed using an extra sum-of-squares F-test (*p* <0.001). LNCaP was significantly more sensitive than PC3 at all doses, with *p values* of 0.001, <0.001, <0.001 and 0.002 at 0.6 Gy, 1.25 Gy, 2.5 Gy and 5 Gy, respectively (Figure 3.3Bii).

3.2.1.3. Sensitivity to radiation of breast adenocarcinoma cell lines.

Ten days post-treatment, the surviving fraction of MDA-MB-231 cells was 0.81 (±0.10), 0.63 (±0.07), 0.40 (±0.09) and 0.18 (±0.06) after 0.6, 1.25, 2.5 and 5 Gy doses, respectively. When compared to the untreated control, the reduction in viability is statistically significant at all doses of ionising radiation, with *p values* of 0.029 at 0.6 Gy and <0.001 at 1.25 Gy, 2.5 Gy and 5 Gy (Figure 3.3Biii). For MCF-7 cells, the surviving fraction was 0.83 (±0.04), 0.69 (±0.08), 0.46 (±0.10) and 0.19 (±0.08) after treatment with 0.6, 1.25, 2.5 and 5 Gy doses of γ-radiation, respectively. The reduction in viability was statistically significant at all doses of treatment when compared to the untreated control, with *p values* of 0.044 at 0.6 Gy and <0.001 for the remaining doses (Figure 3.3Biii). There were no significant differences between the responses of the two cell lines (Figure 3.3Biii).

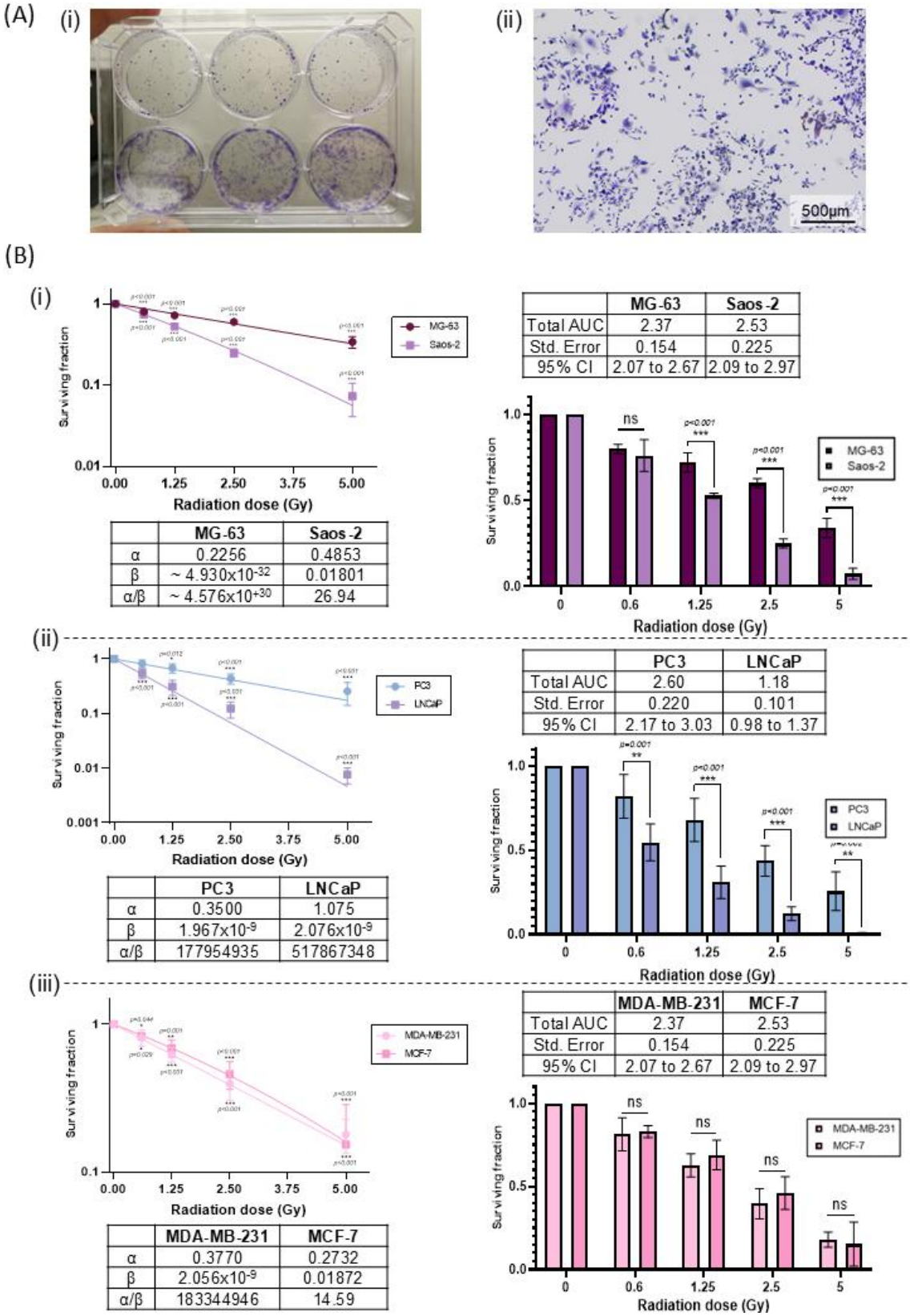

	MG-63	Saos-2
Total AUC	2.37	2.53
Std. Error	0.154	0.225
95% CI	2.07 to 2.67	2.09 to 2.97

	MG-63	Saos-2
α	0.2256	0.4853
β	~ 4.930×10^{-32}	0.01801
α/β	~ $4.576 \times 10^{+30}$	26.94

	PC3	LNCaP
Total AUC	2.60	1.18
Std. Error	0.220	0.101
95% CI	2.17 to 3.03	0.98 to 1.37

	PC3	LNCaP
α	0.3500	1.075
β	1.967×10^{-9}	2.076×10^{-9}
α/β	177954935	517867348

	MDA-MB-231	MCF-7
Total AUC	2.37	2.53
Std. Error	0.154	0.225
95% CI	2.07 to 2.67	2.09 to 2.97

	MDA-MB-231	MCF-7
α	0.3770	0.2732
β	2.056×10^{-9}	0.01872
α/β	183344946	14.59

Figure 3.3 - Cell viability of human osteosarcoma, prostate and breast cancer cell lines 10 days following radiation exposure. (A) colonies were stained with 0.5% crystal violet **(i)** and visualised under the microscopy for colony counting – 10x objective, Cytation5 imaging system, scale bar represents 500 µm **(ii)**. **(B)** Surviving fraction of monolayer cultures 10 days post-treatment. Logarithmic quadratic (LQ) curves were plotted for each cancer type to calculate α/β ratios and area undercurve. The same data from the LQ curve was also

plotted as a bar graph for comparison of responses from cell lines from the same cancer type to each radiation dose. **(i)** LQ, α/β ratio, AUC and Sidak multiple comparisons results from Osteosarcoma cell lines (MG-63 and Saos-2). Surviving fraction data is presented as median ± range, and individual values represent n=3 independent experiments with 3 technical repeats.

3.2.2. Sensitivity of cell lines to radiation treatments in multicellular tumour spheroids 24h post irradiation.

Contrary to observations in monolayer culture, and because of their relatively recent use, there is no *gold standard* method of measuring cell viability in 3D cultures post-radiation treatment. Therefore, it was decided that a simple live/dead stain might be a reliable and reproducible method of assessing cell response to irradiation.

To analyse cell viability, MCTS were generated using the method described in 2.1.6.1. and irradiated using doses of 2.5 Gy, 5 Gy, 10 Gy and 20 Gy. Spheroids were stained with Hoechst33342/PI 24h post-irradiation and imaged on Cytation 5 (Figure 3.4).

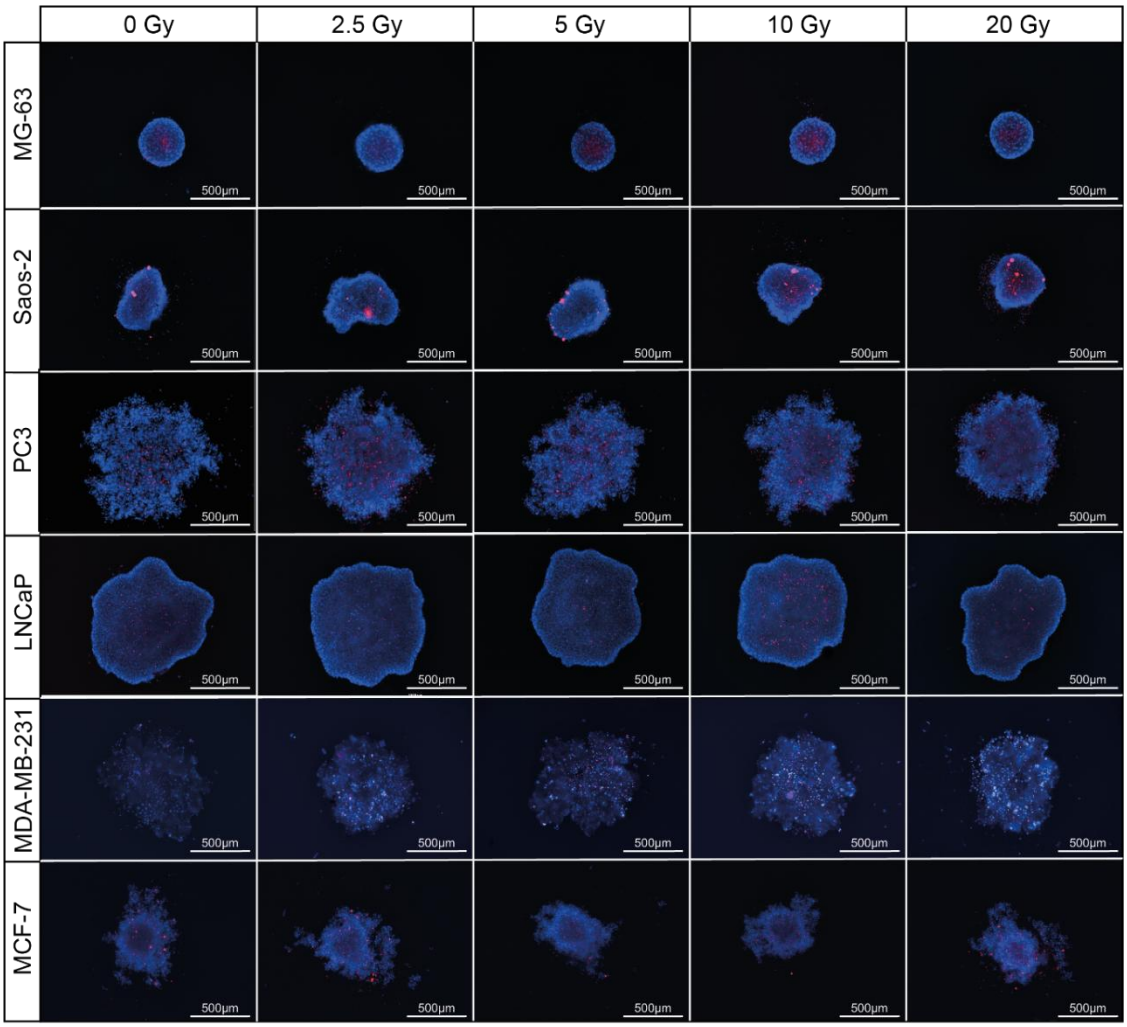

Figure 3.4 - Cell viability of human osteosarcoma, prostate, and breast cancer cell lines, cultured in MCTS, 24h post-radiation treatment. Spheroids from all cell lines remain viable after every treatment dose, as evidenced by the predominance of blue cells (Hoechst 33342-stained, indicating live cells) in comparison to the relatively low number of red cells (PI-stained, indicating dead cells). Cytation 5 imaging system, 4x objective, Z-stack of DAPI and Texas Red channels. Scale bar represents 500µm.

Relative percentage of viable cells was calculated by dividing the area of dead cells – stained with PI - by the total area of the spheroid – stained with Hoechst 33342. These areas were measured using ImageJ (Figure 3.5).

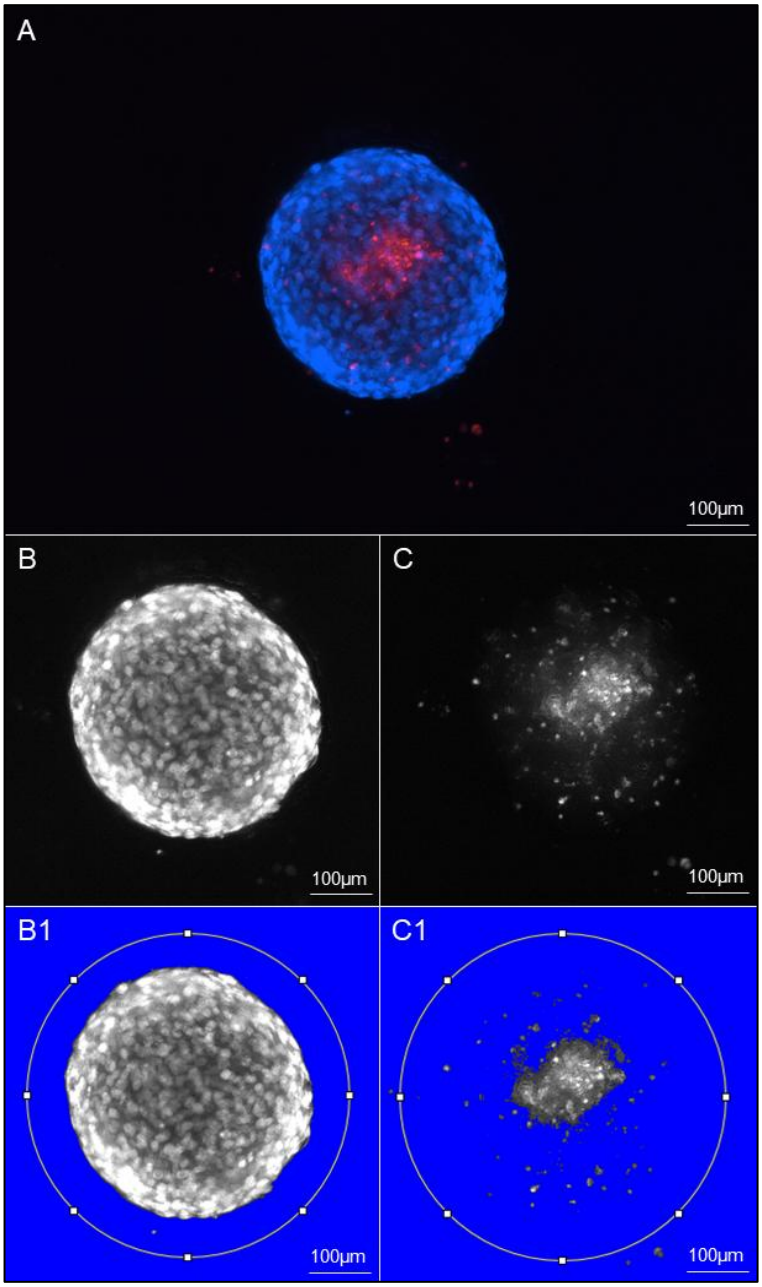

Figure 3.5 - Viability in MCTS after treatment is measured by determining the Hoechst 33342- and PI-stained areas using ImageJ. Starting from the Z-stack image acquired using DAPI and Texas Red **(A)**, the first step is to split these channels into individual images. Once a greyscale of the blue channel **(B)** is obtained, the threshold is adjusted, removing the background, and leaving only the stained spheroid, around which a region of interest (ROI) is drawn **(B1)**. It is then possible to measure the area of blue stained cells. This process is repeated, using a greyscale of the red channel **(C)**. The same ROI and threshold values are then used to measure the area of dead cells **(C1)**. Z-stack images captured using DAPI and Texas Red channels on the Cytation 5 imaging system, 4x objective. Scale bar represents 100 µm.

The viability of each cell line after treatment with each dose of radiation was normalized against its respective untreated control, and the data was plotted as a percentage with the corresponding non-linear regression curves of dose vs. normalised responses (Figure 3.6). The IC50 values were calculated by GraphPad Prism 5.0, with a confidence interval of 95% (Figure 3.6).

All cell lines showed no significant decrease in viability 24h-post treatment when cultured in MCTS, with the IC50 assuming values of 275.1 Gy±124.4 Gy for MG-63, 607.3 Gy±278.4 Gy for Saos-2, 519.9±104.2 Gy for PC3, 796.7±154.2 Gy for LNCaP, 359.2±72.9 Gy for MDA-MB-231 and 753.7±238 Gy for MCF-7. However, these values show no true meaning, due to the lack of dose-dependent response.

Analysis of each cell line's response to different radiation doses was also conducted, and the sensitivity of cell lines of the same cancer type was compared. Due to the skewness of the results, non-parametric tests were used to investigate the level of significance of sensitivity to each radiation dose. Each cell line's responses were analysed using a Kruskal-Wallis test. Additionally, datasets were subjected to multiple comparisons, using the Dunn's correction as a post-hoc test, to assess the significance of the response to each dose, when compared to the untreated control. To compare the sensitivity of cell lines of the same cancer type to each dose of ionising radiation, analysis was conducted using multiple *t-tests* corrected using the Holme-Sidak method with a 95% confidence interval.

Osteosarcoma cell lines showed no sensitivity to treatment at any dose of radiation, with normalised viability of MG-63 being 0.96±0.02, 0.93±0.07, 0.92±0.08, and 0.97±0.05 at 2.5 Gy, 5 Gy, 10 Gy and 20 Gy, respectively (Figure 3.9A), and 1.00±0.01 at 2.5 Gy, 1.00±0.03 at 5 Gy, 0.98±0.04 at 10 Gy, and 0.97±0.05 at 20 Gy for Saos-2 (Figure 3.9C-ii). When compared, the two cell lines showed no significant difference in sensitivity at any dose (Figure 3.6A).

The same was observed in prostate cell lines. For PC3, viability values were 0.98±0.02, 0.98±0.01, 0.97±0.01, and 0.97±0.01 at 2.5 Gy, 5 Gy, 10 Gy and 20 Gy, respectively (Figure 3.6B). For LNCaP these assumed values of 1.00±0.01, 0.99±0.01, 0.99±0.02, and 0.98±0.02 at 2.5 Gy, 5 Gy, 10 Gy and 20 Gy, respectively (Figure 3.6B). Comparing the two, no significant differences are observed (Figure 3.6B).

Breast cell lines also showed the same pattern. MDA-MB-231 cells presented a viability of 0.98±0.02, 0.99±0.02, 0.98±0.01, and 0.95±0.04 at 2.5 Gy, 5 Gy, 10 Gy and 20 Gy, respectively (Figure 3.6C). For MCF-7, viability values were as follows: 0.99±0.01 at 2.5 Gy, 1.00±0.01 at 5 Gy, 1.00±0.01 at 10 Gy, and 0.97±0.03 at 20 Gy (Figure 3.6B). As observed in all the cell lines from other cancer types, the breast cell lines MCF-7 and MBA-MB-231 showed no difference in sensitivity when compared (Figure 3.6B).

.

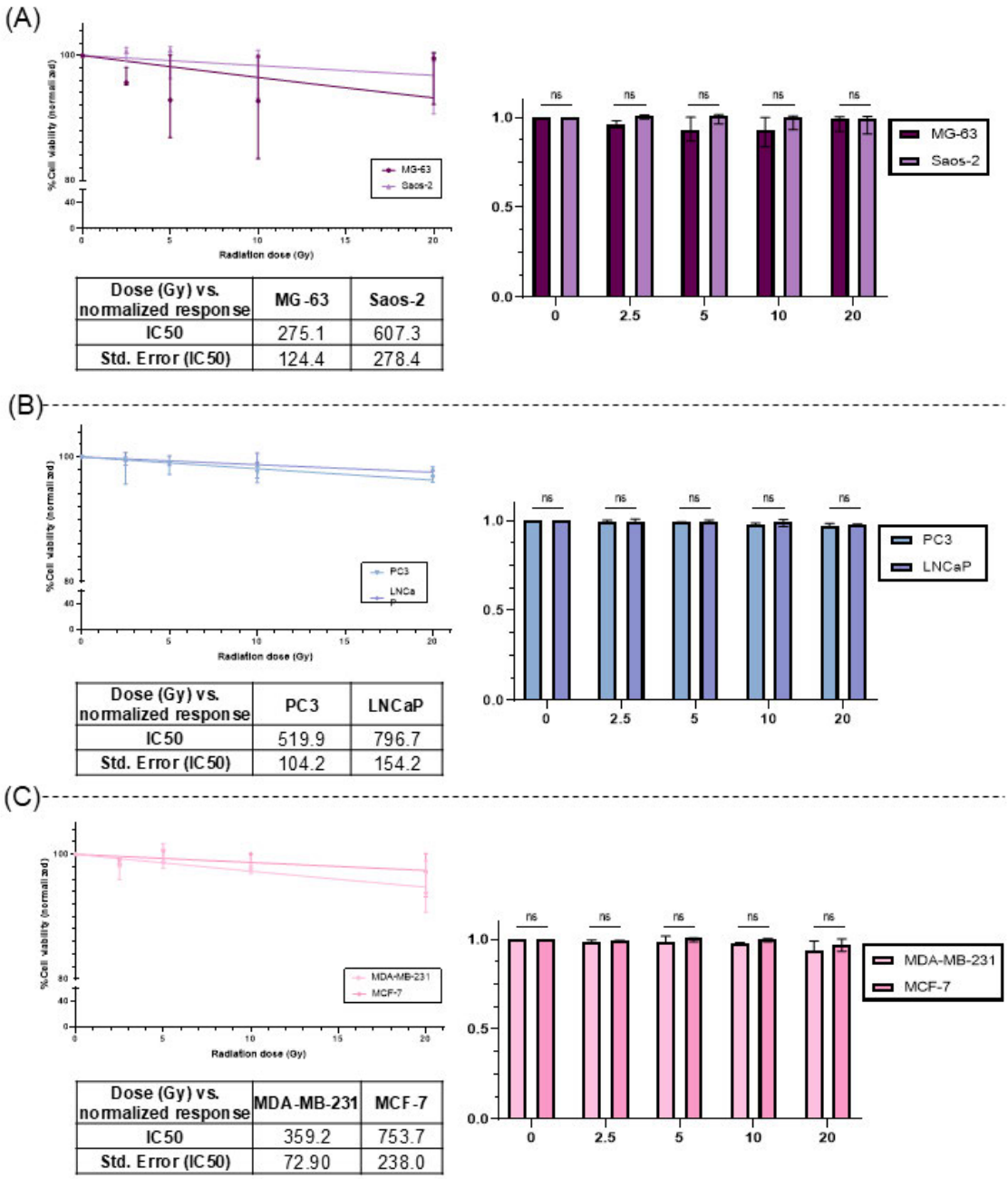

Dose (Gy) vs. normalized response	MG-63	Saos-2
IC50	275.1	607.3
Std. Error (IC50)	124.4	278.4

Dose (Gy) vs. normalized response	PC3	LNCaP
IC50	519.9	796.7
Std. Error (IC50)	104.2	154.2

Dose (Gy) vs. normalized response	MDA-MB-231	MCF-7
IC50	359.2	753.7
Std. Error (IC50)	72.90	238.0

Figure 3.6 – Viability of cells grown in MCTS 24h-post treatment with ionizing radiation. Cell lines present no significant increase in sensitivity with higher doses of radiation. Cell viability of MCTS cultures 24h post-treatment. Scatter plot, percentage cell viability data is presented as median ±range, individual values represent n=3 independent experiments with 3 technical repeats. From the non-linear regression curve, IC50 values were obtained using a 95% confidence interval **(A)** Non-linear regression curve, IC50 values, and Column bar graph, Kruskal-Wallis followed by Dunn's multiple comparisons test (*P<0.05) from Osteosarcoma cell lines (MG-63 and Saos-2). **(B)** Non-linear regression curve, IC50 values, and Column bar graph, Kruskal-Wallis followed by Dunn's multiple comparisons test (*P<0.05) from Prostate adenocarcinoma cell lines (PC3 and LNCaP). **(C)** Non-linear regression curve, IC50 values, and Column bar graph, Kruskal-Wallis followed by Dunn's multiple comparisons test (*P<0.05) from Breast adenocarcinoma cell lines (MDA-MB-231 and MCF-7).

3.2.3. Sensitivity of cell lines to radiation treatments in alginate spheres 24h post irradiation.

Prior to treatment, alginate spheres were prepared using the method described in 2.1.6.2. and irradiated using doses of 2.5 Gy, 5 Gy, 10 Gy and 20 Gy. To assess cell viability after irradiation, alginate spheres were stained with Hoechst 33342/PI 24h post-treatment and imaged on Cytation 5 (Figure 3.7).

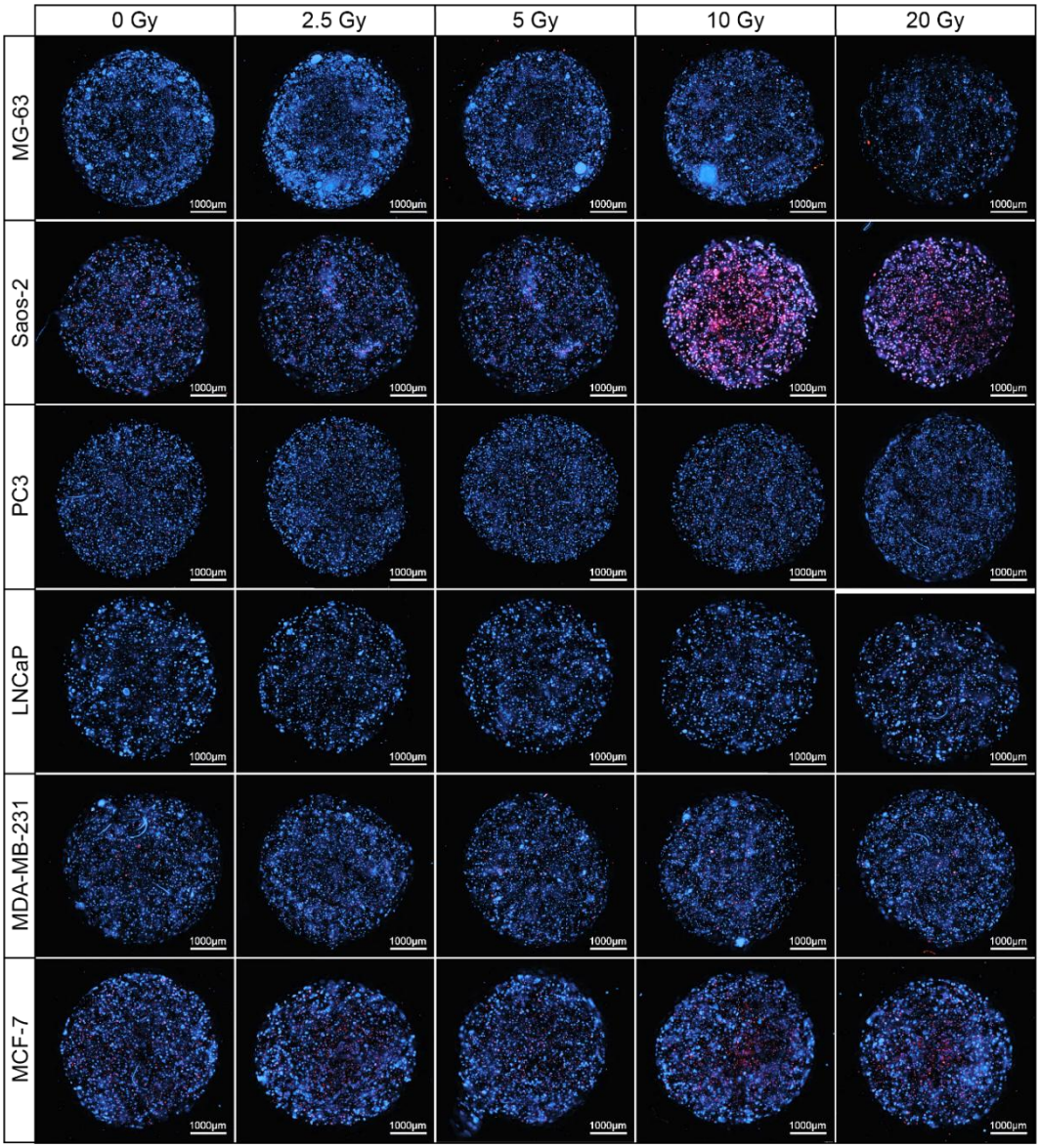

Figure 3.7 - Cell viability of human osteosarcoma, prostate, and breast cancer cell lines, cultured in alginate spheres, 24h post-radiation treatment. Colonies grown in alginate spheres remain viable after every treatment dose, with the majority of cells within the colonies only staining blue (Hoechst 33342 – live cells). This pattern holds true for all cell lines, except for Saos-2 - as the radiation doses increase, there is a noticeable rise in cell death in these colonies, evidenced by the growing number of cells stained with Propidium Iodide (red). Cytation 5 imaging system, 4x objective, Z-stack of DAPI and Texas Red channels. Scale bar represents 1000 µm.

Relative percentage of viable cells was calculated by dividing the number of dead cells – stained with PI - by the total number of cells, stained with Hoechst 33342. These were measured using ImageJ (Figure 3.8).

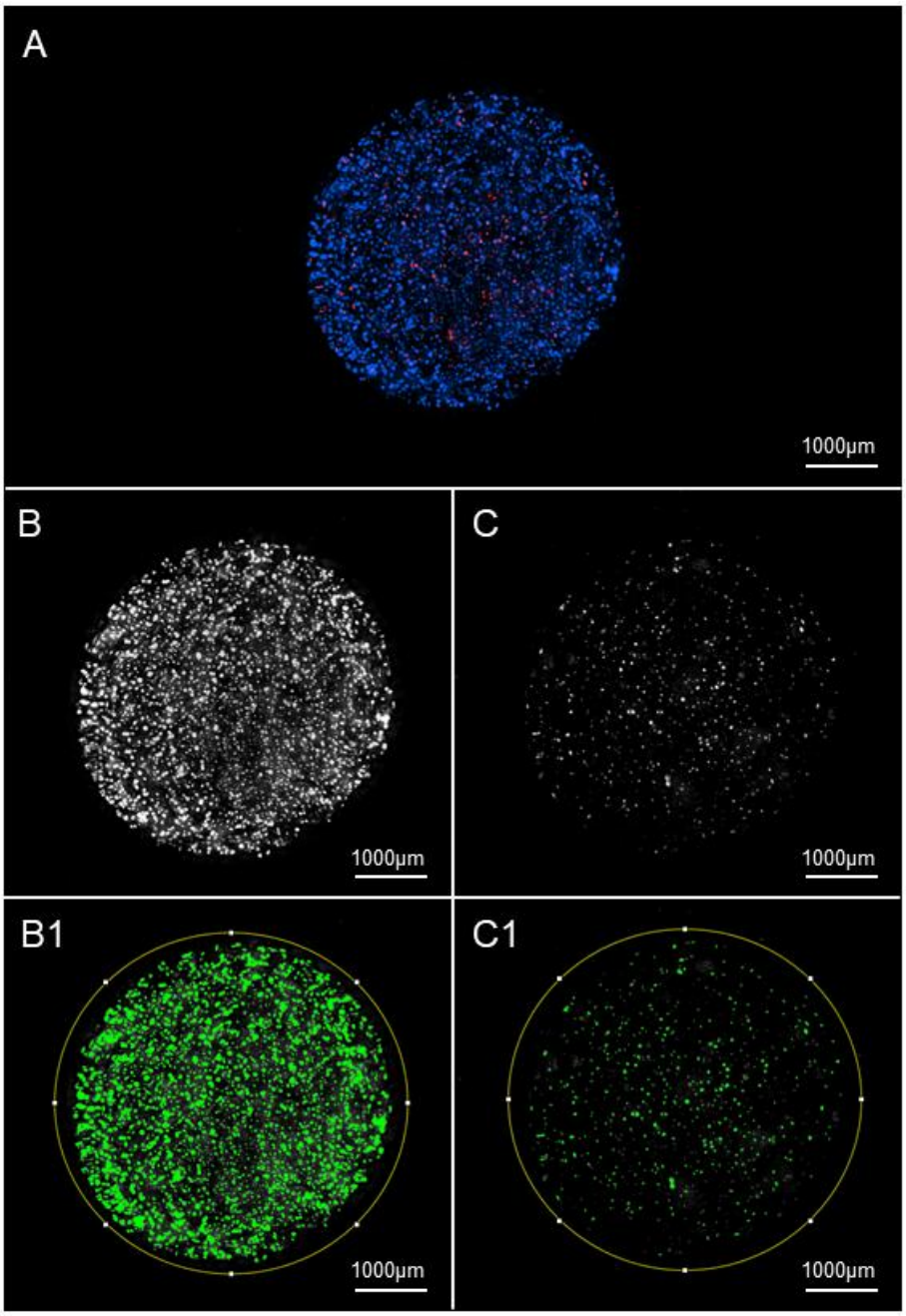

Figure 3.8 - Viability after treatment of colonies grown in alginate spheres is measured by determining what cells present a Hoechst 33342 or PI stain using ImageJ. The Z-stack image acquired using DAPI and Texas Red **(A)**, is uploaded to the software and it is split into the two channels: blue **(B)** and red **(C)**. The threshold is adjusted using the same value for each channel, so the cells stained in blue **(B1)** and red **(C1)** are highlighted and a ROI is drawn around the whole alginate sphere and added to both images. The highlighted areas are then measured by the software. Z-stack images captured using DAPI and Texas Red channels on the Cytation 5 imaging system, 4x objective. Scale bar represents 1000 µm.

The cell viability after radiation exposure of each of the six cell lines used was normalised against each of the untreated controls. The data was graphed as a percentage and non-linear regression curves of dose vs. normalised response were drawn (Figure 3.9). The respective IC50 values were calculated, with a confidence interval of 95% (Figure 3.9). Since only Saos-2 cells showed any sensitivity to treatment, this is the only IC50 value that can be taken into consideration. For the other five cell lines, due to a lack of dose-dependent response, these values hold no true meaning.

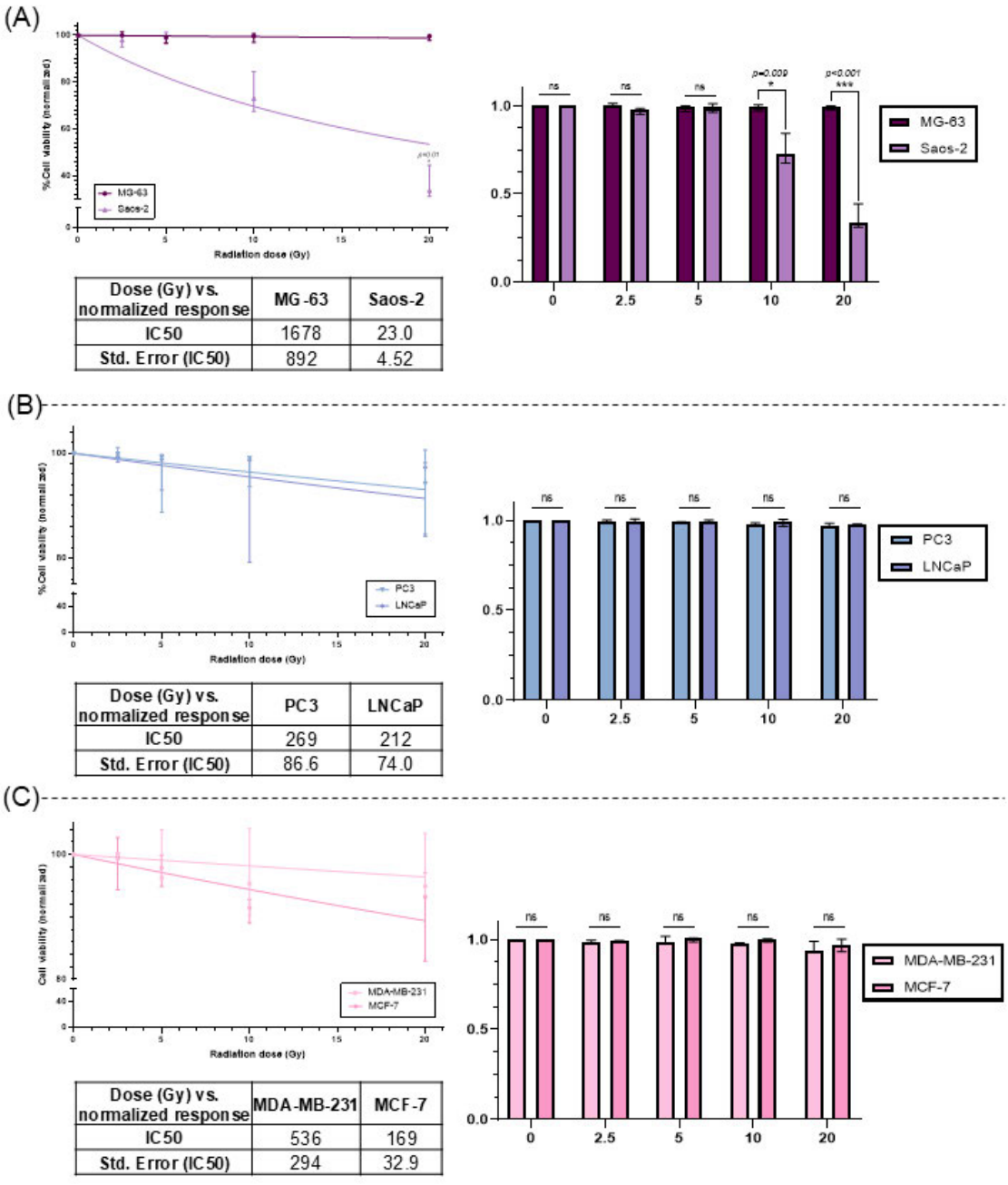

Dose (Gy) vs. normalized response	MG-63	Saos-2
IC50	1678	23.0
Std. Error (IC50)	892	4.52

Dose (Gy) vs. normalized response	PC3	LNCaP
IC50	269	212
Std. Error (IC50)	86.6	74.0

Dose (Gy) vs. normalized response	MDA-MB-231	MCF-7
IC50	536	169
Std. Error (IC50)	294	32.9

Figure 3.9 – Sensitivity of cells cultured in 3D alginate spheres to irradiation 24h post-treatment. Apart from Saos-2, cell lines present no significant increase in sensitivity with higher doses of radiation. Cell viability of alginate sphere

cultures 24h post-treatment. Scatter plot, percentage cell viability data is presented as median ±range, individual values represent n=3 independent experiments with 3 technical repeats. From the non-linear regression curve, IC50 values were obtained using a 95% confidence interval **(A)** Non-linear regression curve, IC50 values, and Column bar graph, Kruskal-Wallis followed by Dunn's multiple comparisons test (*P<0.05) from Osteosarcoma cell lines (MG-63 and Saos-2). **(B)** Non-linear regression curve, IC50 values, and Column bar graph, Kruskal-Wallis followed by Dunn's multiple comparisons test (*P<0.05) from Prostate adenocarcinoma cell lines (PC3 and LNCaP). **(C)** Non-linear regression curve, IC50 values, and Column bar graph, Kruskal-Wallis followed by Dunn's multiple comparisons test (*P<0.05) from Breast adenocarcinoma cell lines (MDA-MB-231 and MCF-7).

Analysis of each cell line's response to the different radiation doses was conducted using a Kruskal-Wallis non-parametric test, due to the skewness of the results. Additionally, datasets were subjected to multiple comparisons, using Dunn's correction as a post-hoc test, to assess the significance of the response to each dose, when compared to the untreated control (0 Gy).

To analyse the response of cell lines of the same cancer type to each radiation dose these were compared using multiple *t-tests*, corrected using the Holme-Sidak method with a 95% confidence interval.

Twenty-four hours post-irradiation, MG-63 cells show a normalised viability of 1.00±0.01, 0.99±0.02, 0.99±0.02, and 0.99±0.01 at 2.5 Gy, 5 Gy, 10 Gy and 20 Gy, respectively. When compared to the untreated control, no significant reduction in viability was observed (Figure 3.9A). Their counterpart, Saos-2, shows no significant decrease in sensitivity to treatment with the first three doses, with the viability of these cells assuming values of 0.97±0.02 at 2.5 Gy, 0.99±0.02 at 5 Gy and 0.75±0.09 at 10 Gy. However, at 20Gy, resistance of these cells to treatment decreases significantly, when compared to the untreated control, with only a 0.36±0.07 fraction of cells remaining viable after treatment. Statistical significance was confirmed with a Kruskal-Wallis test, followed by Dunn's correction, with a *p value* of 0.01 (Figure 3.9A). When compared, Saos-2 proved to be significantly more sensitive than MG-63 at 10 Gy and 20 Gy doses, with *p values* of 0.09 and <0.001, respectively (Figure 3.9A).

For PC3, normalised viability presented values of 1.00±0.01, 0.96±0.06, 0.97±0.03, and 0.93±0.08 at 2.5 Gy, 5 Gy, 10 Gy and 20 Gy, respectively. After statistical analysis, these revealed to be non-significant (Figure 3.9B). For LNCaP viability assumed values of 0.99±0.01, 0.97±0.04, 0.93±0.11, and 0.93±0.07 at

2.5 Gy, 5 Gy, 10 Gy and 20 Gy, respectively (Figure 3.9B). Comparing the two, no significant differences are observed (Figure 3.9B).

Twenty-four hours post-treatment, MDA-MB-231 presented no significant reduction in viability, with the fraction of viable cells being 1.00±0.01, 0.99±0.05, 0.97±0.07, and 0.97±0.07 at 2.5 Gy, 5 Gy, 10 Gy and 20 Gy, respectively (Figure 3.9C). For MCF-7, the viability assumed values of 0.99±0.04, 0.98±0.03, 0.91±0.02, and 0.91±0.07 at 2.5 Gy, 5 Gy, 10 Gy and 20 Gy, respectively. Even though the reduction in viability at 10Gy appears to be statistically significant, when compared to the untreated control, this reduction is biologically insignificant, considering 91% of cells remain viable after treatment (Figure 3.9C). When compared, despite not showing any significant differences at each individual dose (Figure 3.9C), the one-way ANOVA analysis of the overall sensitivity indicates a significant difference in response between MDA-MB-231 and MCF-7 cells, illustrated by a *p value* lower than 0.001.

3.2.4. Resistance to ionising radiation of human osteosarcoma, prostate and breast adenocarcinoma cell lines cultured in 3D models.

Normalised viability in 3D (24h post-irradiation) was compared to the surviving fraction of cells grown in monolayer cultures (10 days post-irradiation) using a two-way ANOVA for comparison of two independent variables (culture model and radiation dose). Sphericity was not assumed; therefore, the Geisser-Greenhouse correction was used. The datasets were then subjected to multiple comparisons, using the Tukey correction method, with a confidence level of 0.05. When compared to monolayer culture, all cell lines show higher resistance to treatment to both 2.5 Gy and 5 Gy radiation doses when cultured in MCTS and alginate spheres (Figure 3.10).

For the MG-63 cell line, the significance of these results is translated into *p values* of 0.001 for both models at 2.5 Gy and of 0.025 and 0.002 at 5 Gy in MCTS and alginate spheres, respectively. In Saos-2, the difference in response is even more accentuated, with *p* assuming values smaller than 0.001 for both models at 2.5 Gy. When irradiated with a dose of 5 Gy, the *p value* of 2D vs. MCTS is once again smaller than 0.001; for 2D vs. alginate spheres significance is shown by a *p value* of 0.02.

Regarding the prostate cancer cell lines: for PC3 cells, the difference in sensitivity is significant at 2.5 Gy for both MCTS and alginate spheres (p=0.016 and p=0.015, respectively). The same occurs at 5 Gy, for both models (p=0.014, comparing 2D vs. MCTS and p=0.015, comparing 2D vs. alginate spheres). As for the LNCaP cell line, both 3D models showed a significantly higher resistance to treatment with both radiation doses, with a *p value* smaller than 0.001 for every comparison.

The breast cancer cell lines showed a similar pattern. In the MDA-MB-231 cell line, MCTS present higher resistance to ionising radiation than 2D models at both 2.5 Gy and 5 Gy (p=0.013 and p=0.004, respectively). Responses in 2D are also more effective than in alginate spheres, with *p values* of 0.013 and 0.002 at 2.5 Gy and 5 Gy, correspondingly. The same is true for MCF-7 cells – when comparing 2D with MCTS models, the difference in response is significant at both 2.5 Gy (p=0.022) and 5 Gy (p=0.002); as for alginate spheres, these also show a higher resistance to treatment when compared to 2D cultures, translated by *p values* of 0.040 at 2.5Gy and 0.003 at 5 Gy.

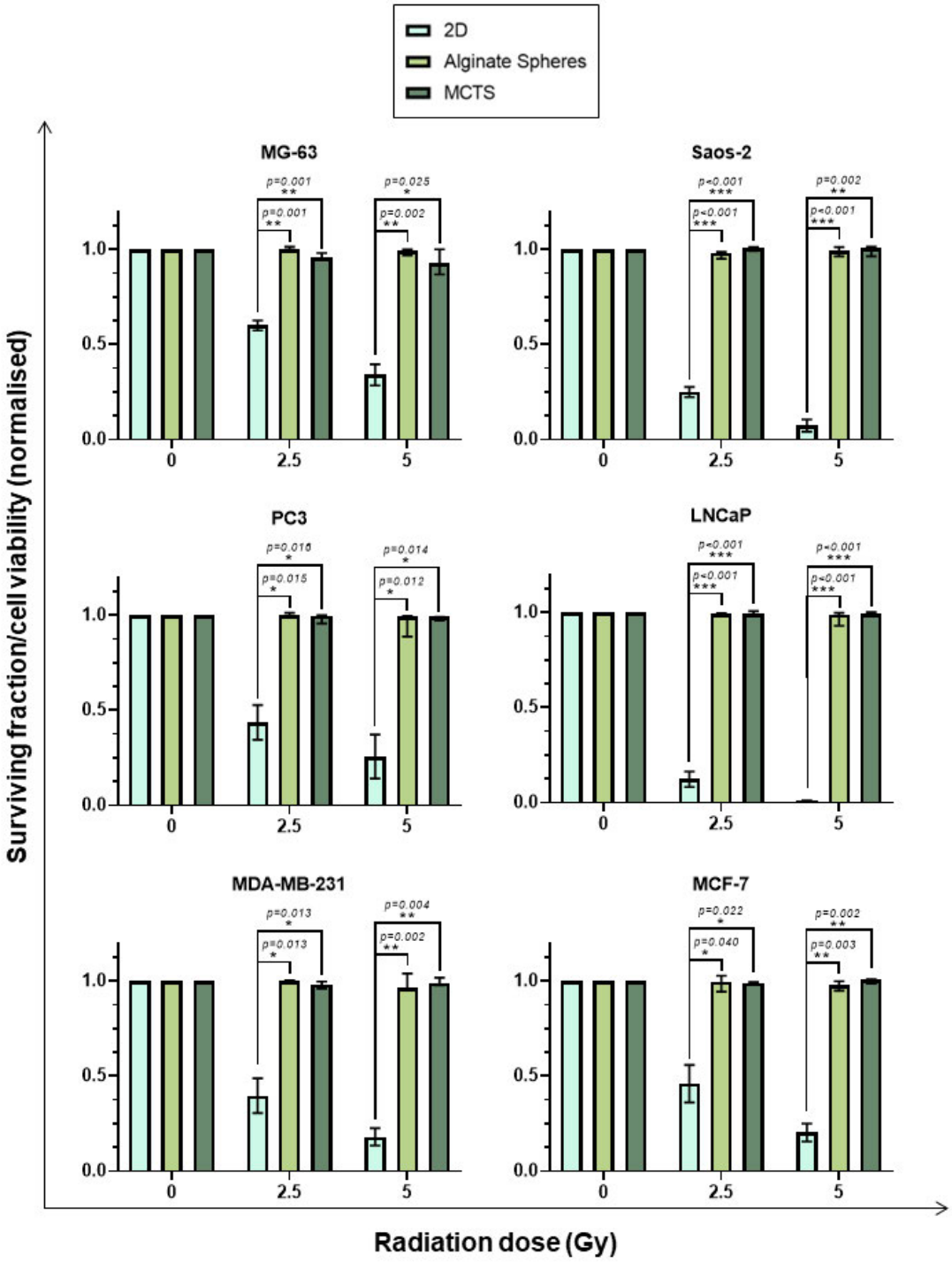

Figure 3.10 - Comparison of responses to ionising radiation between monolayer (after 10 days) and 3D cell culture systems (after 24h). All cell lines show significantly higher sensitivity to treatment when cultured in 2D. Interleaved bars, two-way ANOVA corrected with Geisser-Greenhouse method. Statistical significance corrected using the Tukey method of multiple comparisons, with alpha=0.05. (*P<0.05). 2D data is presented as mean ±SD. 3D data is presented as median ±range and individual values represent n=3 independent experiments with 3 technical repeats. The data presented in this graph has been previously shown in this chapter.

3.2.5. Acute responses to irradiation in 2D cell culture.

After assessing the results of colony formation in 2D it was clear that cells responded to treatment, with the number of colonies decreasing with each increasing radiation dose. Cell viability in 3D cultures was assessed via a live/dead stain that evaluated the acute response of these platforms. Cell viability was measured 24h post-treatment in 3D, rather than 10 days, like in 2D cultures. Therefore, comparing cell viability to colony formation might not be the best indicator of response.

For this reason, acute response to treatment was also measured in 2D, using a Hoechst 33342/PI viability assay 24h after radiation exposure. Due to the increasing volume of samples to be tested and the similar responses between the two breast cancer cell lines, it was decided that moving forward, only prostate cancer and osteosarcoma cell lines would be used. Cells were plated at a density of $1x10^4$ cells/well in a 96-well plate and irradiated with 1.25 Gy, 2.5 Gy, and 5 Gy doses.

To assess response to treatment, the Hoechst/PI-stained cells were imaged on the Cytation 5 (Figure 3.11A) and the percentage of viability was calculated using the instrument's software – Gen5 – that automatically calculates the number of red (dead) and blue cells (total population). The results were normalised against the untreated control and plotted as a dose-response curve (Figure 3.11B) from which the respective IC50 values were calculated (Figure 3.11C).

Contrary to the output from the clonogenic assay, no cell lines showed any sign of sensitivity to treatment 24h post-irradiation, with cell viability remaining above 90% at all radiation doses, for all cell lines. For MG-63, 99.7±0.24%, 99.5±0.25% and 99.5±0.12% viable following 1.25 Gy, 2.5 Gy and 5 Gy doses, respectively. Saos-2 cells showed a viability of 93.9±2.2% at 1.25 Gy, 91.8±1.83% at 2.5 Gy and 91.6±2.3% at 5 Gy. Prostate cancer cell lines showed similar results, with PC3 and LNCaP cells showing viability percentages of 100±0.15% and 99.3±0.18 at 1.25 Gy, 99.3±0.34% and 98.7±0.25% at 2.5 Gy and 99.7±0.11% and 99.7±0.37% at 5 Gy, respectively. Due to the absence of a dose-dependent response, the calculated IC50 values do not have any biological relevance.

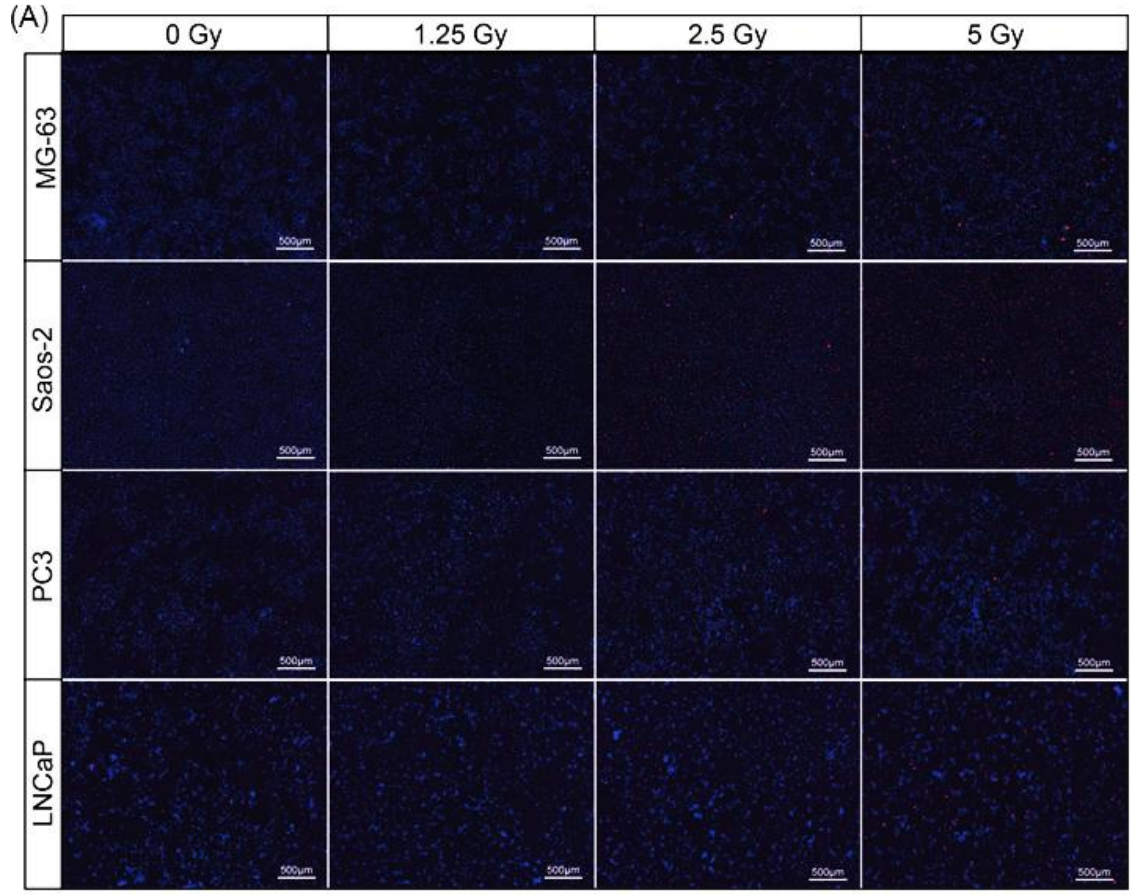

(B) **Cell viability 24h post-treatment in 2D cultures**

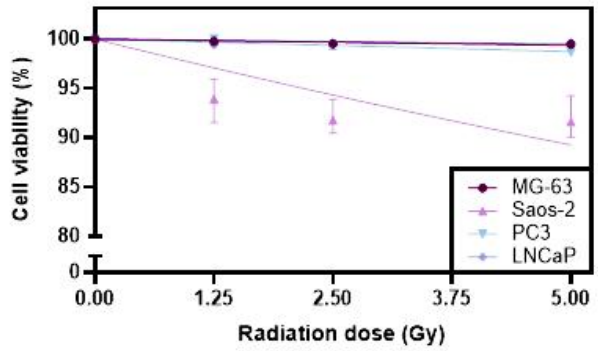

(C)

Dose (Gy) vs. normalized response	MG-63	Saos-2	PC3	LNCaP
IC50	788.2	41.56	388.5	1016
Std. Error (IC50)	120.6	6.16	42.82	338.8

Figure 3.11 - Cell viability of human osteosarcoma and prostate cancer cell lines, cultured in monolayer, 24h post-radiation treatment. (A) All cell lines remain viable after every treatment dose, demonstrated by the majority of live cells (Hoechst-stained) in comparison to the low number of dead cells (PI-stained). Cytation 5 imaging system, 4x objective, Z-stack of DAPI and Texas Red channels. Scale bar represents 500 µm. **(B)** Cell lines show no significant increase in sensitivity with higher doses of radiation. Cell viability of 2D cultures 24h post-treatment. Scatter plot, percentage cell viability data is presented as median ±range, individual values represent n=3 independent experiments with 3 technical repeats. **(C)** IC50 values calculated from the non-linear regression inhibitor (dose) vs. normalised response with 95% confidence.

To ensure the accuracy of results and avoid subjective cell counting by using a more objective method, these were confirmed with flow cytometry. MG-63 and Saos-2 cell lines were harvested 24h post-treatment and stained with Annexin V and Propidium Iodide. Following sample run on the FACSCalibur™, results were graphed using the FloJo software. The data was compensated using single colour controls, populations gated using the FSC and SSC, cell counts for each channel (FL4 – Annexin V; FL3 – PI) were graphed in a dot plot (Figure 3.12A), and the apoptotic profiles of both cell lines 24h-post treatment were plotted (Figure 3.12B).

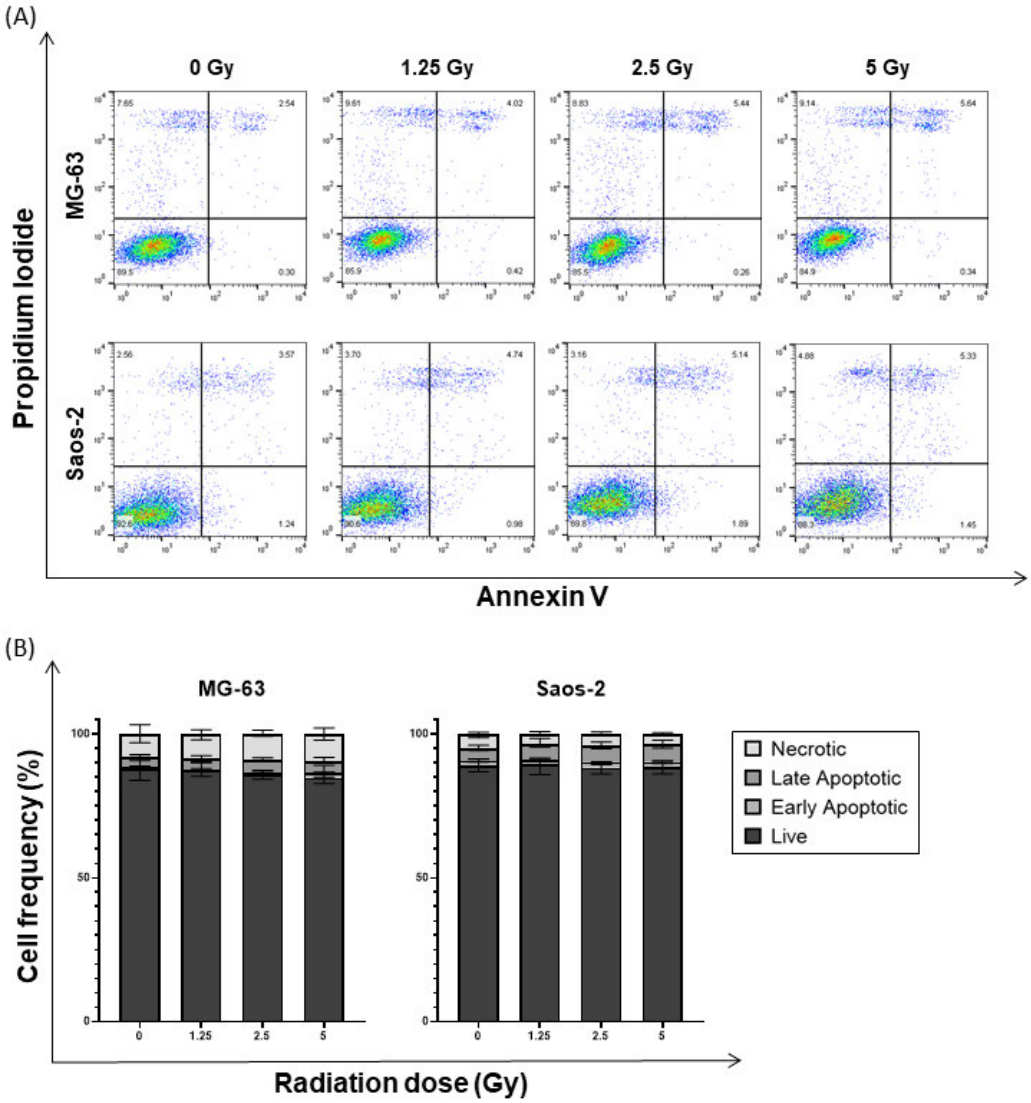

Figure 3.12 Apoptotic profile of osteosarcoma cell lines 24h following irradiation. Both MG-63 and Saos-2 show no significant dose-dependent decrease in viability, with a low percentage of apoptotic/necrotic cells following irradiation. (A) populations were gated to determine apoptotic stage. Dot plot of Annexin V (FL4 channel) vs. PI (FL3 channel). (B) Percentage of live cells is unaltered after irradiation in both cell lines. Stacked bars, percentage data is presented as mean ±range, individual values represent n=3 independent experiments with 3 technical repeats.

Both osteosarcoma cell lines show similar apoptotic profiles, with viability percentages surpassing 85% at all radiation doses for both MG-63 and Saos-2, proving the accuracy and reproducibility of the H/PI assay.

3.2.6. Radio-sensitivity of cells cultured in alginate spheres assessed by colony growth measurements.

In light of cells exhibiting no immediate responsiveness to treatment in 2D, it became essential to establish a reliable and reproducible platform for evaluating colony growth in three dimensions, to facilitate comparison of the radio-sensitivity between the two culture systems. Currently, there is no universally accepted standard for gauging clonogenic potential in three dimensions. Therefore, I opted to capitalize on the colony growth capacity of the alginate model. To achieve this, instead of allowing the alginate spheres to incubate for long enough to generate sizeable colonies, their growth was limited to only 3 days – this ensured the colonies present would be sufficiently young to retain growth potential following treatment (Figure 3.13A). Colony diameter was measured on the day of treatment and the spheres were subsequently irradiated with doses of 2.5 Gy, 5 Gy and 20 Gy. Following treatment, the samples were incubated for a further 10 days, when the colonies were measured again (Figure 3.13B).

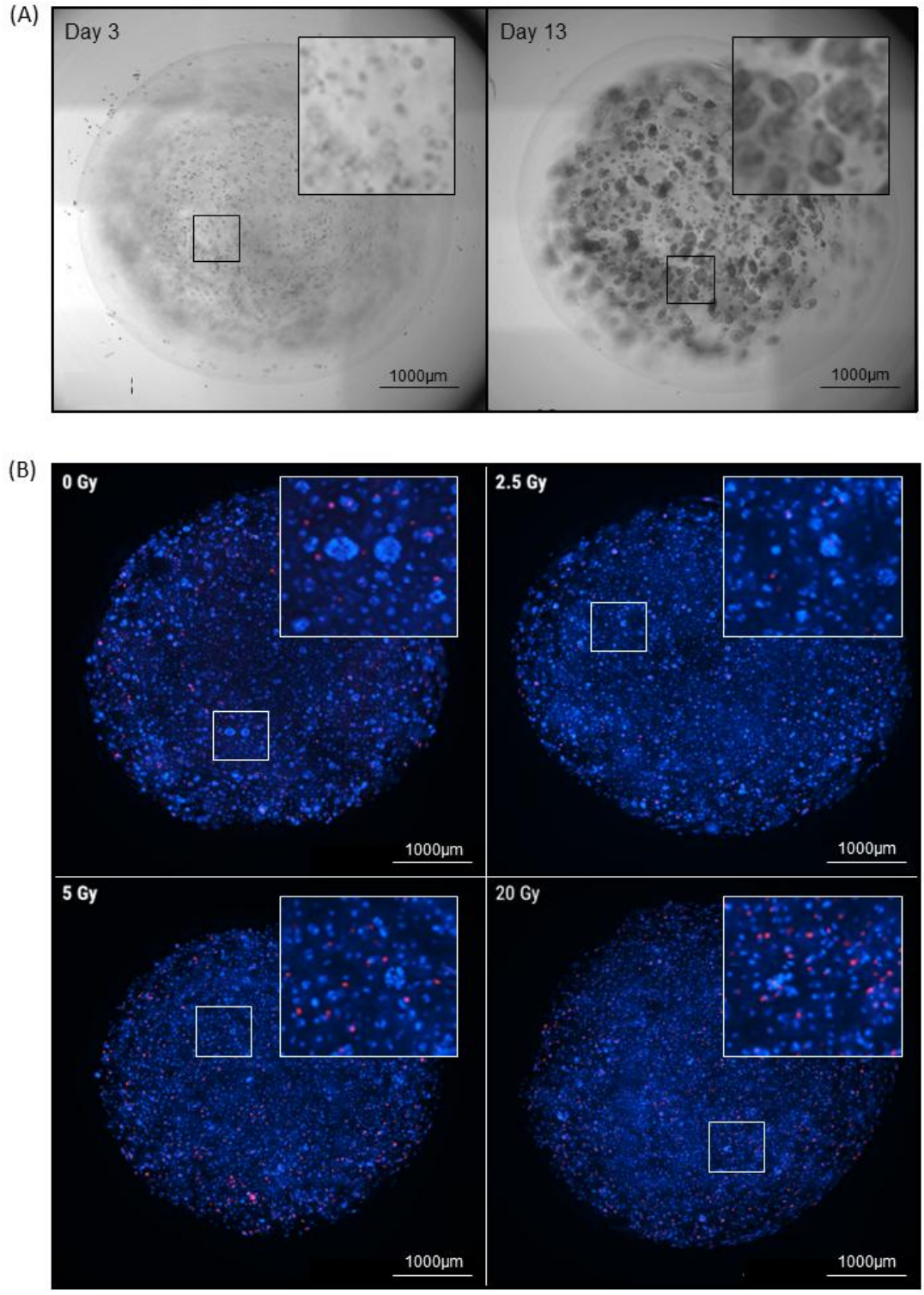

Figure 3.13 - Colony growth in alginate spheres. (A) After 3 days, cells grown in alginate spheres produce colonies young enough to sustain growth potential, which is achieved in full after 10 days. Cytation 5 imaging system, 4x objective, Z-stack of brightfield channel. Scale bar represents 1000 µm. **(B)** 10 days post-treatment, alginate spheres were stained with Hoechst/PI and a dose-dependent difference in colony size is noticeable. Cytation 5 imaging system, 4x objective, Z-stack of DAPI and Texas Red channels. Scale bar represents 1000 µm.

Prior to treatment, MG-63 colonies measured, on average, 31.7±1.2 μm in diameter. 10 days following treatment, untreated colonies tripled in size, measuring on average 92±5.8 μm. Colonies treated with a 2.5 Gy only doubled in size, with the average diameter being 57.1±1.9 μm. After 5 Gy, colonies measured 49.6±1.6 μm in diameter, and colonies treated with 20 Gy did not grow, with their average diameter being 33.7±0.9 μm 10 days post-treatment.

The same trend was observed in Saos-2 cells. On the day of treatment, colonies measured on average 24.5±0.7 μm. 10 days later, untreated spheres doubled in size, exhibiting an average diameter of 55±2.3 μm. In the treated spheres, colonies measured on average 28.5±0.4 μm, 27.2±1 μm and 21.7±0.6 μm after 2.5 Gy, 5 Gy and 20 Gy doses, respectively.

Regarding PC3 cells, their average diameter on day 0 was 16.5±4.2 μm, and five times larger 10 days later, in untreated spheres (77.6±1.9 μm). Colonies treated with 2.5 Gy measured on average 49.8±1.6 μm, 35.1±1.7 μm with 5 Gy and 30±1.1 μm with 20 Gy.

Finally, LNCaP cells presented a diameter of 34.7±1.8 μm on the day of treatment. 10 days post-irradiation, the diameter of untreated colonies measured 105.5±2.9 μm on average. In the treated spheres, colonies measured 65.8±2.3 μm, 53.9±3.3 μm and 24.4±3.7 μm after 2.5 Gy, 5 Gy and 20 Gy doses, respectively.

Each dataset was normalised against their untreated control and a scatter plot with bars was generated. The data was analysed using a Kruskal-Wallis test for non-parametric data, followed by multiple comparisons corrected with Dunn's method. All cell lines showed dose-dependent decrease in colony size, which was significant at 20 Gy (p=0.006 in MG-63, PC3 and LNCaP and p=0.009 in Saos-2) (Figure 3.14).

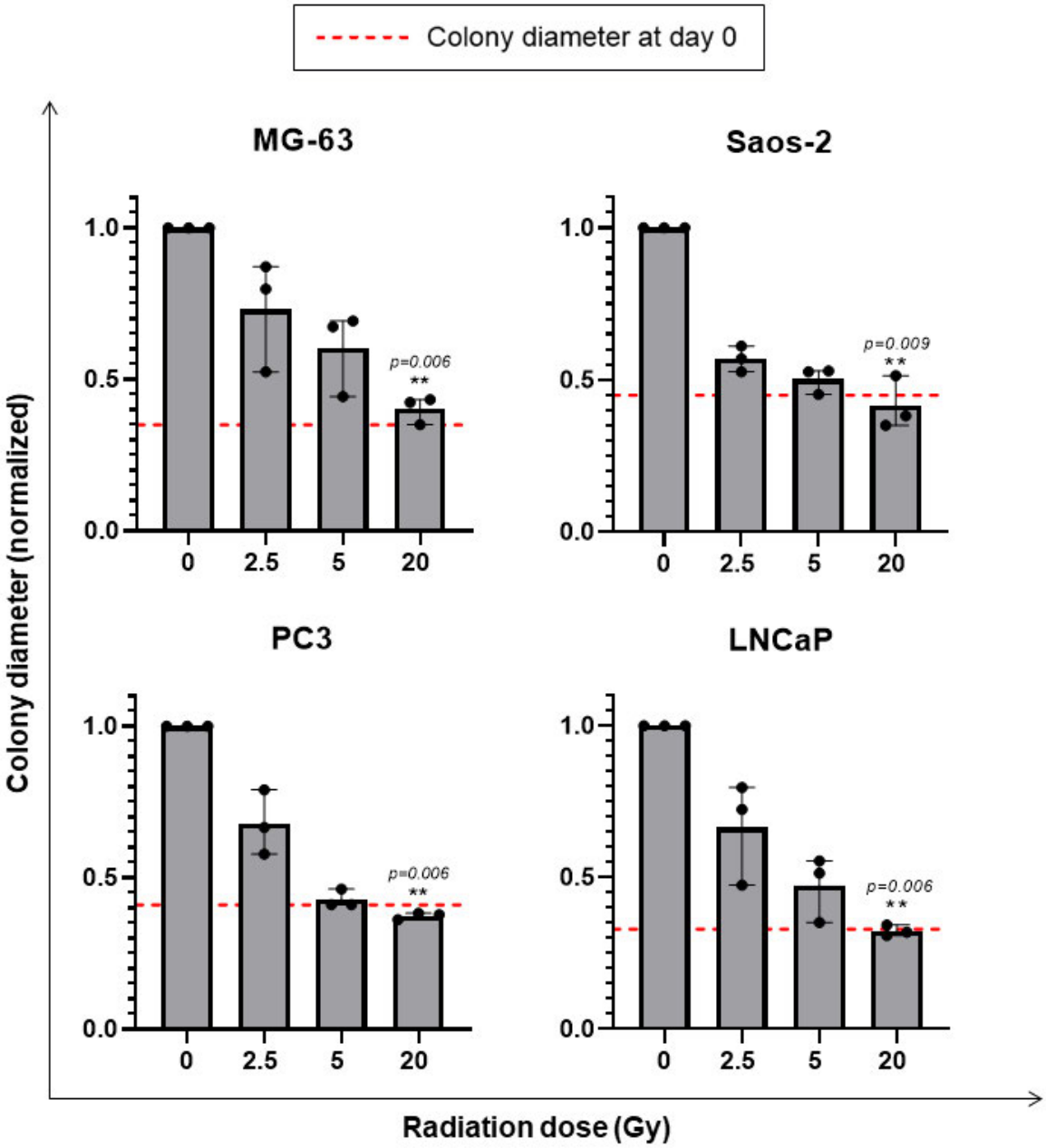

Figure 3.14 – Diameter of colonies grown in alginate spheres 10 days post-irradiation. All cell lines show a significant decrease in colony diameter at the highest radiation dose**.** Scatter plots with bars of normalised data, Kruskal-Wallis followed by Dunn's post-hoc test (*P<0.05).

3.2.7. Comparison of radio-sensitivity between cells grown in monolayer and in 3D alginate spheres.

The resulting data from the 2D clonogenic assays was compared to the colony growth in alginate spheres data using multiple *t* tests. The results show that all cell lines show higher sensitivity to treatment when cultured in monolayer (Figure 3.15). At a 2.5 Gy radiation dose, this difference is significant for Saos-2, PC3 in LNCaP cell lines, with *p* values lower than 0.001 for Saos-2 and LNCaP, and of 0.002 for PC3.

After being treated with a 5 Gy dose, all cell lines show a significantly higher sensitivity in 2D, with *p* values of 0.006 in MG-63, 0.016 in PC3 and lower than 0.001 in both Saos-2 and LNCaP cell lines.

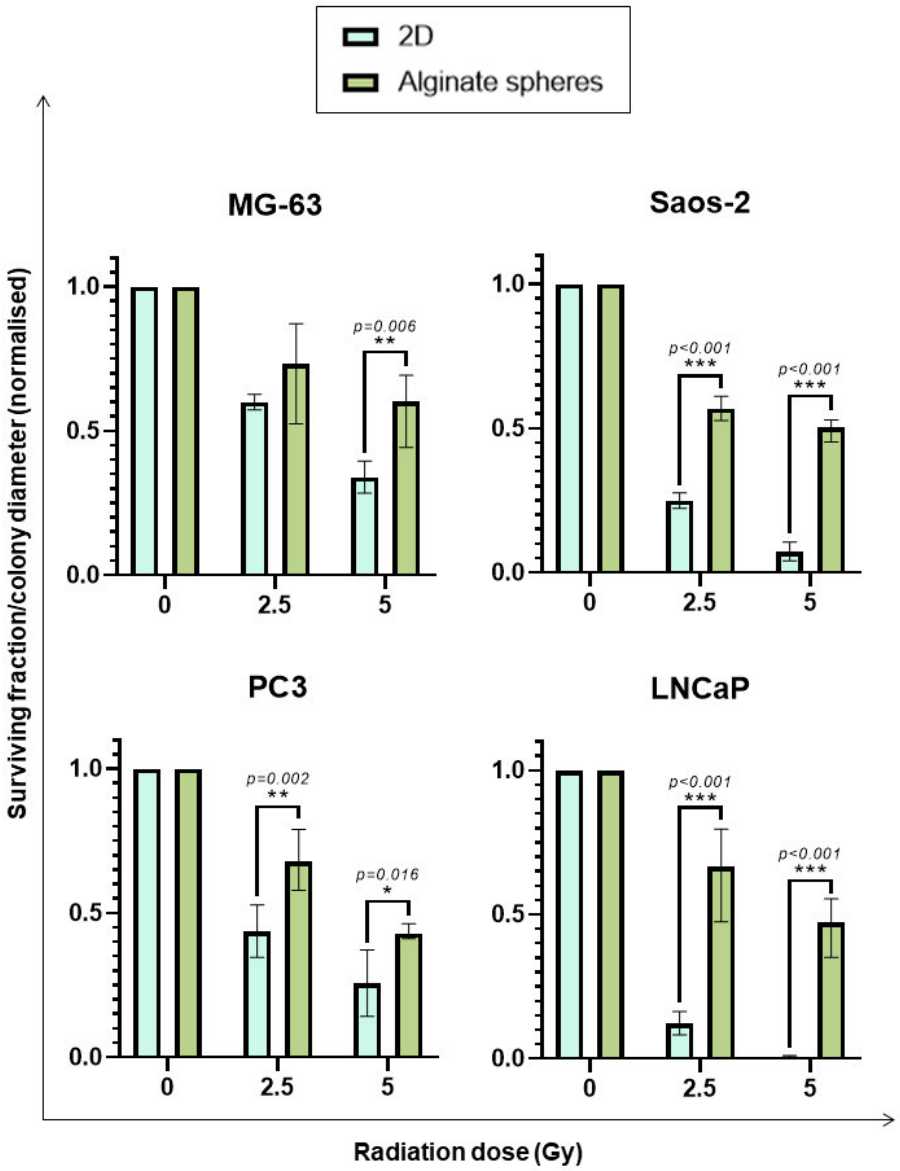

Figure 3.15 - Comparison of responses to ionising radiation between cells cultured in monolayer and alginate spheres 10 days post-irradiation. All cell lines show significantly higher sensitivity to treatment when cultured in 2D. Interleaved bars, multiple *t-tests*. Statistical significance corrected using the Holme-Sidak method of multiple comparisons, with alpha=0.05. (*P<0.05). 2D data is presented as mean ±SD. 3D data is presented as median ±range and individual values represent n=3 independent experiments with 3 technical repeats. The data presented in this graph has been previously shown in this chapter.

3.2.8. Differences in cell cycle distribution following radiation treatment.

Following treatment with ionising radiation, the cell cycle distribution of each of the treated cell lines was investigated by propidium iodide staining and flow cytometry analysis, as described in section 2.3.6.

Regarding cells grown in 2D cultures, following single-cell population gating (Figure 3.16A), the cells were then gated according to cell cycle stage. The percentage of cells in each stage was subsequently plotted as bar graphs and submitted to multiple *t-tests* to investigate statistical significance between untreated cells and cells treated with a 5Gy radiation dose (Figure 3.16B).

Data shows that after a 5Gy dose:

- There is a significant increase in the percentage of MG-63 cells in the G2/M stage of the cell cycle (p=0.037).
- The number of Saos-2 cells in the G0/1 stage sees a reduction of approximately 24% (p<0.001), accompanied by an increase of approximately 27% of cells in G2/M (p<0.001).
- The number of PC3 cells in G0/1 also decreases (≈10%, p<0.001). Inversely, the number of cells in G2/M increases (≈7%, p=0.001).
- There is no statistically significant shift in cell populations of LNCaP in any of the cell cycle stages.

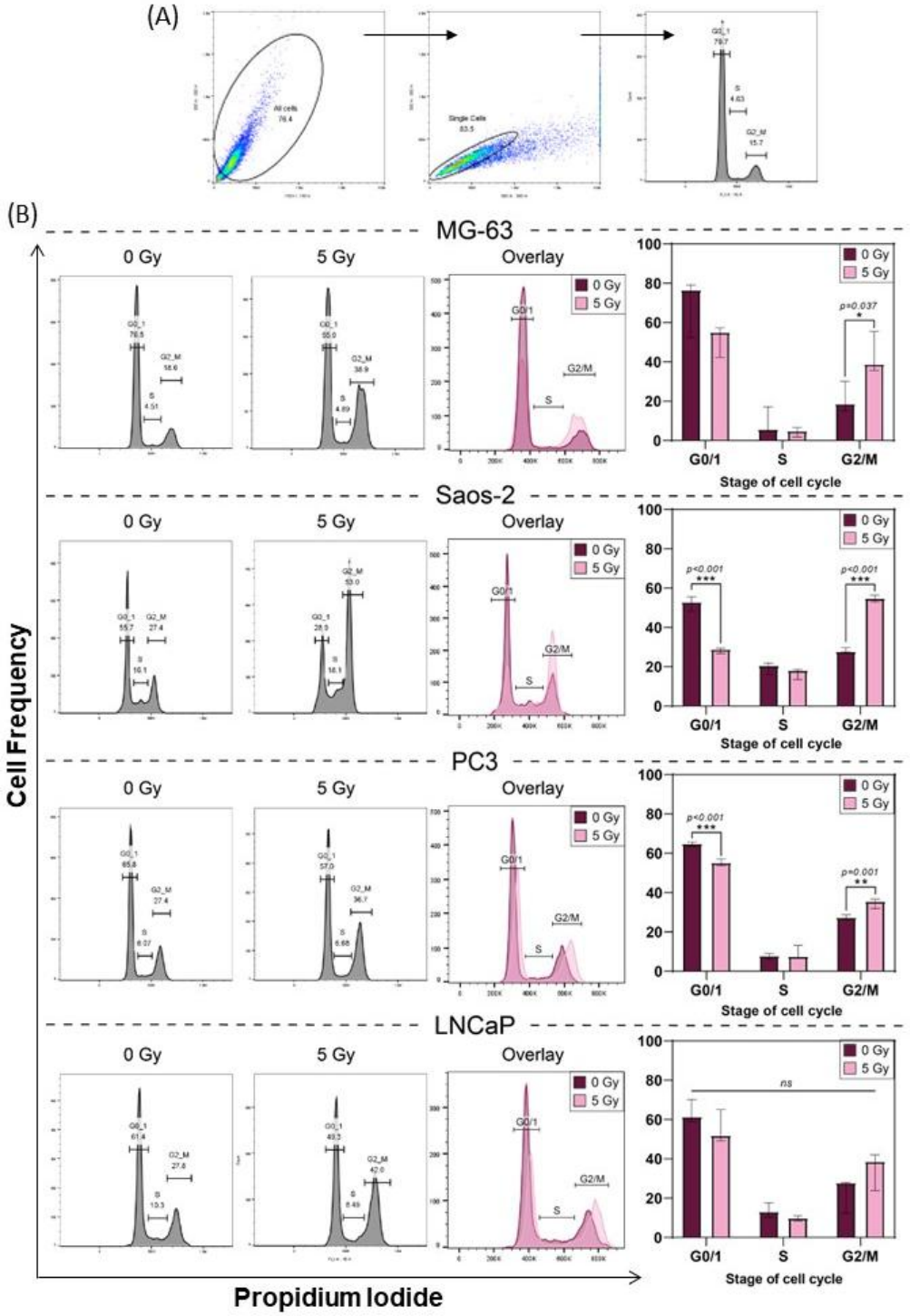

Figure 3.16. Differences in cell cycle distribution of cell lines cultured in 2D 24h following ionising radiation. (A) To obtain the cell cycle distribution histograms, the cell populations are firstly gated using the Forward Scatter Channel (FSC) and Side Scatter Channel (SSC), which generates the viable cell population. A gate is then drawn on this population to isolate the single cells. These are graphed as a histogram using cell frequency as the y axis against PI intensity, measured by the PE channel, on the x asis. (B) From the cell frequency vs. PE histograms it is then possible to gate the cells in each stage of the cell cycle. The histograms obtained from the same cell line (untreated and treated with a 5Gy dose) are then overlaid to obtain a visual representation of the different distributions. The percentage of cells in each stage were also plotted as bar

graphs that show the differences in cell cycle distribution between cells treated with 5 Gy and untreated cells of the same cell line. Interleaved bars, multiple *t-tests*. Statistical significance corrected using the Holme-Sidak method of multiple comparisons, with alpha=0.05. (*P<0.05). Data is presented as median ±range and individual values represent n=3 independent experiments with 3 technical repeats.

The same procedure was carried out for cells cultured in MCTS (Figure 3.17) and alginate spheres (Figure 3.18). Due to time constraints, only a n=1 test was conducted. Even though no statistical analysis was possible, preliminary data shows that:

- The distribution of MG63 cells in the different stages of the cell cycle suffers seemingly negligible alterations post-treatment, when cultured in spheroids. When cultured in alginate spheres, the percentage of cells is slightly lower in G1/0 and higher in G2/M.
- Saos-2 cells show a decrease in the number of cells in G0/1, with an increase in G2/M numbers following treatment. This shift is accentuated in cells grown in alginate spheres.
- When cultured in MCTS, PC3 cells show a minor decrease in cells in G0/1 accompanied by a small increase in cells in G2/M. Contrarily, when cultured in alginate spheres, PC3 cells suffer an increase in the G0/1 population which is complemented by a decrease in the number of cells in S and G2/M phases.
- When cultured in MCTS, LNCaP cells follow the same trend as Saos-2 and PC3, showing a slight decrease in G0/1 cells and an increase in S and G2/M cell populations. Due to time constraints, the analysis of cell cycle distribution of LNCaP cells cultured in alginate spheres was not carried out.

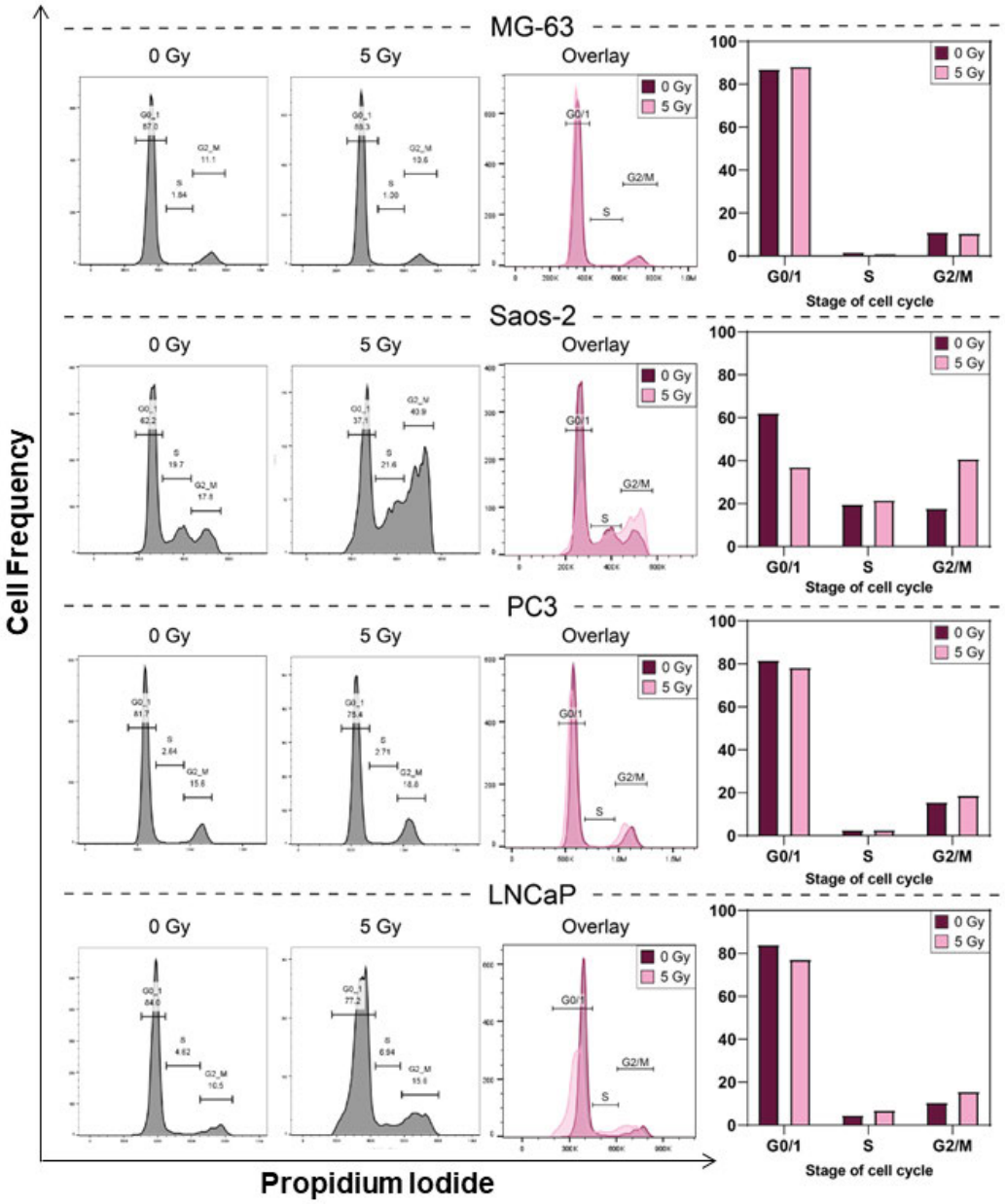

Figure 3.17. Cell cycle distribution of cell lines cultured in multicellular tumour spheroids 24h following irradiation. Histograms of cell frequency vs. PE intensity of untreated cells and treated with a 5 Gy radiatin dose are overlaid to obtain a visual representation of both distributions. The percentage of cells in each stage were plotted as bar graphs that illustrate the differences in cell cycle distribution between cells treated with 5 Gy and untreated cells of the same cell line. Data is presented as individual values representing n=1.

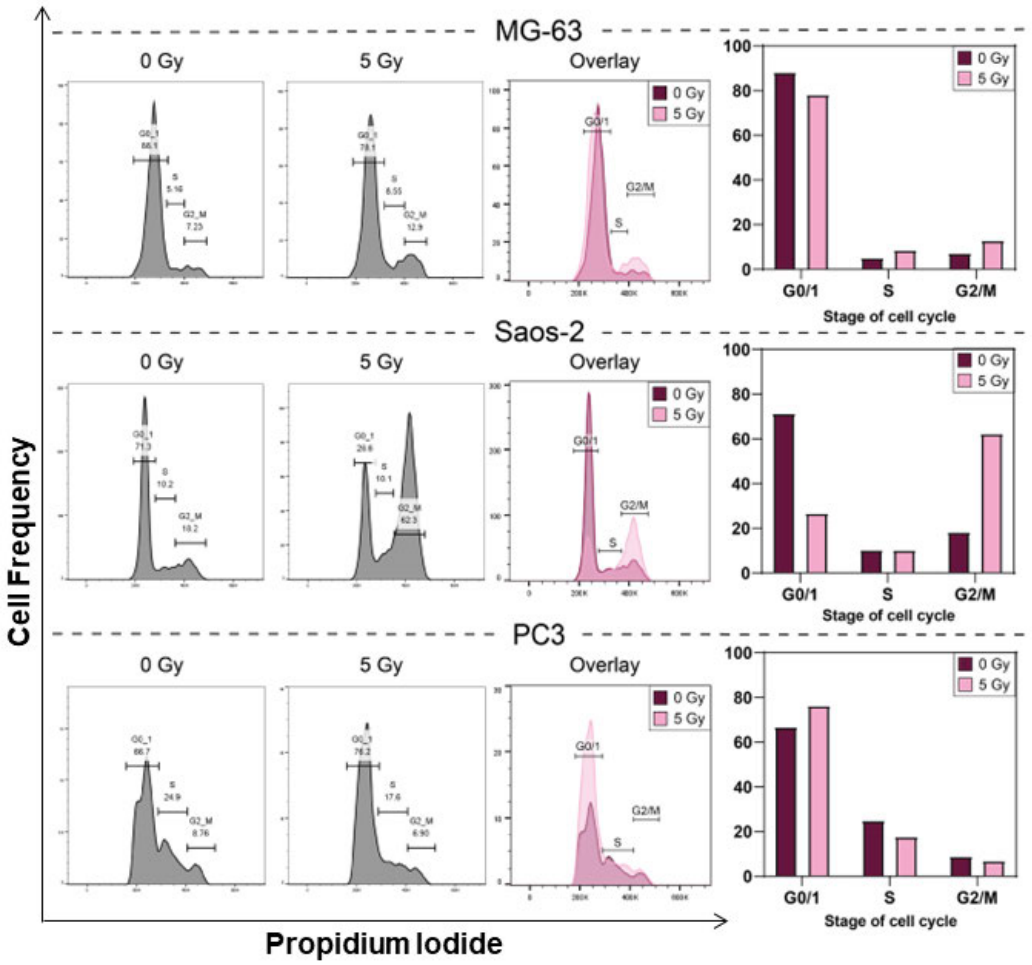

Figure 3.18. Post-treatment cell cycle distribution of cell lines cultured in alginate spheres. Histograms of cell frequency vs. PE intensity and overlay of untreated and 5 Gy-treated cell lines cultured in alginate. Bar graphs representing percentage of cells in each stage of the cell cycle. Data is presented as individual values representing n=1.

3.2.9. γ-H2AX quantification via Western-blot.

Cells were subjected to lysis, protein quantification and Western blot analysis of the γ-H2AX protein to investigate the existence of radiation-induced double strand breaks, as described in section 2.3.5.1.

Due to the small amount of protein present, this analysis was inconclusive, with the only cell line showing any bands corresponding to γ-H2AX being LNCaP (Figure 3.19). Because of time constraints, this analysis was not repeated.

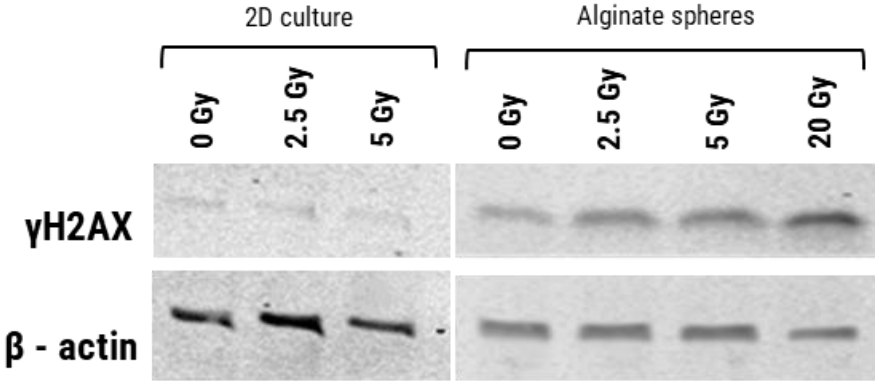

Figure 3.19 - Western blot analysis of γ-H2AX protein shows an increase in protein concentration with increasing radiation doses in LNCaP cells cultured in alginate spheres 24h post-treatment. However, due to the inconsistency of the β-actin control bands, it is not possible to reach any reliable conclusions.

3.2.10. Localization of γ-H2AX foci following irradiation.

To investigate γ-H2AX foci localisation, the cell preparations were subjected to Immunofluorescence assays, 24h post-treatment, as described in section 2.3.5.2. The resulting confocal images (Figure 3.20) were analysed using the Zeiss Zen 2.3 (blue edition) software (Carl Zeiss) by quantification of the number of H2AX foci per cell nucleus.

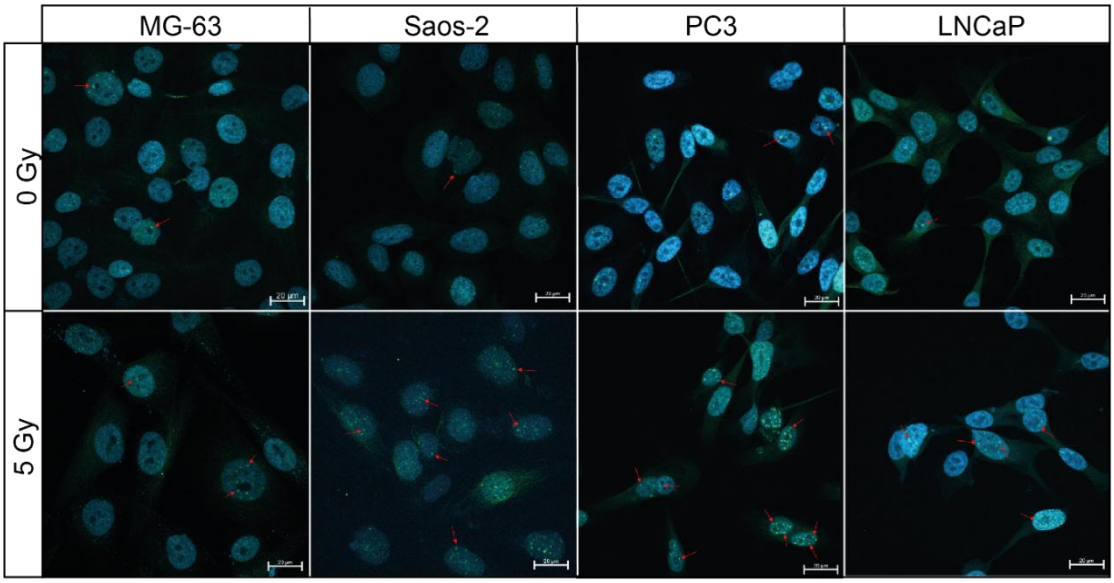

Figure 3.20 – Confocal images of γ-H2AX detection in human osteosarcoma and prostate adenocarcinoma cell lines. Cells were stained with an anti-Human Histone H2AX [p Ser139] primary antibody, AlexaFluor™ 488 secondary antibody (green) and counterstained with DAPI (blue). Images show an increase in the number of H2AX foci (red arrows) in cells treated with 5Gy of ionising radiation, compared to untreated cells. Zeiss LSM 800 confocal microscope, 40x objective, Z-stack of DAPI and AF488 channels. Scale bar represents 20 μm.

Results were graphed as violin plots and analysed using unpaired *t* tests of the means of three repeats in GraphPad Prism (Figure 3.21).

Apart from MG-63, the number of H2AX foci significantly increased post-radiation treatment in all cell lines. With a 5 Gy dose, MG-63 cells had an average of 0.84 foci per cell, compared to 0.48 in untreated cells (p=0.250). 73% of untreated MG-63 cells did not show any foci, with treated cells seeing this percentage reduced to 56%. Untreated Saos-2 cells presented, on average, 0.86 foci per cell, with 56% not showing any foci. After a 5 Gy radiation dose, the percentage of cells without foci dropped to 28% and the average number of foci per cell increased to 2.54, (p=0.037). For PC3 cells, the average number of H2AX foci in untreated cells was 1.36, which saw an increase of 26% following radiation treatment – cells treated with a 5 Gy dose showed an average of 3.52 foci per cell (p=0.003). The percentage of cells without foci saw a reduction, with 39% for untreated populations and 20% for irradiated cell populations. Finally, irradiated LNCaP cells also saw a rise in the number of H2AX foci – 2.88 – compared to untreated cells – 0.48 (p<0.001). For this cell line, the percentage of cells without foci was 65% before treatment and 27% after.

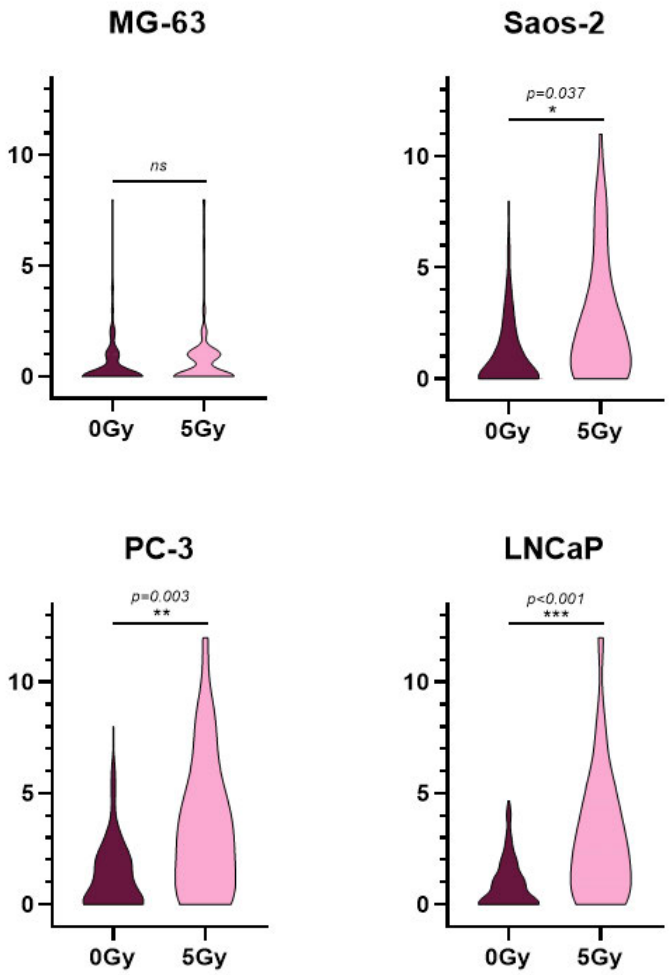

Figure 3.21 - Number of H2AX foci in cells treated with ionising radiation 24h post exposure. All cell lines show an increase in DNA damage following radiation, translated by an increased number of H2AX foci, with MG-63 being the most resistant cell line. Violin plots, unpaired *t* tests. Statistical significance calculated as a two-tailed *p* value, with a confidence level of 95% (*P<0.05) based on the means of 3 repeats.

3.3. Discussion

3.3.1. Colony formation assays of irradiated monolayer cultures.

The findings of this study show that, when grown in monolayer, there is a direct correlation between higher doses of gamma radiation and a reduction in cell proliferation. However, despite the existence of a dose-dependent effect in every cell line, some are more sensitive than others.

Osteosarcoma cell lines are notably resistant to radiation treatments, a phenomenon related to several mechanisms (Kim et al., 2022a). For instance, Eliseev *et al* (2005) demonstrated that resistance to radiation in the Saos-2 cell line could be related to the upregulation of the transcription factor NF-κB, which inhibits the *c-Jun* N-terminal kinase signalling pathway, strongly related to radiation-induced apoptosis (Eliseev et al., 2005). Additionally, studies led by Li (2015) and Mamo (2017) suggest that both MG-63 and Saos-2, respectively, show a higher level of expression of DNA-PK_{CS} – a DNA-dependent protein kinase involved in DNA repair mechanisms, which relates to radio-resistance (Li et al., 2015; Mamo et al., 2017). Nonetheless, despite the overall resistance of these cell lines, Saos-2 has proven to be significantly more sensitive to ionising radiation, compared to its counterpart. Due to the lack of radio-biology studies using these cell lines, it is difficult to pinpoint where this difference in treatment response may reside. However, and even though further studies would be required, it may be linked to their different expression of hypoxia-inducible factors (HIF). A study led by Flint (2021), where different metabolites were investigated by multimodal mass spectrometry imaging, has shown that the Glut1 gene is overexpressed across MG63 aggregated spheroids, in correlation with a constant stability of HIF-1α. This suggests that cells are able to proliferate under extreme hypoxic conditions, due to high glucose levels imported but the overexpressed Glut1. In contrast, imaging data of Saos-2 ‘aggregoids’ indicates a lower Glut1 expression, restricted to the spheroid cores (Flint et al., 2021). Higher levels of hypoxia are tendentially correlated with higher resistance to radiation and poorer treatment outcomes (Raitanen et al., 2023).

Following irradiation, PC3 cells demonstrated higher resistance to treatment then LNCaP. This difference in radiosensitivity was expected, due to the different inherent biological characteristics of these prostate adenocarcinoma cell lines. Firstly, the main characteristic that sets these two cell lines apart is their expression of androgen receptors (AR) – while LNCaP cells are androgen-

sensitive, PC3 are androgen-independent (Tai et al., 2011). A study conducted by Xie et al has previously shown that cells that not reliant on androgens for growth and survival are less susceptible to radiation-induced damage (Xie et al., 2010). Moreover, androgen signalling can influence the expression of DNA repair genes, which are crucial for the cell's ability to repair DNA damage induced by radiation. Likewise, genomic analysis of different prostate cancer cell lines by Jividen *et al* (2018) revealed that LNCaP cells have several mutations in DNA repair genes, which could compromise their DNA repair capacity, potentially increasing their vulnerability to radiation-induced cell death (Jividen et al., 2018). Lastly, despite there being no significant differences between the sensitivity of both breast cancer cell lines to radiation at each individual dose, when analysing the overall sensitivity, MDA-MB-231 cells are significantly more resistant to radiation than MCF-7. These findings align with established literature, which indicates that due to their more aggressive phenotype, MDA-MB-231 cells present higher resistance to radiotherapy when compared to the non-invasive MCF-7 cell line (Chen, X. et al., 2017). The triple-negative status of MDA-MB-231 cells implies the lack of molecular targets that could be exploited by radiation-induced damage (Lee et al., 2020). Additionally, these cells often exhibit more robust DDR mechanisms, further enhancing their resistance capabilities (Wong et al., 2022).

3.3.2. Acute sensitivity of 3D models to radiation.

As demonstrated in the results section of this chapter, it is evident that the impact of radiation is negligible in cells cultured in 3D models. Apart from Saos-2 cells grown in alginate spheres, all other cell lines exhibit resistance to treatment in both models, maintaining normalized cell viability values consistently close to 1.00 across various doses. Regarding Saos-2 cells, while existing literature does not definitively explain their increased sensitivity when cultured as alginate spheroids, several hypotheses can be proposed:

- Different 3D models can trigger the expression of different markers - the microenvironment and cell-cell interactions within 3D cultures can significantly influence gene expression and protein production. Factors such as matrix composition, oxygen availability, nutrient gradients, and mechanical cues can contribute to this variability (Edmondson et al.,

2014). Since the spatial arrangement of cells cultured in alginate is substantially different from MCTS, this can greatly impact cell behaviour.

- Differentiated cancer cells may exhibit altered radiation sensitivity – research indicates that triggering the osteogenic differentiation process in osteosarcoma cells, enhances their sensitivity to radiation (Luce et al., 2021). If Saos-2 cells undergo differentiation when cultured in alginate, this might alter their sensitivity to treatment.
- Matrix stiffness can influence various cell behaviours, including response to stressors such as radiation – studies show that changes in matrix stiffness can profoundly affect tumour cells' response to treatment by triggering several pathways that ultimately impact DNA repair, thereby increasing sensitivity to genotoxic agents (Deng, B. et al., 2022). Moreover, matrix stiffness can generate mechanical cues to which cells respond through mechanotransduction pathways, stimulating cell transdifferentiation and metabolic reprogramming (Jiang, Y. et al., 2022). Therefore, Saos-2 cells may be particularly sensitive to the stiffness of the alginate matrix in which they are cultured, leading to the increased sensitivity to high doses of γ-radiation.

Expanding on the observations regarding Saos-2 cells, it is crucial to acknowledge that the resistance seen in other cell lines within 3D models, compared to their 2D counterparts, is in line with anticipated outcomes. It has long been established that due to the inherent spatial configuration of 3D models, these more accurately mimic the tumour microenvironment as well as its heterogeneity and mechanisms of cell-cell communication and are, therefore, notably more resistant to therapeutic interventions than the gold standard monolayer cultures (Fontana et al., 2020; Raitanen et al., 2023). As expected, my findings align with this premise.

Research using breast cancer cell lines has demonstrated that three-dimensional cultures showcase differential cellular responses to radiation. For instance, in 2021 Manda et al compared the radiosensitivity of MCF-7 cells cultured in monolayer and in Matrigel™, concluding that cells grown in a 3D environment present higher resistance to treatment doses ranging between 2 and 6 Gy (Manda et al., 2021). Additionally, a study conducted by Dubois and collaborators, where MDA-MB-231 cells were cultured in 2D and 3D spheroids,

found that at a single dose of radiation, the cell survival rate is not affected in 3D – these cultures required fractionated doses over multiple consecutive days to show any sensitivity to radiation, and even then, their sensitivity was significantly lower than that of the monolayer cultures (Dubois et al., 2019).

Regarding prostate cancer cell lines, a study conducted by Raitanen and colleagues (2023) has demonstrated that both PC3 and LNCaP cells cultured in spheroids exhibit high resistance to treatment at doses up to 8 Gy, only showing some sensitivity, more pronounced in LNCaP cells, at a 20 Gy dose. It is important to note, however, that the decrease in cell viability and metabolic activity is only significant when evaluated 15- and 21-days post irradiation treatment (Raitanen et al., 2023).

Since osteosarcoma cells are inherently resistant to radiotherapy, there is a gap in the literature when it comes to studies investigating their sensitivity to radiation when cultured in three-dimensional platforms. However, a study led by Reichl (2020) found that MG-63 cells grown in spheroids retained their growth potential after treatment with doses ranging between 2 Gy and 6 Gy of photon radiation (Reichl, 2020).

The findings of this study are supported by previous research, showing that cell lines cultured in 3D exhibit greater resistance to treatment compared to those cultured in two dimensions. Nonetheless, it is important to refer that 2D viability was determined based on colony growth potential, whereas in 3D cultures it was assessed acutely, through a live/dead stain. Therefore, to enhance this study's robustness, acute response in 2D and growth potential of colonies in alginate were also investigated.

3.3.3. Acute cell viability of monolayer cultures.

To ensure a valid comparison of radiotherapy responses between 2D and 3D cell models, cells grown in monolayers were irradiated, and their viability was measured 24 hours post-treatment using the same method applied to the 3D cell models. The results indicated that, at 24 hours, the 2D models showed no difference in viability compared to the untreated controls. The observed discrepancy between cell viability 24 hours post-irradiation and their dose-dependent colony formation ability 10 days post-treatment can be attributed to several factors:

- Radiation frequently triggers delayed cellular responses. Gamma radiation, known for inducing DNA damage, may not immediately show its

effects. For example, damaged DNA can result in defective cell cycle checkpoints, allowing cells to proceed into mitosis with unrepaired genetic material. This can lead to mitotic catastrophe, a mechanism that controls cells unable to complete mitosis properly. (Sia et al., 2020).

- Cell cycle arrest. Ionizing radiation disturbs the normal progression of the cell cycle by causing DNA damage, which initiates a protective response aimed at maintaining genomic integrity. If the DDR mechanisms are effective, the cell progresses further in the cycle, while if the repair is unsuccessful the cell may exit the cycle and undergo programmed cell death, or proceed with unresolved damage, potentially leading to genome instability. Both outcomes can result in reduced in cell proliferation (Lonati et al., 2021).

These findings illustrate that while 2D and 3D cell models exhibited similar viability 24 hours post-irradiation, the observed disparity in long-term colony formation underscores the impact of delayed cellular responses and cell cycle disturbances induced by radiation. To further investigate these mechanisms, cell cycle distribution post-irradiation and DNA damage, illustrated by gamma H2AX presence, were also analysed.

3.3.4. Comparison of prolonged effects of radiation in 2D and alginate sphere cultures.

To effectively compare the clonogenic results from monolayer cultures to their three-dimensional counterparts, alginate spheres were irradiated at a young stage and the cells were allowed to proliferate for a further 7 days following treatment. The results indicate that, even though there is a dose-dependent decrease in colony diameter this is only significant at 20Gy. When compared to cells grown in 2D, the alginate model has, as expected, showed a higher rate of cell proliferation, translated by colony growth. These findings align with the high resistance of 3D models to radiation previously described in literature and detailed in section 3.4.2. Nonetheless, it is important to note that while both assays assess colony growth, the comparison between the two is not direct. In monolayer, clonogenic capability is measured via colony survival; in alginate spheres, the diameter of pre-formed colonies is measured. Due to the large size of the spheres and the limited imaging capabilities, an accurate colony count in 3D would be challenging to achieve. Therefore, measuring colony growth over

time is the closest representation of a clonogenic assay in three-dimensions. Had colony survival in 3D been measured with a size threshold, the trend could have been similar to that observed in monolayer.

3.3.5. Cell cycle distribution following irradiation.

To further investigate the discrepancy between the high acute viability and the long-term loss in colony growth, the cell cycle distribution of irradiated cell populations was assessed through flow cytometry. The findings of this thesis indicate a shift in the number of cells at each stage of the cell cycle, in both 2D and 3D models. When cultured in monolayer, the number of cells in the G0/1 stage decreased in all cell lines. The reduction suggests that cells are either not remaining in the initial growth stage or are being forced out of this phase in response to DNA damage. Concurrently, there was an increase in the number of cells in G2/M, suggesting a cycle arrest at this stage. The accumulation of cells in the G2/M phase likely results from the activation of the G2/M checkpoint, a moment during the cell cycle which ensures that cells do not enter mitosis with damaged DNA. This may be reflecting a cellular response to radiation-induced DNA damage, and the attempt to repair it. These findings are consistent with several radiobiology studies that also indicate a correlation between irradiation and G2/M cell cycle arrest (Keam et al., 2022; Liu et al., 2019; Yan et al., 2007). These results corroborate the observed discrepancy observed between the cells' high viability 24 post-treatment and the dose-dependent decrease in clonogenic capability: they suggest that radiation-induced damage causes cells to arrest in the G2/M phase, where cells are unable to complete repair, ultimately leading to a decrease in cell proliferation. In 3D, all cell lines show a similar trend – apart from alginate-cultured PC3 cells – despite the percentage difference between untreated and treated cells being smaller. However, since the sample size does not allow statistical analysis, it is impossible to infer if these differences are significant or not. Interestingly, my findings indicate that, when cultured in alginate, PC3 cells seem to arrest their cell cycle progression at the G0/1 stage, a deviation from the typical G2/M arrest seen in response to radiation-induced damage. Usually, this arrest occurs in response to genotoxic stress, and it is primarily triggered by the p53 protein – when the DNA is critically damaged, elevated levels of p53 prompt the arrest of the cell cycle in G0/1, allowing cells to repair the damage before DNA replication occurs (Pellegata et al., 1996).

However, the PC3 cell line lacks functional TP53, which rules out this p53-dependent mechanism. Despite the absence of functional p53, the increase in the G0/1 population could be attributed to the cells' arrest in the G0 phase. This phase represents a state of metabolic quiescence – if reversible – or senescence – a potentially irreversible state characterised by basal metabolic activity –, as a response to the stress conditions induced by radiation (Wiecek et al., 2023). The colony growth results detailed in section 3.3.6 show a dose-dependent reduction in the proliferation rate of PC3 cells cultured in alginate. This observation suggests that the potential arrest in G0 may be correlated with the cells entering a senescent state in response to genotoxic stress. To confirm this hypothesis, further studies are necessary. These studies should not only increase the sample size to enable robust statistical analysis but also include additional experiments to verify the senescence hypothesis. Techniques such as transcriptomics could provide insights into the gene expression profiles associated with senescence, helping to confirm whether the observed G0 arrest in PC3 cells is indeed linked to a senescent state.

3.3.6. γ-H2AX foci quantification.

H2AX is a protein that plays a pivotal role in the packaging of DNA into chromatin with the cell nucleus. The occurrence of DSBs trigger the initiation of a cellular response to signal and repair the damage. γ-H2AX, resulting from the phosphorylation of H2AX at the Ser139 residue, is one of the specific markers of DSBs and its accumulation at the break site form visible foci, detected through immunofluorescence. These foci serve as recruitment sites for a variety of DNA repair proteins, facilitating the efficient repair of damaged DNA (Podhorecka et al., 2010).

The results presented in this thesis indicate that, following irradiation, all cell lines show a significant increase in the average number of γ-H2AX foci per cell and a decrease of the percentage of cells without foci. This indicates that a significant amount of DSBs have occurred, and the DDR pathways have been activated – the cells have recognised the DNA damage, and the repair process has initiated. These findings align with the cell cycle analysis results discussed above: cells are accumulating in the G2/M phase, indicating they have activated the G2/M checkpoint and are attempting to repair the radiation-damaged DNA. However, the dose-dependent decrease in proliferation highlighted in section 3.4.1.

suggests that, despite being activated, the repair mechanisms may not be successfully resolving the DNA damage.

3.4. Conclusion

In this chapter, I have explored the responses of different cell lines cultured in 2D and 3D models to radiation treatment. While none of the models showed an immediate response to radiation 24 hours post-treatment, they exhibited a decrease in proliferation after 10 days. Comparative analysis revealed that 3D-cultured cells are more resistant to radiation treatment compared to their 2D counterparts. However, it is important to consider that this is not a direct comparison (colony number vs. colony diameter).

This increased resistance is further supported by cell cycle studies, which demonstrate a G2/M arrest in response to 5Gy radiation in both 2D and 3D cultures. However, an exception was observed in one cell line that exhibited a G0/G1 arrest in 3D culture, highlighting potential variations in radiation response mechanisms among different cell lines. The G2/M arrest indicates that cells are attempting to repair DNA damage before entering mitosis, while the G0/G1 arrest in PC3 suggests an alternative response mechanism possibly linked to a prolonged repair process or entry into a senescent state.

Furthermore, gamma H2AX immunofluorescence assays showed a dose-dependent increase in foci number for all cell lines. This dose-dependent increase suggests that radiation induces significant DNA damage, which cells attempt to repair over time, accounting for the delayed decrease in proliferation observed in long-term assays.

These results collectively suggest that while short-term viability may not be immediately affected, long-term proliferation and cell cycle dynamics reveal significant insights into the radiation response of cells, with 3D cultures exhibiting greater resilience. This highlights the importance of 3D cell models in studying radiotherapy responses, as they more accurately mimic the in vivo tumour environment and may better predict clinical outcomes. However, it is important to note that due to COVID-19 restrictions and resulting time constraints, only single-dose radiotherapy responses were evaluated. Ideally, responses to fractioned dosing RT should also have been investigated as it better mimics what is often done in a clinical setting (The Royal College of Radiologists, 2024), which is concomitantly supported by *in vitro* radiobiology research. For instance, Dubois

et al have demonstrated that 3D spheroids exposed to daily 2 Gy radiation doses exhibit a progressively greater reduction in viability with each additional day of treatment (Dubois et al., 2019). Moreover, Cosme et al (2021) have also shown that fractioned dosing of photodynamic therapy (PDT) enhances toxicity, leading to a decrease in spheroid viability (Aguilar Cosme et al., 2021). Despite the differences between RT and PDT treatment modalities, both involve mechanisms that produce reactive oxygen species to induce cell death.

Building on the insights gained from the differential radiation responses of 2D and 3D cell models, both 3D models will be used for the following chapters. As the responses seen in MCTS and alginate spheres don't necessarily correlate but both offer important outputs, I determined it would be beneficial to carry both platforms to the next phase of the study. Moreover, it was determined that the most representative and reproducible technique for cell viability assessment was the clonogenic assay for 2D and colony growth monitoring for 3D. Still, our group is also interested in investigating if the presence of gold nanoparticles produces an acute sensitising effect. Therefore, even though colony formation/growth assays are the primary concern, live/dead assessments will also be performed in all models. Furthermore, cell cycle distribution and gamma h2ax foci presence will too be investigated.

The next chapter will examine the potential of gold nanoparticles, known radiosensitizers, which have shown promise in enhancing the effects of radiation therapy by increasing DNA damage. With the aim to overcome the resistance observed in the 3D models and improve therapeutic outcomes, this approach could provide a novel strategy for sensitising tumour cells to radiotherapy, offering new avenues for effective cancer treatment.

Chapter 4. Assessing *in vitro* radio-sensitivity in gold nanoparticle-treated cell models

4.1. Introduction

Over the past few decades, numerous nanomaterials have been developed for nanomedicine applications (Soares et al., 2018). Among these, gold nanoparticles have gained particular prominence in cancer therapeutics due to their distinctive features, including excellent biocompatibility, low toxicity, straightforward synthesis, unique optoelectronic properties, and ease of surface functionalisation (Sell et al., 2023). Moreover, even in the absence of functionalisation, once in the blood stream, AuNPs tend to passively accumulate in the tumour site – due to tumoral vasculature defectiveness and permeability, nanoparticles tend to extravasate the blood vessels, lodging in the diseased tissue. Furthermore, tumours often have poor lymphatic drainage and AuNPs present low diffusivity, which means that once they enter the tumour site, they are likely to be retained for longer periods, providing the possibility of delivering drugs or other compounds with low solubility, poor pharmacokinetics, or susceptibility to enzymatic degradation (Jain et al., 2012; Yao et al., 2020). Due to all these unique characteristics, gold nanoparticles are promising enhancers for cancer therapy and can be used as drug carriers and photothermal agents but also as imaging agents and radiosensitisers (Burlec et al., 2023).

Gold nanoparticles are proven radio-sensitisers at kilovoltage (kV) and megavoltage (MV) photon energies, with higher radio-sensitization observed at kV photon energies (Chen et al., 2020b). This enhanced radio-sensitisation occurs due to gold's high atomic number (Z), which allows it to absorb more radiation compared to tissues. When interfacing with radiation, gold nanoparticles (AuNPs) release low-energy electrons through the Auger effect. These electrons can cause damage to the DNA chain by either directly interacting with it, leading to strand breaks, or by reacting with the most abundant component in the cell – water. When a low-energy electron reacts with a water molecule, a hydroxyl radical (•OH) is produced and these highly reactive molecules can subsequently damage the DNA chain. In addition, the production of •OH leads to the release of a second electron that could directly interact with the DNA or with another water molecule. This creates a chain reaction, this way contributing to the overall effectiveness of radiation (Chen et al., 2020b; Penninckx et al., 2020).

Results in monolayer cultures show that gold nanoparticles cause an enhancement of the susceptibility of tumour cells to radiation, therefore improving cell killing (Chen et al., 2020b). This mainly occurs due to their capacity of initiating Auger cascades when interacting with ionizing radiation, magnifying its effect - AuNPs produce reactive oxygen species that mediate DNA damage and cell death through oxidative stress (Tabatabaie et al., 2022). Although there is still an insufficient number of studies regarding the use of gold nanoparticles as radiation absorbers in three-dimensional cell culture models, some research groups have started to explore this possibility. For instance, Igaz et al. (2020) demonstrated the radiosensitising potential of gold nanoparticles in the recognised radio-resistant A-549 lung cancer cells cultured in 3D spheroids. This effect was further enhanced by treating the cells in combination with SAHA (Suberoylanilide hydroxamic acid), a histone deacetylase inhibitor, showcasing the potential of gold nanoparticles to produce synergistic effects when combined with well-researched antineoplastic agents (Igaz et al., 2020). Furthermore, Alhussan et al. (2023) have shown that co-culturing pancreatic cancer cell lines with patient-derived cancer-associated fibroblasts in 3D spheroids enhances gold nanoparticle uptake, which translates into a higher radiosensitising effect (Alhussan et al., 2023). Bromma et al. (2020) have also shown that both cancer cells and CAFs internalise AuNPs more effectively than normal fibroblasts, which cements the role of gold nanoparticles in enhancing the local radiotherapy dose while sparing the surrounding normal tissue (Bromma et al., 2020). These findings strengthen the potential of introducing gold nanoparticles in *in vivo* therapeutic regimens, in combination with radiotherapy. Table 4.1 outlines important advances achieved by several research groups regarding the use of gold nanoparticles in the context of radiobiology.

Table 4.1 - Studies investigating the radiosensitising potential of AuNPs in 2D and 3D cultures.

Research Group	Cell line(s)	Culture method		Nanoparticle size (concentration)	Radiation dose	Results
		2D	3D			
(Rahman et al., 2009)	Bovine aortic endothelial cells (BAECs)	✓		1.9 nm (0.125-1.0 mM)	1-5 Gy	Lower doses of radiation induce the same amount of cell death when AuNPs are present as do higher radiation doses without AuNPs.
(Teraoka et al., 2018)	HSC-3 (oral squamous carcinoma)	✓		5 nm (1.0 nM)	2, 4 and 8 Gy	AuNPs enhanced the cytotoxic effect of radiation through the induction of apoptosis but not inhibition of cell proliferation.
(Kazmi et al., 2020)	U87 (glioblastoma)	✓		42 nm (100 µg/mL)	2-8 Gy	AuNPs enabled radiosensitisation of U87 cells at 2Gy.
(Igaz et al., 2020)	A549 (lung adenocarcinoma) DU-145 + PC3 (prostate adenocarcinoma) MCF-7 (breast adenocarcinoma)	✓	✓	10 nm (6.8 µM)	2 and 4 Gy	AuNPs are effective in sensitising A549 cells to radiation in both 2D and 3D

(Musielak et al., 2023)	MCF-7 (breast adenocarcinoma)	✓	✓	10 nm and 30 nm (0.4-1.2 μg/mL)	2 Gy	AuNPs induce radiosensitisation in 2D, with size and length of PEG chain having a significant impact.
(Alhussan et al., 2023)	MIA PaCa-2 (pancreatic cancer) and CAF co-culture		✓	13 nm (7.5 μg/mL)	2 Gy	AuNPs sensitise 3D spheroids to radiation, with a greater effect observed in co-culture.

For AuNPs to function effectively as radiosensitisers, their precise localization within biological models is crucial. The penetration of gold nanoparticles into 3D cell platforms is influenced by various factors such as size, shape, and surface properties. For instance, a study by Rane and Armani (2016) showed that 30nm nanoparticles tend to penetrate HCT116 (colorectal carcinoma) 3D spheroids more efficiently than 10 nm, 50 nm and 70 nm AuNPs. Interestingly, functionalisation with oligonucleotides increased the penetration rate of 10nm and 50nm nanoparticles but reduced it for 30 nm and 70 nm AuNPs. However, none of the nanoparticles were able to penetrate the core of the spheroid, accumulating mainly on the outer ring (Rane & Armani, 2016). This finding is corroborated by a very recent study by Chen et al. (2024), which demonstrated that 15 nm, 22 nm and 60 nm nanoparticles primarily accumulated in the outer regions of MDA-MB-231 spheroids, with only a small fraction of 15 nm AuNPs penetrating the spheroid core (Chen et al., 2024). These findings demonstrate that the penetration rate of gold nanoparticles is not only dependent on the structure of spheroids, i.e. how tightly the cells aggregate, allowing for more or less effective AuNP penetration, but also on the properties of the nanoparticles themselves.

4.1.1. Gold-nanoparticle detection methods

Understanding the distribution of AuNPs within 3D models and cellular structures, their penetration, and intracellular location prior to radiation treatments is vital for optimizing their use as radiosensitizers. As nanoparticles enhance radiation effects by interacting with it and releasing electrons that react with DNA chains and other cell components, their location within cells plays a determinant role in their efficacy. This knowledge can provide insights into their impact on therapeutic outcomes (Lee et al., 2022).

Traditionally, the location of gold nanoparticles within cells is determined by transmission electron microscopy (TEM) or fluorescent microscopy, as nanoparticles are frequently functionalised with fluorescent markers to facilitate their tracking within subcellular structures (Kapara et al., 2020; Qu et al., 2020). However, since TEM is an expensive technique that relies on intricate sample preparation and ultramicrotomy, and fluorescent microscopy often presents imaging challenges, mainly on 3D models, new methods of AuNP detection have been emerging (Kapara et al., 2020). Some of these methods are:

- Raman Spectroscopy – a non-destructive, high-resolution spectroscopic technique used to study the interactions of gold nanoparticles with biological components, mapping their intracellular distribution and giving label-free and chemically specific information about biological samples (Aldosari, 2022). Surface-enhanced Raman Spectroscopy can be used to enhance the signal, allowing AuNP detection and mapping at low concentrations. A three-dimensional method of SERS was introduced by Kapara and colleagues (2020) to track the uptake and subcellular localisation of AuNPs in MCF-7 cells (Kapara et al., 2020).
- Dark Field Microscopy (DFM) - uses scattered light to create images of nanoparticles., which due to their size and optical properties, scatter light in a way that can be distinguished from the background. This method provides high-contrast images of nanoparticles and allows for their visualization and tracking within cells and 3D models in real-time. However, since the scattering of the cells themselves can interfere with the readings, DFM alone is not fully reliable. To overcome this limitation, Rodríguez-Fajardo et al. developed a novel two-colour DF technique that bypasses these challenges by offering more contrast and reducing the cell scattering (Rodríguez-Fajardo et al., 2018). DFM can also be used in combination with hyperspectral microscopy.
- Hyperspectral microscopy - advanced imaging technique that captures a wide spectrum of light for each pixel, allowing precise identification and localization of gold nanoparticles within cells and 3D models based on their unique spectral signatures. This method provides high sensitivity and comprehensive spatial-spectral data without the need for labelling, preserving sample integrity. This technique uses DFM to detect AuNP based on their scattering cross section and confirms their presence using a spectre angle mapping (SAM), which confirms internalisation and intracellular location of AuNPs by comparing the unknown spectra in the acquired hyperspectral image against a defined spectral library (Feng et al., 2023).
- Laser Ablation Inductively Coupled Plasma Mass Spectrometry Imaging (LA-ICP-MSI) – a highly sensitive technique that can be used to detect and quantify gold nanoparticles within biological samples. By ablating the sample with a laser, it vaporizes material which is then analysed by ICP-

MS to determine its elemental composition and concentration. This method provides precise spatial distribution data of nanoparticles within cells and tissues, allowing nanoparticle uptake and distribution assessment in biological systems (Arakawa et al., 2019; Hsiao et al., 2016).

4.1.2. Aims of this chapter

The aim of this chapter is to determine the radio-sensitising potential of non-functionalised (naked) gold nanoparticles in human osteosarcoma and prostate adenocarcinoma cell lines cultured in monolayer and 3D platforms. To investigate this, the different models were treated with 50 nm gold nanoparticles using what has been described in literature as the biologically relevant concentration. To allow for cell penetration, each model was incubated with the appropriate media containing 10 µg/mL AuNPs for 24h. Penetration of the nanoparticles into cells and spheroids/alginate spheres was assessed using LA-ICP-MS/MSI, electron microscopy and hyperspectral microscopy. Once it was confirmed the AuNP treatment had been successful, the gold-containing samples were irradiated with doses up to 20 Gy. Following treatment, cell viability was determined using the methods previously described for both 2D and 3D models. The presence of γ-H2AX foci and cell cycle distribution were also evaluated in 2D via immunofluorescence and flow cytometry analysis, respectively.

4.2. Results

4.2.1. Uptake of gold nanoparticles by 2D and 3D cell cultures.

Prior to irradiation, monolayer, multi-cellular tumour spheroid and alginate cultures were treated with 50 nm gold nanoparticles (Sigma), and their uptake was evaluated using LA-ICP-MS and hyperspectral microscopy.

4.2.1.1. Laser Ablation Inductively Coupled Plasma Mass Spectrometry (LA-ICP-MS) of 2D cultures.

LA-ICP-MS was used to determine if monolayer cultures were successfully internalising the gold-nanoparticles. Following treatment with 10 µg/mL for 24h, the cells were harvested, and microscopy slides were prepared by incorporating the cell pellet in Histogel® prior to sectioning, as described in section 2.7.2. For this analysis, isotopes ^{13}C, ^{66}Zn and ^{197}Au were monitored to determine cellular uptake of gold. The carbon isotope was used as a gate for samples (present in both cells and embedding matrix) and the zinc isotope was used as a cellular

marker. The sample was ablated using a 20 µm/sec scan speed. Data shows that, in 2D, all cell lines show successful gold nanoparticle uptake, as demonstrated by the high ^{197}Au signal (Figure 4.1). The ^{13}C signal increase around the 20-50sec mark indicates the start of sample ablation and stays constant through time, only decreasing when the laser passes from the sample to the glass slide. The ^{66}Zn signal increase around the 30-80sec mark in cell line samples (not as perceptible due to scale) happens when the laser moves from matrix to cell pellet, decreases when the laser moves to matrix and again from matrix to glass slide. A gold-nanoparticle pellet was used as a positive control.

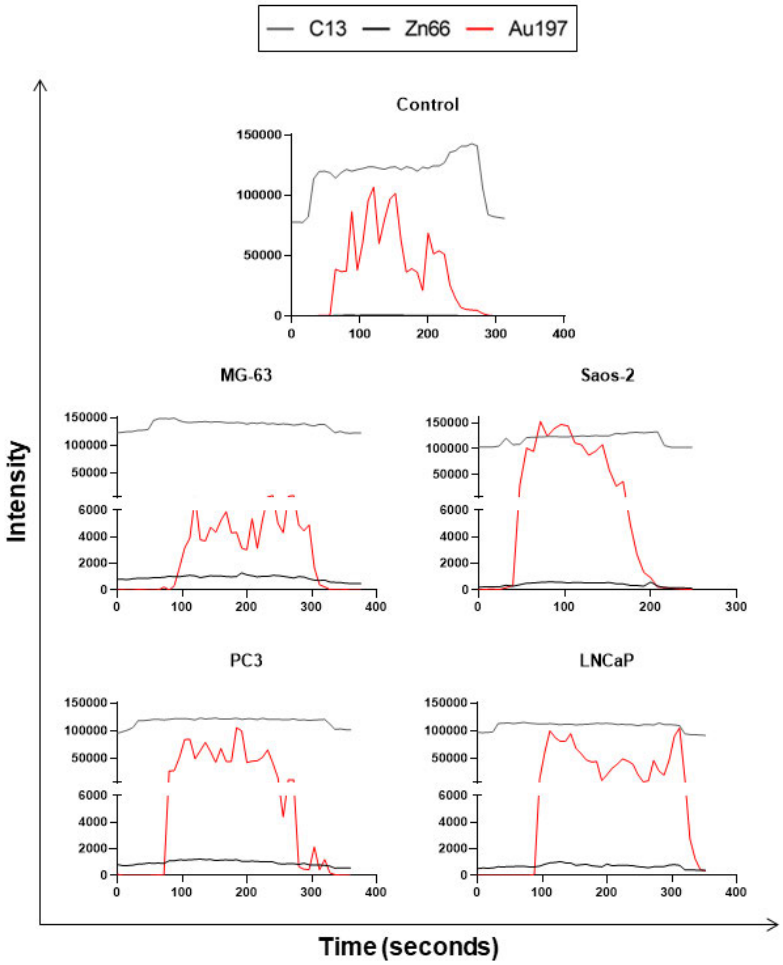

Figure 4.1 - LA-ICP-MS detection of gold nanoparticles in 2D cultures. Quantification of gold nanoparticle uptake in 2D cell pellets of human osteosarcoma and prostate adenocarcinoma cell lines via laser ablation analysis. Intensity vs. time profile of the ablated line in control and cell pellet samples show a successful uptake of AuNPs by all cell lines, demonstrated by the peaks in signal of ^{197}Au (red). 20 µm/sec scan speed.

4.2.1.2. Laser Ablation Inductively Coupled Plasma Mass Spectrometry Imaging (LA-ICP-MSI) of 3D models.

To determine the uptake and localization of gold nanoparticles in cells cultured within MCTS and alginate spheres, sections of both 3D models were analysed using LA-ICP-MS. Untreated controls were used to verify the specificity of the results and the subsequent data can be found in Appendix A of this thesis. The ICP-MS data was plotted as intensity vs. time graphs, using GraphPad Prism, and spectral images were generated to map the localization of each isotope within the samples.

4.2.1.2.1. Multicellular Tumour Spheroids

Data shows that when cultured in MCTS, all cell lines are able to uptake AuNPs. In MG-63 gold nanoparticles failed to penetrate the spheroid core, accumulating in the outer ring (Figure 4.2). In Saos-2, despite the penetration rate being seemingly higher than in MG-63, AuNPs also failed to reach the core of the spheroid (Appendix B). For PC3 MCTS, the processing of samples prior to ICP-MS analysis led to the disruption of the spheroid integrity, making it difficult to determine the precise location of the gold nanoparticles. Nonetheless, the resulting images seem to point to a somewhat even distribution of AuNPs (Appendix B). Finally, for LNCaP, some gold nanoparticles were able to penetrate the spheroid core (Figure 4.3).

4.2.1.2.2. Alginate Spheres

In alginate spheres, only LNCaP cells appear to effectively internalise AuNPs (Figure 4.4). Even though gold uptake is identifiable in MG-63 (Figure 4.5), Saos-2 and PC3 alginate spheres (Appendix C), the intensity of the pulses is much lower, compared to monolayer and MCTS cultures.

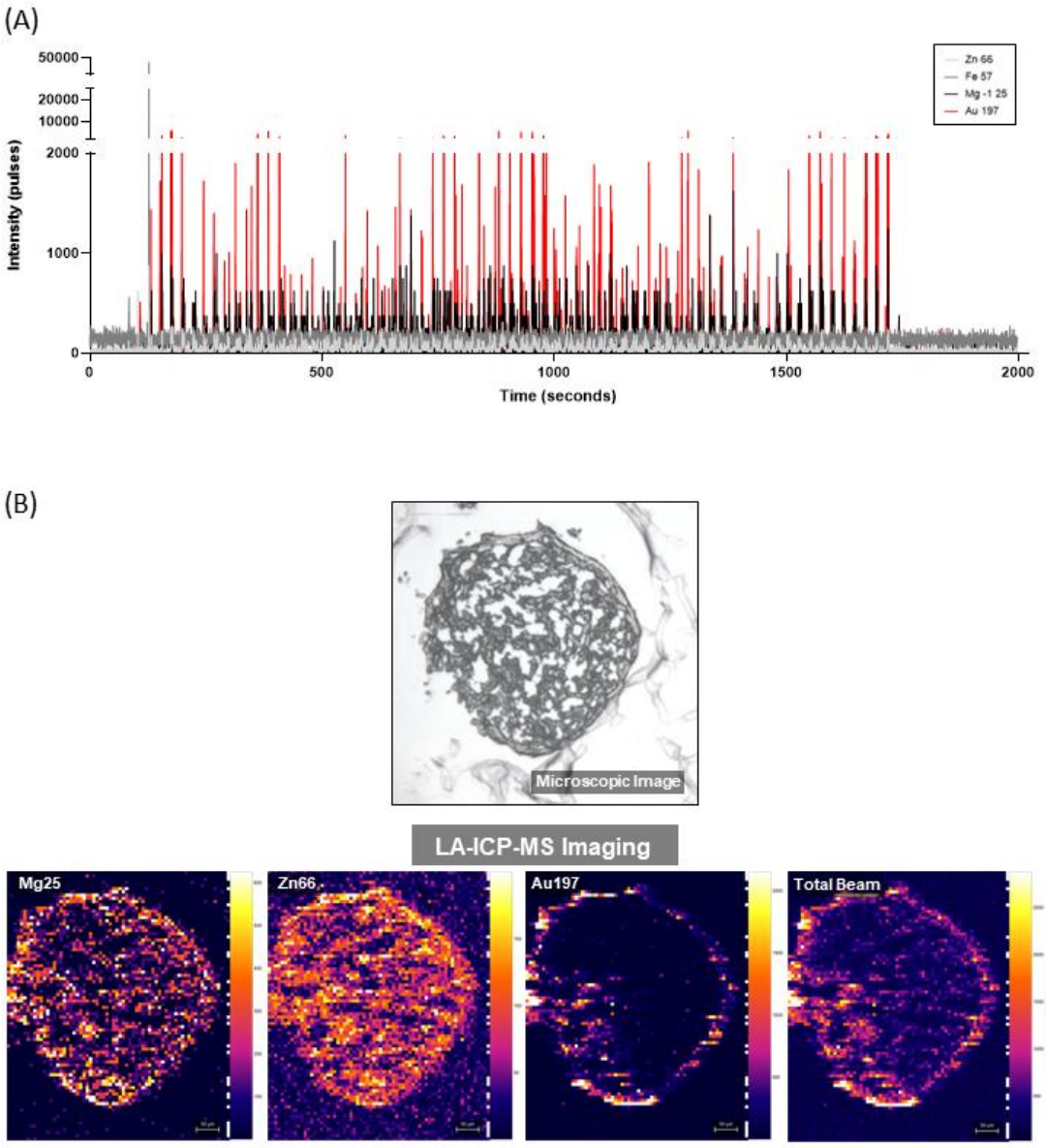

Figure 4.2 - LA-ICP-MS detection and localization of gold nanoparticles in MG-63 MCTS. (A) Intensity vs. time profile of ablated raster shows uptake of AuNPs demonstrated by the ^{197}Au spectrum (red). 20 µm/sec scan speed. **(B)** LA-ICP-MSI of AuNP treated MG-63 spheroid. Pre-ablation optical image (20X objective) and elemental maps of ^{66}Zn, ^{25}Mg, ^{197}Au, and total beam. Scale bar represents 50µm.

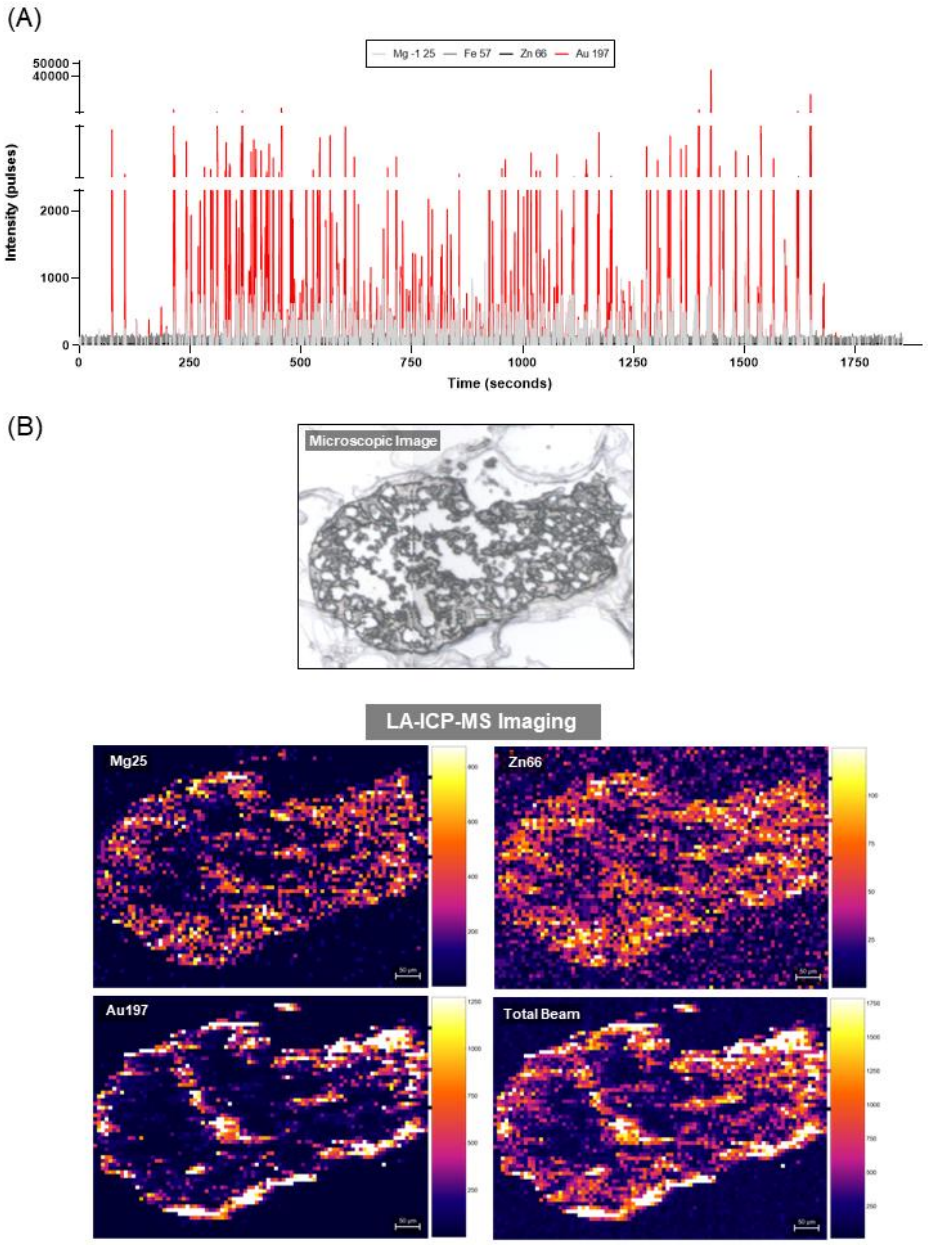

Figure 4.3 - LA-ICP-MS detection and localization of gold nanoparticles in LNCaP MCTS. (A) Intensity vs. time profile of ablated raster shows uptake of AuNPs demonstrated by the ^{197}Au spectrum (red). 20 µm/sec scan speed. **(B)** LA-ICP-MSI of AuNP treated LNCaP spheroid. Pre-ablation optical image (20X objective) and elemental maps of ^{66}Zn, ^{25}Mg, ^{197}Au, and total beam. Scale bar represents 50µm.

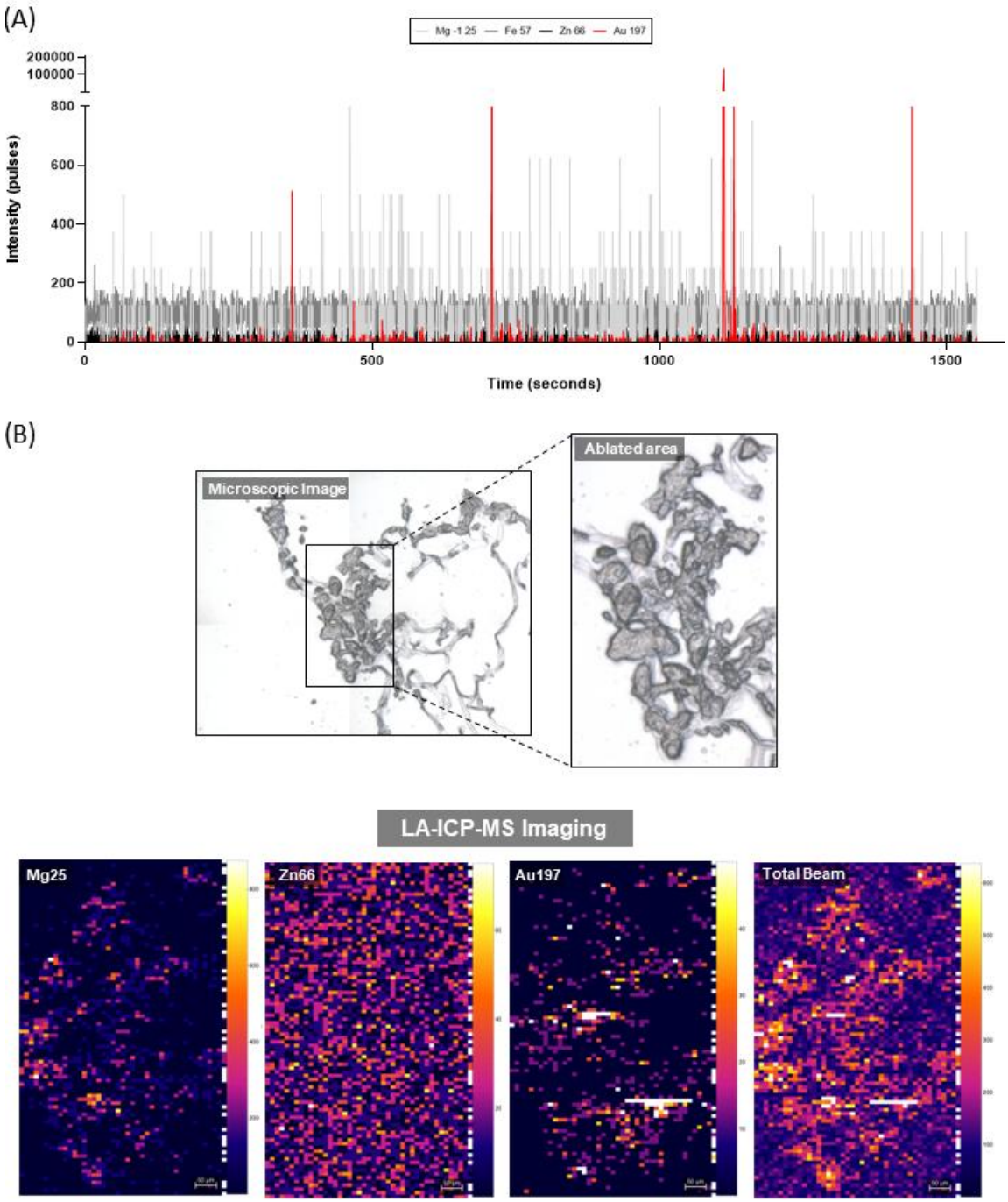

Figure 4.4 - LA-ICP-MS detection and localization of gold nanoparticles in LNCaP alginate spheres. (A) Intensity vs. time profile of ablated raster shows uptake of AuNPs demonstrated by the ^{197}Au spectrum (red). 20 µm/sec scan speed. **(B)** LA-ICP-MSI of AuNP treated LNCaP colonies grown in alginate matrix. Pre-ablation optical image (20X objective) and elemental maps of ^{66}Zn, ^{25}Mg, ^{197}Au, and total beam. Scale bar represents 50µm.

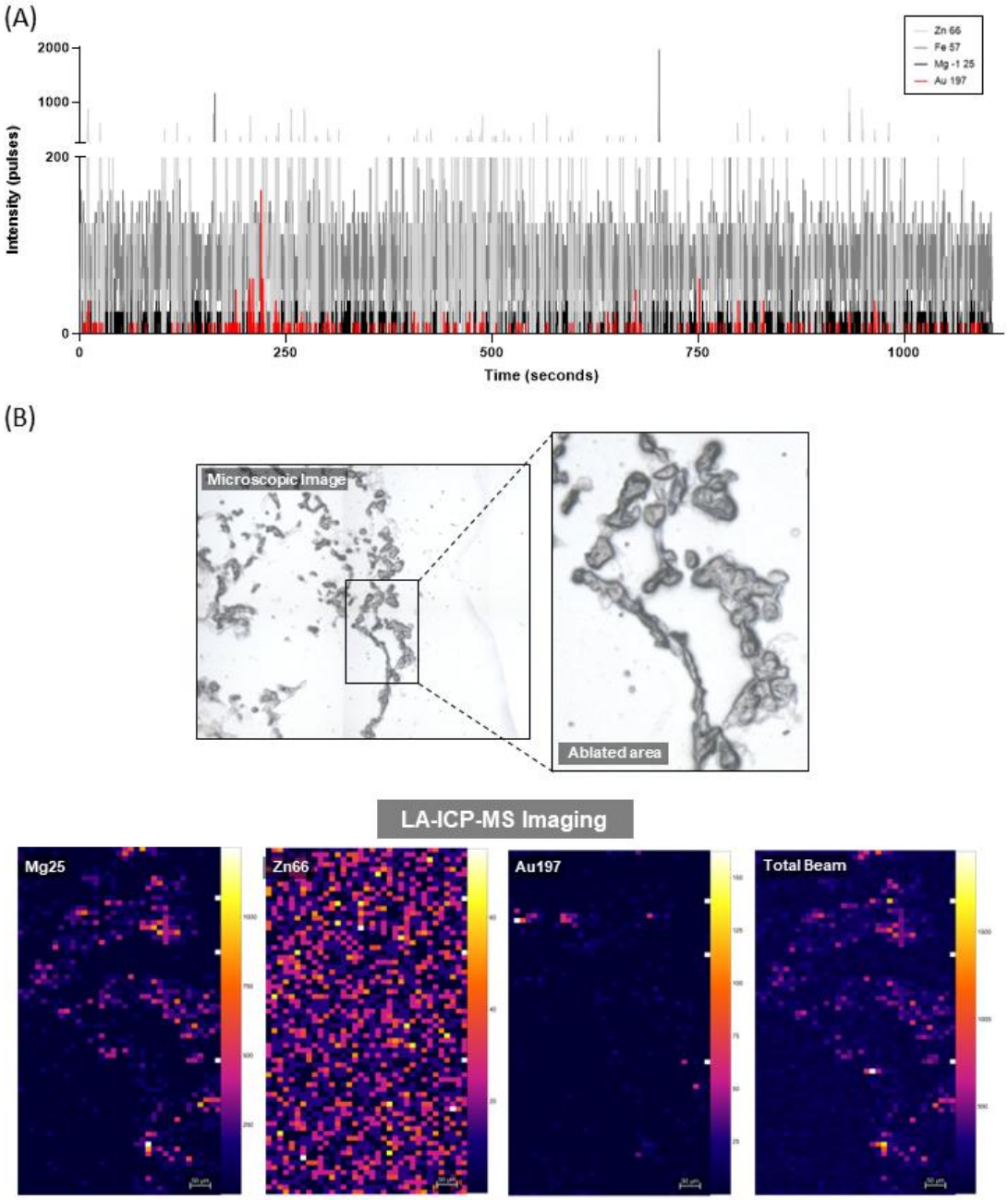

Figure 4.5 – LA-ICP-MS detection and localization of gold nanoparticles in MG-63 alginate spheres. (A) Intensity vs. time profile of ablated raster shows uptake of AuNPs demonstrated by the ^{197}Au spectrum (red). 20 µm/sec scan speed. **(B)** LA-ICP-MSI of AuNP treated MG-63 colonies grown in alginate matrix. Pre-ablation optical image (20X objective) and elemental maps of ^{66}Zn, ^{25}Mg, ^{197}Au, and total beam. Scale bar represents 50µm.

4.2.1.3. Hyperspectral imaging of monolayer and spheroid cultures.

To visualise cellular uptake of gold nanoparticles, monolayer and MCTS samples were imaged via hyperspectral microscopy, a technique that integrates hyperspectral imaging (HSI) with advanced optics, often utilizing specialized dark-field reflectance systems. Resorting to advanced optics and algorithms, HSI allows for the capture of entire spectra in a single pixel, enabling the identification and quantification of different compounds within a sample based on their unique spectral signatures (Roth et al., 2015).

All HSI work was performed by Dr Naill Byrne and his team at Queen's University Belfast. Due to sample availability and time constraints only PC3 monolayer cultures and MG-63 spheroids were analysed, and the resulting figures can be found in Appendix D.

Results indicate that, as seen in LA-ICP-MS data, monolayer cultures are able to successfully internalise gold nanoparticles, demonstrated by the spectral angle mapping (SAM) resulting from HSI of 2D culture slides (Figure 4.6D).

As for MCTS, these findings indicate that although MG-63 cells effectively uptake AuNPs, most fail to penetrate the depth of the spheroid, not reaching the core and accumulating instead in the outer area, as depicted in the enhanced darkfield images (Figure 4.3A) and confirmed by the HSI ensuing SAM (Figure 4.7D). These findings align with the LA-ICP-MSI results.

4.2.2. Assessment of gold nanoparticles as radio-sensitisers in 2D cultures.

Monolayer cultures of osteosarcoma (MG-63 and Saos-2) and prostate adenocarcinoma cell lines (PC3 and LNCaP) were treated with 10 µg/mL of 50 nm diameter gold nanoparticles for 24 hours. After gold treatment, the cells were irradiated with doses of 1.25, 2.5, and 5 Gy, followed by a 10-day incubation period. Cell viability was then assessed using a colony formation assay. Due to the number of samples, and to account for colony variability between cell lines, cells were plated in 96-well plates and colony growth was assessed by measuring the absorbance of each well following crystal violet staining. Absorbance readings were corrected using blank wells and normalised towards the untreated control. To assess how the presence of gold affected the radiosensitivity of each cell line, LQ curves were compared using an extra sum of squares test. The dose enhancement factor was also calculated from the IC50 values of untreated and gold-treated cells using the following formula:

$$Dose\ Enhancement\ Factor\ (DEF) = \frac{IC50_{control}}{IC50_{AuNP}}$$

Responses to each radiation dose of untreated and AuNP-treated cells were compared using multiple *t-tests*, followed by multiple comparisons using the Holme-Sidak method with a 95% confidence interval (Figure 4.6). The toxicity of the AuNP treatment was also assessed to ensure the nanoparticles alone did not hinder cell viability, which was confirmed. The results can be found in Appendix K of this thesis.

Results show that following irradiation the surviving fraction of untreated MG-63 cells was 0.92 ± 0.04, 0.61 ± 0.23, and 0.28 ± 0.13 at 1.25, 2.5 and 5 Gy doses, respectively. This equated to an IC50 of 3.67 ± 0.89 Gy. AuNP-treated MG-63 cells presented a surviving fraction of 0.54 ± 0.11 after a 1.25 Gy dose, 0.27 ± 0.13 after 2.5 Gy, and 0.09 ± 0.03 after 5 Gy, which corresponded to an IC50 of 1.08 ± 0.17 Gy. Comparing the responses of untreated and AuNP-treated cells, it was possible to observe a radiosensitising effect of the gold nanoparticles (p<0.001). The difference in sensitivity was significant at 1.25 Gy (p=0.006). Overall, the presence of gold nanoparticles enhanced the radiation dose effect by a factor of 3.4 in MG-63 cells. To confirm the level of significance of the interaction between gold nanoparticles and radiation, a two-way ANOVA test was also conducted. The results showed a statistically significant interaction between

irradiation and AuNP treatment (p=0.044). The fraction of cells that survived irradiation in untreated Saos-2 was 0.77 ± 0.18 after 1.25 Gy, 0.37 ± 0.19 after 2.5 Gy and 0.13 ± 0.03 after 5 Gy (IC50=1.86 ± 0.45 Gy). For AuNP treated cells, the surviving fraction assumed values of 0.39 ± 0.3, 0.21 ± 0.12 and 0.09 ± 0.06 following 1.25, 2.5 and 5 Gy doses, respectively (IC50=0.71 ± 0.19 Gy). The presence of gold increased the sensitivity of Saos-2 cells by a factor of 2.6, and the sensitising effect was statistically significant (p=0.023). For the prostate cancer cell lines, the radiosensitising effect of gold was statistically significant in PC3 (p=0.012) but not in LNCaP, with a DEF of 1.67 and 1.81 for PC3 and LNCaP, respectively. Untreated PC3 cells presented a surviving fraction of 0.75 ± 0.15, 0.53 ± 0.11, and 0.23 ± 0.06 following 1.25, 2.5 and 5 Gy doses, respectively (IC50=2.57 ± 0.41 Gy). With AuNP treatment, the surviving fraction was 0.67 ± 0.04 after 1.25 Gy, 0.32 ± 0.13 after 2.5 Gy and 0.14 ± 0.08 after 5Gy, thus equating to an IC50 of 1.54 ± 0.19 Gy. As for LNCaP, the surviving fraction untreated cells was 0.60 ± 0.21 Gy after 1.25 Gy. This value saw a reduction of 27% following a 2.5 Gy dose (0.45 ± 0.14) and of 83% after 5 Gy (0.10 ± 0.05), translating to an IC50 value of 1.58 ± 0.45 Gy. For gold-treated LNCaP cells, the surviving fraction after 1.25 Gy was 0.43 ± 0.07, 0.30 ± 0.07 after 2.5 Gy and 0.07 ± 0.02 following a 5 Gy radiation dose, which reflected an IC50 value of 0.87 ± 0.19 Gy.

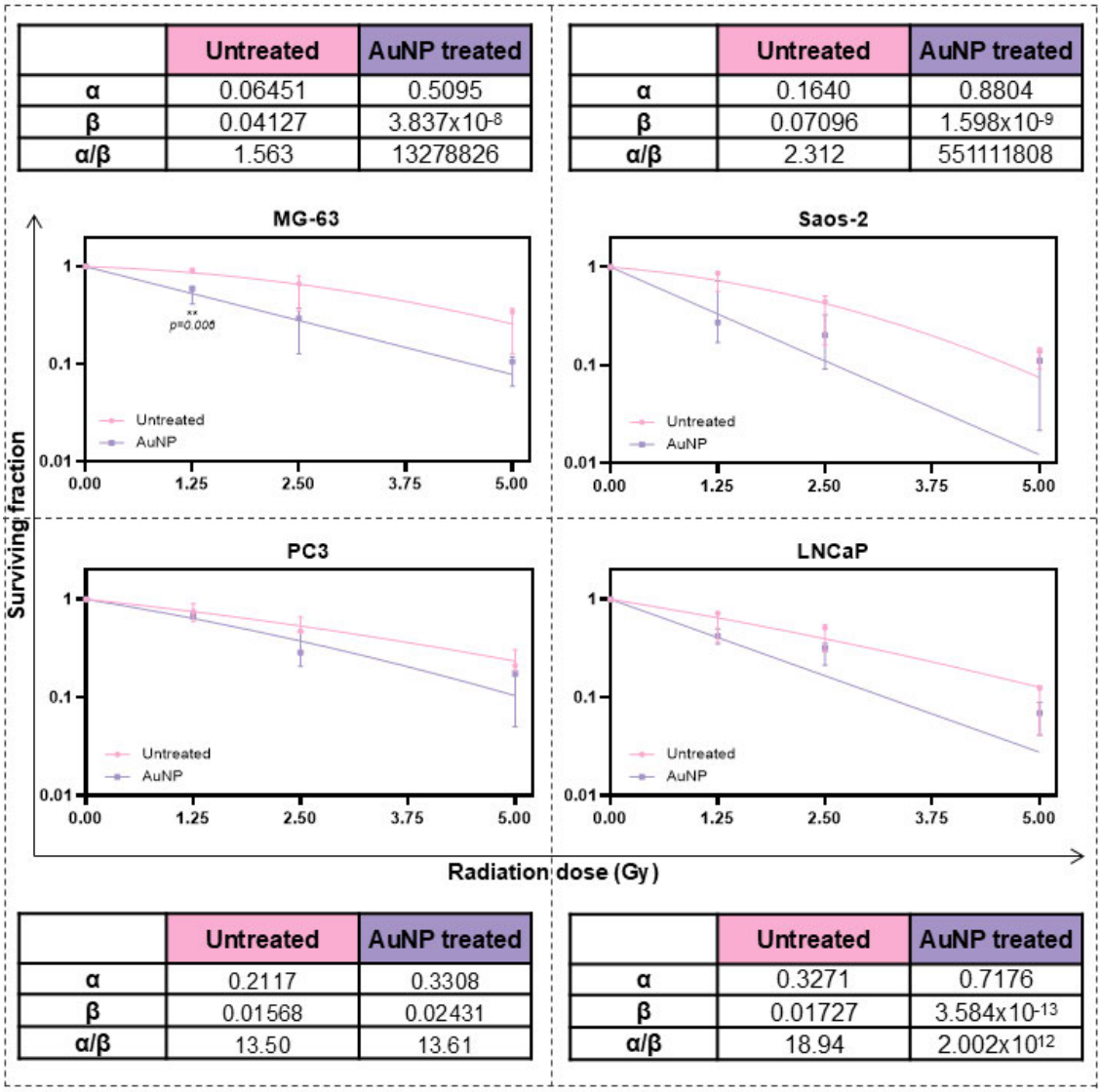

	Untreated	AuNP treated
α	0.06451	0.5095
β	0.04127	3.837×10^{-8}
α/β	1.563	13278826

	Untreated	AuNP treated
α	0.1640	0.8804
β	0.07096	1.598×10^{-9}
α/β	2.312	551111808

	Untreated	AuNP treated
α	0.2117	0.3308
β	0.01568	0.02431
α/β	13.50	13.61

	Untreated	AuNP treated
α	0.3271	0.7176
β	0.01727	3.584×10^{-13}
α/β	18.94	2.002×10^{12}

Figure 4.6 - Cell viability of AuNP-treated osteosarcoma and prostate adenocarcinoma cell lines cultured 10 days post-irradiation. Surviving fractions of AuNP-treated monolayer cultures with increasing doses of radiation. Gold nanoparticle treatment increases the sensitivity of all cell lines to radiation. This difference is significant at 1.25 Gy in MG-63 cells. Scatter plots, surviving fraction data is presented as mean ±SD, individual values represent n=3 independent experiments with 3 technical repeats. Statistical significance determined by multiple *t-tests* and corrected using the Holme-Sidak method of multiple comparisons, with alpha=0.05. (*P<0.05). From the LQ curves, α and β values were calculated using a 95% confidence interval.

4.2.3. Assessment of gold nanoparticles as radio-sensitisers in alginate sphere cultures.

Alginate spheres of MG-63, Saos-2, PC3, and LNCaP cells were prepared and incubated until young colonies were formed (≈3 days). Twenty-four hours prior to irradiation, the spheres were treated with 50 nm diameter gold nanoparticles at a concentration of 10 μg/mL in appropriate cell culture media. On irradiation day, the colonies were measured and treated with doses of 2.5, 5 and 20 Gy. Colonies were allowed to grow for a further 7 days, after which colony diameter was measured once more. The values were normalised towards the untreated control and a non-linear regression curve was plotted for both the untreated and the AuNP-treated populations to determine the IC50 for each cell line. The radiosensitising effect of the gold nanoparticles was quantified by determining the dose enhancement factor using the formula mentioned in the previous section of this chapter. The responses of each untreated and AuNP-treated cell line were compared at each dose using multiple *t-tests* and statistical significance was determined using the Holme-Sidak method, with alpha=0.05. Each row was analysed individually (Figure 4.9).

Results show that gold nanoparticles did not produce a significant radio-sensitising effect in any of the cell lines. Prior to irradiation, the average colony diameter of untreated MG-63 cells was 40.4±2.1 μm (Figure 4.9). After 7 days, untreated colonies nearly doubled, presenting an average diameter of 79.6±2.2 μm, while the colonies in AuNP-treated spheres measured, on average, 56.7±10.5 μm. Following irradiation, untreated colonies measured 57.1±8.4 μm, 47.2±6.5 μm and 31.8±1.3 μm after 2.5, 5 and 20 Gy doses, respectively, which translated to an IC50 of 9.15±1.72 Gy. AuNP-treated colonies measured 49.5±6.5μm following a 2.5 Gy dose, 37.6±4.7 μm at 5 Gy and 30.1±0.7 μm with 20 Gy, meaning the IC50 for gold-treated MG63 colonies was 11.3±1.13 Gy. The difference in response between untreated and AuNP-treated cells was not significant.

Before irradiation, Saos-2 colonies measured 27.9±1.4 μm (Figure 4.9). After a 7-day incubation period, untreated colonies measured 60.3±5.4 μm and AuNP treated measured 62.4±9.9 μm in diameter. Following a 2.5 Gy dose, untreated colonies measured 38.5±1.8 μm and gold-treated colonies measured 40.2±2.3 μm. After 5 Gy, the colony diameter was 35.2±2.6 μm and 32.3±1.8 μm for untreated and AuNP-treated cells, respectively. With a 20 Gy dose, untreated

colonies measured 30.6±2.0 μm and gold-treated colonies presented an average diameter of 31.5±2.5 μm. The IC50 values were 5.7±1.2 Gy and 6.3±1.6 Gy for untreated and gold-treated colonies, respectively. The difference in radio-sensitivity between untreated and AuNP treated Saos-2 alginate spheres was not significant.

PC3 colonies measured 35.8±3.7 μm prior to irradiation (Figure 4.9). The following week, the diameter of untreated colonies increased to 83.5±2.0 μm while AuNP-treated colonies only grew to 60±5.7 μm. Following exposure to radiation, untreated colonies measured 59.8±7.2 μm, 41.5±3.1 μm and 37.5±0.2 μm with doses of 2.5, 5 and 20 Gy, respectively. The diameters of gold-treated colonies were 51.3±1.6 μm, 36.9±0.5 μm and 36.2±2.8 μm following doses of 2.5, 5 and 20 Gy, respectively. The IC50 value of irradiation for untreated colonies was 5.6±0.9 Gy and 5.9±0.8 Gy for AuNP-treated colonies. The difference in response between untreated and gold-treated cells was not significant.

On the day of irradiation, LNCaP colonies measured, on average, 44.7±2.8 μm (Figure 4.9). Following irradiation, untreated colonies exposed to a 2.5 Gy radiation dose measured 75.8±10.3 μm. With a 5 Gy dose, the diameter lowered to 57±7.1 μm and to 42.6±3.1 μm with 20 Gy. Colonies that were not irradiated measured 120.3±11.3 μm. Gold-treated colonies measured 89.5±1.2μm and following doses of 2.5, 5 and 20 Gy, their average diameter was 46.3±5.8 μm, 43.9±1.6 μm, and 45.1±1.4 μm, respectively. The IC50 for untreated colonies was 5.53±0.9 Gy and 3.33±0.6 for AuNP-treated LNCaP cells. Even though the gold nanoparticles seem to have produced a minor radiosensitising effect, translated by a DEF of 1.68, this was not statistically significant.

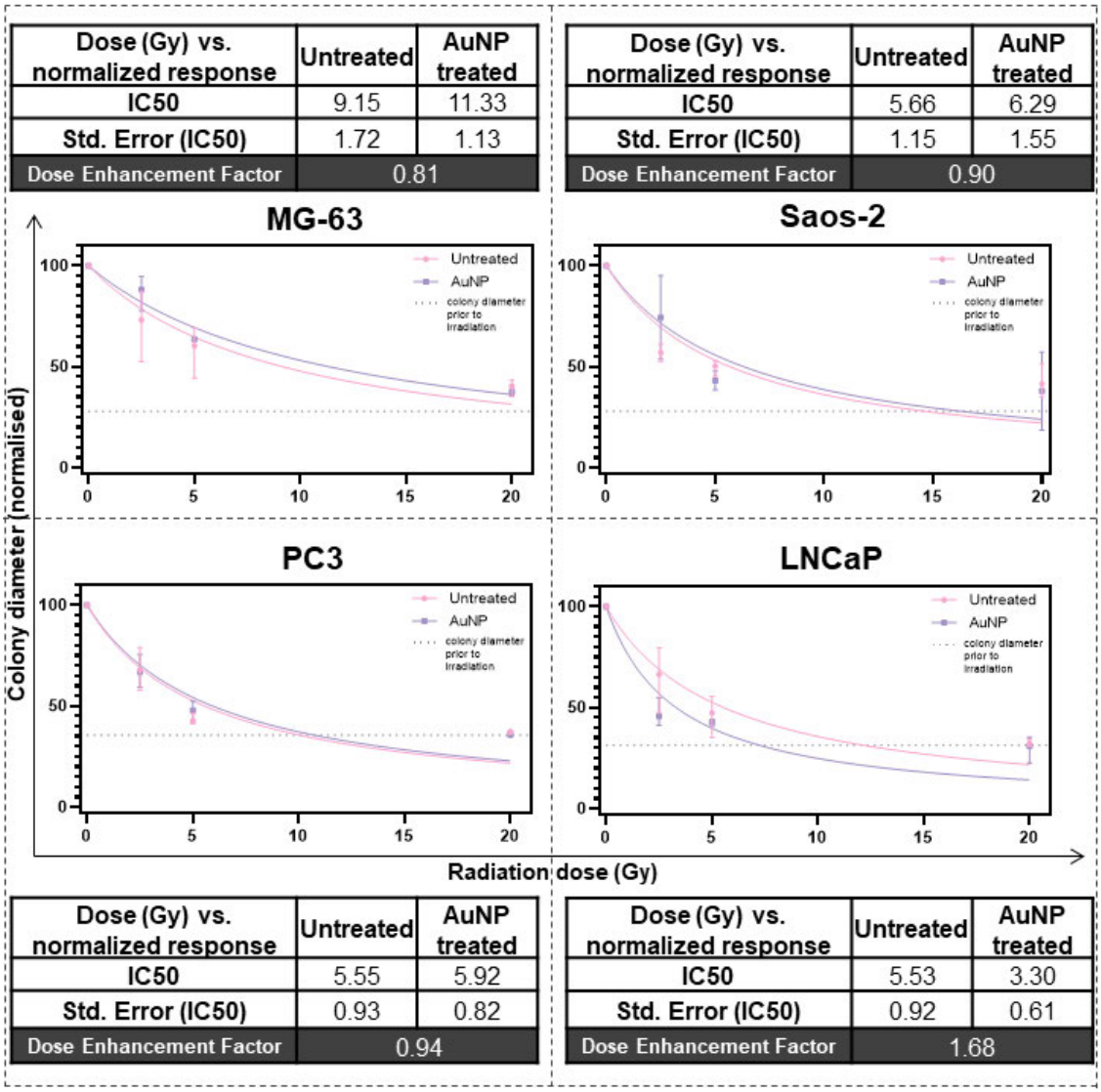

Figure 4.7 – Colony diameter of AuNP-treated osteosarcoma and prostate adenocarcinoma cells grown in alginate spheres 7 days post-irradiation. Normalised colony diameter of AuNP-treated alginate sphere cultures with increasing doses of radiation. Gold nanoparticle treatment does not produce a significant difference in response to radiation. Scatter plots, normalised colony diameter is presented as percentage median ±range, individual values represent n=3 independent experiments with 3 technical repeats. Statistical significance determined by multiple *t-tests* and corrected using the Holme-Sidak method of multiple comparisons, with alpha=0.05. (*P<0.05). From the non-linear regression curves, IC50 values were calculated using a 95% confidence interval.

4.2.4. Comparison of radio-sensitivity between AuNP-treated monolayer and alginate sphere cultures.

The data from the clonogenic assays (2D) and colony diameter measurements (alginate spheres) was compared using multiple *t-tests* and corrected with the Holm-Sidak method for multiple comparisons, with alpha=0.05. The response of monolayer and alginate cultures was analysed at each dose individually. The results show that the difference in radio-sensitivity between 2D and 3D models is significant at 5 Gy for all cell lines, with *p* values lower than 0.001 for MG-63 and LNCaP cells, 0.014 for Saos-2 and 0.003 for PC3. With a 2.5Gy dose the difference in response is significant for all cell lines except LNCaP, with *p* values of 0.02 for MG-63, 0.017 for Saos-2 and 0.018 for PC3 (Figure 4.10).

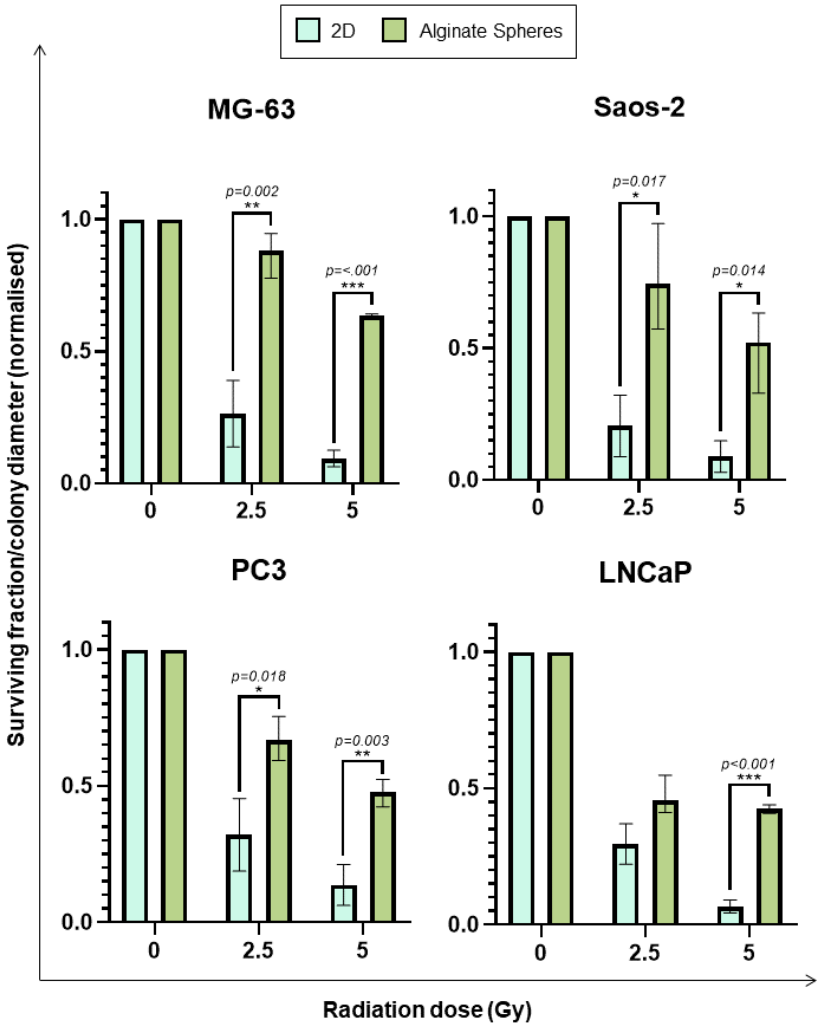

Figure 4.8 - Comparison of responses to ionising radiation between gold-treated cells cultured in monolayer and alginate spheres 10 days post-irradiation. Interleaved bars, multiple *t-tests*. Statistical significance corrected using the Holme-Sidak method of multiple comparisons, with alpha=0.05. (*P<0.05). 2D data is presented as mean ±SD. 3D data is presented as median ±range and individual values represent n=3 independent experiments with 3 technical repeats.

4.2.5. Acute responses of gold-treated MCTS to radiation.

To determine if the gold nanoparticles produced an acute radio-sensitising effect in multicellular tumour spheroids, these were treated with 50 nm diameter gold nanoparticles at a concentration of 10 μg/mL in appropriate cell culture media for 24h. The spheroids were then irradiated with doses of 2.5, 5 and 20 Gy and their viability was measured a Hoechst 33342 and PI live/dead assay (Figure 4.11). The blue (all cells) and red (dead cells) areas were measured, the cell viability was calculated and normalised against the untreated controls and plotted as a percentage with the corresponding non-linear regression curves of dose vs. normalised. The IC50 values were calculated with a confidence interval of 95% (Figure 4.12A) and the sensitivity of gold-treated MCTS to each radiation dose was analysed using a Kruskal-Wallis non-parametric test followed by a Dunn's multiple comparisons test. The viability of AuNP-treated MCTS with each dose was then compared to the one of untreated cultures with multiple *t-tests* corrected using the Holme-Sidak method for multiple comparisons with a 95% confidence interval (Figure 4.12B).

Results show that AuNP-treated osteosarcoma cell lines show a decrease in viability following increasing doses of radiation. After exposure, MG-63 MCTS' viability reduced to 95.1±2.3%, 92.1±5.3%, and 66.9±8.3% after 2.5, 5, and 20 Gy doses of radiation (Figure 4.12A). This reduction is statistically significant at 20 Gy (p=0.06). The viability of Saos-2 MCTS treated with gold was 91.8±12.4% after 2.5 Gy, 76±3.6% with 5 Gy and 39.8±10% following a 20 Gy dose, which was statistically significant (p=0.019) (Figure 4.12A). For AuNP-treated MG-63 MCTS, the IC50 was 42.7±1.6 Gy and 15.3±1.2 Gy for Saos-2. Furthermore, data shows that AuNP-treated osteosarcoma MCTS present a higher acute sensitivity to radiation than untreated MCTS of the same cell lines. This difference in sensitivity is significant at 20 Gy for MG-63 (p=0.05) and at 5 and 20 Gy for Saos-2 (p<0.001) (Figure 4.12B).

Prostate cell lines were not radio-sensitised by the gold nanoparticles, with the calculated IC50 for AuNP-treated PC3 MCTS being 148.9±2.2 Gy and 493.6±2.7 Gy for LNCaP. Given the dimension of these values (>20 Gy) they hold no real biological meaning and were only calculated for completeness of results. The viability of PC3 was 99.3±3.3%, 91.4±5.6%, and 89.6±4.3% after 2.5, 5 and 20 Gy radiation doses, respectively (Figure 4.13A). The difference in viability between the control and the 20 Gy treated spheroids was statistically significant

(p=0.05) but not biologically relevant, since the average viability was still approximately 90%. For LNCaP, spheroid viability remained similar regardless of radiation dose, with average values of 97.2±2.7%, 94.8±1.8%, and 97.5±0.7% with 2.5, 5 and 20 Gy doses, respectively (Figure 4.12A). Following exposure with a 5 Gy dose, there is a significant difference in sensitivity between the control and radiation exposed spheroids. However, this difference is merely mathematical and not biologically relevant, as MCTS still present a viability of approximately 95% and no significant difference is observed at 20 Gy (Figure 4.12B).

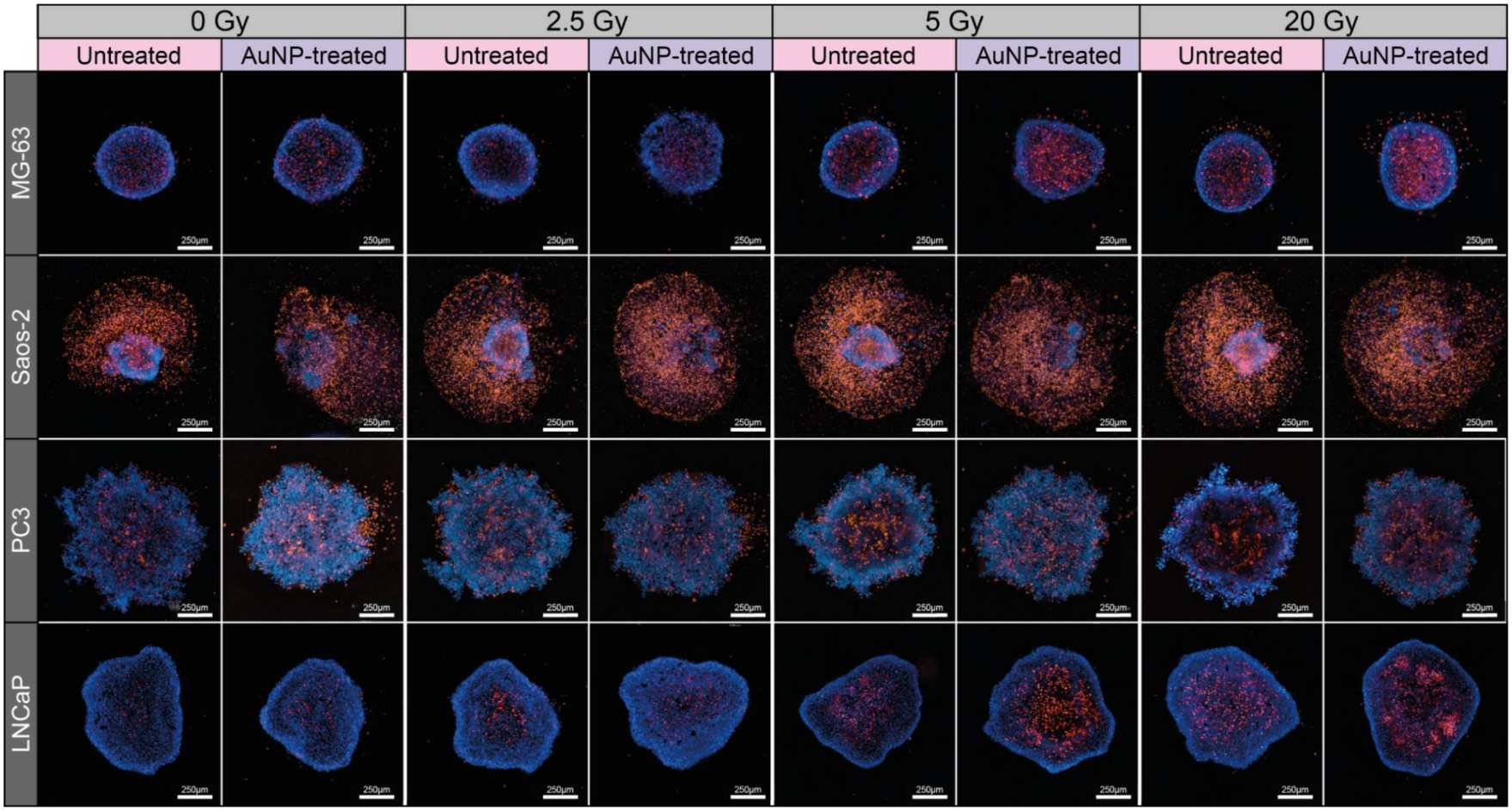

Figure 4.9 - Cell viability of human osteosarcoma and prostate cancer cell lines cultured in MCTS and treated with AuNPs, 24h post-irradiation. Multicellular tumour spheroids were stained with Hoechst 33342 (blue cells) and Propidium Iodide (red cells). Cytation 5 imaging system, 4x objective, Z-stack of DAPI and Texas Red channels. Scale bar represents 250 µm.

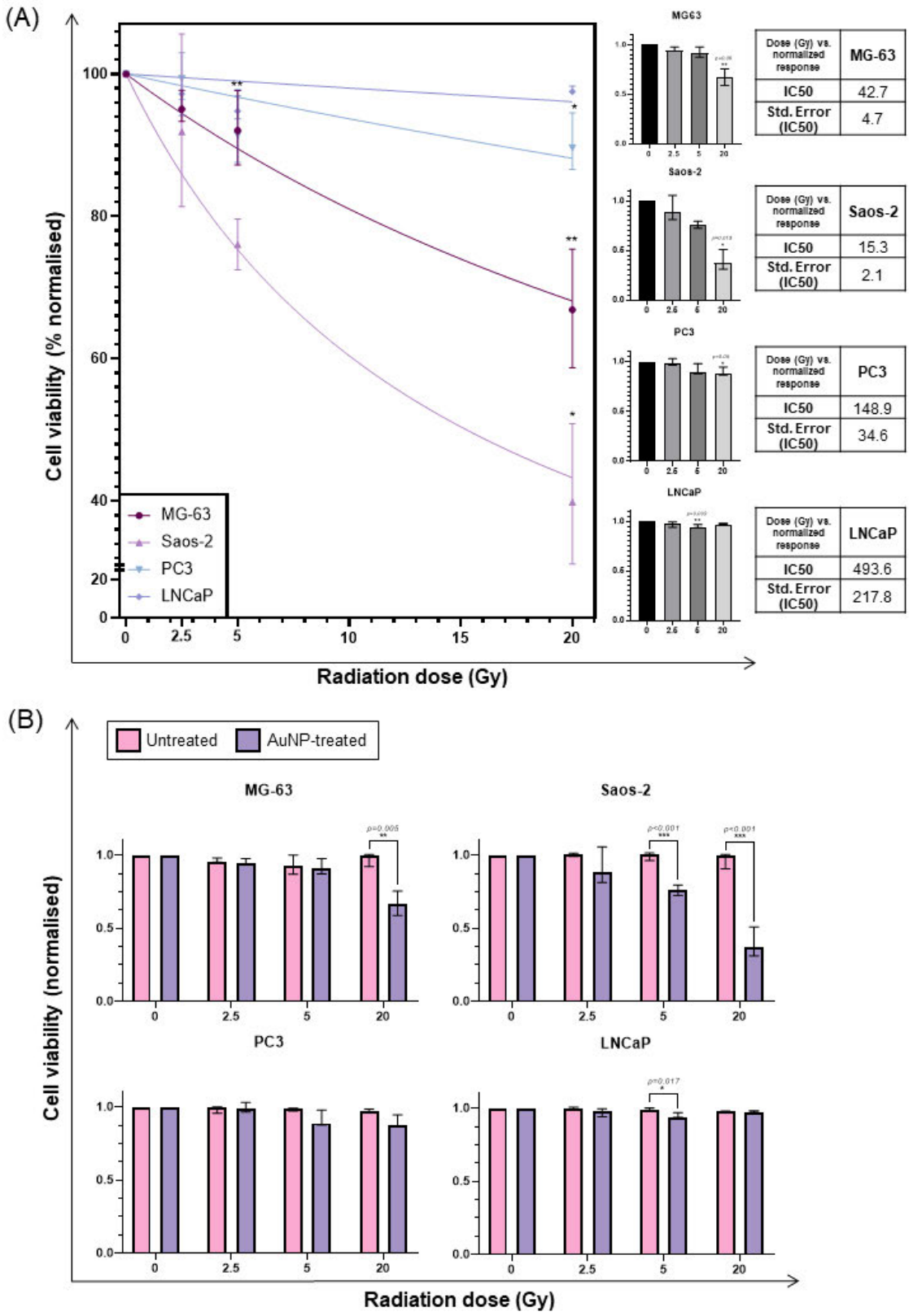

Figure 4.10 - Viability of cells grown in MCTS and treated with AuNPs 24h-post ionising radiation exposure. (A) Cell lines present a reduction in viability with increasing doses of radiation. Scatter plot and non-linear regression curve, percentage cell viability data is presented as median ±range, individual values represent n=3 independent experiments with 3 technical repeats. Individually analysed responses of MG-63, Saos-2, PC3, and LNCaP show a significant reduction in viability at individual doses. Column bar graph, Kruskal-Wallis followed by Dunn's multiple comparisons test (*P<0.05). **(B)** Comparison

between untreated and AuNP-treated MCTS of each cell line. Interleaved bars, multiple *t-tests*. Statistical significance corrected using the Holm-Sidak method of multiple comparisons, with alpha=0.05. (*P<0.05). All data is presented as median ±range and individual values represent n=3 independent experiments with 3 technical repeats. Untreated data has been shown in previous chapters as all measurements were done at the same time.

4.2.6. Acute responses of gold-treated alginate spheres to radiation.

Prior to ionising radiation exposure, alginate spheres were prepared using the method described in 2.1.6.2. and treated with 50 nm diameter gold nanoparticles at a concentration of 10 μg/mL in appropriate cell culture media for 24h. The alginate spheres were then irradiated using doses of 2.5 Gy, 5 Gy, and 20 Gy. To assess cell viability after irradiation, the cultures were stained with Hoechst 33342/PI 24h post-treatment and imaged on Cytation 5 (Figure 4.13). Relative percentage of viable cells was calculated by dividing the number of dead cells – stained with PI - by the total number of cells, stained with Hoechst 33342, and normalised towards the respective untreated control. The data was graphed as a percentage in a scatter plot and non-linear regression curves of dose vs. normalised response were drawn. The respective IC50 values were calculated, with a confidence interval of 95% (Figure 4.14). Analysis of each gold-treated cell line's response to the different radiation doses was conducted using a Kruskal-Wallis non-parametric test, due to the skewness of the results. Additionally, datasets were subjected to multiple comparisons, using Dunn's correction as a post-hoc test, to assess the significance of the response to each dose, when compared to the untreated control (0Gy). The response of gold-treated alginate spheres was compared with that of the untreated models of the same cell line for each radiation dose using multiple t-tests and corrected using the Holme-Sidak method with a 95% confidence interval.

Results show that all cell lines suffer a decrease in viability following irradiation. MG-63 colonies present average viability values of 95.1±2.5%, 84.5±8%, and 64.3±2.2% after exposure to 2.5, 5, and 20 Gy radiation doses, respectively (Figure 4.14A). This reduction in viability was significant at 20 Gy (p=0.006) and the IC50 for MG-63 cells grown in alginate spheres was 34.6±3.1 Gy. When compared to untreated models, AuNP-treated alginate spheres show a significant reduction in viability with every dose with p values of 0.024 at 2.5 Gy, 0.041 at 5 Gy and lower than 0.001 at 20 Gy (Figure 4.14B). Saos-2 cells also show a decrease in viability with each increasing dose: 76.6±20% with 2.5 Gy,

50.1±15.6% with 5 Gy, and 32.8±18.1% following a dose of 20 Gy (Figure 4.14A). The latter held statistical significance, with a *p* value of 0.009. The IC50 value for Saos-2 alginate spheres was 6.9±1.6 Gy. The comparison between the responses of gold-treated alginate spheres with those of untreated models revealed a radiosensitising effect of AuNPs, which was statistically significant at 20 Gy (p=0.006) (Figure 4.14B). The reduction in viability of PC3 cells grown in alginate spheres was less pronounced than in the previously mentioned cell lines. Following a dose of 2.5 Gy, the viability of PC3 cells remained at 95±5.7%, and 95.2±1.8% with 5 Gy. After being exposed to 20 Gy the viability was significantly reduced (p=0.006) to 78.4±4% (Figure 4.14A). The IC50 for AuNP-treated PC3 alginate spheres was 73.8±5.4 Gy and when compared to their untreated counterparts the cell viability remained similar – even though there is a statistically significant difference in viability between untreated and AuNP-treated PC3 alginate spheres at 2.5 Gy, this is not biologically relevant as approximately 95% of cells remain viable (Figure 4.14B). Following irradiation, the viability of gold-treated LNCaP alginate spheres decreased to 97.8±2.4%, 90±3.2%, and 68.7±18.4% with 2.5, 5, and 20 Gy doses, respectively, which was statistically significant for the latter (p=0.009) (Figure 4.14A). The IC50 value was 41.8±8.4 Gy. When comparing gold-treated to untreated LNCaP alginate spheres at each radiation dose, a radiosensitising effect of AuNPs is observed. This is significant a 5 Gy, with a *p* value of 0.006 (Figure 4.14B).

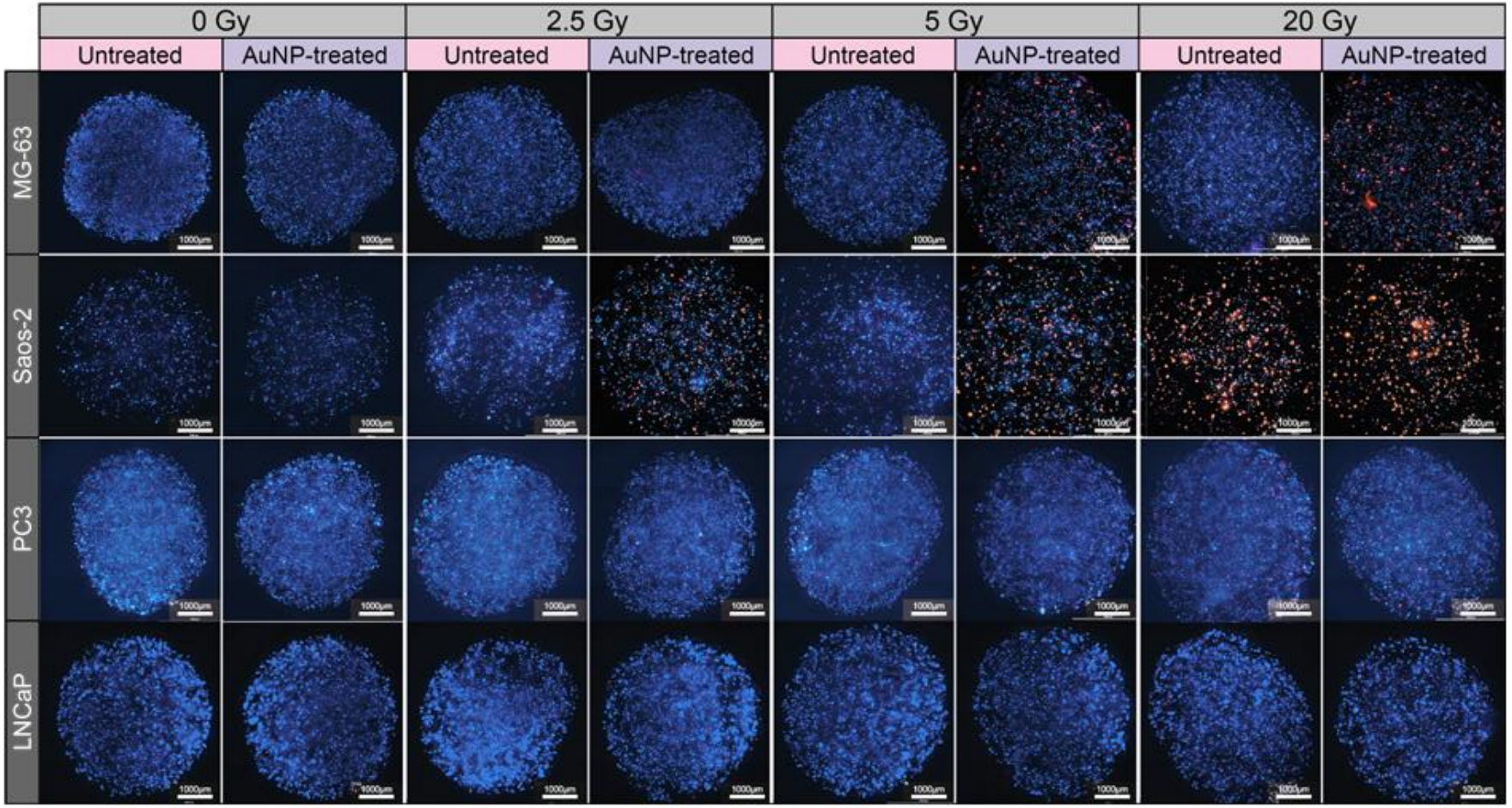

Figure 4.11 - Cell viability of human osteosarcoma and prostate cancer cell lines cultured in alginate spheres and treated with AuNPs, 24h post-irradiation. Colonies were stained with Hoechst 33342 (blue cells) and Propidium Iodide (red cells). Cytation 5 imaging system, 4x objective, Z-stack of DAPI and Texas Red channels. Scale bar represents 1000 µm.

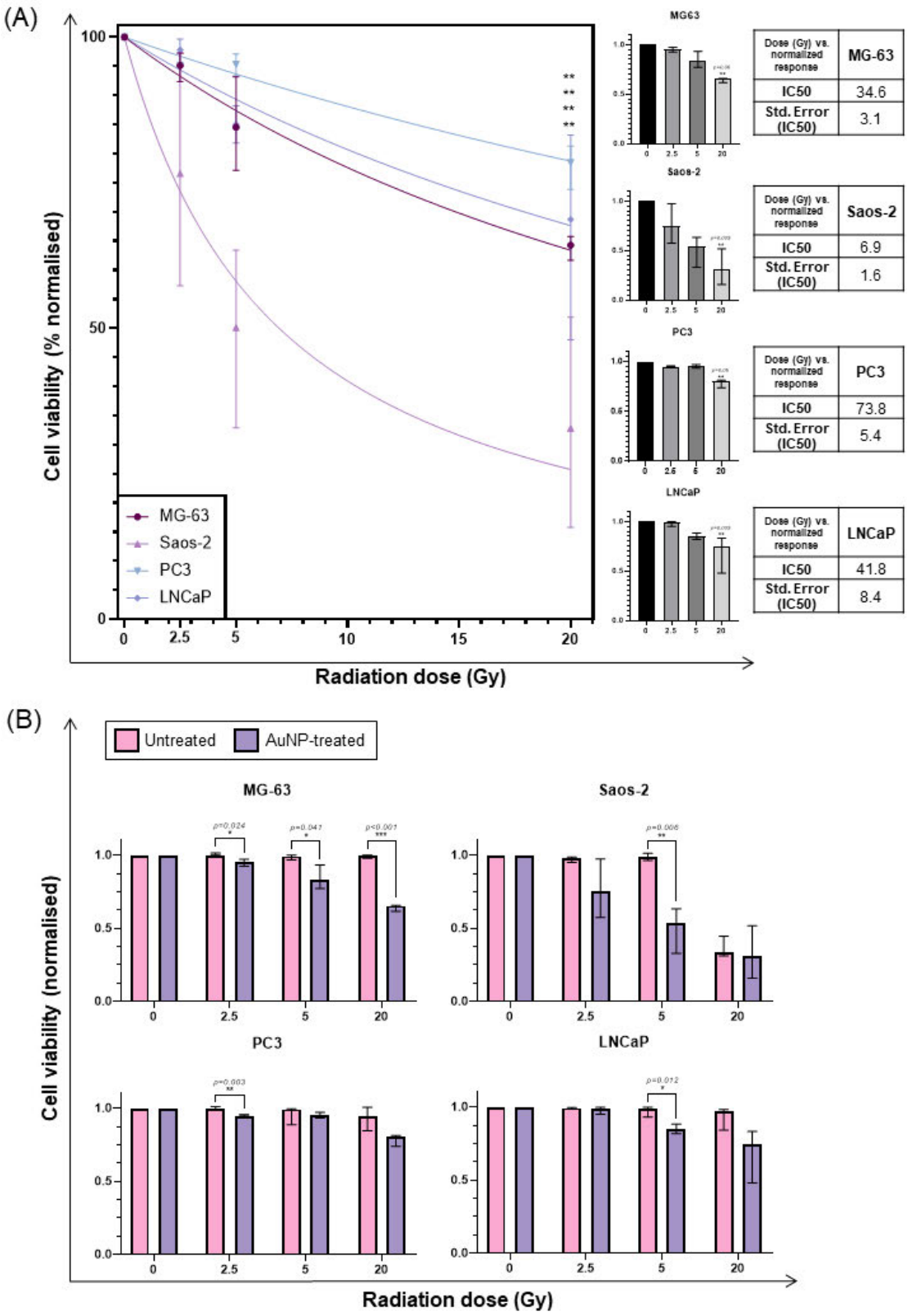

Figure 4.12 - Viability of cells grown in alginate spheres and treated with AuNPs 24h-post ionising radiation exposure. (A) Cell lines present a reduction in viability with increasing doses of radiation. Scatter plot and non-linear regression curve, percentage cell viability data is presented as median ±range, individual values represent n=3 independent experiments with 3 technical repeats. Individually analysed responses of MG-63, Saos-2, PC3, and LNCaP show a significant reduction in viability at individual doses. Column bar graph, Kruskal-Wallis followed by Dunn's multiple comparisons test (*P<0.05). **(B)**

Comparison between untreated and AuNP-treated alginate spheres of each cell line. Interleaved bars, multiple *t-tests*. Statistical significance corrected using the Holm-Sidak method of multiple comparisons, with alpha=0.05. (*P<0.05). All data is presented as median ±range and individual values represent n=3 independent experiments with 3 technical repeats. Untreated data has been shown in previous chapters as all measurements were done at the same time.

4.2.7. Differences in cell cycle distribution between AuNP-treated and untreated cells in 2D and 3D models.

Following treatment with 50 nm gold nanoparticles for 24h, monolayer cultures and both 3D models were exposed to a 5 Gy dose of ionising radiation. The cell cycle distribution of each of the treated cell lines was investigated by propidium iodide staining and flow cytometry analysis, as described in section 2.3.6. Due to time constraints, this analysis was only conducted once meaning that no descriptive statistics were performed. Even though a larger sample size would be necessary to draw solid conclusions, the data acquired provides an insight into the impact the radio-sensitising effect of AuNPs have on cell cycle distribution.

4.2.7.1. Effect of AuNPs and irradiation on cell cycle distribution in monolayer cultures.

Twenty-four hours after irradiation, 2D samples were stained with Propidium Iodide according to the method described in section 2.3.6.2. and analysed using flow cytometry. Single-cell populations were gated as described in section 3.2.8. and then gated according to cell cycle stage. The percentage of cells in each stage was then plotted as bar graphs (Figure 4.13A). Data shows that after a 5Gy dose, the percentage of cells in G0/1 and S phases decreases and increases in G2/M for MG-63 (63.5% vs. 10.6% in G0/1, 8.9% vs. 1.7% in S, and 27.6% vs. 87.7% in G2/M), Saos-2 63 (44.1% vs. 25% in G0/1, 24.1% vs. 11.8% in S, and 30.2% vs. 60.8% in G2/M) and PC3 cells 63 (55.6% vs. 45.7% in G0/1, 12.1% vs. 8.9% in S, and 31.6% vs. 44.8% in G2/M). For LNCaP cells, the opposite happens: an increase in the G1/0 population (64.4% vs. 78.3%) is accompanied by a decrease in the percentage of cells in S (10.6% vs. 6.6%) and G2/M (24.2% vs. 15.1%).

When comparing the cell cycle distribution of untreated populations with AuNP-treated cells it is possible to infer the presence of gold is affecting the way cells are dividing (Figure 4.13B). For MG-63, it is clear that the gold is enhancing the effects of radiation, as a higher percentage of cells accumulated in G2/M and very few are present in G0/1. In Saos-2, even though there is a slight decrease in the

G0/1 and S populations, and a small increase in the percentage of cells in G2/M, the difference seems minute. For PC3, the same AuNP radio-enhancing trend can be observed, as the cell population in G0/1 decreases and the one in G2/M increases. In contrast, in LNCaP the presence of gold nanoparticles seems to have a contrary effect to what was observed in untreated populations, with the percentage of cells in G0/1 increasing, accompanied by a decrease in the G2/M population.

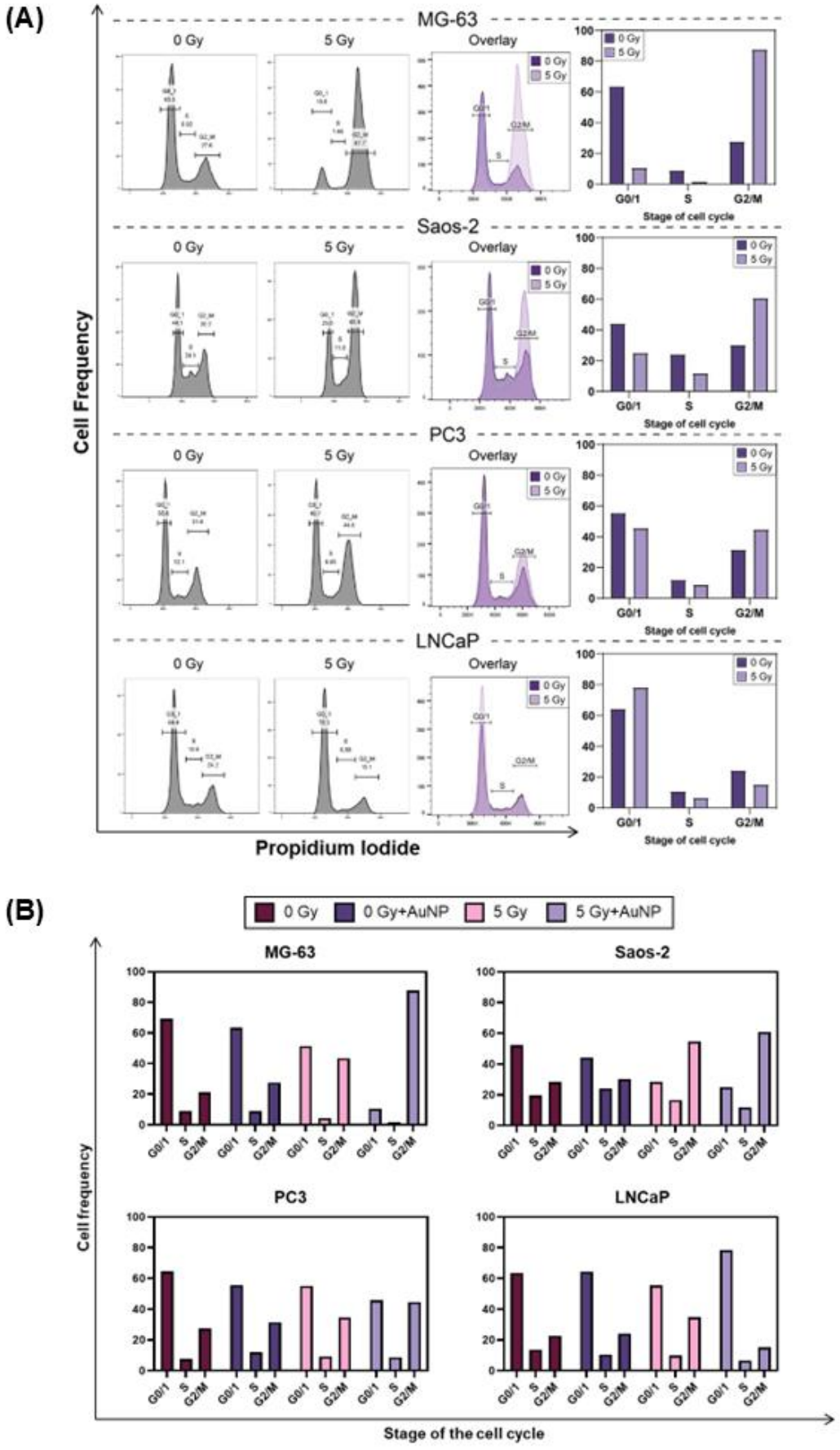

Figure 4.13 - Differences in cell cycle distribution of AuNP-treated cell lines cultured in 2D 24h following ionising radiation. Cells were gated according to their DNA content (stained with PI), i.e. the stage of the cell cycle in which they

were in 24h post-irradiation. **(A)** Histograms of irradiated untreated and gold-treated populations were overlaid for visual representation of different distributions. The percentages of cells in each stage were plotted as interleaved bar graphs of n=1. **(B)** Comparison of cell cycle distribution between untreated and AuNP-treated cells cultured in 2D exposed to 5 Gy radiation**.** For MG-63, Saos-2 and PC3, the presence of gold nanoparticles appears to enhance the effects of radiation in cell cycle distribution. For LNCaP, however, it seems to have an opposing effect. Interleaved bars, n=1. Untreated data has been shown in previous chapters as all measurements were done at the same time.

4.2.7.2. Effect of AuNPs and irradiation on cell cycle distribution in 3D cell models.

Gold-treated multicellular tumour and alginate sphere cultures were also analysed using the protocol detailed above. Due to time constraints only MG-63 and PC3 alginate spheres were tested. Preliminary data shows that in AuNP-treated MCTS, a 5Gy dose produces minor changes in the cell cycle distribution of these cultures. In MG-63 and LNCaP cell lines, a minor increase in the G0/1 population and subsequent decrease in S and G2/M populations was observed (87.6% vs. 89.6% in G0/1, 1.32% vs. 1.06% in S, and 11.1% vs. 9.29% in G2/M; and 78.1% vs. 75.6% in G0/1, 10.8% vs. 5.5% in S, and 9.77% vs. 17.9% in G2/M, respectively). In PC3, the AuNP-treated cells' percentage showed no overt difference in G0/1 (82.1% vs. 79%), S (2.54% vs. 3.13%) and G2/M (15.2% vs. 17.9%) populations. In Saos-2, despite the differences shown in the interleaved bar graph, due to sample loss, the irradiated cell population was too small to draw any conclusions (Figure 4.14A).

When comparing untreated with gold-treated MCTS' response to ionising radiation, and even though further studies with a larger sample size would be required, it is possible to observe that the presence of AuNPs does not produce major changes in cell cycle distribution following irradiation (Figure 4.19). In MG-63 and LNCaP, AuNPs seems to slightly amplify the effects of radiation, with a minor increase in the G0/1 population and a low decrease in the percentage of cells in G2/M in MG-63, and the opposite for LNCaP. In PC3, the presence of AuNPs seems to counteract radiation effects, bringing the percentages of cells in each stage of the cell cycle closer to pre-irradiation levels. However, since these are differences are minimal, it is not possible to conclusively attribute them to AuNP treatment. These values might change with additional repeats, as the standard deviation values seen in previous experiments of n=3 were high enough to potentially affect the results. For Saos-2, despite the clear differences

observed, and as stated before, the number of gated cells was too small to draw any conclusions.

In alginate spheres, both gold-treated MG-63 and PC3 cells saw a small observed difference in the percentage of cells in G0/1, S and G2/M populations. For MG-63, the percentage of cells in G0/1 decreased 2.4% following a 5 Gy dose and increased 0.2% and 3.7% in S and G2/M phases, respectively. PC3 cell populations saw a 2.1% decrease in G0/1 following irradiation and an increase of 1% in both S and G2/M phases after a 5 Gy dose (Figure 4.15A When comparing untreated with gold-treated alginate spheres' response to ionising radiation, gold appears to produce a similar effect as observed in LNCaP MCTS (Figure 4.15B). The number of AuNP-treated cells in each stage of the cell cycle is closer to pre-irradiation values than that of untreated cells exposed to the same radiation dose. However, due to the limited sample size no statistical analysis can be performed and it is impossible to rule out potential bias in these results.

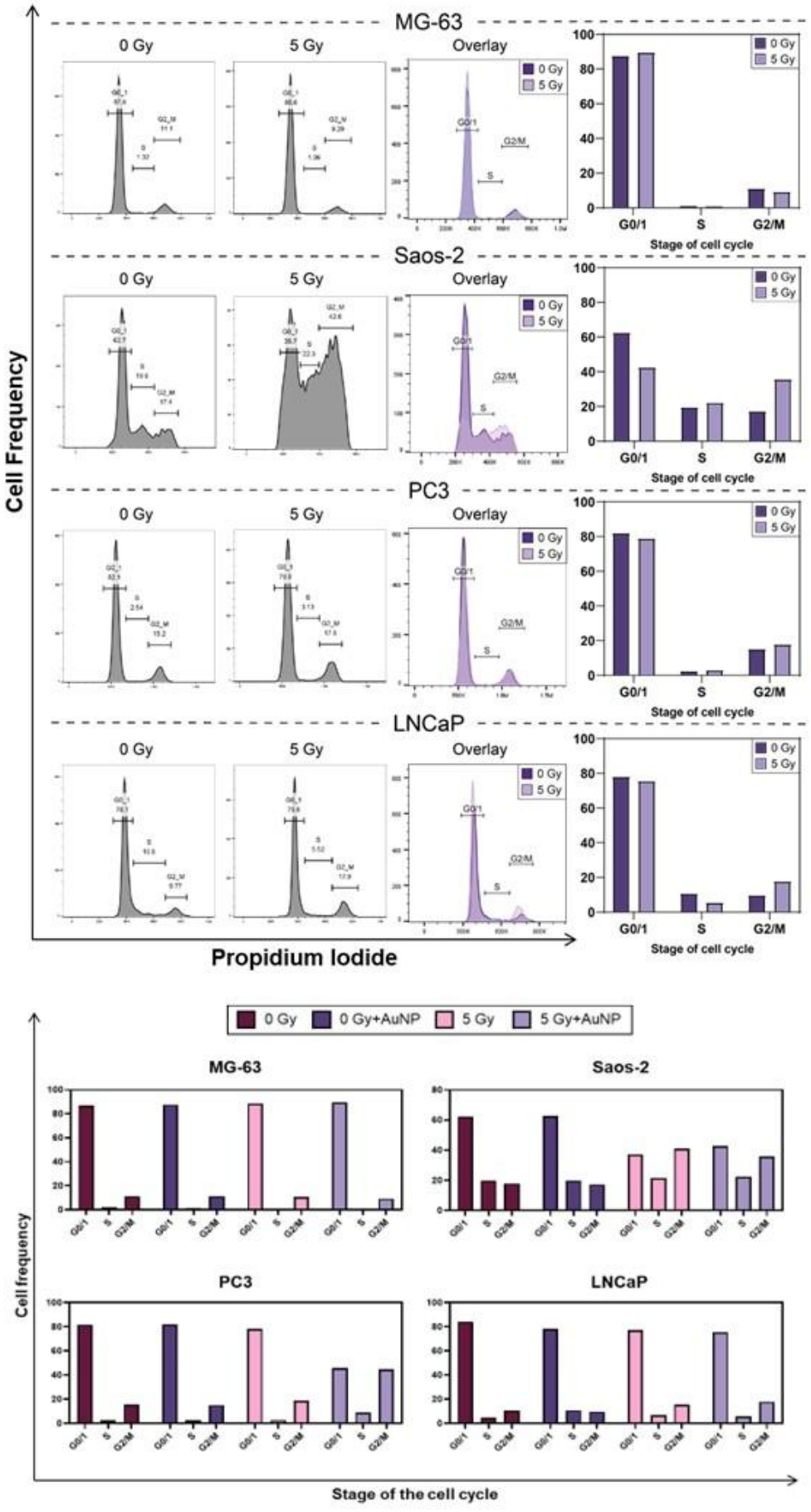

Figure 4.14 - Differences in cell cycle distribution of AuNP-treated cell lines cultured in MCTS 24h following ionising radiation. Single cell-suspensions of

irradiated spheroids were analysed 24h post-irradiation. **(A)** Cells were gated according to the stage of the cell cycle in which they were in, and histograms of irradiated untreated and gold-treated populations were overlaid for visual representation of different distributions. The percentages of cells in each stage were plotted as interleaved bar graphs of n=1. **(B)** Comparison of cell cycle distribution between untreated and AuNP-treated cells cultured in MCTS exposed to 5 Gy radiation. For MG-63 and LNCaP, the presence of gold nanoparticles appears to enhance the effects of radiation in cell cycle distribution. For PC3, it seems to have an opposing effect. Despite the evident differences between untreated and gold-treated Saos-2 cells, the sample size is too small to be representative of the whole population. Interleaved bars, n=1. Untreated data has been shown in previous chapters as all measurements were done at the same time.

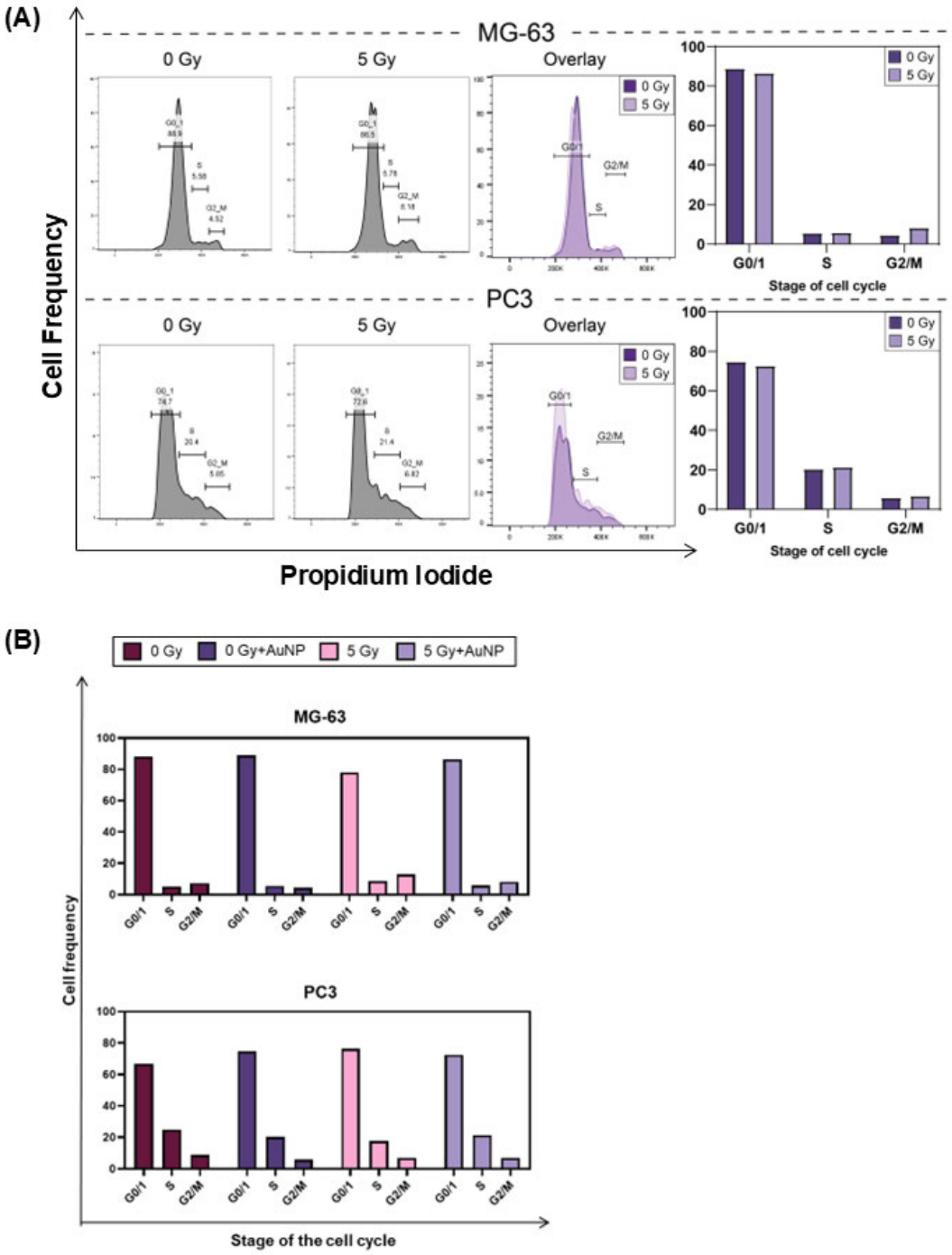

Figure 4.15 - Comparison of cell cycle distribution between untreated and AuNP-treated cells cultured in alginate spheres exposed to 5 Gy radiation. **(A)** AuNP-treatment seems to counteract the effect of radiation, with the cell cycle stage distribution of gold-treated cells being more similar to pre-irradiation levels compared to untreated cells. Nevertheless, the small sample size precludes any conclusions. Interleaved bars, n=1. **(B)** Differences in cell cycle distribution of AuNP-treated cell lines cultured in alginate spheres following ionising radiation. Cells were gated according to the intensity of the PI signal, i.e. the stage of the cell cycle in which they were in 24h post-irradiation. Histograms of irradiated untreated and gold-treated populations were overlaid for visual representation of different distributions. The percentages of cells in each stage were plotted as interleaved bar graphs of n=1.

4.2.8. Localization of γ-H2AX foci in AuNP-treated samples following irradiation.

To assess if AuNPs induced a higher amount of DNA damage in irradiated cells, cell preparations of AuNP-treated monolayer cultures were subjected to Immunofluorescence assays, 24h post-treatment, as described in section 2.3.5.2., to investigate γ-H2AX foci localisation. The resulting confocal images (Figure 4.17) were analysed using the Zeiss Zen 2.3 (blue edition) software (Carl Zeiss) by quantification of the number of H2AX foci per cell nucleus. The results were graphed as violin plots and the means of the 3 repeats were compared to untreated samples of the same cell line using Kruskal-Wallis tests followed by Dunn's multiple comparisons (Figure 4.18).

Results show that AuNP treatment enhances the radio-sensitivity of MG-63 and Saos-2 cells, demonstrated by an increase in the number of cells showing γ-H2AX foci, as well as an increase in the average number of foci per cell. For both cell lines, AuNP treatment without radiation exposure does not significantly affect the number of foci per cell or the number of cells showing foci. Untreated MG-63 cells showed an average of 0.48 foci per cell, with 73% of cells showing no foci, while gold-treated cells had an average of 0.44 foci per cell, with 69% presenting no γ-H2AX foci. Untreated Saos-2 cells showed an average of 1.1 foci per cell, with 53% of cells being negative for γ-H2AX foci, whereas gold-treated cells had an average of 0.5 foci per cell, with 70% of cells not presenting any foci. Following a 5 Gy radiation dose, the average number of foci was significantly higher for both untreated (0.85) and gold-treated MG-63 cells (2.7, $p<0.001$). Comparing untreated and AuNP-treated cells, the number of foci increased significantly in cells treated with gold nanoparticles ($p=0.004$). Moreover, the percentage of γ-H2AX-positive cells was 1.5 times higher in AuNP-treated (68.3%) compared to untreated cells (44.3%). In Saos-2, the average number of foci per cell also increased significantly in both untreated (2.5, $p=0.015$) and gold-treated cells (3.6, $p=0.037$). When comparing radiation-exposed untreated and AuNP-treated Saos-2 cells, the average number of foci per cell was not significantly higher in the presence of gold. Additionally, the number of γ-H2AX-negative cells decreased by 10%, with 28.5% of untreated cells showing no foci compared to 18.4% of gold-treated cells. For PC3, untreated cells had on average 3.5 foci per cell following irradiation ($p=0.003$), and AuNP-treated cells presented an average of 2.5 foci per cell ($p=0.016$), compared to cells that did not receive any radiation,

which showed an average of 1.3 γ-H2AX foci. Even though the AuNP treatment decreased the average number of foci per cell following exposure to a 5 Gy radiation dose, it increased the number of γ-H2AX-positive cells: 88% of AuNP-treated cells showed 1 or more foci, in contrast to 80% of untreated cells. In LNCaP cells, the average number of foci per cell was 0.6 prior to irradiation. Following radiation exposure, in untreated cells that number was 4 times higher (2.8, $p<0.001$), and 5 times in AuNP-treated cells (3.2, $p=0.022$). Similarly to what happened in PC3 cells, the average number of foci was not significantly higher in gold-treated cells, but the number of γ-H2AX-negative cells saw a 9.4% decrease (26.9% for untreated and 17.5% for AuNP-treated cells) after radiation exposure.

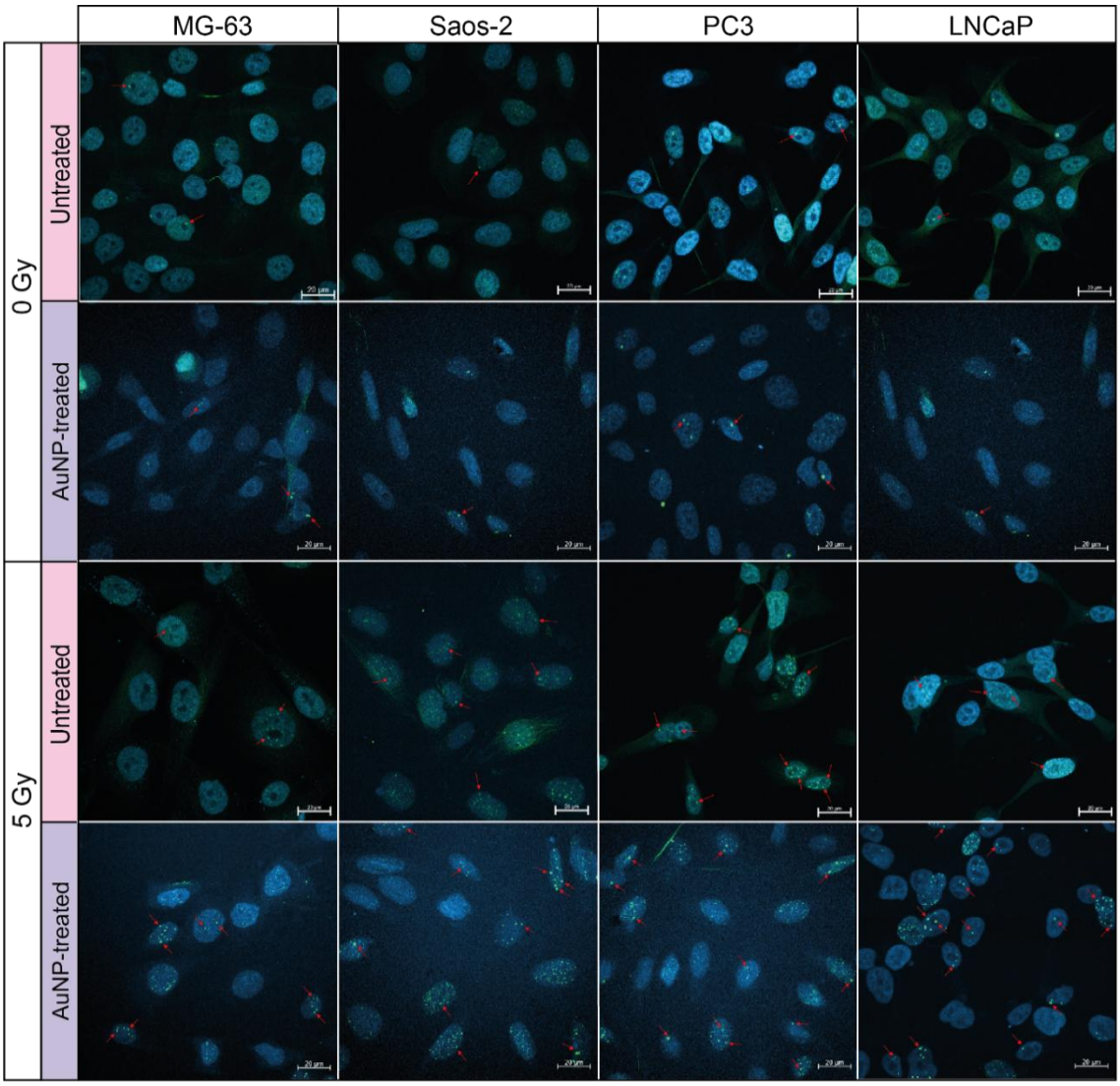

Figure 4.16 - Confocal images of γ-H2AX detection in AuNP-treated human osteosarcoma and prostate adenocarcinoma cell lines. Cells were stained with an anti-Human Histone H2AX [p Ser139] primary antibody, AlexaFluor™ 488 secondary antibody (green) and counterstained with DAPI (blue). Images show an increase in the number of H2AX foci (red arrows) in cells irradiated with 5Gy of ionising radiation, compared to unirradiated cells. Zeiss LSM 800 confocal microscope, 40x objective, Z-stack of DAPI and AF488 channels. Scale bar represents 20 μm.

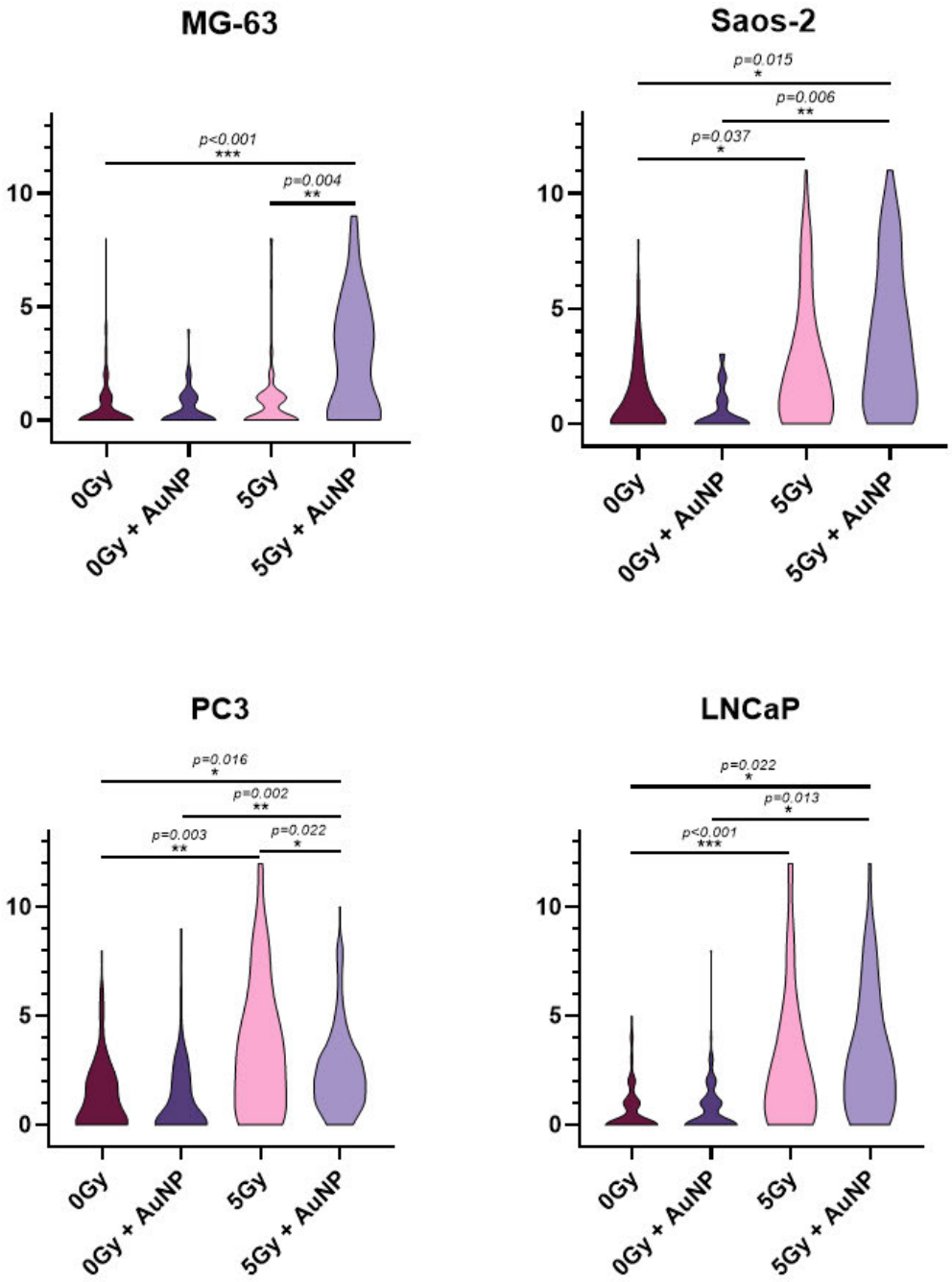

Figure 4.17 - Number of H2AX foci in AuNP-treated cells 24h following ionising radiation. All cell lines show an increase in DNA damage following radiation, translated by an increased number of H2AX foci. When comparing gold-treated to untreated cells, there is a significant increase in the average number of foci in MG-63 and Saos-2 cells. Violin plots, Kruskal-Wallis with Dunn's multiple comparisons. Statistical significance calculated as a two-tailed p value, with a confidence level of 95% (*P<0.05) based on the means of 3 repeats.

4.2.9. TEM imaging of AuNPs and AuNP-treated cells.

To confirm cellular internalisation and pinpoint the intracellular localization of the gold nanoparticles, transmission electron microscopy (TEM) images were captured (Appendix E). The TEM work was performed by Dr Francis Sweeney at the Mechanical Engineering Research Institute of Sheffield Hallam University and Dr Christopher Hill at the University of Sheffield. Due to sample availability and time constraints, only PC3 monolayer cultures were imaged and used as a representative example. Results show that gold nanoparticles are being internalised by the cells and localised in small intracellular vesicles of size range ~300-600 nm.

4.3. Discussion

4.3.1. Gold nanoparticle uptake and localization

In this study 50nm gold nanoparticles were selected for treatment, based on information from previous studies concerning cellular uptake efficiency, cytotoxicity, and potential for later intracellular targeting. Particle size is a key factor in determining the interaction of AuNPs with biological systems and ultimately influences their uptake and toxicity (Xia et al., 2019). In an early study, Chithrani et al. (2006) showed that intracellular uptake of gold nanoparticles by HeLa cells is linked to their size and shape, with 50nm nanoparticles having the highest internalisation rate when compared to AuNPs measuring 14, 30, 74, and 100 nm (Chithrani et al., 2006). This was later confirmed by Yue et al. (2017) that also demonstrated that 50 nm is the ideal diameter for AuNP cellular uptake, this time using U87 glioblastoma cells (Yue et al., 2017). Moreover, studies looking at size-dependent cytotoxicity have shown that smaller particles produce higher levels of cell death compared to AuNPs with a larger diameter. For example, Liu et al. (2014) demonstrated that the growth of A549 lung cancer cells was inhibited by 5nm AuNPs comparatively to a treatment with 40 nm and 50 nm AuNPs, which did not produce this effect (Liu et al., 2014). Another study led by Xia (2018) confirmed this, with 5nm AuNPs exhibiting greater cytotoxicity than 20 nm and 50 nm nanoparticles in HepG2 hepatic cancer cells and L02 normal cells (Xia et al., 2019).

To determine the ideal concentration of AuNPs to promote radio-sensitisation of cell models without hindering cell viability, optimisation experiments should have been performed. However, due to time constraints, this could not have been achieved in a timely manner. Instead, a thorough literature review was conducted

not only to understand the correlation between AuNP concentration and cytotoxicity, but also to investigate what concentrations have been previously used to test similar hypotheses. Studies investigating the radio-sensitising potential of AuNPs have used a range of concentrations, with some treating cells with lower concentrations of gold nanoparticles (5-10μg/mL) (Alhussan et al., 2023; Igaz et al., 2020) and others reaching up to 200μg/mL (Feng et al., 2023; Kazmi et al., 2020; Tudda et al., 2022). However, while higher concentrations of AuNPs have shown to enhance the radio-sensitivity of cancer cells, they have also been associated with increased cytotoxicity, as demonstrated in a study led by Ozcicek (2021), where a high concentration of AuNPs – 100μg/mL – led to a higher production of intracellular ROS, inducing oxidative stress and loss of cell viability (Ozcicek et al., 2021). Furthermore, the internalisation of AuNPs by cancer cells usually occurs through receptor-mediated endocytosis. These receptors have a limited capacity, meaning that higher concentrations of AuNPs can saturate these mechanisms, decreasing the uptake rate (Oliveira et al., 2024). Therefore, to avoid cytotoxic effects while ensuring adequate nanoparticle uptake and effective sensitisation, a concentration of 10 μg/mL was deemed optimal. Additionally, there is a precedent for using this concentration effectively across different experimental models, as an investigation conducted by Wolfe (2015) demonstrated radio-sensitisation effects of gold nanorods at a 10 μg/mL dose in prostate cancer, both *in vitro* and *in vivo* (Wolfe et al., 2015).

Following AuNP treatment, the uptake of the nanoparticles was evaluated through LA-ICP-MSI and hyperspectral imaging and results showed that gold was present in monolayer, spheroids and alginate sphere cultures. In three-dimensional platforms, the rate of penetration was different between cell lines and different models. In MCTS, osteosarcoma cell lines showed an accumulation of gold nanoparticles in the outer rings of the spheroids, whereas in prostate MCTS, the AuNPs were able to penetrate the spheroid core. This is likely due to the differences in structure and density between the spheroids of the two cancer types. While MG-63 and Saos-2 form more compact spheroids, PC3 and LNCaP cells aggregate more loosely. Osteosarcoma cells are notable for the production of extracellular matrix rich in collagen, often associated with the invasiveness, metastasis, and low survival rates of these tumours (Cui et al., 2020). *In vitro*, this dense ECM can act as a physical barrier, limiting the diffusion of gold nanoparticles into the deeper layers of the spheroid (Bromma et al., 2021).

In alginate spheres, even though AuNPs were uniformly distributed, the counts of Au^{197} were significantly lower than in monolayer and MCTS cultures, meaning that less nanoparticles were incorporated by the colonies growing in the alginate matrix. Considering the successful uptake of AuNPs by cells cultured in 2D and in spheroids, the reduced levels of gold found in alginate cultures could be linked to the alginate matrix itself, mainly to factors like porosity and electrostatic interactions. Alginate gels usually present a pore size of ≈5 nm, which allows the efficient diffusion of small molecules through the gel (Lee & Mooney, 2012) and a study led by Siboro (2021) showed that tuning the porosity of this matrix by adjusting the amount of cross-linking can significantly influence drug release (Siboro et al., 2021). Therefore, it is possible that the degree of cross-linking with Ca^{2+} ions in the alginate gels used for these experiments was hindering the diffusion of AuNPs, physically trapping them within the matrix. Moreover, alginate gels are overall negatively charged, due to the presence of carboxylate groups ($-COO^-$). Even though the cross-linking with positive calcium ions on the gel formation neutralises some of the negative charges, some may remain within the structure (Lee & Mooney, 2012; Tyagi et al., 2022). Since gold nanoparticles also have a negative surface charge, due to citrate capping, this could lead to electrostatic repulsion (Sheridan et al., 2022), impeding the nanoparticles to penetrate the alginate matrix and reach the colonies.

4.3.2. Gold nanoparticle radio-sensitisation of monolayer cultures.

To determine the radio-sensitising effect of non-functionalised gold nanoparticles in monolayer cultures of osteosarcoma (MG-63 and Saos-2) and prostate adenocarcinoma (PC3 and LNCaP) cell lines, cells were treated with 50nm AuNPs and irradiated with doses raging from 1.25 to 5 Gy. Their survival was measured through clonogenic assays and compared to the surviving fraction of untreated cells irradiated with the same doses. Results showed that although the difference in sensitivity between untreated and AuNP-treated cells was not statistically significant for most conditions, it is important to acknowledge the dose enhancement factor produced by the nanoparticles, which was greater than 1 across all cell lines, as determined by the IC50 values. This suggests that the presence of AuNPs contributes to an increased radiation effect, when compared to untreated cells. Moreover, it is important to recognise that measuring clonogenic growth through absorbance readings, despite having its advantages

such as reducing human error and accounting for colony variability between cell lines, also produces inherent variability related to cell proliferation, translating to large error bars. Therefore, further studies should be carried out with a more robust sample size to remove outliers. Nevertheless, results have shown a statistically significant difference in the viability of MG-63 cells treated with AuNP following radiation, compared to untreated and irradiated cells, as well a statistically significant interaction between gold treatment and irradiation, meaning that the impact of radiation dose in cell viability is influenced by the gold nanoparticle treatment, i.e. AuNPs are producing a significant radio-sensitising effect in MG-63 cells. This result confirms the relevance of utilising AuNPs as radio-sensitising agents as MG-63 are notably resistant to irradiation, as shown in the previous chapter of this thesis as well as described in literature (Feng et al., 2016; Li et al., 2015). In fact, the reason radiotherapy is not routinely used as a primary treatment for osteosarcoma is due to the inherent radio-resistance of OS cells (Spałek et al., 2021), meaning the findings of this study could lead to new therapeutic strategies. Following an extensive literature review, no studies using MG-63 cells and AuNPs as radio-sensitisers have been found. However, other research groups have explored this hypothesis in other cell lines. For example, Kazmi et al. (2017) have demonstrated the radio-sensitising potential of AuNPs in U87 cells, an aggressive and radio-resistant glioblastoma cell line. In this study, the group used 42nm gold nanoparticles at a concentration of 100µg/mL dose and irradiated the cells with a 6MV photon beam in doses ranging from 2 to 8 Gy. Their findings showed a significant increase in the sensitivity U87 cells at 2 and 6 Gy doses when treated with gold nanoparticles.

Since external beam radiation therapy or EBRT with brachytherapy are primary treatment modalities for prostate cancer patients with localized or advanced disease, the radio-sensitisation of prostate cancer cell lines has been a topic of interest for multiple research groups (Khoo et al., 2017; Moris et al., 2020). For instance, a recent study by Soares et al. (2023) has demonstrated a significant radio-sensitising effect of PEGylated 50 nm AuNPs in both PC3 and LNCaP cells, irradiated with a 6 MV photon beam in fractioned doses of 2.5 Gy each, completing a total irradiation dose of 7.5 Gy. Even though the results of this study follow the same trend, the observed radiation effects in AuNP-treated cells were not as pronounced. This could be related to the lack of PEG coating of the gold nanoparticles used for the experiment – PEG can stabilise the nanoparticles and

prevent them from aggregating – which has been shown to greatly influence the efficiency of AuNP in radio-sensitising cells (Musielak et al., 2023); or to the fact the radiation treatment was administered as a single-dose, rather than fractioned dosing – while a single-dose of radiation may produce acute effects, fractioned dosing allows cells to accumulate sub-lethal damage that can overwhelm the cell's repair mechanisms in the long term (Dale, 2019).

4.3.3. Effects of gold nanoparticles in three-dimensional models following radiation exposure.

To assess the sensitising effect of AuNP in three-dimensional platforms both MCTS and alginate spheres were treated with gold nanoparticles before irradiation. Cell viability was investigated acutely in spheroids and colonies grown in an alginate matrix. Colony diameter was also measured in alginate spheres seven days following radiation exposure.

4.3.3.1. Acute and prolonged effects of radiation exposure in AuNP-treated alginate spheres.

The effects of radiation exposure were analysed in alginate spheres 24h and 7 days post-treatment. Alginate spheres with 10-day old colonies were irradiated and their viability was measured acutely using a Hoechst 33342/PI stain. For colony diameter measurements spheres containing young colonies were irradiated and allowed to proliferate for a further 7 days to assess the prolonged effects of gold radiation through colony diameter measurements. Results showed that while AuNP-treatment in 2D demonstrated a sensitising effect, in alginate sphere cultures only LNCaP cells saw their colony diameter reduced when compared to untreated and irradiated cells, even though this difference was not significant. For the other cell lines, AuNP treatment not only failed to produce radiosensitisation, but colonies treated with gold nanoparticles presented a higher average diameter following irradiation. Nonetheless, this difference was so minor that more repeats could potentially attenuate it even more. Therefore, it is possible to conclude that gold nanoparticle treatment of cells grown in alginate spheres does not affect colony growth following irradiation. As to my knowledge, there are currently no studies investigating radiosensitising potential of gold nanoparticles in alginate cultures so there is no data to compare the one obtained from this study to. Furthermore, due to the lack of research using this culture platform, there is no unified method of measuring clonogenicity in three-

dimensions and further studies would be necessary to investigate different methods to create a standardised technique. When comparing these results to the ones obtained from clonogenic assays in 2D it is possible to observe that, once more, there is a significant difference in radio-sensitivity between cells cultured in monolayer and alginate spheres, with 2D cultures being significantly more sensitive at the doses administered.

As for acute responses, a significant difference in viability was observed between untreated and AuNP-treated osteosarcoma (MG-63 and Saos-2) cells following increasing doses of radiation. Considering these results, it would be expected that the gold nanoparticle treatment produced a proportional difference in average colony diameter. However, as previously mentioned, there were no significant differences between the average colony diameter of untreated and AuNP-treated osteosarcoma cells following irradiation. A possible explanation for this is the amount of DNA damage that is being induced with or without gold nanoparticle treatment: in untreated colonies, the acute cell viability of MG-63 cells remained high with every radiation dose and in Saos-2 it only reduced at 20 Gy. However, results from colony diameter measurements revealed a decrease in colony diameter proportional to the increasing radiation doses. Therefore, it is possible to infer that the radiation-induced damage in MG-63 and Saos-2 cells was not severe enough to cause acute cell death but rather inhibited cell proliferation, possibly inducing senescence (Kim, J. H. et al., 2023). In AuNP-treated cells, on the other hand, the presence of gold nanoparticles amplified the radiation effects, inducing significant DNA damage to lead to immediate cell death, rather than simply inhibiting proliferation. The similar averages of colony diameter of AuNP-treated cells might indicate that while most cells die, the survivors continue to proliferate and form colonies, i.e. the average colony diameter being similar between treated and non-treated groups might mask the variability within the treated group. If many cells die, but a few larger colonies emerge from surviving cells, the average might not reflect the extent of damage or loss of proliferation capabilities. To investigate this further, it would be important to gain more insight into the surviving populations, for example, by looking into senescence markers such as p16 and p21, as well as markers of cell cycle progression, to investigate the possibility of arrest (Wagner & Wagner, 2022). As previously stated, the novelty of the alginate sphere culturing platform as a model to investigate radiotherapy responses limits the extrapolation of

conclusions, but these findings offer interesting insights into the different responses between different 3D cell culture models and create a precedent for future research.

4.3.3.2. Acute effects of radiation exposure in AuNP-treated MCTS.

The viability of AuNP-treated multicellular tumour spheroids was assessed 24h-post irradiation, using a Hoechst 33342/PI stain. Results show that while in AuNP-treated prostate (PC3 and LNCaP) MCTS there was no significant difference in viability with increasing doses of radiation, the gold nanoparticles produced a radio-sensitising effect in MG-63 and Saos-2 spheroids, significant at 20 Gy. When compared to the response of untreated MCTS, the viability of AuNP-treated MG-63 spheroids was significantly lower following a 20 Gy dose. Likewise, the viability of AuNP-treated Saos-2 spheroids was significantly lower than their untreated counterparts following doses of 5 and 20 Gy. The responses of both prostate cell lines are in concordance with existing literature. A study by Igaz et al. (2020) had previously shown that undecorated AuNPs do not enhance radiation treatments at doses of 2 and 4 Gy, and a sensitising effect is only observed when LNCaP and PC3 spheroids were treated with both AuNPs and the histone deacetylase inhibitor SAHA prior to irradiation (Igaz et al., 2020). In a study conducted by Bromma et al. (2023) results showed that treatment with AuNPs led to a radiosensitising effect at 5 Gy in LNCaP spheroids. However, the cell viability assays were conducted 13 days post-irradiation (Bromma et al., 2023). Considering the results of this study it is possible to assume that even though acute viability remained similar to that of untreated spheroids, the synergistic action of gold nanoparticles and radiation might be producing long-term effects, a possibility supported by the clonogenic studies previously described. Studies to investigate levels of DNA damage could confirm this hypothesis, however, due to time constraints, the quantification of γ-H2AX foci was not possible in spheroid samples.

4.3.4. Cell cycle distribution of AuNP-treated cells following radiation exposure.

Following irradiation with a 5 Gy dose, AuNP-treated monolayer, alginate sphere, and MCTS cultures were stained with PI to assess cell distribution in the different stages of the cell cycle. Due to time constraints, this experiment was only carried out once, making statistical analysis impossible. Nonetheless, preliminary data

shows that in 2D, the gold nanoparticle treatment is enhancing the radiation effects in MG-63, Saos-2, and PC3 cell lines. As demonstrated in Figure 4.15, AuNP-treated cells show a more pronounced decrease in the cell populations in the G0/1 and S phases, accompanied by an increase in the percentage of cells in G2/M. As described in section 3.3.5, this might be due to the lack of functional p53 in all three cell lines – in normal conditions, p53 is activated in response to DNA damage, leading to the transcription of CDKN1A (which encodes p21 – a CDK inhibitor). Active p21 blocks the activity of cyclin-CDK complexes responsible for the progression from G1 to S phase, which prevents the replication of damaged DNA. In cells lacking functional p53, this G1 checkpoint is compromised, and cells are allowed to move on to the S phase (Chen, 2016; Keam et al., 2022). The results presented in this thesis show that while this was already visible in untreated cells irradiated with 5 Gy, gold-nanoparticle treatment is enhancing this effect through the higher levels of DNA damage produced. Since the decrease in G0/1 and S phase populations is accompanied by an increase in the percentage of cells in G2/M it is possible to infer that the AuNP-treated cells are enhancing the activation of the G2/M checkpoint, which is not p53-dependent, in response to the severe DNA damage. With higher levels of damage induced by the synergistic action of the radiation and gold nanoparticles, produced by secondary electrons and ROS causing DSBs, the cells arrest the cell cycle in G2/M in an attempt to repair the damage and prevent mitotic entry. Concomitantly, because cells are more sensitive to DNA damage when in G2/M, this could also explain the late effects translated by a decrease in proliferation seen in the clonogenic analysis. These results are corroborated by a study led by Roa (2009) that showed that irradiated AuNP-treated DU-145 cells – which have TP53 mutations resulting in a non-functional p53 protein – do not show acute cell death at 24h but suffer a decrease in proliferation accompanied by an increase of the cell population in G2/M (Roa et al., 2009). On the other hand, in LNCaP cells, which are p53 proficient, seem to be accumulating in G0/1 rather than G2/M.

As for 3D models, there were no substantial differences between responses of untreated and AuNP-treated MCTS or alginate sphere cultures irradiated with a 5 Gy dose. These results align with the cell viability and colony diameter data at the same dose – both cell viability and colony diameter suffer minor alterations with a dose of 5 Gy. To further confirm this, repeating this analysis would be

beneficial. Furthermore, repeating the irradiation treatments using fractioned doses rather than a single dose could potentially alter the results, as this would allow for reoxygenation of hypoxic cells, enhancing the effectiveness of radiation-induced damage, as well as cell cycle redistribution – cells that were stuck in G0/1 may resume cell cycle progression into G2/M, a phase where cells are more sensitive to radiation due to chromatin condensation (Bleaney et al., 2024; Kepka & Socha, 2021).

4.3.5. Increase in γ-H2AX foci in all gold-treated cell lines.

Following irradiation, DNA damage was investigated by γ-H2AX foci quantification via immunofluorescence. These results show that in AuNP-treated MG-63 and Saos-2 cells irradiated with 5 Gy, there was a significant increase of the number of γ-H2AX foci, which correlates with the radio-sensitisation seen in the colony formation assays. Contrarily, AuNP-treated PC3 and LNCaP cells did not enhance the production of γ-H2AX foci following radiation exposure. These findings align with those published by Tremi et al. (2022) in a study where unfunctionalised gold nanoparticles failed to produce a significant increase in the number of γ-H2AX foci in PC3 cells (Tremi et al., 2022). Even though the difference in average number of γ-H2AX foci/cell was not significant in PC3 and LNCaP cells, it is important to note that both cell lines showed a decrease in the number of γ-H2AX-negative cells, revealing a minor sensitising effect of AuNPs, albeit not statistically significant. To the best of my knowledge, no studies have been published on the quantification and localisation of γ-H2AX foci following the use of unfunctionalised gold nanoparticles to enhance radiation treatments in MG-63 or Saos-2 cells.

4.3.6. Intracellular location of gold nanoparticles.

On a cellular level, TEM images confirmed internalisation, with AuNPs being mainly located in membranous vesicles in the cytoplasm. These findings align with what has been previously described in the literature - studies led by Peckys and de Jonge (2011) and Yue (2017) have used TEM to demonstrate that AuNPs enter the cells through endocytosis and accumulate inside endosomes (Peckys & de Jonge, 2011; Yue et al., 2017).

4.4. Conclusion

The aim of this chapter was to assess the radio-sensitising potential of non-functionalised gold nanoparticles in 2D and 3D cell models of human prostate adenocarcinoma and osteosarcoma cell lines. The findings of this thesis show that in two-dimensions AuNPs enhance the effects of radiation, translated by a decrease in colony proliferation, a shift in cell cycle distribution and an increase in the average number of γ-H2AX foci per cell. This enhancement of radiation-induced damage was statistically significant in osteosarcoma (OS) cell lines, both in 2D and acutely in 3D. Due to the lack of research using these cell lines in radio-biology studies, because of their inherent radio-resistant characteristics, the findings of these study offer interesting insights into their interaction with gold nanoparticles and radiation. However, it is important to underscore that since there is a gap in knowledge when it comes to comprehensively address radio-sensitisation by AuNPs in three-dimensional platforms, there is no unified way of measuring radiation-responses in 3D and to track gold nanoparticles within these models, which is why I aimed to develop standardised methodologies for this type of *in-vitro* work. In conclusion, the results of this study regarding AuNP radiosensitisation of OS cells represent an exciting finding that might lead to advances in therapeutic strategies for these radio-resistant cancers. Despite not having an effect on the proliferating ability of cells grown in 3D, the treatment with gold nanoparticles produced a significant decrease in cell viability of OS cells following irradiation, which could make a case for their use in clinic in combination with other therapies.

Seeing that undecorated gold nanoparticles proved to enhance radio-sensitivity, the next logical step was to target them to DNA containing organelles – the nucleus and the mitochondria – to investigate if the proximity to DNA would further enhance radiation-induced damage.

Chapter 5. Investigating the radio-sensitising potential of nuclear-targeted gold nanoparticles in 2D and 3D cell models

5.1. Introduction

It has been previously shown that undecorated gold nanoparticles can enhance radiation-induced damage and increase the levels of tumour cell killing, when compared to radiotherapy treatments alone. However, the level of radio-response enhancement is often weak and fails to eliminate all tumour cells, meaning cells that only acquire sub-lethal damage can often repair it and continue proliferating, increasing the risk of radio-resistance. Additionally, effective AuNP-induced radio-sensitisation has so far failed to translate to clinic (Özçelik & Pratx, 2020; Patil et al., 2023). To improve the radio-sensitising potential of gold nanoparticles, surface functionalisation with different molecules is one of the strategies to enhance their efficiency, either by increasing their stability and blood circulation time, or cellular uptake, through passive or active targeting, to specific cells or organelles within them (Chen et al., 2020).

It has been discussed that the efficiency of AuNPs as radio-sensitisers relies on the fact that they can not only absorb higher levels of radiation than soft tissue, therefore increasing the deposition of energy at the tumour site, but also in their capacity of initiating Auger cascades that lead to direct DNA damage or production of ROS that interact with the DNA chain (Haume et al., 2016; Penninckx et al., 2020). Even though Auger electrons possess a high linear energy transfer (LET) – the ratio of energy transferred from a charged particle to other atoms as it passes through tissue –, they typically have low kinetic energy, which limits how far they can travel (Bardane et al., 2024). For example, a study by McMahon et al. (2011) has shown that the average energy deposit of a 20nm AuNP following a single ionising event by a 40 keV photon is 0.025 keV at the AuNP site. The further away from the nanoparticle, the less energy is deposit, with only 0.002 keV being recorded 300nm away from the AuNP (McMahon et al., 2011). Therefore, one of the strategies that has been gaining interest in recent years is to target them to the cell nucleus, locating them near DNA to maximise dose enhancement, producing fatal damage (Özçelik & Pratx, 2020). To achieve nuclear localisation, AuNPs must be functionalised with specific molecules that

guide them from the cytosol to the cell nucleus – nuclear localisation signal (NLS) peptides. The most commonly used NLS peptides are the adenovirus-derived CGGFSTSLRARKA, the HIV-1 Tat protein-derived CGGRKKRRQRRRAP, and the SV40 large T-antigen-derived CGGGPKKKRKVGG (Ali et al., 2017; Al-Wassiti et al., 2021; Berry et al., 2007; Mackey et al., 2013; Tkachenko et al., 2003). Once in the cell, the transport of NLS peptides into the nucleus is mediated by members of the importin family: NLS binds to importin-α, which forms a complex with importin-β. Even though importin-β does not interact with the NLS peptide, it directs importin-α through the nuclear pore complex (NPC) – a multimeric structure that acts as a barrier between the cytoplasm and the nucleoplasm, regulating the transport of molecules to and from the cell nucleus. The translocation of the NLS/importin-α/importin-β trimeric complex is mediated by nucleoporins which line the nuclear pores and contain phenylalanine-glycine (FG) repeats. Importin-β binds to these FG repeats, acting as docking points that allow the complex to move through the NPC. Once inside the nucleus, Ran-GTP binds to importin-β, causing a conformational change that leads to the dissociation of importin-β from importin-α. At the same time, Nup50 and the cellular apoptosis susceptibility protein (CAS) work with Ran-GTP to release importin-α from the cargo, ensuring the NLS-peptide remains inside the nucleus. This prevents re-export of the cargo back to the cytoplasm, avoiding consecutive cycles of import and export. Once Ran-GTP has facilitated the cargo release, it is transported back to the cytoplasm where Ran-GAP (Ran GTPase-activating protein) hydrolyses Ran-GTP to Ran-GDP, resetting the Ran cycle. This conversion frees up importin-β and importin-α to engage in subsequent rounds of nuclear import by binding new NLS-bearing cargos (Cross, 2019; Lu et al., 2021).

NLS-functionalisation of AuNPs can be achieved through covalent bonding, usually by modifying the NLS peptides to contain a thiol group that binds to the surface of the nanoparticle; amide bonds, by functionalising the AuNPs with carboxyl groups (-COOH) that bind to the amine groups ($-NH_2$) of the NLS peptide; or PEGylation, by coating the surface of AuNPs with PEG molecules modified with a thiol group on one end and a -COOH/$-NH_2$ on the other end, that bind to the NLS peptide (Lu et al., 2021; Mackey et al., 2013; Peng et al., 2014; Wang & Wang, 2014). Even though it has been proven that functionalisation with

NLS peptides localises gold nanoparticles in the cell nucleus, there are several challenges the AuNPs need to overcome, mainly crossing the cell membrane – which can be facilitated by the combined functionalisation with peptides such as RGD, that target integrins on the cell surface, allowing cell internalisation via receptor-mediated endocytosis –, and avoiding sequestration in endosomes – which can be overcome by coating the surface of AuNPs with polycationic materials like polyethyleneimine (PEI), that induce the influx of protons and water causing endosomal rupture by osmotic swelling (Chen et al., 2014; Nie et al., 2023).

Despite the promising characteristics of NLS-tagged AuNPs there is still a lack of research of their use as radio-sensitising agents. To the best of my knowledge only one research article has been published on the use of nuclear-targeted gold nanoparticles to enhance radiosensitisation. In this study, Özçelik and Pratx (2020) demonstrated that by treating A549 lung cancer cells with 40nm NLS-RGD-PEG-AuNPs at a 10μg/mL concentration and irradiating the cultures with doses of 4 and 8 Gy, the cell viability was significantly reduced (Özçelik & Pratx, 2020).

5.1.1. Aims of this chapter

Considering the gap in knowledge that exists in the study of nuclear-targeted AuNPs as radiosensitisers, in both monolayer and three-dimensional platforms, the aim of this chapter was to test the hypothesis that targeting gold nanoparticles to the cell nucleus results in higher levels of DNA damage and, therefore, cell killing. To that effect, I aimed to determine the radio-sensitising potential of NLS-tagged gold nanoparticles in human osteosarcoma and prostate adenocarcinoma cell lines cultured in monolayer and 3D cell culture models. To achieve this, the different models were treated with NLS-modified 50nm gold nanoparticles (Nanopartz) using the same concentration and method described in the previous chapter. Penetration of the nanoparticles and their distribution in spheroids and alginate spheres was assessed using LA-ICP-MSI, and electron microscopy. NLS-AuNP-containing samples were irradiated with doses up to 20 Gy. Following treatment, cell viability was determined the methods previously described for both 2D and 3D models. The presence of γ-H2AX foci and cell cycle distribution were also evaluated in 2D via immunofluorescence and flow cytometry analysis, respectively.

5.2. Results

5.2.1. Attempt to functionalise commercially available 50nm gold nanoparticles with RGD and NLS peptides.

In pursuance of targeting AuNPs to the cells' nuclei, RGD and NLS peptides were custom made and purchased from ThermoFisher. The rationale behind this functionalisation was to PEG-coat the 50nm AuNPs purchased from Sigma for stabilisation and tag both RGD (RGDRGDRGDRGDPGC) – for cell internalisation – and NLS (CGGGPKKKRKVGG) – for nuclear targeting – peptides. To allow tracking of these nanoparticles within cells using confocal microscopy, the NLS peptide was modified with a FITC molecule on the C-Terminal. The functionalisation was carried out by coating the 50nm nanoparticles with PEG and subsequently adding the RGD and NLS peptides in molar excess, according to the method described in section 2.5.1.2. Following several attempts in different vessels made of different materials, the functionalisation proved to be unachievable as the gold nanoparticles stuck to the walls of whatever vessel used, impeding the collection of the prepared AuNP-RGD-NLS solutions (Figure 5.1).

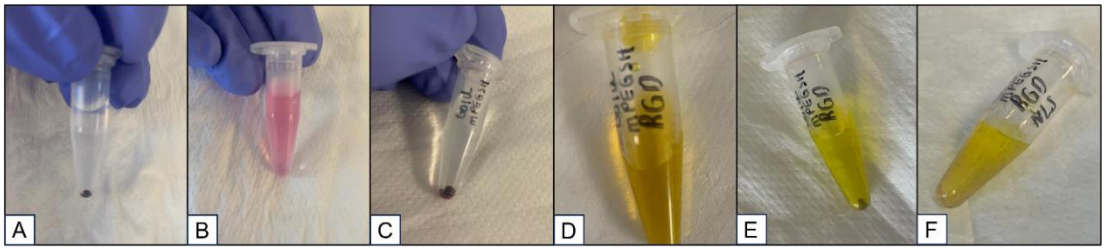

Figure 5.1 - PEG-RGD-NLS AuNP functionalisation. (A) 50nm gold pellet following 12000 x g centrifugation. **(B)** m-PEG-SH was added to 50nm AuNPs and incubated for 24h. **(C)** PEG-AuNP pellet following 12000 x g centrifugation. **(D)** RGD and NLS peptides were added to PEG-AuNPs in molar excess. **(E)** NLS-RGD-PEG-AuNP pellet following 12000 x g centrifugation. The functionalised nanoparticles start adhering to the walls of the tube. **(F)** The pellet was resuspended in dH_2O. Following several rounds of pipetting and scrapping, the nanoparticles do not detach or solubilise.

Due to the unsuccessful attempts at functionalising the 50nm nanoparticles with the custom-made peptides, pre-functionalised and PEGylated FITC-NLS-AuNPs were purchased from Nanopartz.

5.2.2. Uptake of nuclear-targeted gold nanoparticles by 2D and 3D cell models.

Prior to irradiation, monolayer, multi-cellular tumour spheroid and alginate cultures were treated with 50nm NLS-AuNP (Nanopartz) and their uptake was evaluated using LA-ICP-MS and TEM.

5.2.2.1. LA-ICP-MSI of 3D cell models

To determine the uptake and localization of nuclear-targeted gold nanoparticles in cells cultured within MCTS and alginate spheres, sections of both 3D models were analysed using LA-ICP-MS and compared to untreated controls (Appendix A) to ensure specificity of results. The ICP-MS data was plotted as intensity vs. time graphs, using GraphPad Prism, and spectral images were generated to map the localization of each isotope within the samples. To map out the localisation of the isotope of interest (^{197}Au), ^{66}Zn, ^{25}Mg isotopes were also analysed to serve as a cellular control.

5.2.2.1.1. Multicellular Tumour Spheroid

Results show that when cultured in MCTS, all cell lines are able to uptake NLS-AuNPs. In MG-63, the majority of functionalised gold nanoparticles failed to penetrate the spheroid core, accumulating in the outer ring (Figure 5.2). In Saos-2, despite the penetration rate being seemingly higher than in MG-63, the majority of NLS-AuNPs also failed to reach the core of the spheroid (Appendix D). For PC3 MCTS, AuNPs were uniformly distributed through the spheroid (Figure 5.3). Finally, for LNCaP, even though gold concentration was high throughout the entirety of the spheroid, the counts of ^{197}Au reached their peak on the outer regions of the spheroid, suggesting a higher concentration of NLS-functionalised nanoparticles accumulated in the outer regions of LNCaP MCTS (Appendix D).

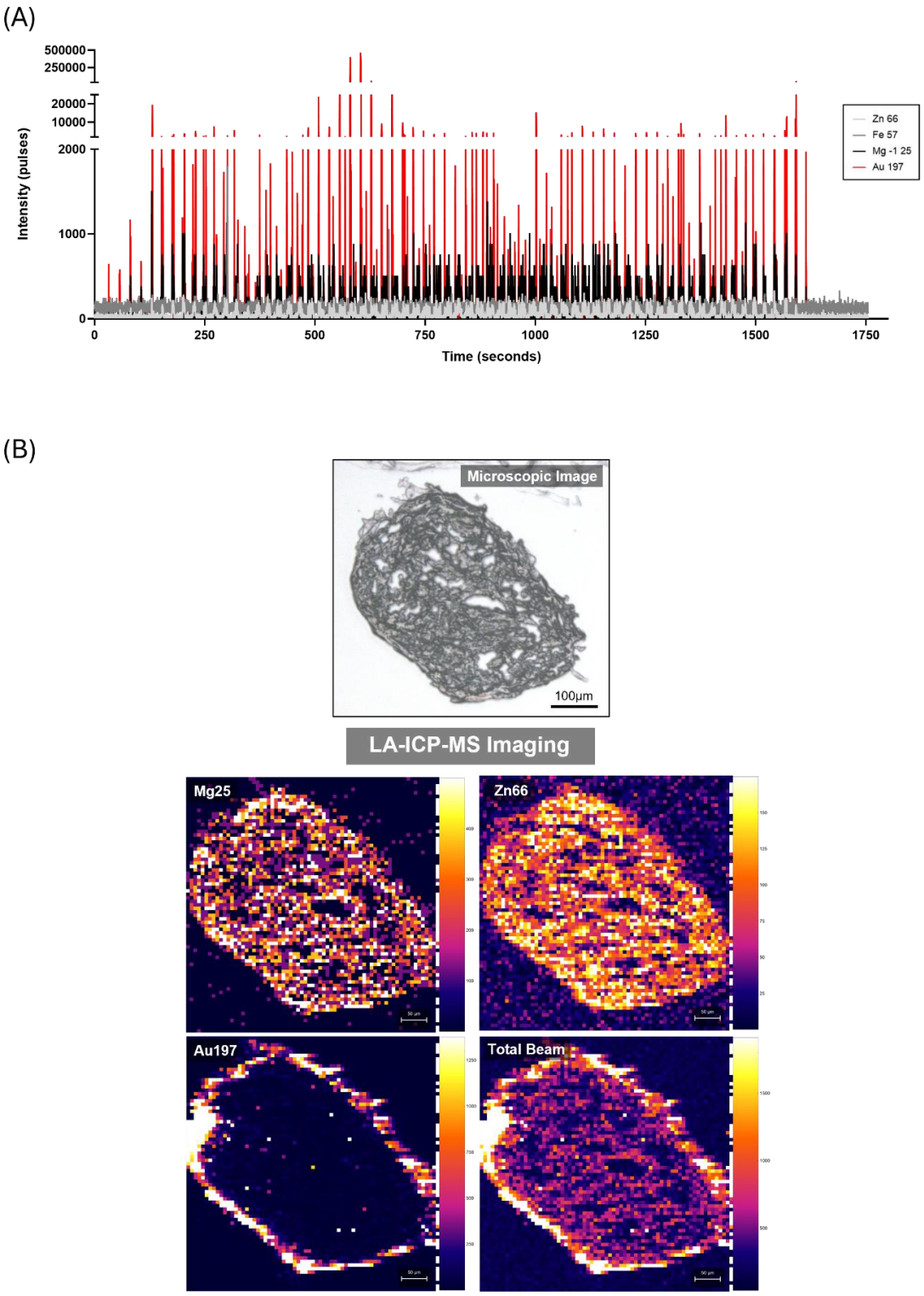

Figure 5.2 - LA-ICP-MS detection and localization of NLS-tagged gold nanoparticles in MG-63 MCTS. (A) Intensity vs. time profile of ablated raster shows uptake of NLS-AuNPs demonstrated by the ^{197}Au spectrum (red). 20µm/sec scan speed**. (B)** LA-ICP-MSI of NLS-AuNP treated MG-63 spheroid. Pre-ablation optical image (20X objective - scale bar represents 100µm) and elemental maps of ^{66}Zn, ^{25}Mg, ^{197}Au, and total beam. Scale bar represents 50µm.

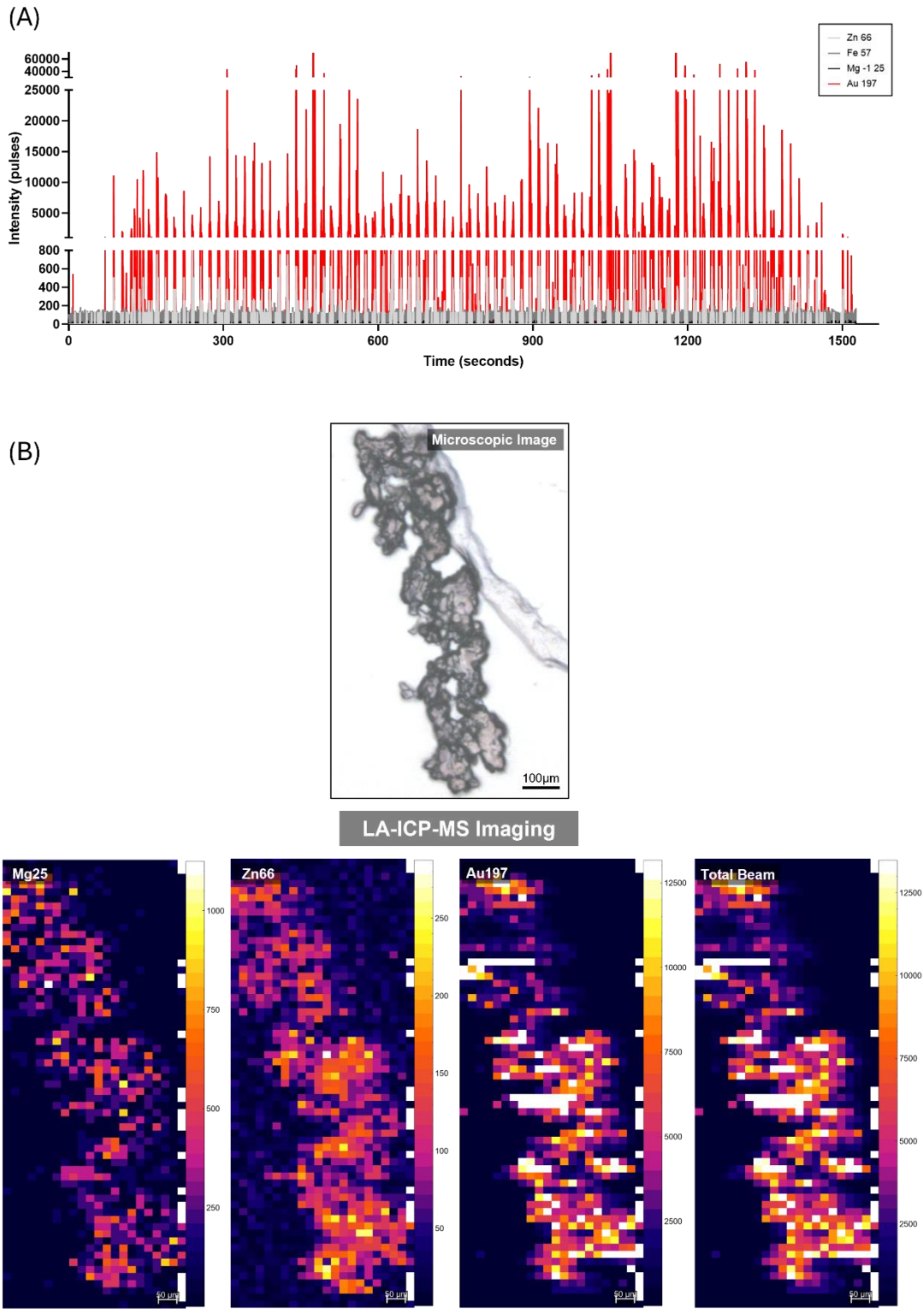

Figure 5.3 - LA-ICP-MS detection and localization of NLS-tagged gold nanoparticles in PC3 MCTS. (A) Intensity vs. time profile of ablated raster shows uptake of NLS-AuNPs demonstrated by the ^{197}Au spectrum (red). 20µm/sec scan speed. **(B)** LA-ICP-MSI of NLS-AuNP treated PC3 spheroid. Pre-ablation optical image (20X objective - scale bar represents 100µm) and elemental maps of ^{66}Zn, ^{25}Mg, ^{197}Au, and total beam. Scale bar represents 50µm.

5.2.2.1.2. Alginate Spheres

For alginate spheres, MG-63 (Figure 5.4), Saos-2 (Appendix E) and PC3 (Appendix E) cell lines showed similar AuNP uptake ratio, demonstrated by ^{197}Au intensities of 200 pulses on average. Even though most LNCaP cells showed the same average intensity of gold, in some the intensity increased to ≈900 pulses (Figure 5.5).

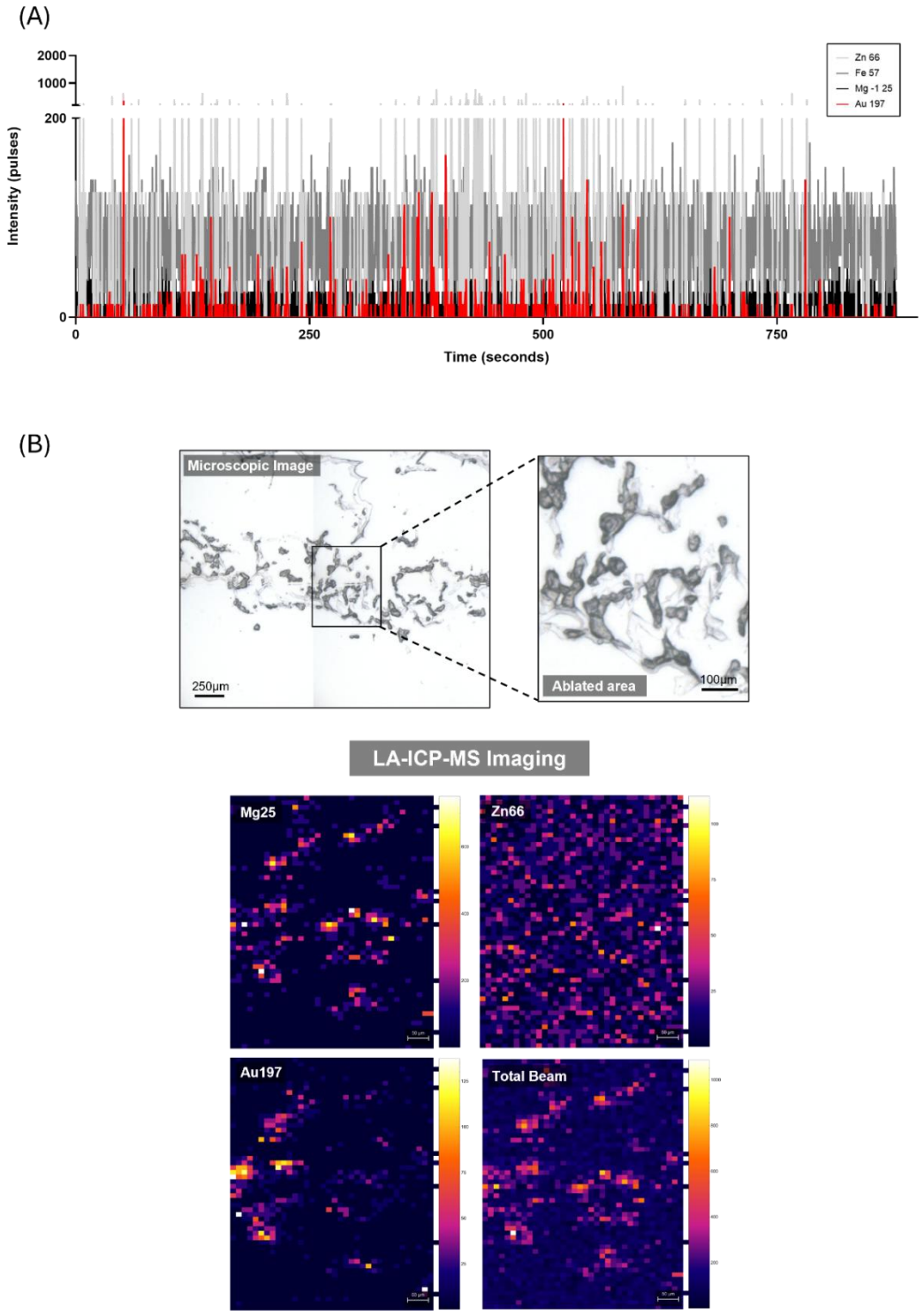

Figure 5.4 - LA-ICP-MS detection and localization of NLS-tagged gold nanoparticles in MG-63 alginate spheres. (A) Intensity vs. time profile of ablated raster shows uptake of NLS-AuNPs demonstrated by the ^{197}Au spectrum (red). 20µm/sec scan speed. **(B)** LA-ICP-MSI of NLS-AuNP treated MG-63 colonies grown in alginate. Pre-ablation optical image (20X objective - scale bars represent 250µm and 100µm) and elemental maps of ^{66}Zn, ^{25}Mg, ^{197}Au, and total beam. Scale bar represents 50µm.

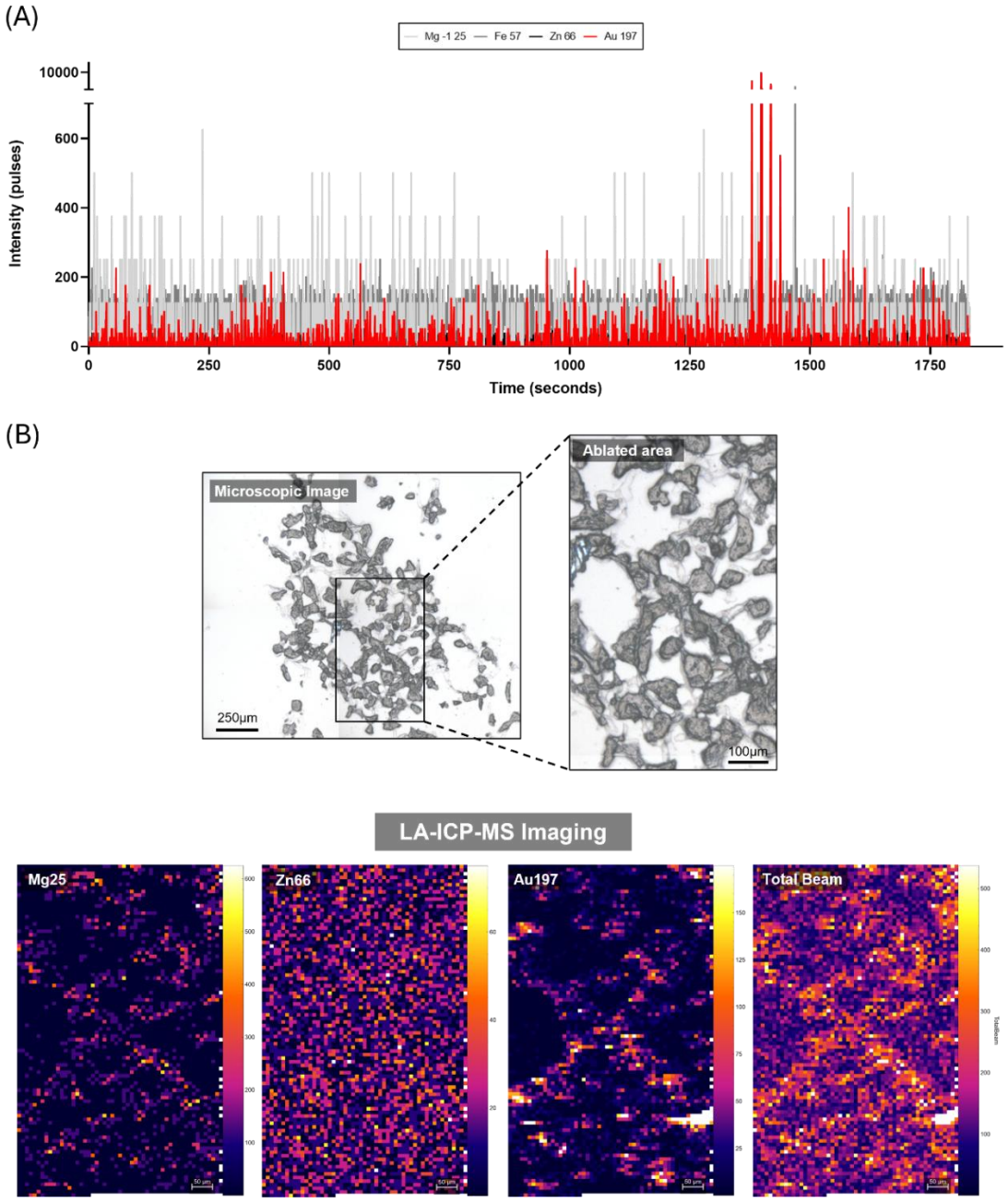

Figure 5.5 - LA-ICP-MS detection and localization of NLS-tagged gold nanoparticles in LNCaP alginate spheres. (A) Intensity vs. time profile of ablated raster shows uptake of NLS-AuNPs demonstrated by the ^{197}Au spectrum (red). 20µm/sec scan speed. **(B)** LA-ICP-MSI of NLS-AuNP treated LNCaP colonies grown in alginate. Pre-ablation optical image (20X objective - scale bars represent 250µm and 100µm) and elemental maps of ^{66}Zn, ^{25}Mg, ^{197}Au, and total beam. Scale bar represents 50µm.

5.2.3. Assessment of radio-sensitising effect of NLS-AuNP in 2D cultures.

Prior to radiation exposure, monolayer cultures of MG-63, Saos-2, PC3 and LNCaP cell lines were incubated for 24 hours with a 10 μg/mL solution of NLS-AuNPs, followed by irradiation with doses of 1.25, 2.5 and 5 Gy. Cell viability was measured 10 days post-treatment using a colony formation assay. Following the same method described in the previous chapter, colonies were stained with 0.5% crystal violet and the absorbance of each well was measured, appropriately blank-corrected and normalised towards the untreated control. LQ curves were drawn and compared using an extra sum of squares test. The responses of untreated and NLS-AuNP-treated samples were compared for each radiation dose using multiple *t-tests*, followed by the Holme-Sidak method for multiple comparisons, with α=0.05 (Figure 5.6). The toxicity of the NLS-AuNP treatment was also assessed to ensure the nanoparticles alone did not hinder cell viability, which was confirmed. The results can be found in Appendix K of this thesis.

Results show that following irradiation the surviving fraction of untreated MG-63 cells was 0.92 ± 0.04, 0.61 ± 0.23, and 0.28 ± 0.13 at 1.25, 2.5 and 5 Gy doses, respectively. This equated to an IC50 of 3.67 ± 0.89 Gy. NLS-AuNP-treated MG-63 cells presented a surviving fraction of 0.92 ± 0.42 after a 1.25 Gy dose, 0.61 ± 0.23 after 2.5 Gy, and 0.28 ± 0.13 after 5 Gy, which corresponded to an IC50 of 3.96 ± 1.00 Gy. Comparing the responses of both untreated and NLS-AuNP-treated MG-63 cells, it was possible to conclude the presence of NLS-tagged AuNPs did not produce a radio-sensitising effect (p=0.927). The fraction of cells that survived irradiation in untreated Saos-2 was 0.77 ± 0.18 after 1.25 Gy, 0.37 ± 0.19 after 2.5 Gy and 0.13 ± 0.03 after 5 Gy (IC50=1.86 ± 0.45 Gy). Saos-2 cells treated with NLS-tagged gold nanoparticles presented a surviving fraction value of 0.77 ± 0.18 after 1.25 Gy, 0.37 ± 0.19 after 2.5 Gy and 0.13 ± 0.03 after a 5 Gy dose, which equated to an IC50 of 1.39 ± 0.34 Gy. Comparing the responses of untreated and AuNP-treated cells, it was possible to observe a minor radiosensitising effect of the NLS-tagged gold nanoparticles (DEF=1.34), illustrated by the shift of the non-linear regression curve to the left of the x axis. Nevertheless, this difference in sensitivity was not statistically significant (p= 0.462). For PC3, the surviving fraction of untreated cells following 1.25, 2.5, and 5Gy irradiation doses was 0.75 ± 0.15, 0.53 ± 0.11, and 0.23 ± 0.06, respectively, thus equating to an IC50 of 2.57 ± 0.41 Gy. With NLS-AuNP treatment, the

surviving fraction was 0.69 ± 0.15 after 1.25 Gy, 0.51 ± 0.16 after 2.5 Gy and 0.17 ± 0.09 after 5Gy, meaning an IC50 of 2.11 ± 0.38 Gy. Even though the presence of NLS-tagged gold nanoparticles enhanced the IC50 dose by a factor of 1.22, the difference in response between untreated and NLS-AuNP-treated PC3 was not statistically significant at any given dose. The extra sum of squares test confirmed there was no significant difference between untreated and NLS-AuNP-treated PC3 cells (p=0.592). LNCaP cells treated with NLS-tagged AuNPs presented surviving fractions of 0.58 ± 0.20, 0.36 ± 0.06, and 0.09 ± 0.03 following 1.25, 2.5, and 5 Gy irradiation doses, respectively. When compared to the responses of untreated cells (0.60 ± 0.21, 0.45 ± 0.14, and 0.10 ± 0.05 following 1.25, 2.5, and 5 Gy doses, respectively), and despite a DEF of 1.20, the difference in sensitivity was not statistically significant (p=0.652).

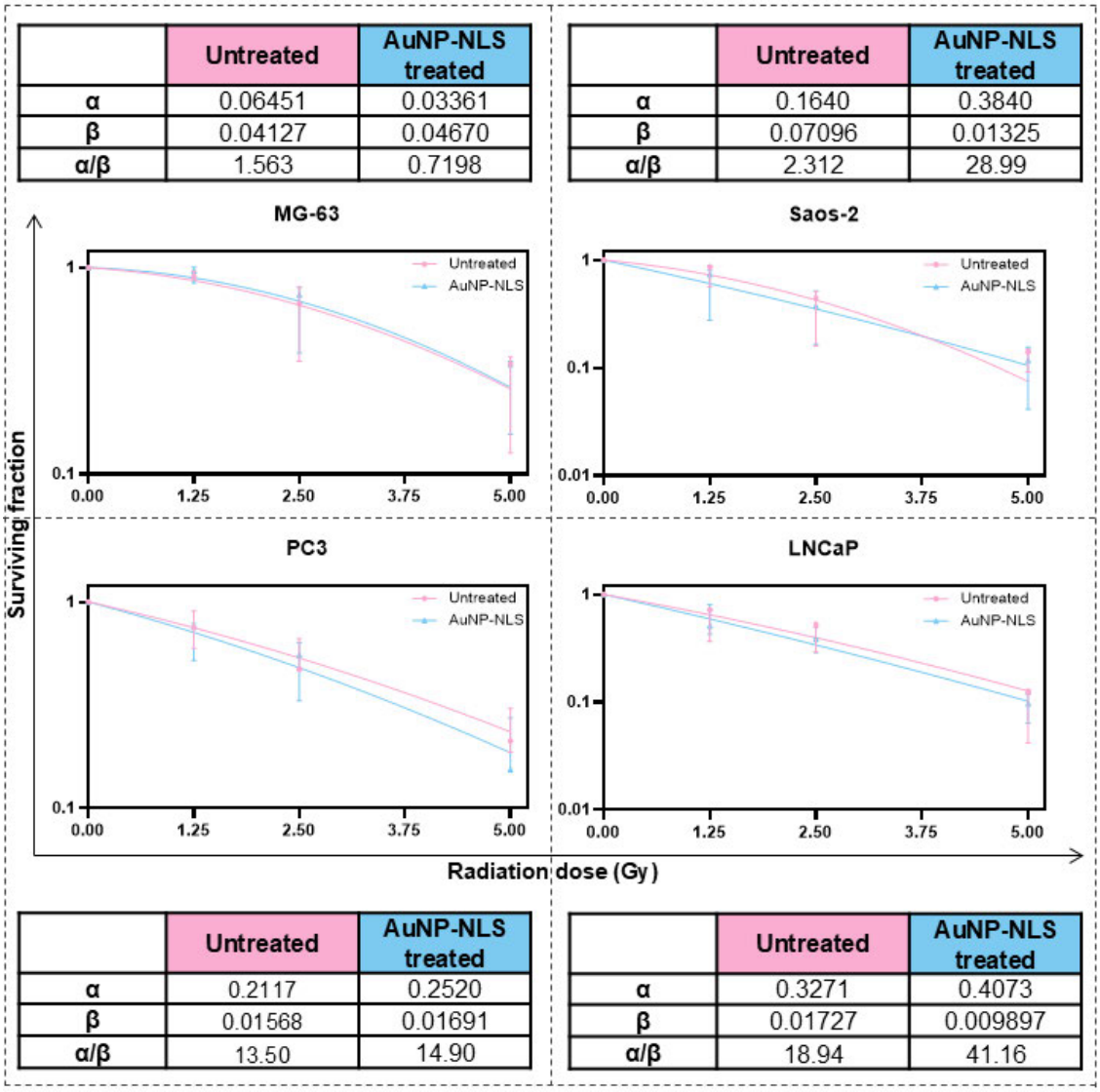

Figure 5.6 - Cell viability of NLS-AuNP-treated osteosarcoma and prostate adenocarcinoma cell lines 10 days post-irradiation. Surviving fractions of NLS-AuNP-treated monolayer cultures with increasing doses of radiation. Albeit producing a minor shift in the survival curves, NLS-tagged gold nanoparticle does not significantly increase the sensitivity of cell lines to radiation. Scatter plots, percentage surviving fraction data is presented as mean ±SD, individual values represent n=3 independent experiments with 3 technical repeats. Statistical significance determined by multiple *t-tests* and corrected using the Holme-Sidak method of multiple comparisons, with alpha=0.05. (*P<0.05). From the LQ curves, α and β values were calculated using a 95% confidence interval. Untreated data has been presented in previous chapters

5.2.4. Comparison of radiation responses between AuNP- and NLS-AuNP treated monolayer cultures.

To investigate the difference in the produced radio-sensitising effect between unfunctionalised and NLS-tagged gold nanoparticles, the proliferating capacity of cells treated with each of the different AuNPs was compared for each radiation dose. Multiple *t-tests* followed by Holme-Sidak correction (α=0.05) revealed that MG-63 cells are significantly more sensitive to a 2.5 Gy radiation dose when treated with unfunctionalised gold nanoparticles. For all other doses, the difference in response was not significant. In the remaining cell lines, there were no significant differences between the response of AuNP- and NLS-AuNP-treated cells, at any given dose (Figure 5.7).

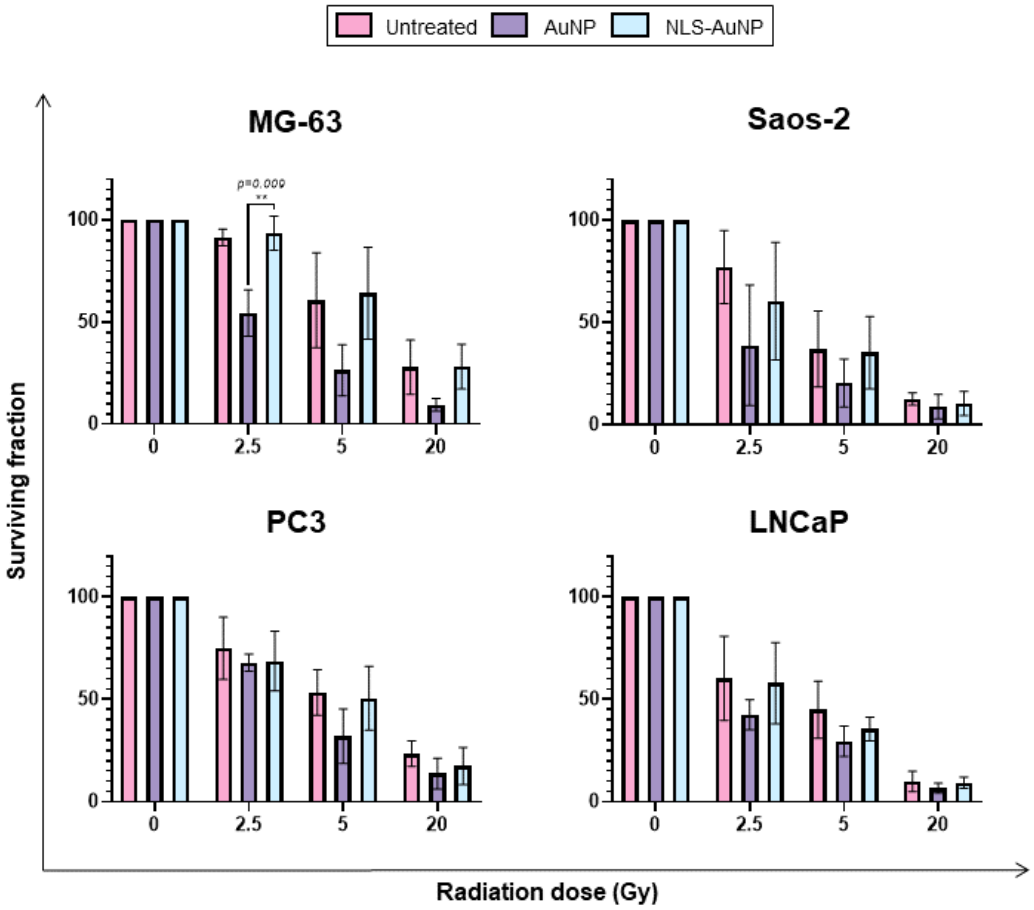

Figure 5.7 - Comparison of radio-responses between AuNP- and NLS-AuNP treated monolayer cultures 10 days post-irradiation. Results show that only MG-63 cells present a significant increase in sensitivity at 2.5 Gy when treated with unfunctionalised AuNPs. Interleaved bars, multiple *t-tests*. Statistical significance corrected using the Holme-Sidak method of multiple comparisons, with alpha=0.05. (*P<0.05). 2D data is presented as mean ±SD and individual values represent n=3 independent experiments with 3 technical repeats. Untreated samples included for baseline response reference. Untreated and AuNP-treated data has been presented in previous chapters.

5.2.5. Assessment of radio-sensitising effect of NLS-AuNP in alginate sphere cultures.

Alginate spheres were prepared and incubated for 3 days to allow the formation of young colonies. There were then incubated for 24h with NLS-tagged 50 nm diameter gold nanoparticles at a concentration of 10 μg/mL in appropriate cell culture media and irradiated with doses ranging between 2.5 and 20 Gy. Following irradiation, the cultures were returned to the incubator and allowed to grow for a further 7 days, after which colony diameter was measured. The values were normalised towards the untreated control and a non-linear regression curve was plotted for both the untreated and the NLS-AuNP-treated populations to determine the IC50 for each cell line. The responses of untreated and NLS-AuNP-treated samples were compared for each radiation dose using multiple *t-tests*, and statistical significance was determined using the Holme-Sidak method, with alpha=0.05 (Figure 5.7).

Results show that untreated colonies are significantly more sensitive to radiation than colonies treated with NLS-tagged gold nanoparticles. Prior to irradiation, the average colony diameter of untreated MG-63 cells was 40.4±2.1μm (Figure 5.8). After 7 days, untreated colonies nearly doubled, presenting an average diameter of 79.6±9.5μm, while the colonies in NLS-AuNP-treated spheres measured, on average, 66.8±9.1μm. Following irradiation with a dose of 2.5 Gy, untreated colonies measured 57.1±8.4μm and NLS-AuNP treated colonies measured 65.8±2.8μm. After 5 Gy, untreated colonies had an average diameter of 47.2±6.5μm while colonies treated with NLS-AuNPs measured 61.4±3.8μm. Following a 20 Gy dose, untreated colonies measured 31.8±1.3μm and the ones treated with NLS-AuNP measured 51.6±6.1μm. This equated to an IC50 of 9.15±1.72 Gy for untreated colonies and 59.19±18.3 Gy for NLS-AuNP treated MG-63 colonies. This difference in sensitivity was statistically significant at a 20 Gy dose (p=0.007). Prior to radiation exposure, Saos-2 colonies measured 27.9±1.4μm. Seven days post-irradiation, untreated Saos-2 colonies measured 60.3±5.4μm and NLS-AuNP treated measured 59.8±5.7μm in diameter. Irradiated untreated colonies measured 38.5±1.8μm, 35.2±2.6μm, and 30.6±2.0μm, with doses of 2.5, 5, and 20 Gy, respectively. Colonies treated with NLS-AuNPs measured 51.3±1.6μm, 36.9±0.5μm, and 36.2±2.9μm, following

doses of 2.5, 5, and 20 Gy, respectively. The IC50 values were 5.7±1.2 Gy and 12.4±2.7 Gy for untreated and NLS-AuNP-treated colonies, respectively. The difference in radio-sensitivity between untreated and NLS-AuNP treated Saos-2 alginate spheres was significant after a 2.5 Gy dose (p=0.015). PC3 colonies measured 35.8±3.7μm prior to irradiation. Seven days following exposure to a 2.5 Gy radiation dose, untreated colonies measured 59.8±7.2μm and NLS-AuNP treated colonies had an average diameter of 50.6±3.4μm. After 5 Gy, the diameters were 41.5±3.1μm for untreated colonies and 47.2±2.6μm for NLS-AuNP treated. With a 20 Gy dose, untreated colonies measured 37.5±0.2μm while colonies treated with NLS-AuNPs measured 47.1±3.6μm. Colonies that were not irradiated measured 83.5±2.0μm without treatment and 57.7±4.9μm when treated with NLS-AuNPs. The difference in sensitivity between untreated and treated cells was significant at 5 Gy (p=0.011) and 20 Gy (p=0.003). The IC50s were 5.6±0.9 Gy and 49.5±14.8 Gy for untreated and treated colonies, respectively. LNCaP colonies measured 44.7±2.8μm on the day of irradiation. The following week, untreated colonies measured 120.3±11.3μm and NLS-AuNP treated colonies had an average diameter of 55.5±0.4μm. After radiation exposure, untreated colonies measured 75.8±10.3μm, 57.0±7.1μm, and 42.6±3.1μm, with doses of 2.5, 5, and 20 Gy, respectively, meaning and IC50 of 5.5±0.9 Gy. The diameters of the colonies treated with NLS-AuNPs were 46.1±4.8μm, 39.9±4.1μm, and 36.0±4.4μm, after a dose of 2.5, 5, and 20 Gy, respectively, which equated to an IC50 of 16.4±1.2 Gy. The difference in sensitivity between untreated and NLS-AuNP-treated colonies was significant at the highest radiation dose (p=0.012).

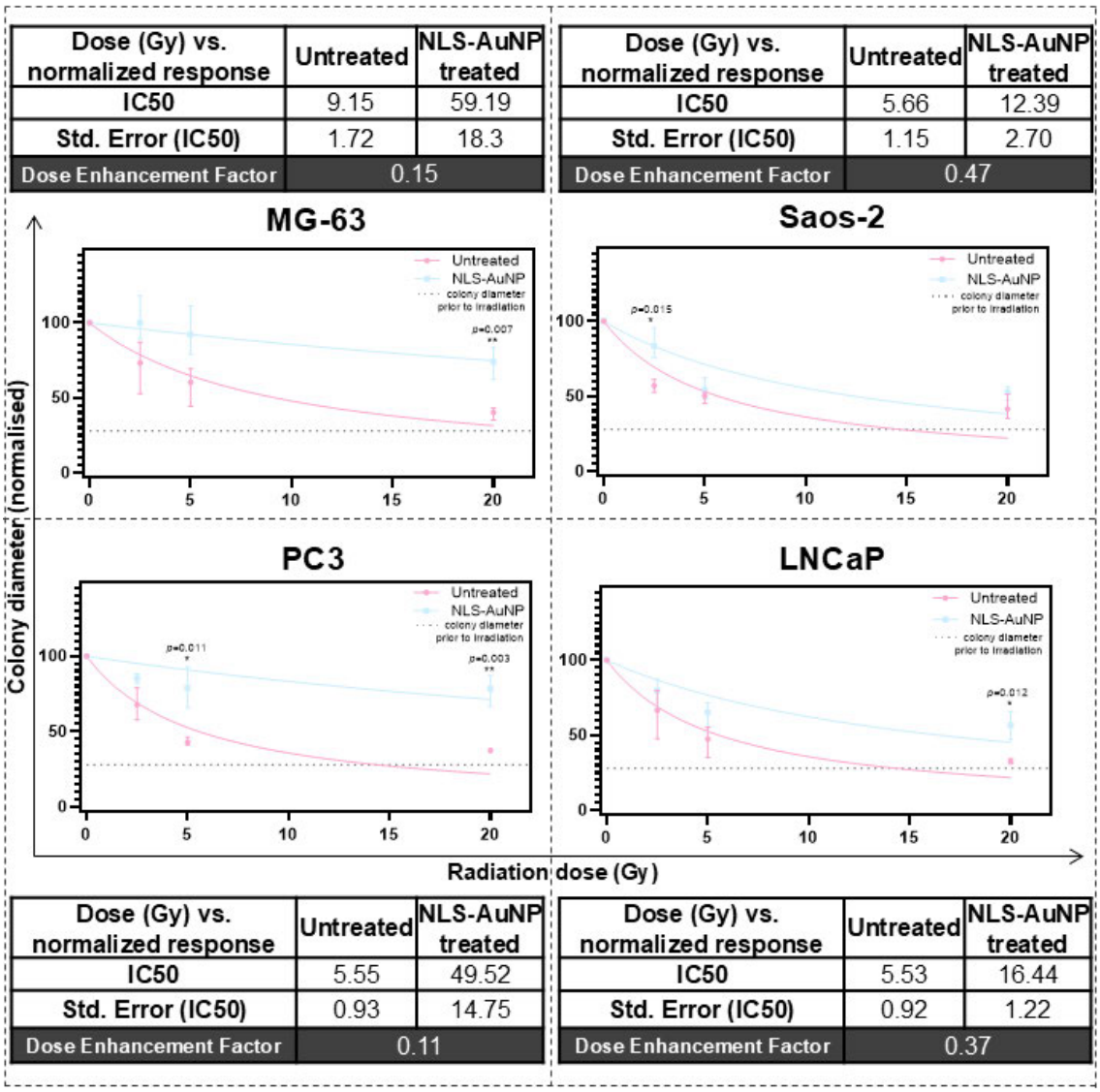

Figure 5.8 - Cell viability of NLS-AuNP-treated osteosarcoma and prostate adenocarcinoma cell lines grown in alginate spheres 10 days post-irradiation. Normalised colony diameters of NLS-AuNP-treated alginate sphere cultures with increasing doses of radiation. Untreated colonies are significantly more sensitive to ~radiation than NLS-AuNP treated colonies. Scatter plots, normalised colony diameter data is presented as percentage mean ±SD, individual values represent n=3 independent experiments with 3 technical repeats. Statistical significance determined by multiple *t-tests* and corrected using the Holme-Sidak method of multiple comparisons, with alpha=0.05. (*P<0.05). From the non-linear regression curves, IC50 values were calculated using a 95% confidence interval. DEF calculated as untreated IC50 ÷ NLS-AuNP treated IC50. Untreated data has been presented in previous chapters.

5.2.6. Comparison of radiation responses between AuNP- and NLS-AuNP-treated alginate spheres.

The radio-responses of AuNP- and NLS-AuNP treated cells were compared for each radiation dose using multiple *t-tests* followed by multiple comparisons using the Holme-Sidak method (α=0.05). Results show that colonies grown in alginate spheres were more sensitive to radiation when treated with unfunctionalized gold nanoparticles. In MG-63, this difference in response was significant at 5 Gy (p=0.042) and 20 Gy (p=0.005). AuNP-treated Saos-2 colonies were significantly more sensitive than NLS-AuNP at 2.5 Gy (p=0.032) and 20 Gy (p=0.30). For PC3, colonies treated with unfunctionalised AuNPs were significantly more sensitive than colonies treated with NLS-AuNPs after a 2.5, 5 and 20 Gy dose (p=0.023, p=0.020, and p=0.002, respectively). In LNCaP, AuNP-treated colonies were significantly more sensitive than colonies treated with NLS-AuNPs at every radiation dose, with p=0.011 with 2.5 Gy, p=0.013 with 5 Gy, and p=0.020 with 20 Gy (Figure 5.9).

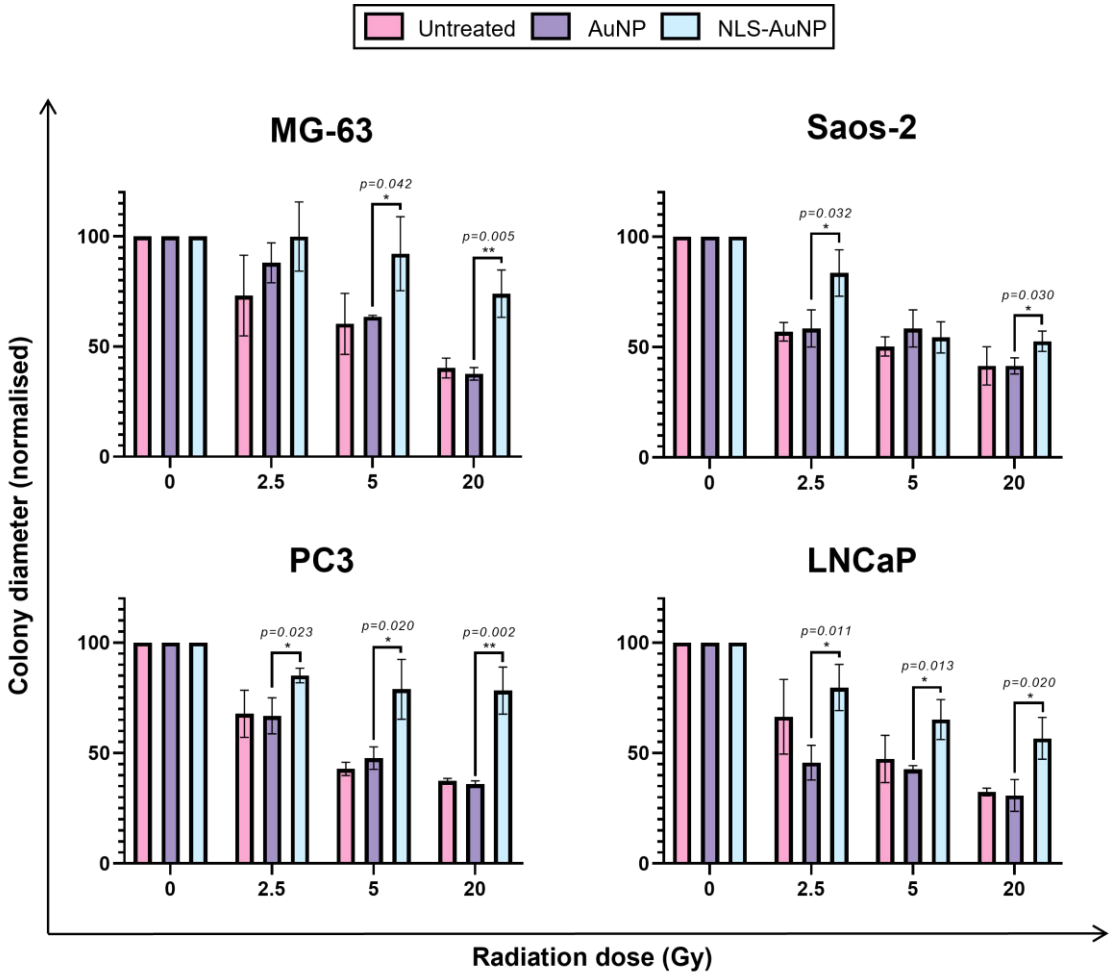

Figure 5.9 - Comparison of radio-responses between AuNP- and NLS-AuNP treated alginate sphere cultures 10 days post-irradiation. Results show that all cell lines present a significant increase in sensitivity when treated with unfunctionalised AuNPs. Interleaved bars, multiple *t-tests*. Statistical significance corrected using the Holme-Sidak method of multiple comparisons, with alpha=0.05. (*P<0.05). 3D data is presented as mean ±SD and individual values represent n=3 independent experiments with 3 technical repeats. Untreated samples included for baseline response reference. Untreated and AuNP-treated data has been presented in previous chapters.

5.2.7. Acute responses of MCTS treated with NLS-tagged AuNPs.

To assess the radio-sensitising effect of nuclear-targeted gold nanoparticles in MCTS, these were treated with NLS-AuNPs (10μg/mL) for 24h and irradiated with doses of 2.5, 5, and 20 Gy. The following day, the spheroids were stained with Hoechst 33342 and PI for a live/dead assay, as previously described (Figure 5.10). Both total and dead cell areas were measured, and cell viability was calculated. The results were plotted as a percentage with corresponding non-linear regression curved, from which IC50 values were calculated. The sensitivity of NLS-AuNP-treated MCTS to each radiation dose was analysed using a Kruskal-Wallis non-parametric test followed by a Dunn's multiple comparisons

test (Figure 5.11A). The viability of NLS-AuNP-treated MCTS with each dose was then compared to the one of untreated cultures with multiple *t-tests* corrected using the Holme-Sidak method for multiple comparisons with a 95% confidence interval (Figure 5.11B).

Results show that the viability of NLS-AuNP-treated MG-63 spheroids declines with each radiation dose, with percentage viability values decreasing to 85.9±3.4%, 81.2±5.1%, and 58.4±5.9% after doses of 2.5, 5, and 20 Gy, translating to an IC50 of 25±2.4 Gy. This reduction in viability is significant at 20 Gy (p=0.006) (Figure 5.11A). Comparing these responses with the ones of untreated spheroids, it is possible to observe a radio-sensitising effect of NLS-AuNPs, with a difference in viability that is significant at 2.5 Gy (p=0.009) and 20 Gy (p<0.001) doses (Figure 5.11B). For Saos-2, the overall viability of spheroids treated with NLS-AuNPs also decreases with increasing radiation doses. After a 2.5 Gy dose the average viability was 63.4±15.9% and with 5 Gy it was reduced to 62.5±12.0%. Following 20 Gy, the average viability of Saos-2 spheroids was 69.2±9.0%, and even though this is slightly higher than the viability after lower irradiation doses, the standard deviation of the results is high, therefore rendering the difference in response between each radiation dose not statistically significant. The IC50 value was 18.46±7.1 Gy (Figure 5.11A). When compared to the response of untreated Saos-2 MCTS, it is possible to visualise a radio-sensitising effect of NLS-AuNPs at every dose (2.5 Gy, p=0.015; 5 Gy, p=0.007; 20 Gy, p=0.010) (Figure 5.11B). The viability of both NLS-AuNP-treated prostate adenocarcinoma spheroids was not affected by irradiation. PC3 spheroids presented an average viability of 100±4.4%, 95.2±2.5%, and 92.8±4.9% following exposure to 2.5, 5, and 20 Gy doses of radiation, respectively (Figure 5.11A). LNCaP spheroids treated with nuclear-targeted nanoparticles were 97.0±2.2%, 99.2±1.6%, and 100±2.3% viable post-irradiation with doses of 2.5, 5, and 20 Gy, respectively (Figure 5.11A). As expected, the difference in viability between untreated and NLS-AuNP-treated spheroids was not significant for any of the prostate cell lines (Figure 5.11B).

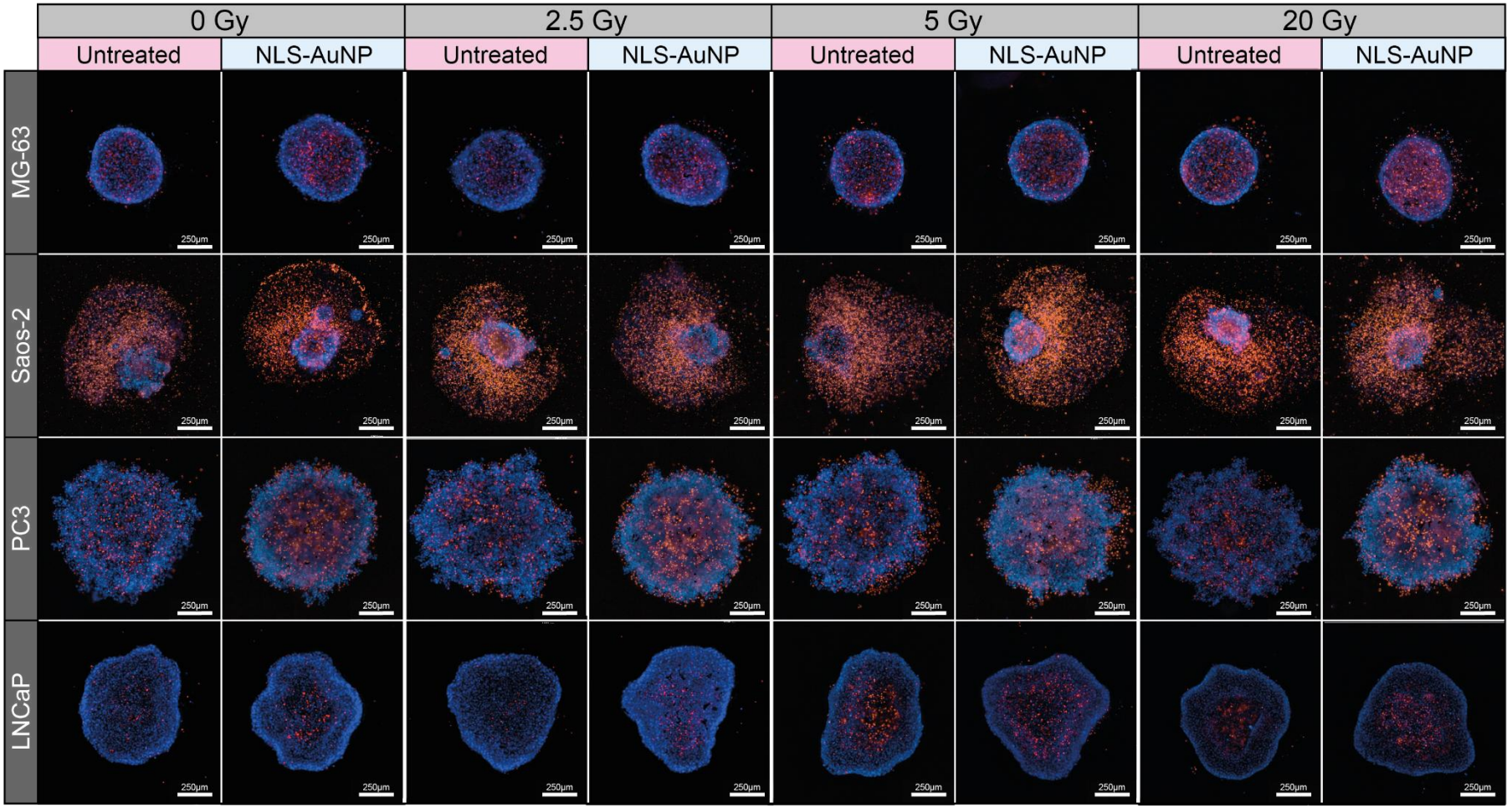

Figure 5.10 - Cell viability of human osteosarcoma and prostate cancer cell lines cultured in MCTS and treated with NLS-AuNPs, 24h post-irradiation. Multicellular tumour spheroids were stained with Hoechst 33342 (blue cells) and Propidium Iodide (red cells). Cytation 5 imaging system, 4x objective, Z-stack of DAPI and Texas Red channels. Scale bar represents 250µm.

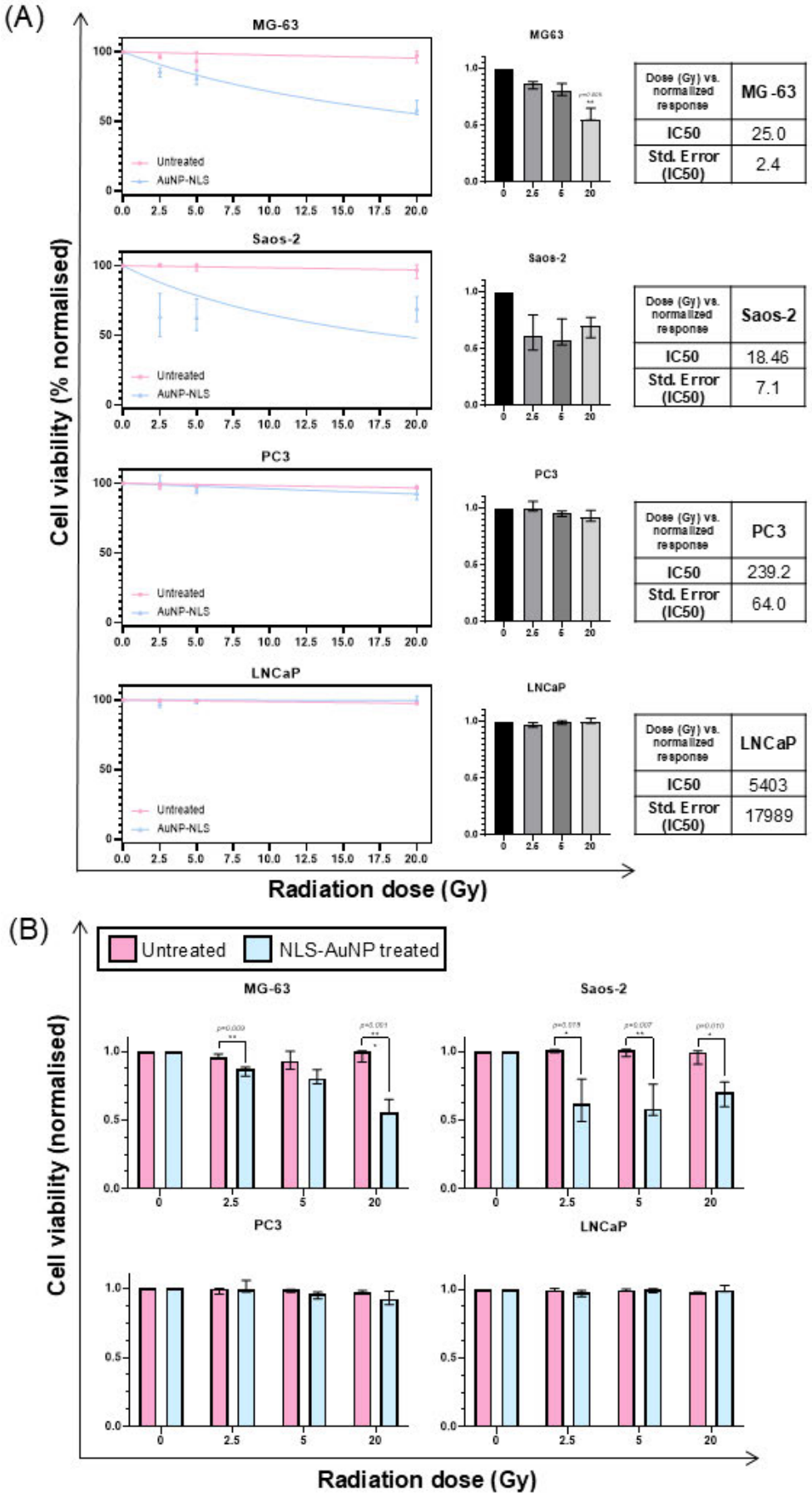

Figure 5.11 - Viability of cells grown in MCTS and treated with NLS-AuNPs 24h-post ionising radiation exposure. (A) Osteosarcoma cell lines present a

reduction in viability with increasing doses of radiation. Scatter plot and non-linear regression curve, percentage cell viability data is presented as median ±range, individual values represent n=3 independent experiments with 3 technical repeats. Individually analysed responses of MG-63, Saos-2, PC3, and LNCaP only show a significant reduction in viability for MG-63 spheroids with a 20 Gy dose. Column bar graph, Kruskal-Wallis followed by Dunn's multiple comparisons test (*P<0.05). **(B)** Comparison between untreated and AuNP-treated MCTS of each cell line showing a radio-sensitisation effect of NLS-AuNPs in MG-63 and Saos-2 spheroids. Interleaved bars, multiple *t-tests*. Statistical significance corrected using the Holm-Sidak method of multiple comparisons, with alpha=0.05. (*P<0.05). All data is presented as median ±range and individual values represent n=3 independent experiments with 3 technical repeats. Untreated data has been presented in previous chapters.

5.2.7.1. Comparison of acute radio-responses between AuNP- and NLS-AuNP-treated MCTS.

To investigate the difference in the produced radio-sensitising effect between unmodified and nuclear targeted gold nanoparticles, the cell viability of spheroids treated with each of the different AuNPs was compared for each radiation dose. Multiple *t-tests* followed by Holme-Sidak correction (α=0.05) revealed that Saos-2 spheroids are significantly more sensitive to a 20 Gy radiation dose when treated with unfunctionalised gold nanoparticles (p=0.020). For all other doses, the difference in response was not significant. In the remaining cell lines, there were no significant differences between the response of AuNP- and NLS-AuNP-treated cells, at any given dose (Figure 5.12).

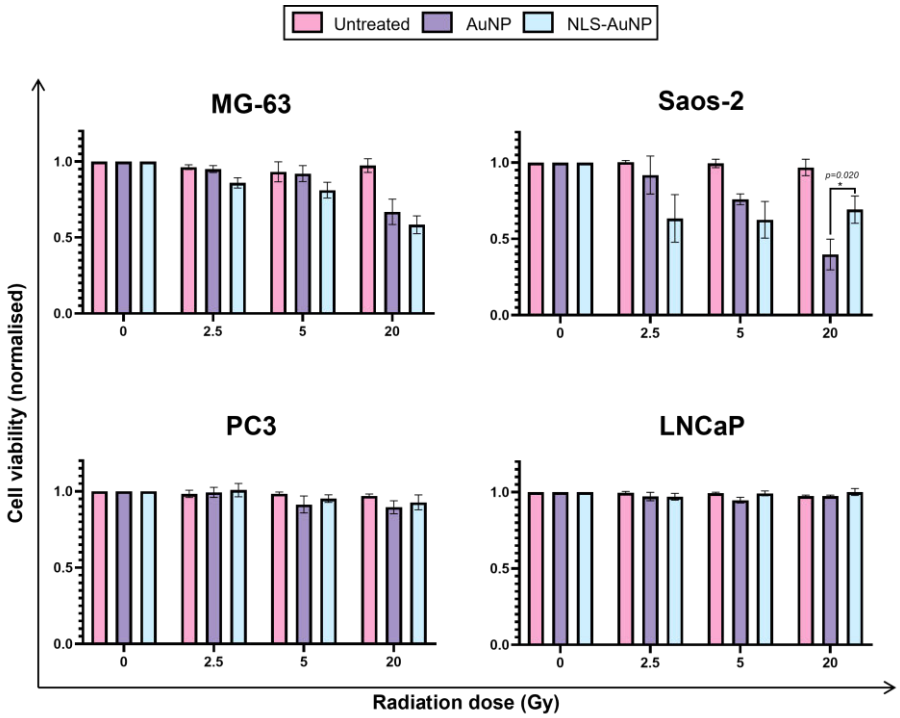

Figure 5.12 - Comparison of acute radio-responses between AuNP- and NLS-AuNP treated MCTS 24h post-irradiation. Only Saos-2 spheroids present a significant increase in sensitivity at 20 Gy when treated with unmodified AuNPs. Interleaved bars, multiple *t-tests*. Statistical significance corrected using the Holme-Sidak method of multiple comparisons, with alpha=0.05. (*P<0.05). 3D data is presented as mean ±SD and individual values represent n=3 independent experiments with 3 technical repeats. Untreated samples included for baseline response reference. Untreated and AuNP-treated data has been presented in previous chapters.

5.2.8. Acute responses of alginate spheres treated with nuclear-targeted gold nanoparticles.

Prior to irradiation, alginate spheres were prepared using the method described in 2.1.6.2. and treated with 50 nm diameter NLS-AuNPs (10 µg/mL) for 24h. The alginate spheres were then irradiated using doses of 2.5 Gy, 5 Gy, and 20 Gy. To assess cell viability after irradiation, the cultures were stained with Hoechst 33342/PI 24h post-treatment and imaged on Cytation 5 (Figure 5.13). Relative percentage of viable cells was calculated and normalised towards the respective untreated control. The data was graphed as a percentage in a scatter plot and non-linear regression curves of dose vs. normalised response were drawn. The respective IC50 values were calculated, with a confidence interval of 95% (Figure 5.14A). Responses of each treated cell line to the different radiation doses were analysed using a Kruskal-Wallis non-parametric test, due to the skewness of the results, followed by multiple comparisons, using Dunn's correction as a post-hoc test, to assess the significance of the response to each dose when compared to

the untreated control (0Gy). The response of NLS-AuNP-treated alginate spheres was compared with that of the untreated models of the same cell line for each radiation dose using multiple t-tests and corrected using the Holme-Sidak method with a 95% confidence interval (Figure 5.14B.

Results show that both osteosarcoma cell lines present a reduction in viability with increasing radiation doses. AuNP-NLS treated MG-63 alginate spheres were 99.1±1.1%, 89.9±11.0%, and 77.4±15.2% viable following exposure to 2.5, 5, and 20 Gy radiation doses, respectively, which equated to an IC50 of 66.2±16.5 Gy. This reduction in viability was significant at 20 Gy (p=0.036) (Figure 5.14A). The viability of NLS-AuNP-treated Saos-2 colonies decreased to 95.8±4.0%, 80.5±10.2%, and 36.6±2.7% after irradiation with 2.5, 5, and 20 Gy doses (IC50 =15.9±2.3 Gy). This reduction in viability was significant at 20 Gy (p=0.006) (Figure 5.14A). In PC3, the decrease in viability was more subtle, with alginate spheres being 97.9±1.4% after a 2.5 Gy dose, 94.6±4.6% with 5 Gy, and 91.5±1.6% with 20 Gy (IC50 = 190.8±33.1 Gy). Despite the significance of the 20 Gy response, this is not biologically relevant, as the viability of NLS-AuNP-treated PC3 alginate spheres was still high (>90%) (Figure 5.14A). Following irradiation with 2.5, 5, and 20 Gy doses, NLS-AuNP-treated LNCaP alginate sphere cultures were 96.5±4.5%, 93.8±6.2%, and 79.6±20% viable (IC50 = 77.5±23.2 Gy). This reduction in viability was significant at 20 Gy (Figure 5.14A). When comparing the responses of NLS-AuNP treated alginate spheres with those of untreated cultures at the same radiation doses, it is possible to observe there were no significant differences in any of the cell lines studied (Figure 5.14B).

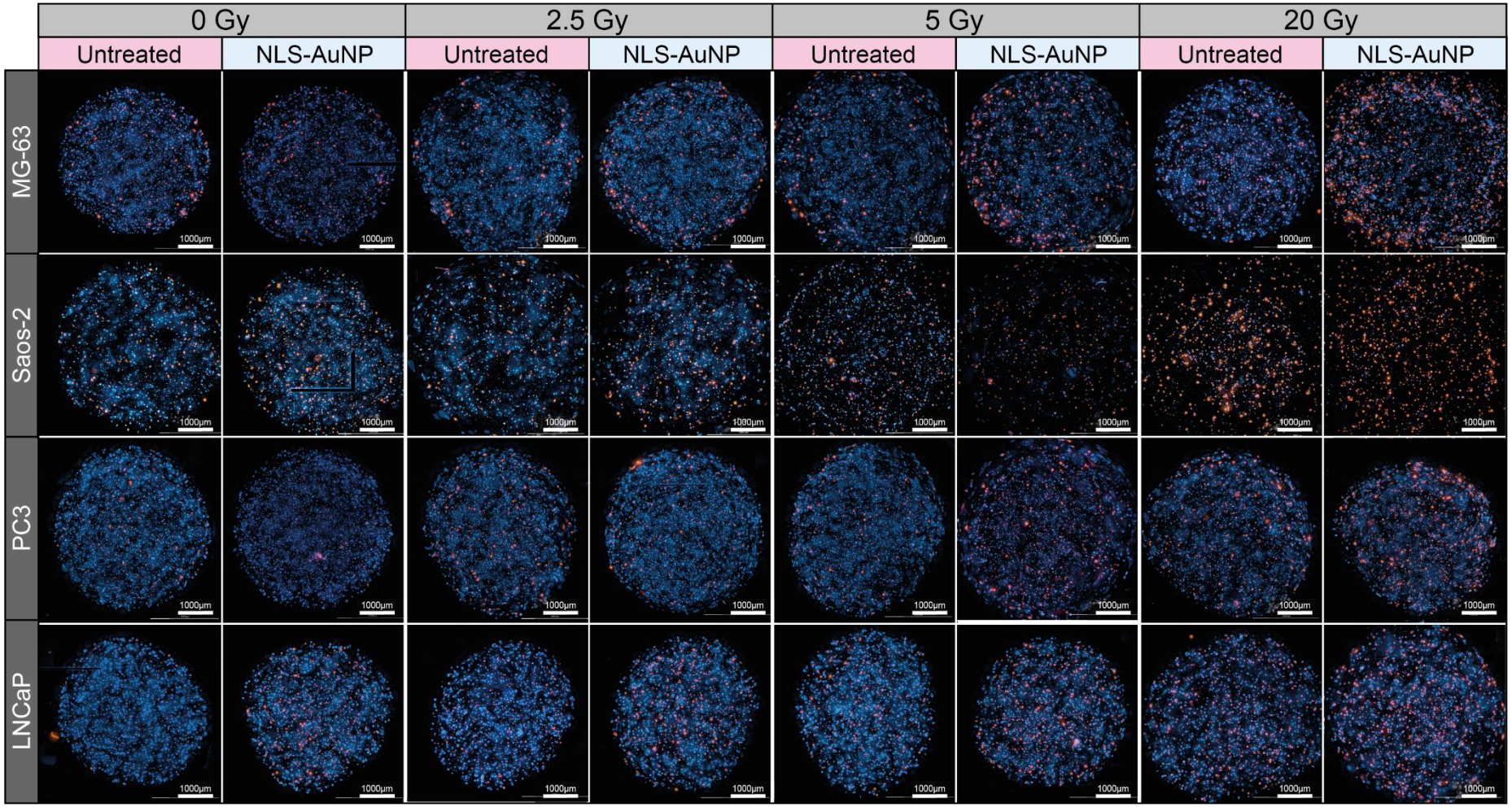

Figure 5.13 - Cell viability of human osteosarcoma and prostate cancer cell lines cultured in alginate spheres and treated with NLS-AuNPs, 24h post-irradiation. Colonies were stained with Hoechst 33342 (blue cells) and Propidium Iodide (red cells). Cytation 5 imaging system, 4x objective, Z-stack of DAPI and Texas Red channels. Scale bar represents 1000µm.

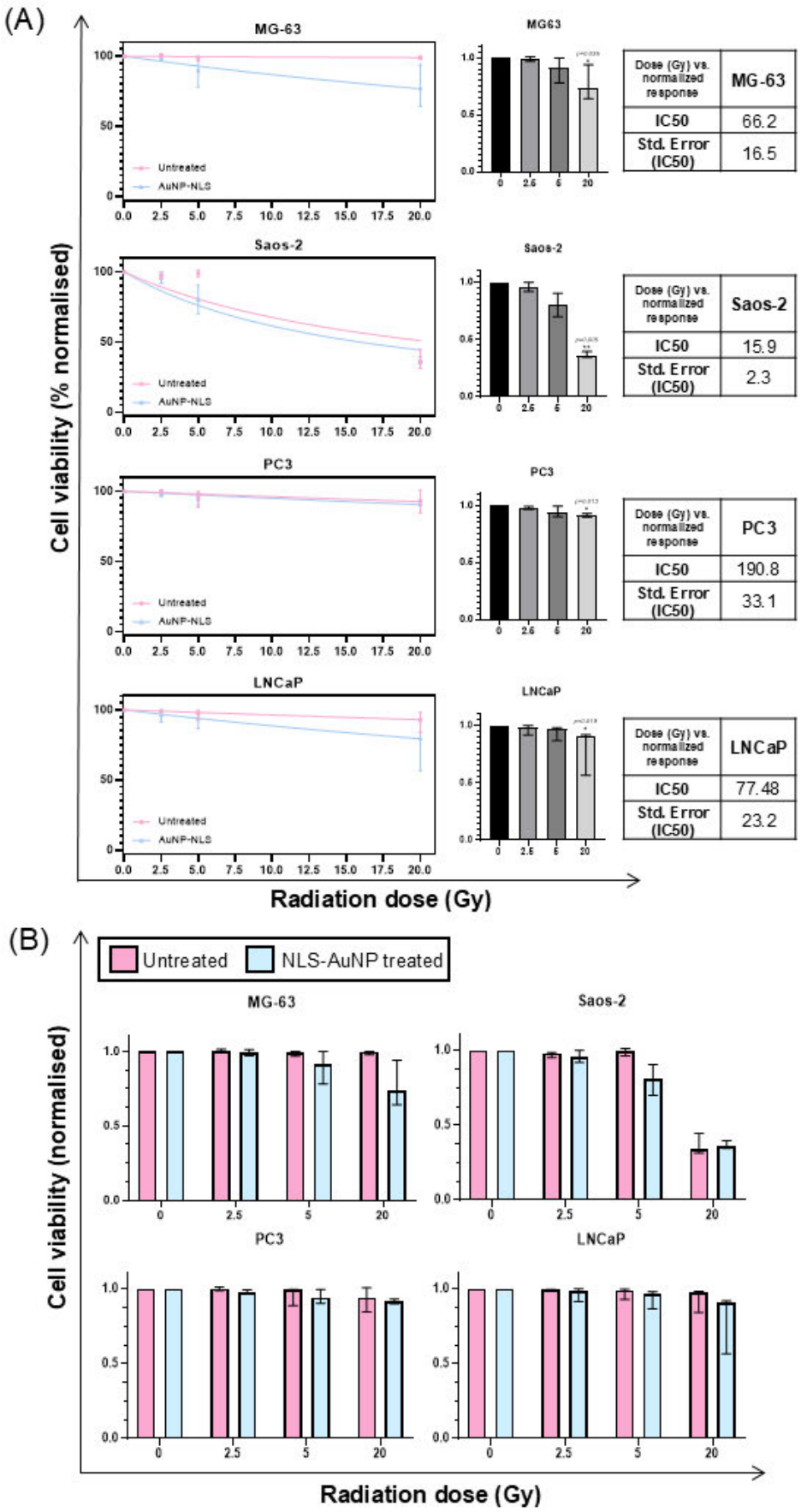

Figure 5.14 - Viability of cells grown in alginate spheres and treated with NLS-AuNPs 24h-post ionising radiation exposure. (A) Cell lines present a reduction in viability with increasing doses of radiation. Scatter plot and non-linear regression curve, percentage cell viability data is presented as median ±range,

individual values represent n=3 independent experiments with 3 technical repeats. Individually analysed responses of MG-63, Saos-2, PC3, and LNCaP show a significant reduction in viability at individual doses. Column bar graph, Kruskal-Wallis followed by Dunn's multiple comparisons test (*P<0.05). **(B)** Comparison between untreated and NLS-AuNP-treated alginate spheres of each cell line. Interleaved bars, multiple *t-tests*. Statistical significance corrected using the Holm-Sidak method of multiple comparisons, with alpha=0.05. (*P<0.05). All data is presented as median ±range and individual values represent n=3 independent experiments with 3 technical repeats. Untreated data has been presented in previous chapters.

5.2.8.1. Comparison of acute radio-responses between AuNP- and NLS-AuNP-treated alginate spheres.

To determine if there was a difference in the produced radio-sensitising effect between unmodified and nuclear-targeted gold nanoparticles, the cell viability of alginate spheres treated with each of the different AuNPs was compared for each radiation dose. Multiple *t-tests* followed by Holme-Sidak correction (α=0.05) revealed that PC3 cells grown in alginate are significantly more sensitive to a 20 Gy radiation dose when treated with unfunctionalised gold nanoparticles (*p*=0.006). For all other doses, the difference in response was not significant. In the remaining cell lines, there were no significant differences between the response of AuNP- and NLS-AuNP-treated cells, at any given dose (Figure 5.15).
0

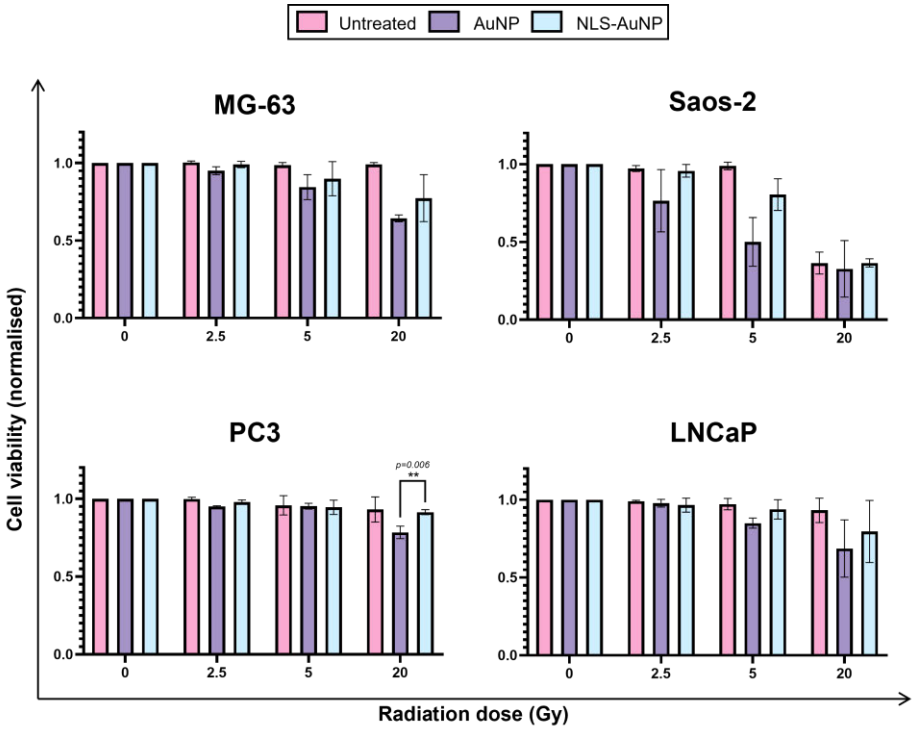

Figure 5.15 - Comparison of acute radio-responses between AuNP- and NLS-AuNP treated alginate spheres 24h post-irradiation. Only PC3 alginate spheres present a significant increase in sensitivity at 20 Gy when treated with

unmodified AuNPs. Interleaved bars, multiple *t-tests*. Statistical significance corrected using the Holme-Sidak method of multiple comparisons, with alpha=0.05. (*P<0.05). 3D data is presented as mean ±SD and individual values represent n=3 independent experiments with 3 technical repeats. Untreated samples included for baseline response reference. Untreated and AuNP-treated data has been presented in previous chapters.

5.2.9. Differences in cell cycle distribution between NLS-AuNP-treated and untreated cells in 2D and 3D.

Following treatment with NLS-tagged 50nm gold nanoparticles for 24h, monolayer cultures and both 3D models were exposed to a 5 Gy dose of ionising radiation. The cell cycle distribution of each of the treated cell lines was investigated by propidium iodide staining and flow cytometry analysis, as described in section 2.3.6. Due to time constraints, this analysis was only conducted once meaning that no descriptive statistics were performed.

5.2.9.1. Effect of NLS-AuNPs on cell cycle distribution of irradiated monolayer cultures.

Cell suspensions were prepared and analysed according to the method described in section 2.3.6.2. Following the gating of cell populations, detailed in section 3.2.8, results of cell cycle distribution revealed that after exposure to a 5 Gy dose the percentage of cells in G0/1 and S phases decreased for MG-63, Saos-2 and PC3 cell lines. Reversely, the percentage of cells in G2/M increased. In LNCaP cells, the percentage of cells in G0/1 increased, the S phase population decreased and the percentage of cells in G2/M remained the same (Figure 5.16A). Comparing the cell cycle distribution of untreated, AuNP-treated and NLS-AuNP-treated populations it is possible to observe that while the unmodified gold nanoparticles changed the way cells were dividing, cells treated with NLS-AuNPs have a similar distribution to untreated cells (Figure 5.16B).

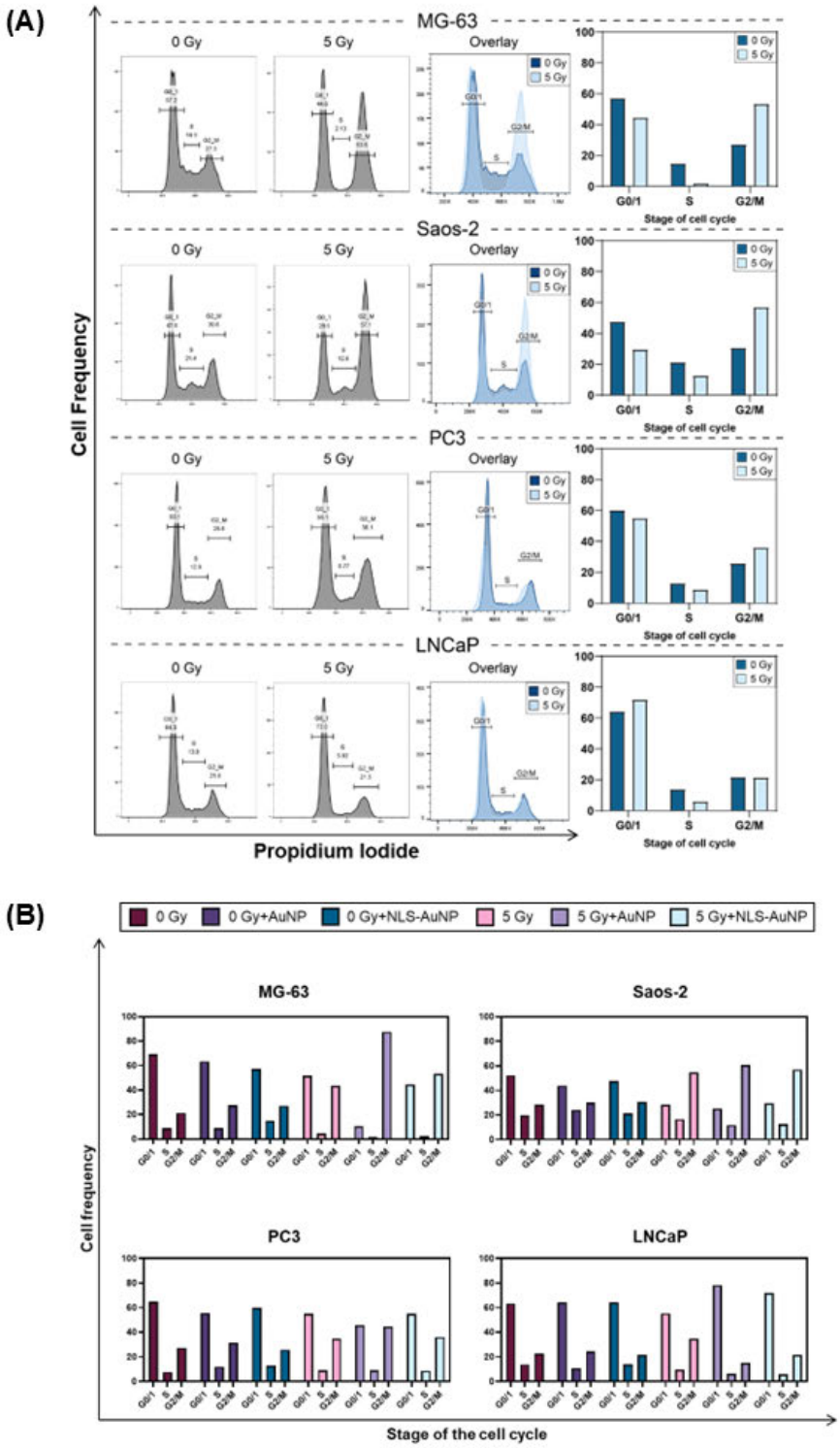

Figure 5.16 - Differences in cell cycle distribution of NLS-AuNP-treated cell lines cultured in 2D 24h following ionising radiation. (A) Cells were gated according to their DNA content (stained with PI), i.e. the stage of the cell cycle in which they were in 24h post-irradiation. Histograms of irradiated untreated and gold-treated populations were overlaid for visual representation of different distributions. The percentages of cells in each stage were plotted as interleaved bar graphs of n=1. **(B)** Comparison of cell cycle distribution between untreated, AuNP-treated and NLS-AuNP-treated cells cultured in 2D exposed to 5 Gy radiation. While the presence of AuNPs seem to enhance the effects of radiation, the distribution of NLS-AuNP treated populations is similar to the distribution of

untreated cells. Interleaved bars, n=1. Untreated and AuNP-treated data has been presented in previous chapters.

5.2.9.2. Effect of AuNPs and irradiation on cell cycle distribution in 3D cell models.

The cell cycle distributions of multicellular tumour spheroids and alginate spheres were also analysed. Due to time constraints only MG-63, Saos-2 and PC3 alginate spheres were tested.

5.2.9.2.1. Multicellular tumour spheroids.

Preliminary data shows that for MG-63 and LNCaP populations, the cell cycle distribution of NLS-AuNP treated cells is similar between unirradiated and irradiated cells. The percentage of Saos-2 cells in G0/1 and S phases decreased, accompanied by an increase in the G2/M population, however it is important to note that the number of 5 Gy-exposed gated cells was low and might not accurately represent the entire population. PC3 cells followed the same trend, albeit in a less pronounced manner (Figure 5.17A). When comparing the cell cycle distribution of NLS-AuNP-treated with AuNP-treated samples, it is possible to observe that NLS-AuNP-treated samples have a much similar distribution to untreated cells than AuNP-treated (Figure 5.17B).

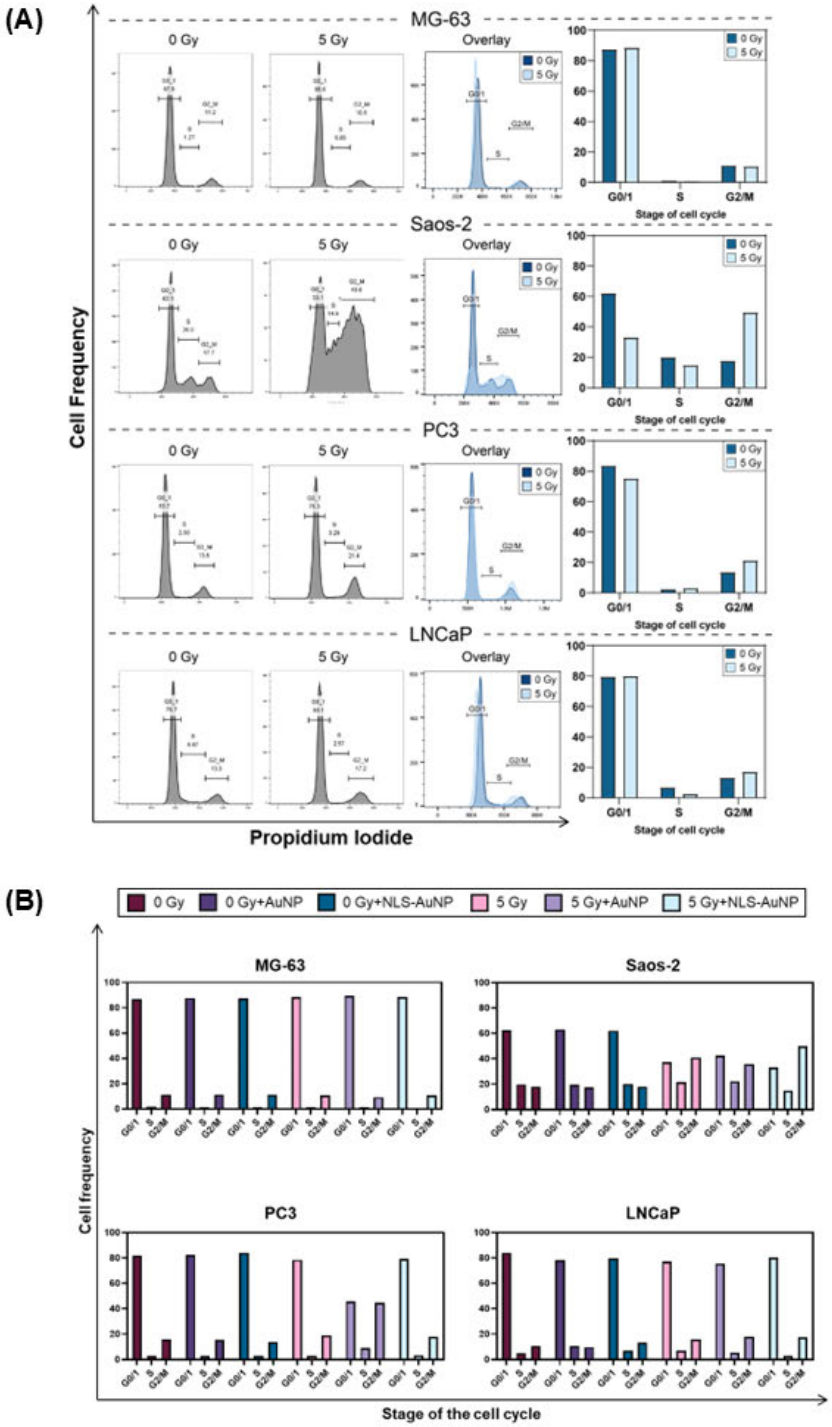

Figure 5.17 - Cell cycle distribution of NLS-AuNP-treated cell lines cultured in MCTS 24h following ionising radiation. (A) Single cell-suspensions of spheroids irradiated with 5 Gy were analysed 24h post-irradiation. Cells were gated according to the stage of the cell cycle in which they were in, and histograms of irradiated untreated and NLS-AuNP-treated populations were overlaid for visual representation of different distributions. The percentages of cells in each stage were plotted as interleaved bar graphs of n=1. **(B)** Comparison of cell cycle distribution between untreated, AuNP-treated and NLS-AuNP-treated spheroids exposed to 5 Gy radiation. While the presence of AuNPs seem to enhance the effects of radiation, the distribution of NLS-AuNP treated populations is similar to the distribution of untreated cells. Interleaved bars, n=1. Untreated and AuNP-treated data has been presented in previous chapters.

5.2.9.2.2. Alginate spheres.

In alginate spheres, MG-63 and PC3 populations did not suffer any pronounced alterations in cell cycle distribution after exposure to a 5 Gy radiation dose. In the Saos-2 population, the percentage of cells in G0/1 decreased along with an increase in the percentage of cells in G2/M (Figure 5.18A). Comparing both AuNP- and NLS-AuNP-treated populations, it is possible to observe that in MG-63 and PC3 populations, while the presence of unmodified gold nanoparticles seemed to return cell cycle distribution to pre-irradiation levels, the NLS-AuNP treatment seems to produce similar results to those seen on the radiation-exposed untreated sample. In Saos-2, since no AuNP-treated sample was analysed, this comparison is not possible. Nonetheless, regarding the NLS-AuNP treatment, it is possible to verify this produces similar outcomes to those of untreated alginate spheres following irradiation (Figure 5.18B).

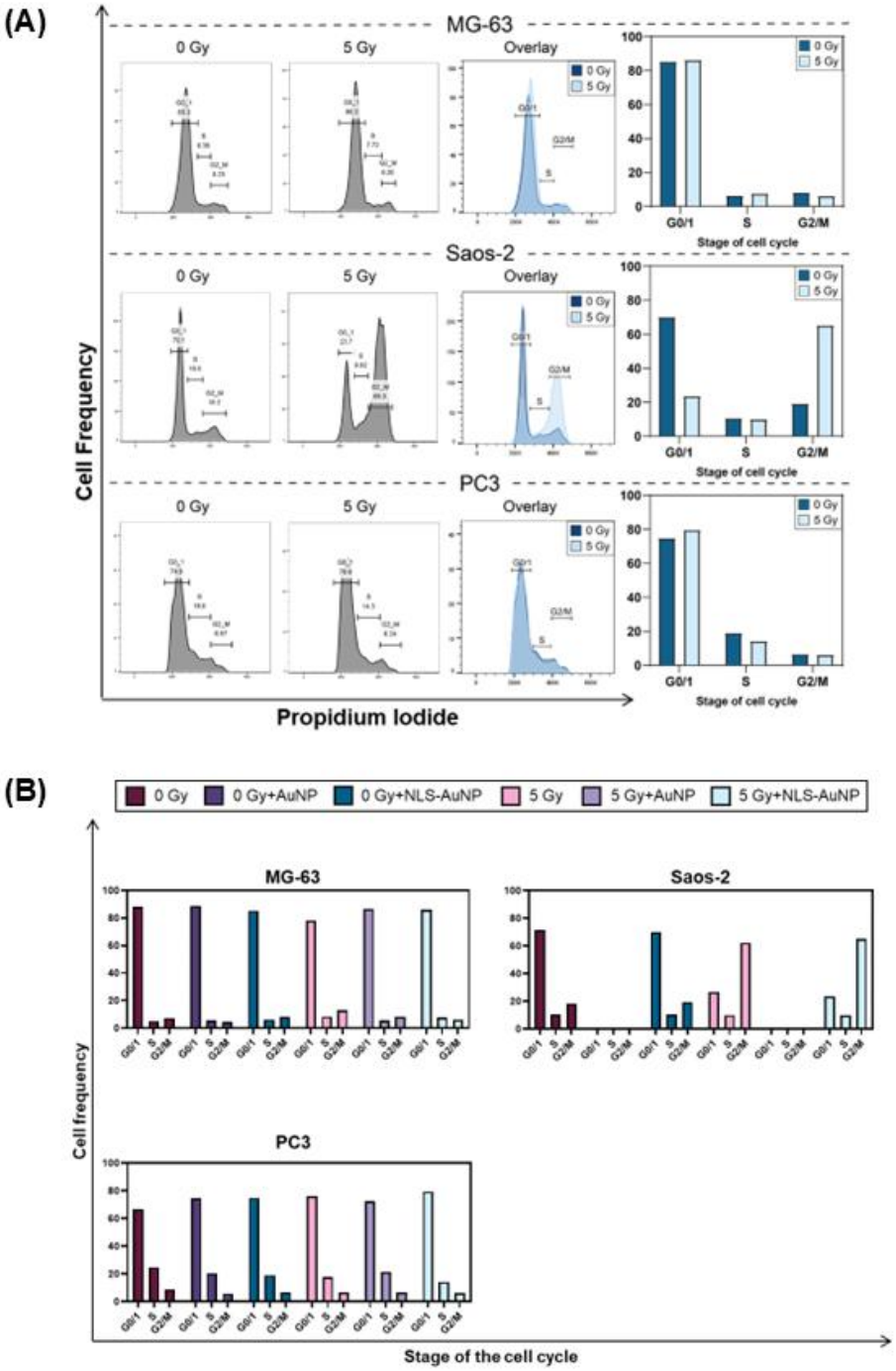

Figure 5.18 - Cell cycle distribution of NLS-AuNP-treated cell lines cultured in alginate spheres 24h following ionising radiation. (A) Cells were gated according to the intensity of the PI signal, i.e. the stage of the cell cycle in which they were in 24h post-irradiation. Histograms of irradiated untreated and gold-treated populations were overlaid for visual representation of different distributions. The percentages of cells in each stage were plotted as interleaved bar graphs of n=1. **(B)** Comparison of cell cycle distribution between untreated, AuNP-treated and NLS-AuNP-treated alginate spheres exposed to 5 Gy radiation. While the presence of AuNPs seem to enhance the effects of radiation, the distribution of NLS-AuNP treated populations is similar to the distribution of untreated cells. Interleaved bars, n=1. Untreated and AuNP-treated data has been presented in previous chapters.

5.2.10. Localisation of γ-H2AX foci in NLS-AuNP-treated samples following irradiation.

To investigate the levels of DNA damage induced by nuclear-targeted gold nanoparticles monolayer cultures were treated with NLS-AuNPs (10μg/mL, 24h) and exposed to a 5 Gy irradiation dose. The presence and location of γ-H2AX foci were investigated through immunofluorescence assays, using the method described in section 2.3.5.2. The resulting confocal images (Figure 5.19) were analysed using the Zeiss Zen 2.3 (blue edition) software (Carl Zeiss) by quantification of the number of H2AX foci per cell nucleus. The results were graphed as violin plots and compared to untreated samples of the same cell line using Kruskal-Wallis tests followed by Dunn's multiple comparisons (Figure 5.20A). To determine if the functionalisation of the nanoparticles produced a higher radio-sensitising effect, the results of NLS-AuNP-treated samples were also compared to those of AuNP treated cells, using Kruskal-Wallis tests followed by Dunn's multiple comparisons (Figure 5.20B).

Results showed that NLS-AuNP sensitise MG-63 cells to radiation, demonstrated by an increase in the average number of foci per cell - 1.5 vs. 0.9 in untreated cells exposed to the same radiation dose – and the total number of cells presenting foci – 44.3% in the untreated cell population vs. 54.6% of NLS-AuNP-treated cells. This difference is statistically significant (p<0.001) (Figure 5.20A). When comparing the responses AuNP- and NLS-AuNP treated MG-63 cells, it is possible to observe that after a 5 Gy radiation dose, the levels of DNA damage – represented by number of γ-H2AX foci – were higher in cells treated with unmodified gold nanoparticles (p<0.001) (Figure 5.20B). In Saos-2, the presence of nuclear-targeted gold nanoparticles did not affect the sensitivity of the cells to radiation. The average number of foci per cell in the untreated population was 2.5 vs. 2.6 in NLS-AuNP treated cells. The percentage of cells presenting foci decreased slightly for the NLS-AuNP treated population, with 68.7% of cells showing one or more foci, compared to 71.5% of untreated cells (Figure 5.20A). When comparing to the levels of DNA damage produced in AuNP-treated cells, it is possible to observe a significantly higher number of γ-H2AX foci in cells treated with unmodified gold nanoparticles (p<0.001) (Figure 5.20B). For PC3 cells, the response produced in NLS-AuNP-treated cells was reduced compared to untreated cells – 80.2% of untreated cells presented one or more γ-H2AX foci, with an average number of 3.5 foci per cell, while only 77.4% of NLS-AuNP-

treated cells were positive for γ-H2AX foci, with and average number of 2.8 foci per cell. However, this difference in DNA damage levels was not statistically significant (Figure 5.20A). When comparing the results to those of AuNP-treated cells, the difference in foci levels was not significant (Figure 5.20B). Finally, the effect of radiation was significantly higher in untreated LNCaP cells than in cells treated with nuclear-targeted gold nanoparticles (p<0.001), with treated cells showing an average of 1.4 foci per cell and 69% γ-H2AX-positive cells, compared to the 73.1% of untreated cells, with an average foci number of 2.8 (Figure 5.20A). Comparing this response to the one of AuNP-treated cells, once more the treatment with unfunctionalised gold nanoparticles proved more effective (p<0.001) (Figure 5.20B).

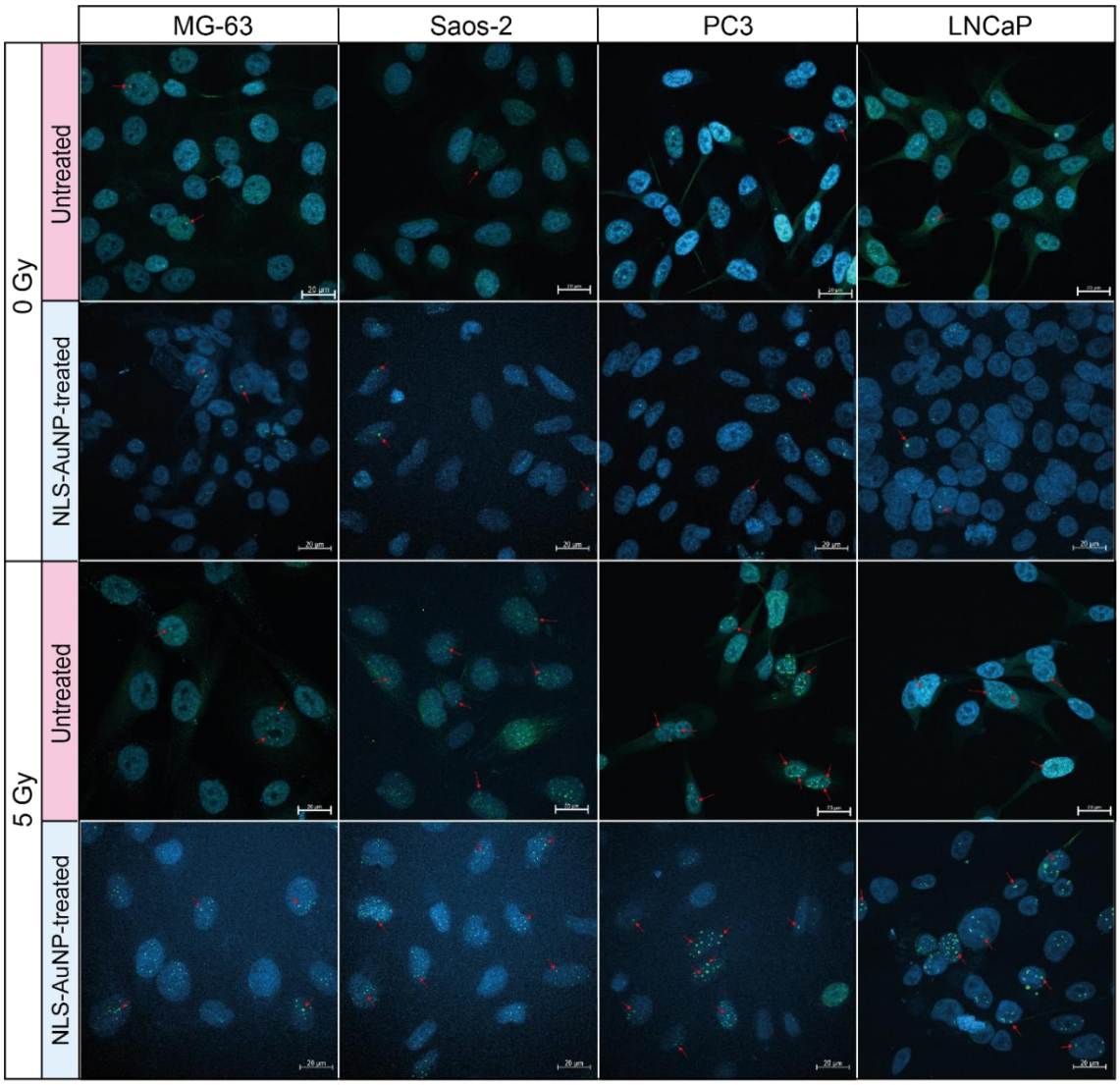

Figure 5.19 - Confocal images of γ-H2AX detection in NLS-AuNP-treated human osteosarcoma and prostate adenocarcinoma cell lines. Cells were stained with an anti-Human Histone H2AX [p Ser139] primary antibody, AlexaFluor™ 488 secondary antibody (green) and counterstained with DAPI (blue). Images show an increase in the number of H2AX foci (red arrows) in cells treated with 5Gy of ionising radiation, compared to untreated cells. Zeiss LSM 800 confocal microscope, 40x objective, Z-stack of DAPI and AF488 channels. Scale bar represents 20μm.

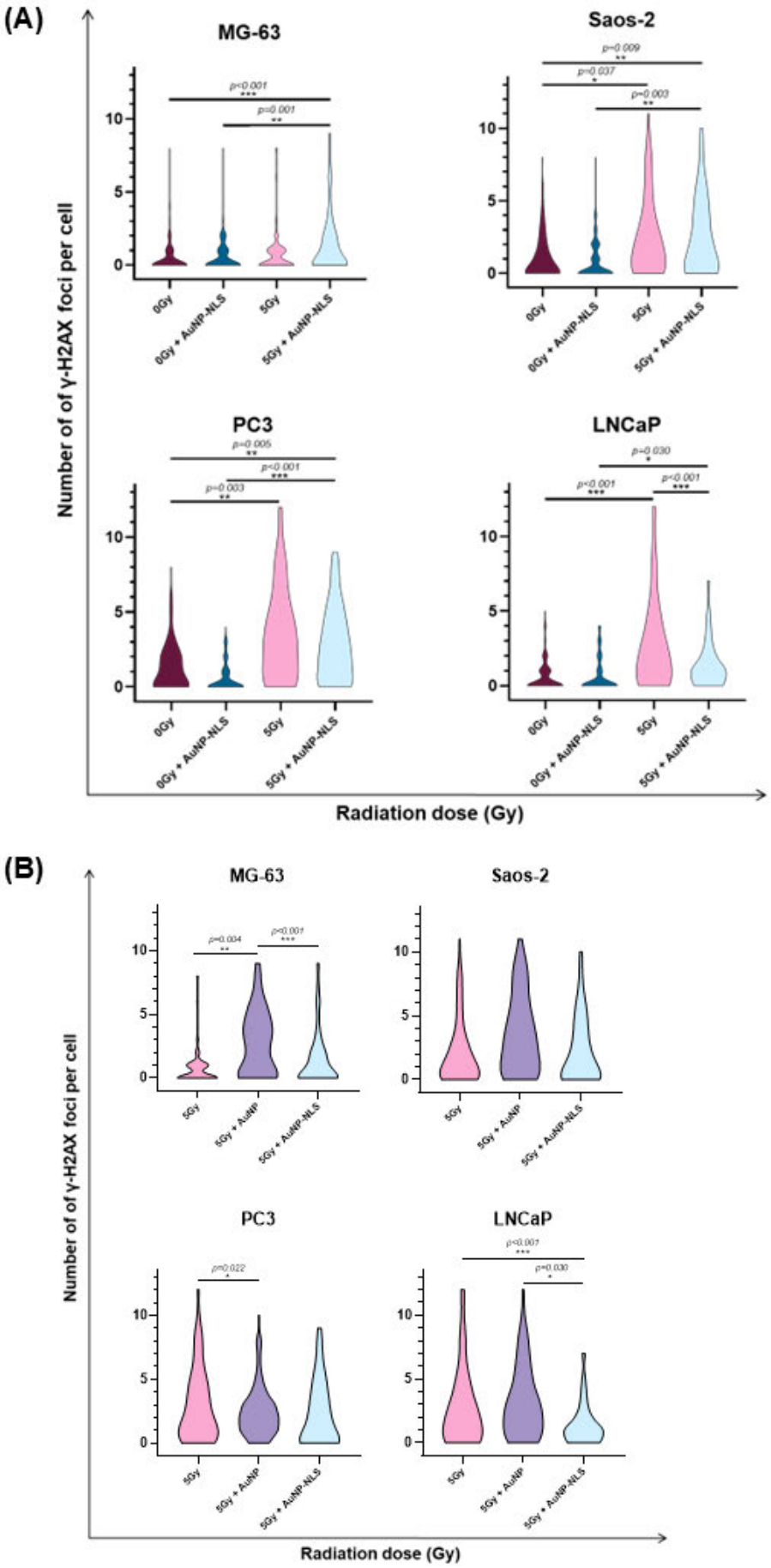

Figure 5.20 - Number of γ-H2AX foci in NLS-AuNP-treated cells 24h following ionising radiation. (A) All cell lines show an increase in DNA damage

following radiation, translated by an increased number of H2AX foci. When comparing NLS-AuNP-treated to untreated cells, there is a significant increase in the average number of foci in MG-63 cells. Violin plots, Kruskal-Wallis with Dunn's multiple comparisons. Statistical significance calculated as *p* value, with a confidence level of 95%. (*P<0.05), based on the means of 3 repeats **(B)** Comparison of H2AX foci between AuNP- and NLS-AuNP treated cells following ionising radiation**.** Apart from in PC3, unmodified gold-nanoparticle treatment produces higher levels of DNA damage than NLS-AuNP treatment. Violin plots, Kruskal-Wallis with Dunn's multiple comparisons. Statistical significance calculated as *p* value, with a confidence level of 95%. (*P<0.05) based on the means of 3 repeats. Untreated and AuNP-treated data has been presented in previous chapters.

5.2.11. TEM imaging of NLS-AuNPs and NLS-AuNP-treated cells.

To assess cellular uptake and intracellular localization of NLS-tagged gold nanoparticles, transmission electron microscopy (TEM) images were captured (Appendix H). The TEM work presented in this chapter was performed by Dr Christopher Hill at the University of Sheffield. Due to sample availability and time constraints, only PC3 monolayer cultures were imaged and used as a representative example. Results show that cells are not successfully internalising NLS-AuNPs.

5.3. Discussion

5.3.1. NLS-tagged gold nanoparticle uptake and localisation within 3D models

Following incubation with a 10µg/mL solution of 50nm NLS-AuNP, localisation of the nanoparticles in 3D models was assessed by LA-ICP-MS. Results showed that similarly to what happened with unfunctionalised gold nanoparticles both 3D models showed a successful uptake. In osteosarcoma spheroids, the majority of nanoparticles accumulated in the outer regions of the spheroid, with only low concentrations making it to the spheroid core. As detailed in the previous chapter, I speculate that is related to the density of OS spheroids, and how tightly they aggregate. As for prostate MCTS, NLS-AuNPs were evenly distributed throughout the entirety of PC3 spheroids; in LNCaP, even though ^{197}Au counts were high across the sample, the peak concentration was attained in the outer regions of the spheroid. This could be explained based on the fact that functionalising 50nm nanoparticles increases the overall size of the construct, making it more challenging for NLS-AuNP to efficiently penetrate the spheroid (Egorova et al., 2020). Additionally, even though LNCaP spheroids are more loosely aggregated than MG-63 or Saos-2, they form denser spheroids than PC3, which could also explain the difference in gold distribution between the two (Grayson et al., 2021).

As for alginate spheres, the results were once again similar to those observed in the previous chapter: despite all cell lines showing uptake of NLS-AuNPs, the ^{197}Au counts were much lower than those observed in MCTS. As previously described, this could be due to the alginate matrix itself entrapping some of the nanoparticles.

5.3.2. Cell internalisation of NLS-tagged gold nanoparticles

Considering the unexpected results of this study, i.e. NLS-tagged gold nanoparticles did not produce a higher radio-sensitising effect than uncoated AuNPs, TEM studies were conducted to investigate the functionalisation of the nanoparticles was successful in enabling their nuclear delivery. Results showed that, unlike naked nanoparticles, NLS-AuNPs did not become internalised by the cell. These results were unexpected, considering the multiple reports of cellular uptake and internalisation of PEGylated NLS-AuNPs (Ali et al., 2017; Drescher et al., 2021; Mackey et al., 2013; Nativo et al., 2008; Özçelik & Pratx, 2020; Xie

et al., 2009). One possible explanation could be the lack of additional functionalisation with a cell penetrating peptide: most studies using nuclear targeted gold nanoparticles utilise a combined functionalisation of NLS and RGD to achieve nuclear delivery. However, in the previously mentioned study by Özçelik and Pratx (2020), the uptake of both RGD-NLS-AuNP and NLS-AuNP was investigated, and the results demonstrated that even though RGD-NLS-AuNP show the maximum uptake rate by A549 cells, NLS-AuNP are still successfully internalised and directed to the cell nucleus (Özçelik & Pratx, 2020). Another factor to consider is the hydrodynamic diameter of the nanoparticle construct and clustering. While the core nanoparticles were the same size as the undecorated ones used in the previous chapter, which cells successfully internalised, the addition of a PEG coating, NLS functionalisation and the tagging of FITC molecules – which were added in an attempt to track the intracellular localisation of NLS-AuNPs – might have increased the overall size of the construct, therefore hindering endocytosis. It has been previously described in a study by Lee et al. (2013) that the main route for 20-100nm AuNP uptake is caveolae-mediated endocytosis, by co-localization of caveolin-1 proteins over internalised nanoparticles found in the caveolae and caveosomes. Furthermore, the group further confirmed this by treating HeLa cells with genistein, an inhibitor of caveolae-mediated endocytosis, in which the uptake of AuNPs significantly decreased (Lee et al., 2013). A study that supports the hypothesis that the overall size of the FITC-NLS-PEG-AuNP nano-construct could be deterring cellular internalisation was led by Noël (2016) – the group showed that while 20nm uncoated AuNPs were able to be internalised by neutrophils, in cytosolic vacuoles, most 70nm AuNPs could not get past the cell membrane (Noël et al., 2016). Therefore, it could possible the functionalisation of the nanoparticles could be increasing the total diameter of the nano-construct, impeding cellular uptake. However, TEM imaging of NLS-AuNP seem to indicate the size of the construct did not change.

In addition to size, surface charge (zeta potential) is another factor that can influence nanoparticle uptake. PEGgylation and NLS functionalisation can alter the surface charge of AuNPs, often resulting in a more neutral or slightly negative zeta potential (El-Baz et al., 2022). This reduction in surface charge may decrease electrostatic interactions with the negatively charged cell membrane,

reducing cellular uptake efficiency. In contrast, uncoated AuNPs typically exhibit a positive surface charge, which may facilitate stronger interactions with the cell membrane and promote internalisation (El-Baz et al., 2022).

5.3.3. Effects of NLS-tagged gold nanoparticles in 2D cell cultures following radiation exposure.

Following treatment and incubation with NLS-AuNP, monolayer cultures were irradiated with doses ranging from 1.25 to 5 Gy their viability was assessed 10 days-post treatment through clonogenic assays. Results showed that albeit producing a minor radio-sensitising effect in Saos-2, PC3 and LNCaP cells, the reduction in the surviving fraction of NLS-AuNP-treated cells was not statistically significant when compared to the response of untreated cells at the same radiation doses. By comparing these results with those obtained from clonogenic assays of cells treated with non-functionalised AuNPs, it is possible to observe that uncoated AuNPs produce a higher radio-sensitising effect than NLS-AuNPs. Had the NLS-tagged nanoparticles successfully internalised the cells, these results would seem counterintuitive. However, due to the lack of intracellular AuNPs it is possible to infer the lack of radio-sensitisation is due to the short-range energy deposition of the Auger electrons produced during the ionisation of the gold nanoparticles.

5.3.4. Effects NLS-AuNPs in three-dimensional models following radiation exposure.

The responses to radiation of cells cultured in alginate spheres were measured acutely, using a H/PI stain 24h post-irradiation; prolonged effects were determined by measuring the diameter of colonies 7-days post-irradiation. Results showed that 24h-post irradiation, there is no significant difference between the responses of untreated and NLS-AuNP-treated cells. However, when measuring colony diameter 7-days post-irradiation, it is possible to observe that average diameter of NLS-AuNP-treated colonies is larger than both untreated and AuNP-treated colonies. Considering the outcome of these experiments, the TEM imaging results, that demonstrated the NLS-AuNP are not internalising the cells, and the LA-ICP-MS data, that showed that the counts of ^{197}Au were reduced in alginate sphere samples compared to MCTS, it is possible to infer that the NLS-tagged gold nanoparticles are being sequestered in the alginate matrix, as discussed in previous chapters. Considering the high cross-

section of gold nanoparticles compared to cells, i.e. AuNPs have a higher probability of interacting with radiation, it is possible to infer the NLS-AuNPs outside the cells are preferentially absorbing the radiation, reducing the ionisation of the colonies inside the alginate matrix. Furthermore, due to the peptide functionalisation of these nanoparticles, it is also possible that NLS peptides, being positively charged, are interacting with and neutralising secondary electrons emitted from the irradiated AuNPs. Moreover, it has been shown that peptides have radical scavenging capabilities, meaning the NLS peptide could also be neutralising the free hydroxyl radicals produce during water radiolysis (Guo et al., 2020; Liu et al., 2021; Shah et al., 2015). This effect reduces the likelihood of secondary electron- and radical-induced ionisation of nearby cells, further shielding them from radiation damage.

In multicellular tumour spheroids, NLS-AuNP produced an acute radio-sensitising effect in MG-63 and Saos-2 cells. LA-ICP-MSI data showed high concentrations of NLS-tagged gold nanoparticles in the outer ring of the spheroids, composed by viable, proliferating cells, as opposed to the core, containing mostly hypoxic cells (Flint et al., 2021). Moreover, the previously mentioned Noël et al. (2016) study demonstrated that 70nm nanoparticles can be 'trapped' in the cell membrane (Noël et al., 2016). Taking this into consideration, it is possible to infer that while NLS-AuNPs are not internalised, they could be located in the cell membrane or in the interstitial space, in close proximity to the cells. Since OS cells aggregate tightly, forming dense spheroids, it is likely that the accumulation of NLS-AuNPs within the viable areas of the MCTS is causing a chain-reaction effect, i.e. γ-rays ionise NLS-AuNPs, causing Auger cascades. The secondary electrons produced react with water creating ROS and more low energy electrons, which will react with water again, amplifying this reaction (Chen et al., 2020). This could mean that even though nuclear localisation of the nanoparticles was ineffective, this chain-reaction could be disrupting the cell membranes, ultimately leading to apoptosis.

5.3.5. Cell cycle distribution of AuNP-treated cells following radiation exposure.

Following irradiation with a 5 Gy dose, NLS-AuNP-treated monolayer, alginate sphere, and MCTS cultures were stained with PI to assess cell distribution in the different stages of the cell cycle. Due to time constraints, this experiment was

only carried out once, making statistical analysis impossible. Preliminary data showed that compared to untreated cells, there were minimal observable differences in NLA-AuNP treated cells. Considering these data sets, a higher sample size would be necessary for a more robust analysis.

5.3.6. Localisation of γ-H2AX foci in NLS-AuNP treated cells.

Following radiation exposure, cells treated with NLS-AuNP were stained with an anti-human γ-H2AX antibody. Immunofluorescence results showed that while NLS-AuNP treatment increased the number of γ-H2AX foci in MG-63 cells, when compared to untreated cells irradiated with the same dose, this did not have an impact on the overall cell survival and proliferation of these cells, as demonstrated by the results of the clonogenic assays. Considering the results, it is possible to infer that these cells either died, allowing for the proliferation of resistant cells; they were able to repair the damage and continue proliferating; or continued to proliferate with unrepaired sub-lethal damage. As expected, there was a significant difference in the number of γ-H2AX foci of NLS-AuNP treated cells when compared to that of cells treated with undecorated AuNPs, which showed significantly higher levels of γ-H2AX.

5.4. Conclusion

Considering the results of this chapter, due to the lack of cellular uptake of NLS-tagged gold nanoparticles it is challenging to come to solid conclusions, as more studies would be required to confirm the hypothesis proposed. To overcome the internalisation issues, further work would be required, either by using smaller gold nanoparticle cores – for instance, 20nm – to prevent issues with hydrodynamic diameter, and/or by combined functionalisation of NLS with cell-penetrating peptides, improving the chances of internalisation.

Below is a summary table of the results obtained from treatment with undecorated and NLS-tagged gold nanoparticles (Table 5.1).

Table 5.1 - Summary of 50 nm AuNP-induced effects on radiosensitivity of cells cultured in 2D and 3D models.

				Compared to 0 Gy	Compared to RT only	
Cell line	2D/3D	Assay		RT	RT+ AuNP	RT+NLS-AuNP
MG-63	2D	Clonogenic assay		↓ (*p<0.001*)	↓ (*p=0.044*) -DEF=3.4	↑ (ns)
		Cell cycle	% G0/1	↓ (ns)	↓ (n=1)	↓ (n=1)
			% S	↓ (ns)	↓ (n=1)	= (n=1)
			% G2/M	↑ (*p=0.037*)	↑ (n=1)	↑ (n=1)
		γ-H2AX foci/cell		↑ (*p=0.003*)	↑ (*p<0.001*)	↑ (*p=0.004*)
	Alginate spheres	Colony diameter		↓ (*p=0.006*)	↑ (*ns*)	↑ (*p=0.007*)
		Acute viability		=	↓ (*p<0.001*)	↓ (*ns*)
		Cell cycle	% G0/1	↓ (n=1)	↑ (n=1)	↑ (n=1)
			% S	↓ (n=1)	= (n=1)	= (n=1)
			% G2/M	↑ (n=1)	↓ (n=1)	↓ (n=1)
	MCTS	Acute viability		=	↓ (*p=0.005*)	↓ (*p<0.001*)
		Cell cycle	% G0/1	= (n=1)	= (n=1)	= (n=1)
			% S	= (n=1)	= (n=1)	= (n=1)
			% G2/M	= (n=1)	= (n=1)	= (n=1)
Saos-2	2D	Clonogenic assay		↓ (*p<0.001*)	↓ (ns) DEF=2.6	↓ (*ns*) DEF = 1.3
		Cell cycle	% G0/1	↓ (*p<0.001*)	↓ (n=1)	= (n=1)
			% S	=	↓ (n=1)	= (n=1)
			% G2/M	↑ (*p<0.001*)	↑ (n=1)	= (n=1)
		γ-H2AX foci/cell		↑ (*p<0.001*)	↑ (*p<0.001*)	=
	Alginate spheres	Colony diameter		↓ (*p=0.009*)	↑ (*ns*)	↑ (*p=0.015*)
		Acute viability		↓ (*p=0.010*)	↓ (*p=0.007*)	↓ (*ns*)
		Cell cycle	% G0/1	↓ (n=1)		= (n=1)
			% S	= (n=1)		= (n=1)
			% G2/M	↑ (n=1)		= (n=1)
	MCTS	Acute viability		=	↓ (*p<0.001*)	↓ (*p=0.007*)

		Cell cycle	% G0/1	↓ (n=1)	↑ (n=1)	↓ (n=1)
			% S	= (n=1)	↓ (n=1)	↓ (n=1)
			% G2/M	↑ (n=1)	↓ (n=1)	↑ (n=1)
PC3	2D	Clonogenic assay		↓ (*p<0.001*)	↓ (ns) DEF=1.7	↓ (*ns*) DEF = 1.2
		Cell cycle	% G0/1	↓ (*p<0.001*)	↓ (n=1)	= (n=1)
			% S	=	↓ (n=1)	= (n=1)
			% G2/M	↑ (*p<0.001*)	↑ (n=1)	= (n=1)
		γ-H2AX foci/cell		↑ (*p<0.001*)	↓ (ns)	↓ (ns)
	Alginate spheres	Colony diameter		↓ (*p=0.006*)	=	↑ (*p=0.003*)
		Acute viability		=	=	=
		Cell cycle	% G0/1	↑ (n=1)	↓ (n=1)	= (n=1)
			% S	↓ (n=1)	↑ (n=1)	↓ (n=1)
			% G2/M	= (n=1)	= (n=1)	= (n=1)
	MCTS	Acute viability		=	=	=
		Cell cycle	% G0/1	= (n=1)	↓ (n=1)	= (n=1)
			% S	= (n=1)	↑ (n=1)	= (n=1)
			% G2/M	= (n=1)	↑ (n=1)	= (n=1)
LNCaP	2D	Clonogenic assay		↓ (*p<0.001*)	↓ (ns) DEF=1.8	↓ (*ns*) DEF = 1.2
		Cell cycle	% G0/1	↓ (*ns*)	↑ (n=1)	↑ (n=1)
			% S	=	↓ (n=1)	= (n=1)
			% G2/M	↑ (*ns*)	↓ (n=1)	↓ (n=1)
		γ-H2AX foci/cell		↑ (*p<0.001*)	↑ (*ns*)	↓ (*p<0.001*)
	Alginate spheres	Colony diameter		↓ (*p=0.006*)	↓ (ns) DEF=1.7	↑ (*p=0.012*)
		Acute viability		=	=	=
		Cell cycle	% G0/1			
			% S			
			% G2/M			
	MCTS	Acute viability		=	=	=
			% G0/1	↓ (n=1)	= (n=1)	= (n=1)

		Cell cycle	% S	= (n=1)	= (n=1)	↓ (n=1)
			% G2/M	↑ (n=1)	↑ (n=1)	= (n=1)

Chapter 6. Investigating the radio-sensitising potential of mitochondrial-targeted gold nanoparticles in 2D and 3D cell models

6.1. Introduction

Targeting the mitochondria in the context of cancer therapeutics has been an area of increasing interest due to their central role in bioenergetics and apoptosis signalling (Oladimeji et al., 2021). Known as “the powerhouse of the cell”, mitochondria are double-membrane intracellular organelles responsible for most of the cell’s energy production, in the form of ATP, through oxidative phosphorylation (OXPHOS). The OXPHOS metabolic pathway generates ATP by transporting electrons through protein complexes in the inner membrane of the mitochondria, known as the Electron Transport Chain (ETC). Glucose metabolism, which takes place in the cytosol, leads to the production of pyruvate, that enters the mitochondria and is converted to acetyl-CoA. Both glycolysis and pyruvate oxidation lead to the production of NADH. Acetyl-CoA fuels the series of reactions of the Krebs cycle (or citric acid cycle), which produces 6 NADH, 2 $FADH_2$ and 2 ATP molecules. OXPHOS is the final step of cellular respiration, and it utilises the NADH and $FADH_2$ molecules produced in the previous steps to transfer electrons through the ETC, creating a proton gradient in the intermembrane space, which generates an electrical and chemical gradient. This gradient forces the translocation of protons from the intermembrane space back into the mitochondrial matrix through the ATP synthase, which catalyses the conversion of ADP to ATP (Liu et al., 2023).

As previously mentioned, deregulating cellular metabolism is one of the hallmarks of cancer – some cancer cells prefer glycolysis over mitochondrial OXPHOS (Warburg effect) – but the mitochondria participate in several other metabolic pathways, such as apoptosis and redox/calcium homeostasis, glucose metabolism, fatty acid β-oxidation, and amino acid metabolism, all of which are important for cancer progression (Wang et al., 2023). Moreover, one of the byproducts of OXPHOS are reactive oxygen species, which as discussed earlier, can lead to DNA damage and apoptosis. However, controlled ROS production can stimulate growth factors, including the vascular endothelial growth factor (VEGF) and HIF-1α transcription factors which stimulate tumour cell metastasis

and cancer progression (Singh & Manna, 2022). Additionally, mitochondria possess their own DNA (mtDNA) which encodes for the subunits of the ETC and ATP synthase and does not possess efficient DNA repair mechanisms. Mutations in mtDNA have been detected in multiple cancers since they can lead to oncogenic transformation and promote tumour progression (Klein et al., 2020). Furthermore, to support cancer cell survival under harsh tumorigenic conditions, such as nutrient depletion and hypoxia, mitochondria can up- or down-regulate several pathways to adapt to these circumstances (Jeena et al., 2019). Therefore, mitochondrial targeted therapeutics are an emerging area, including in the nanomedicine and radiobiology fields (Oladimeji et al., 2021). The use of mitochondrial targeted drugs has been widely investigated, using multiple strategies with different outcomes. For instance, mitochondrial function can be disrupted through the inhibition of the ETC, with drugs including metformin and tamoxifen, which indirectly induce production and accumulation of ROS (Dong et al., 2020). In recent years, nanomedicine has provided novel strategies to enhance the delivery of mitochondrial-target drugs, as demonstrated in a study by Oladimeji et al. (2021) that used gold nanoparticles to deliver Betulinic Acid – which induces membrane permeability transition, ultimately leading to apoptosis – to the mitochondria of MCF-7 breast cancer cells (Oladimeji et al., 2021). Additionally, Gallud et al. (2019) have demonstrated that functionalisation of gold nanoparticles with alkyl ammonium bromide leads to mitochondrial dysfunction and cell death (Gallud et al., 2019). In the context of radiobiology, the use of mitochondrial-target gold nanoparticles to enhance radiosensitivity has been gaining interest. Several studies have now shown that ROS imbalance can disrupt mitochondrial membranes, leading to the release of cytochrome *c*, thus promoting apoptosis. Therefore, localising gold nanoparticles in the mitochondria can enhance *in situ* ROS production upon radiation exposure (Fang et al., 2017; Li et al., 2018; Zhao et al., 2022). Furthermore, targeting nanoparticles to the mitochondria can be a potential mechanism to address radio-resistance. Since it does not solely rely on the enhancement of radiation-induced DNA damage, but instead forces the cancer cells to undergo apoptosis, this approach guarantees that even cells that evade normal mechanisms of DNA damage response, continuing to proliferate regardless of damage, are effectively killed (Li et al., 2018). Table 6.1 summarises recent advances in mitochondrial-targeted AuNP use for radio-sensitisation.

Table 6.1 - Summary of published literature regarding the use of mitochondrial targeted AuNPs as radiosensitisers.

[1] CCYKFR – peptide synthesised by the Fang group to target the mitochondria. No further information was provided.

Research Group	Cell line(s)	Culture method		Nanoparticle size (concentration)	Ligand	Radiation dose	Results
		2D	3D				
Fang et al. (2017)	MCF-7 (human breast adenocarcinoma)	✓		3 nm (40 μg/mL)	CCYKFR [1]	2, 4, 6, and 8 Gy	CCYKFR-AuNP induce radiosensitisation in MCF-7 cells. At a 4 Gy dose AuNPs a significant enhancement of mitochondrial ROS was observed, correlated with severe DNA damage and cell death.
Li et al. (2018)	MCF-7 (human breast adenocarcinoma)	✓	✓ (xenograft)	≈ 18 nm (concentration not stated)	TPP	4 Gy	*In vitro* TPP-AuNP treatment produced high levels of ROS in the mitochondria of irradiated cells resulting in irreversible apoptosis. *In vivo* TPP-AuNP treatment significantly suppressed the irradiated tumour.
Zhao et al. (2022)	4T1 (mouse breast tumour) and 3T3 (mouse fibroblast)	✓		≈ 20 nm (50 μg/mL)	TPP	6 Gy	TPP-AuNP treatment enhances radio-sensitisation of cancer cells and leads to a significant reduction in ATP.

The most common ligand used for mitochondrial targeting is Triphenylphosphine (TPP), a lipophilic cation that accumulates in the mitochondria due to negative membrane potential, which arises due to the constant translocation of protons out of the mitochondrial matrix. Lipophilic cations are attracted to the negative energy potentials of the lipid bilayer because their positive charge is delocalised over a large surface area, meaning the activation energy required for internalisation is lowered. Because the cytoplasmic membrane also has negative potential, TPP is naturally internalised by the cell, and further accumulates in the mitochondria. The use of TPP as a ligand has many advantages, such as easy synthesis and conjugation with gold nanoparticles and high mitochondrial specificity (Chen, 2014).

6.1.1. Aims of this chapter

To test the hypothesis that targeting gold nanoparticles to the mitochondria will result in mitochondrial disruption and, therefore, higher levels of apoptosis, the aim of this chapter was to determine the radio-sensitising potential of TPP-tagged gold nanoparticles in human osteosarcoma and prostate adenocarcinoma cell lines cultured in monolayer and 3D cell culture models. To achieve this, the different models were treated with TPP-functionalised 5nm gold nanoparticles using the same concentration and method described in the previous chapter. Penetration of the nanoparticles and their distribution in spheroids and alginate spheres was assessed using LA-ICP-MSI, and electron microscopy. TPP-AuNP-containing samples were irradiated with doses up to 20 Gy. Following treatment, cell viability was determined by the methods previously described for both 2D and 3D models. The presence of γ-H2AX foci and cell cycle distribution were also evaluated in 2D via immunofluorescence and flow cytometry analysis, respectively.

6.2. Results

6.2.1. Uptake of mitochondrial-targeted gold nanoparticles by 2D and 3D cell models.

Prior to irradiation, monolayer, multi-cellular tumour spheroid and alginate cultures were treated with 5nm TPP-AuNP and their uptake was evaluated using LA-ICP-MS.

6.2.1.1. LA-ICP-MSI of 3D cell models

To determine the uptake and localization of mitochondrial-targeted gold nanoparticles in cells cultured within MCTS and alginate spheres, sections of both 3D models were analysed using LA-ICP-MS and compared to untreated controls (Appendix A) to ensure specificity of results. The ICP-MS data was plotted as intensity vs. time graphs, using GraphPad Prism, and spectral images were generated to map the localization of each isotope within the samples. To map out the localisation of the isotope of interest (^{197}Au), ^{66}Zn, ^{25}Mg isotopes were also analysed to serve as a cellular control.

6.2.1.1.1. Multicellular Tumour Spheroid

Results show that when cultured in MCTS, all cell lines are able to uptake TPP-AuNPs. In MG-63 and LNCaP cell lines, most of the functionalised gold nanoparticles accumulated in the outer rings of the spheroid (Appendix F and Figure 6.1, respectively). In Saos-2, TPP-AuNPs tended to accumulate in the same side of the spheroid (Appendix F), and for PC3 MCTS, TPP-AuNPs were uniformly distributed through the spheroid (Figure 6.2).

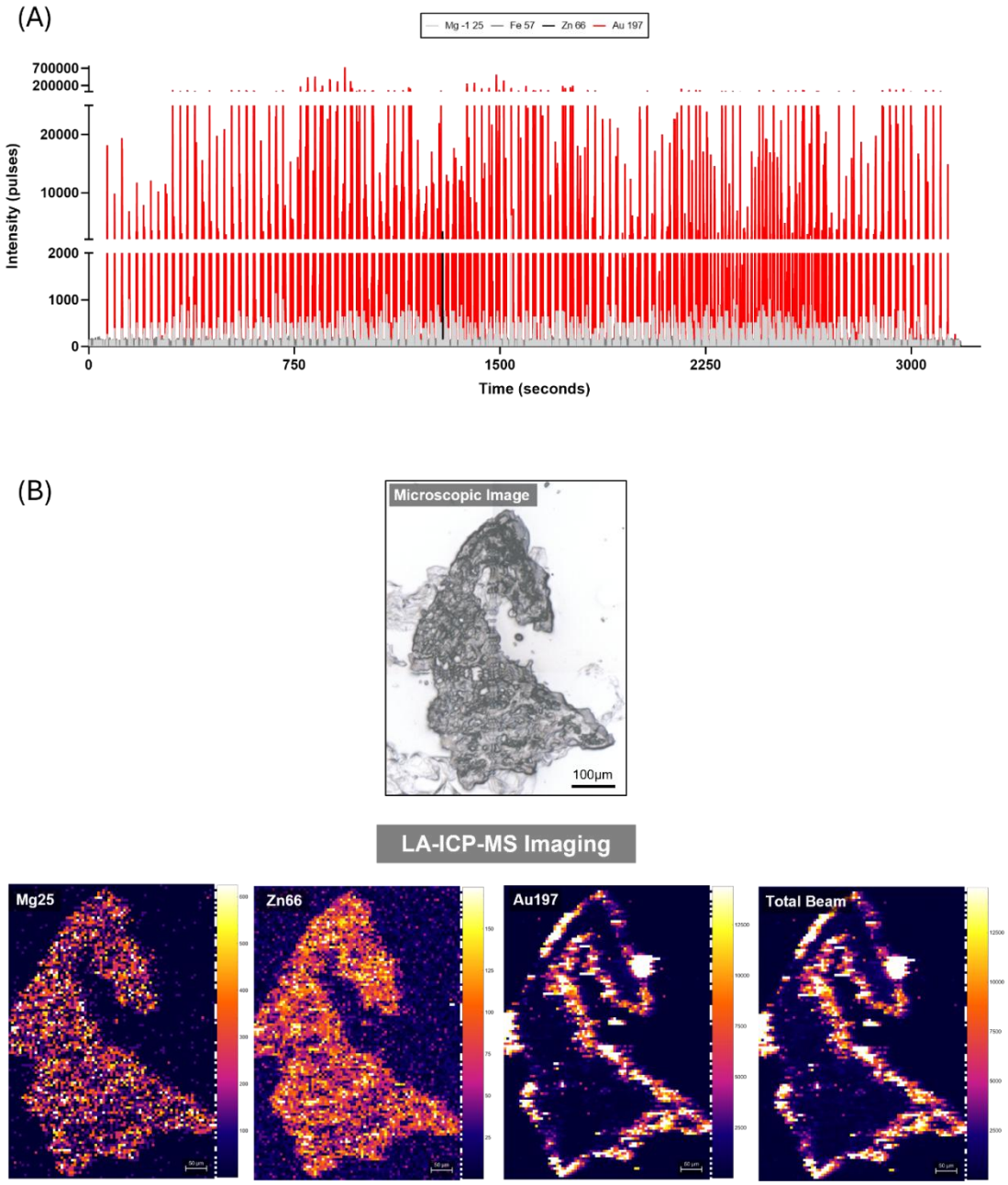

Figure 6.1 - LA-ICP-MS detection and localization of TPP-tagged gold nanoparticles in LNCaP MCTS. (A) Intensity vs. time profile of ablated raster shows uptake of TPP-AuNPs demonstrated by the ^{197}Au spectrum (red). 20µm/sec scan speed. **(B)** LA-ICP-MSI of TPP-AuNP treated LNCaP spheroid. Pre-ablation optical image (20X objective - scale bar represents 100µm) and elemental maps of ^{66}Zn, ^{25}Mg, ^{197}Au, and total beam. Scale bar represents 50µm.

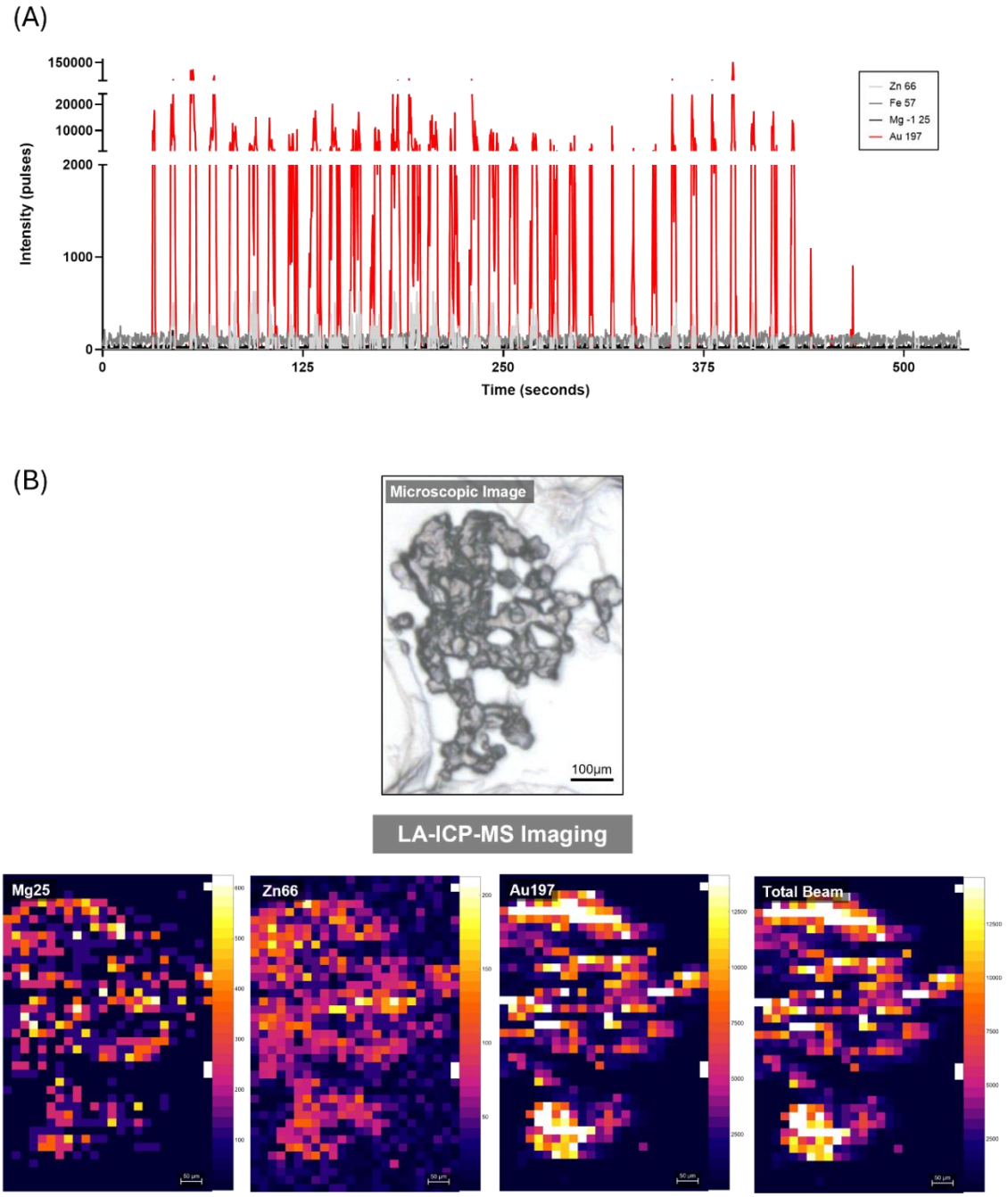

Figure 6.2 - LA-ICP-MS detection and localization of TPP-tagged gold nanoparticles in PC3 MCTS. (A) Intensity vs. time profile of ablated raster shows uptake of TPP-AuNPs demonstrated by the ^{197}Au spectrum (red). 20µm/sec scan speed. **(B)** LA-ICP-MSI of TPP-AuNP treated LNCaP spheroid. Pre-ablation optical image (20X objective - scale bar represents 100µm) and elemental maps of ^{66}Zn, ^{25}Mg, ^{197}Au, and total beam. Scale bar represents 50µm.

6.2.1.1.2. Alginate spheres

For alginate spheres, though the concentration of gold was lower than in spheroid samples, the gold nanoparticles seemed to be evenly distributed though the colonies for all cell lines, represented by LNCaP in Figure 6.3. The remaining data can be found in Appendix G of this thesis.

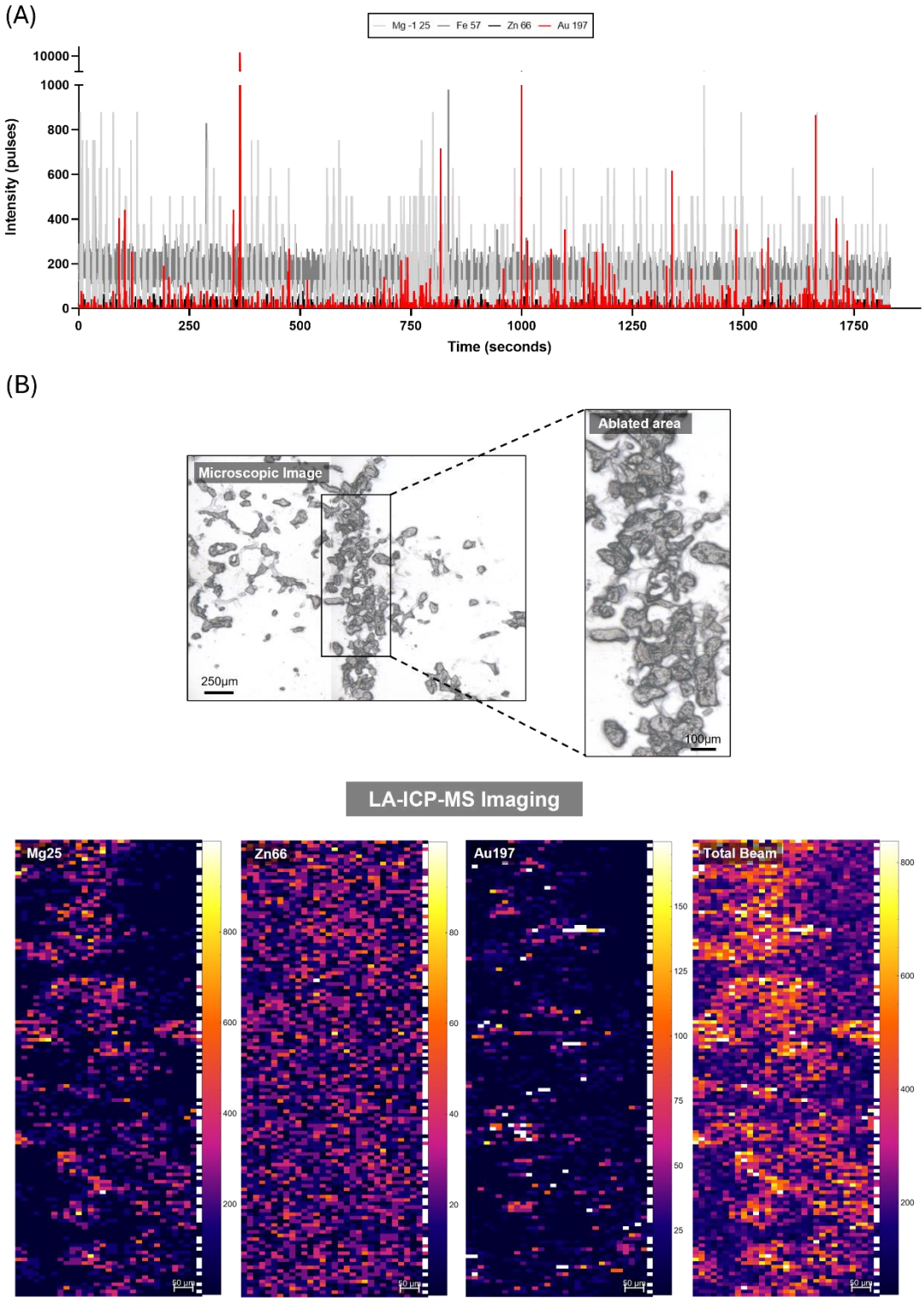

Figure 6.3 - LA-ICP-MS detection and localization of TPP-tagged gold nanoparticles in LNCaP alginate spheres. (A) Intensity vs. time profile of ablated raster shows uptake of TPP-AuNPs demonstrated by the ^{197}Au spectrum (red). 20µm/sec scan speed. **(B)** LA-ICP-MSI of TPP-AuNP treated LNCaP colonies grown in alginate. Pre-ablation optical image (20X objective - scale bars represent 250µm and 100µm) and elemental maps of ^{66}Zn, ^{25}Mg, ^{197}Au, and total beam. Scale bar represents 50µm.

6.2.2. Cell viability of TPP-AuNP treated monolayer cultures post-irradiation.

Osteosarcoma (MG-63 and Saos-2) and prostate adenocarcinoma (PC3 and LNCaP) cell lines were cultured in monolayer and treated with 10μg/mL 5nm TPP-modified gold nanoparticles for 24h. Following treatment, the cells were exposed to radiation using 1.25, 2.5 and 5 Gy doses and allowed to incubate for 10 days, after which cell viability was measured through a colony formation assay. The responses of untreated and TPP-AuNP-treated samples were normalised towards the non-irradiated control, LQ curves were drawn and compared using an extra sum of squares test. Responses were also compared at each radiation dose using multiple *t-tests*, followed by the Holme-Sidak method for multiple comparisons, with α=0.05 (Figure 6.4). Results show a significant decrease in viability in all TPP-AuNP treated cells compared to untreated cultures (p<0.001 for MG-63, Saos-2, PC3 and LNCaP). For MG-63, the surviving fraction of untreated cells was 0.92±0.04 after a 1.25 Gy dose. In TPP-AuNP treated cells, it was three times lower (0.27±0.09). Following a 2.5 Gy dose, untreated cells showed a viability of 0.61±0.23 compared to the 0.24±0.07 of TPP-AuNP-treated cells. After 5 Gy, while untreated cells still presented a surviving fraction of 0.28±0.13, in TPP-AuNP-treated cells it plummeted to 0.02±0.001. This difference in radio-sensitivity was significant at 1.25 Gy (p<0.001). The IC50 of untreated cells was 3.67±0.9 Gy and 0.52±0.1 Gy for the TPP-AuNP-treated population, showing a 7.1 dose enhancement factor of TPP-modified gold nanoparticles (Figure 6.4). For Saos-2, the surviving fraction after 1.25, 2.5, and 5 Gy radiation doses was 0.77±0.18, 0.37±0.19, and 0.13±0.03, respectively. The SF of TPP-AuNP-treated cells was considerably lower, with values of 0.13±0.03, 0.08±0.008, and 0.04±0.001, following doses of 1.25, 2.5, and 5 Gy, respectively. The difference in sensitivity between the two populations was significantly lower at 1.25 Gy (p=0.04) and 5 Gy (p=0.011), with an IC50 of 1.86±0.5 Gy for untreated and 0.19±0.01 Gy for TPP-AuNP-treated Saos-2 cells, which represented a DEF of 9.8 (Figure 6.4). TPP-AuNP-treated PC3 cells showed a significantly higher sensitivity than the untreated population at every radiation dose (p=0.001, p=0.002, and p=0.007 at 1.25, 2.5, and 5 Gy, respectively), with SF values of 0.052±0.006, 0.048±0.006, and 0.036±0.002 following a dose of 1.25, 2.5, and 5 Gy, respectively; versus the untreated surviving fraction of 0.75±0.15, 0.53±0.11, and 0.23±0.06 after the same respective doses. Therefore, the IC50 of the TPP-

AuNP-treated population (0.09±0.01 Gy) was 28.5 times lower than the IC50 of untreated cells (2.57±0.4 Gy) (Figure 6.4). The fraction of cells that survived irradiation in untreated LNCaP cells was 0.60±0.21 after 1.25 Gy, 0.45±0.14 after 2.5 Gy and 0.10±0.05 after 5 Gy (IC50=1.58±0.45 Gy). LNCaP cells treated with TPP-modified gold nanoparticles presented a surviving fraction value of 0.02±0.004 after 1.25 Gy, 0.004±0.0007 after 2.5 Gy and 0.003±0.0009 after a 5 Gy dose, which equated to an IC50 of 0.45±0.002 Gy. Comparing the responses of untreated and TPP-AuNP-treated cells, it was possible to observe a radiosensitising effect of the TPP-functionalised gold nanoparticles (DEF=79), illustrated by the shift of the non-linear regression curve to the left of the x axis (Figure 6.4).

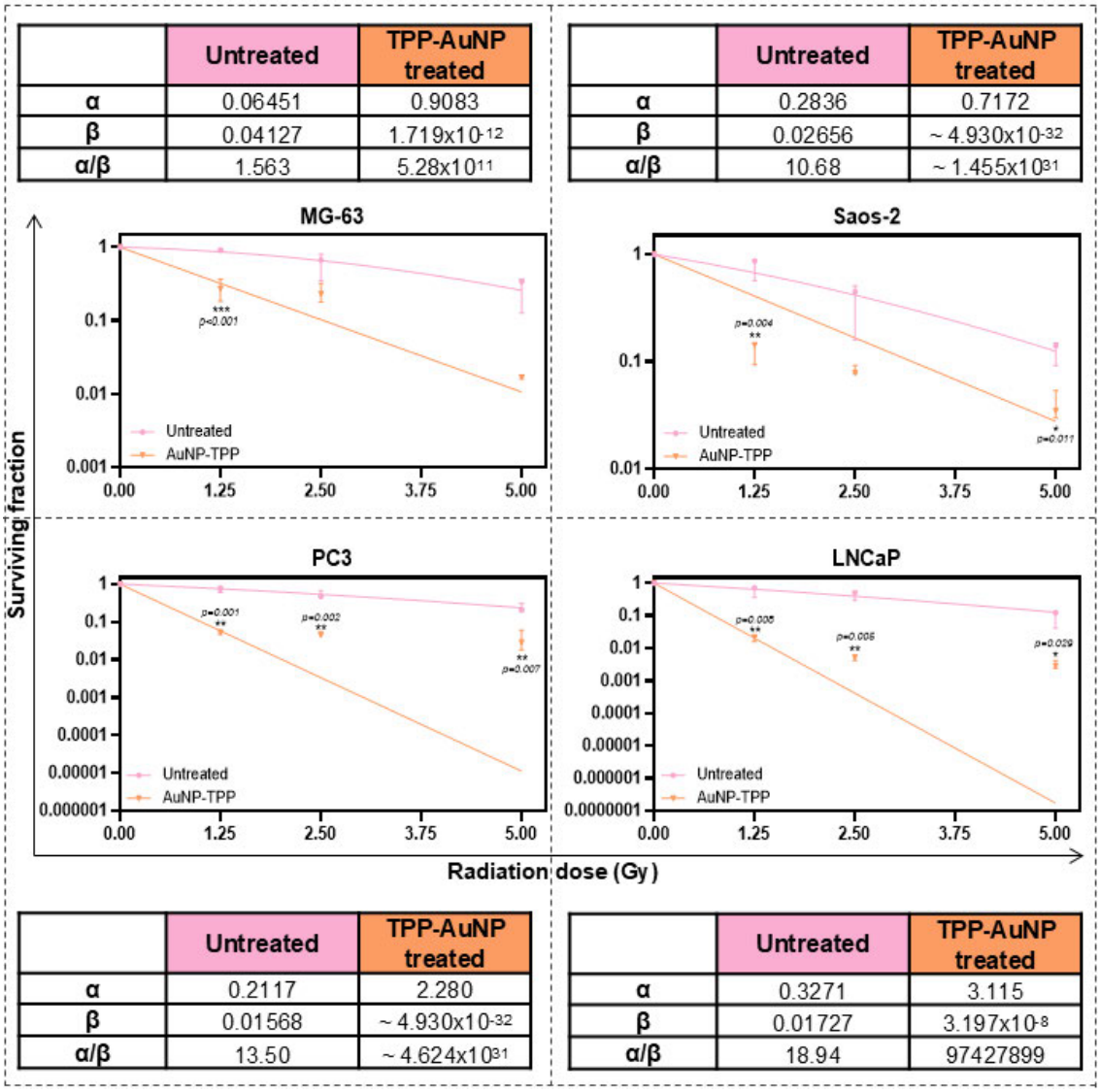

Figure 6.4 - Cell viability of TPP-AuNP-treated osteosarcoma and prostate adenocarcinoma cell lines 10 days post-irradiation. Surviving fractions of TPP-AuNP-treated monolayer cultures with increasing doses of radiation. Results show a sensitising effect of TPP-AuNPs, translated by a significant increase the sensitivity of all cell lines to radiation. Scatter plots, surviving fraction

data is presented as mean ±SD, individual values represent n=3 independent experiments with 3 technical repeats. Statistical significance determined by multiple *t-tests* and corrected using the Holme-Sidak method of multiple comparisons, with alpha=0.05. (*P<0.05). From the non-linear regression curves, IC50 values were calculated using a 95% confidence interval. From the LQ curves, α and β values were calculated using a 95% confidence interval. Untreated data has been presented in previous chapters.

Contrary to the results observed with other AuNP treatments, TPP-tagged AuNP produced a cytotoxic effect in the absence of radiation exposure. Therefore, to illustrate the discrepancy in cell viability prior to irradiation, results were also plotted as normalised viability towards the untreated control (Figure 6.5). A Two-way ANOVA analysis to determine the interaction between irradiation and TPP-AuNP treatment revealed that the treatment with TPP-functionalised gold nanoparticles produced a significant radiosensitisation in all cell lines (MG-63, p=0.004; Saos-2, p<0.001; PC3, p<0.001; LNCaP, p<0.001). Results of toxicity of TPP-AuNP alone can be found in appendix K of this thesis.

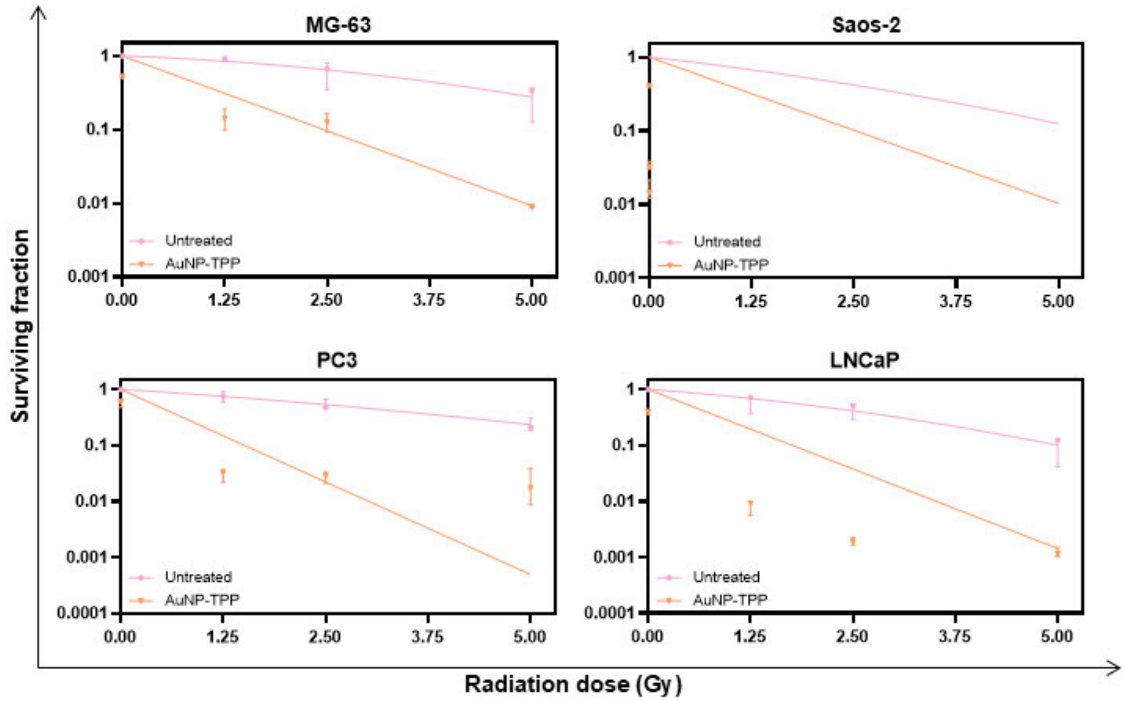

Figure 6.5 - Cell viability of TPP-AuNP-treated osteosarcoma and prostate adenocarcinoma cell lines 10 days post-irradiation, normalised towards the untreated control. Results show a cytotoxic effect of TPP-AuNPs as well as a sensitising effect of TPP-AuNPs. Scatter plots, percentage surviving fraction data is presented as mean ±SD, individual values represent n=3 independent experiments with 3 technical repeats. LQ curves, α and β values were calculated using a 95% confidence interval. Untreated data has been presented in previous chapters.

6.2.3. Assessment of the radio-sensitising effect of TPP-AuNPs in alginate spheres.

Alginate spheres containing young colonies were treated with 5nm TPP-AuNPs (10μg/mL, 24h) and irradiated with 2.5, 5, and 20 Gy doses. The cultures were then incubated for a further 7 days, after which colony diameter was measured and compared to the average diameter of untreated colonies at each radiation dose using multiple *t-tests*, and statistical significance was determined using the Holme-Sidak method, with alpha=0.05. Non-linear regression curves were drawn for both populations to determine the IC50 and DEF of TPP-AuNPs (Figure 6.6). Results show that treating alginate sphere cultures with TPP-modified gold nanoparticles does not significantly affect their radio-sensitivity. Untreated MG-63 cells measured 40.4±2.1μm prior to irradiation. The following week, their size doubled (89.6±2.2μm) whereas TPP-AuNP-treated colonies measured 70.2±8.4μm. After a 2.5 Gy dose, untreated colonies measured on average 67.1±8.4μm and TPP-AuNP treated colonies measured 56.1±3.3μm. Colonies irradiated with 5 Gy measured 57.2±6.5μm if untreated and 46.3±4.2μm when treated with TPP-AuNPs. Following a dose of 20 Gy, untreated MG-63 colonies measured 41.8±1.3μm and TPP-AuNP-treated colonies measured 44.9±4.3μm. The IC50 for untreated colonies was 9.2±1.7 Gy and 15.5±3.9 Gy for colonies treated with TPP-functionalised AuNPs (DEF=0.6). The difference in sensitivity between untreated and treated cells was not statistically significant (Figure 6.6). Saos-2 colonies measured 27.9±1.4μm before radiation exposure. The following week, untreated controls measured 60.3±5.4μm and TPP-AuNP treated colonies measured 61.0±2.8μm. When irradiated, untreated colonies measured 38.5±1.8μm, 35.2±2.6μm, and 30.6±2.0μm, after 2.5, 5, and 20 Gy, respectively. TPP-AuNP-treated colonies measured 39.9±1.0μm after 2.5 Gy, 32.7±0.5μm with 5 Gy, and 30.8±6.1μm after a 20 Gy dose. The IC50 for untreated colonies was 5.7±1.2 Gy and 5.1±1.0 Gy for TPP-AuNP-treated colonies (DEF=1.1). Despite the slight increase in sensitivity, the difference between the responses of untreated and TPP-AuNP treated Saos-2 colonies was not statistically significant at any radiation dose (Figure 6.6). The day before treatment, PC3 colonies measured 35.8±3.7μm. The following week, the diameter of untreated colonies increased to 83.5±2.0μm and after radiation exposure they measured 59.8±7.2μm, 41.5±3.1μm, and 37.5±0.1μm (with 2.5, 5, and 20 Gy, respectively – IC50=5.6±.9 Gy). TPP-AuNP-treated colonies measured an average size of

71.2±6.1μm. After irradiation with doses of 2.5, 5, and 20 Gy, their sizes reduced to 55.5±8.1μm, 47.3±1.0μm, and 40.1±1.3μm, respectively (IC50=11.5±2.0 Gy). These results indicate that the TPP-AuNP treatment not only failed to radio-sensitize PC3 colonies grown in alginate but also made them significantly more resistant to 5 Gy (p=0.006) and 20 Gy (p=0.020) radiation doses (Figure 6.6). LNCaP colonies measured 44.7±2.8μm prior to irradiation. Colonies that were not irradiated measured 120.3±11.3μm without treatment and 73.9±4.2μm when treated with TPP-AuNPs following a 7-day incubation period. After exposure to a 2.5 Gy radiation dose, untreated colonies measured 75.8±10.3μm and TPP-AuNP-treated colonies had an average diameter of 56.7±11.4μm. After 5 Gy, the diameters were 57.0±7.1μm for untreated colonies and 47.5±2.1μm for TPP-AuNP-treated. With a 20 Gy dose, untreated colonies measured 42.6±3.1μm while colonies treated with TPP-AuNPs measured 34.5±4.7μm. The difference in sensitivity between untreated and treated cells was not statistically significant. The IC50s were 5.6±0.9 Gy and 8.9±1.4 Gy for untreated and treated colonies, respectively (Figure 6.6).

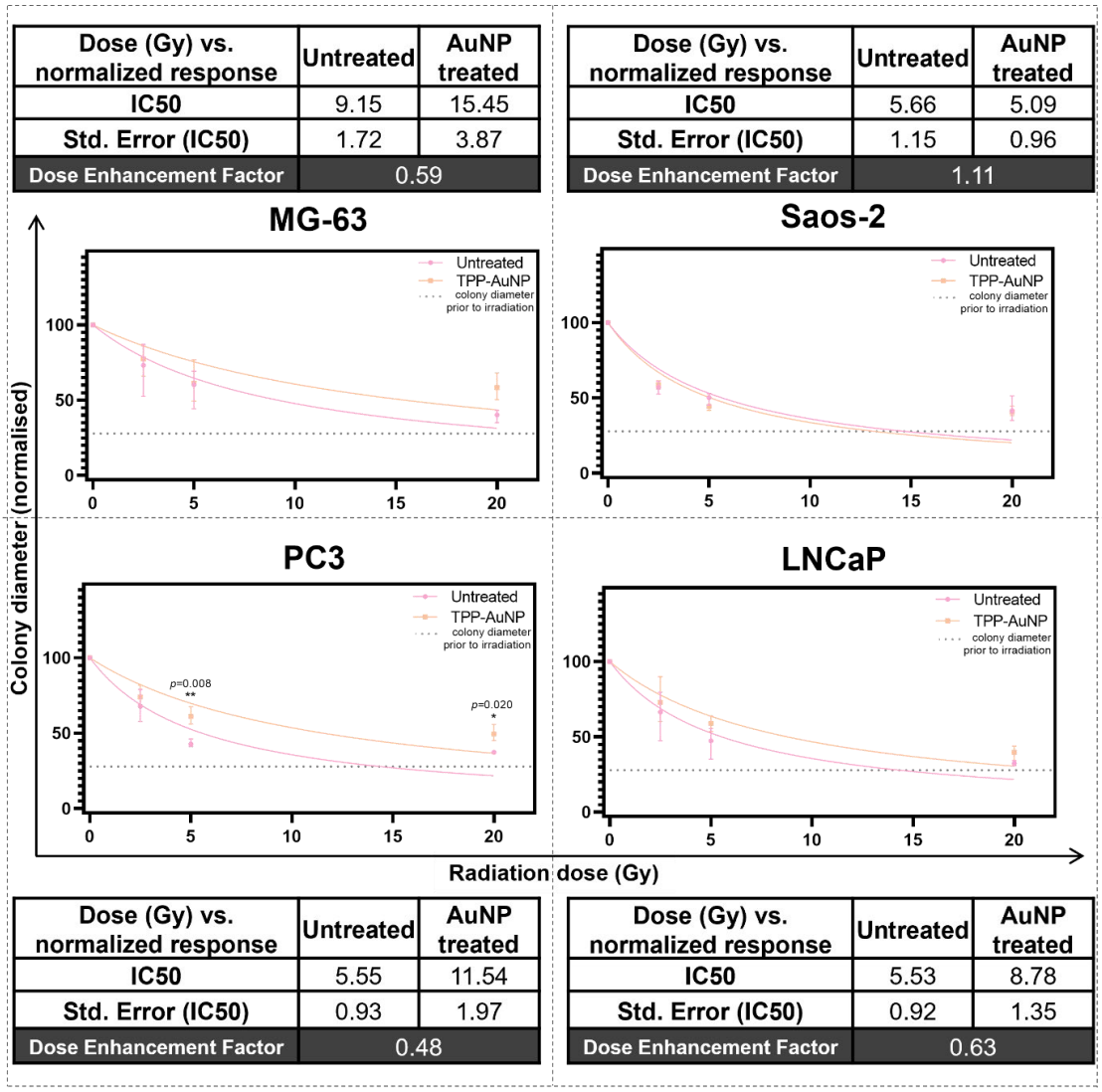

Figure 6.6 - Cell viability of TPP-AuNP-treated osteosarcoma and prostate adenocarcinoma cell lines grown in alginate spheres 10 days post-irradiation. Normalised colony diameters of TPP-AuNP-treated alginate sphere cultures with increasing doses of radiation. PC3 untreated colonies are significantly more sensitive to radiation than TPP-AuNP treated colonies. Other cell lines do not show significant differences in radio-sensitivity between untreated and TPP-AuNP-treated colonies. Scatter plots, normalised colony diameter data is presented as percentage mean ±SD, individual values represent n=3 independent experiments with 3 technical repeats. Statistical significance determined by multiple *t-tests* and corrected using the Holme-Sidak method of multiple comparisons, with alpha=0.05. (*P<0.05). From the non-linear regression curves, IC50 values were calculated using a 95% confidence interval. DEF calculated as untreated IC50 ÷ TPP-AuNP-treated IC50.

6.2.4. Acute responses of TPP-AuNP-treated MCTS to ionising radiation.

To investigate the acute radio-sensitising effect of TPP-functionalised AuNPs in MCTS, these were treated with TPP-AuNPs (10µg/mL) for 24h and irradiated with doses ranging from 2.5 to 20 Gy. Irradiated spheroids were incubated for 24 hours, after which cell viability was assessed through live/dead analysis of a

Hoechst 33342/PI stain (Figure 6.7). The results were plotted as a percentage with corresponding non-linear regression curved, from which IC50 values were calculated. The sensitivity of TPP-AuNP-treated MCTS to each radiation dose was analysed using a Kruskal-Wallis non-parametric test followed by a Dunn's multiple comparisons test (Figure 6.8A). The viability of TPP-AuNP-treated MCTS with each dose was then compared to the one of untreated cultures with multiple *t-tests* corrected using the Holme-Sidak method for multiple comparisons with a 95% confidence interval (Figure 6.8B). Results show that both osteosarcoma cell lines present a significant decrease in viability with increasing doses of radiation. The viability of TPP-AuNP-treated MG-63 spheroids reduced to 93.1±4.8%, 81.9±3.6%, and 65.7±10.8%, following doses of 2.5, 5, and 20 Gy, respectively. This reduction was statistically significant at a 20 Gy dose (p=0.006) (Figure 6.8A). When compared to the responses of untreated spheroids, MG-63 spheroids treated with TPP-modified gold nanoparticles were significantly more sensitive to a 20 Gy radiation dose (p=0.009) (Figure 6.8B). The viability of TPP-AuNP-treated Saos-2 spheroids decreased to 63.4±8.1% after 2.5 Gy, 50.4±16.3% with 5 Gy, and 42.4±3.6% after exposure a 20 Gy radiation dose, the latter being statistically significant (p=0.019) (Figure 6.8A). When compared to the acute response of untreated Saos-2 spheroids, the TPP-AuNP treatment showed a radio-sensitising effect at all doses with p<0.001 at 2.5 Gy, p=0.007 at 5 Gy, and p<0.001 after a 20 Gy dose (Figure 6.8B). PC3 MCTS treated with TPP-AuNPs presented a low reduction in viability with increasing radiation doses (88.9±2.5%, 87.8±0.8%, and 92.2±2.4% at 2.5, 5, and 20 Gy, respectively), albeit statistically significant at 5 Gy (p=0.019). This reduction, however, was not biologically relevant given the high viability of 20 Gy irradiated spheroids (>90%). When compared to the responses of untreated spheroids, the TPP-AuNP treatment showed an acute radio-sensitising effect at all doses with p=0.009 at 2.5 Gy, p<0.001 at 5 Gy, and p=0.035 after a 20 Gy dose (Figure 6.8B). The viability of TPP-AuNP-treated LNCaP spheroids remained high following irradiation with measurements of 99.3±0.7% after 2.5 Gy, 99.9±1% with 5 Gy, and 96.2±3% with 20 Gy. Although the viability decrease at 20 Gy was statistically significant (p=0.026), it is biologically irrelevant given the spheroids' overall high viability rate (Figure 6.8A). There were no statistically significant differences between the responses of TPP-AuNP treated and untreated spheroids (Figure 6.8B).

From the microscopic visualisation of MCTS, represented in Figure 6.7, it is also possible to observe that TPP-AuNP treatment is causing a disruption of the spheroids, which present different morphologies to untreated ones.

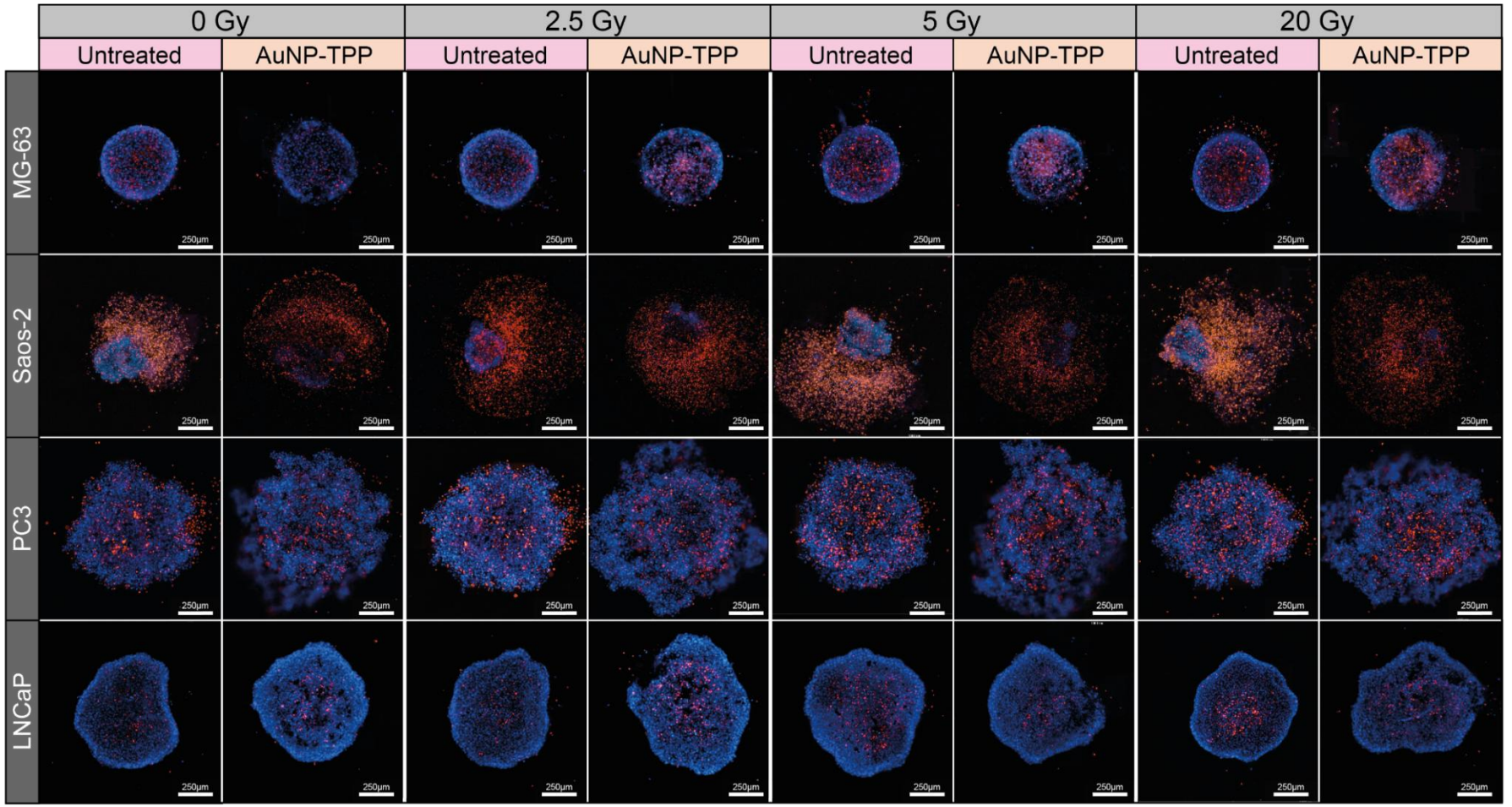

Figure 6.7 - Cell viability of human osteosarcoma and prostate cancer cell lines cultured in MCTS and treated with TPP-AuNPs, 24h post-irradiation. Multicellular tumour spheroids were stained with Hoechst 33342 (blue cells) and Propidium Iodide (red cells). Cytation 5 imaging system, 4x objective, Z-stack of DAPI and Texas Red channels. Scale bar represents 250µm.

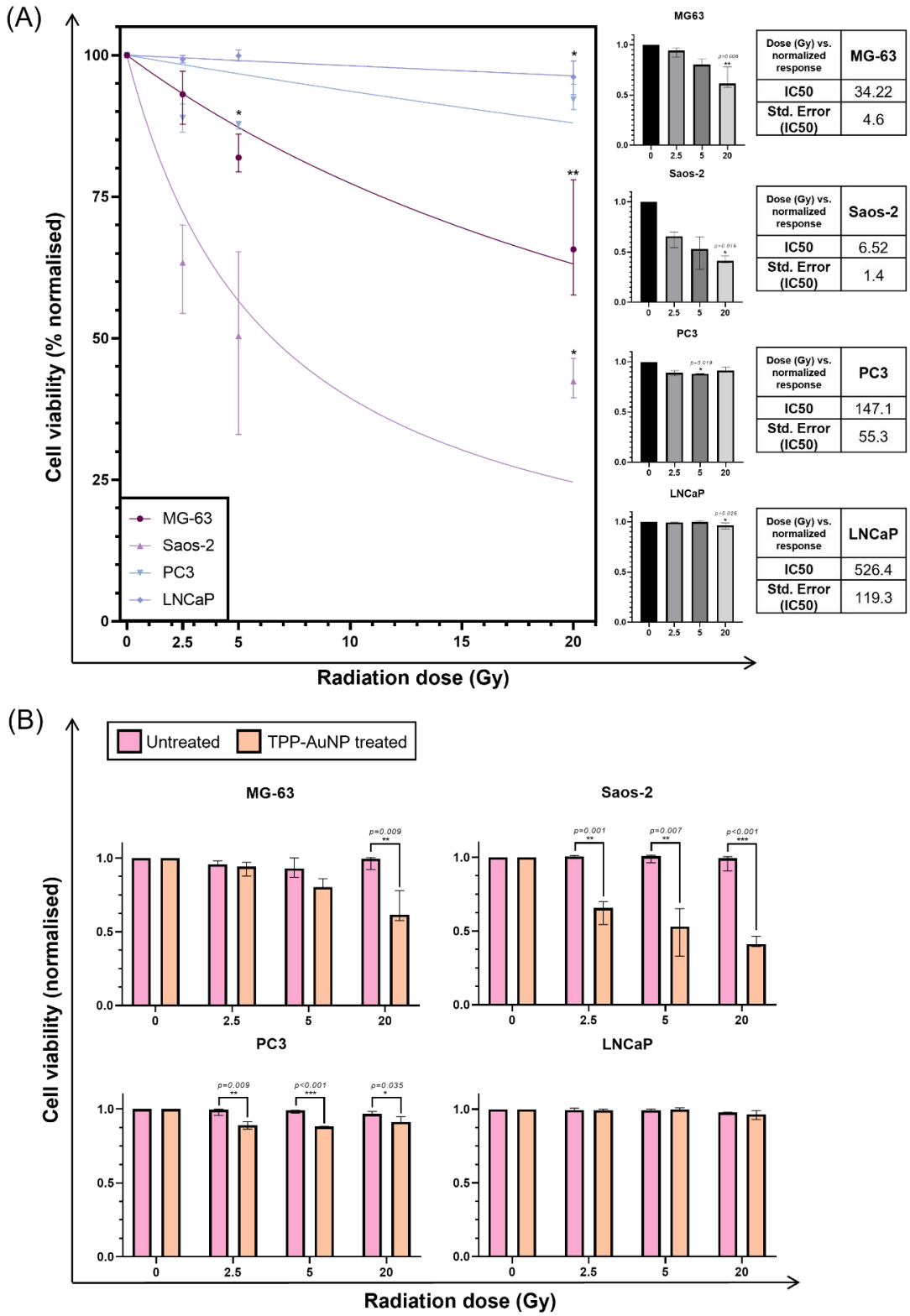

Figure 6.8 - Viability of cells grown in MCTS and treated with TPP-AuNPs 24h-post ionising radiation exposure. (A) Osteosarcoma cell lines present a reduction in viability with increasing doses of radiation. Scatter plot and non-linear regression curve, percentage cell viability data is presented as median ±range, individual values represent n=3 independent experiments with 3 technical repeats. Individually analysed responses of MG-63, Saos-2, PC3, and LNCaP only show a significant reduction in viability for MG-63 and Saos-2 spheroids with a 20 Gy dose. Despite the significance of the responses at 5 and 20 Gy for PC3 and LNCaP, respective, these are not biologically relevant. Column bar graph,

Kruskal-Wallis followed by Dunn's multiple comparisons test (*P<0.05). **(B)** Comparison between untreated and TPP-AuNP-treated MCTS of each cell line showing a radio-sensitisation effect of TPP-AuNPs in MG-63, Saos-2, and PC3 spheroids. Interleaved bars, multiple *t-tests*. Statistical significance corrected using the Holm-Sidak method of multiple comparisons, with alpha=0.05. (*P<0.05). All data is presented as median ±range and individual values represent n=3 independent experiments with 3 technical repeats.

6.2.5. Acute radio-responses of alginate spheres treated with mitochondrial-targeted AuNPs.

Prior to ionising radiation exposure, alginate spheres were treated with 5 nm diameter TPP-modified gold nanoparticles at a concentration of 10 μg/mL in appropriate cell culture media for 24h. The alginate spheres were then irradiated using doses of 2.5 Gy, 5 Gy, and 20 Gy. To assess cell viability after irradiation, the cultures were stained with Hoechst 33342/PI 24h post-treatment and imaged on Cytation 5 (Figure 6.9). Relative percentage of viable cells was calculated and normalised towards the respective untreated control. The data was graphed as a percentage in a scatter plot and non-linear regression curves of dose vs. normalised response were drawn. The respective IC50 values were calculated, with a confidence interval of 95% (Figure 6.10A). Analysis of each TPP-AuNP-treated cell line's response to the different radiation doses was conducted using a Kruskal-Wallis non-parametric test, due to the skewness of the results. Additionally, datasets were subjected to multiple comparisons, using Dunn's correction as a post-hoc test, to assess the significance of the response to each dose, when compared to the untreated control (0Gy). The response of TPP-AuNP-treated alginate spheres was compared with that of the untreated models of the same cell line for each radiation dose using multiple t-tests and corrected using the Holme-Sidak method with a 95% confidence interval (Figure 6.10B).

Results show that all TPP-AuNP-treated colonies show a decrease in viability with increasing radiation doses. The viability of MG-63 colonies was reduced to 92.8±6.3%, 84.7±7.1%, and 74.1±12.4% following doses of 2.5, 5, and 20 Gy, respectively (IC50 = 49.2±9.6 Gy). This reduction in viability was significant at 20 Gy (p=0.013) (Figure 6.10A). Compared to the responses of untreated MG-63 colonies grown in alginate spheres, TPP-AuNP-treated colonies did not present a significant increase in sensitivity (Figure 6.10B). Saos-2 colonies treated with TPP-AuNPs saw their viability reduce to 84.7±11.5% after a 2.5 Gy dose, 58.9±9.9% after 5 Gy, and 35.5±4.7% following exposure to 20 Gy gamma radiation, equating to an IC50 of 9.6±1.3 Gy. The reduction in viability of Saos-2

TPP-AuNP-treated colonies was significant at 20 Gy (p=0.006) (Figure 6.10A). Comparatively to untreated Saos-2 spheres, the colonies grown in TPP-AuNP-treated spheres were significantly more radio-sensitive to a 5 Gy dose (p=0.002) (Figure 6.10B). The viability of PC3 colonies treated with TPP-functionalised AuNPs reduced to 96.8±3.6%, 91.0±0.7%, and 48.7±5.7%, following doses of 2.5, 5, and 20 Gy, respectively, with the latter being statistically significant (p=0.006). The IC50 of TPP-AuNP-treated PC3 colonies was 24.7±1.4 Gy (Figure 6.10A). When compared to untreated colonies, TPP-AuNP-treated colonies of PC3 were significantly more sensitive to a 20 Gy dose (Figure 6.10B). The cell viability of LNCaP cells was 97.6±2.1% after exposure to a 2.5 Gy radiation dose, 94.4±2.2% after 5 Gy, and 71.6±4.9% after 20 Gy, which was statistically significant (p=0.006). The IC50 value for LNCaP colonies treated with TPP-AuNPs was 54.5±4.6 Gy (Figure 6.10A). Comparing these results to those of untreated colonies, it is possible to observe a significant increase in sensitivity of TPP-AuNP-treated spheres after exposure to a dose of 20 Gy (p=0.015) (Figure 6.10B).

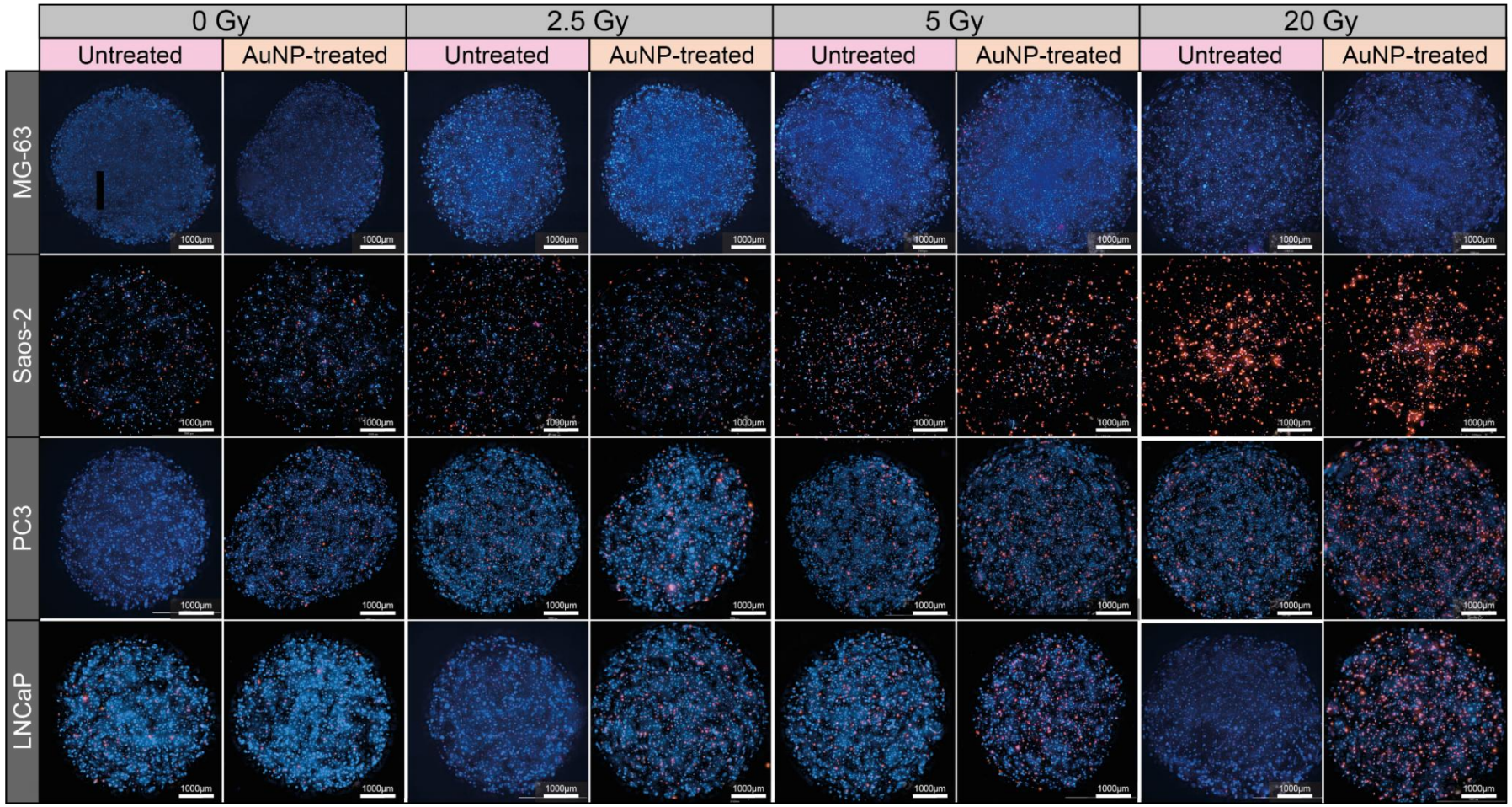

Figure 6.9 - Cell viability of human osteosarcoma and prostate cancer cell lines cultured in alginate spheres and treated with TPP-AuNPs, 24h post-irradiation. Colonies were stained with Hoechst 33342 (blue cells) and Propidium Iodide (red cells). Cytation 5 imaging system, 4x objective, Z-stack of DAPI and Texas Red channels. Scale bar represents 1000µm.

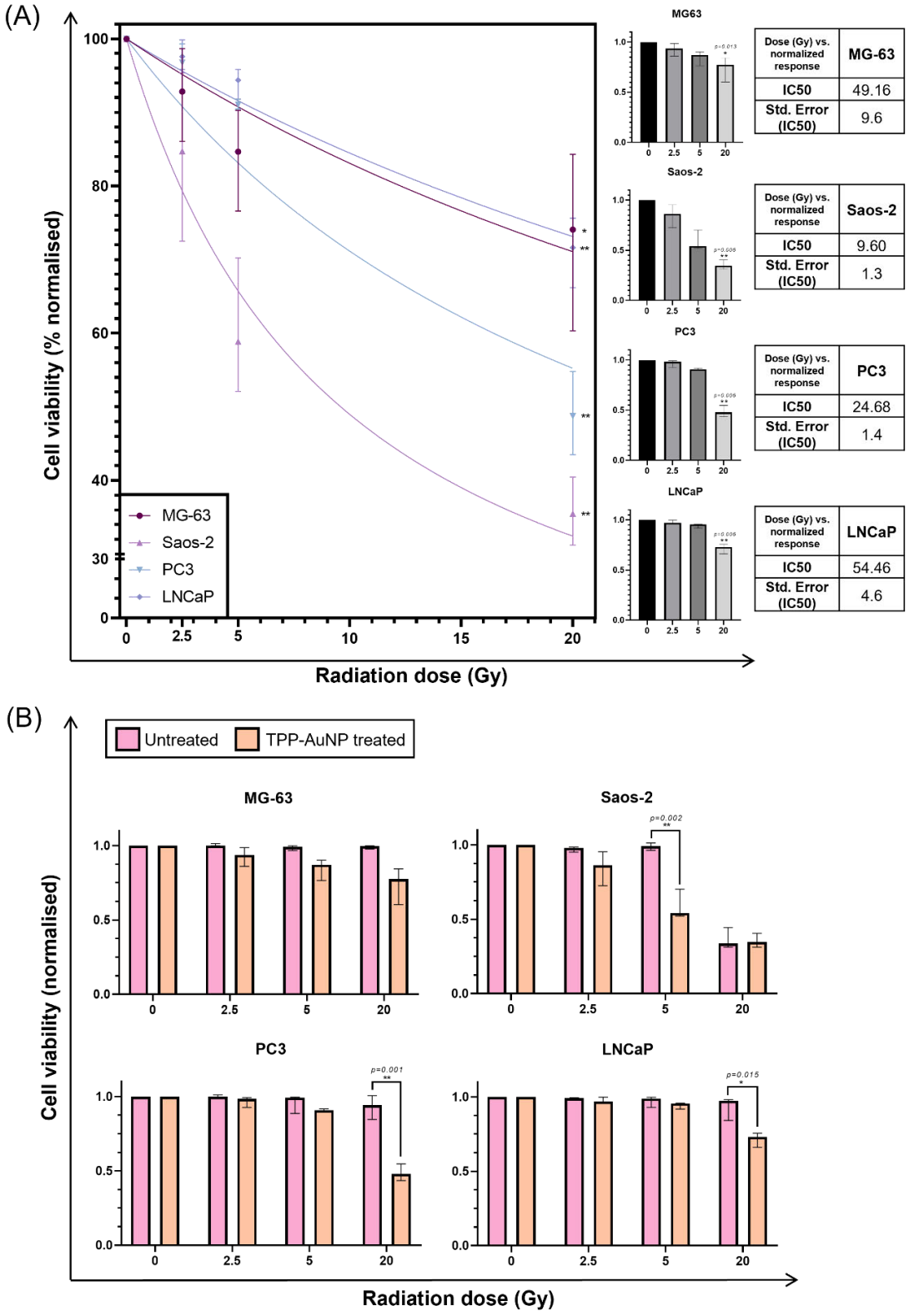

Figure 6.10 - Viability of cells grown in alginate spheres and treated with TPP-AuNPs 24h-post ionising radiation exposure. (A) Cell lines present a reduction in viability with increasing doses of radiation. Scatter plot and non-linear regression curve, percentage cell viability data is presented as median ±range, individual values represent n=3 independent experiments with 3 technical repeats. Individually analysed responses of MG-63, Saos-2, PC3, and LNCaP show a significant reduction in viability at a 20 Gy dose. Column bar graph, Kruskal-Wallis followed by Dunn's multiple comparisons test (*P<0.05). **(B)**

Comparison between untreated and TPP-AuNP-treated alginate spheres of each cell line. Interleaved bars, multiple *t-tests*. Statistical significance corrected using the Holm-Sidak method of multiple comparisons, with alpha=0.05. (*P<0.05). All data is presented as median ±range and individual values represent n=3 independent experiments with 3 technical repeats.

6.2.6. Cell cycle distribution of TPP-AuNP-treated cells in 2D and 3D following radiation exposure.

Following treatment with TPP-modified 5nm gold nanoparticles for 24h, monolayer cultures and both 3D models were exposed to a 5 Gy dose of ionising radiation. The cell cycle distribution of each of the treated cell lines was investigated by propidium iodide staining and flow cytometry analysis, as described in section 2.3.6. Due to time constraints, this analysis was only conducted once meaning that no descriptive statistics were performed.

6.2.6.1. Effect of TPP-AuNP treatment on cell cycle distribution of irradiated monolayer cultures.

Cell suspensions were prepared and analysed according to the method described in section 2.3.6.2. Following the gating of cell populations, detailed in section 3.2.8, results of cell cycle distribution revealed that after exposure to a 5 Gy dose the percentage of cells in G0/1 and S phases decreased for MG-63, Saos-2 and PC3 cell lines. Conversely, the percentage of cells in G2/M increased. These changes were more accentuated in the osteosarcoma cell lines than in PC3. In LNCaP cells, the percentage of cells in G0/1 increased, and the S and G2/M populations decreased (Figure 6.11A). Comparing the cell cycle distributions on untreated and TPP-AuNP-treated monolayer cultures, it is possible to observe that for MG-63 and Saos-2 cell lines TPP-AuNPs seem to enhance the effects of radiation. TPP-AuNP treatment in PC3 cells showed what seems to be a mild radio-sensitising effect, with the percentage of cells in G0/1 decreasing slightly and a minor increase in the G2/M population. In LNCaP cells, treatment with TPP-AuNPs shows the opposite effect of irradiation only in untreated cells (Figure 6.11B).

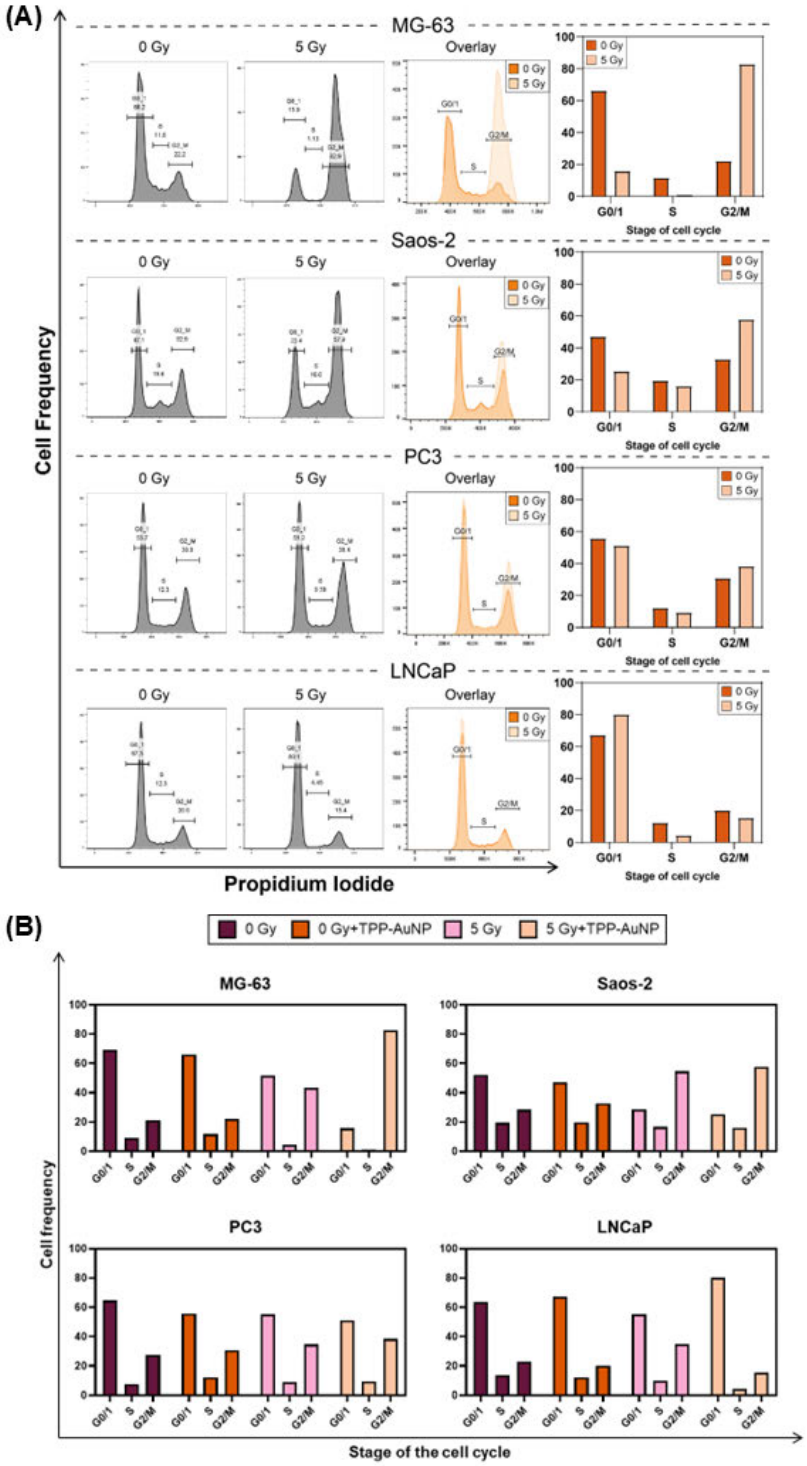

Figure 6.11 - Differences in cell cycle distribution of TPP-AuNP-treated cell lines cultured in 2D 24h following ionising radiation. (A) Cells were gated according to their DNA content (stained with PI), i.e. the stage of the cell cycle in which they were in 24h post-irradiation. Histograms of irradiated untreated and TPP-AuNP-treated populations were overlaid for visual representation of different distributions. The percentages of cells in each stage were plotted as interleaved bar graphs of n=1. **(B)** Comparison of cell cycle distribution between untreated and TPP-AuNP-treated cells cultured in 2D exposed to 5 Gy radiation**.** TPP-AuNPs seem to enhance the effects of radiation in OS cells. In LNCaP cells, it produces the contrary effect. Interleaved bars, n=1.

6.2.6.2. Effect of TPP-AuNP treatment on the cell cycle distribution of irradiated 3D cultures.

The cell cycle distributions of multicellular tumour spheroids and alginate spheres were also analysed. Due to time constraints only MG-63, Saos-2 and PC3 alginate spheres were tested.

6.2.6.2.1. Multicellular tumour spheroids.

Preliminary results showed that TPP-AuNP-treated MG-63 MCTS did not show differences in cell cycle distribution pre- and post-irradiation. Saos-2, PC3 and LNCaP MCTS treated with TPP-modified gold nanoparticles showed a decrease in the G0/1 population accompanied by an increase in the percentage of cells in G2/M (Figure 6.12A). Comparing these responses to untreated spheroids it is possible to observe TPP-modified gold nanoparticles did not alter cell cycle distribution of cells cultured in MCTS (Figure 6.12B).

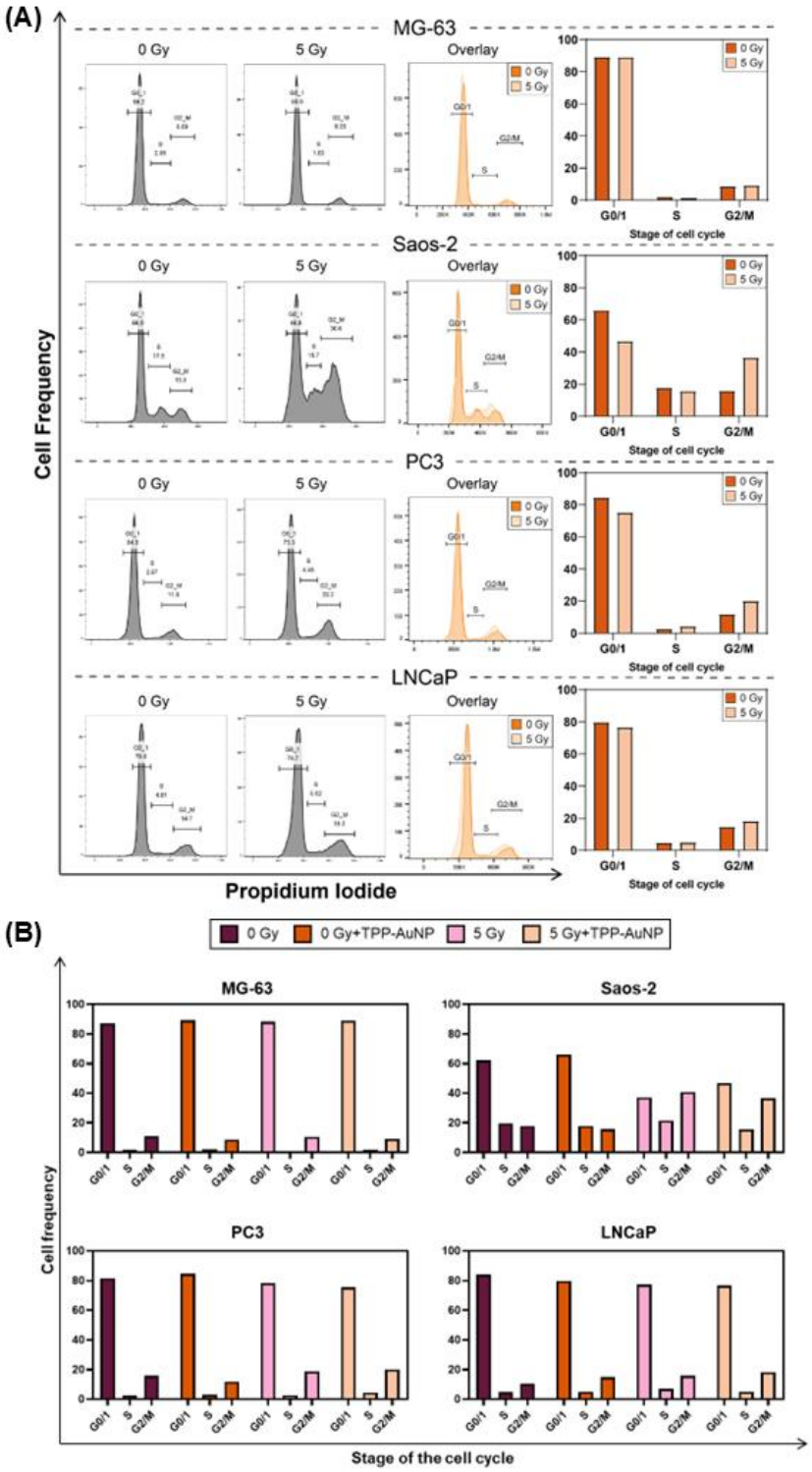

Figure 6.12 - Cell cycle distribution of TPP-AuNP-treated cell lines cultured in MCTS 24h following ionising radiation. (A) Single cell-suspensions of spheroids irradiated with 5 Gy were analysed 24h post-irradiation. Cells were gated according to the stage of the cell cycle in which they were in, and histograms of irradiated untreated and TPP-AuNP-treated populations were overlaid for visual representation of different distributions. The percentages of cells in each stage were plotted as interleaved bar graphs of n=1. **(B)** Comparison of cell cycle distribution between untreated and TPP-AuNP-treated spheroids exposed to 5 Gy radiation. TPP-AuNP treatment does not alter the cell cycle distribution of irradiated spheroids. Interleaved bars, n=1.

6.2.6.2.2. Alginate spheres.

Preliminary data showed that in MG-63 and PC3 alginate spheres, the G0/1 population decreased after irradiation, with an increase in the percentage of cells in G2/M. In PC3, although there was a minor increase in the G2/M population and a slight increase in the percentage of cells in S phase, the G0/1 population was maintained (Figure 6.13A). Comparatively to the responses of untreated spheroids, the TPP-AuNP treatment appeared to have a radio-sensitising effect in MG-63, further decreasing the percentage of cells in G0/1 and increasing those in G2/M. In Saos-2, the results of TPP-AuNP-treated cultures did not overtly affect cell cycle distribution compared to untreated spheroids. In PC3 cells, TPP-AuNP treatment seems to be producing a similar effect, with and without radiation exposure (Figure 6.13B).

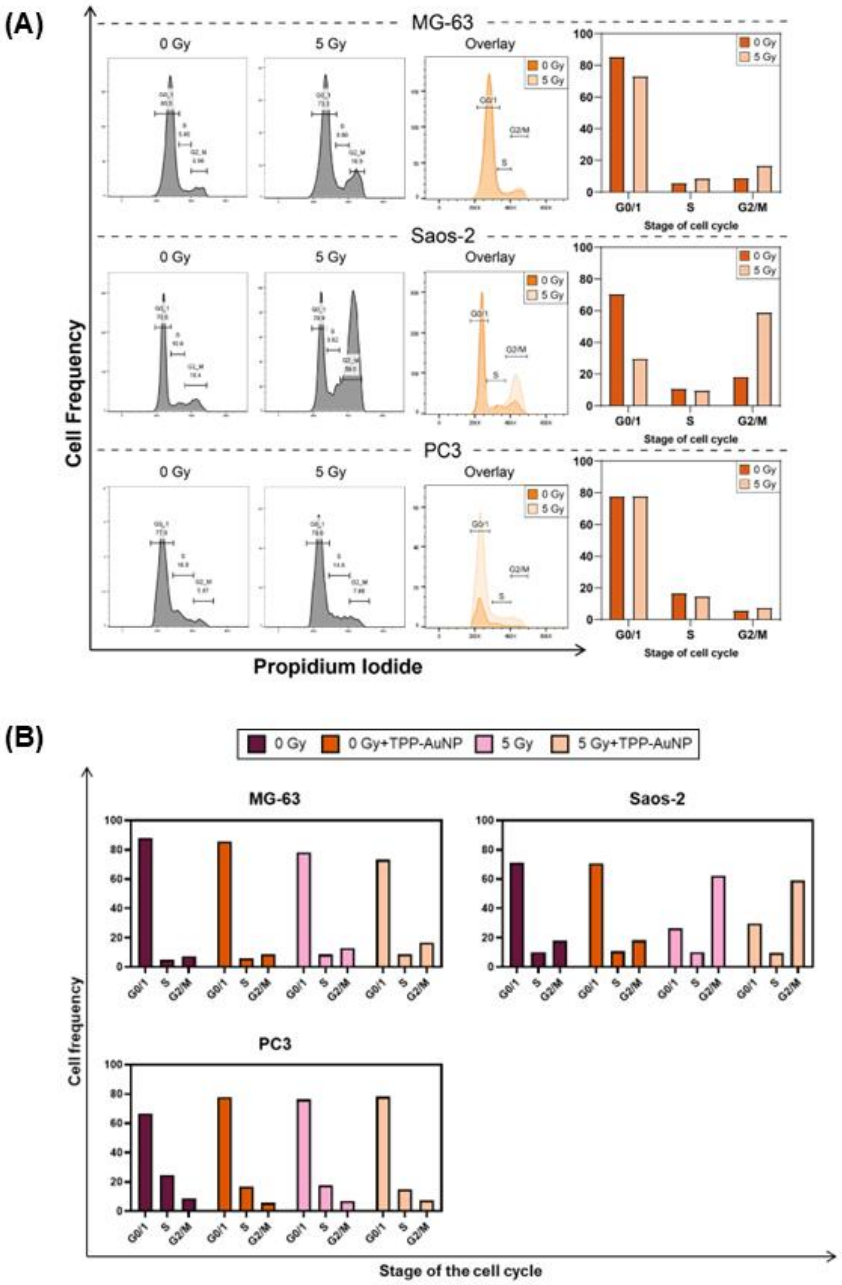

Figure 6.13 - Cell cycle distribution of TPP-AuNP-treated cell lines cultured in alginate spheres 24h following ionising radiation. (A) Cells were gated according to the intensity of the PI signal, i.e. the stage of the cell cycle in which they were in 24h post-irradiation. Histograms of irradiated untreated and gold-treated populations were overlaid for visual representation of different distributions. The percentages of cells in each stage were plotted as interleaved bar graphs of n=1. **(B)** Comparison of cell cycle distribution between untreated and TPP-AuNP-treated alginate spheres exposed to 5 Gy radiation. In MG-63, the presence of TPP-AuNPs seemed to produce a minor radio-sensitising effect; in Saos-2 despite a similar response to untreated and irradiated cells, the percentage of cells in G0/1 increased slightly, accompanied by a minor decrease in the G2/M population. In PC3, the presence of TPP-AuNPs did not majorly affect the cell cycle distribution of irradiated cells.

6.2.7. Localisation of γ-H2AX foci in NLS-AuNP-treated samples following irradiation.

To assess the levels of DNA damage, translated by γ-H2AX foci, induced by TPP-AuNPs, monolayer cultures were treated with TPP-functionalised 5 nm gold nanoparticles (10μg/mL, 24h) and exposed to a 5 Gy irradiation dose. The presence and location of γ-H2AX foci were investigated through immunofluorescence assays, using the method described in section 2.3.5.2. The resulting confocal images (Figure 6.14) were analysed using the Zeiss Zen 2.3 (blue edition) software (Carl Zeiss) by quantification of the number of H2AX foci per cell nucleus. The results were graphed as violin plots and the means of 3 repeats were compared to untreated samples of the same cell line using Kruskal-Wallis tests followed by Dunn's multiple comparisons (Figure 6.15). Results showed that MG-63 cells treated with TPP-AuNPs presented an increase in the average number of γ-H2AX foci per cell following irradiation (2.9 in TPP-AuNP-treated cells vs. 0.86 in untreated cells) as well as a decrease in the number of cells without any foci, which was 12.1% compared to 55.7% of untreated cells. This difference was statistically significant (p=0.004) (Figure 6.15). Saos-2 cells treated with TPP-AuNPs showed a higher number of γ-H2AX foci comparatively to untreated cells (3.4 and 2.5, respectively). This difference was not statistically significant. The number of γ-H2AX foci containing cells also increased, with 71.5% of untreated cells being positive for γ-H2AX compared to 90.8% of TPP-AuNP-treated cells (Figure 6.15). The average number of γ-H2AX foci per cell in TPP-AuNP-treated PC3 cells was 2.8, with only 7.1% of cells not displaying a single focus. The level of DNA damage was not significantly higher in this population compared to untreated cells exposed to the same dose of radiation which despite presenting a higher foci number (3.5 per cell) showed a higher percentage of γ-H2AX-negative cells (19.8%) (Figure 6.15). In LNCaP cells, there were no significant differences in the number of γ-H2AX foci or the percentage of γ-H2AX-positive cells between untreated (2.8, 73.1%) and TPP-AuNP-treated (3.0, 81.6%) cells (Figure 6.15).

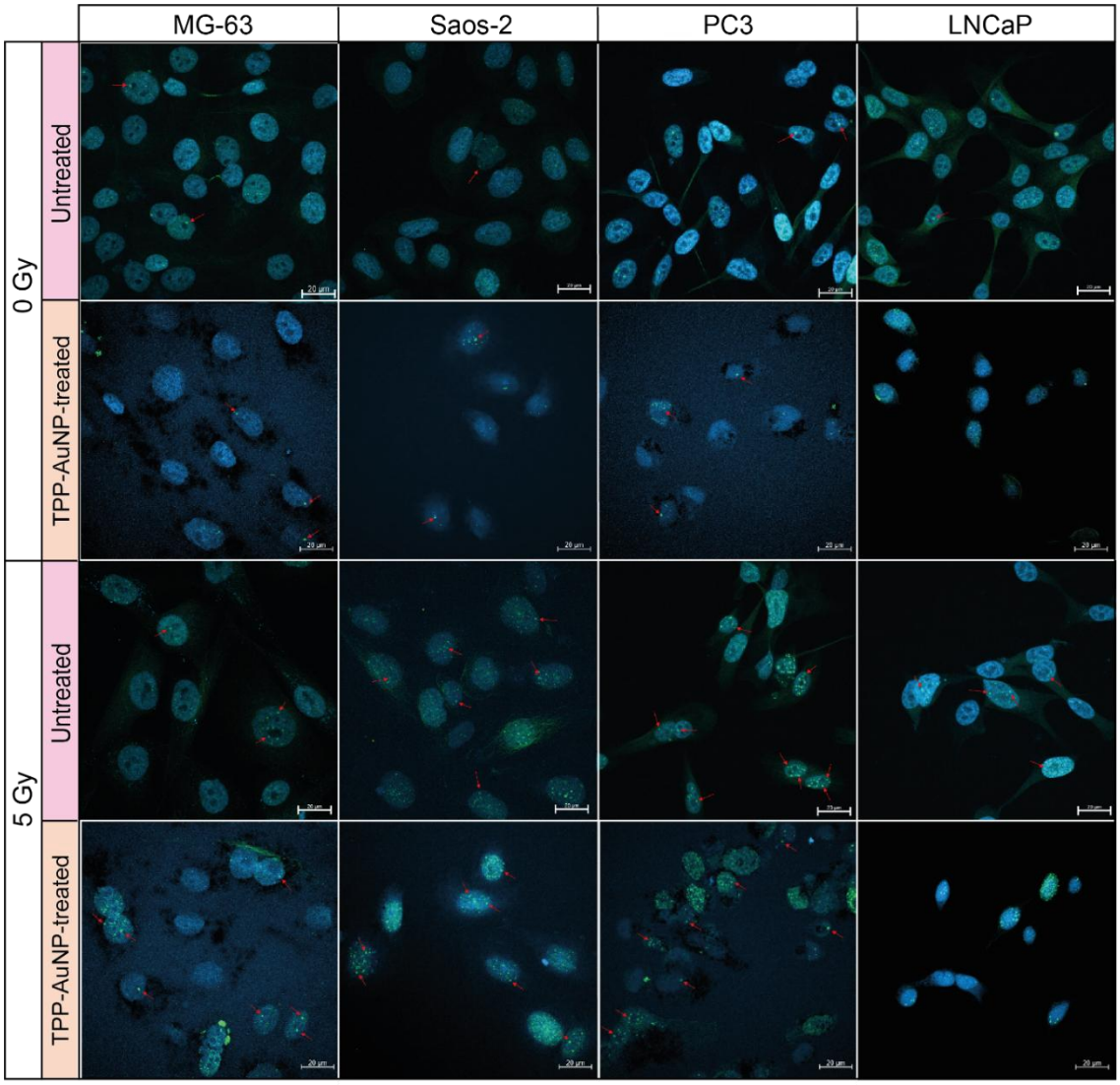

Figure 6.14 - Confocal images of γ-H2AX detection in TPP-AuNP-treated human osteosarcoma and prostate adenocarcinoma cell line. Cells were stained with an anti-Human Histone H2AX [p Ser139] primary antibody, AlexaFluor™ 488 secondary antibody (green) and counterstained with DAPI (blue). Images show an increase in the number of H2AX foci (red arrows) in cells treated with 5Gy of ionising radiation, compared to untreated cells. The dark shadows represent the clustering of TPP-AuNPs, whose absorbance spectrum is between ≈450nm and ≈550nm. Zeiss LSM 800 confocal microscope, 40x objective, Z-stack of DAPI and AF488 channels. Scale bar represents 20μm.

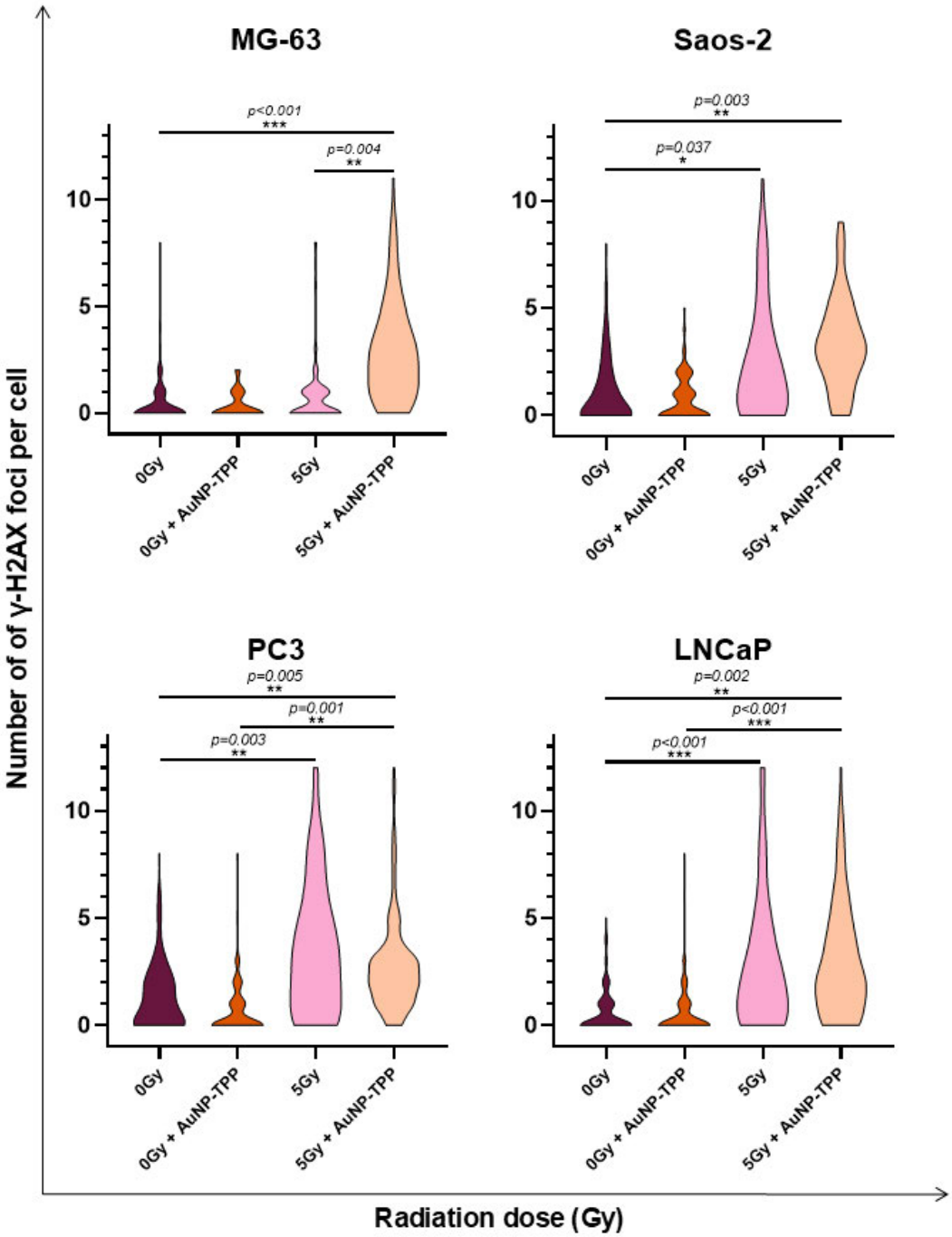

Figure 6.15 - Number of γ-H2AX foci in TPP-AuNP-treated cells 24h following ionising radiation. All cell lines show an increase in DNA damage following radiation, translated by an increased number of H2AX foci. When comparing TPP-AuNP-treated to untreated cells, there is a significant increase in the average number of foci in all cell lines apart from LNCaP. Violin plots, Kruskal-Wallis with Dunn's multiple comparisons. Statistical significance calculated as *p* value, with a confidence level of 95%. (*P<0.05) based on the means of 3 repeats.

6.2.8. TEM imaging of TPP-AuNPs and TPP-AuNP-treated cells.

To assess cellular uptake and intracellular localization of TPP-modified gold nanoparticles, TEM images were captured (Appendix L). The TEM work presented in this chapter was performed by Dr Christopher Hill at the University of Sheffield. Due to sample availability and time constraints, only PC3 monolayer cultures were imaged and used as a representative example. Results show that cells are successfully internalising TPP-AuNPs, with the majority localised in small intracellular vesicles of size range ~300-600nm. The images provided did not show accumulation of TPP-AuNPs in the cell's mitochondria.

6.3. Discussion

6.3.1. Uptake and localisation of TPP-AuNPs in 3D cell culture models.

LA-ICP-MS results demonstrated that while in OS and LNCaP spheroids, AuNPs tended to accumulate in the outer area of the MCTS, with lower concentrations in the core, in PC3 TPP-tagged gold nanoparticles were evenly distributed. As mentioned in previous chapters, this might be due to the tendency these cells have to aggregate more tightly than PC3, which form looser aggregated, allowing easier penetration of nanoparticles. Moreover, despite the smaller size of TPP-AuNPs (5nm), these tend to cluster together, a phenomenon previously described in literature and confirmed by TEM imaging of Figure 6.19 (Dheyab et al., 2022; Pham-Nguyen et al., 2022). The clustering of TPP-AuNPs effectively forms larger constructs, possibly complicating their penetration within sturdier spheroids such as MG-63, Saos-2 and LNCaP.

6.3.2. Intracellular localisation of TPP-AuNP

TEM imaging of PC3 cells confirmed cellular internalisation of TPP-AuNPs, with the highest concentrations of nanoparticles observed in vesicles. In higher magnification images it possible to observe that TPP-coated nanoparticles are encapsulated by single and double membrane, but mitochondrial accumulation was not confirmed since the folded inner membrane of the organelle was not identified. The accumulation of TPP-AuNPs in intracellular vesicles has been previously described in literature. For instance, Chen (2014) demonstrated that treating PC3 cells with 5nm TPP-AuNPs leads to their preferential accumulation in single and double membrane vesicles/organelles, with mitochondrial localisation only being confirmed through uranyl acetate and lead citrate staining (Chen, 2014).

6.3.3. Viability of TPP-AuNP treated cells cultured in 2D and exposed to ionising radiation.

Even though mitochondrial targeting was not confirmed, cellular internalisation was successful. The results obtained from clonogenic assays confirm the hypothesis that treating cells with TPP-AuNPs leads to a radio-sensitising effect, with nanoparticle-treatment producing dose enhancement factors of 7, 8, 29 and 79, in MG-63, Saos-2, PC3, and LNCaP cells, respectively. Assuming that the double-membrane organelles where AuNP accumulated were, in fact,

mitochondria, this radio-sensitising effect could be arising from mitochondrial membrane disruption and release of cytochrome *c*, which binds to Apaf-1 (apoptotic protease activating factor 1), assembling the apoptosome. This platform activates caspase-9, which in turn activates caspase-3, leading to apoptosis. A study by Li et al. (2018) demonstrated that irradiated cells treated with TPP-AuNPs present significantly increased levels of caspase-3 activity, which can result in mitochondrial ETC destruction and regeneration of ROS, inducing a domino effect (Li et al., 2018).

If the membranous vesicles where TPP-AuNPs accumulated were not mitochondria, this significant increase in cell viability loss could also be explained by the radio-sensitising properties of gold nanoparticles, similar to what was observed in chapter 4, when cells were treated with undecorated AuNPs. The higher magnitude of the effect produced by TPP-AuNP could be due to the higher intracellular concentration, as TEM images showed a higher uptake of 5nm TPP-AuNP in comparison to 50nm uncoated nanoparticles. Moreover, it is important to note that while TPP-AuNP treatment did not produce acute cytotoxic effects, clonogenic assay results demonstrated that cells treated with TPP-coated AuNPs presented a reduction in proliferation, even in the absence of radiation exposure. Therefore, it is possible to assume the nanoparticles themselves are affecting cell viability. It has been previously shown that smaller gold nanoparticles can inhibit cell proliferation, as demonstrated in a study by Liu at el. (2014), where the proliferation of A549 lung cancer cells was inhibited when incubated with 5nm AuNP. Additionally, gold nanoparticle treatment also promoted apoptosis and cell cycle arrest. Gold nanoparticles have also been shown to induce cleavage of cytoskeletal proteins and endoplasmic reticulum stress, inducing to the release of Ca^{2+} stores and generalised autolysis (Arvizo et al., 2010; Noël et al., 2016).

6.3.4. Viability of 3D cell models treated with TPP-AuNPs and exposed to γ-radiation

Results obtained from diameter measurements of colonies grown in alginate spheres revealed that TPP-AuNP treatment did not produce a radiosensitising effect, with AuNP-treated colonies of some cell lines being larger than their untreated counterparts. Considering the highly sensitising effect observed in two-dimensions, these results were unexpected. However, when evaluating the acute effect TPP-coated gold nanoparticles had on irradiated alginate spheres, it was

possible to observe that TPP-AuNP treatment produced an increase in immediate cell death. In light of these results, it is possible to infer that while AuNP treatment sensitises some cells, the more resistant clones – or cells were TPP-AuNP uptake was inefficient – continued to proliferate, leading to the growth of larger colonies. As previously mentioned, the alginate matrix can be impacting AuNP diffusion and cellular uptake, and considering TPP moieties have a positive charge – property that allows for their accumulation in the mitochondria – it is possible that TPP-AuNPs could be sequestered in the matrix, explaining the lower counts of ^{197}Au observed in LA-ICP-MS analysis.

Acute sensitivity of TPP-AuNP treated multicellular spheroids was also evaluated, and the results of this assay revealed phosphonium gold nanoparticles produced a radio-sensitising effect in osteosarcoma spheroids. Moreover, even in spheroids where radiosensitisation was not observed, i.e. PC3 and LNCaP MCTS, structural differences were observed, with spheroid integrity being compromised. These are important findings meaning TPP-AuNP treating could be priming these three-dimensional structures for radiation-induced damage. One way to prove this hypothesis would be irradiation with fractioned dosing which, as previously discussed, could potentially improve cell killing.

6.3.5. Cell cycle distribution of TPP-AuNP treated monolayer, alginate and MCTS cultures.

Following irradiation, the cell cycle distribution of 2D and 3D cell models treated with TPP-tagged gold nanoparticles was investigated. Due to time constraints, this experiment was only carried out once, making statistical analysis impossible. Nonetheless, preliminary data showed that TPP-AuNPs enhanced the effects of radiation in MG-63 cells, with an observable decrease of the G0/1 population and concomitant increase of the percentage of cells in the G2/M stage. In contrast, the population of TPP-AuNP-treated LNCaP cells increased in G0/1 and decreased in G2/M. This difference in response to DNA damage could be explained by the p53 status of both of these cell lines, previously detailed in section 4.3.4. of this thesis. In Saos-2 and PC3, no observable differences in cell cycle distribution were detected between TPP-AuNP-treated and untreated cells. In both alginate spheres and MCTS, TPP-AuNPs also failed to produce any differences in cell cycle distribution.

6.3.6. Intracellular localisation of γ-H2AX foci in TPP-AuNP-treated cells.

The amount of radiation-induced damage in TPP-AuNP-treated cells was evaluated by localisation of γ-H2AX foci following irradiation with a 5 Gy dose. These results showed that the average number of foci per cell was significantly higher in all cell lines, when compared to their untreated counterparts, following radiation exposure. These results align with the outcomes of the clonogenic assays, where a significantly radio-sensitising effect of these nanoparticles was observed. These results are corroborated by previous studies using TPP-coated AuNPs to radio-sensitise cancer cells as all confirm an increase in DNA damage, demonstrated by a significantly higher amount of γ-H2AX foci, correlated with an increase of intracellular ROS (Fang et al., 2017; Li et al., 2018; Zhao et al., 2022). It is also important to note that even though a cytotoxic effect of TPP-AuNP was observed, demonstrated by the lower proliferation rate of TPP-AuNP treated cells compared to their untreated counterparts, in the absence of radiation exposure, the amount of DNA damage observed in TPP-AuNP treated cells was similar to the levels seen in untreated cultures. Therefore, it is possible to infer that the cytotoxicity of these nanoparticles is due to mechanisms unrelated to nuclear DNA damage, such as mitochondrial stress and membrane disruption, promoting metabolic imbalance (Bhatti et al., 2017; Zhao et al., 2022); increase in localised ROS which could trigger endoplasmic reticulum stress, leading to an accumulation of misfolded proteins which could in turn enhance apoptotic signalling (Cao & Kaufman, 2014); or cell cycle arrest initiated by mitochondrial dysfunction (Moiseeva et al., 2009) – it is possible to appreciate minor observable shifts in cell cycle distribution of TPP-AuNP-treated PC3 and LNCaP cells that were not exposed to radiation, which could support this hypothesis.

6.4. Conclusion

The aim of this chapter was to assess the radio-sensitising potential of non-functionalised gold nanoparticles in 2D and 3D cell models of human prostate adenocarcinoma and osteosarcoma cell lines. These findings show that in monolayer cultures, TPP-AuNPs effectively enhance radiosensitivity treatment, as demonstrated by a loss in proliferative ability, cell cycle disruption and increased DNA damage. Therefore, the findings of this study offer exciting insights for the use of TPP-functionalised gold nanoparticles as an agent to improve radio-sensitivity of cancer cells: on one hand, due to the inherent radio-sensitising properties of gold nanoparticles, these constructs are able to amplify

radiation-induced direct or indirect damage; additionally, by effectively targeting the mitochondria, TPP-AuNPs can not only enhance the production of localised ROS, ultimately disrupting mitochondrial functions, leading to apoptosis, but also trigger ROS diffusion to other organelles, triggering global oxidative stress. The natural cell's defences such as superoxide dismutase-2, glutathione, and catalase enzyme, which usually act as ROS scavengers to maintain redox balance are often upregulated in cancer cells, allowing them to survive under oxidative stress, contributing to radiation-resistant (Wu et al., 2019). By treating the cells with TPP-AuNPs it is possible to circumvent this – through introducing an overwhelming amount of ROS that the cells cannot neutralise this will inevitably lead to cell death. In three-dimensional platforms, an acute radio-sensitising effect was observed, not only in cell viability loss but also in spheroid integrity, which suggests that repeating this study with fractioned doses could be beneficial as it would limit the time cancer cells have to recover from DNA damage.

Overall, the results of this study have confirmed the potential of TPP-coated gold nanoparticles as promising radiosensitisers. Table 6.2 summarises the results obtained from treatment with undecorated and TPP-tagged gold nanoparticles.

Table 6.2 – Summary of the results obtained from treatment with undecorated and TPP-functionalised gold nanoparticles.

				Compared to 0 Gy	Compared to RT only	
Cell line	2D/3D	Assay		RT	RT+ AuNP	RT+TPP-AuNP
MG-63	2D	Clonogenic assay		↓ (*p<0.001)*	↓ (*p=0.044)* -DEF=3.4	↑ (*p=0.004) DEF=7.1*
		Cell cycle	% G0/1	↓ (ns)	↓ (n=1)	↓ (n=1)
			% S	↓ (ns)	↓ (n=1)	= (n=1)
			% G2/M	↑ (*p=0.037)*	↑ (n=1)	↑ (n=1)
		γ-H2AX foci/cell		↑ (*p=0.003)*	↑ (*p<0.001)*	↑ (*p<0.001)*
	Alginate spheres	Colony diameter		↓ (*p=0.006)*	↑ (*ns)*	↑ (*ns)*
		Acute viability		=	↓ (*p<0.001)*	↓ (*p=0.009)*
		Cell cycle	% G0/1	↓ (n=1)	↑ (n=1)	↓ (n=1)
			% S	↓ (n=1)	= (n=1)	= (n=1)
			% G2/M	↑ (n=1)	↓ (n=1)	↑ (n=1)
	MCTS	Acute viability		=	↓ (*p=0.005)*	↓ (*p=0.009)*
		Cell cycle	% G0/1	= (n=1)	= (n=1)	= (n=1)
			% S	= (n=1)	= (n=1)	= (n=1)
			% G2/M	= (n=1)	= (n=1)	= (n=1)
Saos-2	2D	Clonogenic assay		↓ (*p<0.001)*	↓ (ns) DEF=2.6	↓ (*p<0.001)* DEF = 9.8
		Cell cycle	% G0/1	↓ (*p<0.001)*	↓ (n=1)	= (n=1)
			% S	=	↓ (n=1)	= (n=1)
			% G2/M	↑ (*p<0.001)*	↑ (n=1)	= (n=1)
		γ-H2AX foci/cell		↑ (*p<0.001)*	↑ (*p<0.001)*	↑ (*p<0.001)*
	Alginate spheres	Colony diameter		↓ (*p=0.009)*	↑ (*ns)*	↓ (*ns)*
		Acute viability		↓ (*p=0.010)*	↓ (*p=0.007)*	↓ (*p=0.002)*
		Cell cycle	% G0/1	↓ (n=1)		= (n=1)
			% S	= (n=1)		= (n=1)
			% G2/M	↑ (n=1)		= (n=1)
	MCTS	Acute viability		=	↓ (*p<0.001)*	↓ (*p<0.001)*
		Cell cycle	% G0/1	↓ (n=1)	↑ (n=1)	= (n=1)
			% S	= (n=1)	↓ (n=1)	= (n=1)
			% G2/M	↑ (n=1)	↓ (n=1)	= (n=1)
PC3	2D	Clonogenic assay		↓ (*p<0.001)*	↓ (ns) DEF=1.7	↓ (*ns)* DEF = 1.2

		Cell cycle	% G0/1	↓ (*p<0.001*)	↓ (n=1)	= (n=1)
			% S	=	↓ (n=1)	= (n=1)
			% G2/M	↑ (*p<0.001*)	↑ (n=1)	= (n=1)
		γ-H2AX foci/cell		↑ (*p<0.001*)	↓ (ns)	↓ (ns)
	Alginate spheres	Colony diameter		↓ (*p=0.006*)	=	↓ (*p<0.001*)
		Acute viability		=	=	↓ (*p=0.001*) DEF = 29
		Cell cycle	% G0/1	↑ (n=1)	↓ (n=1)	= (n=1)
			% S	↓ (n=1)	↑ (n=1)	= (n=1)
			% G2/M	= (n=1)	= (n=1)	= (n=1)
	MCTS	Acute viability		=	=	=
		Cell cycle	% G0/1	= (n=1)	↓ (n=1)	= (n=1)
			% S	= (n=1)	↑ (n=1)	= (n=1)
			% G2/M	= (n=1)	↑ (n=1)	= (n=1)
LNCaP	2D	Clonogenic assay		↓ (*p<0.001*)	↓ (ns) DEF=1.8	↓ (*p<0.001*) DEF = 79
		Cell cycle	% G0/1	↓ (*ns*)	↑ (n=1)	↑ (n=1)
			% S	=	↓ (n=1)	= (n=1)
			% G2/M	↑ (*ns*)	↓ (n=1)	↓ (n=1)
		γ-H2AX foci/cell		↑ (*p<0.001*)	↑ (*ns*)	↓ (*p<0.001*)
	Alginate spheres	Colony diameter		↓ (*p=0.006*)	↓ (ns) DEF=1.7	↑ (*ns*)
		Acute viability		=	=	↓ (*p=0.015*)
		Cell cycle	% G0/1			
			% S			
			% G2/M			
	MCTS	Acute viability		=	=	=
		Cell cycle	% G0/1	↓ (n=1)	= (n=1)	= (n=1)
			% S	= (n=1)	= (n=1)	= (n=1)
			% G2/M	↑ (n=1)	↑ (n=1)	= (n=1)

Chapter 7. Final Considerations

The findings of this study offer exciting insights for the use of gold nanoparticles as radiosensitising agents. I demonstrated that the use of these agents can successfully amplify radiation-induced damage, increase the levels of cell death, and most importantly, sensitise inherently radio-resistant cell lines to radiation exposure, an outcome that could potentially lead to new advances on the therapeutic approaches of these types of tumours. It is important to note that the lack of research using three-dimensional platforms as models of tumoral response to AuNP treatment in combination with radiotherapy is still incredibly scarce. While the outcomes of this study contribute with knowledge otherwise inexistent, further work is needed to better understand the behaviour of these models and bridge the gap between *in vitro* and *in vivo* studies.

Prior to studying the effect of gold nanoparticles as radiosensitising agents, I aimed to determine the baseline response to irradiation of both 2D and 3D models to better understand differences in sensitivity as well as how distinct 3D cultures behave. The results of this thesis showed that, as previously described in literature, 3D models present significantly higher resistance to radiation exposure. To better investigate and compare cellular responses between 2D and 3D I used a three-dimensional clonogenic-like model that allowed us to better understand the prolonged effects of radiation exposure in colonies grown in an alginate matrix. Additionally, I have identified that cells grown in alginate spheres and multicellular tumour spheroids behave and respond differently to stress, an important finding that further addresses the intrinsic variability of cancer cells and how they adapt to different environments. Growth of cancer cells in 3D cell culture imparts certain stresses with hypoxia, low glucose and increased ROS production being key features. To overcome the ROS aspect of 3D cell culture, cells can adapt by expressing Nuclear Factor Erythroid 2-Related Factor 2 (Nrf2), which is the master regulator of the antioxidant response. Using a CRISP-R screen, Takahashi et al. (2020) demonstrated that spheroid growth was dependant on Nrf2 expression, in that Nrf2-null clones did not develop 3D structures when grown from isogenic cell clones in Matrigel, a model comparable to the alginate model (Takahashi et al., 2020). This is very different to aggregation 3D cell culture models such as MCTS and hanging drop, where cancer cells are forced together for short periods of time. In clonal growth sphere assays such as alginate and

Matrigel sphere assays, cells lacking Nrf2 do not grow beyond very small spheroid sizes, presumably as a result of excessive ROS impacting on survival, which would normally be removed via Nrf2-driven expression of antioxidant gene expression (such as glutathione-S transferase). This raises the possibility that although 3D cell cultures are more resistant to irradiation (and other stresses) due to environment-induced Nrf2 expression, different 3D cell culture models might respond differently to ROS derived from irradiation in cell culture (Kamble et al., 2021; Qin et al., 2021; Takahashi et al., 2020). In the current study, there were differences between alginate and MCTS responses to irradiation, which also differed depending on AuNP treatment. It is possible that alginate sphere formation might 'select' for intrinsically more ROS-insensitive cells than the unselected monolayer cell culture model. Equally, MCTS might induce considerable Nrf2 expression in the core of the spheroid but exhibit lower levels in the periphery. Whether Nrf2 is higher or lower in different 3D models has not been addressed but could explain differences between radio-responses between different 3D cell models, and Nrf2 is a good candidate for decreased radio-responses in 3D models over 2D cell culture.

Once the baseline response of 2D and 3D cell models was established, undecorated gold nanoparticles were utilised to radio-sensitise the cell models models. While in standard 2D cell culture all cell lines showed to be relatively sensitive, OS cells still presented a higher resistance, with 50% of cells being able to form proliferative colonies. Treating them with gold nanoparticles enhanced their sensitivity by a factor of 3, demonstrated significant reductions in proliferation, accompanied by increases in radiation-induced DNA damage, an exciting outcome that offers new possibilities for the treatment of these tumours. Additionally, the treatment with AuNPs allowed for the acute sensitisation of three-dimensional cultures. While this did not translate in prologued effects, potentially due to cancer cells being able to either repair the induced damage or proliferate regardless of it, creating resistant colonies, these findings show promise when it comes to the use of fractioned dosing – by repeating irradiation with consecutive doses, the cells continue to accumulate damage, which could potentially lead to higher levels of cell death. Moreover, combining a treatment with AuNPs with radiation exposure in fractioned doses, can lead to other mechanisms of priming cells to radiosensitivity. For instance, by altering the expression of microRNAs (miRNA) involved in regulating gene expression which

drives tumorigenesis and cancer progression, as shown by Soares et al. (2024). In this study, gold nanoparticle treatment and irradiation led to modulation of miRNA-106-5p and -541-3p, which heightened the radio-sensitivity of PC3 cells (Soares et al., 2024).

Considering the promising results of treatment with undecorated nanoparticles, I wanted to investigate if targeting them to the cell nucleus or the mitochondria would produce an increase in the radio-sensitising effect already observed with non-functionalised gold nanoparticles. Therefore, I started by treating the cell models previously used with nuclear-targeted nanoparticles. These were functionalised with an NLS peptide, to facilitate nuclear delivery. Unfortunately, I did not observe the desired effects, with NLS-AuNPs not affecting the radio-sensitivity of most models. In light of these results, I investigated intracellular location of the nanoparticles via TEM imaging, which showed that cellular internalisation was unsuccessful. Nevertheless, acute results in OS spheroids still demonstrated a sensitising effect, albeit lower than the one of undecorated nanoparticles, which were internalised by cells.

Finally, I investigated the radio-sensitising potential of mitochondrial-targeted nanoparticles, functionalised with a TPP molecule, known to selectively accumulate in the mitochondria due to negative membrane potential. The results here presented show that although mitochondrial localisation was not confirmed, cellular internalisation was successful. Following clonogenic assays, I determined that these smaller particles not only induced cytotoxicity to cancer cells, but also sensitised them to radiation, enhancing the efficiency of the doses used by a factor of 7, 10, 29, and 79 in MG-63, Saos-2, PC3 and LNCaP, respectively. Additionally, TPP-AuNP treatment significantly increased the number of γ-H2AX foci, showcasing their ability to enhance radiation-induced DNA damage. Treating 3D models with TPP-AuNP also increased their acute sensitivity to radiation, with higher amounts of cell death observed in both alginate spheres and multicellular tumour spheroids.

In conclusion, the outcomes of this study further confirm the radio-sensitising potential of gold nanoparticles, both with and without surface functionalisation. The intrinsic properties of gold nanoparticles, mainly their good biocompatibility, straightforward synthesis and high cross-section interaction with radiation, make them exciting aids for radiotherapy treatments, allowing delivery of lower doses for the same effect, while sparing the normal tissue surrounding the tumour site.

Furthermore, it is also important to highlight that these findings show promise in other areas of cancer treatment, as it is possible to combine the radio-sensitising properties of AuNPs with other agents that will further enhance the overall effectiveness of treatment. For instance, Silva et al. (2022) have shown that combining AuNP with substance P peptides – that target the neurokinin-1 receptor (NK1R), overexpressed in glioblastoma –, and using them as a carrier for radionuclides, allowed for pronounced radiobiological effects in U373 glioblastoma cells (Silva et al., 2022). In a similar fashion, a study by Bavelaar et al. (2021) demonstrated that functionalising AuNPs with radio-labelled oligonucleotides and telomerase inhibitors, produced a significant increase in DSBs and reduction in clonogenic survival of MDA-MB-435 breast cancer cells (Bavelaar et al., 2021).

In this study I have also shown that these radio-sensitising agents have the ability to sensitise known radio-resistant cell lines, creating possibilities of new therapeutic directions for tumours that otherwise have very limited options. All these advantages could ultimately lead to cancer treatment evolution and, hopefully, improvement of the quality of life of cancer patients.

7.1. Limitations of this study and future work.

The first limitation of this study was the lack of an in-house irradiator. As radiation exposure was the main stress inducer, having access to these type of facilities on campus would have facilitated experimental work: on one hand, it would have allowed the exploration of other 3D cell culture modes that, due to their fragile nature, could not withstand travel, e.g. the hanging drop model; additionally, it would have avoided the loss of samples, as many did not survive the travel-related stress, despite all precautions being taken (i.e. temperature maintenance during travel, avoiding excess movement, media loss and drying, etc.); and finally, it would have made the work more time efficient and less costly. The lack of an in-house irradiator also impeded the delivery of radiation treatments in fractioned doses, a method that would have been closer to clinical practice, as it would not have been feasible or practical to transport and treat multiple samples every day. However, I consider that it is important to test the radio-sensitisers used in this study in response to fractioned-dosing. The exciting findings in acute sensitivity suggest that a high radiosensitising effect could potentially be achieved if subsequent radiation doses were administered, preventing cancer cell mechanisms of evading apoptosis.

When comparing radio-responses between 2D and 3D cell models, the limitations lie of the lack of standardised methods to evaluate response to radiation exposure in three-dimensional platforms, and to compared them to the responses of monolayer cultures in a reliable manner. Therefore, I opted to use the alginate sphere model to try to achieve a colony formation assay in three-dimensions. Despite being a model that allows a more reliable comparison to clonogenic assays in 2D, the *gold standard* method of evaluating radio-responses in monolayer, the alginate model comes with its own limitations, mainly selection bias – due to the size of the models, it becomes impossible to determine number of colonies per sphere as well as measuring every single colony within a sphere. Even though I measured 150 colonies per bead, at random (in attempt to minimise this bias as much as possible), there is still an inherent skewness associated. For instance, if the percentage of colonies is reduced due to radiation-induced cell killing, resistant colonies will continue proliferating, increasing in size, which will inevitably condition the average diameter of colonies per bead. However, there is no unified method to determine colony proliferation in 3D and this method is, to the best of my knowledge, the closest way to achieve clonogenic assay-like results in three-dimensional platforms.

Regarding gold nanoparticle synthesis and functionalisation, I had planned to use AuNPs of the same size for every treatment, to allow for effective comparison of all treatments to be able to determine which gold functionalisation produced the highest sensitising effect. Unfortunately, that was not possible, as readily available uncoated 5nm nanoparticles come in highly diluted solutions and I could not centrifuge them at high enough speeds to allow for pellet formation. I also attempted to freeze dry them which led to clustering, a phenomenon I could not overcome and that stopped the AuNPs from being dispersed in solution again. Therefore, for future work, and even though some studies investigate the use of functionalised AuNPs without comparing them to non-functionalised gold responses, I believe it would be beneficial to always have an undecorated nanoparticle of the same size to directly compare to. Another limitation of this study was the repeatedly unsuccessful attempts to functionalise AuNPs with peptide ligands, which ultimately resulted in the purchase of readily available NLS-tagged AuNPs that, in hindsight, might not have been the best choice in terms of size and lack of a cell penetrating peptide, fact that I believe ultimately hindered cellular uptake and nuclear delivery.

Finally, the inability to access TEM facilities for the first two years of the project significantly impacted the results of this study, mainly when it comes to Chapter 5 results. When I began the experiments, the goal was to evaluate cellular uptake prior to any radiation exposure – this would confirm successful internalisation and allow us to modulate subsequent experiments depending on the results obtained. However, the TEM facilities at SHU were not accessible throughout most of the project, meaning I had to instead develop a method for AuNP localisation using instrumentation available, mainly LA-ICP-MSI, that while informing on gold presence, does not offer information about uptake and subcellular localisation. When our electron microscope was finally operational, I wash informed that I did not possess an ultra-microtome, making it impossible to conduct the analysis in-house, eventually having to opt to outsource this work. Unfortunately, this process was slow and TEM images were only authorised towards the end of the deadline, which not only limited the number of samples I could prepare and analyse, but also meant I had no additional time to order in new NLS-AuNP and repeat the experimental work. Thus, I believe further studies using NLS-AuNP are required, possibly using a second peptide, to facilitate endocytosis (e.g. RME or RGD) and TEM images of all cell lines would also be beneficial, as cellular uptake and nuclear delivery could be cell-dependent.

Finally, it would be necessary to complete the experimental panel, in the models and assays where time constraints did not permit a robust data analysis. Additionally, considering the exciting results obtained, I believe it would be advantageous to further investigate the radio-sensitising effects produced by AuNPs, for instance, measuring ROS production or investigating apoptosis markers, such as caspase-3. In the landscape of radio-biology research in three-dimensional *in vitro* platforms, further investigation of how different 3D models behave would be useful. Studying radio-resistance mechanisms and understanding how phenotypes change depending on 3D model of choice could offer important insights into how to make non-animal models resemble *in vivo* tumours in the most accurate possible manner, therefore improving the translation of *in vitro* research into clinic.

Chapter 8. References

Abdal Dayem, A., Hossain, M. K., Lee, S. B., Kim, K., Saha, S. K., Yang, G., Choi, H. Y., & Cho, S. (2017). The Role of Reactive Oxygen Species (ROS) in the Biological Activities of Metallic Nanoparticles. International Journal of Molecular Sciences, 18(1), 120. 10.3390/ijms18010120

Adamo, P., & Ladomery, M. R. (2016). The oncogene ERG: a key factor in prostate cancer. Oncogene, 35(4), 403–414. 10.1038/onc.2015.109

Aguilar Cosme, J. R., Gagui, D. C., Green, N. H., Bryant, H. E., & Claeyssens, F. (2021). In Vitro Low-Fluence Photodynamic Therapy Parameter Screening Using 3D Tumor Spheroids Shows that Fractionated Light Treatments Enhance Phototoxicity. ACS Biomaterials Science & Engineering, 7(11), 5078–5089. 10.1021/acsbiomaterials.1c00690

Ahmad Raus, R., Wan Nawawi, W. M. F., & Nasaruddin, R. R. (2021). Alginate and alginate composites for biomedical applications. Asian Journal of Pharmaceutical Sciences, 16(3), 280–306. 10.1016/j.ajps.2020.10.001

Ahmadi Kamalabadi, M., Neshastehriz, A., Ghaznavi, H., & Amini, S. M. (2022). Folate functionalized gold-coated magnetic nanoparticles effect in combined electroporation and radiation treatment of HPV-positive oropharyngeal cancer. Medical Oncology, 39(12), 196. 10.1007/s12032-022-01780-2

Ai, Y., Meng, Y., Yan, B., Zhou, Q., & Wang, X. (2024). The biochemical pathways of apoptotic, necroptotic, pyroptotic, and ferroptotic cell death. Molecular Cell, 84 https://www.cell.com/molecular-cell/pdf/S1097-2765(23)01017-1.pdf

Alberts, B., Johnson, A., Lewis, J., Raff, M., Roberts, K., & Walter, P. (2002). An Overview of the Cell Cycle. Molecular Biology of the Cell. 4th edition (). Garland Science.

Aldosari, F. M. M. (2022). Characterization of Labeled Gold Nanoparticles for Surface-Enhanced Raman Scattering. Molecules, 27(3), 892. 10.3390/molecules27030892

Alhussan, A., Jackson, N., Calisin, R., Morgan, J., Beckham, W., & Chithrani, D. B. (2023). Utilizing Gold Nanoparticles as Prospective Radiosensitizers in 3D Radioresistant Pancreatic Co-Culture Model. International Journal of Molecular Sciences, 24(15), 12523. 10.3390/ijms241512523

Ali, M. R. K., Wu, Y., Ghosh, D., Do, B. H., Chen, K., Dawson, M. R., Fang, N., Sulchek, T. A., & El-Sayed, M. A. (2017). Nuclear Membrane-Targeted Gold Nanoparticles Inhibit Cancer Cell Migration and Invasion. ACS Nano, 11(4), 3716–3726. 10.1021/acsnano.6b08345

Al-Wassiti, H. A., Thomas, D. R., Wagstaff, K. M., Fabb, S. A., Jans, D. A., Johnston, A. P., & Pouton, C. W. (2021). Adenovirus Terminal Protein Contains a Bipartite Nuclear Localisation Signal Essential for Its Import into the Nucleus. International Journal of Molecular Sciences, 22(7), 3310. 10.3390/ijms22073310

American Cancer Society. (2022, April 12,). Treatment of Breast Cancer Stages I-III. American Cancer Society. Retrieved Sep 18, 2024, from https://www.cancer.org/cancer/types/breast-cancer/treatment/treatment-of-breast-cancer-by-stage/treatment-of-breast-cancer-stages-i-iii.html

Amin, A. R. M. R., Karpowicz, P. A., Carey, T. E., Arbiser, J., Nahta, R., Chen, Z. G., Dong, J., Kucuk, O., Khan, G. N., Huang, G. S., Mi, S., Lee, H., Reichrath, J., Honoki, K., Georgakilas, A. G., Amedei, A., Amin, A., Helferich, B., Boosani, C. S., . . . Shin, D. M. (2015). Evasion of anti-growth signaling: a key step in tumorigenesis and potential target for treatment and prophylaxis by natural compounds. Seminars in Cancer Biology, 35 Suppl, S55–S77. 10.1016/j.semcancer.2015.02.005

Antonelli, F. (2023). 3D Cell Models in Radiobiology: Improving the Predictive Value of In Vitro Research. International Journal of Molecular Sciences, 24(13), 10620. 10.3390/ijms241310620

Arakawa, A., Jakubowski, N., Flemig, S., Koellensperger, G., Rusz, M., Iwahata, D., Traub, H., & Hirata, T. (2019). High-resolution laser ablation inductively coupled plasma mass spectrometry used to study transport of metallic nanoparticles through collagen-rich microstructures in fibroblast multicellular spheroids. Analytical and Bioanalytical Chemistry, 411(16), 3497–3506. 10.1007/s00216-019-01827-w

Arcos Rosero, W. A., Bueno Barbezan, A., Daruich de Souza, C., & Chuery Martins Rostelato, M. E. (2024). Review of Advances in Coating and Functionalization of Gold Nanoparticles: From Theory to Biomedical Application. Pharmaceutics, 16(2), 255. 10.3390/pharmaceutics16020255

Arvizo, R. R., Miranda, O. R., Thompson, M. A., Pabelick, C. M., Bhattacharya, R., Robertson, J. D., Rotello, V. M., Prakash, Y. S., & Mukherjee, P. (2010). Effect of nanoparticle surface charge at the plasma membrane and beyond. Nano Letters, 10(7), 2543–2548. 10.1021/nl101140t

Auger, P. (1975). The Auger effect. Surface Science, 48(1), 1–8. 10.1016/0039-6028(75)90306-4

Babu, A., Muralidharan, R., Amreddy, N., Mehta, M., Munshi, A., & Ramesh, R. (2016). Nanoparticles for siRNA-Based Gene Silencing in Tumor Therapy. IEEE Transactions on Nanobioscience, 15(8), 849–863. 10.1109/TNB.2016.2621730

Bai, X., Wang, Y., Song, Z., Feng, Y., Chen, Y., Zhang, D., & Feng, L. (2020). The Basic Properties of Gold Nanoparticles and their Applications in Tumor Diagnosis and Treatment. International Journal of Molecular Sciences, 21(7), 2480. 10.3390/ijms21072480

Bajracharya, R., Song, J. G., Patil, B. R., Lee, S. H., Noh, H., Kim, D., Kim, G., Seo, S., Park, J., Jeong, S. H., Lee, C. H., & Han, H. (2022). Functional ligands for improving anticancer drug therapy: current status and applications to drug delivery systems. Drug Delivery, 29(1), 1959–1970. 10.1080/10717544.2022.2089296

Bardane, A., Maalej, N., Chakir, E. M., & Ibrahmi, E. M. A. (2024). Gold nanoparticle effect on dose and DNA damage enhancement in the vicinity of gold nanoparticles. Nuclear Analysis, 3(4), 100126. 10.1016/j.nucana.2024.100126

Barrett, A., Dobbs, J., Morris, S., & Roques, T. (2009). Principles of Radiotherapy Planning. In G. Jamieson, E. Senior & J. Silman (Eds.), Practical Radiotherapy Planning, 4th Ed. (pp. 9–31). Hodder Arnold.

Baskar, R., Lee, K. A., Yeo, R., & Yeoh, K. (2012). Cancer and Radiation Therapy: Current Advances and Future Directions. International Journal of Medical Sciences, 9(3), 193–199. 10.7150/ijms.3635

Bavelaar, B. M., Song, L., Jackson, M. R., Able, S., Tietz, O., Skaripa-Koukelli, I., Waghorn, P. A., Gill, M. R., Carlisle, R. C., Tarsounas, M., & Vallis, K. A. (2021). Oligonucleotide-Functionalized Gold Nanoparticles

Baylin, S. B., & Jones, P. A. (2016). Epigenetic Determinants of Cancer. Cold Spring Harbor Perspectives in Biology, 8(9), a019505. 10.1101/cshperspect.a019505

Berardi, R., Morgese, F., Rinaldi, S., Torniai, M., Mentrasti, G., Scortichini, L., & Giampieri, R. (2020). Benefits and Limitations of a Multidisciplinary Approach in Cancer Patient Management. Cancer Management and Research, 12, 9363–9374. 10.2147/CMAR.S220976

Berben, L., Floris, G., Wildiers, H., & Hatse, S. (2021). Cancer and Aging: Two Tightly Interconnected Biological Processes. Cancers, 13(6), 1400. 10.3390/cancers13061400

Berry, C. C., de la Fuente, J. M., Mullin, M., Chu, S. W. L., & Curtis, A. S. G. (2007). Nuclear localization of HIV-1 tat functionalized gold nanoparticles. IEEE Transactions on Nanobioscience, 6(4), 262–269. 10.1109/tnb.2007.908973

Bhatt, A. P., Redinbo, M. R., & Bultman, S. J. (2017). The Role of the Microbiome in Cancer Development and Therapy. CA: A Cancer Journal for Clinicians, 67(4), 326–344. 10.3322/caac.21398

Bhatti, J. S., Bhatti, G. K., & Reddy, P. H. (2017). Mitochondrial dysfunction and oxidative stress in metabolic disorders - A Step towards mitochondria based therapeutic strategies. Biochimica Et Biophysica Acta, 1863(5), 1066–1077. 10.1016/j.bbadis.2016.11.010

Blake, P. (2007). Clinical Introduction to Brachytherapy. In P. Mayles, A. Nahum & J. Rosenwald (Eds.), Handbook of Radiotherapy Physics (pp. 1093–1115). Taylor & Francis.

Blanpain, C., Mohrin, M., Sotiropoulou, P. A., & Passegué, E. (2011). DNA-Damage Response in Tissue-Specific and Cancer Stem Cells. Cell Stem Cell, 8(1), 16–29. 10.1016/j.stem.2010.12.012

Bleaney, C. W., Abdelaal, H., Reardon, M., Anandadas, C., Hoskin, P., Choudhury, A., & Forker, L. (2024). Clinical Biomarkers of Tumour Radiosensitivity and Predicting Benefit from Radiotherapy: A Systematic Review. Cancers, 16(10), 1942. 10.3390/cancers16101942

Bodgi, L., Bahmad, H. F., Araji, T., Al Choboq, J., Bou-Gharios, J., Cheaito, K., Zeidan, Y. H., Eid, T., Geara, F., & Abou-Kheir, W. (2019). Assessing

Radiosensitivity of Bladder Cancer in vitro: A 2D vs. 3D Approach. Frontiers in Oncology, 9, 153. 10.3389/fonc.2019.00153

Bonnet, D., & Dick, J. E. (1997). Human acute myeloid leukemia is organized as a hierarchy that originates from a primitive hematopoietic cell. Nature Medicine, 3(7), 730–737. 10.1038/nm0797-730

Borrego-Soto, G., Ortiz-López, R., & Rojas-Martínez, A. (2015). Ionizing radiation-induced DNA injury and damage detection in patients

Boulefour, W., Rowinski, E., Louati, S., Sotton, S., Wozny, A., Moreno-Acosta, P., Mery, B., Rodriguez-Lafrasse, C., & Magne, N. (2021). A Review of the Role of Hypoxia in Radioresistance in Cancer Therapy. Medical Science Monitor : International Medical Journal of Experimental and Clinical Research, 27, e934116–7. 10.12659/MSM.934116

Brierley, J., Gospodarowicz, M., & O'Sullivan, B. (2016). The principles of cancer staging. Ecancermedicalscience, 10, ed61. 10.3332/ecancer.2016.ed61

Bromma, K., Alhussan, A., Perez, M. M., Howard, P., Beckham, W., & Chithrani, D. B. (2021). Three-Dimensional Tumor Spheroids as a Tool for Reliable Investigation of Combined Gold Nanoparticle and Docetaxel Treatment. Cancers, 13(6), 1465. 10.3390/cancers13061465

Bromma, K., Beckham, W., & Chithrani, D. B. (2023). Utilizing two-dimensional monolayer and three-dimensional spheroids to enhance radiotherapeutic potential by combining gold nanoparticles and docetaxel. Cancer Nanotechnology, 14(1), 80. 10.1186/s12645-023-00231-5

Bromma, K., Cicon, L., Beckham, W., & Chithrani, D. B. (2020). Gold nanoparticle mediated radiation response among key cell components of the tumour microenvironment for the advancement of cancer nanotechnology. Scientific Reports, 10(1), 12096. 10.1038/s41598-020-68994-0

Brown, G. (2021). Oncogenes, Proto-Oncogenes, and Lineage Restriction of Cancer Stem Cells. International Journal of Molecular Sciences, 22(18), 9667. 10.3390/ijms22189667

Brüningk, S. C., Rivens, I., Box, C., Oelfke, U., & ter Haar, G. (2020). 3D tumour spheroids for the prediction of the effects of radiation and hyperthermia treatments. Scientific Reports, 10, 1653. 10.1038/s41598-020-58569-4

Bryant, H. E., Schultz, N., Thomas, H. D., Parker, K. M., Flower, D., Lopez, E., Kyle, S., Meuth, M., Curtin, N. J., & Helleday, T. (2005). Specific killing of BRCA2-deficient tumours with inhibitors of poly(ADP-ribose) polymerase. Nature, 434(7035), 913–917. 10.1038/nature03443

Burlec, A. F., Corciova, A., Boev, M., Batir-Marin, D., Mircea, C., Cioanca, O., Danila, G., Danila, M., Bucur, A. F., & Hancianu, M. (2023). Current Overview of Metal Nanoparticles' Synthesis, Characterization, and Biomedical Applications, with a Focus on Silver and Gold Nanoparticles. Pharmaceuticals (Basel, Switzerland), 16(10), 1410. 10.3390/ph16101410

Cancer Research, U. K. (2014, -10-29T11:54:33+00:00). Stages of cancer. Retrieved Aug 16, 2024, from https://www.cancerresearchuk.org/about-cancer/what-is-cancer/stages-of-cancer

Cancer Research, U. K. (2021, March 17,). Treatment options for bone cancer. Cancer Research UK. Retrieved Sep 18, 2024, from https://www.cancerresearchuk.org/about-cancer/bone-cancer/treatment/treatment-options-for-bone-cancer

Cancer Research, U. K. (2022a, Grade Groups of prostate cancer. Retrieved Aug 16, 2024, from https://www.cancerresearchuk.org/about-cancer/prostate-cancer/stages/grades

Cancer Research, U. K. (2022b, July 05,). Treatment options for prostate cancer. Cancer Research UK. Retrieved Sep 18, 2024, from https://www.cancerresearchuk.org/about-cancer/prostate-cancer/treatment/decisions-about-your-treatment

Cancer Research, U. K. (2023, July 11,). Treatment for breast cancer. Cancer Research UK. Retrieved Sep 18, 2024, from https://www.cancerresearchuk.org/about-cancer/breast-cancer/treatment

Cao, S. S., & Kaufman, R. J. (2014). Endoplasmic Reticulum Stress and Oxidative Stress in Cell Fate Decision and Human Disease. Antioxidants & Redox Signaling, 21(3), 396–413. 10.1089/ars.2014.5851

Capra, M., Nuciforo, P. G., Confalonieri, S., Quarto, M., Bianchi, M., Nebuloni, M., Boldorini, R., Pallotti, F., Viale, G., Gishizky, M. L., Draetta, G. F., & Di Fiore, P. P. (2006). Frequent Alterations in the Expression of Serine/Threonine Kinases

in Human Cancers. Cancer Research, 66(16), 8147–8154. 10.1158/0008-5472.CAN-05-3489

Carbone, A. (2020). Cancer Classification at the Crossroads. Cancers, 12(4), 980. 10.3390/cancers12040980

Carlos-Reyes, A., Muñiz-Lino, M. A., Romero-Garcia, S., López-Camarillo, C., & Hernández-de la Cruz, O. N. (2021). Biological Adaptations of Tumor Cells to Radiation Therapy. Frontiers in Oncology, 1110.3389/fonc.2021.718636

Carter, E. P., Roozitalab, R., Gibson, S. V., & Grose, R. P. (2021). Tumour microenvironment 3D-modelling: simplicity to complexity and back again. Trends in Cancer, 7(11), 1033–1046. 10.1016/j.trecan.2021.06.009

Casimiro, M. C., Crosariol, M., Loro, E., Li, Z., & Pestell, R. G. (2012). Cyclins and Cell Cycle Control in Cancer and Disease. Genes & Cancer, 3(11-12), 649–657. 10.1177/1947601913479022

Cendrowicz, E., Sas, Z., Bremer, E., & Rygiel, T. P. (2021). The Role of Macrophages in Cancer Development and Therapy. Cancers, 13(8), 1946. 10.3390/cancers13081946

Chadha, M. (2011). Breast Cancer. In J. J. Lu, & L. W. Brady (Eds.), Decision Making in Radiation Oncology, Volume 1 (pp. 207–260). Springer. 10.1007/978-3-642-13832-4

Chen, H. H. W., & Kuo, M. T. (2017). Improving radiotherapy in cancer treatment: Promises and challenges. Oncotarget, 8(37), 62742–62758. 10.18632/oncotarget.18409

Chen, J. (2016). The Cell-Cycle Arrest and Apoptotic Functions of p53 in Tumor Initiation and Progression. Cold Spring Harbor Perspectives in Medicine, 6(3), a026104. 10.1101/cshperspect.a026104

Chen, W., Wang, W., Xie, Z., Centurion, F., Sun, B., Paterson, D. J., Tsao, S. C., Chu, D., Shen, Y., Mao, G., & Gu, Z. (2024). Size-Dependent Penetration of Nanoparticles in Tumor Spheroids: A Multidimensional and Quantitative Study of Transcellular and Paracellular Pathways. Small (Weinheim an Der Bergstrasse, Germany), 20(8), e2304693–n/a. 10.1002/smll.202304693

Chen, X., Ma, N., Zhou, Z., Wang, Z., Hu, Q., Luo, J., Mei, X., Yang, Z., Zhang, L., Wang, X., Feng, Y., Yu, X., Ma, J., & Guo, X. (2017). Estrogen Receptor

Mediates the Radiosensitivity of Triple-Negative Breast Cancer Cells. Medical Science Monitor: International Medical Journal of Experimental and Clinical Research, 23, 2674–2683. 10.12659/msm.904810

Chen, Y. (2014). Phosphonium-Functionalised Gold Nanoparticles for Mitochondria Targeted Therapeutics (PhD). https://core.ac.uk/download/154423539.pdf

Chen, Y., Xianyu, Y., & Jiang, X. (2017). Surface Modification of Gold Nanoparticles with Small Molecules for Biochemical Analysis. Accounts of Chemical Research, 50(2), 310–319. 10.1021/acs.accounts.6b00506

Chen, Y., Xianyu, Y., Wu, J., Yin, B., & Jiang, X. (2016). Click Chemistry-Mediated Nanosensors for Biochemical Assays. Theranostics, 6(7), 969–985. 10.7150/thno.14856

Chen, Y., Yang, J., Fu, S., & Wu, J. (2020). Gold Nanoparticles as Radiosensitizers in Cancer Radiotherapy. International Journal of Nanomedicine, 15, 9407–9430. 10.2147/IJN.S272902

Chen, Z., Guan, D., Wang, Z., Li, X., Dong, S., Huang, J., & Zhou, W. (2023). Microbiota in cancer: molecular mechanisms and therapeutic interventions. MedComm, 4(6), e417. 10.1002/mco2.417

Chen, Z., Zhang, L., He, Y., & Li, Y. (2014). Sandwich-type Au-PEI/DNA/PEI-Dexa nanocomplex for nucleus-targeted gene delivery in vitro and in vivo. ACS Applied Materials & Interfaces, 6(16), 14196–14206. 10.1021/am503483w

Chial, H. (2008a). Proto-oncogenes to Oncogenes to Cancer. Nature Education, 1(1), 33. https://www.nature.com/scitable/topicpage/proto-oncogenes-to-oncogenes-to-cancer-883/

Chial, H. (2008b). Tumor Suppressor (TS) Genes and the Two-Hit Hypothesis. Nature Education, 1(1), 177. http://www.nature.com/scitable/topicpage/tumor-suppressor-ts-genes-and-the-two-887

Chino, F., Hijal, T., Pater, J. L. & Tweed, C. (2024, 19/01,). PDQ Breast Cancer Treatment. Bethesda, MD: National Cancer Institute. Retrieved Sep 18, 2024, from https://www.cancer.gov/types/breast/hp/breast-treatment-pdq

Chithrani, B. D., Ghazani, A. A., & Chan, W. C. W. (2006). Determining the Size and Shape Dependence of Gold Nanoparticle Uptake into Mammalian Cells. Nano Letters, 6(4), 662–668. 10.1021/nl052396o

Choi, B. J., Jung, K. O., Graves, E. E., & Pratx, G. (2018). A gold nanoparticle system for the enhancement of radiotherapy and simultaneous monitoring of reactive-oxygen-species formation. Nanotechnology, 29(50), 504001. 10.1088/1361-6528/aae272

Choi, W. H., & Cho, J. (2016). Evolving Clinical Cancer Radiotherapy: Concerns Regarding Normal Tissue Protection and Quality Assurance. Journal of Korean Medical Science, 31(Suppl 1), S75–S87. 10.3346/jkms.2016.31.S1.S75

Chu, X., Tian, W., Ning, J., Xiao, G., Zhou, Y., Wang, Z., Zhai, Z., Tanzhu, G., Yang, J., & Zhou, R. (2024). Cancer stem cells: advances in knowledge and implications for cancer therapy. Signal Transduction and Targeted Therapy, 9(1), 1–63. 10.1038/s41392-024-01851-y

Claridge Mackonis, E., Suchowerska, N., Naseri, P., & McKenzie, D. R. (2012). Optimisation of exposure conditions for in vitro radiobiology experiments. Australasian Physical & Engineering Sciences in Medicine, 35(2), 151–157. 10.1007/s13246-012-0132-6

Congregado Ruiz, B., Rivero Belenchón, I., Lendínez Cano, G., & Medina López, R. A. (2023). Strategies to Re-Sensitize Castration-Resistant Prostate Cancer to Antiandrogen Therapy. Biomedicines, 11(4), 1105. 10.3390/biomedicines11041105

Connolly, J. L., Schnitt, S. J., Wang, H. H., Longtine, J. A., Dvorak, A., & Dvorak, H. F. (2003). Role of the Surgical Pathologist in the Diagnosis and Management of the Cancer Patient. In D. W. Kufe, R. E. Pollock & R. R. Weichselbaum (Eds.), Holland-Frei Cancer Medicine. 6th edition (). BC Decker.

Cooper, G. M. (2000a). The Development and Causes of Cancer. The Cell: A Molecular Approach. 2nd edition. Sinauer Associates.

Cooper, G. M. (2000b). Tumor Suppressor Genes. The Cell: A Molecular Approach. 2nd edition. Sinauer Associates.

Coppé, J., Desprez, P., Krtolica, A., & Campisi, J. (2010). The Senescence-Associated Secretory Phenotype: The Dark Side of Tumor Suppression. Annual Review of Pathology, 5, 99–118. 10.1146/annurev-pathol-121808-102144

Costa, P. M. d. S., Sales, S. L. A., Pinheiro, D. P., Pontes, L. Q., Maranhão, S. S., Pessoa, C. d. Ó, Furtado, G. P., & Furtado, C. L. M. (2023). Epigenetic reprogramming in cancer: From diagnosis to treatment. Frontiers in Cell and Developmental Biology, 11, 1116805. 10.3389/fcell.2023.1116805

Cross, N. (2019). Nuclear Import and Export. Sheffield Hallam University.

Cruz, E., & Kayser, V. (2019). Synthesis and Enhanced Cellular Uptake In Vitro of Anti-HER2 Multifunctional Gold Nanoparticles. Cancers, 11(6), 870. 10.3390/cancers11060870

Cui, J., Dean, D., Hornicek, F. J., Chen, Z., & Duan, Z. (2020). The role of extracelluar matrix in osteosarcoma progression and metastasis. Journal of Experimental & Clinical Cancer Research : CR, 39, 178. 10.1186/s13046-020-01685-w

Cui, L., Her, S., Borst, G. R., Bristow, R. G., Jaffray, D. A., & Allen, C. (2017). Radiosensitization by gold nanoparticles: Will they ever make it to the clinic? Radiotherapy and Oncology, 124(3), 344–356. 10.1016/j.radonc.2017.07.007

D'Acunto, M., Cioni, P., Gabellieri, E., & Presciuttini, G. (2021). Exploiting gold nanoparticles for diagnosis and cancer treatments. Nanotechnology, 32(19), 192001. 10.1088/1361-6528/abe1ed

Dale, R. G. (2019). Radiation repair models for clinical application. The British Journal of Radiology, 92(1093), 20180070. 10.1259/bjr.20180070

Daruich De Souza, C., Ribeiro Nogueira, B., & Rostelato, M. E. C. M. (2019). Review of the methodologies used in the synthesis gold nanoparticles by chemical reduction. Journal of Alloys and Compounds, 798, 714–740. 10.1016/j.jallcom.2019.05.153

Dasgupta, S., Srinidhi, S., & Vishwanatha, J. K. (2012). Oncogenic activation in prostate cancer progression and metastasis: Molecular insights and future challenges. Journal of Carcinogenesis, 11, 4. 10.4103/1477-3163.93001

Debeb, B. G., Xu, W., Mok, H., Li, L., Robertson, F., Ueno, N. T., Reuben, J., Lucci, A., Cristofanilli, M., & Woodward, W. A. (2010). Differential radiosensitizing

effect of valproic acid in differentiation versus self-renewal promoting culture conditions. International Journal of Radiation Oncology, Biology, Physics, 76(3), 889–895. 10.1016/j.ijrobp.2009.09.052

Demaria, S., Guha, C., Schoenfeld, J., Morris, Z., Monjazeb, A., Sikora, A., Crittenden, M., Shiao, S., Khleif, S., Gupta, S., Formenti, S. C., Vikram, B., Coleman, C. N., & Ahmed, M. M. (2021). Radiation dose and fraction in immunotherapy: one-size regimen does not fit all settings, so how does one choose? Journal for Immunotherapy of Cancer, 9(4), e002038. 10.1136/jitc-2020-002038

Deng, B., Zhao, Z., Kong, W., Han, C., Shen, X., & Zhou, C. (2022). Biological role of matrix stiffness in tumor growth and treatment. Journal of Translational Medicine, 20(1), 540. 10.1186/s12967-022-03768-y

Deng, S., Vlatkovic, T., Li, M., Zhan, T., Veldwijk, M. R., & Herskind, C. (2022). Targeting the DNA Damage Response and DNA Repair Pathways to Enhance Radiosensitivity in Colorectal Cancer. Cancers, 14(19), 4874. 10.3390/cancers14194874

Deng, W., McKelvey, K. J., Guller, A., Fayzullin, A., Campbell, J. M., Clement, S., Habibalahi, A., Wargocka, Z., Liang, L., Shen, C., Howell, V. M., Engel, A. F., & Goldys, E. M. (2020). Application of Mitochondrially Targeted Nanoconstructs to Neoadjuvant X-ray-Induced Photodynamic Therapy for Rectal Cancer. ACS Central Science, 6(5), 715–726. 10.1021/acscentsci.9b01121

Dheyab, M. A., Aziz, A. A., Moradi Khaniabadi, P., Jameel, M. S., Oladzadabbasabadi, N., Mohammed, S. A., Abdullah, R. S., & Mehrdel, B. (2022). Monodisperse Gold Nanoparticles: A Review on Synthesis and Their Application in Modern Medicine. International Journal of Molecular Sciences, 23(13), 7400. 10.3390/ijms23137400

Dong, J., Carpinone, P. L., Pyrgiotakis, G., Demokritou, P., & Moudgil, B. M. (2020). Synthesis of Precision Gold Nanoparticles Using Turkevich Method. Kona : Powder Science and Technology in Japan, 37, 224–232. 10.14356/kona.2020011

Dong, L., Gopalan, V., Holland, O., & Neuzil, J. (2020). Mitocans Revisited: Mitochondrial Targeting as Efficient Anti-Cancer Therapy. International Journal of Molecular Sciences, 21(21), 7941. 10.3390/ijms21217941

Dong, Y., Zhou, L., Tian, Q., Zheng, Y., & Sanche, L. (2017). Chemoradiation Cancer Therapy: Molecular Mechanisms of Cisplatin Radiosensitization. The Journal of Physical Chemistry C, 121(32), 17505–17513. 10.1021/acs.jpcc.7b05271

Drescher, D., Büchner, T., Schrade, P., Traub, H., Werner, S., Guttmann, P., Bachmann, S., & Kneipp, J. (2021). Influence of Nuclear Localization Sequences on the Intracellular Fate of Gold Nanoparticles. ACS Nano, 15(9), 14838–14849. 10.1021/acsnano.1c04925

Dubois, C., Martin, F., Hassel, C., Magnier, F., Daumar, P., Aubel, C., Guerder, S., Mounetou, E., Penault-Lorca, F., & Bamdad, M. (2019). Low-Dose and Long-Term Olaparib Treatment Sensitizes MDA-MB-231 and SUM1315 Triple-Negative Breast Cancers Spheroids to Fractioned Radiotherapy. Journal of Clinical Medicine, 9(1), 64. 10.3390/jcm9010064

Duffy, A. M., Bouchier-Hayes, D. J., & Harmey, J. H. (2013). Vascular Endothelial Growth Factor (VEGF) and Its Role in Non-Endothelial Cells: Autocrine Signalling by VEGF. Madame Curie Bioscience Database [Internet] (). Landes Bioscience.

Dulińska-Litewka, J., Felkle, D., Dykas, K., Handziuk, Z., Krzysztofik, M., & Gąsiorkiewicz, B. (2022). The role of cyclins in the development and progression of prostate cancer. Biomedicine & Pharmacotherapy, 155, 113742. 10.1016/j.biopha.2022.113742

Dunne, A. L., Price, M. E., Mothersill, C., McKeown, S. R., Robson, T., & Hirst, D. G. (2003). Relationship between clonogenic radiosensitivity, radiation-induced apoptosis and DNA damage/repair in human colon cancer cells. British Journal of Cancer, 89(12), 2277–2283. 10.1038/sj.bjc.6601427

Edmondson, R., Broglie, J. J., Adcock, A. F., & Yang, L. (2014). Three-Dimensional Cell Culture Systems and Their Applications in Drug Discovery and Cell-Based Biosensors. Assay and Drug Development Technologies, 12(4), 207–218. 10.1089/adt.2014.573

Egorova, E. A., van Rijt, M. M. J., Sommerdijk, N., Gooris, G. S., Bouwstra, J. A., Boyle, A. L., & Kros, A. (2020). One Peptide for Them All: Gold Nanoparticles of Different Sizes Are Stabilized by a Common Peptide Amphiphile. ACS Nano, 14(5), 5874–5886. 10.1021/acsnano.0c01021

Elebiyo, T. C., Rotimi, D., Evbuomwan, I. O., Maimako, R. F., Iyobhebhe, M., Ojo, O. A., Oluba, O. M., & Adeyemi, O. S. (2022). Reassessing vascular endothelial growth factor (VEGF) in anti-angiogenic cancer therapy. Cancer Treatment and Research Communications, 32, 100620. 10.1016/j.ctarc.2022.100620

Eliseev, R. A., Zuscik, M. J., Schwarz, E. M., O'Keefe, R. J., Drissi, H., & Rosier, R. N. (2005). Increased radiation-induced apoptosis of Saos2 cells via inhibition of NFkappaB: a role for c-Jun N-terminal kinase. Journal of Cellular Biochemistry, 96(6), 1262–1273. 10.1002/jcb.20607

Engeland, K. (2022). Cell cycle regulation: p53-p21-RB signaling. Cell Death & Differentiation, 29(5), 946–960. 10.1038/s41418-022-00988-z

European Association of Urology. (2024, EAU Guidelines on Prostate Cancer - Classification and Staging Systems. Retrieved Aug 16, 2024, from https://uroweb.org/guidelines/prostate-cancer/chapter/classification-and-staging-systems

European Commission. (2022, European Cancer Information System. Retrieved Aug 13, 2024, from https://ecis.jrc.ec.europa.eu/factsheets_2022.php

Fadaka, A., Ajiboye, B., Ojo, O., Adewale, O., Olayide, I., & Emuowhochere, R. (2017). Biology of glucose metabolization in cancer cells. Journal of Oncological Sciences, 3(2), 45–51. 10.1016/j.jons.2017.06.002

Fang, X., Wang, Y., Ma, X., Li, Y., Zhang, Z., Xiao, Z., Liu, L., Gao, X., & Liu, J. (2017). Mitochondria-targeting Au nanoclusters enhance radiosensitivity of cancer cells. Journal of Materials Chemistry B, 5(22), 4190–4197. 10.1039/C7TB00422B

Faraday, M. (1857). X. The Bakerian Lecture. —Experimental relations of gold (and other metals) to light. Philosophical Transactions of the Royal Society of London, 147, 145–181. https://doi.org/10.1098/rstl.1857.0011

Fares, J., Fares, M. Y., Khachfe, H. H., Salhab, H. A., & Fares, Y. (2020). Molecular principles of metastasis: a hallmark of cancer revisited. Signal Transduction and Targeted Therapy, 5(1), 1–17. 10.1038/s41392-020-0134-x

Fass, L. (2008). Imaging and cancer: A review. Molecular Oncology, 2(2), 115–152. 10.1016/j.molonc.2008.04.001

Fazeli, G. R., Khoei, S., Nikoofar, A. R., & Goliaei, B. (2007). Reduced DNA damage in tumor spheroids compared to monolayer cultures exposed to ionizing radiation. Iran. J. Radiat. Res., 5(2), 63–69.

Feng, H., Wang, J., Chen, W., Shan, B., Guo, Y., Xu, J., Wang, L., Guo, P., & Zhang, Y. (2016). Hypoxia-induced autophagy as an additional mechanism in human osteosarcoma radioresistance. Journal of Bone Oncology, 5(2), 67–73. 10.1016/j.jbo.2016.03.001

Feng, J., Pathak, V., Byrne, N. M., Wang, T., Yin, C., Medina, R. J., & Coulter, J. A. (2023). Modulating tumour metabolism enhances gold nanoparticle radiosensitisation in HPV-negative head and neck cancer. Cancer Nanotechnology, 14(1), 33–23. 10.1186/s12645-023-00185-8

Fernald, K., & Kurokawa, M. (2013). Evading apoptosis in cancer. Trends in Cell Biology, 23(12), 620–633. 10.1016/j.tcb.2013.07.006

Filippou, C., Themistocleous, S. C., Marangos, G., Panayiotou, Y., Fyrilla, M., Kousparou, C. A., Pana, Z., Tsioutis, C., Johnson, E. O., & Yiallouris, A. (2024). Microbial Therapy and Breast Cancer Management: Exploring Mechanisms, Clinical Efficacy, and Integration within the One Health Approach. International Journal of Molecular Sciences, 25(2), 1110. 10.3390/ijms25021110

Flint, L. E., Hamm, G., Ready, J. D., Ling, S., Duckett, C. J., Cross, N. A., Cole, L. M., Smith, D. P., Goodwin, R. J. A., & Clench, M. R. (2021). Comparison of Osteosarcoma Aggregated Tumour Models with Human Tissue by Multimodal Mass Spectrometry Imaging. Metabolites, 11(8), 506. 10.3390/metabo11080506

Flint, L. E., Hamm, G., Ready, J. D., Ling, S., Duckett, C. J., Cross, N. A., Cole, L. M., Smith, D. P., Goodwin, R. J. A., & Clench, M. R. (2020). Characterization of an Aggregated Three-Dimensional Cell Culture Model by Multimodal Mass Spectrometry Imaging. Analytical Chemistry, 92(18), 12538–12547. 10.1021/acs.analchem.0c02389

Fontana, F., Raimondi, M., Marzagalli, M., Sommariva, M., Gagliano, N., & Limonta, P. (2020). Three-Dimensional Cell Cultures as an In Vitro Tool for Prostate Cancer Modeling and Drug Discovery. International Journal of Molecular Sciences, 21(

Frampton, J. E. (2010). Mifamurtide: a review of its use in the treatment of osteosarcoma. Paediatric Drugs, 12(3), 141–153. 10.2165/11204910-000000000-00000

Francescone, R., Hou, V., & Grivennikov, S. I. (2014). Microbiome, Inflammation and Cancer. Cancer Journal (Sudbury, Mass.), 20(3), 181–189. 10.1097/PPO.0000000000000048

Fuentes-García, J. A., Santoyo-Salzar, J., Rangel-Cortes, E., Goya, G. F., Cardozo-Mata, V., & Pescador-Rojas, J. A. (2021). Effect of ultrasonic irradiation power on sonochemical synthesis of gold nanoparticles. Ultrasonics Sonochemistry, 70, 105274. 10.1016/j.ultsonch.2020.105274

Gallud, A., Klöditz, K., Ytterberg, J., Östberg, N., Katayama, S., Skoog, T., Gogvadze, V., Chen, Y., Xue, D., Moya, S., Ruiz, J., Astruc, D., Zubarev, R., Kere, J., & Fadeel, B. (2019). Cationic gold nanoparticles elicit mitochondrial dysfunction: a multi-omics study. Scientific Reports, 9(1), 4366. 10.1038/s41598-019-40579-6

Gatenby, R. A., & Gillies, R. J. (2004). Why do cancers have high aerobic glycolysis? Nature Reviews Cancer, 4(11), 891–899. 10.1038/nrc1478

Gerken, L. R. H., Gerdes, M. E., Pruschy, M., & Herrmann, I. K. (2023). Prospects of nanoparticle-based radioenhancement for radiotherapy. Materials Horizons, 10(10), 4059–4082. 10.1039/d3mh00265a

Gessner, I., & Neundorf, I. (2020). Nanoparticles Modified with Cell-Penetrating Peptides: Conjugation Mechanisms, Physicochemical Properties, and Application in Cancer Diagnosis and Therapy. International Journal of Molecular Sciences, 21(7), 2536. 10.3390/ijms21072536

Ghaderi, N., Jung, J., Brüningk, S. C., Subramanian, A., Nassour, L., & Peacock, J. (2022). A Century of Fractionated Radiotherapy: How Mathematical Oncology Can Break the Rules. International Journal of Molecular Sciences, 23(3), 1316. 10.3390/ijms23031316

Gong, L., Zhang, Y., Liu, C., Zhang, M., & Han, S. (2021). Application of Radiosensitizers in Cancer Radiotherapy. International Journal of Nanomedicine, 16, 1083–1102. 10.2147/IJN.S290438

Grayson, K. A., Jyotsana, N., Ortiz-Otero, N., & King, M. R. (2021). Overcoming TRAIL-resistance by sensitizing prostate cancer 3D spheroids with taxanes. PLoS ONE, 16(3), e0246733. 10.1371/journal.pone.0246733

Greaves, M., & Maley, C. C. (2012). Clonal evolution in cancer. Nature, 481(7381), 306–313. 10.1038/nature10762

Greten, F. R., & Grivennikov, S. I. (2019). Inflammation and Cancer: Triggers, Mechanisms and Consequences. Immunity, 51(1), 27–41. 10.1016/j.immuni.2019.06.025

Groelly, F. J., Fawkes, M., Dagg, R. A., Blackford, A. N., & Tarsounas, M. (2023). Targeting DNA damage response pathways in cancer. Nature Reviews Cancer, 23(2), 78–94. 10.1038/s41568-022-00535-5

Guo, H., Guo, S., & Liu, H. (2020). Antioxidant activity and inhibition of ultraviolet radiation-induced skin damage of Selenium-rich peptide fraction from selenium-rich yeast protein hydrolysate. Bioorganic Chemistry, 105, 104431. 10.1016/j.bioorg.2020.104431

Gupta, P. B., Pastushenko, I., Skibinski, A., Blanpain, C., & Kuperwasser, C. (2019). Phenotypic plasticity as a driver of cancer formation, progression and resistance to therapy. Cell Stem Cell, 24(1), 65–78. 10.1016/j.stem.2018.11.011

Gupta, T., Agarwal, J., Jain, S., Phurailatpam, R., Kannan, S., Ghosh-Laskar, S., Murthy, V., Budrukkar, A., Dinshaw, K., Prabhash, K., Chaturvedi, P., & D'Cruz, A. (2012). Three-dimensional conformal radiotherapy (3D-CRT) versus intensity modulated radiation therapy (IMRT) in squamous cell carcinoma of the head and neck: a randomized controlled trial. Radiotherapy and Oncology: Journal of the European Society for Therapeutic Radiology and Oncology, 104(3), 343–348. 10.1016/j.radonc.2012.07.001

Hainfeld, J. F., Dilmanian, F. A., Zhong, Z., Slatkin, D. N., Kalef-Ezra, J. A., & Smilowitz, H. M. (2010). Gold nanoparticles enhance the radiation therapy of a murine squamous cell carcinoma. Physics in Medicine and Biology, 55(11), 3045–3059. 10.1088/0031-9155/55/11/004

Hainfeld, J. F., Slatkin, D. N., & Smilowitz, H. M. (2004). The use of gold nanoparticles to enhance radiotherapy in mice. Physics in Medicine and Biology, 49(18), 309. 10.1088/0031-9155/49/18/n03

Hainfeld, J. F., Smilowitz, H. M., O'Connor, M. J., Dilmanian, F. A., & Slatkin, D. N. (2013). Gold nanoparticle imaging and radiotherapy of brain tumors in mice. Nanomedicine (London, England), 8(10), 1601–1609. 10.2217/nnm.12.165

Hanahan, D. (2022). Hallmarks of Cancer: New Dimensions. Cancer Discovery, 12(1), 31–46. 10.1158/2159-8290.CD-21-1059

Hanahan, D., & Weinberg, R. A. (2000). The Hallmarks of Cancer. Cell, 100(1), 57–70. 10.1016/S0092-8674(00)81683-9

Hanahan, D., & Weinberg, R. A. (2011). Hallmarks of Cancer: The Next Generation. Cell, 144(5), 646–674. 10.1016/j.cell.2011.02.013

Hara, D., Tao, W., Schmidt, R. M., Yang, Y., Daunert, S., Dogan, N., Ford, J. C., Pollack, A., & Shi, J. (2022). Boosted Radiation Bystander Effect of PSMA-Targeted Gold Nanoparticles in Prostate Cancer Radiosensitization. Nanomaterials, 12(24), 4440. 10.3390/nano12244440

Haume, K., Rosa, S., Grellet, S., Śmiałek, M. A., Butterworth, K. T., Solov'yov, A. V., Prise, K. M., Golding, J., & Mason, N. J. (2016). Gold nanoparticles for cancer radiotherapy: a review. Cancer Nanotechnology, 7(1), 8. 10.1186/s12645-016-0021-x

Hein, C. D., Liu, X., & Wang, D. (2008). Click Chemistry, a Powerful Tool for Pharmaceutical Sciences. Pharmaceutical Research, 25(10), 2216–2230. 10.1007/s11095-008-9616-1

Helleday, T., Bryant, H. E., & Schultz, N. (2005). Poly(ADP-ribose) polymerase (PARP-1) in homologous recombination and as a target for cancer therapy. Cell Cycle (Georgetown, Tex.), 4(9), 1176–1178. 10.4161/cc.4.9.2031

Hirsch, B., Bro, A., Walker, J., McDaniel, J., & Penrod, D. (2022). Metastatic bone cancer: Consideration for optimal dose fractionation in radiation therapy. Journal of Medical Imaging and Radiation Sciences, 53(2, Supplement), S39–S43. 10.1016/j.jmir.2022.03.009

Hoarau-Véchot, J., Rafii, A., Touboul, C., & Pasquier, J. (2018). Halfway between 2D and Animal Models: Are 3D Cultures the Ideal Tool to Study Cancer-Microenvironment Interactions? International Journal of Molecular Sciences, 19(1), 181. 10.3390/ijms19010181

Hosea, R., Hillary, S., Naqvi, S., Wu, S., & Kasim, V. (2024). The two sides of chromosomal instability: drivers and brakes in cancer. Signal Transduction and Targeted Therapy, 9(1), 1–30. 10.1038/s41392-024-01767-7

Hsiao, I. -., Bierkandt, F. S., Reichardt, P., Luch, A., Huang, Y., Jakubowski, N., Tentschert, J., & Haase, A. (2016). Quantification and visualization of cellular uptake of TiO2 and Ag nanoparticles: comparison of different ICP-MS techniques. Journal of Nanobiotechnology, 14(1), 50. 10.1186/s12951-016-0203-z

Huang, H., Liu, R., Yang, J., Dai, J., Fan, S., Pi, J., Wei, Y., & Guo, X. (2023). Gold Nanoparticles: Construction for Drug Delivery and Application in Cancer Immunotherapy. Pharmaceutics, 15(7), 1868. 10.3390/pharmaceutics15071868

Igaz, N., Szőke, K., Kovács, D., Buhala, A., Varga, Z., Bélteky, P., Rázga, Z., Tiszlavicz, L., Vizler, C., Hideghéty, K., Kónya, Z., & Kiricsi, M. (2020). Synergistic Radiosensitization by Gold Nanoparticles and the Histone Deacetylase Inhibitor SAHA in 2D and 3D Cancer Cell Cultures. Nanomaterials (Basel, Switzerland), 10(1), 158. 10.3390/nano10010158

Jain, S., Hirst, D. G., & O'Sullivan, J. M. (2012). Gold nanoparticles as novel agents for cancer therapy. The British Journal of Radiology, 85(1010), 101–113. 10.1259/bjr/59448833

Jan, R., & Chaudhry, G. (2019). Understanding Apoptosis and Apoptotic Pathways Targeted Cancer Therapeutics. Advanced Pharmaceutical Bulletin, 9(2), 205–218. 10.15171/apb.2019.024

Jeena, M. T., Kim, S., Jin, S., & Ryu, J. (2019). Recent Progress in Mitochondria-Targeted Drug and Drug-Free Agents for Cancer Therapy. Cancers, 12(1), 4. 10.3390/cancers12010004

Jividen, K., Kedzierska, K. Z., Yang, C., Szlachta, K., Ratan, A., & Paschal, B. M. (2018). Genomic analysis of DNA repair genes and androgen signaling in prostate cancer. BMC Cancer, 18, 960. 10.1186/s12885-018-4848-x

Ju-Nam, Y. (2007). Functionalised Metal Nanoparticles as Novel Reagents for Biomedical Analysis (PhD).

Ju-Nam, Y., Bricklebank, N., Allen, D. W., Gardiner, P. H. E., Light, M. E., & Hursthouse, M. B. (2006). Phosphonioalkylthiosulfate zwitterions—new masked

thiol ligands for the formation of cationic functionalised gold nanoparticles. Organic & Biomolecular Chemistry, 4(23), 4345–4351. 10.1039/B610480K

Ju-Nam, Y., Chen, Y., Ojeda, J. J., Allen, D. W., Cross, N. A., Gardiner, P. H. E., & Bricklebank, N. (2012). Water-soluble gold nanoparticles stabilized with cationic phosphonium thiolate ligands. RSC Advances, 2(27), 10345–10351. 10.1039/C2RA21421K

Jung, H., Yoon, S. R., Lim, J., Cho, H. J., & Lee, H. G. (2020). Dysregulation of Rho GTPases in Human Cancers. Cancers, 12(5), 1179. 10.3390/cancers12051179

Jung, M., & Pfeifer, G. P. (2013). CpG Islands. In S. Maloy, & K. Hughes (Eds.), Brenner's Encyclopedia of Genetics (Second Edition) (pp. 205–207). Academic Press.

Jurkovicova, D., Neophytou, C. M., Gašparović, A. Č, & Gonçalves, A. C. (2022). DNA Damage Response in Cancer Therapy and Resistance: Challenges and Opportunities. International Journal of Molecular Sciences, 23(23), 14672. 10.3390/ijms232314672

Kamble, D., Mahajan, M., Dhat, R., & Sitasawad, S. (2021). Keap1-Nrf2 Pathway Regulates ALDH and Contributes to Radioresistance in Breast Cancer Stem Cells. Cells, 10(1), 83. 10.3390/cells10010083

Kang, S., Lee, J., Huh, Y. S., & Takayama, S. (2021). Alginate Microencapsulation for Three-Dimensional In Vitro Cell Culture. ACS Biomaterials Science & Engineering, 7(7), 2864–2879. 10.1021/acsbiomaterials.0c00457

Kapałczyńska, M., Kolenda, T., Przybyła, W., Zajączkowska, M., Teresiak, A., Filas, V., Ibbs, M., Bliźniak, R., Łuczewski, Ł, & Lamperska, K. (2018). 2D and 3D cell cultures – a comparison of different types of cancer cell cultures. Archives of Medical Science: AMS, 14(4), 910–919. 10.5114/aoms.2016.63743

Kapara, A., Brunton, V., Graham, D., & Faulds, K. (2020). Investigation of cellular uptake mechanism of functionalised gold nanoparticles into breast cancer using SERS. Chemical Science, 11(22), 5819–5829. 10.1039/d0sc01255f

Kaur, S., Bronson, S. M., Pal-Nath, D., Miller, T. W., Soto-Pantoja, D. R., & Roberts, D. D. (2021). Functions of Thrombospondin-1 in the Tumor

Microenvironment. International Journal of Molecular Sciences, 22(9), 4570. 10.3390/ijms22094570

Kazmi, F., Vallis, K. A., Vellayappan, B. A., Bandla, A., Yukun, D., & Carlisle, R. (2020). Megavoltage Radiosensitization of Gold Nanoparticles on a Glioblastoma Cancer Cell Line Using a Clinical Platform. International Journal of Molecular Sciences, 21(2), 429. 10.3390/ijms21020429

Keam, S., MacKinnon, K. M., D'Alonzo, R. A., Gill, S., Ebert, M. A., Nowak, A. K., & Cook, A. M. (2022). Effects of Photon Radiation on DNA Damage, Cell Proliferation, Cell Survival, and Apoptosis of Murine and Human Mesothelioma Cell Lines. Advances in Radiation Oncology, 7(6), 101013. 10.1016/j.adro.2022.101013

Keohane, E. M. (2020). Introduction to hematologic neoplasms. In E. M. Keohane, C. N. Otto & J. M. Walenga (Eds.), Rodak's Hematology (Sixth Edition) (pp. 466–476). Elsevier.

Kepka, L., & Socha, J. (2021). Dose and fractionation schedules in radiotherapy for non-small cell lung cancer. Translational Lung Cancer Research, 10(4), 1969–1982. 10.21037/tlcr-20-253

Ketley, R., & Gullerova, M. (2020). Jack of all trades? The versatility of RNA in DNA double-strand break repair. Essays in Biochemistry, 64(5), 721–735. 10.1042/EBC20200008

Khademi, S., Sarkar, S., Shakeri-Zadeh, A., Attaran, N., Kharrazi, S., Ay, M. R., Azimian, H., & Ghadiri, H. (2019). Targeted gold nanoparticles enable molecular CT imaging of head and neck cancer: An in vivo study. The International Journal of Biochemistry & Cell Biology, 114, 105554. 10.1016/j.biocel.2019.06.002

Khoo, A. M., Cho, S. H., Reynoso, F. J., Aliru, M., Aziz, K., Bodd, M., Yang, X., Ahmed, M. F., Yasar, S., Manohar, N., Cho, J., Tailor, R., Thames, H. D., & Krishnan, S. (2017). Radiosensitization of Prostate Cancers In Vitro and In Vivo to Erbium-filtered Orthovoltage X-rays Using Actively Targeted Gold Nanoparticles. Scientific Reports, 7(1), 18044. 10.1038/s41598-017-18304-y

Khorshid, M., Varshosaz, J., Rostami, M., Haghiralsadat, F., Akbari, V., & Khorshid, P. (2023). Anti HER-2 aptamer functionalized gold nanoparticles of

dasatinib for targeted chemo-radiotherapy in breast cancer cells. Biomaterials Advances, 154, 213591. 10.1016/j.bioadv.2023.213591

Kim, J. H., Brown, S. L., & Gordon, M. N. (2023). Radiation-induced senescence: therapeutic opportunities. Radiation Oncology, 18(1), 10. 10.1186/s13014-022-02184-2

Kim, J., Berlow, N. E., Lathara, M., Bharathy, N., Martin, L. R., Purohit, R., Cleary, M. M., Liu, Q., Michalek, J. E., Srinivasa, G., Cole, B. L., Chen, S. D., & Keller, C. (2022). Sensitization of osteosarcoma to irradiation by targeting nuclear FGFR1. Biochemical and Biophysical Research Communications, 621, 101–108. 10.1016/j.bbrc.2022.07.002

Kim, J., Cho, H., Lim, D., Joo, M. K., & Kim, K. (2023). Perspectives for Improving the Tumor Targeting of Nanomedicine via the EPR Effect in Clinical Tumors. International Journal of Molecular Sciences, 24(12), 10082. 10.3390/ijms241210082

Kim, J., Yu, A. M., Kubelick, K. P., & Emelianov, S. Y. (2022). Gold nanoparticles conjugated with DNA aptamer for photoacoustic detection of human matrix metalloproteinase-9. Photoacoustics, 25, 100307. 10.1016/j.pacs.2021.100307

Kim, S. K., & Cho, S. W. (2022). The Evasion Mechanisms of Cancer Immunity and Drug Intervention in the Tumor Microenvironment. Frontiers in Pharmacology, 13, 868695. 10.3389/fphar.2022.868695

Klein, K., He, K., Younes, A. I., Barsoumian, H. B., Chen, D., Ozgen, T., Mosaffa, S., Patel, R. R., Gu, M., Novaes, J., Narayanan, A., Cortez, M. A., & Welsh, J. W. (2020). Role of Mitochondria in Cancer Immune Evasion and Potential Therapeutic Approaches. Frontiers in Immunology, 1110.3389/fimmu.2020.573326

Koch, J., Mönch, D., Maaß, A., Gromoll, C., Hehr, T., Leibold, T., Schlitt, H. J., Dahlke, M., & Renner, P. (2021). Three dimensional cultivation increases chemo- and radioresistance of colorectal cancer cell lines. PLoS ONE, 16(1), e0244513. 10.1371/journal.pone.0244513

Koka, K., Verma, A., Dwarakanath, B. S., & Papineni, R. V. L. (2022). Technological Advancements in External Beam Radiation Therapy (EBRT): An

Indispensable Tool for Cancer Treatment. Cancer Management and Research, 14, 1421–1429. 10.2147/CMAR.S351744

Kong, F., Zhang, J., Li, R., Wang, Z., Wang, W., & Wang, W. (2017). Unique Roles of Gold Nanoparticles in Drug Delivery, Targeting and Imaging Applications. Molecules : A Journal of Synthetic Chemistry and Natural Product Chemistry, 22(9), 1445. 10.3390/molecules22091445

Kumar, V., Abbas, A. K., Aster, J. C., & Perkins, J. A. (2018). Neoplasia. Robbins Basic Pathology (10th ed., pp. 189–242). Elsevier.

Kumar, V., Vashishta, M., Kong, L., Wu, X., Lu, J. J., Guha, C., & Dwarakanath, B. S. (2021). The Role of Notch, Hedgehog, and Wnt Signaling Pathways in the Resistance of Tumors to Anticancer Therapies. Frontiers in Cell and Developmental Biology, 9, 650772. 10.3389/fcell.2021.650772

Kundu, Z. S. (2014). Classification, imaging, biopsy and staging of osteosarcoma. Indian Journal of Orthopaedics, 48(3), 238–246. 10.4103/0019-5413.132491

Kweldam, C. F., van Leenders, G. J., & van der Kwast, T. (2019). Grading of prostate cancer: a work in progress. Histopathology, 74(1), 146–160. 10.1111/his.13767

Ledermann, J. A., Drew, Y., & Kristeleit, R. S. (2016). Homologous recombination deficiency and ovarian cancer. European Journal of Cancer, 60, 49–58. 10.1016/j.ejca.2016.03.005

Lee, E. Y. H. P., & Muller, W. J. (2010). Oncogenes and Tumor Suppressor Genes. Cold Spring Harbor Perspectives in Biology, 2(10), a003236. 10.1101/cshperspect.a003236

Lee, E., Lee, M., Kwon, S., Kim, J., & Kwon, Y. (2022). Systematic and mechanistic analysis of AuNP-induced nanotoxicity for risk assessment of nanomedicine. Nano Convergence, 9(1), 27. 10.1186/s40580-022-00320-y

Lee, J. Y., Bhandare, R. R., Boddu, S. H. S., Shaik, A. B., Saktivel, L. P., Gupta, G., Negi, P., Barakat, M., Singh, S. K., Dua, K., & Chellappan, D. K. (2024). Molecular mechanisms underlying the regulation of tumour suppressor genes in lung cancer. Biomedicine & Pharmacotherapy, 173, 116275. 10.1016/j.biopha.2024.116275

Lee, J., Twomey, M., Machado, C., Gomez, G., Doshi, M., Gesquiere, A. J., & Moon, J. H. (2013). Caveolae-Mediated Endocytosis of Conjugated Polymer Nanoparticles. Macromolecular Bioscience, 13(7), 913–920. 10.1002/mabi.201300030

Lee, K. J., Mann, E., Wright, G., Piett, C. G., Nagel, Z. D., & Gassman, N. R. (2020). Exploiting DNA repair defects in triple negative breast cancer to improve cell killing. Therapeutic Advances in Medical Oncology, 12, 1758835920958354. 10.1177/1758835920958354

Lee, K. Y., & Mooney, D. J. (2012). Alginate: properties and biomedical applications. Progress in Polymer Science, 37(1), 106–126. 10.1016/j.progpolymsci.2011.06.003

Lee, Y. J., Ahn, E., & Park, Y. (2019). Shape-dependent cytotoxicity and cellular uptake of gold nanoparticles synthesized using green tea extract. Nanoscale Research Letters, 14(1), 129. 10.1186/s11671-019-2967-1

Lee, Y., Cho, J., Sai, S., Oh, J. Y., Park, J., Oh, S. J., Park, M., Kwon, J., Shin, U. S., Baek, J., Lim, S. H., Song, J., Hwang, S., & Kim, E. H. (2019). 5-Fluorouracil as a Tumor-Treating Field-Sensitizer in Colon Cancer Therapy. Cancers, 11(12), 1999. 10.3390/cancers11121999

Li, N., Yu, L., Wang, J., Gao, X., Chen, Y., Pan, W., & Tang, B. (2018). A mitochondria-targeted nanoradiosensitizer activating reactive oxygen species burst for enhanced radiation therapy. Chemical Science, 9(12), 3159–3164. 10.1039/C7SC04458E

Li, W., & Chen, X. (2015). Gold nanoparticles for photoacoustic imaging. Nanomedicine (London, England), 10(2), 299–320. 10.2217/nnm.14.169

Li, X., Tian, J., Bo, Q., Li, K., Wang, H., Liu, T., & Li, J. (2015). Targeting DNA-PKcs increased anticancer drug sensitivity by suppressing DNA damage repair in osteosarcoma cell line MG63. Tumor Biology, 36(12), 9365–9372. 10.1007/s13277-015-3642-5

Li, Z., Xiong, W., Liang, Z., Wang, J., Zeng, Z., Kołat, D., Li, X., Zhou, D., Xu, X., & Zhao, L. (2024). Critical role of the gut microbiota in immune responses and cancer immunotherapy. Journal of Hematology & Oncology, 17(1), 33. 10.1186/s13045-024-01541-w

Liberti, M. V., & Locasale, J. W. (2016). The Warburg Effect: How Does it Benefit Cancer Cells? Trends in Biochemical Sciences, 41(3), 211–218. 10.1016/j.tibs.2015.12.001

Lilienthal, I., & Herold, N. (2020). Targeting Molecular Mechanisms Underlying Treatment Efficacy and Resistance in Osteosarcoma: A Review of Current and Future Strategies. International Journal of Molecular Sciences, 21(18), 6885. 10.3390/ijms21186885

Lim, Y. K., & Kim, D. (2021). Brachytherapy: A Comprehensive Review. Progress in Medical Physics, 32(2), 25–39. 10.14316/pmp.2021.32.2.25

Liu, C., Nie, J., Wang, R., & Mao, W. (2019). The Cell Cycle G2/M Block Is an Indicator of Cellular Radiosensitivity. Dose-Response, 17(4), 1559325819891008. 10.1177/1559325819891008

Liu, Q., Luo, M., Huang, C., Chen, H., & Zhou, Z. (2021). Epigenetic Regulation of Epithelial to Mesenchymal Transition in the Cancer Metastatic Cascade: Implications for Cancer Therapy. Frontiers in Oncology, 1110.3389/fonc.2021.657546

Liu, R., Bian, Y., Liu, L., Liu, L., Liu, X., & Ma, S. (2022). Molecular pathways associated with oxidative stress and their potential applications in radiotherapy (Review). International Journal of Molecular Medicine, 49(5), 65. 10.3892/ijmm.2022.5121

Liu, X., Zhu, N., Hao, Y., Yu, X., Li, Z., Mao, R., Liu, R., Kang, J., Hu, J., & Li, Y. (2021). Radioprotective Effect of Whey Hydrolysate Peptides against γ-Radiation-Induced Oxidative Stress in BALB/c Mice. Nutrients, 13(3), 816. 10.3390/nu13030816

Liu, Y., Sun, Y., Guo, Y., Shi, X., Chen, X., Feng, W., Wu, L., Zhang, J., Yu, S., Wang, Y., & Shi, Y. (2023). An Overview: The Diversified Role of Mitochondria in Cancer Metabolism. International Journal of Biological Sciences, 19(3), 897–915. 10.7150/ijbs.81609

Liu, Y., Zheng, C., Huang, Y., He, M., Xu, W. W., & Li, B. (2021). Molecular mechanisms of chemo- and radiotherapy resistance and the potential implications for cancer treatment. MedComm, 2(3), 315–340. 10.1002/mco2.55

Liu, Z., Wu, Y., Guo, Z., Liu, Y., Shen, Y., Zhou, P., & Lu, X. (2014). Effects of Internalized Gold Nanoparticles with Respect to Cytotoxicity and Invasion Activity in Lung Cancer Cells. PloS One, 9(6), e99175. 10.1371/journal.pone.0099175

Llauradó, M., Ruiz, A., Majem, B., Ertekin, T., Colás, E., Pedrola, N., Devis, L., Rigau, M., Sequeiros, T., Montes, M., Garcia, M., Cabrera, S., Gil-Moreno, A., Xercavins, J., Castellví, J., Garcia, A., Ramón y Cajal, S., Moreno, G., Alameda, F., Reventós, J. (2012). Molecular bases of endometrial cancer: New roles for new actors in the diagnosis and the therapy of the disease. Molecular and Cellular Endocrinology, 358(2), 244–255. 10.1016/j.mce.2011.10.003

Lonati, L., Barbieri, S., Guardamagna, I., Ottolenghi, A., & Baiocco, G. (2021). Radiation-induced cell cycle perturbations: a computational tool validated with flow-cytometry data. Scientific Reports, 11(1), 925. 10.1038/s41598-020-79934-3

Lu, J., Wu, T., Zhang, B., Liu, S., Song, W., Qiao, J., & Ruan, H. (2021). Types of nuclear localization signals and mechanisms of protein import into the nucleus. Cell Communication and Signaling, 19(1), 60. 10.1186/s12964-021-00741-y

Luan, S., Xie, R., Yang, Y., Xiao, X., Zhou, J., Li, X., Fang, P., Zeng, X., Yu, X., Chen, M., Gao, H., & Yuan, Y. (2022). Acid-Responsive Aggregated Gold Nanoparticles for Radiosensitization and Synergistic Chemoradiotherapy in the Treatment of Esophageal Cancer. Small (Weinheim an Der Bergstrasse, Germany), 18(19), e2200115–n/a. 10.1002/smll.202200115

Luce, A., Lama, S., Millan, P. C., Itro, A., Sangiovanni, A., Caputo, C., Ferranti, P., Cappabianca, S., Caraglia, M., & Stiuso, P. (2021). Polydatin Induces Differentiation and Radiation Sensitivity in Human Osteosarcoma Cells and Parallel Secretion through Lipid Metabolite Secretion. Oxidative Medicine and Cellular Longevity, 2021, 3337013. 10.1155/2021/3337013

Luo, D., Wang, X., Burda, C., & Basilion, J. P. (2021). Recent Development of Gold Nanoparticles as Contrast Agents for Cancer Diagnosis. Cancers, 13(8), 1825. 10.3390/cancers13081825

Ma, N., Wu, F., Zhang, X., Jiang, Y., Jia, H., Wang, H., Li, Y., Liu, P., Gu, N., & Chen, Z. (2017). Shape-Dependent Radiosensitization Effect of Gold Nanostructures in Cancer Radiotherapy: Comparison of Gold Nanoparticles,

Nanospikes, and Nanorods. ACS Applied Materials & Interfaces, 9(15), 13037–13048. 10.1021/acsami.7b01112

Mackey, M. A., Saira, F., Mahmoud, M. A., & El-Sayed, M. A. (2013). Inducing Cancer Cell Death by Targeting Its Nucleus: Solid Gold Nanospheres versus Hollow Gold Nanocages. Bioconjugate Chemistry, 24(6), 897–906. 10.1021/bc300592d

Mah, L., El-Osta, A., & Karagiannis, T. C. (2010). γH2AX: a sensitive molecular marker of DNA damage and repair. Leukemia, 24, 679–686. https://doi.org/10.1038/leu.2010.6

Mamo, T., Mladek, A. C., Shogren, K. L., Gustafson, C., Gupta, S. K., Riester, S. M., Maran, A., Galindo, M., van Wijnen, A. J., Sarkaria, J. N., & Yaszemski, M. J. (2017). Inhibiting DNA-PKCS radiosensitizes human osteosarcoma cells. Biochemical and Biophysical Research Communications, 486(2), 307–313. 10.1016/j.bbrc.2017.03.033

Manda, K., Juerß, D., Fischer, P., Schröder, A., Koenen, A., & Hildebrandt, G. (2021). Simvastatin treatment varies the radiation response of human breast cells in 2D or 3D culture. Investigational New Drugs, 39(3), 658–669. 10.1007/s10637-020-01046-6

Marcu, L. G. (2010). Altered fractionation in radiotherapy: From radiobiological rationale to therapeutic gain. Cancer Treatment Reviews, 36(8), 606–614. 10.1016/j.ctrv.2010.04.004

Martin, T. A., Ye, L., Sanders, A. J., Lane, J., & Jiang, W. G. (2013). Cancer Invasion and Metastasis: Molecular and Cellular Perspective. Madame Curie Bioscience Database [Internet] (). Landes Bioscience.

Maxim, L. D., Niebo, R., & Utell, M. J. (2014). Screening tests: a review with examples. Inhalation Toxicology, 26(13), 811–828. 10.3109/08958378.2014.955932

Mbemi, A., Khanna, S., Njiki, S., Yedjou, C. G., & Tchounwou, P. B. (2020). Impact of Gene–Environment Interactions on Cancer Development. International Journal of Environmental Research and Public Health, 17(21), 8089. 10.3390/ijerph17218089

McMahon, S. J., Hyland, W. B., Muir, M. F., Coulter, J. A., Jain, S., Butterworth, K. T., Schettino, G., Dickson, G. R., Hounsell, A. R., O'Sullivan, J. M., Prise, K. M., Hirst, D. G., & Currell, F. J. (2011). Biological consequences of nanoscale energy deposition near irradiated heavy atom nanoparticles. Scientific Reports, 1(1), 18. 10.1038/srep00018

Mehta, S. R., Suhag, V., Semwal, M., & Sharma, N. (2010). Radiotherapy: Basic Concepts and Recent Advances. Medical Journal, Armed Forces India, 66(2), 158–162. 10.1016/S0377-1237(10)80132-7

Moiseeva, O., Bourdeau, V., Roux, A., Deschênes-Simard, X., & Ferbeyre, G. (2009). Mitochondrial dysfunction contributes to oncogene-induced senescence. Molecular and Cellular Biology, 29(16), 4495–4507. 10.1128/MCB.01868-08

Monitoring of Tumor Progression. Biomacromolecules, 23(8), 3130–3141. 10.1021/acs.biomac.2c00169

Moore, L. D., Le, T., & Fan, G. (2013). DNA Methylation and Its Basic Function. Neuropsychopharmacology, 38(1), 23–38. 10.1038/npp.2012.112

Moris, L., Cumberbatch, M. G., Van den Broeck, T., Gandaglia, G., Fossati, N., Kelly, B., Pal, R., Briers, E., Cornford, P., De Santis, M., Fanti, S., Gillessen, S., Grummet, J. P., Henry, A. M., Lam, T. B. L., Lardas, M., Liew, M., Mason, M. D., Omar, M. I., . . . Wiegel, T. (2020). Benefits and Risks of Primary Treatments for High-risk Localized and Locally Advanced Prostate Cancer: An International Multidisciplinary Systematic Review. European Urology, 77(5), 614–627. 10.1016/j.eururo.2020.01.033

Musielak, M., Boś-Liedke, A., Piwocka, O., Kowalska, K., Markiewicz, R., Szymkowiak, B., Bakun, P., & Suchorska, W. M. (2023). The Role of Functionalization and Size of Gold Nanoparticles in the Response of MCF-7 Breast Cancer Cells to Ionizing Radiation Comparing 2D and 3D In Vitro Models. Pharmaceutics, 15(3), 862. 10.3390/pharmaceutics15030862

Muz, B., de la Puente, P., Azab, F., & Azab, A. K. (2015). The role of hypoxia in cancer progression, angiogenesis, metastasis, and resistance to therapy. Hypoxia, 3, 83–92. 10.2147/HP.S93413

National Cancer Institute. (2018, May 1,). External Beam Radiation Therapy for Cancer. National Cancer Institute. Retrieved Sep 20, 2024, from

https://www.cancer.gov/about-cancer/treatment/types/radiation-therapy/external-beam

Nativo, P., Prior, I. A., & Brust, M. (2008). Uptake and Intracellular Fate of Surface-Modified Gold Nanoparticles. ACS Nano, 2(8), 1639–1644. 10.1021/nn800330a

Nickoloff, J. A., Taylor, L., Sharma, N., & Kato, T. A. (2021). Exploiting DNA repair pathways for tumor sensitization, mitigation of resistance, and normal tissue protection in radiotherapy. Cancer Drug Resistance, 4(2), 244–263. 10.20517/cdr.2020.89

Nie, Y., Fu, G., & Leng, Y. (2023). Nuclear Delivery of Nanoparticle-Based Drug Delivery Systems by Nuclear Localization Signals. Cells, 12(12), 1637. 10.3390/cells12121637

Noël, C., Simard, J., & Girard, D. (2016). Gold nanoparticles induce apoptosis, endoplasmic reticulum stress events and cleavage of cytoskeletal proteins in human neutrophils. Toxicology in Vitro, 31, 12–22. 10.1016/j.tiv.2015.11.003

Oike, T., Komatsu, S., Komatsu, Y., Nachankar, A., Darwis, N. D. M., Shibata, A., & Ohno, T. (2020). Reporting of methodologies used for clonogenic assays to determine radiosensitivity. Journal of Radiation Research, 61(6), 828–831. 10.1093/jrr/rraa064

Okła, E., Białecki, P., Kędzierska, M., Pędziwiatr-Werbicka, E., Miłowska, K., Takvor, S., Gómez, R., de la Mata, F. J., Bryszewska, M., & Ionov, M. (2023). Pegylated Gold Nanoparticles Conjugated with siRNA: Complexes Formation and Cytotoxicity. International Journal of Molecular Sciences, 24(7), 6638. 10.3390/ijms24076638

Oladimeji, O., Akinyelu, J., Daniels, A., & Singh, M. (2021). Modified Gold Nanoparticles for Efficient Delivery of Betulinic Acid to Cancer Cell Mitochondria. International Journal of Molecular Sciences, 22(10), 5072. 10.3390/ijms22105072

Oliveira, B. B., Fernandes, A. R., & Baptista, P. V. (2024). Assessing the gene silencing potential of AuNP-based approaches on conventional 2D cell culture versus 3D tumor spheroid. Frontiers in Bioengineering and Biotechnology, 12, 1320729. 10.3389/fbioe.2024.1320729

Orozco-García, E., van Meurs, D. J., Calderón, J., Narvaez-Sanchez, R., & Harmsen, M. C. (2023). Endothelial plasticity across PTEN and Hippo pathways: A complex hormetic rheostat modulated by extracellular vesicles. Translational Oncology, 31, 101633. 10.1016/j.tranon.2023.101633

Overgaard, J., Sand Hansen, H., Lindeløv, B., Overgaard, M., Jørgensen, K., Rasmusson, B., & Berthelsen, A. (1991). Nimorazole as a hypoxic radiosensitizer in the treatment of supraglottic larynx and pharynx carcinoma. First report from the Danish Head and Neck Cancer Study (DAHANCA) protocol 5-85. Radiotherapy and Oncology: Journal of the European Society for Therapeutic Radiology and Oncology, 20 Suppl 1, 143–149. 10.1016/0167-8140(91)90202-r

Özçelik, S., & Pratx, G. (2020). Nuclear-targeted gold nanoparticles enhance cancer cell radiosensitization. Nanotechnology, 31(41), 415102. 10.1088/1361-6528/aba02b

Ozcicek, I., Aysit, N., Cakici, C., & Aydeger, A. (2021). The effects of surface functionality and size of gold nanoparticles on neuronal toxicity, apoptosis, ROS production and cellular/suborgan biodistribution. Materials Science & Engineering C, 128, 112308. 10.1016/j.msec.2021.112308

Patil, T., Gambhir, R., Vibhute, A., & Tiwari, A. P. (2023). Gold Nanoparticles: Synthesis Methods, Functionalization and Biological Applications. Journal of Cluster Science, 34(2), 705–725. 10.1007/s10876-022-02287-6

Paul, M. K., & Mukhopadhyay, A. K. (2004). Tyrosine kinase – Role and significance in Cancer. International Journal of Medical Sciences, 1(2), 101–115. https://www.ncbi.nlm.nih.gov/pmc/articles/PMC1074718/

PDQ Adult Treatment Editorial Board. (2023, February 16,). PDQ Prostate Cancer Treatment. Bethesda,MD: National Cancer Institute. Retrieved Sep 18, 2024, from https://www.cancer.gov/types/prostate/patient/prostate-treatment-pdq

Peckys, D. B., & de Jonge, N. (2011). Visualizing Gold Nanoparticle Uptake in Live Cells with Liquid Scanning Transmission Electron Microscopy. Nano Letters, 11(4), 1733–1738. 10.1021/nl200285r

Pellegata, N., Antoniono, R., Redpath, J. , & Stanbridge, E. (1996). DNA damage and p53-mediated cell cycle arrest: A reevaluation. Proceedings of the National

Academy of Sciences of the United States of America, 93(26), 15209–15214. 10.1073/pnas.93.26.15209

Peng, L., Niu, J., Zhang, C., Yu, W., Wu, J., Shan, Y., Wang, X., Shen, Y., Mao, Z., Liang, W., & Gao, J. (2014). TAT conjugated cationic noble metal nanoparticles for gene delivery to epidermal stem cells. Biomaterials, 35(21), 5605–5618. 10.1016/j.biomaterials.2014.03.062

Penninckx, S., Heuskin, A., Michiels, C., & Lucas, S. (2020). Gold Nanoparticles as a Potent Radiosensitizer: A Transdisciplinary Approach from Physics to Patient. Cancers, 12(8), 2021. 10.3390/cancers12082021

Penninckx, S., Pariset, E., Cekanaviciute, E., & Costes, S. V. (2021). Quantification of radiation-induced DNA double strand break repair foci to evaluate and predict biological responses to ionizing radiation. NAR Cancer, 3(4), zcab046. 10.1093/narcan/zcab046

Pham-Nguyen, O., Shin, J., Park, Y., Jin, S., Kim, S. R., Jung, Y. M., & Yoo, H. S. (2022). Fluorescence-Shadowing Nanoparticle Clusters for Real-Time photon irradiation (Masters).

Pierotti, M. A., Sozzi, G., & Croce, C. M. (2003). Mechanisms of oncogene activation. In D. W. Kufe, R. E. Pollock, R. R. Weichselbaum & O. N. Hamilton (Eds.), Holland-Frei Cancer Medicine. 6th edition (). BC Decker.

Poch, B., Gansauge, F., Schwarz, A., Seufferlein, T., Schnelldorfer, T., Ramadani, M., Beger, H. G., & Gansauge, S. (2001). Epidermal Growth Factor Induces Cyclin D1 in Human Pancreatic Carcinoma: Evidence for a Cyclin D1–Dependent Cell Cycle Progression. Pancreas, 23(3), 280. https://journals.lww.com/pancreasjournal/fulltext/2001/10000/epidermal_growth_factor_induces_cyclin_d1_in_human.9.aspx

Podhorecka, M., Skladanowski, A., & Bozko, P. (2010). H2AX Phosphorylation: Its Role in DNA Damage Response and Cancer Therapy. Journal of Nucleic Acids, 2010, 920161. 10.4061/2010/920161

Prasanna, P. G., Citrin, D. E., Hildesheim, J., Ahmed, M. M., Venkatachalam, S., Riscuta, G., Xi, D., Zheng, G., Deursen, J. v., Goronzy, J., Kron, S. J., Anscher, M. S., Sharpless, N. E., Campisi, J., Brown, S. L., Niedernhofer, L. J., O'Loghlen, A., Georgakilas, A. G., Paris, F., . . . Coleman, C. N. (2021). Therapy-Induced

Senescence: Opportunities to Improve Anticancer Therapy. JNCI: Journal of the National Cancer Institute, 113(10), 1285–1298. 10.1093/jnci/djab064

Prostate Cancer, U. K. (2024, Active Surveillance Evidence Base and Best Practice. Prostate Cancer UK. Retrieved Sep 18, 2024, from https://prostatecanceruk.org/for-health-professionals/resources/active-surveillance-hub/evidence-based-resources/

Qian, S., Wei, Z., Yang, W., Huang, J., Yang, Y., & Wang, J. (2022). The role of BCL-2 family proteins in regulating apoptosis and cancer therapy. Frontiers in Oncology, 12, 985363. 10.3389/fonc.2022.985363

Qin, S., He, X., Lin, H., Schulte, B. A., Zhao, M., Tew, K. D., & Wang, G. Y. (2021). Nrf2 inhibition sensitizes breast cancer stem cells to ionizing radiation via suppressing DNA repair. Free Radical Biology & Medicine, 169, 238–247. 10.1016/j.freeradbiomed.2021.04.006

Qiu, S., & Huang, J. (2021). MRN complex is an essential effector of DNA damage repair. Journal of Zhejiang University. Science. B, 22(1), 31–37. 10.1631/jzus.B2000289

Qu, D., Liao, L., & Ding, Q. (2020). Targeting of ovarian cancer cell through functionalized gold nanoparticles by novel glypican-3- binding peptide as a ultrasound contrast agents. Process Biochemistry, 98, 51–58. 10.1016/j.procbio.2020.07.019

Rahman, W. N., Bishara, N., Ackerly, T., He, C. F., Jackson, P., Wong, C., Davidson, R., & Geso, M. (2009). Enhancement of radiation effects by gold nanoparticles for superficial radiation therapy. Nanomedicine: Nanotechnology, Biology, and Medicine, 5(2), 136–142. 10.1016/j.nano.2009.01.014

Raitanen, J., Barta, B., Hacker, M., Georg, D., Balber, T., & Mitterhauser, M. (2023). Comparison of Radiation Response between 2D and 3D Cell Culture Models of Different Human Cancer Cell Lines. Cells, 12(3), 360. 10.3390/cells12030360

Rane, T. D., & Armani, A. M. (2016). Two-Photon Microscopy Analysis of Gold Nanoparticle Uptake in 3D Cell Spheroids. Plos One, 11(12), e0–e0167548. 10.1371/journal.pone.0167548

Rathore, R., & Van Tine, B. A. (2021). Pathogenesis and Current Treatment of Osteosarcoma: Perspectives for Future Therapies. Journal of Clinical Medicine, 10(6), 1182. 10.3390/jcm10061182

Read, G. H., Miura, N., Carter, J. L., Kines, K. T., Yamamoto, K., Devasahayam, N., Cheng, J. Y., Camphausen, K. A., Krishna, M. C., & Kesarwala, A. H. (2018). Three-dimensional alginate hydrogels for radiobiological and metabolic studies of cancer cells. Colloids and Surfaces. B, Biointerfaces, 171, 197–204. 10.1016/j.colsurfb.2018.06.018

Reichl, J. (2020). Generation of a 3D model of osteosarcoma

Reznickova, A., Slavikova, N., Kolska, Z., Kolarova, K., Belinova, T., Hubalek Kalbacova, M., Cieslar, M., & Svorcik, V. (2019). PEGylated gold nanoparticles: Stability, cytotoxicity and antibacterial activity. Colloids and Surfaces A: Physicochemical and Engineering Aspects, 560, 26–34. 10.1016/j.colsurfa.2018.09.083

Ribatti, D., Tamma, R., & Annese, T. (2020). Epithelial-Mesenchymal Transition in Cancer: A Historical Overview. Translational Oncology, 13(6), 100773. 10.1016/j.tranon.2020.100773

Roa, W., Zhang, X., Guo, L., Shaw, A., Hu, X., Xiong, Y., Gulavita, S., Patel, S., Sun, X., Chen, J., Moore, R., & Xing, J. Z. (2009). Gold nanoparticle sensitize radiotherapy of prostate cancer cells by regulation of the cell cycle. Nanotechnology, 20(37), 375101. 10.1088/0957-4484/20/37/375101

Rodríguez-Fajardo, V., Sanz, V., de Miguel, I., Berthelot, J., Aćimović, S. S., Porcar-Guezenec, R., & Quidant, R. (2018). Two-color dark-field (TCDF) microscopy for metal nanoparticle imaging inside cells. Nanoscale, 10(8), 4019–4027. 10.1039/c7nr09408f

Rosen, R. D., & Sapra, A. (2024). TNM Classification. StatPearls (). StatPearls Publishing.

Rosenberg, L. E., & Rosenberg, D. D. (2012). The Genetics of Cancer. In L. E. Rosenberg, & D. D. Rosenberg (Eds.), Human Genes and Genomes (pp. 259–288). Academic Press.

Roth, G. A., Tahiliani, S., Neu-Baker, N. M., & Brenner, S. A. (2015). Hyperspectral microscopy as an analytical tool for nanomaterials. Wiley

Interdisciplinary Reviews. Nanomedicine and Nanobiotechnology, 7(4), 565–579. 10.1002/wnan.1330

Sadida, H. Q., Abdulla, A., Marzooqi, S. A., Hashem, S., Macha, M. A., Akil, A. S. A., & Bhat, A. A. (2023). Epigenetic modifications: Key players in cancer heterogeneity and drug resistance. Translational Oncology, 39, 101821. 10.1016/j.tranon.2023.101821

Saini, R., Saini, S., & Sharma, S. (2010). Nanotechnology: The Future Medicine. Journal of Cutaneous and Aesthetic Surgery, 3(1), 32–33. 10.4103/0974-2077.63301

Salamone, T. A., Rutigliano, L., Pennacchi, B., Cerra, S., Matassa, R., Nottola, S., Sciubba, F., Battocchio, C., Marsotto, M., Del Giudice, A., Chumakov, A., Davydok, A., Grigorian, S., Canettieri, G., Agostinelli, E., & Fratoddi, I. (2023). Thiol functionalised gold nanoparticles loaded with methotrexate for cancer treatment: From synthesis to in vitro studies on neuroblastoma cell lines. Journal of Colloid and Interface Science, 649, 264–278. 10.1016/j.jcis.2023.06.078

Saman, H., Raza, S. S., Uddin, S., & Rasul, K. (2020). Inducing Angiogenesis, a Key Step in Cancer Vascularization, and Treatment Approaches. Cancers, 12(5), 1172. 10.3390/cancers12051172

Samani, R. K., Tavakoli, M. B., Maghsoudinia, F., Motaghi, H., Hejazi, S. H., & Mehrgardi, M. A. (2020). Trastuzumab and folic acid functionalized gold nanoclusters as a dual-targeted radiosensitizer for megavoltage radiation therapy of human breast cancer. European Journal of Pharmaceutical Sciences, 153, 105487. 10.1016/j.ejps.2020.105487

Schirripa, A., Sexl, V., & Kollmann, K. (2022). Cyclin-dependent kinase inhibitors in malignant hematopoiesis. Frontiers in Oncology, 12, 916682. 10.3389/fonc.2022.916682

Schmitt, C. A., Wang, B., & Demaria, M. (2022). Senescence and cancer — role and therapeutic opportunities. Nature Reviews Clinical Oncology, 19(10), 619–636. 10.1038/s41571-022-00668-4

Sell, M., Lopes, A. R., Escudeiro, M., Esteves, B., Monteiro, A. R., Trindade, T., & Cruz-Lopes, L. (2023). Application of Nanoparticles in Cancer Treatment: A Concise Review. Nanomaterials, 13(21), 2887. 10.3390/nano13212887

Seoane, J., & Gomis, R. R. (2017). TGF-β Family Signaling in Tumor Suppression and Cancer Progression. Cold Spring Harbor Perspectives in Biology, 9(12), a022277. 10.1101/cshperspect.a022277

Sgouros, G., Bodei, L., McDevitt, M. R., & Nedrow, J. R. (2020). Radiopharmaceutical therapy in cancer: clinical advances and challenges. Nature Reviews Drug Discovery, 19(9), 589–608. 10.1038/s41573-020-0073-9

Shackleton, M., Quintana, E., Fearon, E. R., & Morrison, S. J. (2009). Heterogeneity in Cancer: Cancer Stem Cells versus Clonal Evolution. Cell, 138(5), 822–829. 10.1016/j.cell.2009.08.017

Shah, A., Adhikari, B., Martic, S., Munir, A., Shahzad, S., Ahmad, K., & Kraatz, H. (2015). Electron transfer in peptides. Chemical Society Reviews, 44(4), 1015–1027. 10.1039/c4cs00297k

Sharma, A., Boise, L. H., & Shanmugam, M. (2019). Cancer Metabolism and the Evasion of Apoptotic Cell Death. Cancers, 11(8), 1144. 10.3390/cancers11081144

Sheridan, A. J., Thompson, K. C., & Slater, J. M. (2022). Interaction of negatively and positively capped gold nanoparticle with different lipid model membranes. Biophysical Chemistry, 290, 106896. 10.1016/j.bpc.2022.106896

Sherr, C. J., & McCormick, F. (2002). The RB and p53 pathways in cancer. Cancer Cell, 2(2), 103–112. 10.1016/S1535-6108(02)00102-2

Shiue, A., Chen, J., Chang, C., Chang, S., Hwa, K., Chin, K., & Leggett, G. (2020). Synthesis and cytotoxic analysis of thiolated xylose derivatives decorated on gold nanoparticles. Biotechnology Reports, 28, e00549. 10.1016/j.btre.2020.e00549

Shortt, J., & Johnstone, R. W. (2012). Oncogenes in Cell Survival and Cell Death. Cold Spring Harbor Perspectives in Biology, 4(12), a009829. 10.1101/cshperspect.a009829

Sia, J., Szmyd, R., Hau, E., & Gee, H. E. (2020). Molecular Mechanisms of Radiation-Induced Cancer Cell Death: A Primer. Frontiers in Cell and Developmental Biology, 8, 41. 10.3389/fcell.2020.00041

Siboro, S. A. P., Anugrah, D. S. B., Ramesh, K., Park, S., Kim, H., & Lim, K. T. (2021). Tunable porosity of covalently crosslinked alginate-based hydrogels and

its significance in drug release behavior. Carbohydrate Polymers, 260, 117779. 10.1016/j.carbpol.2021.117779

Siddique, S., & Chow, J. C. L. (2020). Gold Nanoparticles for Drug Delivery and Cancer Therapy. Applied Sciences, 10(11), 3824. 10.3390/app10113824

Silva, F., D'Onofrio, A., Mendes, C., Pinto, C., Marques, A., Campello, M. P. C., Oliveira, M. C., Raposinho, P., Belchior, A., Di Maria, S., Marques, F., Cruz, C., Carvalho, J., & Paulo, A. (2022). Radiolabeled Gold Nanoseeds Decorated with Substance P Peptides: Synthesis, Characterization and In Vitro Evaluation in Glioblastoma Cellular Models. International Journal of Molecular Sciences, 23(2), 617. 10.3390/ijms23020617

Sim, S., & Wong, N. K. (2021). Nanotechnology and its use in imaging and drug delivery (Review). Biomedical Reports, 14(5), 42. 10.3892/br.2021.1418

Singh, R., & Manna, P. P. (2022). Reactive oxygen species in cancer progression and its role in therapeutics. Exploration of Medicine, 3(1), 43–57. 10.37349/emed.2022.00073

Sinkala, M. (2023). Mutational landscape of cancer-driver genes across human cancers. Scientific Reports, 13, 12742. 10.1038/s41598-023-39608-2

Smeland, S., Bielack, S. S., Whelan, J., Bernstein, M., Hogendoorn, P., Krailo, M. D., Gorlick, R., Janeway, K. A., Ingleby, F. C., Anninga, J., Antal, I., Arndt, C., Brown, K. L. B., Butterfass-Bahloul, T., Calaminus, G., Capra, M., Dhooge, C., Eriksson, M., Flanagan, A. M., . . . Marina, N. (2019). Survival and prognosis with osteosarcoma: outcomes in more than 2000 patients in the EURAMOS-1 (European and American Osteosarcoma Study) cohort. European Journal of Cancer, 109, 36–50. 10.1016/j.ejca.2018.11.027

Soares, S., Aires, F., Monteiro, A., Pinto, G., Faria, I., Sales, G., Correa-Duarte, M. A., Guerreiro, S., & Fernandes, R. (2024). Radiotherapy Metastatic Prostate Cancer Cell Lines Treated with Gold Nanorods Modulate miRNA Signatures. International Journal of Molecular Sciences, 25(5), 2754. 10.3390/ijms25052754

Soares, S., Sousa, J., Pais, A., & Vitorino, C. (2018). Nanomedicine: Principles, Properties, and Regulatory Issues. Frontiers in Chemistry, 6, 360. 10.3389/fchem.2018.00360

Song, X., Sun, Z., Li, L., Zhou, L., & Yuan, S. (2023). Application of nanomedicine in radiotherapy sensitization. Frontiers in Oncology, 13, 1088878. 10.3389/fonc.2023.1088878

Soto, A. M., & Sonnenschein, C. (2011). The tissue organization field theory of cancer: A testable replacement for the somatic mutation theory. BioEssays : News and Reviews in Molecular, Cellular and Developmental Biology, 33(5), 332–340. 10.1002/bies.201100025

Spałek, M. J., Poleszczuk, J., Czarnecka, A. M., Dudzisz-Śledź, M., Napieralska, A., Matysiakiewicz, J., Chojnacka, M., Raciborska, A., Sztuder, A., Maciejczyk, A., Szulc, A., Skóra, T., Cybulska-Stopa, B., Winiecki, T., Kaźmierska, J., Tomasik, B., Fijuth, J., & Rutkowski, P. (2021). Radiotherapy in the Management of Pediatric and Adult Osteosarcomas: A Multi-Institutional Cohort Analysis. Cells, 10(2), 366. 10.3390/cells10020366

Sriramulu, S., Thoidingjam, S., Brown, S. L., Siddiqui, F., Movsas, B., & Nyati, S. (2023). Molecular targets that sensitize cancer to radiation killing: From the bench to the bedside. Biomedicine & Pharmacotherapy, 158, 114126. 10.1016/j.biopha.2022.114126

Stanciu, I., Parosanu, A. I., Orlov-Slavu, C., Iaciu, I. C., Popa, A. M., Olaru, C. M., Pirlog, C. F., Vrabie, R. C., & Nitipir, C. (2023). Mechanisms of Resistance to CDK4/6 Inhibitors and Predictive Biomarkers of Response in HR+/HER2- Metastatic Breast Cancer—A Review of the Literature. Diagnostics, 13(5), 987. 10.3390/diagnostics13050987

Stewart, B. W. (2019). Mechanisms of carcinogenesis: from initiation and promotion to the hallmarks. In R. A. Baan, B. W. Stewart & K. Straif (Eds.), Tumour Site Concordance and Mechanisms of Carcinogenesis (). International Agency for Research on Cancer.

Stish, B. J., Davis, B. J., Mynderse, L. A., McLaren, R. H., Deufel, C. L., & Choo, R. (2018). Low dose rate prostate brachytherapy. Translational Andrology and Urology, 7(3), 341–356. 10.21037/tau.2017.12.15

Tabatabaie, F., Franich, R., Feltis, B., & Geso, M. (2022). Oxidative Damage to Mitochondria Enhanced by Ionising Radiation and Gold Nanoparticles in Cancer Cells. International Journal of Molecular Sciences, 23(13), 6887. 10.3390/ijms23136887

Tai, S., Sun, Y., Squires, J. M., Zhang, H., Oh, W. K., Liang, C., & Huang, J. (2011). PC3 Is a Cell Line Characteristic of Prostatic Small Cell Carcinoma. The Prostate, 71(15), 1668–1679. 10.1002/pros.21383

Takahashi, H., Oshi, M., Asaoka, M., Yan, L., & Takabe, K. (2020). Molecular biological features of Nottingham histological Grade 3 breast cancers. Annals of Surgical Oncology, 27(11), 4475–4485. 10.1245/s10434-020-08608-1

Takahashi, N., Cho, P., Selfors, L. M., Kuiken, H. J., Kaul, R., Fujiwara, T., Harris, I. S., Zhang, T., Gygi, S. P., & Brugge, J. S. (2020). 3D Culture Models with CRISPR Screens Reveal Hyperactive NRF2 as a Prerequisite for Spheroid Formation via Regulation of Proliferation and Ferroptosis. Molecular Cell, 80(5), 828–844.e6. 10.1016/j.molcel.2020.10.010

Tang, M., Lu, X., Zhang, C., Du, C., Cao, L., Hou, T., Li, Z., Tu, B., Cao, Z., Li, Y., Chen, Y., Jiang, L., Wang, H., Wang, L., Liu, B., Xu, X., Luo, J., Wang, J., Gu, J., Zhu, W. (2017). Downregulation of SIRT7 by 5-fluorouracil induces radiosensitivity in human colorectal cancer. Theranostics, 7(5), 1346–1359. 10.7150/thno.18804

Taniere, P., O'Sullivan, B., Evans, M., & Hughes, F. (2019). Molecular pathology. In S. K. Suvarna, C. Layton & J. D. Bancroft (Eds.), Bancroft's Theory and Practice of Histological Techniques (Eighth Edition) (pp. 395–433). Elsevier.

Taylor, B. C., & Balko, J. M. (2022). Mechanisms of MHC-I Downregulation and Role in Immunotherapy Response. Frontiers in Immunology, 1310.3389/fimmu.2022.844866

Teh, B. S., Blanco, A. I., Paulino, A. C., & Butler, E. B. (2011). Prostate Cancer. In J. J. Lu, & L. W. Brady (Eds.), Decision Making in Radiation Oncology, Volume 2 (pp. 567–610). Springer. 10.1007/978-3-642-13832-4

Teraoka, S., Kakei, Y., Akashi, M., Iwata, E., Hasegawa, T., Miyawaki, D., Sasaki, R., & Komori, T. (2018). Gold nanoparticles enhance X-ray irradiation-induced apoptosis in head and neck squamous cell carcinoma in vitro. Biomedical Reports, 9(5), 415–420. 10.3892/br.2018.1142

The Royal College of Radiologists. (2024). Radiotherapy dose fractionation (4th ed.). Clinical Oncology.

Thomas, S. K., Lee, J., & Beatty, G. L. (2020). Paracrine and cell autonomous signalling in pancreatic cancer progression and metastasis. EBioMedicine, 53, 102662. 10.1016/j.ebiom.2020.102662

Tímár, J., Honn, K. V., Hendrix, M. J. C., Marko-Varga, G., & Jalkanen, S. (2023). Newly identified form of phenotypic plasticity of cancer: immunogenic mimicry. Cancer Metastasis Reviews, 42(1), 323–334. 10.1007/s10555-023-10087-1

Tkachenko, A. G., Xie, H., Coleman, D., Glomm, W., Ryan, J., Anderson, M. F., Franzen, S., & Feldheim, D. L. (2003). Multifunctional Gold Nanoparticle−Peptide Complexes for Nuclear Targeting. Journal of the American Chemical Society, 125(16), 4700–4701. 10.1021/ja0296935

Tomlins, S. A., Rhodes, D. R., Perner, S., Dhanasekaran, S. M., Mehra, R., Sun, X., Varambally, S., Cao, X., Tchinda, J., Kuefer, R., Lee, C., Montie, J. E., Shah, R. B., Pienta, K. J., Rubin, M. A., & Chinnaiyan, A. M. (2005). Recurrent Fusion of TMPRSS2 and ETS Transcription Factor Genes in Prostate Cancer. Science, 310(5748), 644–648. 10.1126/science.1117679

Tremi, I., Havaki, S., Georgitsopoulou, S., Terzoudi, G., Lykakis, I. N., Iliakis, G., Georgakilas, V., Gorgoulis, V. G., & Georgakilas, A. G. (2022). Biological Response of Human Cancer Cells to Ionizing Radiation in Combination with Gold Nanoparticles. Cancers, 14(20), 5086. 10.3390/cancers14205086

Tudda, A., Donzelli, E., Nicolini, G., Semperboni, S., Bossi, M., Cavaletti, G., Castriconi, R., Mangili, P., Vecchio, A. d., Sarno, A., Mettivier, G., & Russo, P. (2022). Breast radiotherapy with kilovoltage photons and gold nanoparticles as radiosensitizer: An in vitro study. Medical Physics (Lancaster), 49(1), 568–578. 10.1002/mp.15348

Tunç, C. Ü, & Aydin, O. (2022). Co-delivery of Bcl-2 siRNA and doxorubicin through gold nanoparticle-based delivery system for a combined cancer therapy approach. Journal of Drug Delivery Science and Technology, 74, 103603. 10.1016/j.jddst.2022.103603

Tyagi, N., Gambhir, K., Pandey, R., Gangenahalli, G., & Verma, Y. K. (2022). Minimizing the negative charge of Alginate facilitates the delivery of negatively charged molecules inside cells. Journal of Polymer Research, 29(1)10.1007/s10965-021-02813-6

van Dooijeweert, C., van Diest, P. J., & Ellis, I. O. (2022). Grading of invasive breast carcinoma: the way forward. Virchows Archiv, 480(1), 33–43. 10.1007/s00428-021-03141-2

Varma, M., Delahunt, B., Cheng, L., Chetty, R., Compérat, E., Deshpande, V., Egevad, L., van der Kwast, T. H., Lopez-Beltran, A., & McCluggage, W. G. (2023). Tumour grading: communication is the key. Journal of Clinical Pathology, 76(5), 291–292. 10.1136/jcp-2023-208824

Verma, M., Sheoran, P., & Chaudhury, A. (2018). Application of Nanotechnology for Cancer Treatment. In S. K. Gahlawat, J. S. Duhan, R. K. Salar, P. Siwach, S. Kumar & P. Kaur (Eds.), Advances in Animal Biotechnology and its Applications (pp. 161–178). Springer.

Victorelli, S., & Passos, J. F. (2017). Telomeres and Cell Senescence - Size Matters Not. EBioMedicine, 21, 14–20. 10.1016/j.ebiom.2017.03.027

Villalobos Gutiérrez, P. T., Muñoz Carrillo, J. L., Sandoval Salazar, C., Viveros Paredes, J. M., & Gutiérrez Coronado, O. (2023). Functionalized Metal Nanoparticles in Cancer Therapy. Pharmaceutics, 15(7), 1932. 10.3390/pharmaceutics15071932

Vines, J. B., Yoon, J., Ryu, N., Lim, D., & Park, H. (2019). Gold Nanoparticles for Photothermal Cancer Therapy. Frontiers in Chemistry, 710.3389/fchem.2019.00167

Wagner, K., & Wagner, N. (2022). The Senescence Markers p16INK4A, p14ARF/p19ARF, and p21 in Organ Development and Homeostasis. Cells, 11(12), 1966. 10.3390/cells11121966

Wainwright, E. N., & Scaffidi, P. (2017). Epigenetics and Cancer Stem Cells: Unleashing, Hijacking, and Restricting Cellular Plasticity. Trends in Cancer, 3(5), 372–386. 10.1016/j.trecan.2017.04.004

Wang, B., Guo, H., Yu, H., Chen, Y., Xu, H., & Zhao, G. (2021). The Role of the Transcription Factor EGR1 in Cancer. Frontiers in Oncology, 1110.3389/fonc.2021.642547

Wang, E. C., & Wang, A. Z. (2014). Nanoparticles and Their Applications in Cell and Molecular Biology. Integrative Biology : Quantitative Biosciences from Nano to Macro, 6(1), 9–26. 10.1039/c3ib40165k

Wang, H., Guo, M., Wei, H., & Chen, Y. (2023). Targeting p53 pathways: mechanisms, structures, and advances in therapy. Signal Transduction and Targeted Therapy, 8(1), 92. 10.1038/s41392-023-01347-1

Wang, L., Wu, C., Rajasekaran, N., & Shin, Y. (2018). Loss of Tumor Suppressor Gene Function in Human Cancer: An Overview. Cellular Physiology and Biochemistry, 51(6), 2647–2693. 10.1159/000495956

Wang, S., Tseng, L., & Lee, H. (2023). Role of mitochondrial alterations in human cancer progression and cancer immunity. Journal of Biomedical Science, 30(1), 61. 10.1186/s12929-023-00956-w

Wang, W., Li, L., & Cui, J. (2020). Chromosome structural variation in tumorigenesis: mechanisms of formation and carcinogenesis. Epigenetics & Chromatin, 13(1), 1–17. 10.1186/s13072-020-00371-7

Wang, Z. (2021). Regulation of Cell Cycle Progression by Growth Factor-Induced Cell Signaling. Cells, 10(12), 3327. 10.3390/cells10123327

Wiecek, A. J., Cutty, S. J., Kornai, D., Parreno-Centeno, M., Gourmet, L. E., Malagoli Tagliazucchi, G., Jacobson, D. H., Zhang, P., Bond, G. L., Barr, A. R., & Secrier, M. (2023). Genomic hallmarks and therapeutic implications of G0 cell cycle arrest in cancer. Genome Biology, 24(128). 10.1186/s13059-023-02963-4

Wishart, G., Gupta, P., Schettino, G., Nisbet, A., & Velliou, E. (2021). 3d tissue models as tools for radiotherapy screening for pancreatic cancer. The British Journal of Radiology, 94(1120), 20201397. 10.1259/bjr.20201397

Wolfe, T., PhD, Chatterjee, D., PhD, Lee, J., MD, Grant, J. D., MD, Bhattarai, S., PhD, Tailor, R., PhD, Goodrich, G., PhD, Nicolucci, P., PhD, & Krishnan, S., MD. (2015). Targeted gold nanoparticles enhance sensitization of prostate tumors to megavoltage radiation therapy in vivo. Nanomedicine, 11(5), 1277–1283. 10.1016/j.nano.2014.12.016

Wong, W., Guerra Liberal, F. D. C., & McMahon, S. J. (2022). DNA Repair Inhibitors Potentiate Fractionated Radiotherapy More Than Single-Dose Radiotherapy in Breast Cancer Cells. Cancers, 14(15), 3794. 10.3390/cancers14153794

Wu, P., Onodera, Y., Ichikawa, Y., Rankin, E. B., Giaccia, A. J., Watanabe, Y., Qian, W., Hashimoto, T., Shirato, H., & Nam, J. (2017). Targeting integrins with

RGD-conjugated gold nanoparticles in radiotherapy decreases the invasive activity of breast cancer cells. International Journal of Nanomedicine, 12, 5069–5085. 10.2147/IJN.S137833

Wu, S., Lu, H., & Bai, Y. (2019). Nrf2 in cancers: A double-edged sword. Cancer Medicine, 8(5), 2252–2267. 10.1002/cam4.2101

Wu, Y., Song, Y., Wang, R., & Wang, T. (2023). Molecular mechanisms of tumor resistance to radiotherapy. Molecular Cancer, 22(1), 96. 10.1186/s12943-023-01801-2

Xia, Q., Huang, J., Feng, Q., Chen, X., Liu, X., Li, X., Zhang, T., Xiao, S., Li, H., Zhong, Z., & Xiao, K. (2019). Size- and cell type-dependent cellular uptake, cytotoxicity and in vivo distribution of gold nanoparticles. International Journal of Nanomedicine, 14, 6957–6970. 10.2147/IJN.S214008

Xiao, S., Qin, D., Hou, X., Tian, L., Yu, Y., Zhang, R., Lyu, H., Guo, D., Chen, X., Zhou, C., & Tang, J. (2023). Cellular senescence: a double-edged sword in cancer therapy. Frontiers in Oncology, 13, 1189015. 10.3389/fonc.2023.1189015

Xie, B., Zhang, H., Yu, L., Wang, J., Pang, B., Wu, R., Qian, X., Li, S., Shi, Q., Wang, L., & Zhou, J. (2010). The radiation response of androgen-refractory prostate cancer cell line C4-2 derived from androgen-sensitive cell line LNCaP. Asian Journal of Andrology, 12(3), 405–414. 10.1038/aja.2009.91

Xie, W., Wang, L., Zhang, Y., Su, L., Shen, A., Tan, J., & Hu, J. (2009). Nuclear Targeted Nanoprobe for Single Living Cell Detection by Surface-Enhanced Raman Scattering. Bioconjugate Chemistry, 20(4), 768–773. 10.1021/bc800469g

Xu, X., Peng, Q., Jiang, X., Tan, S., Yang, Y., Yang, W., Han, Y., Chen, Y., Oyang, L., Lin, J., Xia, L., Peng, M., Wu, N., Tang, Y., Li, J., Liao, Q., & Zhou, Y. (2023). Metabolic reprogramming and epigenetic modifications in cancer: from the impacts and mechanisms to the treatment potential. Experimental & Molecular Medicine, 55(7), 1357–1370. 10.1038/s12276-023-01020-1

Yafout, M., Ousaid, A., Khayati, Y., & El Otmani, I. S. (2021). Gold nanoparticles as a drug delivery system for standard chemotherapeutics: A new lead for targeted pharmacological cancer treatments. Scientific African, 11, e00685. 10.1016/j.sciaf.2020.e00685

Yan, Y., Black, C. P., & Cowan, K. H. (2007). Irradiation-induced G2/M checkpoint response requires ERK1/2 activation | Oncogene. Oncogene, 26, 4689–4698. 10.1038/sj.onc.1210268

Yang, T., Zhai, J., Hu, D., Yang, R., Wang, G., Li, Y., & Liang, G. (2022). “Targeting Design” of Nanoparticles in Tumor Therapy. Pharmaceutics, 14(9), 1919. 10.3390/pharmaceutics14091919

Yao, Y., Zhou, Y., Liu, L., Xu, Y., Chen, Q., Wang, Y., Wu, S., Deng, Y., Zhang, J., & Shao, A. (2020). Nanoparticle-Based Drug Delivery in Cancer Therapy and Its Role in Overcoming Drug Resistance. Frontiers in Molecular Biosciences, 7, 193. 10.3389/fmolb.2020.00193

Yaswen, P., MacKenzie, K. L., Keith, W. N., Hentosh, P., Rodier, F., Zhu, J., Firestone, G. L., Matheu, A., Carnero, A., Bilsland, A., Sundin, T., Honoki, K., Fujii, H., Georgakilas, A. G., Amedei, A., Amin, A., Helferich, B., Boosani, C. S., Guha, G., . . . Yang, X. (2015). Therapeutic targeting of replicative immortality. Seminars in Cancer Biology, 35(Suppl), S104–S128. 10.1016/j.semcancer.2015.03.007

Yu, W., Hua, Y., Qiu, H., Hao, J., Zou, K., Li, Z., Hu, S., Guo, P., Chen, M., Sui, S., Xiong, Y., Li, F., Lu, J., Guo, W., Luo, G., & Deng, W. (2020). PD-L1 promotes tumor growth and progression by activating WIP and β-catenin signaling pathways and predicts poor prognosis in lung cancer. Cell Death & Disease, 11(7), 1–16. 10.1038/s41419-020-2701-z

Yu, Y., Liu, S., Yang, L., Song, P., Liu, Z., Liu, X., Yan, X., & Dong, Q. (2024). Roles of reactive oxygen species in inflammation and cancer. MedComm, 5(4), e519. 10.1002/mco2.519

Yue, J., Feliciano, T. J., Li, W., Lee, A., & Odom, T. W. (2017). Gold Nanoparticle Size and Shape Effects on Cellular Uptake and Intracellular Distribution of siRNA Nanoconstructs. Bioconjugate Chemistry, 28(6), 1791–1800. 10.1021/acs.bioconjchem.7b00252

Żelechowska-Matysiak, K., Wawrowicz, K., Wierzbicki, M., Budlewski, T., Bilewicz, A., & Majkowska-Pilip, A. (2023). Doxorubicin- and Trastuzumab-Modified Gold Nanoparticles as Potential Multimodal Agents for Targeted Therapy of HER2+ Cancers. Molecules, 28(6), 2451. 10.3390/molecules28062451

Zhang, T., Ma, C., Zhang, Z., Zhang, H., & Hu, H. (2021). NF-κB signaling in inflammation and cancer. MedComm, 2(4), 618–653. 10.1002/mco2.104

Zhao, G., Feng, L., Ye, T., Liu, Y., Fan, L., Ye, C., & Chen, J. (2023). Cetuximab enhances radiosensitivity of esophageal squamous cell carcinoma cells by G2/M cycle arrest and DNA repair delay through inhibiting p-EGFR and p-ERK. Thoracic Cancer, 14(22), 2127–2138. 10.1111/1759-7714.14995

Zhao, H., Wu, L., Yan, G., Chen, Y., Zhou, M., Wu, Y., & Li, Y. (2021). Inflammation and tumor progression: signaling pathways and targeted intervention. Signal Transduction and Targeted Therapy, 6(1), 1–46. 10.1038/s41392-021-00658-5

Zhao, Y., Feng, Y., Li, J., Cui, C., Wang, A., Fang, J., Zhang, Y., Ye, S., Mao, Q., Wang, X., & Shi, H. (2022). Endogenous ROS-Mediated Covalent Immobilization of Gold Nanoparticles in Mitochondria: A “Sharp Sword” in Tumor Radiotherapy. ACS Chemical Biology, 17(8), 2355–2365. 10.1021/acschembio.2c00475

Zheng, Y., & Sanche, L. (2023). Mechanisms of Nanoscale Radiation Enhancement by Metal Nanoparticles: Role of Low Energy Electrons. International Journal of Molecular Sciences, 24(5), 4697. 10.3390/ijms24054697

APPENDICES

Appendix A – untreated controls for LA-ICP-MSI analysis.

(A)

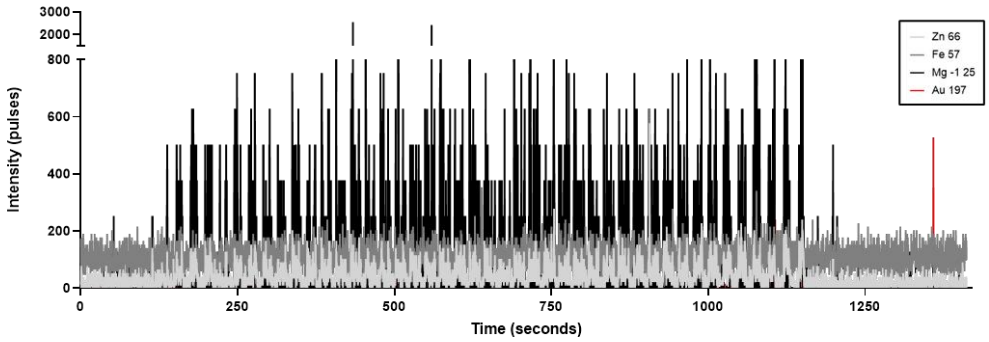

(B)

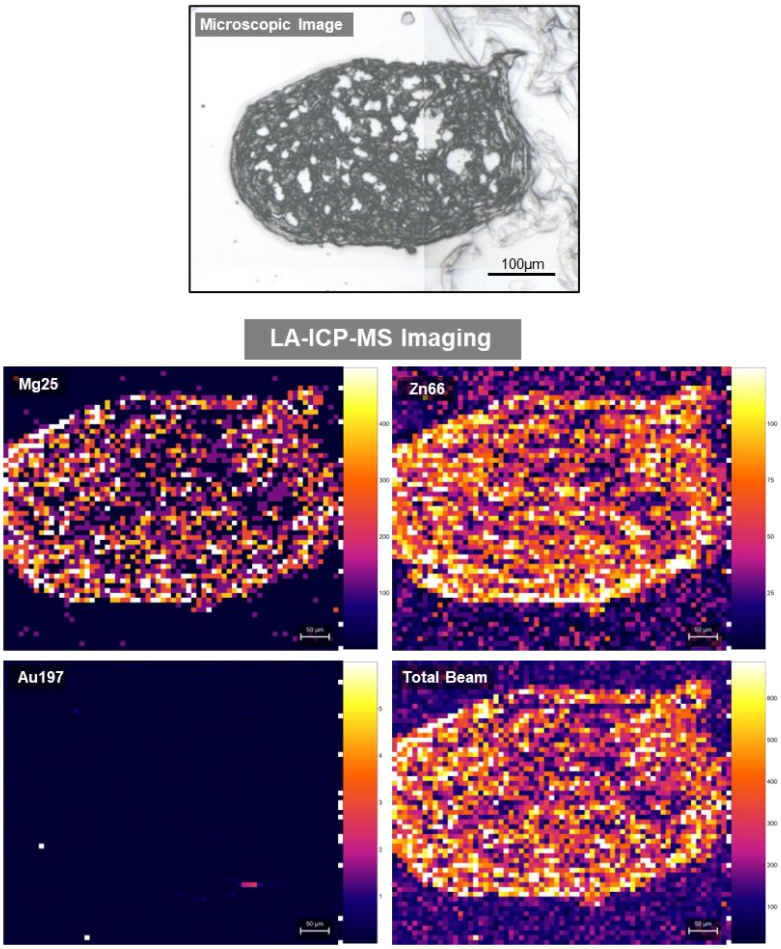

Figure XVI – LA-ICP-MSI analysis of untreated MG-63 spheroid. . (A) Intensity vs. time profile of ablated raster shows uptake of AuNPs demonstrated by the ^{197}Au spectrum (red). 20µm/sec scan speed. **(B)** LA-ICP-MSI of AuNP treated MG-63 spheroid. Pre-ablation optical image (20X objective) and elemental maps of ^{66}Zn, ^{25}Mg, ^{197}Au, and total beam. Scale bar represents 50µm.

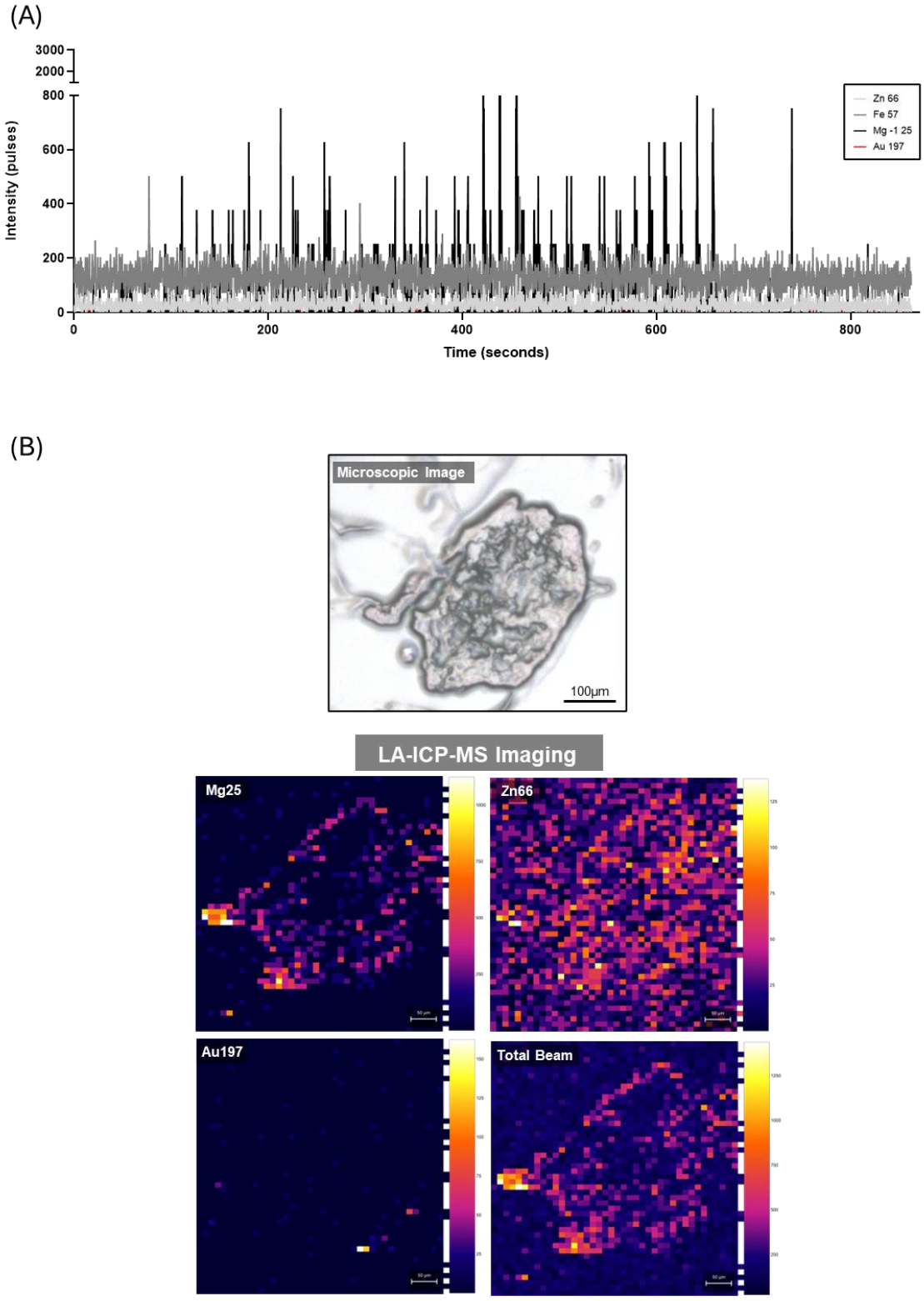

Figure XVII - LA-ICP-MSI analysis of untreated Saos-2 spheroid. (A) Intensity vs. time profile of ablated raster shows uptake of AuNPs demonstrated by the ^{197}Au spectrum (red). 20µm/sec scan speed. **(B)** LA-ICP-MSI of AuNP treated MG-63 spheroid. Pre-ablation optical image (20X objective) and elemental maps of ^{66}Zn, ^{25}Mg, ^{197}Au, and total beam. Scale bar represents 50µm.

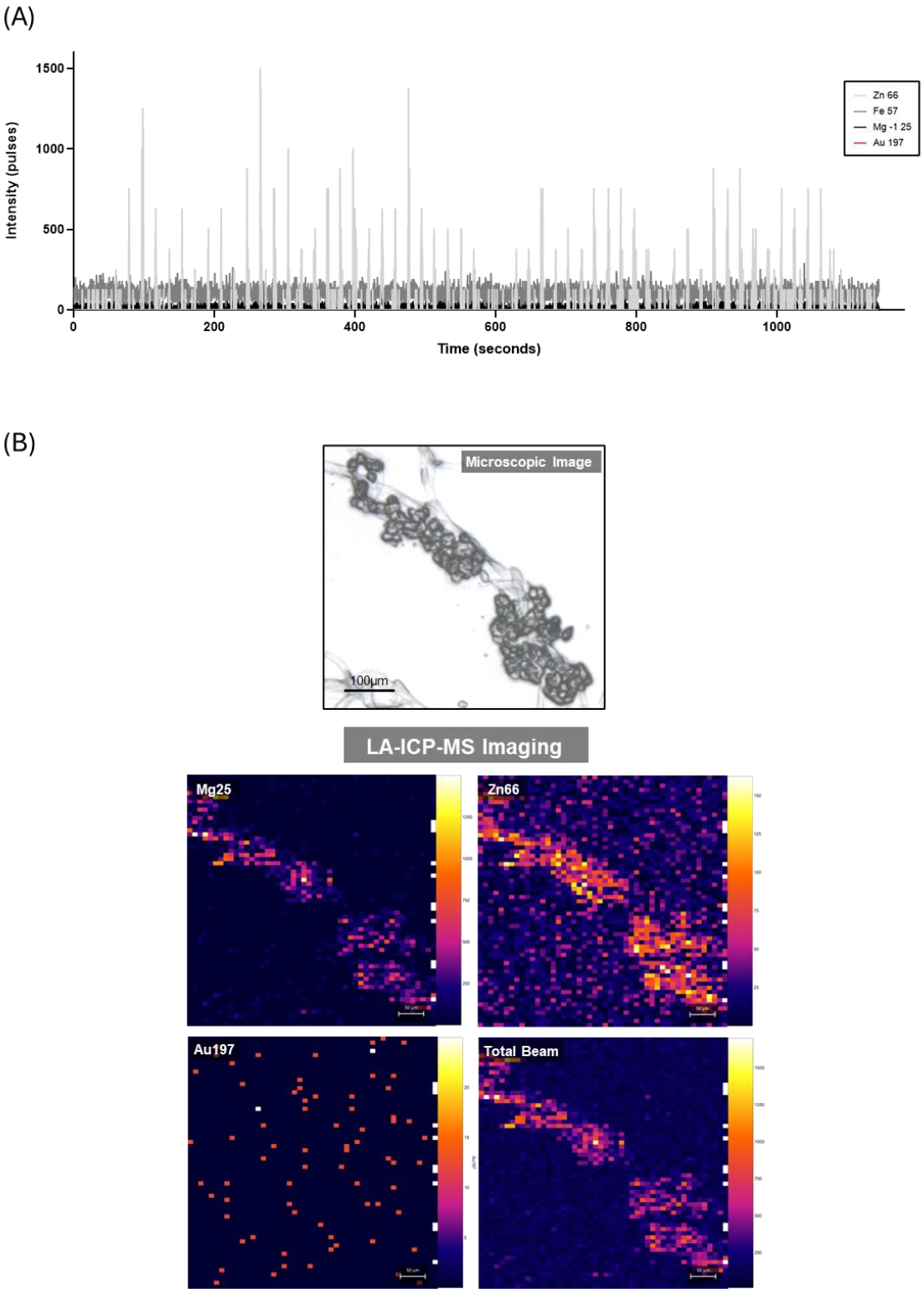

Figure XVIII - LA-ICP-MSI analysis of untreated PC3 spheroid. (A) Intensity vs. time profile of ablated raster shows uptake of AuNPs demonstrated by the ^{197}Au spectrum (red). 20µm/sec scan speed. **(B)** LA-ICP-MSI of AuNP treated MG-63 spheroid. Pre-ablation optical image (20X objective) and elemental maps of ^{66}Zn, ^{25}Mg, ^{197}Au, and total beam. Scale bar represents 50µm.

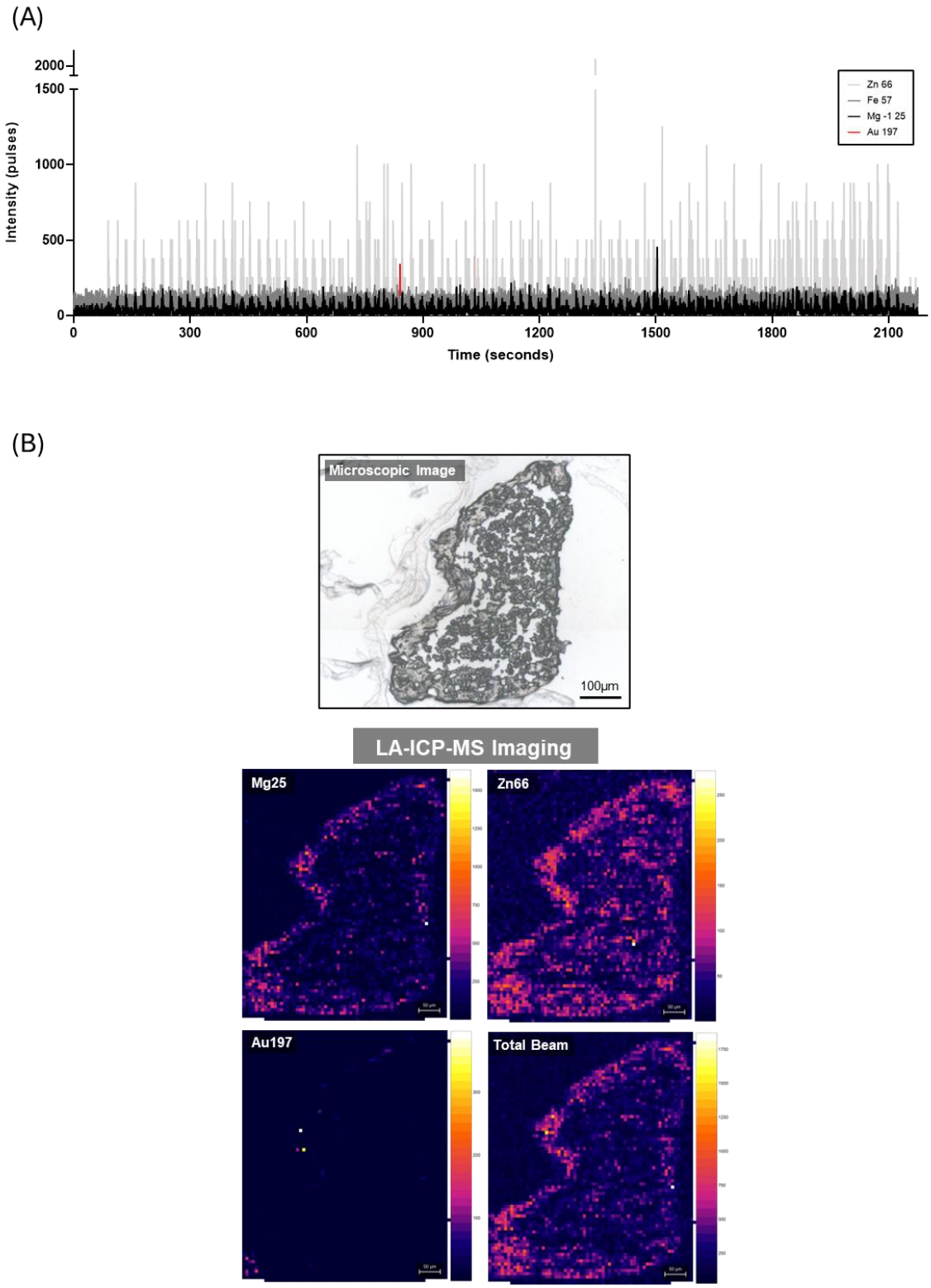

Figure XIX - LA-ICP-MSI analysis of untreated LNCaP spheroid. (A) Intensity vs. time profile of ablated raster shows uptake of AuNPs demonstrated by the ^{197}Au spectrum (red). 20µm/sec scan speed. **(B)** LA-ICP-MSI of AuNP treated MG-63 spheroid. Pre-ablation optical image (20X objective) and elemental maps of ^{66}Zn, ^{25}Mg, ^{197}Au, and total beam. Scale bar represents 50µm.

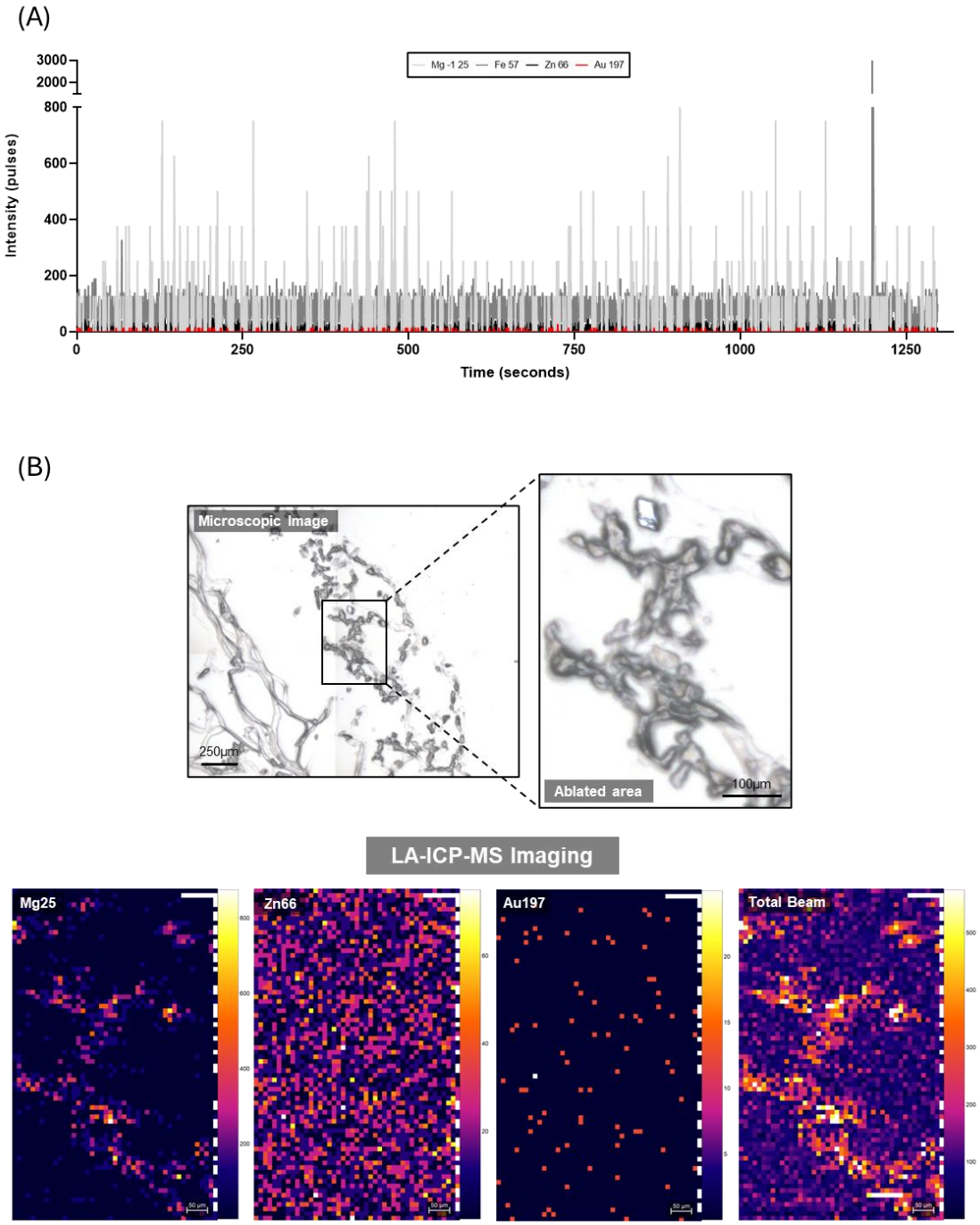

Figure XX - LA-ICP-MSI analysis of untreated MG-63 alginate sphere. (A) Intensity vs. time profile of ablated raster shows uptake of AuNPs demonstrated by the ^{197}Au spectrum (red). 20µm/sec scan speed. **(B)** LA-ICP-MSI of AuNP treated MG-63 spheroid. Pre-ablation optical image (20X objective) and elemental maps of ^{66}Zn, ^{25}Mg, ^{197}Au, and total beam. Scale bar represents 50µm.

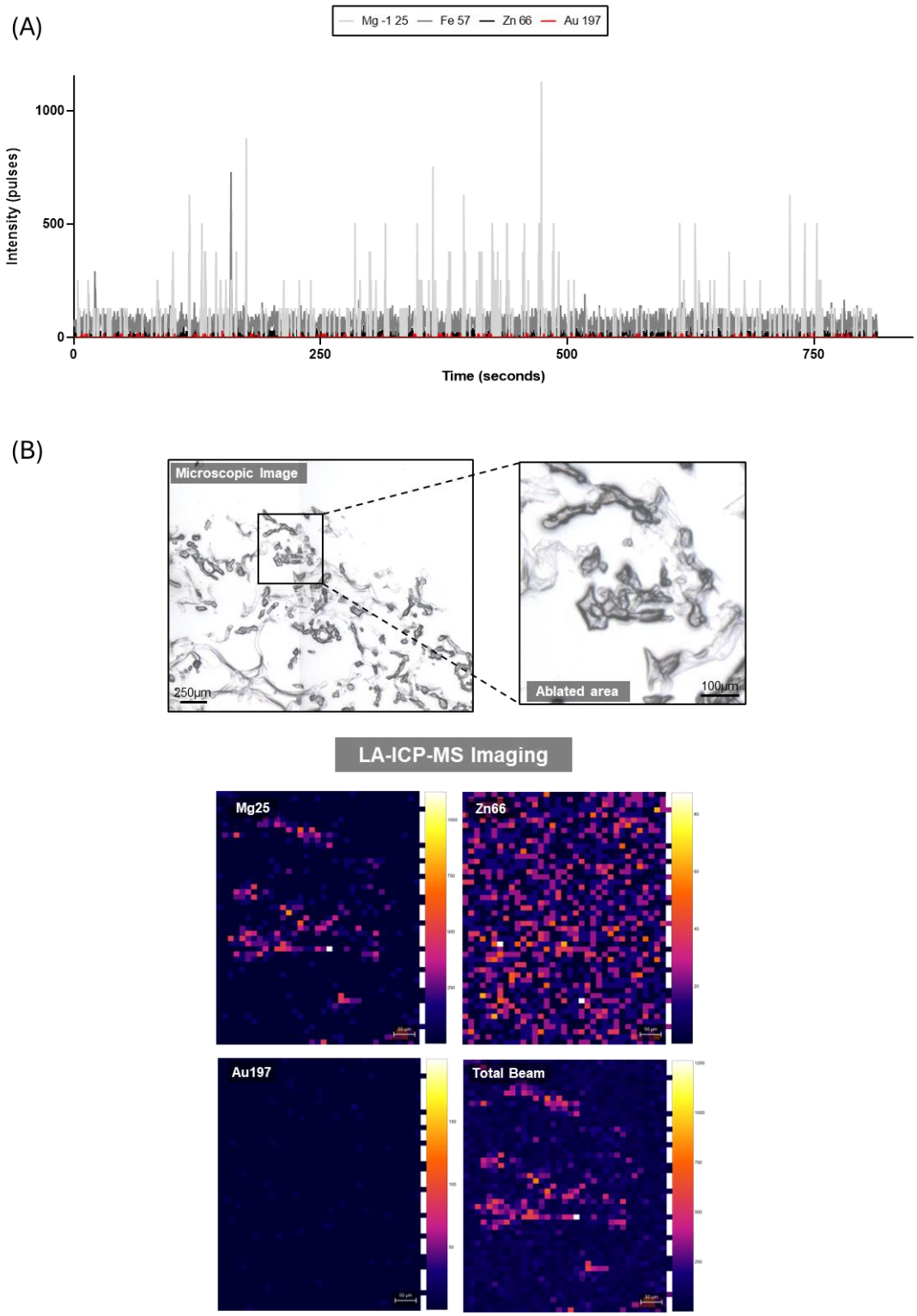

Figure XXI - LA-ICP-MSI analysis of untreated Saos-2 alginate sphere. (A) Intensity vs. time profile of ablated raster shows uptake of AuNPs demonstrated by the ^{197}Au spectrum (red). 20µm/sec scan speed. **(B)** LA-ICP-MSI of AuNP treated MG-63 spheroid. Pre-ablation optical image (20X objective) and elemental maps of ^{66}Zn, ^{25}Mg, ^{197}Au, and total beam. Scale bar represents 50µm.

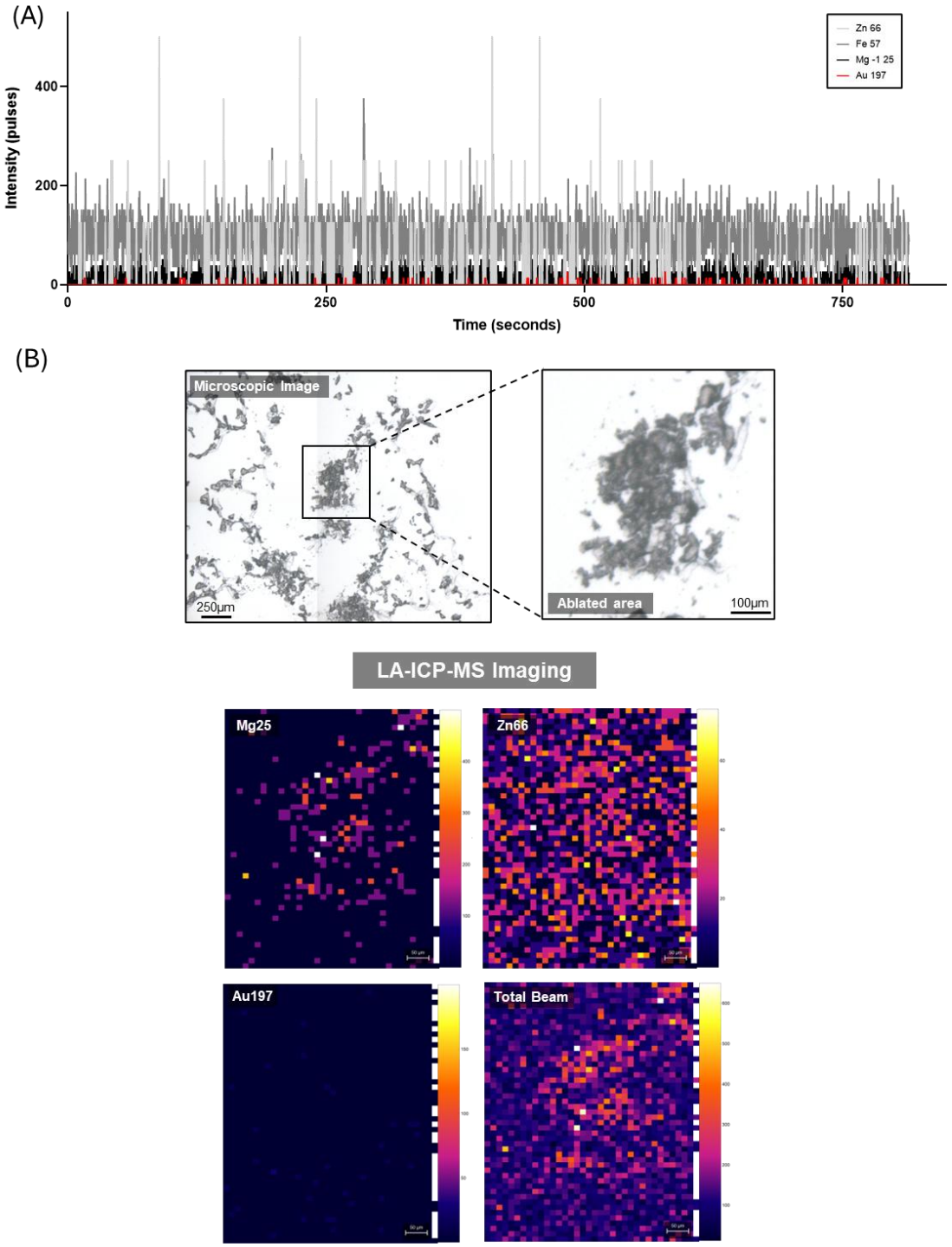

Figure XXII - LA-ICP-MSI analysis of untreated PC3 alginate sphere. (A) Intensity vs. time profile of ablated raster shows uptake of AuNPs demonstrated by the ^{197}Au spectrum (red). 20µm/sec scan speed. **(B)** LA-ICP-MSI of AuNP treated MG-63 spheroid. Pre-ablation optical image (20X objective) and elemental maps of ^{66}Zn, ^{25}Mg, ^{197}Au, and total beam. Scale bar represents 50µm.

Appendix B – LA-ICP-MSI analysis of spheroids treated with undecorated 50nm AuNPs.

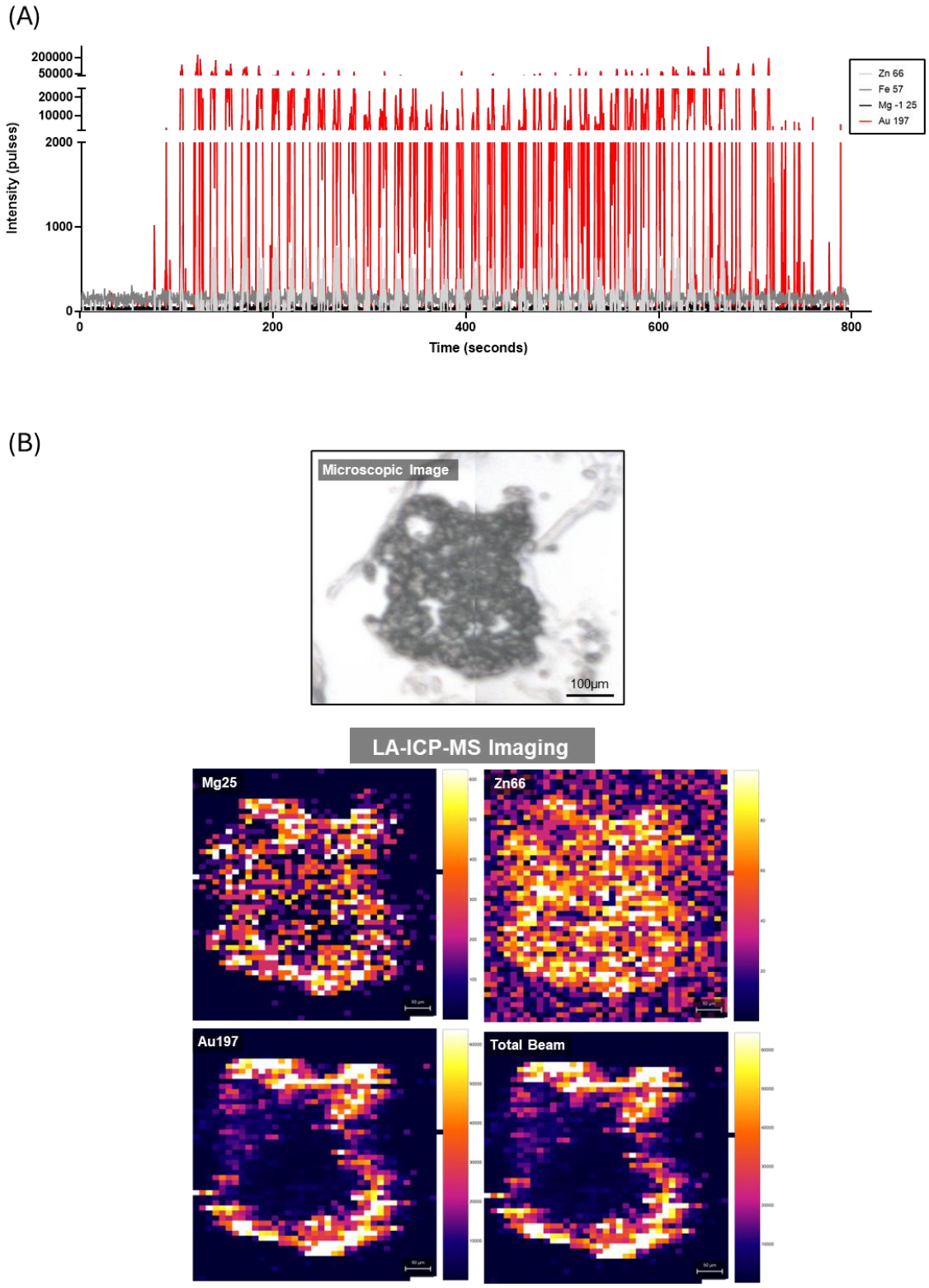

Figure XXIII - LA-ICP-MSI analysis of AuNP-treated Saos-2 spheroid. (A) Intensity vs. time profile of ablated raster shows uptake of AuNPs demonstrated by the ^{197}Au spectrum (red). 20µm/sec scan speed. **(B)** LA-ICP-MSI of AuNP treated MG-63 spheroid. Pre-ablation optical image (20X objective) and elemental maps of ^{66}Zn, ^{25}Mg, ^{197}Au, and total beam. Scale bar represents 50µm.

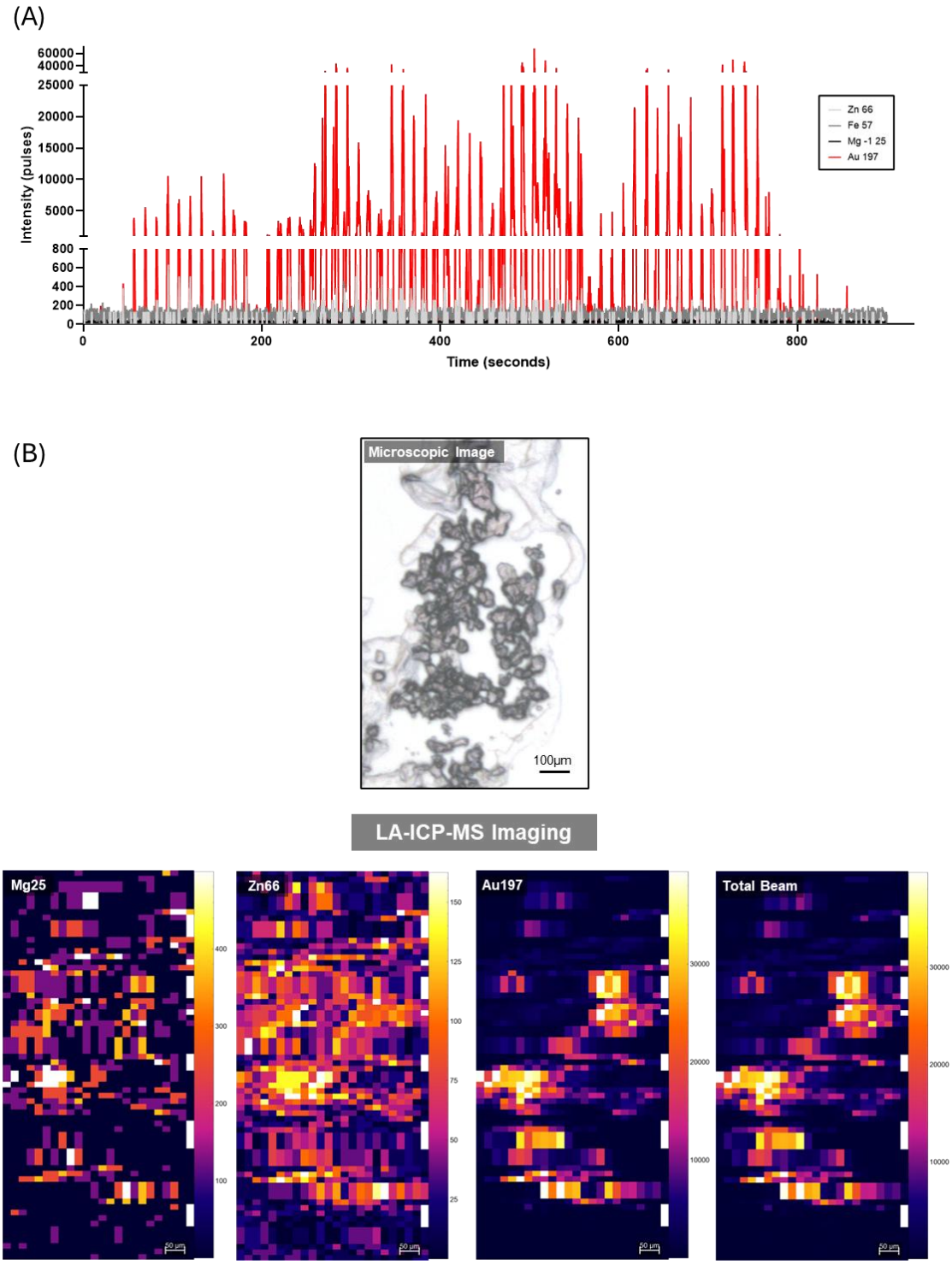

Figure XXIV - LA-ICP-MSI analysis of AuNP-treated PC3 spheroid. (A) Intensity vs. time profile of ablated raster shows uptake of AuNPs demonstrated by the ^{197}Au spectrum (red). 20µm/sec scan speed. **(B)** LA-ICP-MSI of AuNP treated MG-63 spheroid. Pre-ablation optical image (20X objective) and elemental maps of ^{66}Zn, ^{25}Mg, ^{197}Au, and total beam. Scale bar represents 50µm.

Appendix C – LA-ICP-MSI analysis of alginate spheres treated with undecorated 50nm AuNPs.

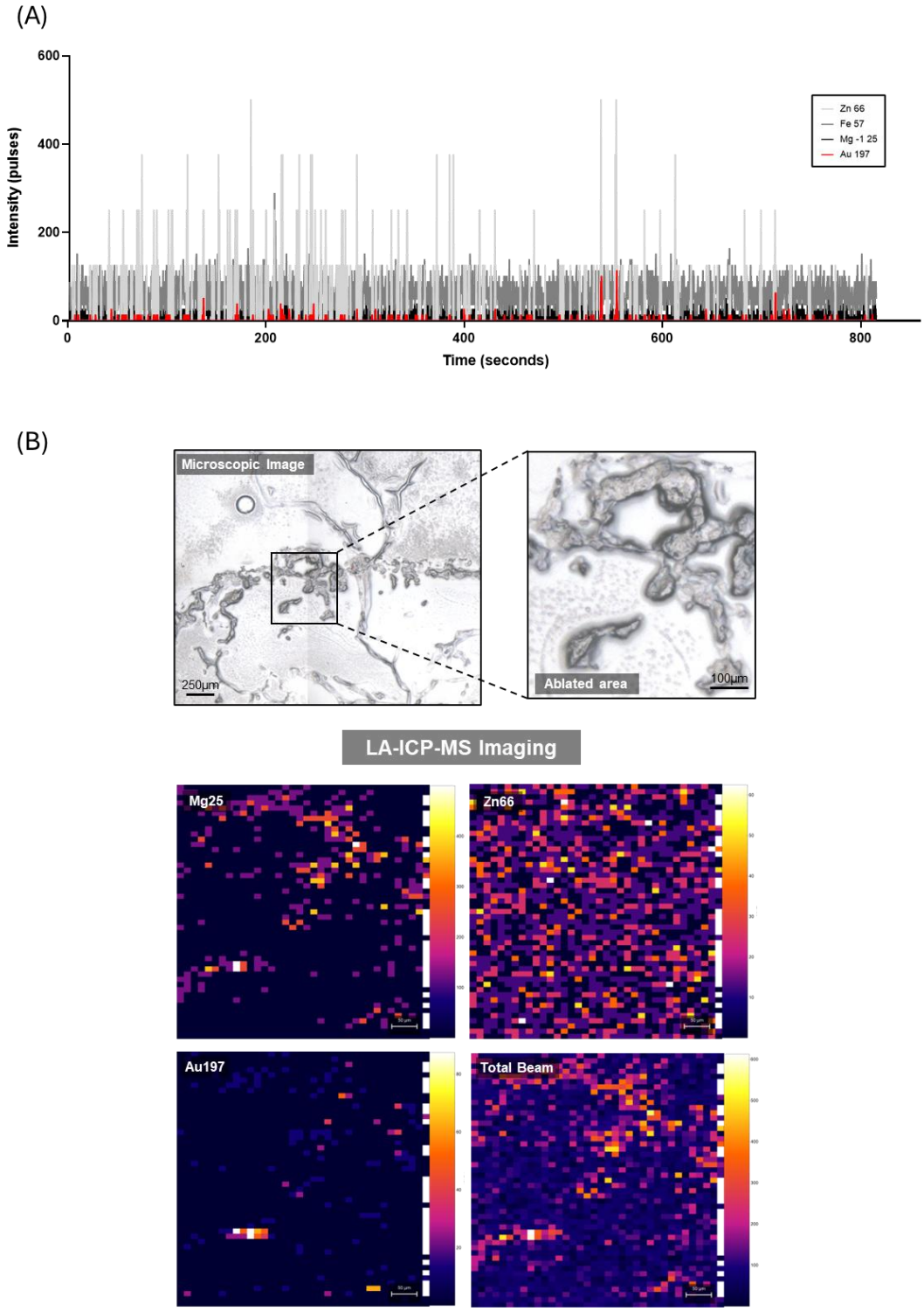

Figure XXV - LA-ICP-MSI analysis of AuNP-treated Saos-2 alginate sphere. **(A)** Intensity vs. time profile of ablated raster shows uptake of AuNPs demonstrated by the ^{197}Au spectrum (red). 20µm/sec scan speed. **(B)** LA-ICP-MSI of AuNP treated MG-63 spheroid. Pre-ablation optical image (20X objective)

and elemental maps of ^{66}Zn, ^{25}Mg, ^{197}Au, and total beam. Scale bar represents 50μm.

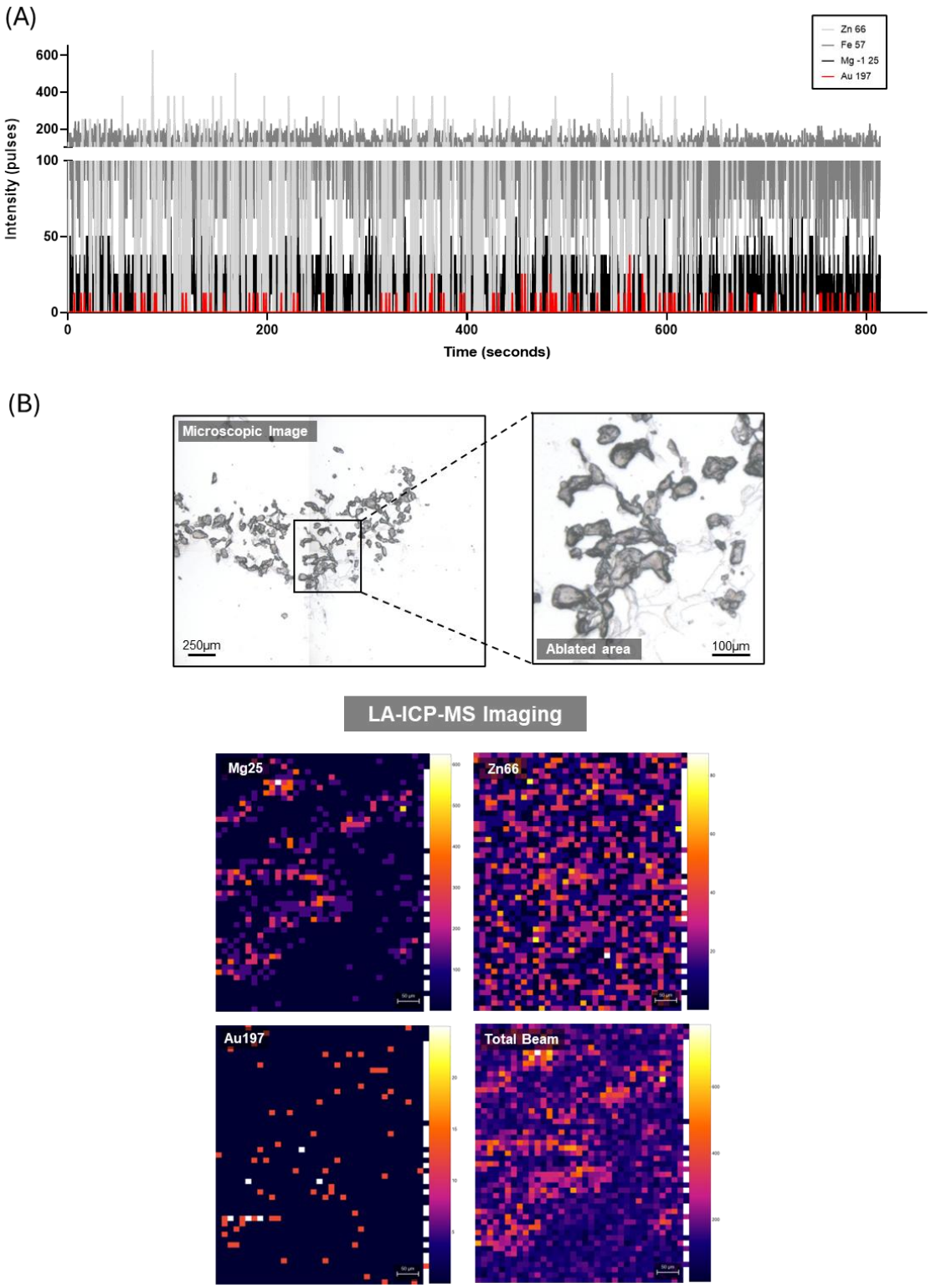

Figure XXVI - LA-ICP-MSI analysis of AuNP-treated PC3 alginate sphere. (A) Intensity vs. time profile of ablated raster shows uptake of AuNPs demonstrated by the ^{197}Au spectrum (red). 20µm/sec scan speed. **(B)** LA-ICP-MSI of AuNP treated MG-63 spheroid. Pre-ablation optical image (20X objective) and elemental maps of ^{66}Zn, ^{25}Mg, ^{197}Au, and total beam. Scale bar represents 50µm

Appendix D – Hyperspectral imaging of AuNP-treated cells

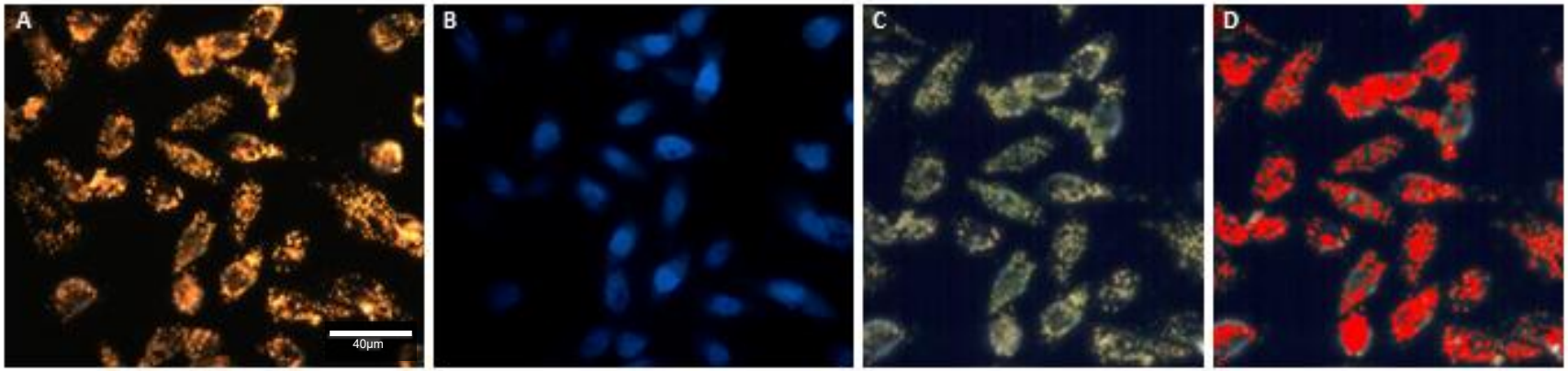

Figure XXVII- Darkfield, fluorescent and hyperspectral imaging of AuNP treated PC3 cells. Cells were treated with a 10 µg/mL solution of 50 nm AuNPs for 24h and imaged for gold detection and localization. 60X objective. **(A)** Enhanced darkfield image. AuNP in a brighter orange colour than cells (faded orange) due to higher light-scattering properties. **(B)** Fluorescent image. DAPI stained PC3 cells (blue). **(C)** Hyperspectral image. DAPI stained PC3 cells in blue and AuNPs in yellow. **(D)** Sample angle mapping. Gold detection (red) based on unique spectral signal (Envi 4.8 Software).

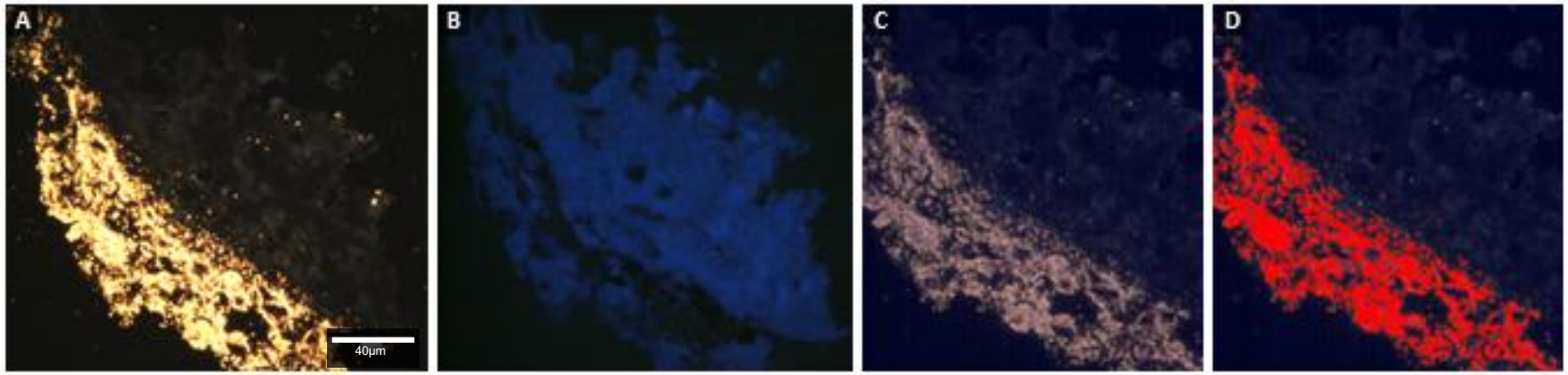

Figure XXVIII - Darkfield, fluorescent and hyperspectral imaging of AuNP treated MG-63 spheroids. MCTS were treated with a 10 µg/mL solution of 50 nm AuNPs for 24h and imaged for gold detection and localization. 60X objective. **(A)** Enhanced darkfield image. AuNP in bright orange. **(B)** Fluorescent image. DAPI stained MG-63 cells (blue**). (C)** Hyperspectral image. DAPI stained MG-63 cells in blue and AuNPs in pink. **(D)** Sample angle mapping. Gold detection (red) based on unique spectral signal (Envi 4.8 Software).

Appendix E – TEM imaging of AuNPs and AuNP-treated cells.

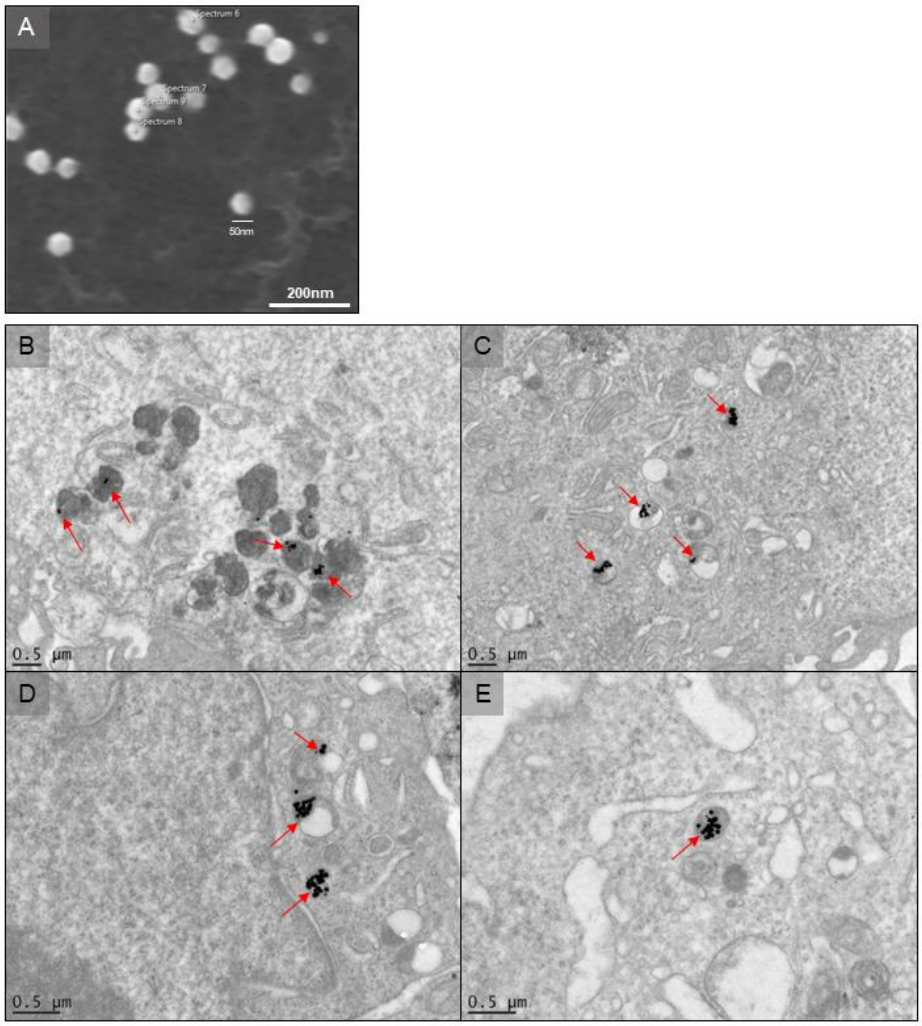

Figure XXIX - TEM studies of cell uptake of gold nanoparticles. (A) TEM image of 50nm diameter gold nanoparticles – MERI, Sheffield Hallam University. **(B-E)** Cell uptake of 50nm AuNP in intracellular vesicles (red arrows). FEI Tecnai TEM with Gatan digital camera – University of Sheffield. (B-C) 2900X objective (D-E) 4800X objective.

Appendix F - LA-ICP-MSI analysis of spheroids treated with NLS-functionalised 50nm AuNPs.

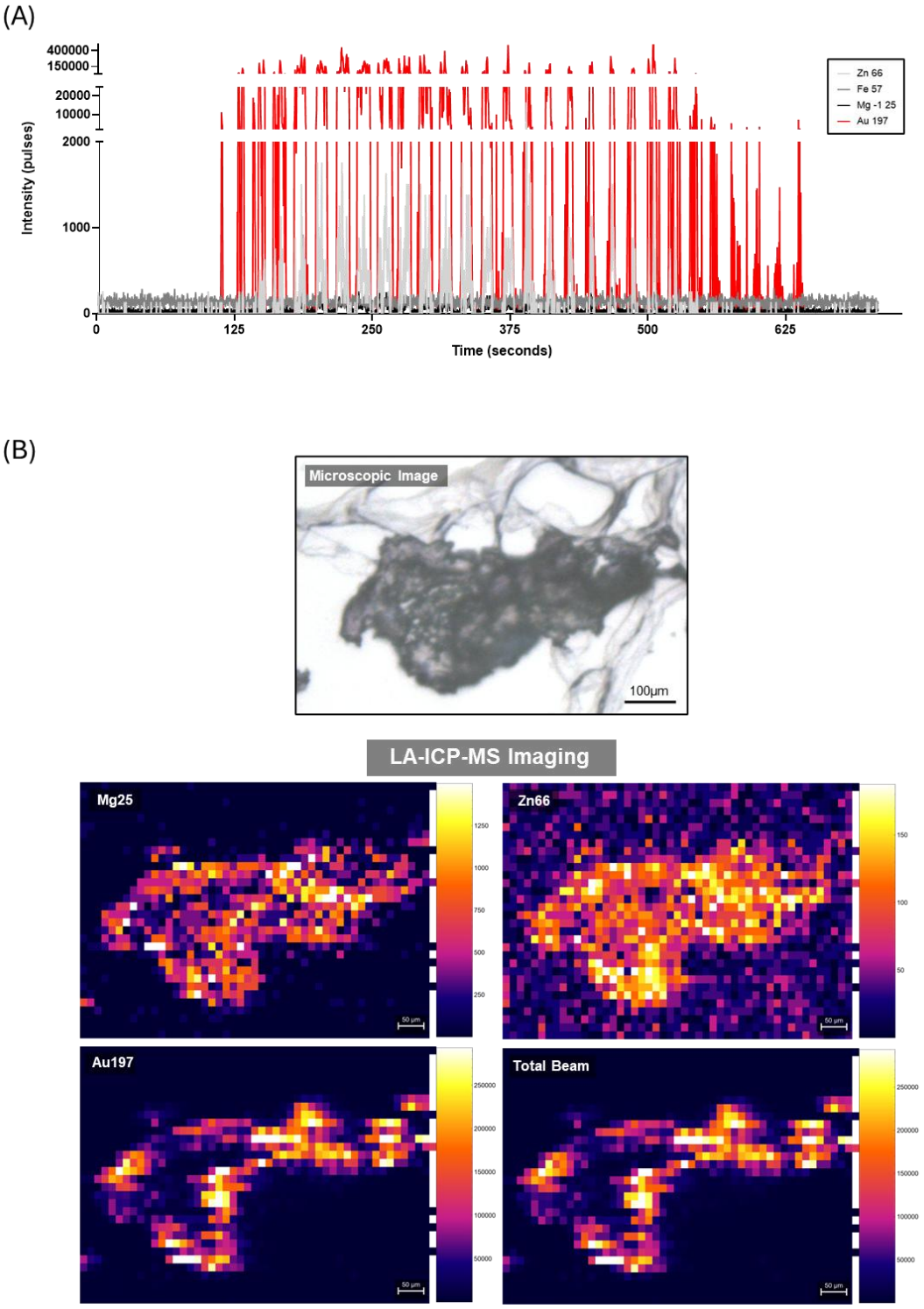

Figure XXX - LA-ICP-MSI analysis of NLS-AuNP-treated Saos-2 spheroid. (A) Intensity vs. time profile of ablated raster shows uptake of AuNPs demonstrated by the ^{197}Au spectrum (red). 20µm/sec scan speed. **(B)** LA-ICP-MSI of AuNP treated MG-63 spheroid. Pre-ablation optical image (20X objective) and elemental maps of ^{66}Zn, ^{25}Mg, ^{197}Au, and total beam. Scale bar represents 50µm.

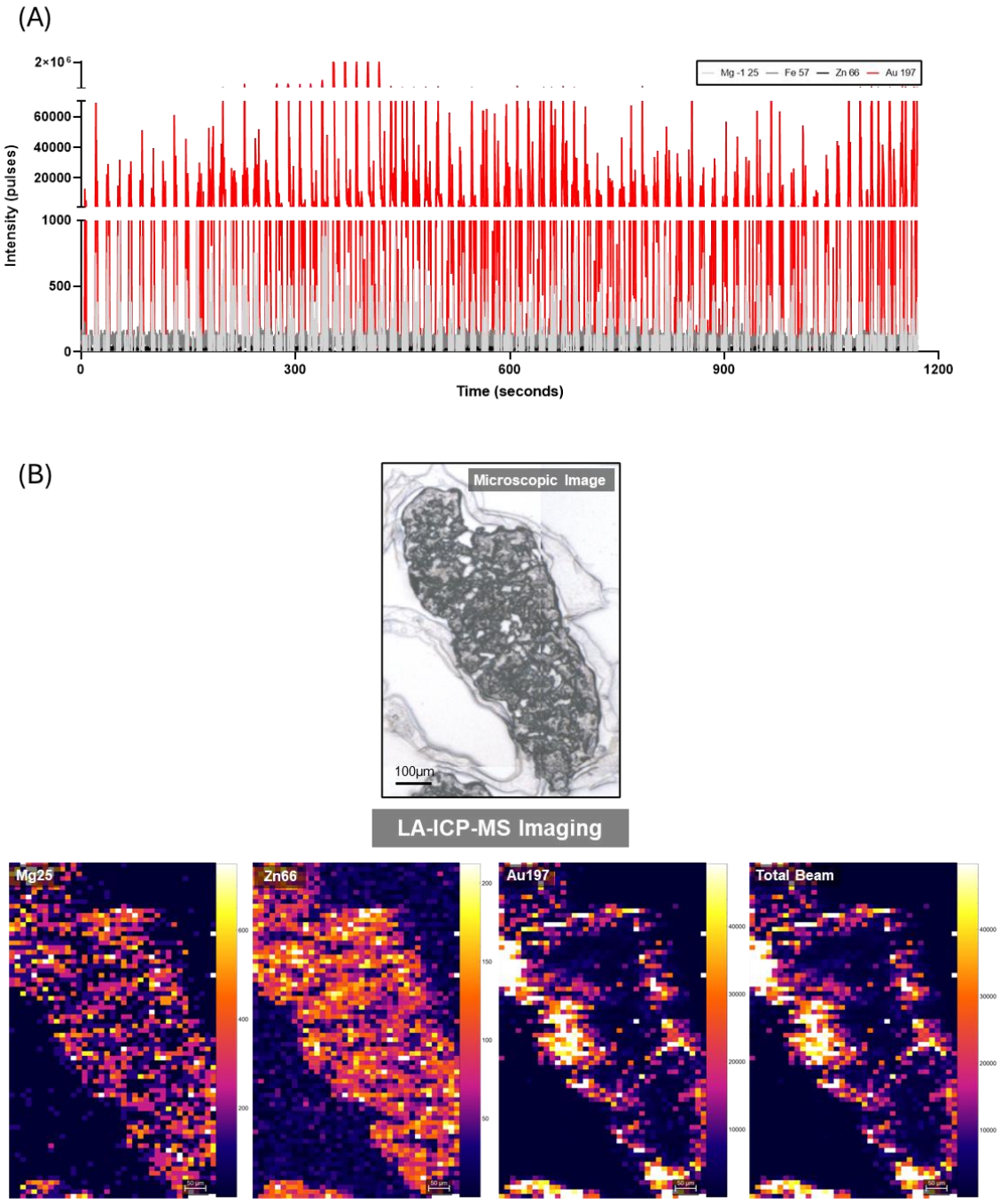

Figure XXXI - LA-ICP-MSI analysis of NLS-AuNP-treated LNCaP spheroid. (A) Intensity vs. time profile of ablated raster shows uptake of AuNPs demonstrated by the ^{197}Au spectrum (red). 20µm/sec scan speed. **(B)** LA-ICP-MSI of AuNP treated MG-63 spheroid. Pre-ablation optical image (20X objective) and elemental maps of ^{66}Zn, ^{25}Mg, ^{197}Au, and total beam. Scale bar represents 50µm.

Appendix G - LA-ICP-MSI analysis of alginate spheres treated with NLS-functionalised 50nm AuNPs.

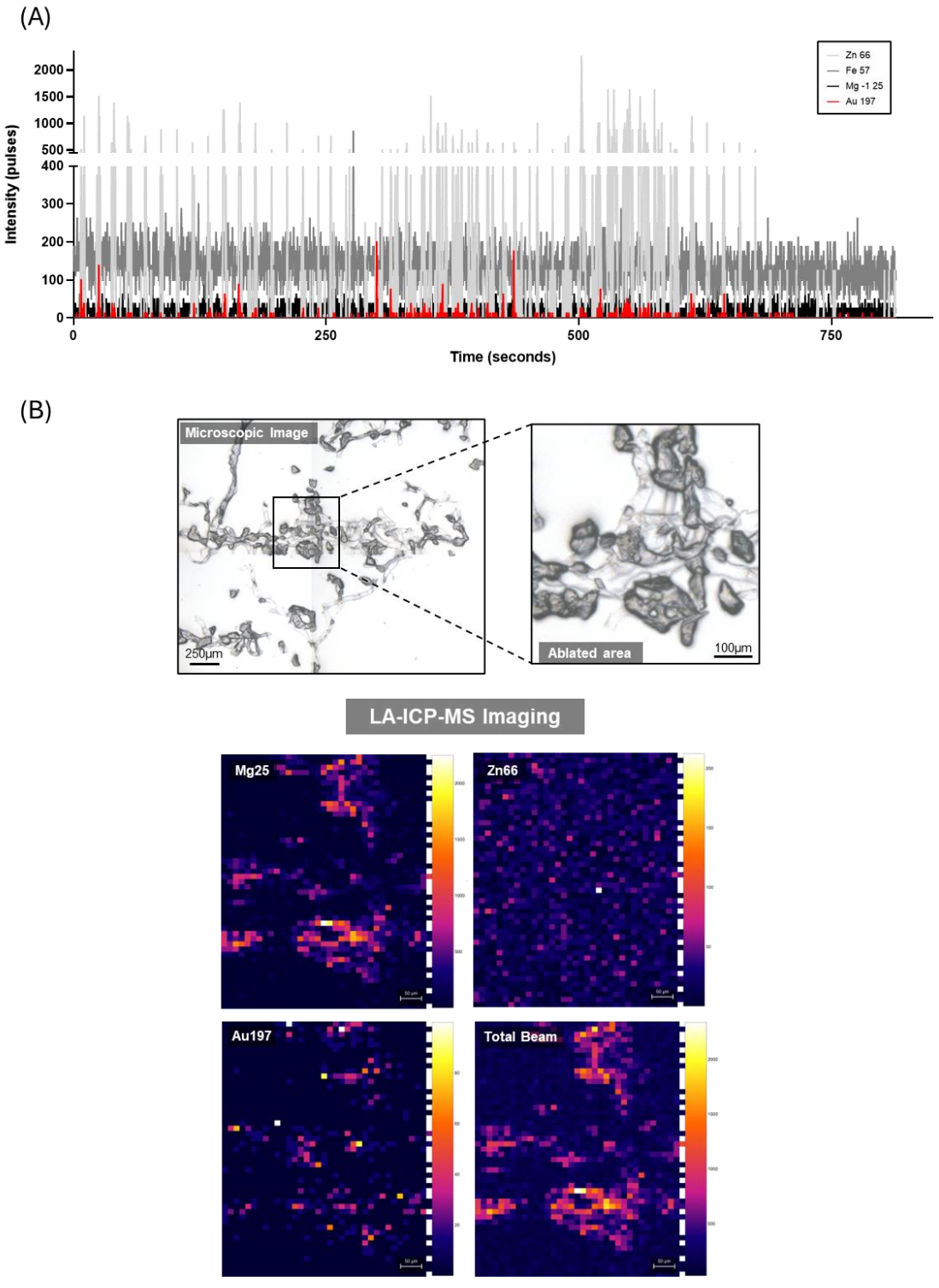

Figure XXXII - LA-ICP-MSI analysis of NLS-AuNP-treated Saos-2 alginate sphere. (A) Intensity vs. time profile of ablated raster shows uptake of AuNPs demonstrated by the ^{197}Au spectrum (red). 20µm/sec scan speed. **(B)** LA-ICP-MSI of AuNP treated MG-63 spheroid. Pre-ablation optical image (20X objective) and elemental maps of ^{66}Zn, ^{25}Mg, ^{197}Au, and total beam. Scale bar represents 50µm.

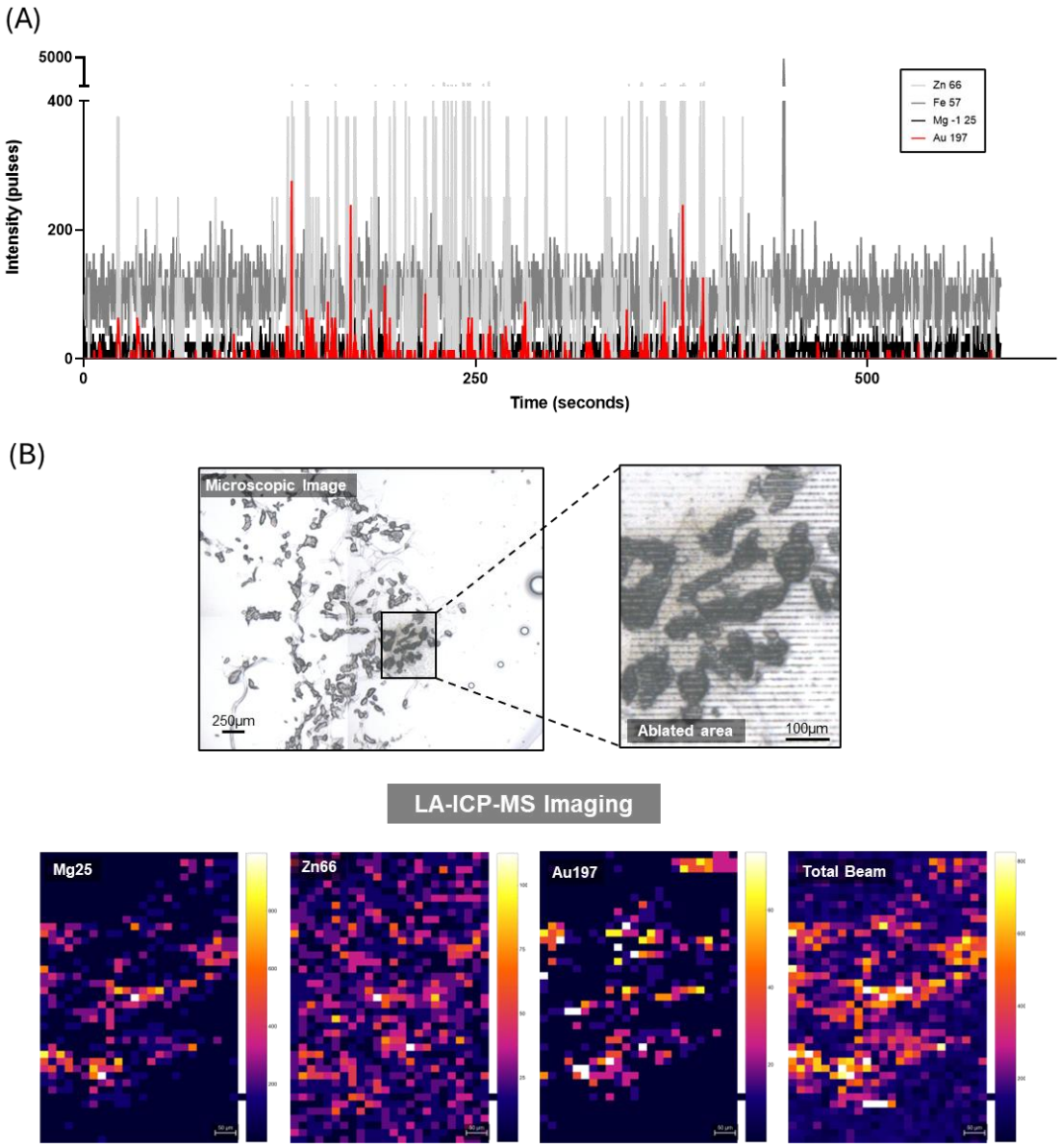

Figure XXXIII - LA-ICP-MSI analysis of NLS-AuNP-treated Saos-2 alginate sphere. (A) Intensity vs. time profile of ablated raster shows uptake of AuNPs demonstrated by the ^{197}Au spectrum (red). 20µm/sec scan speed. **(B)** LA-ICP-MSI of AuNP treated MG-63 spheroid. Pre-ablation optical image (20X objective) and elemental maps of ^{66}Zn, ^{25}Mg, ^{197}Au, and total beam. Scale bar represents 50µm.

Appendix H - TEM imaging of NLS-AuNPs and NLS-AuNP-treated cells.

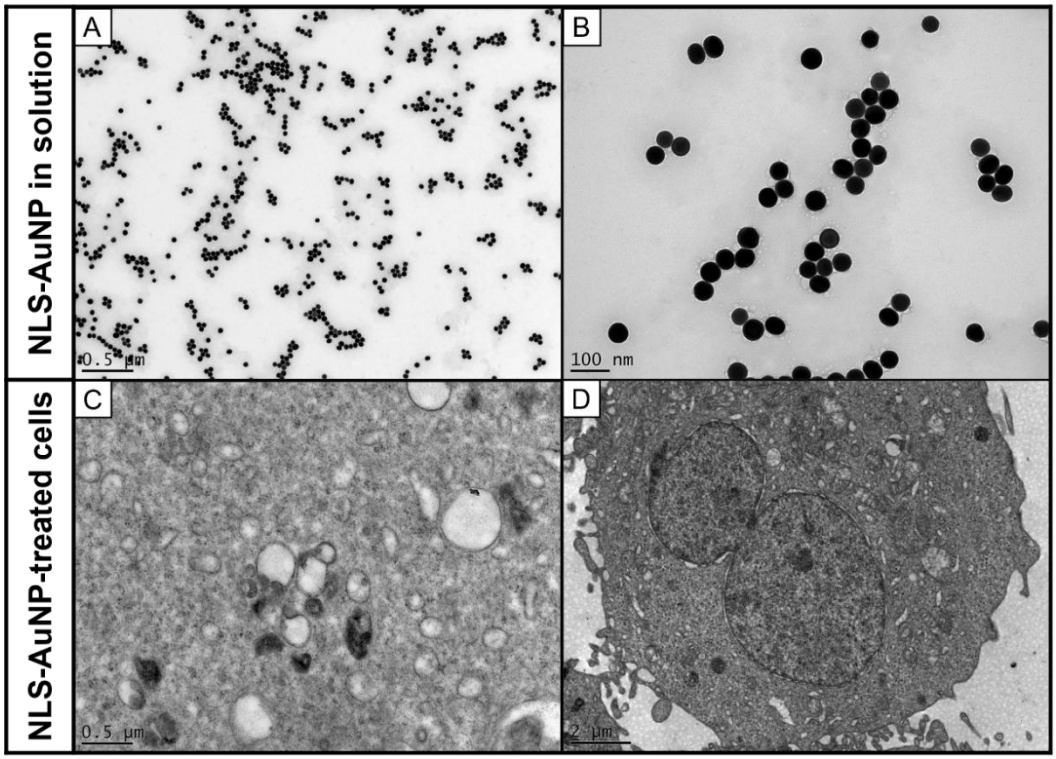

Figure XXXIV - TEM studies of cell uptake of NLS-tagged gold nanoparticles. (A-B) TEM image of 50nm NLS-AuNP in suspension with a 4800X objective (A) and a 18500X objective (B). **(C-D)** Cell images with 4800X (C) and 1400X objectives show unsuccessful cellular internalisation of NLS-AuNPs. FEI Tecnai TEM with Gatan digital camera – University of Sheffield.

Appendix I - LA-ICP-MSI analysis of spheroids treated with TPP-functionalised 5nm AuNPs.

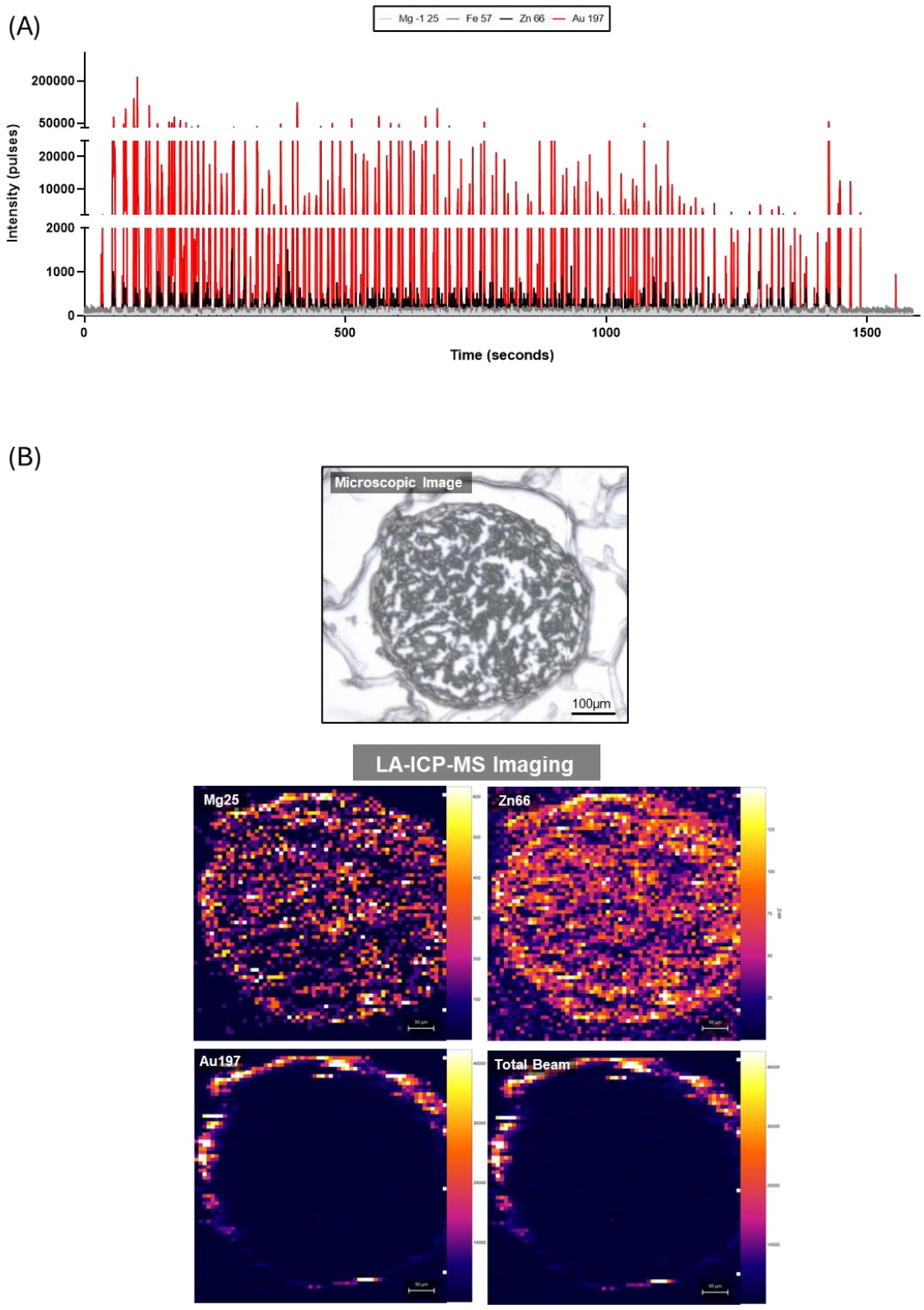

Figure XXXV - LA-ICP-MSI analysis of TPP-AuNP-treated MG-63 spheroid. (A) Intensity vs. time profile of ablated raster shows uptake of AuNPs demonstrated by the ^{197}Au spectrum (red). 20µm/sec scan speed. **(B)** LA-ICP-MSI of AuNP treated MG-63 spheroid. Pre-ablation optical image (20X objective) and elemental maps of ^{66}Zn, ^{25}Mg, ^{197}Au, and total beam. Scale bar represents 50µm.

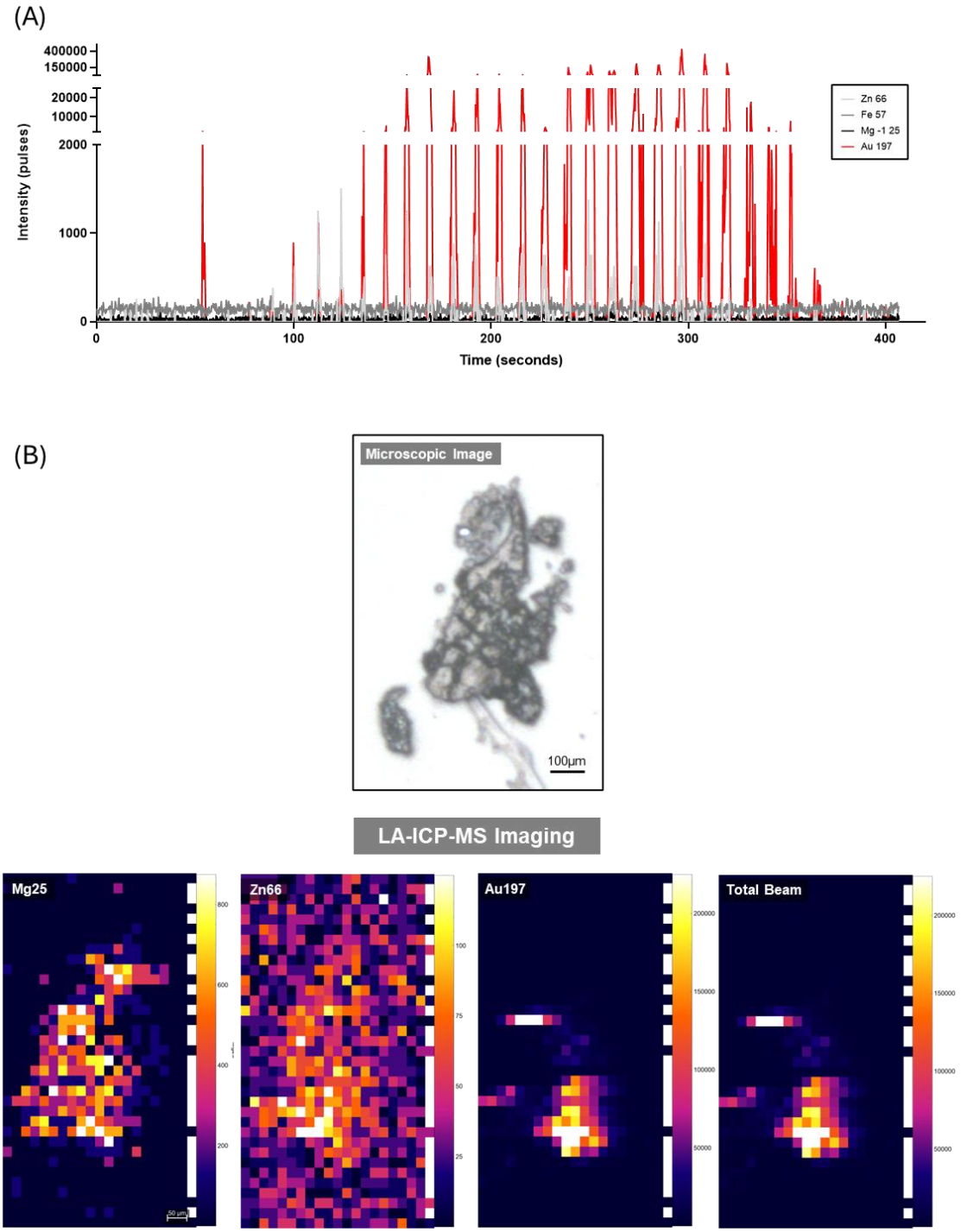

Figure XXXVI - LA-ICP-MSI analysis of TPP-AuNP-treated MG-63 spheroid. **(A)** Intensity vs. time profile of ablated raster shows uptake of AuNPs demonstrated by the ^{197}Au spectrum (red). 20µm/sec scan speed. **(B)** LA-ICP-MSI of AuNP treated MG-63 spheroid. Pre-ablation optical image (20X objective) and elemental maps of ^{66}Zn, ^{25}Mg, ^{197}Au, and total beam. Scale bar represents 50µm.

Appendix J - LA-ICP-MSI analysis of alginate spheres treated with TPP-functionalised 5nm AuNPs.

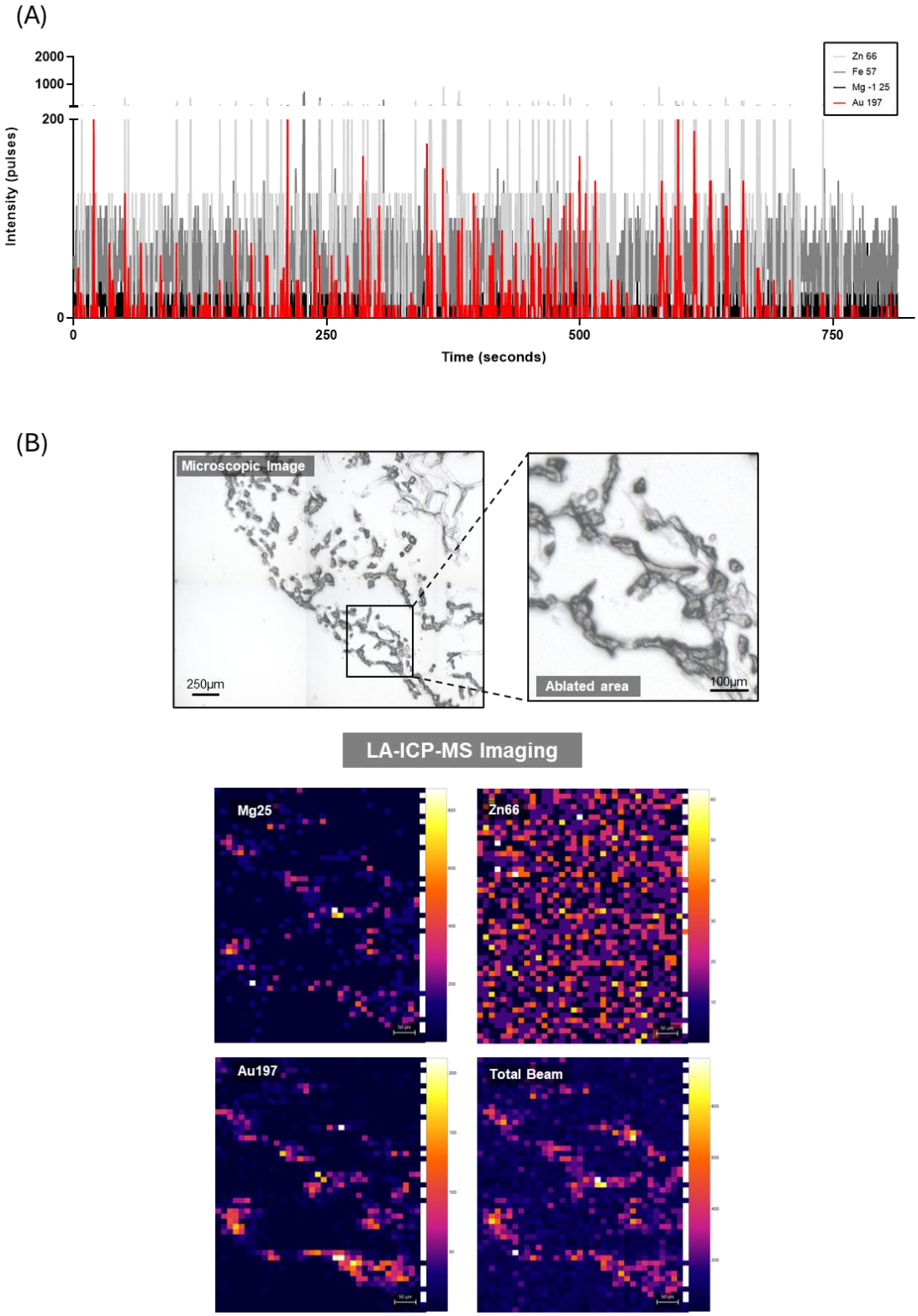

Figure XXXVII - LA-ICP-MSI analysis of TPP-AuNP-treated MG-63 alginate sphere. (A) Intensity vs. time profile of ablated raster shows uptake of AuNPs demonstrated by the ^{197}Au spectrum (red). 20µm/sec scan speed. **(B)** LA-ICP-MSI of AuNP treated MG-63 spheroid. Pre-ablation optical image (20X objective) and elemental maps of ^{66}Zn, ^{25}Mg, ^{197}Au, and total beam. Scale bar represents 50µm.

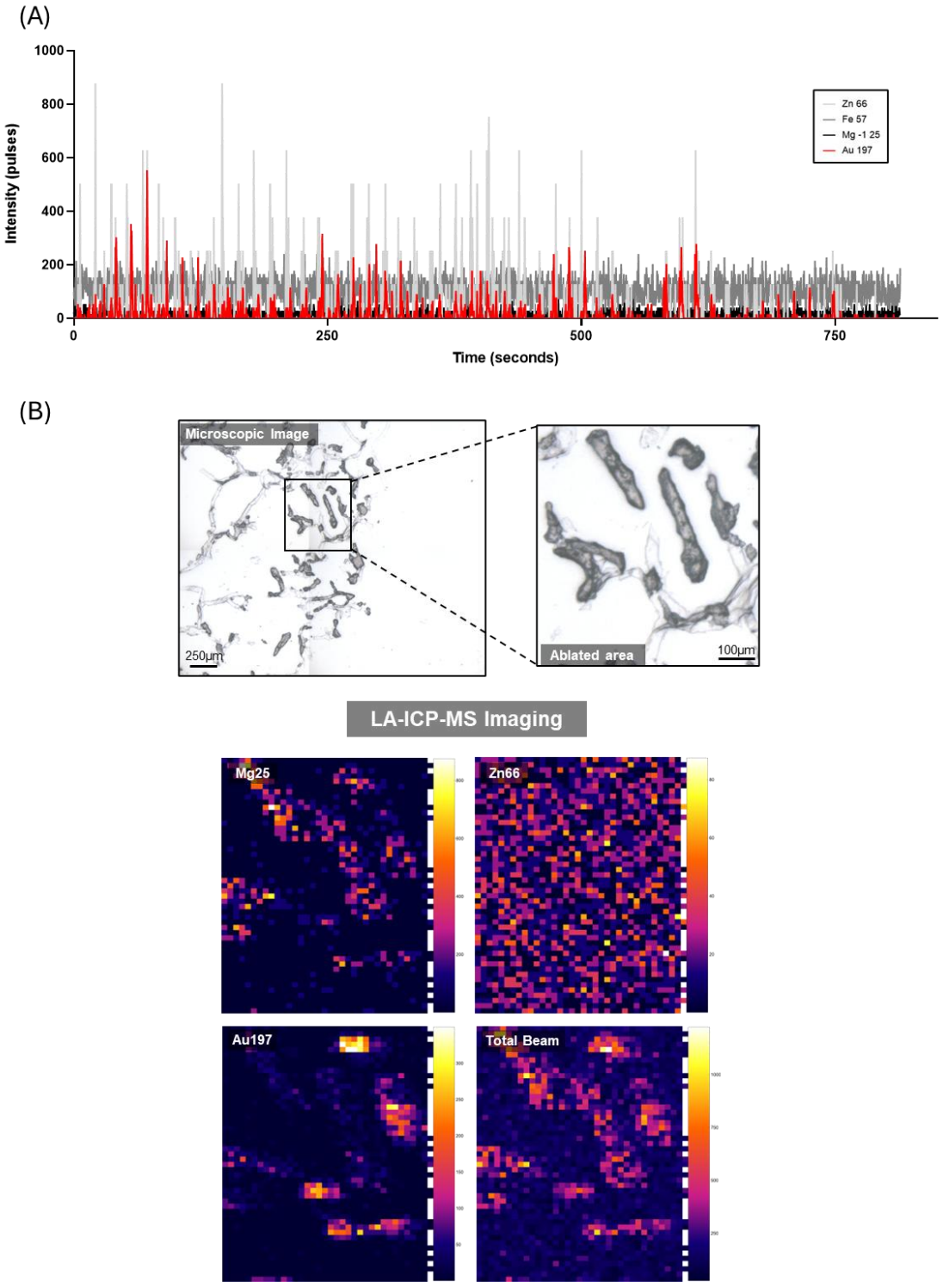

Figure XXXVIII - LA-ICP-MSI analysis of TPP-AuNP-treated Saos-2 alginate sphere. (A) Intensity vs. time profile of ablated raster shows uptake of AuNPs demonstrated by the ^{197}Au spectrum (red). 20µm/sec scan speed. **(B)** LA-ICP-MSI of AuNP treated MG-63 spheroid. Pre-ablation optical image (20X objective) and elemental maps of ^{66}Zn, ^{25}Mg, ^{197}Au, and total beam. Scale bar represents 50µm.

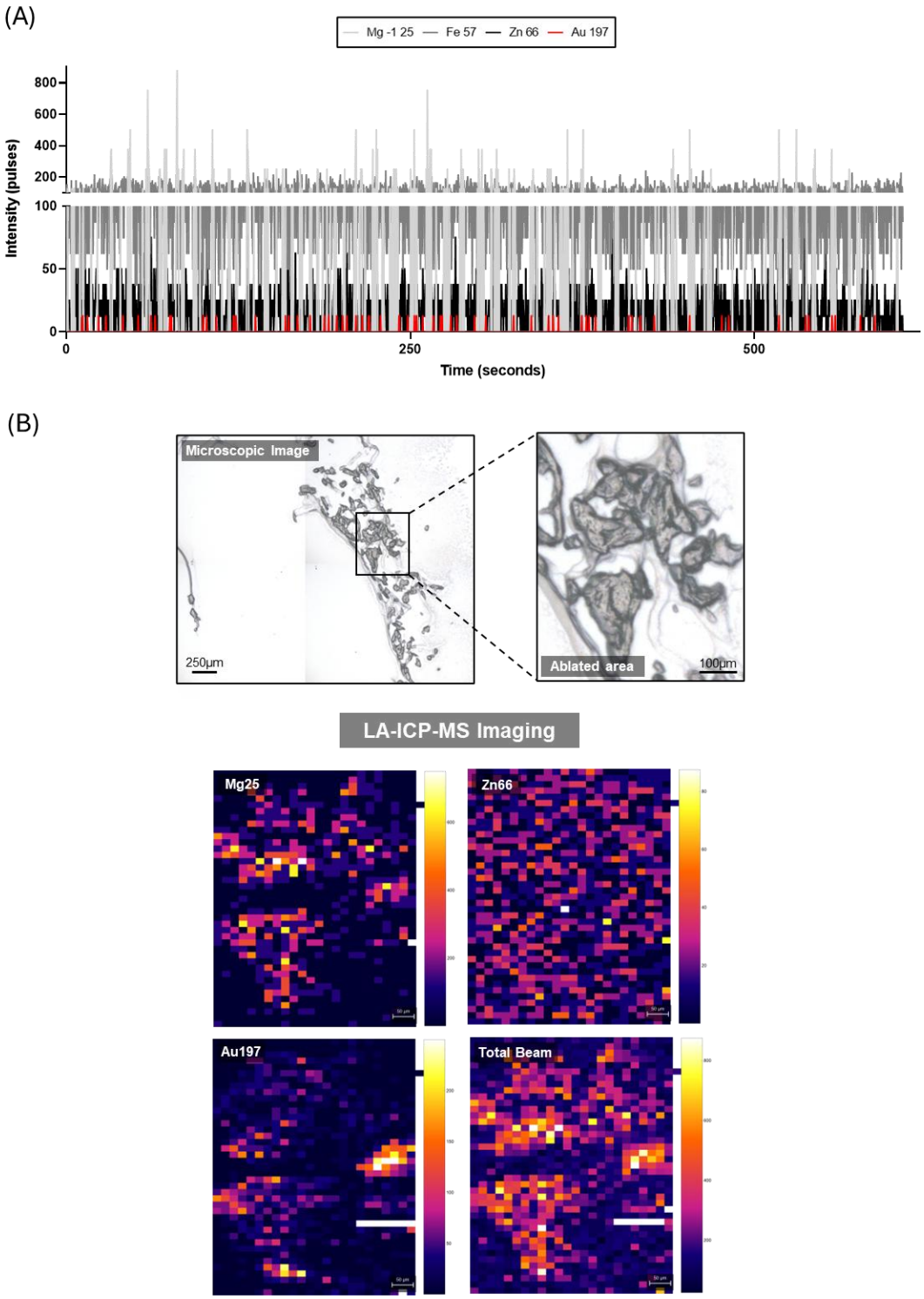

Figure XXXIX - LA-ICP-MSI analysis of TPP-AuNP-treated PC3 alginate sphere. (A) Intensity vs. time profile of ablated raster shows uptake of AuNPs demonstrated by the ^{197}Au spectrum (red). 20µm/sec scan speed. **(B)** LA-ICP-MSI of AuNP treated MG-63 spheroid. Pre-ablation optical image (20X objective) and elemental maps of ^{66}Zn, ^{25}Mg, ^{197}Au, and total beam. Scale bar represents 50µm.

Appendix K – Toxicity of AuNP, NLS-AuNP, and TPP-AuNP treatment.

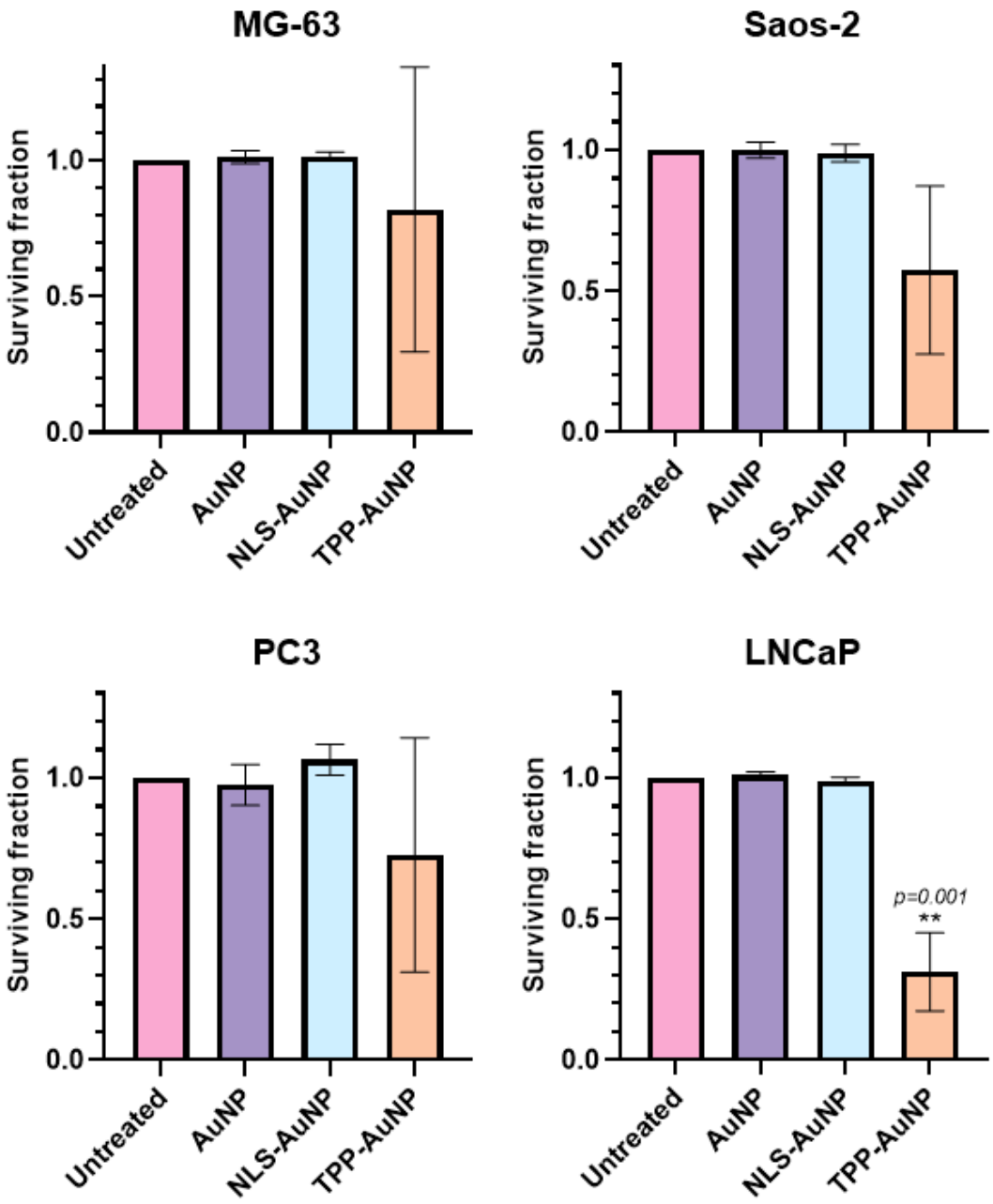

Figure XL – Surviving fraction of AuNP, NLS-AuNP, and TPP-AuNP treated osteosarcoma and prostate adenocarcinoma cell lines in the absence of radiation exposure 10 days post-plating. Unfunctionalised and NLS-tagged gold nanoparticles do not produce cytotoxic effects. Toxicity of TPP-AuNP significant in LNCaP cells. Interleaved bars, multiple *t-tests*. Statistical significance corrected using the Holm-Sidak method of multiple comparisons, with alpha=0.05. (*P<0.05). All data is presented as median ±range and individual values represent n=3 independent experiments with 3 technical repeats.

Appendix L - TEM imaging of TPP-AuNPs and TPP-AuNP-treated cells.

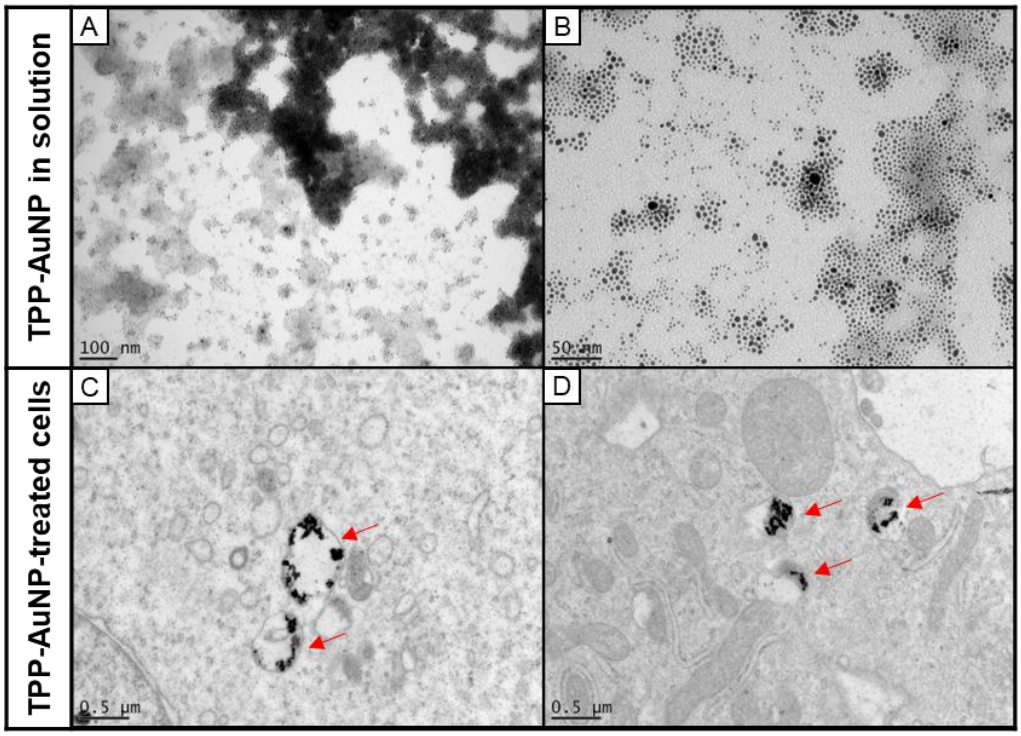

Figure XLI - TEM studies of cell uptake of TPP-tagged gold nanoparticles. (A-B) TEM image of 5nm TPP-AuNP in suspension with a 4800X objective (A) and a 18500X objective (B). **(C-D)** Cell images with 4800X objectives show successful cellular internalisation of TPP-AuNPs into small vesicles. FEI Tecnai TEM with Gatan digital camera – University of Sheffield.